frontiers | Research Topics

Understanding geomaterial instability: physics and mechanics of landslides and seismic events

Edited by
Yifei Sun, Sanjay Shrawan Nimbalkar, Huiming Tan,
Shao-Heng He, Zhijun Liu and Jiancheng Zhang

Published in
Frontiers in Physics
Frontiers in Earth Science

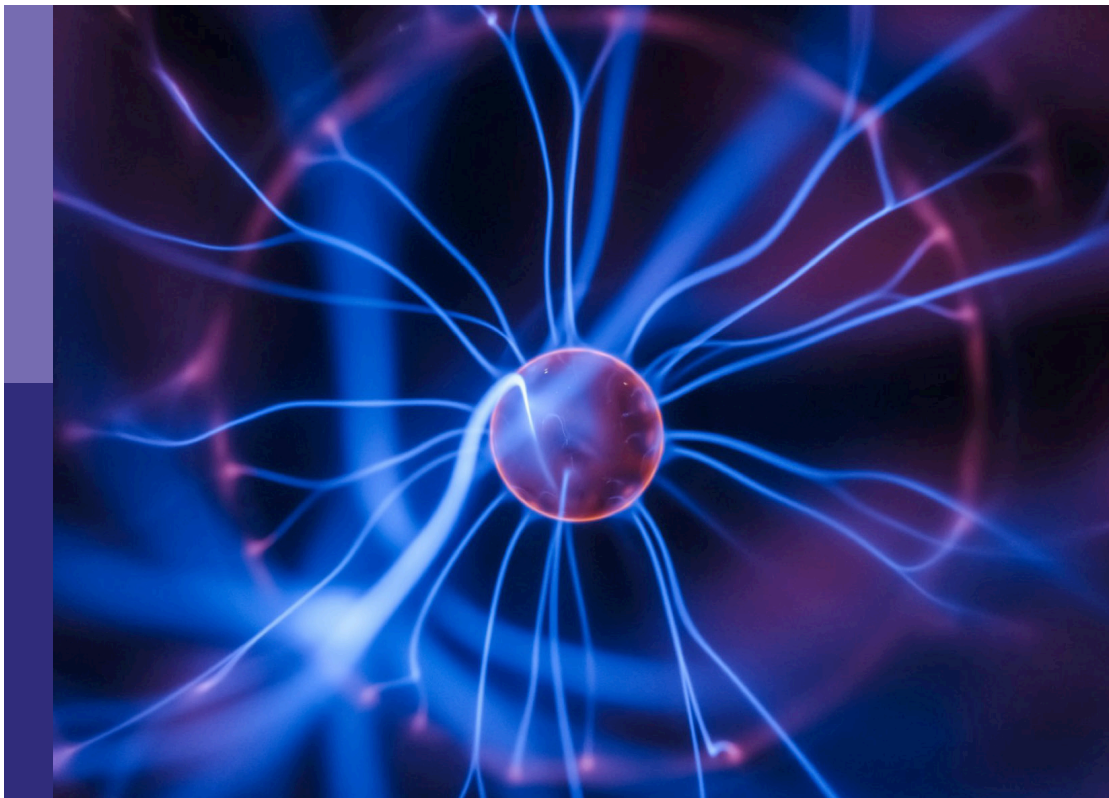

ISSN 1664-8714
ISBN 978-2-8325-6934-4
DOI 10.3389/978-2-8325-6934-4

Generative AI statement
Any alternative text (Alt text) provided alongside figures in the articles in this ebook has been generated by Frontiers with the support of artificial intelligence and reasonable efforts have been made to ensure accuracy, including review by the authors wherever possible. If you identify any issues, please contact us.

About Frontiers

Frontiers is more than just an open access publisher of scholarly articles: it is a pioneering approach to the world of academia, radically improving the way scholarly research is managed. The grand vision of Frontiers is a world where all people have an equal opportunity to seek, share and generate knowledge. Frontiers provides immediate and permanent online open access to all its publications, but this alone is not enough to realize our grand goals.

Frontiers journal series

The Frontiers journal series is a multi-tier and interdisciplinary set of open-access, online journals, promising a paradigm shift from the current review, selection and dissemination processes in academic publishing. All Frontiers journals are driven by researchers for researchers; therefore, they constitute a service to the scholarly community. At the same time, the *Frontiers journal series* operates on a revolutionary invention, the tiered publishing system, initially addressing specific communities of scholars, and gradually climbing up to broader public understanding, thus serving the interests of the lay society, too.

Dedication to quality

Each Frontiers article is a landmark of the highest quality, thanks to genuinely collaborative interactions between authors and review editors, who include some of the world's best academicians. Research must be certified by peers before entering a stream of knowledge that may eventually reach the public - and shape society; therefore, Frontiers only applies the most rigorous and unbiased reviews. Frontiers revolutionizes research publishing by freely delivering the most outstanding research, evaluated with no bias from both the academic and social point of view. By applying the most advanced information technologies, Frontiers is catapulting scholarly publishing into a new generation.

What are Frontiers Research Topics?

Frontiers Research Topics are very popular trademarks of the *Frontiers journals series*: they are collections of at least ten articles, all centered on a particular subject. With their unique mix of varied contributions from Original Research to Review Articles, Frontiers Research Topics unify the most influential researchers, the latest key findings and historical advances in a hot research area.

Find out more on how to host your own Frontiers Research Topic or contribute to one as an author by contacting the Frontiers editorial office: frontiersin.org/about/contact

Understanding geomaterial instability: physics and mechanics of landslides and seismic events

Topic editors

Yifei Sun — Taiyuan University of Technology, China
Sanjay Shrawan Nimbalkar — University of Technology Sydney, Australia
Huiming Tan — Hohai University, China
Shao-Heng He — Zhejiang University, China
Zhijun Liu — CCCC Fourth Harbor Engineering Institute Co., Ltd, China
Jiancheng Zhang — Jiangsu University of Science and Technology, China

Citation

Sun, Y., Nimbalkar, S. S., Tan, H., He, S.-H., Liu, Z., Zhang, J., eds. (2025). *Understanding geomaterial instability: physics and mechanics of landslides and seismic events*. Lausanne: Frontiers Media SA. doi: 10.3389/978-2-8325-6934-4

Table of contents

frontiers | Frontiers in Physics

TYPE Editorial
PUBLISHED 23 September 2025
DOI 10.3389/fphy.2025.1696671

OPEN ACCESS

EDITED AND REVIEWED BY
Alex Hansen,
NTNU, Norway

*CORRESPONDENCE
Yifei Sun,
yifei.sun@hhu.edu.cn

RECEIVED 01 September 2025
ACCEPTED 05 September 2025
PUBLISHED 23 September 2025

CITATION
Sun Y, Nimbalkar S, Tan H, He S-H, Liu Z and Zhang J (2025) Editorial: Understanding geomaterial instability: physics and mechanics of landslides and seismic events. *Front. Phys.* 13:1696671.
doi: 10.3389/fphy.2025.1696671

Editorial: Understanding geomaterial instability: physics and mechanics of landslides and seismic events

Yifei Sun[1]*, Sanjay Nimbalkar[2], Huiming Tan[3], Shao-Heng He[4], Zhijun Liu[5] and Jiancheng Zhang[6]

[1]College of Civile Engineering, Taiyuan University of Technology, Taiyuan, China, [2]School of Civil and Environmental Engineering, University of Technology Sydney (UTS), Sydney, NSW, Australia, [3]College of Harbour, Coastal and Offshore Engineering, Hohai University, Nanjing, China, [4]Department of Civil Engineering, Zhejiang University City College, Hangzhou, China, [5]CCCC Fourth Harbor Engineering Institute Co., Ltd., Guangzhou, China, [6]School of Naval Architecture and Civil Engineering, Jiangsu University of Science and Technology, Zhangjiagang, China

KEYWORDS

geomaterial, landslide, seismic event, numerical simulation, soil-improvement

Editorial on the Research Topic
Understanding geomaterial instability: physics and mechanics of landslides and seismic events

Geomaterial instability, manifesting as catastrophic events like landslides and seismic activities, induces profound socioeconomic disruptions through the destruction of critical infrastructure and loss of human life. Understanding the underlying physics and mechanics of these failure processes is therefore essential for advancing predictive capabilities and developing effective risk mitigation strategies in vulnerable regions.

Previous studies have substantially advanced the understanding of geomaterial instability across multiple fronts. Notably, Hu Wei's team [1] identified a metastable state preceding seismic shear failure, uncovering mechanisms of co-seismic weakening and post-seismic healing that refined the classical Newmark sliding-block model [2, 3]. Research under extreme thermo-hydro-mechanical-chemical (THMC) coupled conditions has improved predictions of deformation and failure in deep geological environments, directly supporting the safety assessment of energy reservoirs and subsurface storage projects [4, 5]. Meanwhile, satellite-based InSAR monitoring has been operationalized for large-scale slope stability assessment, providing millimeter-resolution deformation data essential for regional early warning systems [6, 7]. Further contributions include innovative slope stabilization methods using lightweight geofoam [8] and models quantifying freeze-thaw damage in cold regions [9], forming a multifaceted foundation for hazard mitigation. Nevertheless, further research is essential to advance the fundamental understanding of the mechanisms governing geomaterial instability under multi-physical coupling conditions.

This Research Topic seeks to advance our understanding of the fundamental physics and mechanics underlying geomaterial instability, with the goal of clarifying its implications for geohazard mitigation and its significance within broader physical research. The Research Topic currently features 16 papers spanning the fields of geology, physics, mechanics, and

engineering, reflecting the key emerging themes and interdisciplinary nature of research in geomaterial instability.

The dynamic responses of foundations and slopes were examined. It was found by Tao and Gao through numerical simulation that the displacements of suction-bucket foundations in saturated sand peak synchronously with peak ground acceleration, and that liquefaction leads to marked settlement and loss of bearing capacity. Likewise, it was shown by Wang and Wen via shaking-table tests that rocky slopes subjected to seismic loading undergo a three-stage failure sequence characterized by crack opening, sliding, and shear failure. Chen et al. demonstrated by limit-equilibrium analysis that non-uniform geosynthetic (anchor) pullout strength reduces the seismic stability margin of slopes, suggesting that the common assumption of uniform strength may overestimate seismic performance.

Several papers investigated novel soil-improvement techniques. For instance, Yan et al. reported that expansive soil stabilized with industrial by-products (CKD+CCS) at a 10% CKD + 9% CCS ratio exhibits substantially increased strength and suppressed swelling. Additionally, an electrochemical stabilization method combining a movable anode with $CaCl_2$ injection was proposed by Han et al. Sang et al. showed that the addition of a low-concentration PVA solution together with plant fibers to sandy soils markedly enhances strength and ductility; and Tao and Gao found that increasing polymer content in polyurethane-reinforced granular materials reduces porosity and permeability, for which a pore-constriction model was advanced to explain the observed effect.

Advances in reinforced structures and embankment systems were also reported. Hu et al. introduced a non-foamed polyurethane-bonded gravel pile material that, relative to ordinary gravel, exhibits higher strength and stiffness while retaining high permeability, making it suitable for rapid construction. Zhao and Zheng found from field data that a well-compacted geogrid-reinforced soil platform beneath pile-supported embankments can significantly reduce lateral displacement of the embankment, with geogrid stiffness and interface friction identified as key controlling factors.

Moreover, seismic-wave propagation and crustal imaging were addressed. Qiu and Zhang developed a model for the reflection and transmission of obliquely incident P-waves at an elastic–saturated-porous interface, and showed that incidence angle, frequency and related parameters substantially influence wave propagation. Hu et al. applied double-difference tomography in the Huoshan region and found that mid-strong earthquake epicenters coincide with gradients in seismic velocity and Poisson's ratio. Huang et al. used Rayleigh-wave tomography to reveal fault-geometry-controlled differential subsidence and noted that the previously active Sankeshu pull-apart basin is approaching dormancy.

Several studies developed predictive models for fracture and failure processes in geomaterials. Lei et al., using an elastic wellbore model, showed that drilling-induced fractures can evolve into "J"-shaped cracks, providing a basis for their identification; Deng et al. proposed a nonlinear Mohr–Coulomb criterion to describe unloading-induced failure in frozen weakly cemented sandstone; Gu et al. observed that pervasive micro-fissures in deep columnar-jointed basalts lead to rapid post-unloading relaxation and reductions in acoustic velocity; and Liu et al., employing SPH simulations of high-pressure jet grouting, found that tensile failure predominates in the soil under jet action.

We sincerely thank all contributing authors, the anonymous reviewers for their rigorous evaluations, and the editorial staff for their invaluable efforts. It is hoped that this Research Topic will inform and inspire future research and engineering practice in advancing the analysis of geomaterial instability.

Author contributions

YS: Writing – original draft, Investigation, Conceptualization. SN: Writing – review and editing. HT: Writing – review and editing. SH: Writing – review and editing. ZL: Writing – review and editing. JZ: Writing – review and editing.

Funding

The author(s) declare that no financial support was received for the research and/or publication of this article.

Conflict of interest

Author ZL was employed by CCCC Fourth Harbor Engineering Institute Co., Ltd.

The remaining authors declare that the research was conducted in the absence of any commercial or financial relationships that could be construed as a potential conflict of interest.

Generative AI statement

The author(s) declare that no Generative AI was used in the creation of this manuscript.

Any alternative text (alt text) provided alongside figures in this article has been generated by Frontiers with the support of artificial intelligence and reasonable efforts have been made to ensure accuracy, including review by the authors wherever possible. If you identify any issues, please contact us.

Publisher's note

References

1. Li Y, Hu W, Xu Q, Luo H, Chang C, Jia X. Metastable state preceding shear zone instability: implications for earthquake-accelerated landslides and dynamic triggering. *Proc Natl Acad Sci U S A* (2024) 122:e2417840121. doi:10.1073/pnas.2417840121

2. Chen S, Miao ZL, Wu LX. A method for seismic landslide hazard assessment using simplified Newmark displacement model based on modified strength parameters of rock mass. *Acta Seismol Sin* (2022) 44:512–27. doi:10.11939/jass.20210008

3. Newmark NM. Effects of earthquakes on dams and embankments. *Géotechnique* (1965) 15:139–60. doi:10.1680/GEOT.1965.15.2.139

4. Kim K-I, Lee C, Cho D, Rutqvist J. Enhancement of disposal efficiency for deep geological repositories based on three design factors – Decay heat optimization, increased thermal limit of the buffer and double-layer concept. *Tunnelling Under. Space Technol.* (2024) 153:106017. doi:10.1016/j.tust.2024.106017

5. Sasaki T, Yoon S, Rutqvist J. Modelling of failure and fracture development of the Callovo-Oxfordian claystone during an *in-situ* heating experiment associated with geological disposal of high-level radioactive waste. *Geomechanics Energy Environ* (2024) 38:100546. doi:10.1016/j.gete.2024.100546

6. Dun J, He J, Lombardo L, Chang L, Feng W, Tanyas H. Forecasting InSAR-derived slope movement from climate records at Baihetan reservoir. *Eng Geol* (2025) 356:108302. doi:10.1016/j.enggeo.2025.108302

7. He J, Tanyas H, Dahal A, Huang D, Lombardo L. Spatial prediction of InSAR-derived hillslope velocities via deep learning. *Bull Eng Geol Environ* (2025) 84:131. doi:10.1007/s10064-025-04161-x

8. Özer AT, Akay O, Fox GA, Bartlett SF, Arellano D. A new method for remediation of sandy slopes susceptible to seepage flow using EPS-block geofoam. *Geotext Geomembr* (2014) 42:166–80. doi:10.1016/j.geotexmem.2014.01.003

9. Ren L, Zhao L-Y, Niu F-J. A physically-based elastoplastic damage model for quasi-brittle geomaterials under freeze-thaw cycles and loading. *Appl Math Model* (2022) 106:276–98. doi:10.1016/j.apm.2022.02.006

frontiers | Frontiers in Physics

TYPE Original Research
PUBLISHED 13 September 2024
DOI 10.3389/fphy.2024.1458844

OPEN ACCESS

EDITED BY
Huiming Tan,
Hohai University, China

REVIEWED BY
Yifei Sun,
Hohai University, China
Zhouchuan Huang,
Nanjing Normal University, China
Yunpeng Zhang,
China Earthquake Administration, China

*CORRESPONDENCE
Xiaoping Fan,
nj_fxp@njtech.edu.cn
Wei Fu,
fuwei@njtech.edu.cn

RECEIVED 03 July 2024
ACCEPTED 27 August 2024
PUBLISHED 13 September 2024

CITATION
Huang Q, Fan X, Fu W, Zhang P, Zheng T, Liu Y, Zhang T, Ren S, Wang Q, Liu Z and Qian T (2024) Shallow crustal structure detection of the upper crust at Anqiu-Juxian Fault in the Tanlu fault zone.
Front. Phys. 12:1458844.
doi: 10.3389/fphy.2024.1458844

Shallow crustal structure detection of the upper crust at Anqiu-Juxian Fault in the Tanlu fault zone

Qilong Huang[1], Xiaoping Fan[1]*, Wei Fu[1]*, Peng Zhang[1], Tuo Zheng[1], Yunze Liu[1], Tiantian Zhang[1], Shiyu Ren[1], Qinghui Wang[1], Zhiwen Liu[1] and Ting Qian[2]

[1]College of Transportation Engineering, Nanjing Tech University, Nanjing, China, [2]Earthquake Administration of Jiangsu Province, Nanjing, China

Within the Tan-Lu Fault Zone, the largest active tectonic belt in eastern China, the Anqiu-Juxian Fault exhibits the most recent activity period, evident surface traces, and highest seismic hazard, making it a Holocene active fault. This study utilized the vertical component continuous data observed by 100 short-period temporary stations from August 1–21, 2023, and extracted 1,944 Rayleigh wave group velocity dispersion curves within the period of 0.2–4 s. Using the direct surface wave tomography method, we calculated a high-resolution 3-D shear-wave velocity structure at depths of 0.2–1.25 km within the study area. Our results are summarized as follows: 1) The development of faults F_1, F_2, and F_5 in the Tan-Lu Fault Zone highly correlated with the shear-wave velocity anomalies at depths >0.8 km. Specifically, fault F_5 comprised two boundary faults, $F_{5\text{-}1}$ and $F_{5\text{-}2}$, which together controlled a Cenozoic depression covered by a thick, low-velocity sediment layer. 2) The complex velocity structure characteristics in the Suqian area revealed that the influence of faults on the sedimentary layers in the Suqian area was not expressed as an overall uplift or subsidence of the block but rather as differential subsidence. 3) Near Sankeshu, the F_5 fault formed a small pull-apart basin. The latest activity in this pull-apart basin has shifted to the fault in the center of the basin, indicating that the pull-apart basin has entered the extinction stage.

KEYWORDS

Tanlu fault zone, Anqiu-Juxian fault, ambient noise tomography, shallow crustal structure, shear-wave velocity

1 Introduction

The Tan-Lu Fault Zone is the largest active fault zone in eastern China, extending from Luobei in Heilongjiang Province in the north to Guangji in Hubei Province in the south, spanning a length of up to 2,400 km, being an important tectonic boundary. It traverses the eastern part of mainland China, influencing crustal development, tectonic evolution, and seismic activity [1, 2]. Numerous destructive earthquakes have been recorded along the Tan-Lu Fault Zone, such as the Tancheng M8.5 earthquake on 25 July 1668, the Bohai Sea M7.5 earthquake on 13 June 1888, and the Haicheng M7.3 earthquake on 24 February 1975. Based on the tectonic activity characteristics, the Tan-Lu Fault Zone can be divided into four segments from north to south (Figure 1A) 1) the Hegang-Tieling segment, 2) the XiaLiaohe-

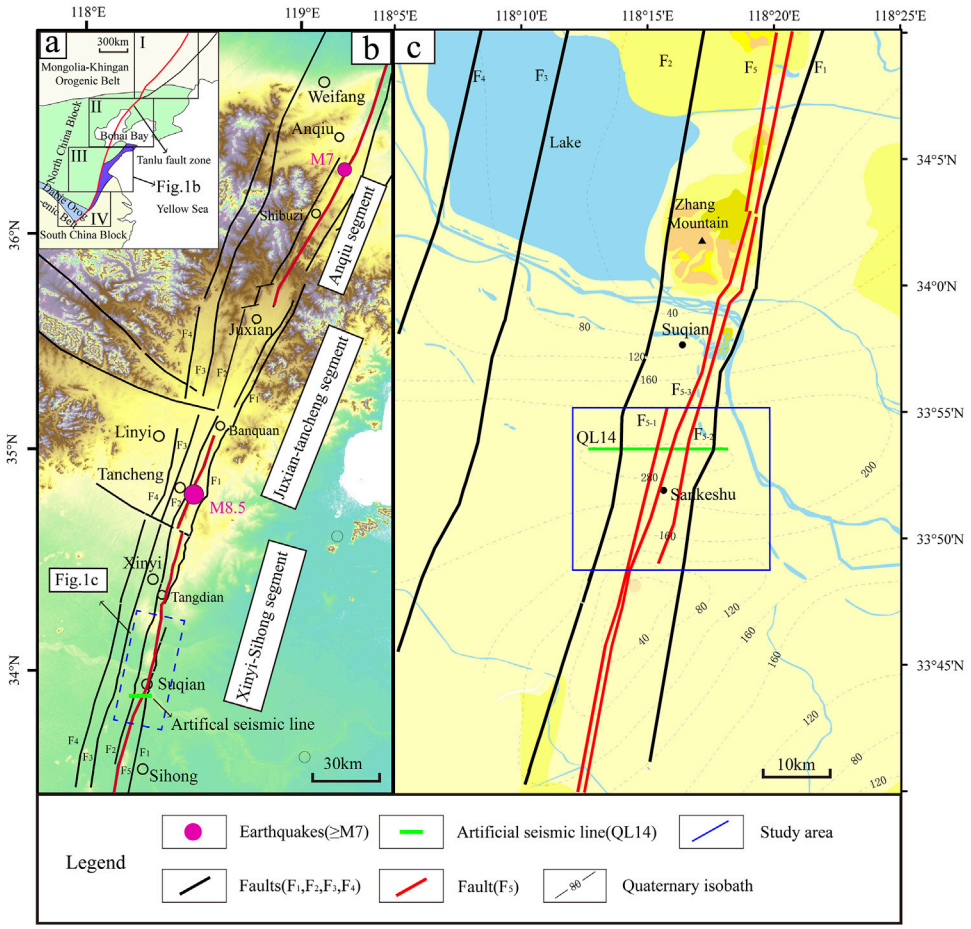

FIGURE 1
(A) Topographic map. **(B)** Fault distribution map of the Weifang–Jiashan segment of the Tanlu fault zone. F_1: Shanzuokou-Sihong Fault; F_2: Xinyi-Xindian Fault; F_3: Mohe-Lingcheng Fault; F_4: Jiji-Wangji Fault; F_5: Anqiu-Juxian Fault. **(C)** Tectonic distribution of the Suqian segment of Anqiu-Juxian Fault. The blue box indicates our study area. (Adapted from Zhang et al. (2023)) [3].

LaizhouWan segment, 3) the Weifang-Jiashan segment, and 4) the Jiashan-Guangji segment. Among these segments, the Weifang-Jiashan segment is recognized as the most tectonically active [4, 5] and consists of the following five major faults, from east to west: the Shanzuokou-Sihong Fault (F_1), the Anqiu-Juxian Fault (F_5), the Xinyi-Xindian Fault (F_2), the Mohe-Lingcheng Fault (F_3), and–the Wangji Fault (F_4). Among these faults, fault F_5 is the most recently active Holocene fault among the Weifang-Jiashan segment of the Tan-Lu Fault Zone, exhibiting the most evident surface traces and the highest seismic hazard (Figure 1B) [3, 6].

The Anqiu M7 earthquake in 70 BCE (before common era) and the Tancheng M8.5 earthquake in 1668 were both associated with fault F_5 [4, 7]. The Jiangsu segment of fault F_5 is located between fault F_1 and fault F_2. Based on the spatial distribution and activity period, fault F_5 consists of three segments in a north-south direction: the Anqiu, Juxian-Tancheng, and Xinyi-Sihong segments (Figure 1B) [8, 9]. The late Quaternary activity characteristics of fault F_5 indicate that a major paleoseismic event has occurred since the Holocene [10, 11]. Several fault profiles were found from Nanmaling Mountain to Chonggang Mountain, these profiles suggest significant Holocene activity along the Jiangsu segment of fault F_5, with the most recent activity primarily characterized by thrusting movement, with a maximum displacement of 1 m. Overall, the Quaternary activity of fault F_5 was characterized by dextral strike-slip combined with thrusting movement, whereas localized regions were characterized by strike-slip with normal faulting. Since the late Pleistocene, fault F_5 has experienced multiple activities, showed significant activity during the Holocene, with seismic activity characterized by high intensity and low frequency [12].

Owing to its complex crustal structure and intense tectonic activity, numerous studies have been conducted on fault F_5 by previous researchers. For instance, Xu et al. (2016) performed a shallow seismic exploration of fault F_5 to determine its precise localization and development characteristics [13]. However, their study was limited to providing evidence of the existence, exact position, and recent activities of fault F_5 in Suqian area without further investigation. Cao et al. (2015) have reported major findings in the precise fault localization and activity research of the Suqian segment of fault F_5 through shallow seismic exploration and drilling combined profiling [14]. However, the limited coverage of shallow seismic profiles limits our understanding of continuity and variations in large horizontal strata. Meng et al. (2019) utilized ambient noise tomography to obtain a 3-D S-wave (shear-wave) velocity model for the central-southern section of the Tan-Lu Fault

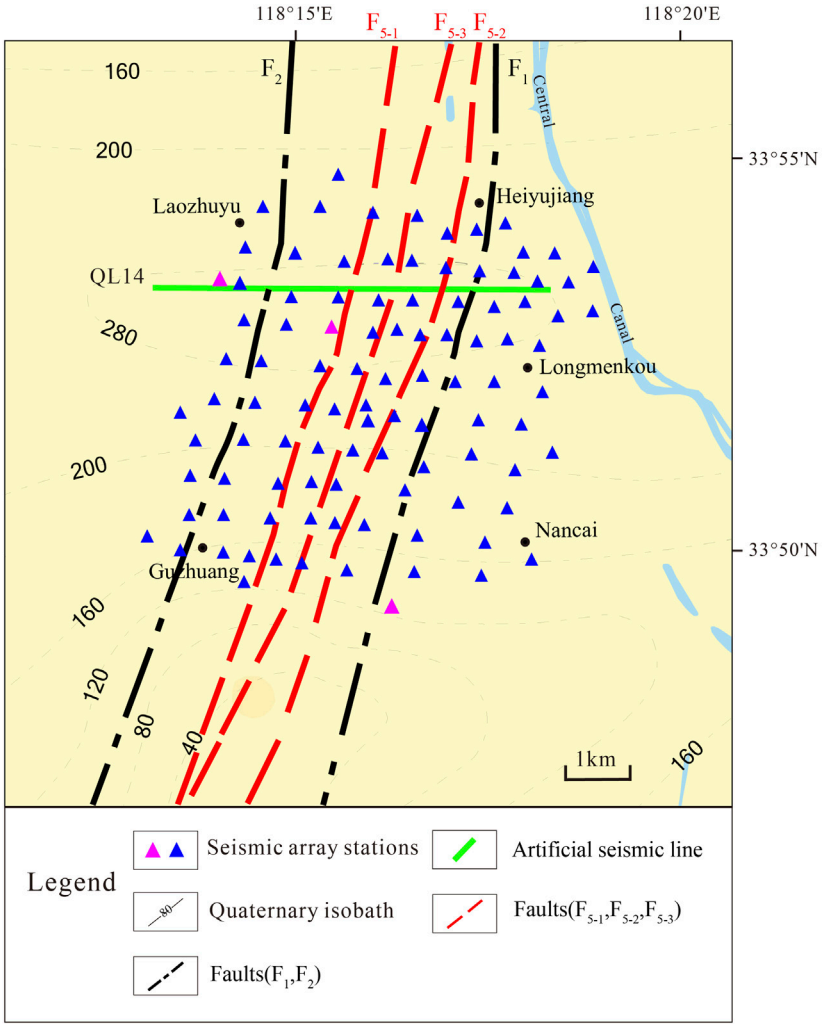

FIGURE 2
Station distribution in the Suqian area. The blue triangles represent the stations, the pink triangles represent stations G002, G008 and G048; the green line represents the artificial seismic line QL14 (Figure 11).

Zone [15]. Although the imaging results included our study area, the resolution of the shallow structures was low. Qin et al. (2020) obtained the shallow primary-wave velocity structure of the Tan-Lu Fault Zone using a first-break wave imaging method [16]; however, their study depth was primarily within 0.8 km, and there is a lack of research in deeper regions. Therefore, high-resolution 3-D S-wave velocity structures for the shallow part of the Suqian segment of fault F_5 remain warranted. Consequently, ambient noise tomography was used to investigate the shallow crustal structure of the Suqian segment of fault F_5 (Figure 1C).

This ambient noise tomography was first implemented in California, United States, in 2005 [17] and has since been widely accepted and extensively applied by seismologists. Using dispersion data within medium- or long-period ranges can invert the upper mantle and crustal velocity structure to investigate geodynamic processes underlying plate motion, earthquake nucleation, and magma transfer [18–21]. Utilizing dispersion data within short-period ranges can be inverted for high-resolution shear-wave velocity structures near the surface or in shallow parts of the crust, detection of hidden faults, geological disaster assessment, and 3D geological modeling [22–26].

This study used ambient noise data from a short-period dense array deployed in the Suqian segment of fault F_5. Our study area ranges from 118.2°E to 118.325°E and 33.815°N to 33.92°N (Figure 1C). We inverted the shallow S-wave velocity structure of the area by applying direct surface wave tomography [19]. By combining the velocity model with the regional tectonic background, we clarified the shallow crustal structure of the Suqian segment of fault F_5 and its influence on the sedimentary layers of the Suqian area. Our study findings will facilitate future studies on the extension characteristics of the Suqian segment of fault F_5 and aid in assessing seismic hazards.

2 Methods

In this study, we deployed 100 SmartSolo digital seismic stations with a main frequency of 5 Hz across fault F_5. The sampling rate was

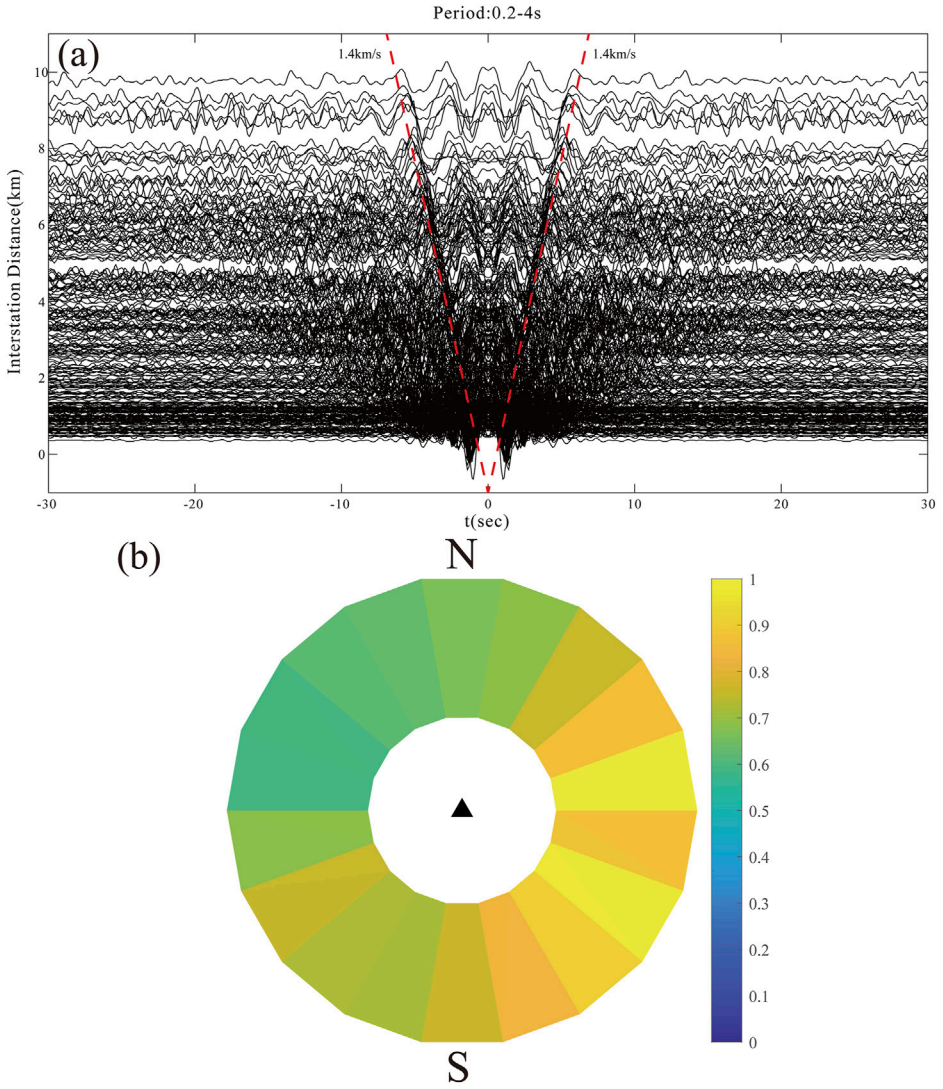

FIGURE 3
(A) Cross-correlation functions (CFs) with signal-to-noise ratio (SNR) > 4.5 in the 0.2–4 s period band obtained using the normalized linear stacking method. **(B)** Azimuthal dependence of the normalized amplitudes of CFs for all station pairs in the 0.2–4 s period band.

set at 1000 Hz (dt = 1 ms). Data recording was commenced on 1 August 2023 and concluded on 21 August 2023 covering a total duration of 20 days. The average station spacing was approximately 0.7 km. The station distribution is shown in Figure 2.

To increase the signal-to-noise ratio (SNR) and reduce computational time, the raw data from each station were decimated to 10 samples per period. Subsequently, the mean value and trend of the data were removed, then bandpass filtered in the period band 0.2–4 s. Besides, we performed the spectral whitening and temporal normalization before the calculation of cross-correlation in order to avoid the effects of earthquakes [27, 28]. Finally, cross-correlation was conducted to obtain the time-domain cross-correlation functions (CFs) between the two stations for each daily data. Figure 3A illustrates the CFs with SNR >4.5 in the period band of 0.2–4 s, revealing prominent Rayleigh surface-wave signals of 1.4 km/s. Figure 3B shows the normalized amplitudes of the CFs for all station pairs. It can be observed that most values of relative amplitude ratios are between 0.5 and 1, which means the differences in amplitude between positive- and negative-time CFs are insignificant. This indicates there will hardly be any significant bias in surface-wave dispersion measurements [29].

We employed a quick tracing method and an image analysis technique to extract the Rayleigh wave group velocity dispersion curves from the Empirical Green's functions (EGFs) of all station pairs [18]. Two quality control criteria were followed during selection of the dispersion curves to get reasonable dispersion curves, which will be used to invert the S-wave model. Firstly, considering the far-field approximation, we excluded records where the interstation distance was less than twice the wavelength [22]. Secondly, for the inversion results to closely approximate the real conditions, only the dispersion curves with SNR >4.5 was used in this study.

Figure 4A represents the group velocity dispersion curves in the 0.2–4 s period band after quality control, and the dispersion data reveal significant velocity variations. Figures 4B, C represent examples of interstation (G002-G008 and G008-G048) Rayleigh

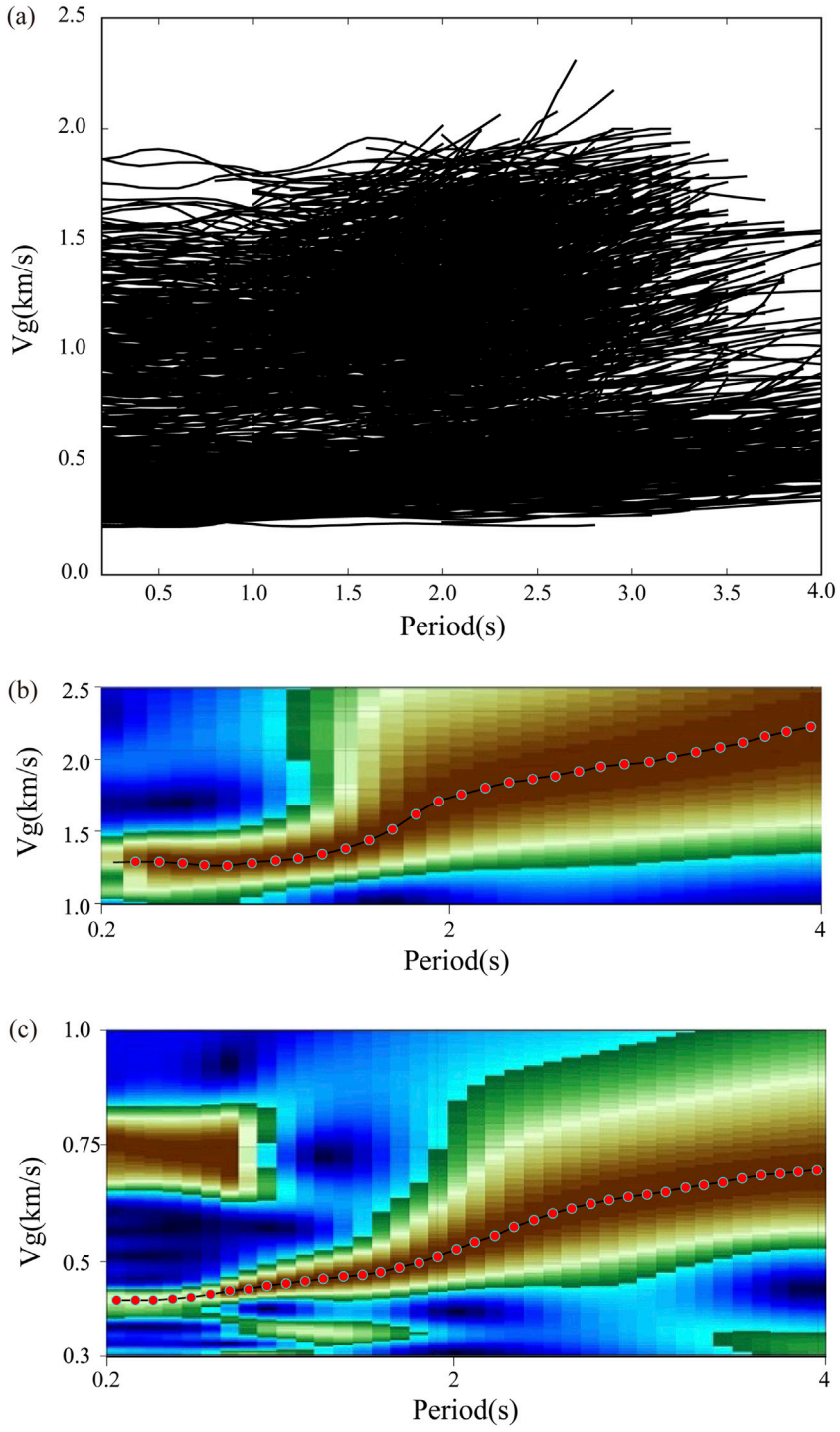

FIGURE 4
(A) Group velocity dispersion curves in the 0.2–4s period band. **(B)** Example of interstation (G002-G008) Rayleigh wave group velocity dispersion curve. **(C)** Example of interstation (G008-G048) Rayleigh wave group velocity dispersion curve. Red asterisks represent the extracted dispersion points.

wave group velocity dispersion curves. Within the period band, the group velocity varied from 0.2 km/s to 2.0 km/s, indicating significant medium heterogeneity.

This study employed a direct surface-wave tomography method to invert all group velocity dispersion curves for the shear-wave velocity structure [19] without the intermediate inversion step for group or phase velocity maps. This method, widely applied in different regions [30–34], employs the fast-marching method proposed for ray tracing to simulate the actual propagation paths of surface waves [35]. It considers that some ray paths will bend away from great-circle paths in the shallow surface based on the fast-marching method [19]. To obtain an optimal model m, this method minimizes differences between the observed travel-times t_i^{obs} and the predicted travel-times $t_i(\omega)$ calculated from the reference model for all frequencies ω.

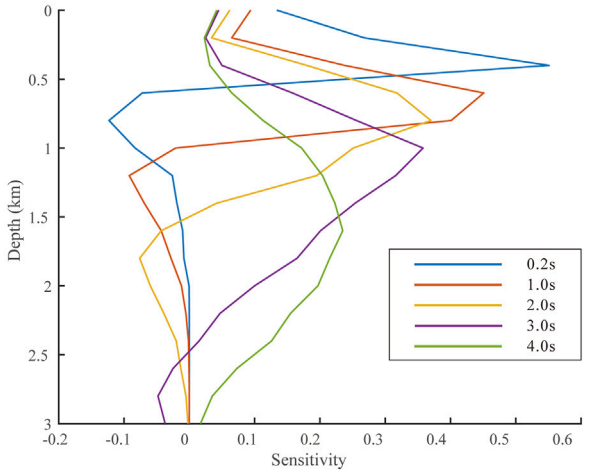

FIGURE 5
Depth sensitivity kernels for group velocity at 0.2, 1.0, 2.0, 3.0, and 4.0 s.

$$\delta t_i(\omega) = t_i^{obs} - t_i(\omega) \approx -\sum_{k=1}^{K} v_{ik} \frac{\delta C_k(\omega)}{C_k^2(\omega)} \tag{1}$$

where v_{ik} is the bilinear interpolation coefficients along the ray path associated with the ith travel-time data and $\delta C_k(\omega)$ is perturbation of group velocity $C_k(\omega)$ at the kth 2-D surface grid point at angular frequency ω. Since this method only inverts for shear-wave velocity, it couples the compressional-wave velocity and density with the shear-wave velocity [36]. Thus, Equation (1) can be further transformed to:

$$\begin{aligned} \delta t_i(\omega) &= \sum_{k=1}^{K} \left(-\frac{v_{ik}}{C_k^2(\omega)} \right) \sum_{j=1}^{J} \left[R_\alpha'(z_i) \frac{\partial C_k(\omega)}{\partial \alpha_k(z_j)} + R_\rho'(z_i) \frac{\partial C_k(\omega)}{\partial \rho_k(z_j)} + \frac{\partial C_k(\omega)}{\partial \beta_k(z_j)} \right] \Big|_{\theta_k} \\ \delta \beta_k(z_j) &= \sum_{l=1}^{M} \mathbf{G}_{il} \mathbf{m}_l \end{aligned} \tag{2}$$

where α, β and ρ are respectively compressional-wave velocity, mass density, and shear-wave velocity, $\frac{\partial C_k(\omega)}{\partial \alpha_k(z)}$, $\frac{\partial C_k(\omega)}{\partial \beta_k(z)}$ and $\frac{\partial C_k(\omega)}{\partial \rho_k(z)}$ are the group velocity depth sensitivity kernels to them. θ_k denotes the 1-D layered reference model at the kth surface grid point on the surface. R_α' and R_ρ' are the scaling factors derived from the empirical relationships [19]. $\delta \beta_k(z_j)$ represents the shear-wave velocity perturbation at the jth depth grid and kth surface grid point. J is the number of grid nodes in the depth direction and M is the total number of grid points in the 3-D model. Equation 2 above gives the final surface wave travel-time perturbation after the discretization of the shear-wave velocity in the depth and horizontal directions.

The average group velocity dispersion curves were used to identify the most reasonable 1D model. We considered it as the initial model to invert the near-surface shear velocity structures. For the inversion grid, the grid interval was 0.0073° along the latitude and 0.0067° along the longitude (which amounts to 18 × 18 grid points). In addition, from 0.2 km to 1.25 km we also placed nine grid points along the depth direction.

Rayleigh wave group velocity values at different periods reflect the characteristics of shear-wave velocity changes within a specific depth range, with the penetration depth increasing as the period lengthens. Therefore, it is necessary to provide sensitivity kernel functions for the group velocities at various depth periods when correlating surface-wave group velocities with S-wave velocities. Figure 5 shows the depth sensitivity kernels for Rayleigh wave group velocities at five periods (0.2, 1.0, 2.0, 3.0, and 4.0 s) and indicates that in the period range of 0.2–4 seconds, our dispersion data can be resolved well down to depths >1.4 km.

Figure 6 presents the path coverage of group velocity measurements at four selected periods based on the final 3D velocity model. It can be clearly seen that the path number decreases with the increase of the period. And generally speaking, the ray coverage at these periods is relatively good except for some marginal area, indicating that in the most of the study area, this dataset has the capability to resolve the structure of our study area.

Then a checkerboard resolution test was typically used to evaluate the resolution and errors of data at different depths to test the impact of ray paths and station distribution. This study employed this method to test the reliability of dispersion data, the maximum strength of the shear-wave velocity anomaly was ±50%. With increasing inversion depth, the model resolution gradually decreases (Figure 7). Moreover, Checkerboard models in the middle part of the study area recovered better than the models of the marginal part (Figure 8). Considering that the ray-paths covered more densely in the middle part than in the marginal part of the study area, the checkerboard resolution is generally combined with the ray-path coverage. Owing to the relatively dense data coverage, the velocity anomalies in most of the inversion region can be resolved well.

Finally, we used the group dispersion data in the inversion. Regularization parameters were carefully selected through a trade-off analysis for the inversion [37]. After inversion, the root-mean-square (RMS) residual value decreased from 2.0 s to 1.27 s and remained stable (Figure 9). In the first two iterations, the RMS rapidly reduced. Then it decreased slowly and converged after the 10th iteration, showing that after multiple iterations, the inversion results converged to a stable state.

3 Results

The S-wave model at different depths is shown in Figure 10. The velocity structure exhibited significant lateral heterogeneity in the study area, with variations in velocity structure at various depths. At a depth of 0.2 km (Figure 10A), the S-wave velocity was generally low, with a spatial distribution showing lower velocities in the eastern area and higher velocities in the western area. In the study area, the depth to the bedrock was approximately 0.28 km, thus the velocity structure at this depth reflected variations in the medium structure of the bottom strata in the Neogene. At 0.35 km depth, velocity anomalies appeared in the study area (Figure 10B), with relatively higher velocities on the west and east sides and a predominance of low velocity anomalies in the middle. Since the depth of 0.2 km is located in the upper part of the bedrock region, the low-velocity anomaly zone in the middle might reflect the development of a fractured zone. At depths >0.65 km (Figures 10D–H), the S-wave velocities showed band-like features, with a west-to-east velocity structure characterized by low-high-low-high-velocity distributions. Based on the development characteristics in the study area, at depths >0.65 km, the high-velocity anomaly in the

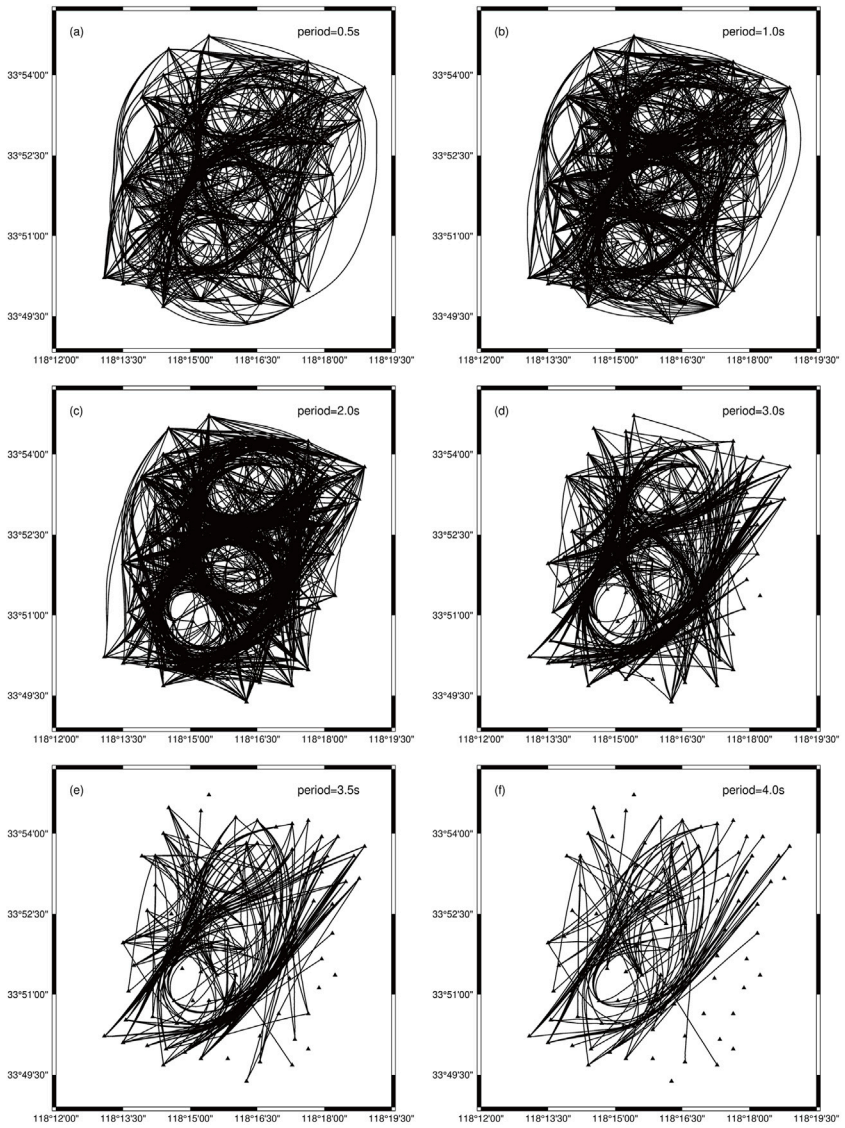

FIGURE 6
Ray-path coverage for six selected periods **(A)** 0.5 s, **(B)** 1.0 s, **(C)** 2.0 s, **(D)** 3.0 s, **(E)** 3.5 s, and **(F)** 4.0 s. Triangles represent stations, and black lines represent ray paths.

Daluo region was related to the metamorphic rocks of the Archean-Proterozoic Jiaodong Group (Ar-Pt_2), and the band-like high-velocity anomaly in the Heiyuwang-Nancai area was associated with the Mesozoic Wangshi Formation sandstone (K_2w).

4 Discussion

4.1 Spatial distribution and structural characteristics of fault F_5

Using ambient noise tomography, recent studies investigating shallow velocity structures have shown that shallow crustal velocity structures typically correlate well with structural units. For instance, in 3-D S-wave velocity structures, the orientation and location of the significant high- and low-velocity anomalies often match faults passing through the study area [38]. Owing to the evident lateral heterogeneity of S-wave velocities within the study area, we inferred that the distribution of velocity anomalies, combined with previous research on fault distribution characteristics in the Suqian area, can be used to determine the orientation and location of faults within the study area. Based on the S-wave velocity distribution characteristics (Figure 10), it can be inferred that fault F_1 is distributed along the western boundary of the high-velocity anomaly located in the Longmenkou-Nancai area, and fault F_2 is distributed along the eastern boundary of the low-velocity anomaly located in the Laozhuyu area.

A north-south trending low-velocity anomaly zone developed in the Sankeshu area; the eastern and western boundaries of this low-velocity anomaly zone were inferred to be faults $F_{5\text{-}1}$ and $F_{5\text{-}2}$, respectively. This low-velocity anomaly is associated with the fractured zone between the two faults. Overall, at least four faults

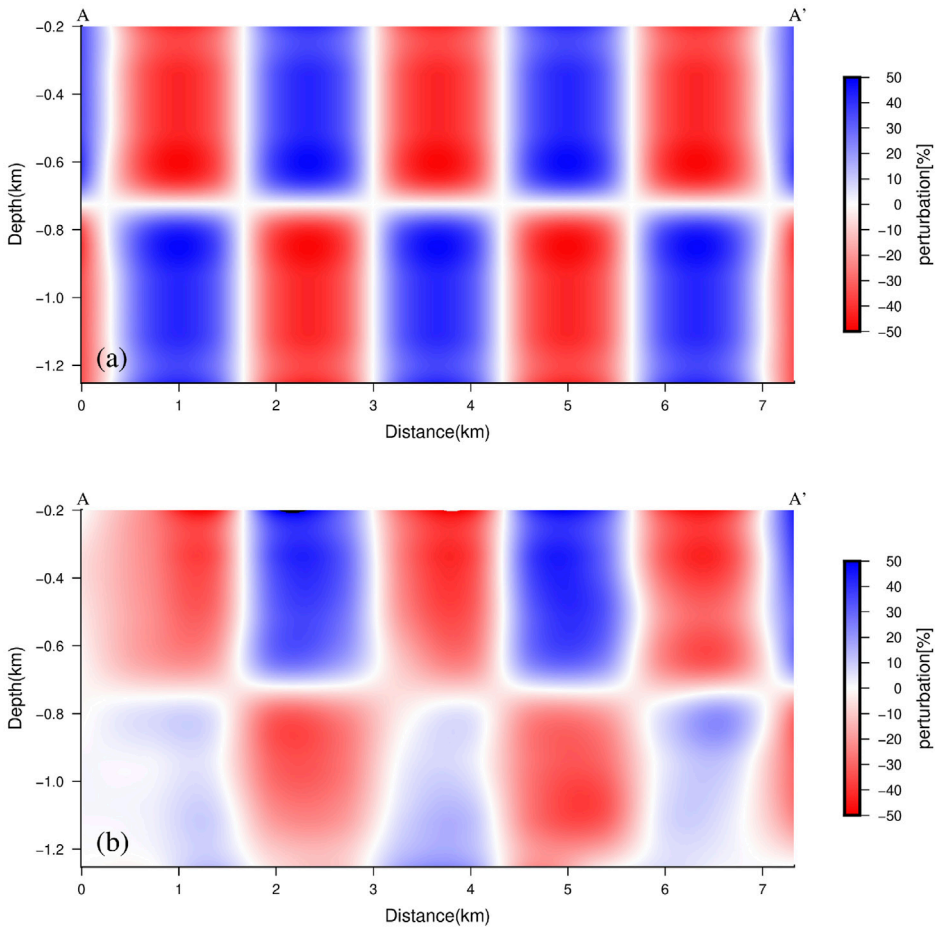

FIGURE 7
Checkerboard resolution tests in the vertical direction beneath profile AA' (Figure 2). **(A)** Initial model, **(B)** Recovered model.

were identified within the study area, namely F_1, F_5 ($F_{5\text{-}1}$, $F_{5\text{-}2}$), and F_2, generating a series of NNE trends (Figure 10).

To validate the reasonableness of the inferred fault locations, we compared the results of this study with those of previous studies on fault F_5. Xu et al. (2016) conducted a shallow seismic exploration along the reflection seismic profile QL14 (Figure 11C) [13]. Fault F_5 is composed of multiple-branch faults: fault $F_{5\text{-}1}$ develops at trace number 4150, fault $F_{5\text{-}2}$ develops at trace number 6700, and fault $F_{5\text{-}3}$ develops at trace number 5700. The locations of trace numbers 4150 and 6700 are shown in Figure 10A. By comparing the interpreted locations of faults $F_{5\text{-}1}$ and $F_{5\text{-}2}$ from reflection seismic profile QL14 with the fault locations inferred from the map view of the S-wave velocity model, it was observed that the interpretations of faults $F_{5\text{-}1}$ and $F_{5\text{-}2}$ from these two profiles were consistent. Therefore, we will subsequently conduct a joint discussion of the results from the QL14 profile and the imaging results presented in this paper. As shown in Figure 11C, the $F_{5\text{-}1}$ and $F_{5\text{-}2}$ faults dip towards each other, while the $F_{5\text{-}3}$ fault is nearly vertical. There are evident fault diffraction waves at the interface of the bedrock and overlying strata along the $F_{5\text{-}3}$ fault, which is a clear indicator of active faults on the seismic profile. Additionally, the arcuate characteristics of the reflectors within the fault also strongly indicate significant bending and deformation of the strata due to tectonic activity, further confirming the more intense activity of the $F_{5\text{-}3}$ fault compared to $F_{5\text{-}1}$ and $F_{5\text{-}2}$.

To better study the fault zone and its velocity structure characteristics, we showed the vertical resolution beneath two profiles traversing the region from west to east, AA' and BB' (Figures 11A, B). The locations of these profiles are shown in Figure 10B. Figure 11A shows that fault F_5 is a fault zone composed of two faults, with $F_{5\text{-}1}$ marked as the western boundary and $F_{5\text{-}2}$ marked as the eastern boundary. The fractured zone between $F_{5\text{-}1}$ and $F_{5\text{-}2}$ exhibited a significant low-velocity anomaly. Faults $F_{5\text{-}1}$ and $F_{5\text{-}2}$ likely controlled the Cenozoic depression, which was covered by a thick low-velocity sediment layer. Fault F_5 in the study area comprises two faults that dip in opposite directions, with a deep depression in the middle, consistent with a previous understanding of the distribution characteristics of fault F_5 in the area [10]. Figure 11C shows that a near-vertical fault $F_{5\text{-}3}$ developed between faults $F_{5\text{-}1}$ and $F_{5\text{-}2}$. However, fault $F_{5\text{-}3}$ is not clearly shown in the AA' and BB' profiles, possibly owing to the poor integrity of the rocks within the fractured zone where fault $F_{5\text{-}3}$ is located and the relatively low transverse velocity heterogeneity. In contrast, the lithological and velocity differences on either side of faults $F_{5\text{-}1}$ and $F_{5\text{-}2}$ were more significant, exacerbating the differences in the transverse velocity in the AA' and BB' profiles.

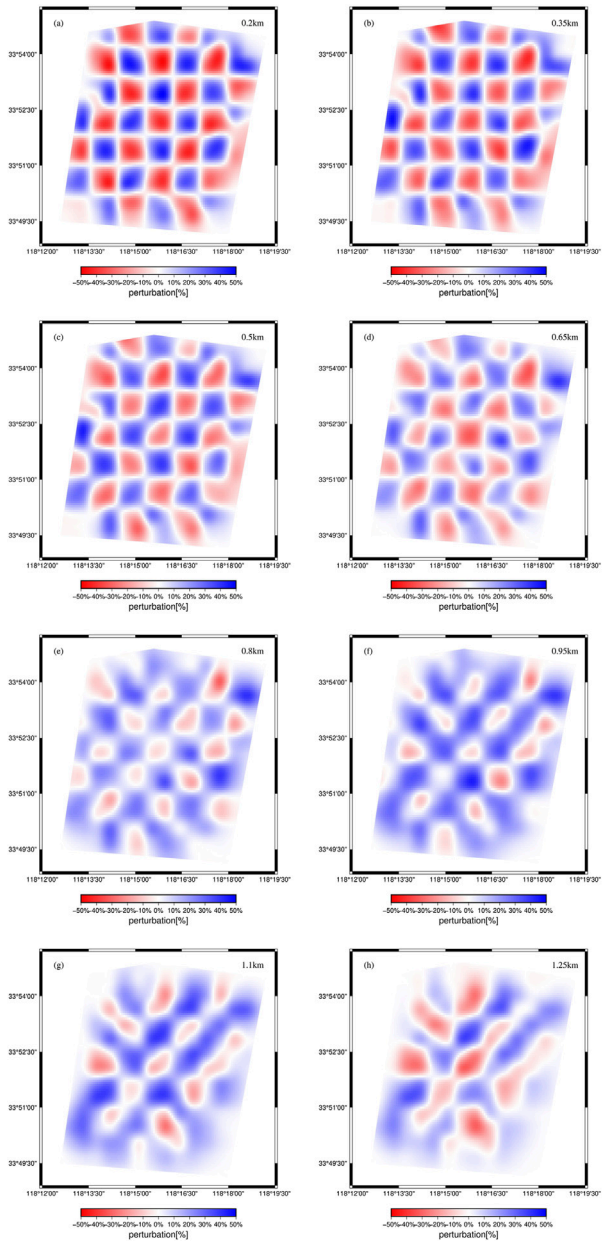

FIGURE 8
Checkerboard resolution tests of the inversion at depth of **(A)** 0.20 **(B)** 0.35, **(C)** 0.50, **(D)** 0.65, **(E)** 0.80, **(F)** 0.95, **(G)** 1.1, and **(H)** 1.25 km.

Hence, the imaging results and the inferred spatial distribution of faults in this study showed a relatively good consistency with those of previous studies. Therefore, subsequent discussions combine the reflection seismic profile QL14 with the imaging results of this study.

The imaging results in this study revealed the development characteristics and spatial distribution of fracture structures within the Neogene (N) and its underlying bedrock (K2w, Ar). Based on comprehensive shallow seismic exploration results and S-wave velocity imaging, it is found that faults F_1, F_2, and F_5 extended downward to the depth of 1.25 km and below. Faults $F_{5\text{-}1}$ and $F_{5\text{-}2}$ collectively controlled a Cenozoic depression with a thick, low-velocity sediment layer. These two boundary faults may merge into a single fracture at greater depths.

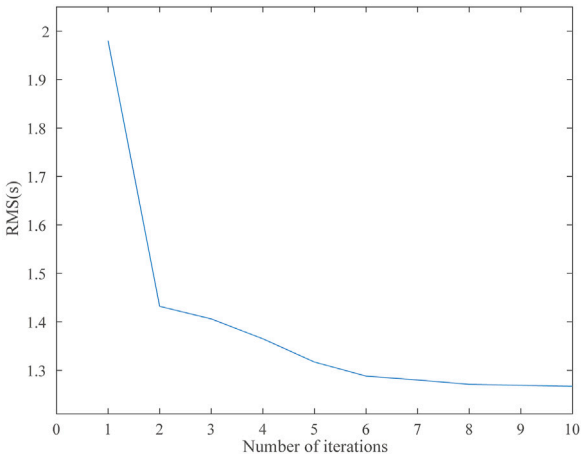

FIGURE 9
Variation of the RMS value of surface-wave travel-time residuals through the iterations.

4.2 The control of fault F_5 on sediment in the Suqian area

The AA' profile (Figure 11A) traverses the low-velocity anomaly bodies controlled by faults F_2 and F_5. The boundary characteristics of these low-velocity anomalies were distinct. The orientations of faults F_2, $F_{5\text{-}1}$, and $F_{5\text{-}2}$ are highly consistent with the dip directions of the boundaries, each forming a separate low-velocity anomaly center. Among these, the low-velocity anomaly between faults $F_{5\text{-}1}$ and $F_{5\text{-}2}$ was more pronounced, extending to depths >1.2 km in the crust, whereas the anomalous body near fault F_2 extended only to approximately 1 km, indicating relatively shallower burial and a smaller extent. Therefore, local sedimentary centers might develop on either side of fault F_2, with a more extensive sedimentary area associated with fault F_5, reflecting the significant control of fault F_5 on the sedimentary thickness of the strata.

The velocity structure along the profiles AA' and BB' is consistent with the horizontal velocity structures, revealing a velocity structure which showed low-high-low-high velocity distributions in west-east direction. This suggests that the control of faults on sedimentary layers in the Suqian area does not manifest as an overall uplift or subsidence of the block but rather as differential subsidence. The alternating activity of faults in the Suqian area has formed a tectonic structure characterized by alternating horsts and grabens. Within fault-controlled zones, the sediment in the shallow layers is highly uneven, which could pose challenges for construction projects, necessitating a more detailed geological survey.

4.3 Discussion on the pull-apart basin centered around Sankeshu

Findings from previous research near the Sankeshu area have indicated that three right-stepping faults compose fault F_5, these three faults formed a pull-apart basin which controls the deposition of Neogene and Quaternary strata [13]. Our imaging results

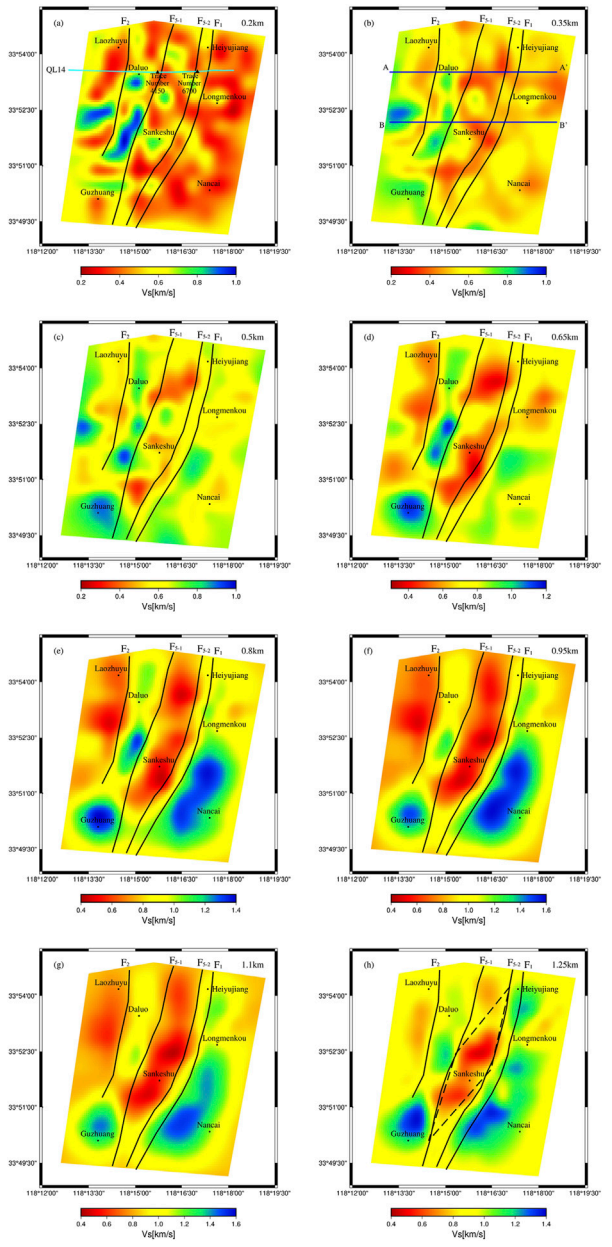

FIGURE 10
Map view of the shear-wave velocity model at depth of **(A)** 0.20, **(B)** 0.35, **(C)** 0.50, **(D)** 0.65, **(E)** 0.80, **(F)** 0.95, **(G)** 1.1, and **(H)** 1.25 km.

indicated that at depths 0.8–1.25 km, the band-like low-velocity anomaly located at Sankeshu diminished with increasing depth. At a depth of 1.25 km, only a portion of the low-velocity anomaly centered around Sankeshu remained (Figure 10H). Combined with our previous conclusion that faults $F_{5\text{-}1}$ and $F_{5\text{-}2}$ control a Cenozoic depression with a thick low-velocity sediment layer, this supports the presence of a pull-apart basin and suggests that the basement of the basin lies below 1.25 km. Furthermore, utilizing the map view of the S-wave model (Figure 10) and the reflection seismic profile (Figure 11C), the scale of the pull-apart basin can be roughly determined, as indicated in Figure 10H. The boundary faults of the pull-apart basin are faults $F_{5\text{-}1}$ and $F_{5\text{-}2}$, which delineate the western and eastern boundaries of the basin, respectively. In contrast, its northern and southern boundaries correspond to the northern and southern extents of the low-velocity anomaly. Since the reflection seismic profile indicated the presence of reflection wave groups below fault $F_{5\text{-}1}$, Fault $F_{5\text{-}1}$ might exert a stronger control over the pull-apart basin, making it the main fault on the eastern edge of the basin. In the early stages, this fault controlled the development of other faults, as well as the formation and evolution of the pull-apart basin.

Fault $F_{5\text{-}3}$ exhibits the highest activity from the reflection seismic profile, whereas faults $F_{5\text{-}1}$ and $F_{5\text{-}2}$ were relatively less active. Based on the positions of these faults within the pull-apart basin and the understanding of similar basins from previous studies [39], we hypothesized that faults $F_{5\text{-}1}$ and $F_{5\text{-}2}$ represent early basin-controlling boundary faults and currently show less activity. In contrast, fault $F_{5\text{-}3}$, located in the central part of the basin, represents a newly developed strike-slip fault, indicating that the recent activity of the pull-apart basin was mainly expressed on this fault, which serves as the main throughgoing fault of this basin.

Given that the extinction of a pull-apart basin commonly manifests as the development of a new strike-slip fault diagonally across the basin [40], we hypothesized that this basin's latest activity has shifted to the central fault $F_{5\text{-}3}$. This fault, being an extensional-shear strike-slip, effectively diminishes normal faulting activity along the basin boundary faults as well as within the basin, signalling the basin's late-stage evolution towards extinction. This transition implies a higher seismic hazard potential for central fault $F_{5\text{-}3}$. Structurally, the formation and increased activity of the new fault exacerbate seismic risks. Therefore, it is essential to monitor the activity of fault $F_{5\text{-}3}$ and evaluate its seismic risk. Detailed studies of the geometric characteristics, historical activity, and current stress state of the fault are crucial for developing earthquake disaster prevention and mitigation strategies in the Suqian area.

5 Conclusion

This study utilized continuous vertical component ambient noise waveforms recorded by 100 short-period temporary stations to investigate the shallow crustal structure of the upper crust of fault F_5 in the Suqian area, China. We obtained a 3-D S-wave velocity model for the 0.2–1.25 km depth range in this region. The following results were obtained:

The velocity structure exhibited strong lateral heterogeneity. The development of faults F_1, F_2, and F_5 shows a high degree of consistency with S-wave velocity anomalies. Fault F_5 was composed of two boundary faults $F_{5\text{-}1}$ and $F_{5\text{-}2}$, which together controlled a Cenozoic depression covered by a thick low-velocity sediment layer. These two faults might gradually merge into a single fault in the deeper crust.

On either side of fault F_2, localized sedimentary centers have developed. Notably, the sedimentary extent at fault F_5 was relatively larger, which reflected the significant control that fault F_5 exerts over the sedimentary thickness of the strata. The velocity structures along the profiles AA' and BB' displayed a low-high-low-high velocity distribution from west to east across the study area. This pattern indicated that the control exerted by the faults over the sedimentary layers in the Suqian region was not manifesting as an overall uplift or subsidence of the block, but rather as differential subsidence. The

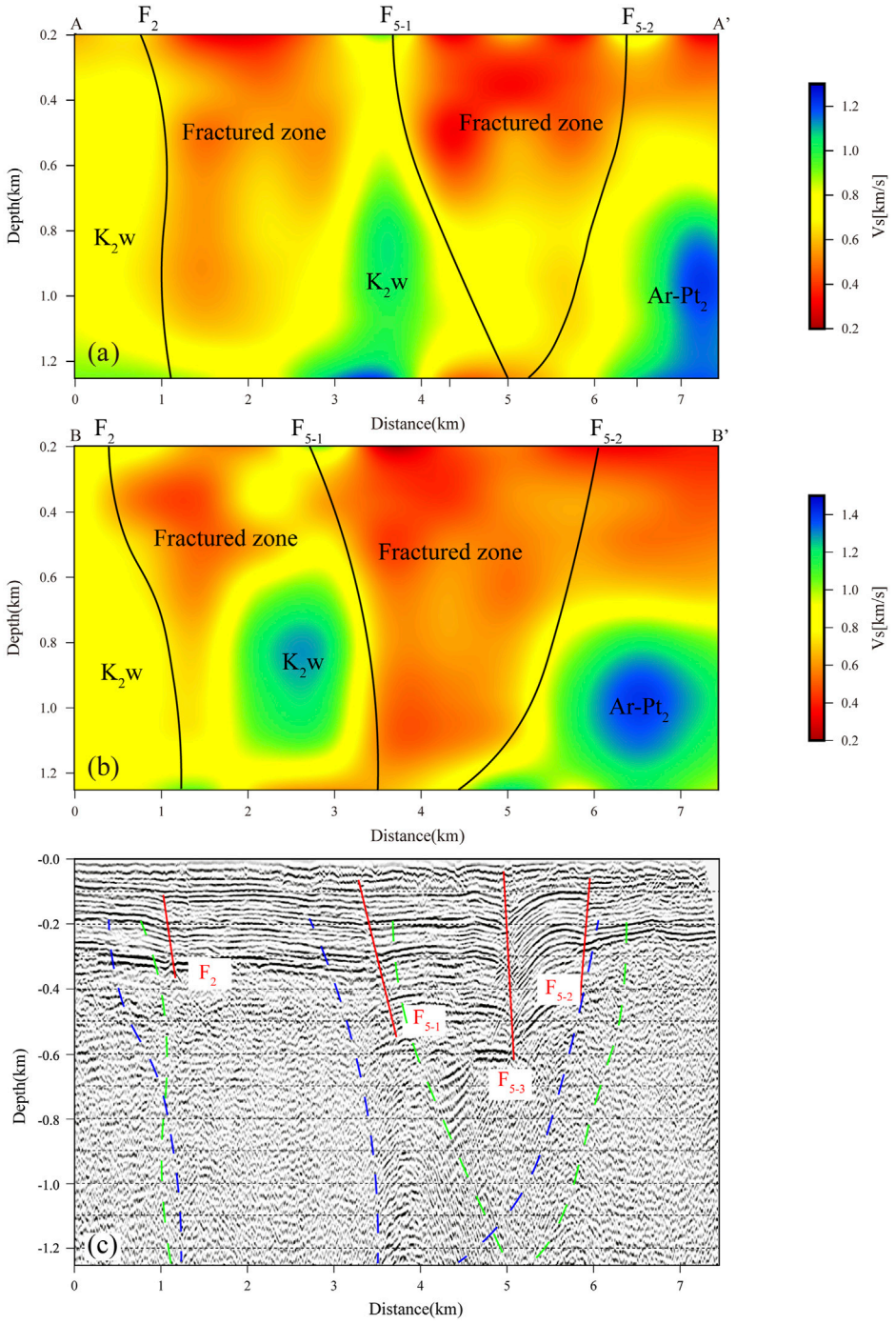

FIGURE 11
Cross-section of the shear-wave velocity model along **(A)** AA′ and **(B)** BB′ and **(C)** the reflection seismic profile QL14. The red lines represent faults F_2, F_{5-1}, F_{5-2} and F_{5-3} shown in the reflection seismic profile QL14, the green dotted lines represent faults F_2, F_{5-1} and F_{5-2} shown in Figure 11, the blue dotted lines represent faults F_2, F_{5-1} and F_{5-2} shown in Figure 11.

alternating activity of faults in the Suqian area has formed a tectonic structure characterized by alternating horsts and grabens.

The boundary faults of the pull-apart basin formed by fault F_5 are F_{5-1} and F_{5-2}. Among these two faults, fault F_{5-1} served as the primary fault zone on the eastern edge of the basin and has played a dominant role in the development of other faults as well as in the formation and evolution of the entire basin during its early stages, while fault F_{5-3} exhibited the highest activity and is a newly developing strike-slip fault within the center of the basin. The latest activity of the pull-apart basin has shifted to fault F_{5-3}. We hypothesized that its dextral strike-slip movement has decomposed the normal fault activity of the boundary faults, leading to the basin entering a stage of extinction.

Data availability statement

The raw data supporting the conclusions of this article will be made available by the authors, without undue reservation.

Author contributions

QH: Conceptualization, Data curation, Formal Analysis, Investigation, Software, Supervision, Validation, Visualization, Writing–original draft, Writing–review and editing. XF: Data curation, Funding acquisition, Project administration, Software, Supervision, Writing–review and editing. WF: Data curation, Formal Analysis, Software, Supervision, Visualization, Writing–review and editing. PZ: Resources, Supervision, Writing–review and editing. TZ: Supervision, Writing–review and editing. YL: Data curation, Resources, Writing–review and editing. TZ: Data curation, Resources, Writing–review and editing. SR: Data curation, Resources, Writing–review and editing. QW: Data curation, Resources, Writing–review and editing. ZL: Data curation, Resources, Writing–review and editing. TQ: Data curation, Resources, Writing–review and editing.

Funding

The author(s) declare that financial support was received for the research, authorship, and/or publication of this article. This study was supported by the National Natural Science Foundation of China (Grant Nos 42104099 and 41874051).

Conflict of interest

The authors declare that the research was conducted in the absence of any commercial or financial relationships that could be construed as a potential conflict of interest.

Publisher's note

All claims expressed in this article are solely those of the authors and do not necessarily represent those of their affiliated organizations, or those of the publisher, the editors and the reviewers. Any product that may be evaluated in this article, or claim that may be made by its manufacturer, is not guaranteed or endorsed by the publisher.

References

1. Zhu G, Wang D, Liu G, Song C, Xu J, Niu M. Extensional activities along the Tan-Lu fault zone and its geodynamic setting. *Chin J Geol* (2001) 36:269–78.

2. Deng Y, Fan W, Zhang Z, Badal J. Geophysical evidence on segmentation of the Tancheng-Lujiang fault and its implications on the lithosphere evolution in East China. *J Asian Earth Sci* (2012) 78:263–76. doi:10.1016/j.jseaes.2012.11.006

3. Zhang H, Li L, Jiang X, Zhang D, Xu H. New progress in paleoearthquake studies of the Jiangsu segment of the Anqiu-Juxian Fault in the Tanlu fault zone. *Seismol Geol* (2023) 45:880–95. doi:10.3969/j.issn.0253-4967.2023.04.005

4. Chao HT, Li J, Cui Z, Zhao Q. Discussion on several problems related to the seismic fault of the 1688 Tancheng earthquake (M= 8½). *North China Earthquake Sci* (1997) 15: 18–25.

5. Shi W, Zhang Y, Dong S. Quaternary activity and segmentation behavior of the middle portion of the Tan-Lu fault zone. *Acta Geosci Sin* (2003) 24:11–8.

6. Liu B, Feng S, Ji J, Shi J, Tan Y, Li Y. Fine lithosphere structure beneath the middle-southern segment of the Tan-Lu fault zone. *Chin J Geophys* (2015) 58:1610–21. doi:10.6038/cjg20150513

7. Wang H, Geng J. Some features of 1668 Tancheng earthquake (M= 8½) fault. *North China Earthquake Sci* (1992) 10:34–42.

8. Chao H, Li J, Cui Z, Zhao Q. Characteristic slip behavior of the Holocene fault in the central section of the Tan-Lu fault zone and the characteristic earthquakes. *Inland Earthquake* (1994) 8:297–30.

9. Li J, Chao H, Cui Z, Zhao Q. Segmentation of active fault along the Tancheng-Lijiang fault zone and evaluation of strong earthquake risk. *Seismol Geol* (1994) 16: 121–6.

10. Zhang P, Li L, Ran Y, Cao J, Xu H, Jiang X. Research on characteristics of late quaternary activity of the Jiangsu segment of Anqiu-Juxian fault in the Tanlu fault zone. *Seismol Geol* (2015) 37:1162–76. doi:10.3969/j.issn.0253-4967.2015.04.018

11. Zhang P, Zhang Y, Li L, Jiang X, Meng K. New evidences of Holocene activity in the Jiangsu segment of Anqiu-Juxian fault of the Tanlu fault zone. *Seismol Geol* (2019) 41:576–86. doi:10.3969/j.issn.0253-4967.2019.03.003

12. Zhang P, Li L, Zhang J, Jiang W, Chen D, Li J, et al. A discuss of the characteristics of activities in quaternary for the Jiangsu segment of Tan-Lu fault zone and its geodynamic setting. *J Disaster Prev Mitigation Eng* (2011) 31:389–96. doi:10.3969/j.issn.1672-2132.2011.04.007

13. Xu H, Fan X, Ran Y. New evidences of the Holocene fault in Suqian segment of the Tanlu fault zone discovered by shallow seismic exploration method. *Seismol Geol* (2016) 38:31–43. doi:10.3969/j.issn.0253-4967.2016.01.003

14. Cao J, Ran Y, Xu H, Li Y, Zhang P, Ma X, et al. Typical case analysis on application of multi-method detection technique to active fault exploration in Suqian city. *Seismol Geol* (2015) 37:430–9. doi:10.3969/j.issn.0253-4967.2015.02.007

15. Meng Y, Yao H, Wang X, Li L, Feng J, Hong D, et al. Crustal velocity structure and deformation features in the central-southern segment of Tanlu fault zone and its adjacent area from ambient noise tomography. *Chin J Geophys* (2019) 62:2490–509. doi:10.6038/cjg2019M0189

16. Qin J, Liu B, Xu H, Shi J, Tan Y, He Y, et al. Exploration of shallow structural characteristics in the Suqian segment of the TanLu fault zone based on seismic refraction and reflection method. *Chin J Geophys* (2020) 63:505–16. doi:10.6038/cjg2020N0144

17. Sabra KG, Gerstoft P, Roux P, Kuperman WA, Fehler MC. Surface wave tomography from microseisms in Southern California. *Geophys Res Lett* (2005) 32: L14311. doi:10.1029/2005GL023155

18. Yao H, Van Der Hilst RD, De Hoop MV. Surface-wave array tomography in SE Tibet from ambient seismic noise and two-station analysis—I. Phase velocity maps. *Geophys J Int* (2006) 166:732–44. doi:10.1111/j.1365-246X.2006.03028.x

19. Fang H, Yao H, Zhang H, Huang Y, Van Der Hilst RD. Direct inversion of surface wave dispersion for three-dimensional shallow crustal structure based on ray tracing: methodology and application. *Geophys J Int* (2015) 201:1251–63. doi:10.1093/gji/ggv080

20. Zhou L, Xie J, Shen W, Zheng Y, Yang Y, Shi H, et al. The structure of the crust and uppermost mantle beneath South China from ambient noise and earthquake tomography. *Geophys J Int* (2012) 189:1565–83. doi:10.1111/j.1365-246X.2012.05423.x

21. Li C, Yao H, Fang H, Huang X, Wan K, Zhang H, et al. 3D near-surface shear-wave velocity structure from ambient noise tomography and borehole data in the Hefei urban area, China. *Seismol Res Lett* (2016) 87:882–92. doi:10.1785/0220150257

22. Yao H, Gouédard P, Collins JA, McGuire JJ, Van Der Hilst RD. Structure of young East Pacific Rise lithosphere from ambient noise correlation analysis of fundamental- and higher-mode Scholte-Rayleigh waves. *C R Géoscience* (2011) 343:571–83. doi:10.1016/j.crte.2011.04.004

23. Lin F, Li D, Clayton RW, Hollis D. High-resolution 3D shallow crustal structure in Long Beach, California: application of ambient noise tomography on a dense seismic array. *Geophysics* (2013) 78:Q45–Q56. doi:10.1190/geo2012-0453.1

24. Chmiel M, Mordret A, Boue P, Brenguier F, Lecocq T, Courbis R, et al. Ambient noise multimode Rayleigh and Love wave tomography to determine the shear velocity structure above the Groningen gas field. *Geophys J Int* (2019) 218:1781–95. doi:10.1093/gji/ggz237

25. Gu N, Wong N, Gao J, Ding N, Yao H, Zhang H. Shallow crustal structure of the Tanlu Fault Zone near Chao Lake in eastern China by direct surface wave tomography from local dense array ambient noise analysis. *Pure Appl Geophys* (2019) 176:1193–206. doi:10.1007/s00024-018-2041-4

26. Wei Z, Chu R, Chen L, Wu S. Crustal structure in the middle-southern segments of the Tanlu Fault Zone and adjacent regions constrained by multifrequency receiver

function and surface wave data. *Phys Earth Planet Inter* (2020) 301:106470. doi:10.1016/j.pepi.2020.106470

27. Bensen GD, Ritzwoller MH, Barmin MP, Levshin AL, Lin F, Moschetti MP, et al. Processing seismic ambient noise data to obtain reliable broad-band surface wave dispersion measurements. *Geophys J Int* (2007) 169:1239–60. doi:10.1111/j.1365-246X.2007.03374.x

28. Zhang Y, Yao H, Yang H, Cai H, Fang H, Xu J, et al. 3-D crustal shear-wave velocity structure of the Taiwan Strait and Fujian, SE China, revealed by ambient noise tomography. *JGR Solid Earth* (2018) 123:8016–31. doi:10.1029/2018JB015938

29. Yao H, Van Der Hilst RD. Analysis of ambient noise energy distribution and phase velocity bias in ambient noise tomography, with application to SE Tibet. *Geophys J Int* (2009) 179:1113–32. doi:10.1111/j.1365-246X.2009.04329.x

30. Huang Y, Yao H, Huang B, Van Der Hilst RD, Wen K, Huang W, et al. Phase velocity variation at periods of 0.5–3 seconds in the Taipei Basin of Taiwan from correlation of ambient seismic noise. *Bull Seismol Soc Am* (2010) 100:2250–63. doi:10.1785/0120090319

31. Liu C, Yao H, Yang H, Shen W, Fang H, Hu S, et al. Direct inversion for three-dimensional shear wave speed azimuthal anisotropy based on surface wave ray tracing: methodology and application to Yunnan, southwest China. *JGR Solid Earth* (2019) 124:11394–413. doi:10.1029/2018JB016920

32. Gu Q, Ding Z, Kang Q, Li D. Group velocity tomography of Rayleigh wave in the middle-southern segment of the Tan-Lu fault zone and adjacent regions using ambient seismic noise. *Chin J Geophys* (2020) 63:1505–22. doi:10.6038/cjg2020N0117

33. Luo S, Yao H, Li Q, Wang W, Wan K, Meng Y, et al. High-resolution 3D crustal S-wave velocity structure of the Middle-Lower Yangtze River Metallogenic Belt and implications for its deep geodynamic setting. *Sci China Arth Sci* (2019) 62:1361–78. doi:10.1007/s11430-018-9352-9

34. Zheng L, Fan X, Zhang P, Hao J, Qian H, Zheng T. Detection of urban hidden faults using group-velocity ambient noise tomography beneath Zhenjiang area, China. *Sci Rep* (2021) 11:987. doi:10.1038/s41598-020-80249-6

35. Rawlinson N, Sambridge M. Wave front evolution in strongly heterogeneous layered media using the fast marching method. *Geophys J Int* (2004) 156:631–47. doi:10.1111/j.1365-246X.2004.02153.x

36. Brocher TM. Empirical relations between elastic wavespeeds and density in the Earth's crust. *Bull Seismol Soc Am* (2005) 95:2081–92. doi:10.1785/0120050077

37. Aster RC, Borchers B, Thurber CH. *Parameter estimation and inverse problems*. 2nd ed. Academic (2013).

38. Jin J, Luo S, Yao H, Tian X. Dense array ambient noise tomography reveals the shallow crustal velocity structure and deformation features in the Weifang segment of the Tanlu fault zone. *Chin J Geophys* (2023) 66:558–75. doi:10.6038/cjg2022P0934

39. Shu P, Xu X, Feng S, Liu B, Li K, Tapponnier P, et al. Sedimentary and tectonic evolution of the Banquan pull-apart basin and implications for Late Cenozoic dextral strike-slip movement of the Tanlu Fault Zone. *Sci China (Earth Sci.)* (2023) 66:797–820. doi:10.1007/s11430-022-1028-5

40. Zhang P, Burchfiel BC, Chen S, Deng Q. Extinction of pull-apart basins. *Geology* (1989) 17:814–7. doi:10.1130/0091-7613(1989)017<0814:eopab>2.3.co;2

frontiers | Frontiers in Physics

TYPE Original Research
PUBLISHED 30 October 2024
DOI 10.3389/fphy.2024.1497190

OPEN ACCESS

EDITED BY
Huiming Tan,
Hohai University, China

REVIEWED BY
Yongfeng Deng,
Southeast University, China
Xingyue Li,
Tongji University, China

*CORRESPONDENCE
Peiqing Wang,
497450734@qq.com

RECEIVED 16 September 2024
ACCEPTED 16 October 2024
PUBLISHED 30 October 2024

CITATION
Sang D, Wang P, Chen L, Zhang W, Liu Z and Wang Q (2024) Analysis of the mechanical properties and micro-reinforcement mechanisms of loose accumulated sandy soil improved with polyvinyl alcohol and sisal fiber. *Front. Phys.* 12:1497190.
doi: 10.3389/fphy.2024.1497190

Analysis of the mechanical properties and micro-reinforcement mechanisms of loose accumulated sandy soil improved with polyvinyl alcohol and sisal fiber

Ding Sang[1,2], Peiqing Wang[1,2]*, Liang Chen[1,2], Wengang Zhang[3], Zhen Liu[1,2] and Qi Wang[1,2]

[1]College of Water Conservancy and Civil Engineering, Xizang Agriculture and Animal Husbandry University, Linzhi, China, [2]Research Center of Civil, Hydraulic and Power Engineering of Xizang, Xizang Agriculture and Animal Husbandry University, Linzhi, China, [3]School of Civil Engineering, Chongqing University, Chongqing, China

As one of the world's most fragile and sensitive ecological regions, Xizang risks significant environmental damage from using traditional materials, including cement and lime, to improve and reinforce loose accumulated sandy soil slopes. To address this issue, this study utilized a low-concentration biodegradable polyvinyl alcohol (PVA) solution combined with sisal fibers (SFs) to stabilize loose accumulated sand in southeastern Xizang. A series of physical, mechanical, and microscopic analyses was conducted to evaluate the properties of the treated sand. The results indicated the following. 1) The stress-strain curves of the improved samples exhibited an elastic-plastic relationship. Failure was observed in two stages. At a strain of 3% or less, the samples demonstrated elastic deformation with a linear increase in stress, whereas the deviator stress increased rapidly and linearly with an increase in axial strain. Once the strain exceeded 3%, the deformation became plastic with a nonlinear increase in the stress-strain relationship, and the growth rate of the deviator stress gradually decreased and leveled off. 2) Under varying confining pressure conditions, the relationship curve between the maximum $(\sigma_1\text{-}\sigma_3)_{max}$~$\sigma_3$ for both untreated loose accumulated sandy soil and soil improved with the PVA solution, and the sisal fiber was approximately linear. 3) The SFs created a skeletal-like network that encased the soil particles, and the hydroxyl functional groups in the PVA molecules bonded with both the soil particles and the fiber surface, thereby enhancing the interfacial properties. This interaction resulted in a tighter connection between the soil particles and SFs, which improved the stability of the structure. 4) The incorporation of a PVA solution and SFs significantly enhanced the mechanical strength and deformation resistance of the loose accumulated sandy soil. The optimal ratio for the improved soil was S_P = 3% and S_L = 15 mm, which increased the cohesion from 24.54 kPa in untreated loose accumulated sandy soil to 196.03 kPa. These findings could be applied in

engineering practices to improve and reinforce loose accumulated sandy soil slopes in southeastern Xizang and provide a theoretical basis for such applications.

KEYWORDS

southeastern xizang, loose accumulated sandy soil, polyvinyl alcohol, sisal fiber, triaxial test, mechanism analysis

1 Introduction

The southeastern region of Xizang is characterized by rugged mountains and intricate valleys, where diverse topographies and highland environments create a complex and unique climate that accelerates rock erosion and weathering. Over time, geological processes have transformed landscapes, resulting in extensive loose accumulation of sandy soil slopes after weathering. Sandy soil, as a typical non-cohesive soil, has a loose structure and low cohesion [1], making it prone to rainfall-induced erosion, which can lead to landslides and debris flows, posing significant threats to the lives and properties of local residents [2–10]. Therefore, research on the improvement and reinforcement of loose accumulated soil is crucial to mitigate landslides and debris flows triggered by rainfall.

As global ecological issues escalate, countries are advancing their environmental protection strategies. Scholars are exploring new high-polymer materials and natural fibers as alternatives to traditional soil reinforcement materials such as cement and lime [11–13]. Polymer-based reinforcement techniques are environmentally friendly, in which polymers facilitate chemical reactions that transform liquid substances into solid forms, thereby binding loose sandy soil into a more robust structure. Polyvinyl alcohol (PVA) is a polymer that enhances soil water stability by forming a gel-soil bonding system with soil particles, thus improving both strength and water stability [14–17]. Cherdsak et al. [18] demonstrated a significant increase in the unconfined compressive strength of soil with the addition of PVA, and Cruz et al. [19] developed a novel biopolymer hydrogel using PVA to enhance soil water retention. Owing to their degradability, renewability, cost-effectiveness, and strong mechanical properties [13, 20–22], natural fibers are a major focus of geotechnical engineering. Various natural fibers, including palm, sisal, bamboo, and areca, have been employed for soil improvement with satisfactory reinforcement results [13, 23, 24]. Sisal fiber (SF) known for its toughness, strength, and resistance to wear and corrosion under harsh conditions is increasingly being applied as a reinforcement material for both inorganic and organic binding agents [25]. The high-strength characteristics of sisal fibers are closely related to their chemical composition and structure. They mainly contain components, such as cellulose, hemicellulose, pectin, and lignin, which together constitute a robust framework for fibers. Cellulose, as the primary structural component, endows sisal fibers with high strength and elasticity, and hemicellulose, pectin, and lignin further enhance their wear and corrosion resistance [26]. For instance, Sharanabasava Patil et al. [27] adopted SFs to enhance coarse aggregates in fly ash-red soil concrete, promoting sustainable concrete development. Song H et al. [28] employed the SFs to reinforce the synthesized aggregates. Aimin Z et al. [29] replaced the traditional steel fibers with mixed SFs to create UHPC materials, utilizing long (12 mm) and short (6 mm) fibers (2% fiber content). Additionally, Ekkachai Y et al. [30] demonstrated that SFs improved the structural performance of reinforced concrete columns, and Lima R P et al. [31] evaluated their effectiveness in enhancing the bending strength of one-way precast concrete slabs after cracking.

The aforementioned studies suggest that both PVA and SFs are eco-friendly materials for soil improvement. However, little research has focused on the mechanisms by which soil, fibers, and polymers interact to enhance loose accumulated sandy soils. This study addressed this gap by employing varying concentrations of PVA solutions and different lengths of SFs to improve sandy soil, quantitatively analyzing their effects on the mechanical properties of the improved soil, and investigating the intrinsic microstructural changes in the reinforced soil. These findings provide a theoretical basis and practical guidance for protecting and reinforcing loose accumulated sandy soil slopes in southeastern Xizang.

2 Experimental overview

2.1 Experimental materials

The sandy soil adopted in this experiment was sourced from loose accumulated sandy soil slopes along National Highway 318 in Bomi County, southeastern Xizang (Latitude 30°16′78″, Longitude 94°94′35″), at a sampling depth of approximately 2 m. After the soil

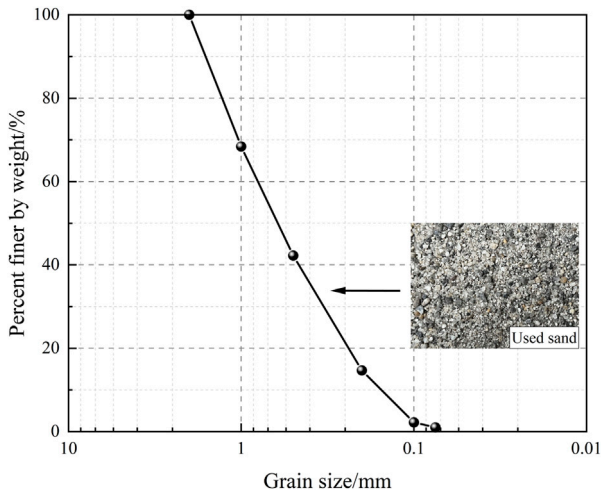

FIGURE 1
Grain size distribution curve of test sandy soil.

TABLE 1 Main physical and mechanical properties of sandy soils.

$\rho_{d\,max}$/ (g.cm^{-3})	ρ_d/ (g.cm^{-3})	$\rho_{d\,min}$/ (g.cm^{-3})	ω/ %	D_{50}/ mm	C_u	C_c
2.13	1.93	1.72	1.15	0.614	2.4	0.9

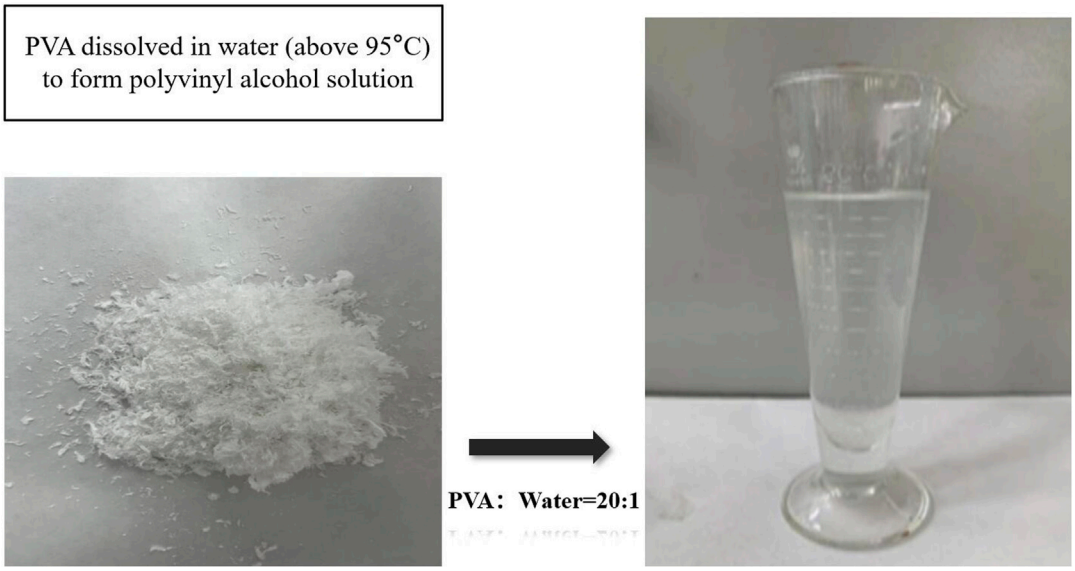

FIGURE 2
Polyvinyl alcohol solution.

TABLE 2 Basic physical properties of polyvinyl alcohol.

Viscosity/ mPa.s	Volatile matter/%	Ash content/%	pH
34.0-42.2	5	0.5	5.0-7.0

samples were retrieved, they were dried in an oven and subjected to sieve analysis according to the "Standard for Geotechnical Testing Methods" (GB/T 50123-2019) [32], resulting in the cumulative particle size distribution curve shown in Figure 1. Additional basic physical properties of the sandy soil are listed in Table 1.

The polymer utilized in this experiment was PVA (Figure 2). It is a polyhydroxy polymer valued for its water solubility, barrier properties, and biodegradability, and has the chemical formula $[C_2H_4O]_n$. It appears as a white, flaky, fibrous, or powdered solid that is odorless and soluble in water at temperatures above 95°C. In the experiment, the PVA solution was prepared by dissolving PVA in boiling water at a specific ratio. PVA has a lower degree of hydrolysis and retains some hydroxyl groups, enhancing its cohesive properties. The reaction process is shown in Equation 1, and the physical parameters are summarized in Table 2.

$$(C_2H_4O)_n + nH_2O \rightarrow nC_2H_50H + OH^- \quad (1)$$

where $(C_2H_4O)_n$ represents PVA; H_2O represents water molecules; C_2H_5OH signifies the ethanol; and OH^- denotes the hydroxide ions.

The SFs used in this experiment were natural bundled fibers, widely recognized for their advantages, such as low energy consumption, low manufacturing costs, high elasticity, large elastic modulus, acid and base resistance, and rapid water absorption. Considered ideal reinforcement materials for both inorganic and organic binders, their strength increased by 10%–15% in water compared to their dry strength [33]. These fibers were environmentally friendly with a rough surface texture, good dispersion, an average diameter of approximately 0.2 mm, and biodegradability. For the experiment, SFs with lengths of 6 mm, 9 mm, 12 mm, and 15 mm were selected (Figure 3). This study examined the effect of SFs length (S_L) on the mechanical properties of reinforced sandy soil, with the SFs content (S_F) defined as the ratio of the mass of SFs (m_d) to the mass of dry sand (m_s), calculated using the following Equation 2.

$$S_F = \frac{m_d}{m_s} \quad (2)$$

2.2 Experimental instruments

The triaxial shear test was performed using a 6T-type fully automatic triaxial shear apparatus consisting of three main components: a pressure chamber, a pressure volume controller, and a data processing system. The sample parameters were initialized using software, and various sensors automatically collected the data via a data processing system. The equipment used is illustrated in Figure 4. To analyze the microstructural changes in the loose accumulated sandy soil reinforced with SFs and PVA solution, a CX-200PLUS tungsten filament scanning electron microscope (SEM) was employed on the shear-tested samples. This SEM included an electron gun, a sample stage, electron lenses, detectors, an electron scanning system, a control system, a display, and image processing software (Figure 5).

2.3 Experimental procedure

Before the experiment, sandy soil was prepared according to the cumulative curve of the particle size distribution. To ensure a

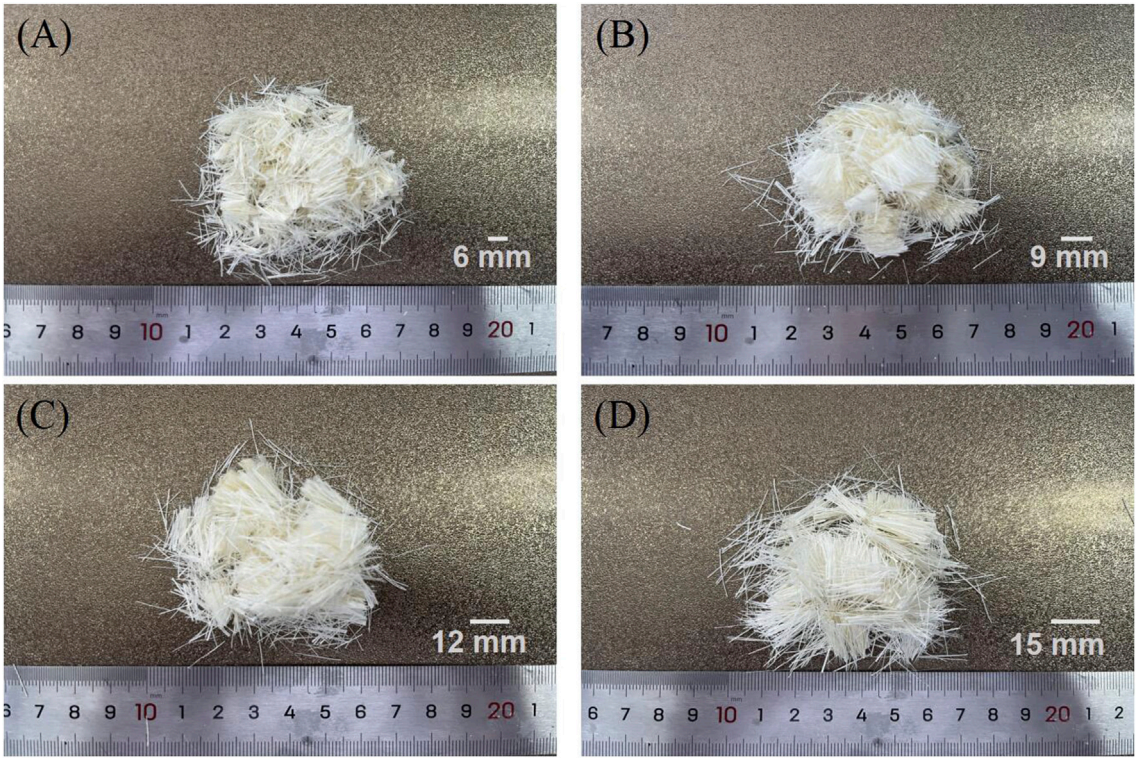

FIGURE 3
Sisal fiber. **(A)** S_L = 6 mm, **(B)** S_L = 9 mm, **(C)** S_L = 12 mm, **(D)** S_L = 15 mm.

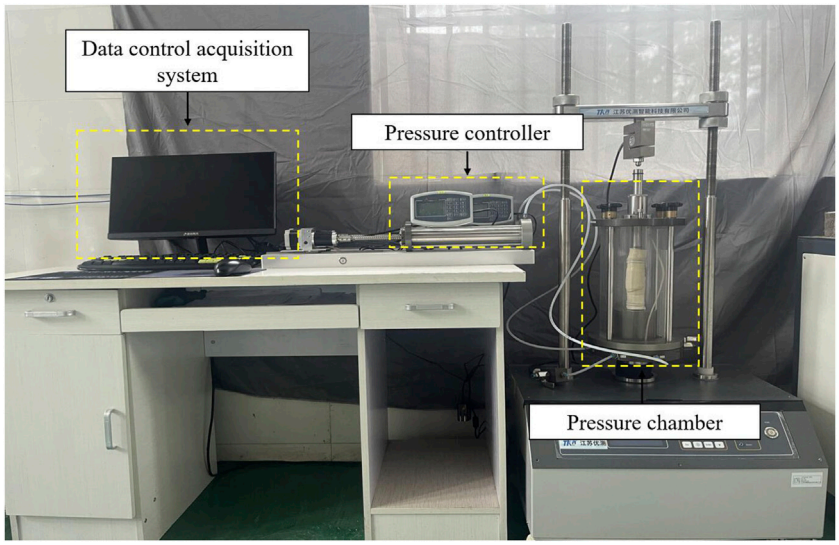

FIGURE 4
Fully automatic triaxial shear apparatus.

uniform distribution of SFs within the sandy soil, dry sand was thoroughly mixed with the fibers, followed by the addition of water and PVA solution to the mixture. The obtained soil-fiber mixture was compacted into a cylindrical mold in four layers, with each layer scarified using a soil cutter. The final cylindrical samples measured φ39.1 mm × h 80 mm. Triaxial shear tests were conducted using a 6T fully automatic triaxial apparatus, whereas microstructural analysis was performed using a CX-200PLUS tungsten filament scanning electron microscope (SEM). Each sample with identical parameters underwent three independent trials, and the most statistically

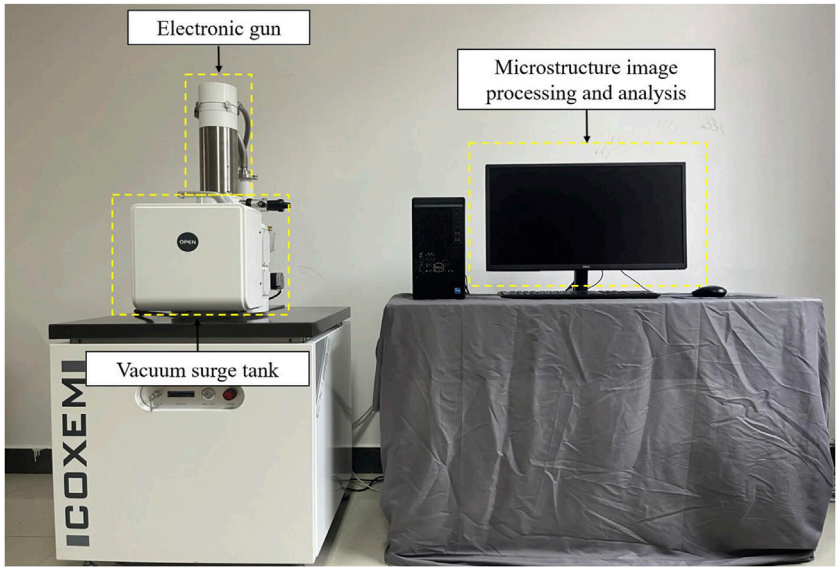

FIGURE 5
SEM scanning electron microscope.

significant data were selected for analysis. The detailed experimental procedure is as follows.

2.3.1 Triaxial shear test

A total of 25 groups of samples were prepared for this study, consisting of one group of untreated loose accumulated sandy soil and four groups of PVA-treated loose accumulated sandy soil.

The study prepared 4 groups of SFs-treated loose accumulated sandy soil and 16 groups of PVA and SF-reinforced loose accumulated sandy soil. Each group underwent consolidation drained shear testing under confining pressures of 100 kPa, 200 kPa, 300 kPa, and 400 kPa, following the "Standard for Geotechnical Testing Methods" (GB/T 50123—2019). The shear strain rate was set at 0.08 mm/min, and the testing was stopped when the strain (ε) reached 15%. To evaluate the effects of the PVA solution content (S_P) and SFs length (S_L) on the strength of the reinforced sandy soil, PVA solution contents of 1%, 2%, 3%, and 4% and SFs lengths of 6 mm, 9 mm, 12 mm, and 15 mm were tested, while the SFs content (S_F) remained constant at 0.8% (both PVA and fiber contents were percentages of the total sample mass). The initial moisture content was controlled at w = 1.15% and the density at ρ_d = 1.93 g/cm^3, with the untreated sandy soil of the same moisture content and density serving as a control.

2.3.2 Microstructural analysis

To prepare the samples for SEM observation, they were air-dried to remove moisture, volatile substances, and magnetic materials. After drying, internal samples of dimensions 10 mm × 5 mm × 2 mm were extracted for analysis. Because the sandy materials were non-conductive, directly placing them under the electron microscope could cause damage to the electron beam and reduce the edge resolution. To obtain high-quality images, the surfaces of the samples were coated with a metallic layer to minimize electron beam penetration and enhance the edge resolution, thus protecting the sensitive samples. CX-200PLUS SEM was then applied to observe the microstructural characteristics of the loose accumulated sandy soil before and after reinforcement with PVA solution and SFs, with a particular focus on the reinforcement mechanism.

3 Test results and analysis

3.1 Characteristics of deviator stress and axial strain curves

The deviator stress-strain curves for untreated loose accumulated sandy soil and sandy soil reinforced with PVA solution and SFs were plotted based on the results of triaxial consolidated drained shear tests (CD) (Figure 6).

In Figure 6A, the deviator stress-strain curve for the untreated loose accumulated sandy soil demonstrated that under varying confining pressures, the samples primarily exhibited strain softening. Initially, the samples exhibited elastic deformation with a linear increase in the strain. Once the strain exceeded 2%, the curve entered a nonlinear phase, where the rate of increase in the deviator stress gradually decreased, and higher confining pressures required greater axial strain to achieve the peak deviator stress. Figures 6B, C present the deviator stress-strain curves for sandy soil reinforced with a PVA solution, where the samples also demonstrated strain softening. At confining pressures of 100 and 200 kPa, the peak deviator stress fluctuated with increasing PVA solution content. In contrast, at 300 and 400 kPa, it gradually increased with increasing PVA content, whereas the peak values did not exhibit a significant improvement compared with the untreated sandy soil. The post-peak softening phenomenon improved, although the extent of this improvement was relatively modest. Figures 6D,E illustrate the

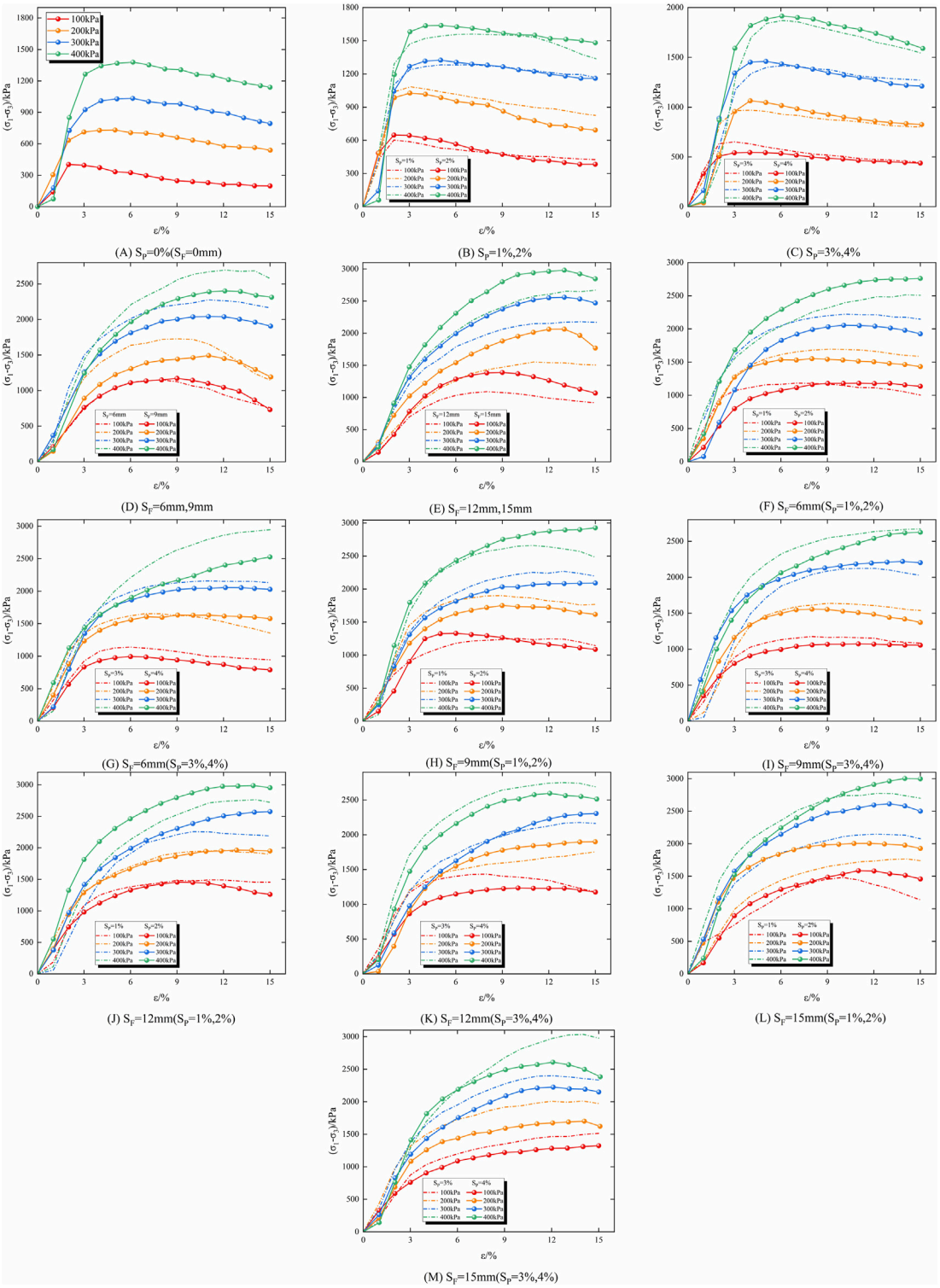

FIGURE 6
Deviator stress-strain curves of untreated loose accumulated sandy soil and modified loose accumulated sandy soil with PVA and SFs. Note: S_F is the length of sisal fiber, and S_P is the content of polyvinyl alcohol. **(A)** Untreated loose accumulated soil. **(B)** Modified loose accumulated sandy soil with PAV solution content of 1% and 2%. **(C)** Modified loose accumulated sandy soil with PAV solution content of 3% and 4%. **(D)** Modified loose accumulated sandy soil with SFs lengths of 6 mm and 9 mm. **(E)** Modified loose accumulated sandy soil with SFs lengths of 12 mm and 15 mm. **(F)** Modified loose accumulated sandy soil with SFs length of 6 mm and PAV solution content of 1% and 2%. **(G)** Modified loose accumulated sandy soil with SFs length of 6mm and PAV solution content of 3% and 4%. **(H)** Modified loose accumulated sandy soil with SFs length of 9mm and PAV solution content of 1% and 2%. **(I)** Modified loose accumulated sandy soil with SFs length of 9 mm and PAV solution content of 3% and 4%. **(J)** modified loose accumulated sandy soil with SFs length of 12 mm and PAV solution content of 1% and 2%. **(K)** modified loose accumulated sandy soil with SFs length of 12 mm and PAV solution content of 3% and 4%. **(L)** Modified loose accumulated sandy soil with SFs length of 15 mm and PAV solution content of 1% and 2%. **(M)** Modified loose accumulated sandy soil with SFs length of 15 mm and PAV solution content of 3% and 4%View less.

TABLE 3 Peak deviator stress of untreated loose accumulated soil and modified loose accumulated sandy soil with PVA solution and SFs.

Number	S_P/%	S_L/mm	S_F/%	Confining pressure/kPa			
				100	200	300	400
S-1	—	—	—	424	744	1,042	1,390
S-2	1	—	—	612	1,104	1,301	1,580
S-3	2	—	—	663	1,049	1,337	1,665
S-4	3	—	—	667	1,065	1,435	1887
S-5	4	—	—	558	1,081	1,472	1927
S-6	—	6	—	1,164	1749	2,296	2,729
S-7	—	9	—	1,184	1,496	2080	2,428
S-8	—	12	—	1,199	1873	2,188	2,685
S-9	—	15	—	1,405	2095	2,575	3,015
S-10	1	6	0.8	1,197	1716	2,231	2,538
S-11	2	6	0.8	1,197	1,565	2070	2,788
S-12	3	6	0.8	1,149	1,670	2,177	2,959
S-13	4	6	0.8	1,009	1,651	2076	2,750
S-14	1	9	0.8	1,266	1911	2,287	2,674
S-15	2	9	0.8	1,344	1755	2,107	2,928
S-16	3	9	0.8	1,192	1,650	2,142	2,691
S-17	4	9	0.8	1,088	1,577	2,233	2,646
S-18	1	12	0.8	1,510	1968	2,279	2,783
S-19	2	12	0.8	1,473	1976	2,594	3,002
S-20	3	12	0.8	1,410	1783	2,193	2,785
S-21	4	12	0.8	1,245	1919	2,323	2,610
S-22	1	15	0.8	1,497	1878	2,224	2,810
S-23	2	15	0.8	1,601	2023	2,721	3,020
S-24	3	15	0.8	1,517	2,116	2,418	3,056
S-25	4	15	0.8	1,353	1811	2,244	2,625

deviator stress-strain curves for the sandy soil reinforced with SFs, increasing the peak deviator stress compared with the untreated sandy soil. However, once the peak strength was reached, the deviator stress decreased sharply. Figures 6F–M depict the deviator stress-strain curves for the sandy soil reinforced with a combination of PVA solution and SFs, revealing an elastic-plastic stress-strain relationship. The failure of these samples occurred in two phases. For strains less than or equal to 3%, the samples exhibited elastic deformation with a linear increase in the deviator stress, whereas beyond 3% strain, they underwent plastic deformation. In this phase, the stress-strain relationship exhibited a nonlinear upward trend with a gradual decrease in the rate of increase in deviator stress, resulting in a plateau. The curves exhibited a clear inflection point and maintained a softening characteristic, indicating a distinct peak in the deviator stress, followed by only slight reductions post-peak.

3.2 Relationship between peak deviator stress and confining pressure

According to the "Standard for Geotechnical Testing Methods" (GB/T 50123—2019), the peak strength was recorded at the moment of peak during the shear process of the sample. If no peak strength was evident, the strength corresponding to ε = 15% was used as the peak strength. Table 3 presents the peak deviator stress for the untreated loose accumulated sandy soil and sandy soil reinforced with the PVA solution and SFs under various confining pressures. The table indicates that the peak deviator stress for the sandy soil reinforced with the combination of PVA solution and SFs increased monotonically with the PVA content and length of the SFs. For the PVA contents of S_P = 2% and S_P = 3% and the SF length of S_L = 15 mm, the peak deviator stresses reached 1,601 kPa, 2023 kPa, 2,721 kPa, and 3,020 kPa under different confining pressures. For S_L = 15 mm, the corresponding values were 1,517 kPa, 2,116 kPa, 2,418 kPa, and 3,056 kPa. Compared with the peak deviator stress of the untreated sandy soil (424 kPa, 744 kPa, 1,042 kPa, and 1,390 kPa), these values represented increases of 377%, 271%, 261%, and 217%, and 357%, 284%, 232%, and 219%, respectively. As the confining pressure increased, the peak deviator stress of the samples also increased, whereas the relative increase compared to the untreated sandy soil showed a declining trend.

The data in Table 3 were plotted in the $(\sigma_1 - \sigma_3)_{max} \sim \sigma_3$ relationship graph. Figure 7 demonstrates that the $(\sigma_1 - \sigma_3)_{max} \sim \sigma_3$ relationship curves for both the untreated sandy soil and the sandy soil reinforced with PVA solution and SFs exhibited a nearly linear relationship, influenced by the soil particle arrangement and aggregation. The fluctuating characteristics of the slope and intercept of the regression equation for the peak deviator stress can be analyzed using linear regression principles based on the least-squares method. The coefficient R^2 indicated the correlation between the fitted line and the experimental points, with a value closer to 1 representing a higher degree of fit. Figure 7 reveals that all the fitted lines had determination coefficients R^2 higher than 0.958, indicating a high degree of fit that could be used to predict the trends in the peak deviator stress for the untreated loose accumulated sandy soil and the variations in the PVA solution content and SF length under different confining pressures. To represent the relationship between the peak deviator stress changes influenced by both factors simultaneously, a simple linear model was employed, as described by the following Equation 3.

$$(\sigma_1 - \sigma_3)_{max} = a\sigma_3 + b \tag{3}$$

where a and b are the parameters associated with the characteristics of untreated loose accumulated sandy soil and sandy soil reinforced with PVA solution and SFs, respectively.

The relationship between parameters a and b with respect to the concentration of the PVA solution is illustrated using samples with varying concentrations of PVA solution and a SFs length of S_L = 15 mm (Figure 8). The results is shown in Equations 3, 4.

$$a = 0.1804x + 4.056 \tag{4}$$

$$b = 135.2x + 610.6 \tag{5}$$

where x is the PVA solution content (%).

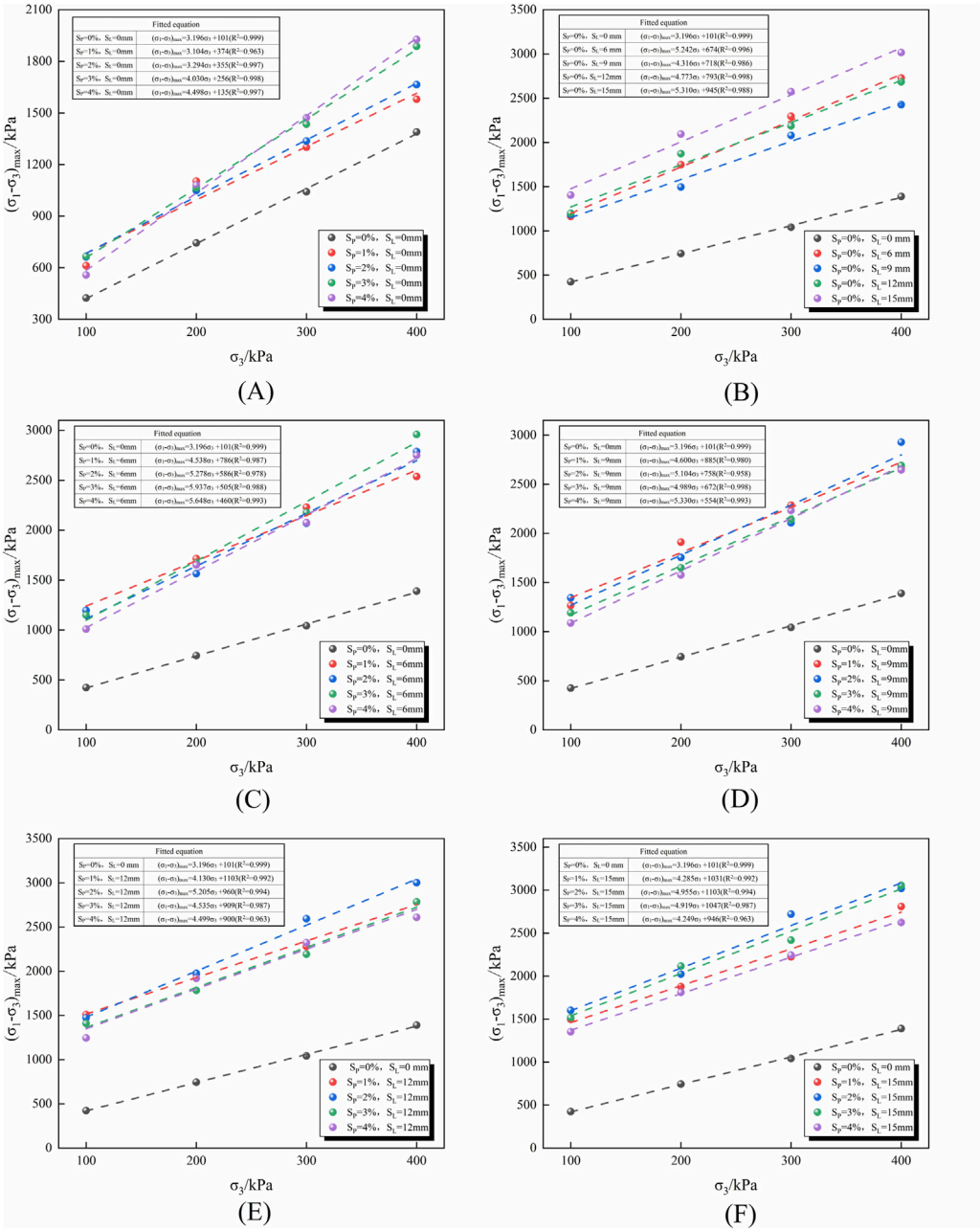

FIGURE 7
$(\sigma_1-\sigma_3)_{max}-\sigma_3$ relationship curve of untreated loose accumulated soil and modified loose accumulated sandy soil with PVA and SFs. **(A)** $(\sigma_1-\sigma_3)_{max}-\sigma_3$ relationship curve of untreated loose accumulated soil and modified loose accumulated sandy soil with different PVA solution contents **(B)** $(\sigma_1-\sigma_3)_{max}-\sigma_3$ relationship curve of untreated loose accumulated soil and modified loose accumulated sandy soil with different lengths of SFs **(C)** $(\sigma_1-\sigma_3)_{max}-\sigma_3$ relationship curve of untreated loose accumulated soil and modified loose accumulated sandy soil with S_L=6mm and different PVA solution contents **(D)** $(\sigma_1-\sigma_3)_{max}-\sigma_3$ relationship curve of untreated loose accumulated soil and modified loose accumulated sandy soil with S_L=9mm and different PVA solution contents **(E)** $(\sigma_1-\sigma_3)_{max}-\sigma_3$ relationship curve of untreated loose accumulated soil and modified loose accumulated sandy soil with S_L=12mm and different PVA solution contents **(F)** $(\sigma_1-\sigma_3)_{max}-\sigma_3$ relationship curve of untreated loose accumulated soil and modified loose accumulated sandy soil with S_L=15mm and different PVA solution contents.

3.3 Shear strength characteristics

Shear strength is a crucial index in geotechnics, represented by shear strength parameters. To elucidate the influence of the PVA solution content and SFs length on these parameters, the cohesion (c) and internal friction angle (φ) values were calculated for both untreated loose accumulated sandy soil and sandy soil reinforced with PVA solution and SFs.

Figure 9 presents a bar chart illustrating the relationship between the shear strength parameters and varying PVA solution content, including the parameters for the untreated loose accumulated sandy soil for comparison. As shown in Figure 9A, incorporating the PVA

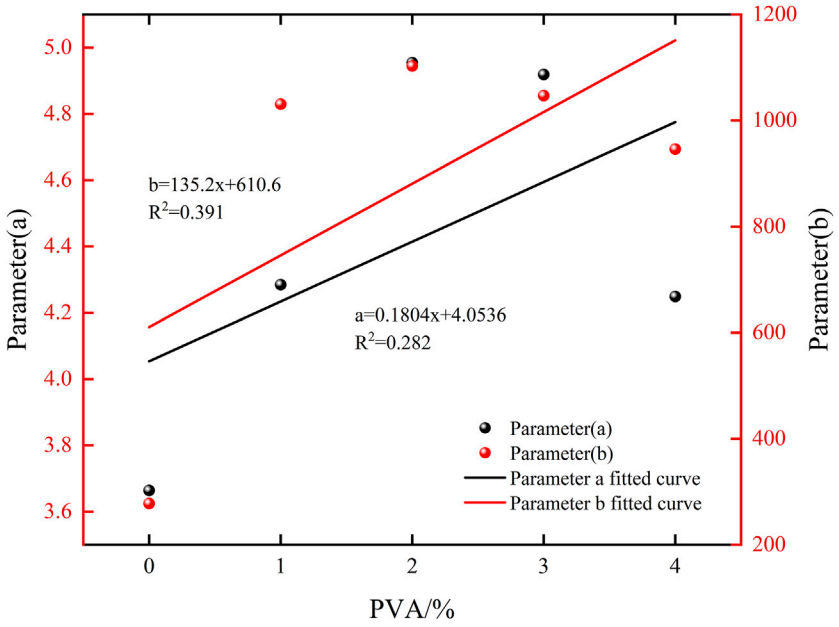

FIGURE 8
Curve fitting for the effect of peak bias stress with different PVA content at S_L = 15 mm.

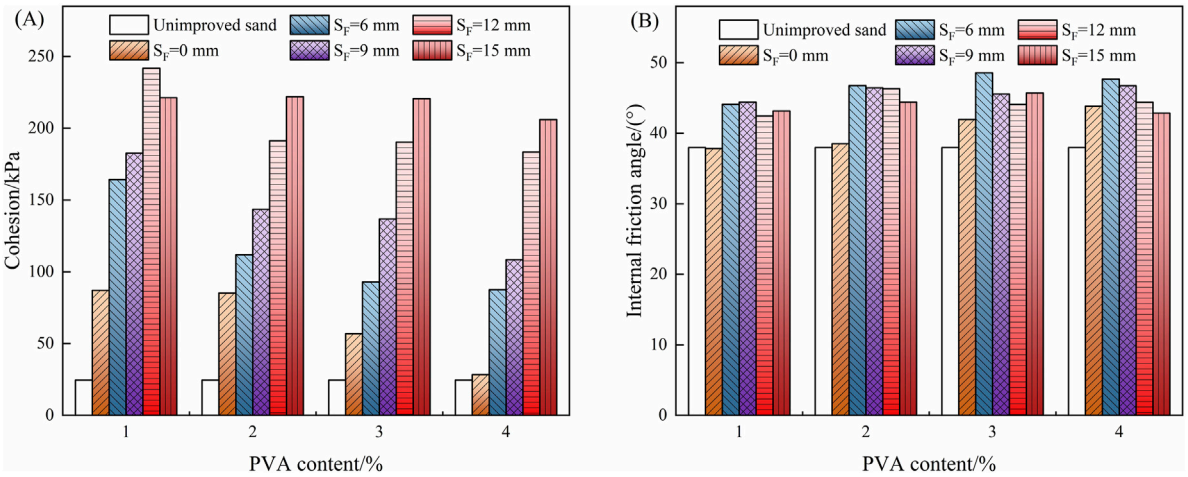

FIGURE 9
Relationship between shear strength parameters and PVA content. **(A)** relationship between cohesion and PVA content, **(B)** relationship between internal friction angle and PVA content.

solution significantly enhanced the cohesion of the samples compared with that of the untreated sandy soil. However, as the PVA content increased, the cohesion decreased. This trend suggested that while excess PVA effectively coated and intertwined the sandy particles, its wet and slippery characteristics during shear caused sliding among the PVA-coated particles, weakening their interconnections and reducing their cohesion. Conversely, Figure 9B illustrates that for the samples compounded with both the PVA solution and SFs, the internal friction angle initially increased with the PVA content but then decreased. The fluctuations in this parameter were relatively small, indicating that the significant changes observed in the cohesion were not reflected in the internal friction angle.

Figure 10 presents a bar chart illustrating the relationship between the shear strength parameters and varying SFs lengths, with untreated sandy soil parameters for comparison. Figure 10A reveals that with a constant PVA solution content, the cohesion of the reinforced sandy soil increased as the length of the SFs increased, peaking at 241.76 kPa for S_L = 12 mm (S_P = 1%). However, as the SFs length continued to increase, the cohesion decreased, with S_L = 15 mm (S_P = 1%) showing a cohesion value of 221.34 kPa. These values represented 985% and 901% of the cohesion of untreated sandy soil (24.54 kPa). The cohesion trend for the S_L = 12 mm sample exhibited a rapid initial increase that gradually stabilized, in contrast to the trend for the S_L = 15 mm sample.

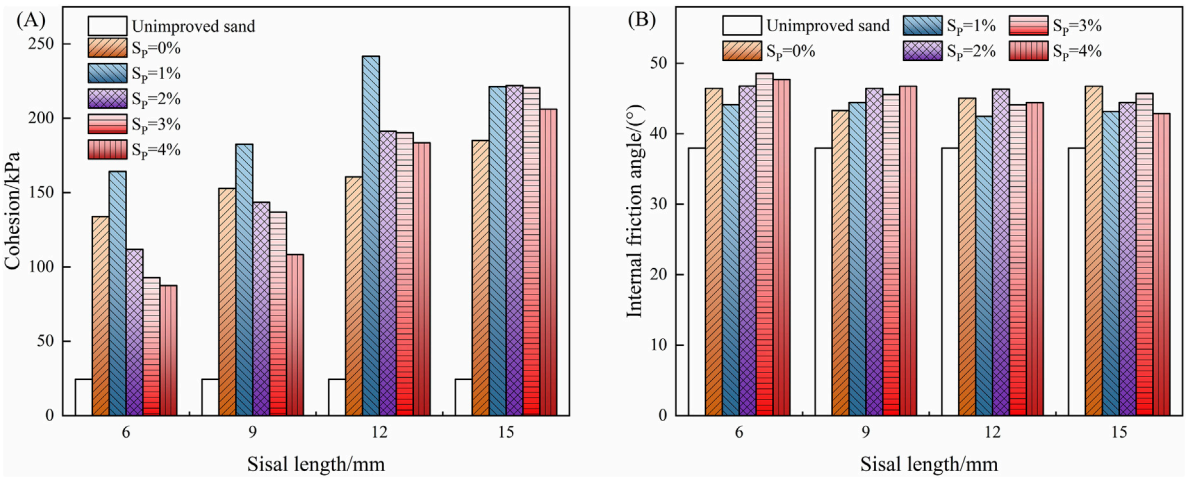

FIGURE 10
Relationship between shear strength parameters and SFs lengths. **(A)** relationship between cohesion and SFs length, **(B)** relationship between internal friction angle and SFs length.

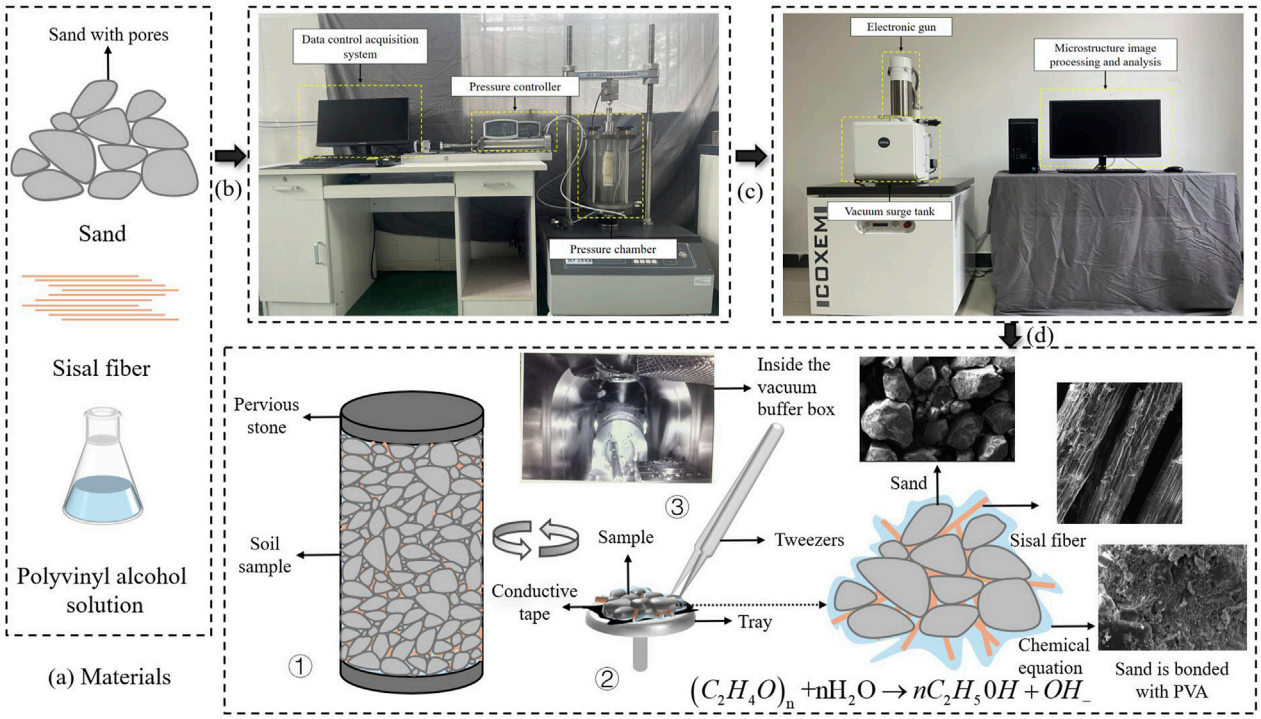

FIGURE 11
Schematic diagram of the mechanism of reinforcing sandy soil with PVA and SFs composite. **(A)** Experimental materials. **(B)** Triaxial test. **(C)** SEM experiment. **(D)** Microscopic analysis.

Figure 10B shows that the internal friction angle of the reinforced sandy soil exhibited a waveform pattern as the SFs length increased with minimal overall fluctuation. The changes in the internal friction angles were all less than 4°. This indicated that the PVA solution improved the bonding between the SFs and soil particles, thereby reducing the particle spacing. During shear, this enhanced the interlocking and friction intensity among the soil particles, leading to variations in the internal friction angle.

4 Mechanism analysis and discussion

4.1 Microscopic mechanism analysis

The mechanism of reinforcing loose accumulated sandy soil using a composite of PVA solution and SFs is illustrated in the schematic diagram in Figure 11. To analyze the microscopic structural characteristics of untreated loose accumulated sandy

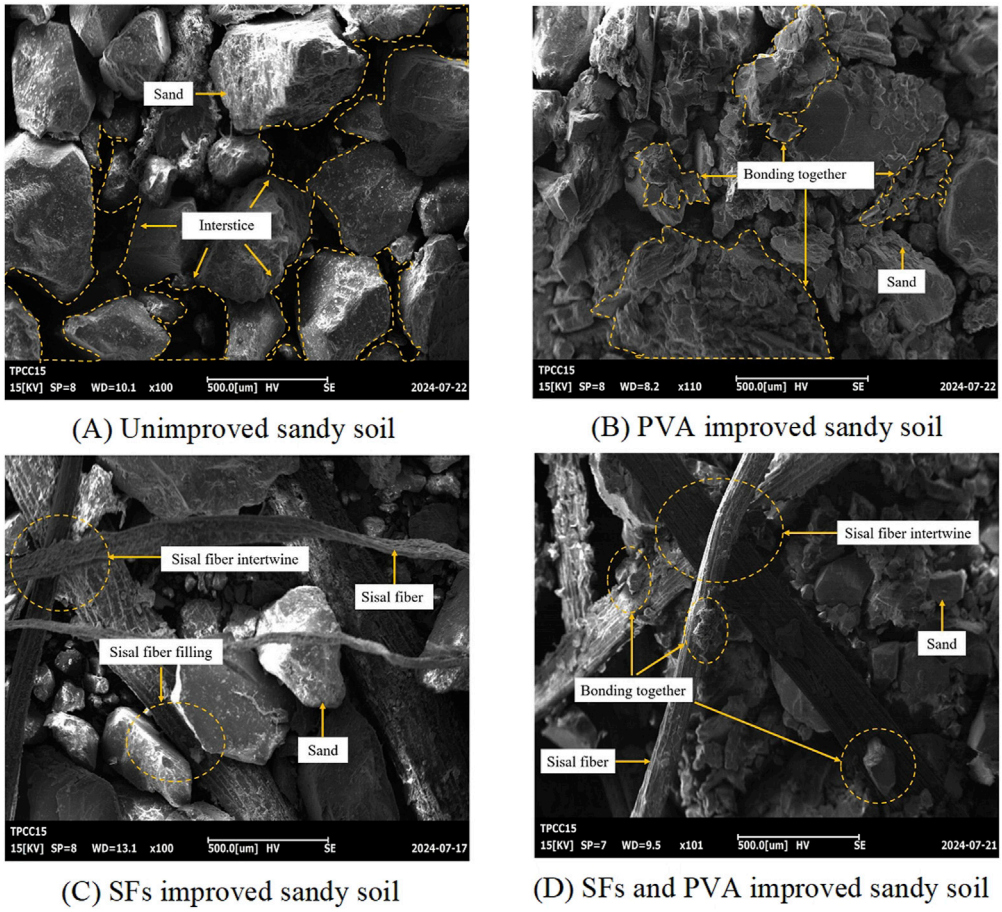

FIGURE 12
SEM images of untreated loose accumulated soil and modified loose accumulated sandy soil with PVA solution and SFs. **(A)** Unimproved sandy soil **(B)** PVA improved sandy soil **(C)** SFs improved sandy soil **(D)** SFs and PVA improved sandy soil.

soil, PVA solution, and SF-reinforced sandy soil, SEM with a tungsten filament (CX-200PLUS) was used (Figure 12). Sandy soil primarily consisted of sand grains that were non-cohesive and relied on particle interlocking and friction for stability. Figure 12A shows that the untreated loose accumulated sandy soil had a loose structure with a wide distribution of pore spaces between the particles. The cohesive PVA solution wrapped around and intertwined the sandy particles, improving their arrangement and facilitating more compact packing, thereby reducing the pore spaces. Figure 12B demonstrates how the PVA solution formed a solidified membrane around the sand grains, tightly bonding them to create a "granular structure" with enhanced strength and shape stability. Loose accumulated sandy soil, characterized by rough, angular particle surfaces, consists of debris that remained in its original position after weathering, leading to certain voids between bonded sand grains. As an ideal reinforcing material with both inorganic and organic binding properties, SFs were randomly distributed among the sandy particles, forming a woven "net" that enveloped the soil and reduced displacement and deformation. Figure 12C presents the SFs filling the spaces between the soil particles intersecting to form a fibrous network binding the grains together. These fibers distributed within the pores restricted radial deformation and enhanced the overall stability of the soil structure. The cohesion provided by the PVA solution synergized with the SFs anchoring effect, resulting in a stable structure that significantly improved the mechanical properties of the loose accumulated sandy soil.

Figure 12D shows that the soil particles were interconnected through the bonds among themselves, between the soil particles and fibers, and among the fibers. The voids between the sand grains were filled with SFs and the PVA solution. The intertwined SFs were effectively anchored within the adhesive formed by the PVA solution, enhancing the particle cohesion. The exceptional toughness of the SFs allowed them to connect across the fractures like "spider silk," providing the tensile strength and preventing the deformation of the sandy soil. The PVA solution exhibited strong adhesion to the fiber-containing materials, with hydroxyl functional groups bonding with the surfaces of both the soil particles and fibers, improving the interfacial properties and creating a tighter connection. This enhanced bonding significantly increased the stability of the composite structure formed by the SFs and sandy soil. The incorporation of the PVA solution and SFs formed a stable composite structure, improving the overall stability and safety of the soil matrix. The synergistic effect of the PVA solution and SFs enhanced the mechanical properties of the soil and contributed to its resilience to deformation and failure under load.

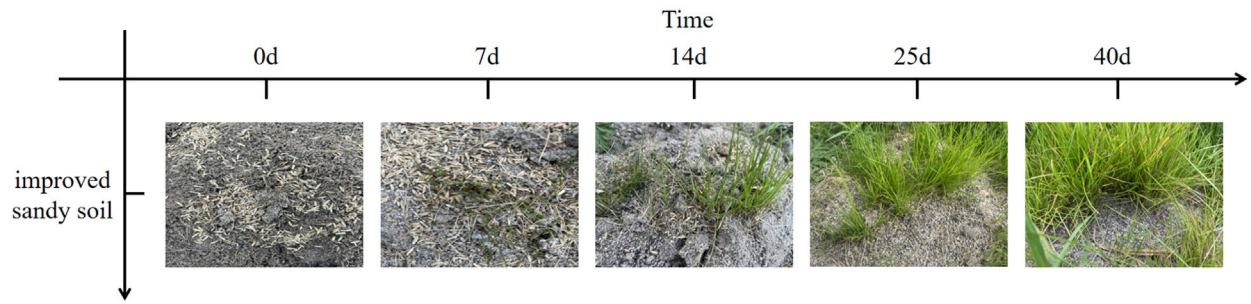

FIGURE 13
Outdoor planting in modified sandy soil.

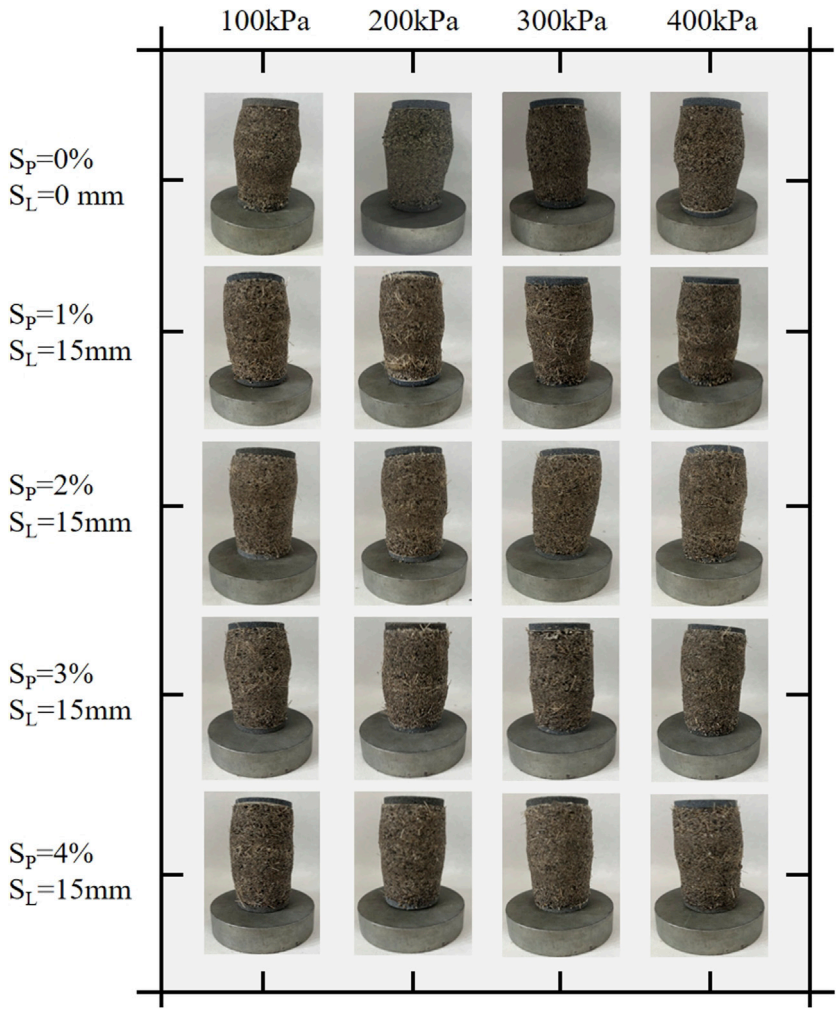

FIGURE 14
Specimen drawing after triaxial shear.

4.2 Discussion

Before conducting the experiments, outdoor seeding was performed on the PVA solution and the SF-reinforced loose accumulated sandy soil to ensure the adaptability of the materials to the high-altitude environment without harming the surrounding ecology. This seeding, performed in May during a period of ample rainfall and sufficient sunlight, resulted in the growth of native plants in reinforced sandy soil. The successful growth of these plants indicated that the modified materials were environmentally benign,

rendering them suitable for improving and reinforcing the loose slopes in the southeastern Xizang Region (Figure 13).

Ma K et al. [34] explored the potential of using polyurethane organic polymer and sisal fiber to improve the mechanical performance of sand. The results indicated a significant increase in the UCS and DTS of the reinforced sand with increasing polymer content, fiber content, and dry density. This study utilized a composite of PVA and SFs to effectively enhance the properties of loose accumulated sandy soils. Notably, when SFs with a length of S_L = 15 mm were combined with various PVA solution concentrations, the cohesion exhibited stable fluctuations, with the peak shear strength occurring at the PVA concentrations of S_P = 2% and S_P = 3%. Examination of the shear behavior of the untreated sandy soil and the modified sandy soil with 15 mm SFs at different PVA concentrations revealed that the failure mode of the samples was dominant, with no shear failure planes identified. Compared with the untreated sandy soil, the modified sandy soil exhibited a significantly reduced failure mode. At a confining pressure of 400 kPa, visible deformation was observed in the modified samples, indicating that the uneven dispersion of SFs during preparation caused aggregation and shear deformation under high confining pressures. Nevertheless, the samples with S_L = 15 mm (S_P = 3%) exhibited an improved overall stability and less noticeable compressive deformation at different confining pressures (Figure 14).

In practical engineering applications, both cost-effectiveness and safety stability are crucial. The multiphase and variable nature of geological materials can contribute to their inherent uncertainty, which is why geotechnical engineering lacks the rigor of other disciplines. As a highly practical field that operates on a conceptual design framework, geotechnical engineering relies on robust theories, reasonable experiments, and validation through practical experience as the essential foundations for successful applications.

5 Conclusion

Based on the principles of "ecological priority and green development," this study focused on modifying the loose accumulated sandy soil in southeastern Xizang using a composite of PVA solution and SFs. Various consolidated drained triaxial compression tests were performed under different confining pressures to examine the effects of varying PVA solution concentrations and SFs lengths on the strength characteristics of the modified sandy soil. SEM was employed to analyze the internal structures of the samples after shear testing. The experimental results led to the following conclusions.

(1) The stress-strain curves of the modified loose accumulated sandy soil, under varying PVA solution concentrations and SFs lengths, exhibited strain-softening behavior, characterized by a distinct peak in the deviator stress. The stress-strain relationship demonstrated elastic-plastic characteristics. The failure of the samples occurred in two main stages. At strains less than or equal to 3%, the samples were in the elastic deformation stage with a linear increase in the deviator stress. As the strain exceeded 3%, the deformation became plastic, and the deviator stress-strain relationship exhibited a nonlinear increase, with the rate of deviator stress growth gradually decreasing and trending towards a smooth decline.

(2) The incorporation of PVA solution and SFs significantly affected the peak deviator stress of the samples. As the concentration of the PVA solution and length of the SFs increased, the peak deviator stress also increased under a constant confining pressure. The relationship curve between $(\sigma_1-\sigma_3)_{max}$~$\sigma_3$ for both the untreated loose accumulated sandy soil and the modified sandy soil with the PVA solution and SFs approximated a linear trend.

(3) SEM analysis revealed that the pores between the sand particles were filled with SFs and PVA solution. The interwoven SFs bonded effectively within the adhesive formed by the PVA solution, thereby increasing the cohesion between the particles. The improved toughness of the fibers enabled them to connect both sides of the fracture surface, similar to "spider silk," providing the tensile strength that mitigated the soil deformation. Additionally, the water-soluble PVA exhibited strong adhesion to both fibers and soil particles. The hydroxyl groups in the PVA molecules bonded with the surfaces of the soil particles and fibers, enhancing the interfacial properties and improving the connection between the SFs and soil particles, which increased the overall structural stability.

(4) This study analyzed the loose accumulated sandy soil in southeastern Xizang and discovered that composite modification using a PVA solution and SFs was highly effective. The optimal combination for practical engineering reinforcement was a PVA solution concentration of S_P = 3% and SFs length of S_L = 15 mm. The modified soil exhibited a significant increase in the cohesion, rising from 24.54 kPa in the untreated sandy soil to 196.03 kPa, thus achieving both economic and reinforcement effectiveness.

Data availability statement

The original contributions presented in the study are included in the article/supplementary material, further inquiries can be directed to the corresponding author.

Author contributions

DS: Conceptualization, Data curation, Methodology, Validation, Writing–original draft, Writing–review and editing. PW: Conceptualization, Funding acquisition, Supervision, Writing–review and editing. LC: Conceptualization, Formal Analysis, Funding acquisition, Resources, Supervision, Visualization, Writing–review and editing. WZ: Conceptualization, Methodology, Supervision, Validation, Writing–review and editing. ZL: Conceptualization, Data curation, Writing–review and editing. QW: Conceptualization, Data curation, Investigation, Visualization, Writing–review and editing.

Funding

The author(s) declare that financial support was received for the research, authorship, and/or publication of this article. Key Program of Natural Foundation of Science and Technology Department of Xizang Autonomous Region, China (XZ202201ZR0068G); National Natural Science Foundation of China - Regional Innovation and Development Joint Fund Key Program (U22A20594); Key Program of Natural Foundation of Science and Technology Department of Xizang Autonomous Region, China (XZ202301ZR0033G); Sponsored by the Graduate Education Innovation Program of Xizang Agricultural and Animal Husbandry College (YJS2024-45).

Acknowledgments

We gratefully acknowledge financial support from the National Natural Science Foundation of China - We also extend our heartfelt thanks to the two participants who willingly participated in the on-site experiment and to the experts who generously shared their insights during the online survey. Additionally, we thank Wang Jiahui from Hohai University and Li Zhongyao from Chongqing Jiaotong University for their valuable insights and encouragement, which contributed to my development as a researcher.

Conflict of interest

The authors declare that the research was conducted with no commercial or financial relationships that could be perceived as potential conflicts of interest.

Publisher's note

References

1. Wang LW, Liu J, Xi LZ, Wu LL, Zheng C, Qi CQ, et al. Study on triaxial shear test of improved sandy soil based on polymer composite materials. *Hydrogeology Eng Geology* (2020) 47(04):149–157. doi:10.16030/j.cnki.issn.1000-3665.201911005

2. Yuan Y, Wang C, Liang FY. Erosion characterization of sandy soil particles based on improved SSRT test method. *Chin J Geotechnical Eng* (2020) 42(S1):198–202. doi:10.11779/CJGE2020S1039

3. Wu Z, Liu J, He Y, Wei JH, Song ZZ, Sun R, et al. Polymer curing agent vegetation composite improvement of sand erosion resistance characteristics. *Progr. Water Conser. Hydropower. Techno* (2021) 41(05):28–33+70. doi:10.3880/j.issn.1006.7647.2021.05.005

4. Yang F, Li ML, Wang X, Wu E, Wang F, Lv J, et al. Physical modeling test of rainfall on loess fill slopes based on NbS structure[J/OL]. *Adv Eng Sci* (2021)(05):24–34. doi:10.15961/j.jsuese.202300560

5. He J, Huang A, Ji J, Qu S, Hang L. Enzyme induced carbonate precipitation with fibers for the improvement of clay soil slopes against rainfall and surface runoff erosions. *Transportation Geotechnics* (2023) 42:101074. doi:10.1016/j.trgeo.2023.101074

6. Wang G, Sassa K. Study on the excess pore pressure generation at failure and the resulting movement of sandy slope in flume test by rainfall. *Landslides* (2000) 37(2):40–7. doi:10.3313/jls1964.37.2_40

7. Wang TL, Liu JK, Tian YG. Study on static properties of cement and lime-amended soil under freeze-thaw. *Rock Soil Mech* (2011) 32(01):193–8. doi:10.16285/j.rsm.2011.01.010

8. Wang L, Zhang K, Chen Y, Wang S, Tian D, Li X, et al. Progressive deformation mechanism of colluvial landslides induced by rainfall: insights from long-term field monitoring and numerical study. *Landslides* (2024) 1–18. doi:10.1007/s10346-024-02344-3

9. Jia K, Bingcheng W, Zhiqiu G, Zhou S, Chen H, Shen H. Research on machine learning forecasting and early warning model for rainfall-induced landslides in Yunnan province. *Scientific Rep* (2024) 14(1):14049. doi:10.1038/S41598-024-64679-0

10. Peng T, Chen N, Hu G, Tian S, Ni H, Huang L. New rulers for estimating the magnitude of catastrophic debris flows. *Nat Hazards* (2024) 1–14. doi:10.1007/S11069-024-06795-8

11. Wang S, Xue Q, Zhu Y, Li G, Wu Z, Zhao K. Experimental study on material ratio and strength performance of geopolymer-improved soil. *Construction Building Mater* (2020) 267:120469. doi:10.1016/j.conbuildmat.2020.120469

12. Williams KA, Ruiz SA, Petroselli C, Walker N, Fletcher DM, Pileio G, et al. Physical characterisation of chia mucilage polymeric gel and its implications on rhizosphere science - integrating imaging, MRI, and modelling to gain insights into plant and microbial amended soils. *Soil Biol Biochem* (2021) 162. doi:10.1016/J.SOILBIO.2021.108404

13. Bai Y, Liu J, Song Z, Chen Z, Jiang C, Lan X, et al. Unconfined compressive properties of composite sand stabilized with organic polymers and natural fibers. *Polymers* (2019) 11(10):1576. doi:10.3390/polym11101576

14. Ren F, Ding H, Dong B, Qian X, Liu J, Tan J. Study on the improvement of soil properties using hydrophilic-hydrophobic biopolymer crosslinking. *Construction Building Mater* (2024) 415:415135101. doi:10.1016/J.CONBUILDMAT.2024.135101

15. Zhang JR, Liu JH, Cheng Y, Jiang T, Sun D, Saberian M, et al. Water-retention behaviour and microscopic analysis of two biopolymer-improved sandy soils. *Construction Building Mater* (2023) 403. doi:10.1016/J.CONBUILDMAT.2023.133202

16. Li Z, Zhao Z, Shi H, Li W, Wang B, Wang P. Experimental investigation of mechanical, permeability, and microstructural properties of PVA-improved sand under dry-wet cycling conditions. *Front Phys* (2021) 9:761754. doi:10.3389/fphy.2021.761754

17. Zhao Z, Li W, Shi H, Li Z, Li J, Zhao C, et al. Strength of coarse-grained soil stabilized by poly (vinyl alcohol) solution and silica fume under wet–dry cycles. *Polymers* (2022) 14(17):3555. doi:10.3390/polym14173555

18. Cherdsak S, Suksun H, Chakkrid Y, Arul A Evaluation of polyvinyl alcohol and high calcium fly ash based geopolymer for the improvement of soft Bangkok clay. *Transportation Geotechnics* (2021):27100476. doi:10.1016/j.trgeo.2020.100476

19. Fabian DRC, Durpekova S, Dusankova M, Hanusova D, Bergerova ED, Sedlacik M, et al. Renewable whey-based hydrogel with polysaccharides and polyvinyl alcohol as a soil amendment for sustainable agricultural application. *Int J Biol macromolecules* (2024) 259:129056. doi:10.1016/J.IJBIOMAC.2023.129056

20. Tang C, Shi B, Gao W, Chen F, Cai Y. Strength and mechanical behavior of short polypropylene fiber reinforced and cement stabilized clayey soil. *Geotextiles and Geomembranes* (2006) 25(3):194–202. doi:10.1016/j.geotexmem.2006.11.002

21. Oliveira VJP, Correia SAA, Teles CPNMJ, Custódio GD. Effect of fibre type on the compressive and tensile strength of a soft soil chemically stabilised. *Geosynthetics Int* (2016) 23(3):171–82. doi:10.1680/jgein.15.00040

22. Memon A, Nakai A. Fabrication and mechanical properties of jute spun yarn/PLA unidirection composite by compression molding. *Energy Proced* (2013) 34:34830–8. doi:10.1016/j.egypro.2013.06.819

23. Marandi S, Bagheripour MH, Rahgozar R, Zare H. Strength and ductility of randomly distributed palm fibers reinforced silty-sand soils. *Am J Appl Sci* (2008) 5(3):209–20. doi:10.3844/ajassp.2008.209.220

24. Sudhakaran PS, Sharma KA, Kolathayar S. Soil stabilization using bottom ash and areca fiber: experimental investigations and reliability analysis. *J Mater Civil Eng* (2018) 30(8). doi:10.1061/(asce)mt.1943-5533.0002326

25. Almajed AA. *Enzyme induced carbonate precipitation (EICP) for soil improvement* (doctoral dissertation). Arizona State University, Tempe, AZ, United States (2017).

26. Huang Z. *Preparation and properties of the sword-hemp fiber-enhanced polymer-based composites [D]*. Jinan: University of (2017).

27. Patil S, Bhaskar R, Xavier RJ. Optimization of rheological and mechanical properties of sustainable lateritic self-compacting concrete containing sisal fiber using response surface methodology. *J Building Eng* (2024) 84:84108574. doi:10.1016/J.JOBE.2024.108574

28. Song H, Liu T, Gauvin F, Brouwers H. Investigation of sisal fiber incorporation on engineering properties and sustainability of lightweight aggregates produced from municipal solid waste incinerated bottom ash. *Construction Building Mater* (2024) 413:413134943. doi:10.1016/J.CONBUILDMAT.2024.134943

29. Zhang A, Liu K, Li J, Song R, Guo T, et al. Static and dynamic tensile properties of ultra-high performance concrete (UHPC) reinforced with hybrid sisal fibers. *Construction Building Mater* (2024) 411:134492. doi:10.1016/J.CONBUILDMAT.2023.134492

30. Ekkachai Y, Pongsak W, Amorn P. A use of natural sisal and jute fiber composites for seismic retrofitting of nonductile rectangular reinforced concrete columns. *J Building Eng* (2022) 52:104521. doi:10.1016/J.JOBE.2022.104521

31. Lima RP, Barros AJ, Roque BA, Fontes CM, Lima JM. Short sisal fiber reinforced recycled concrete block for one-way precast concrete slabs. *Construction Building Mater* (2018) 187:187620–34. doi:10.1016/j.conbuildmat.2018.07.184

32. GB/T 50123-2019,Standard for geotechnical testing method[S].

33. Wu XF, Luo ZX, Chen HY. Production and application of sisal fiber. *China Fiber Inspection* (2010)(03) 59–61. doi:10.14162/j.cnki.11-4772/t.2010.03.005

34. Ma K, Liu J, Jiang CY, Ma XF, Huang LH, He CZ, et al. Experimental study on the strength of sand improved by polyurethane curing agent and sisal fiber. *J Cent South Univ* (2022) 29(02):528–545. doi:10.1007/s11771-022-4909-9

frontiers | Frontiers in Earth Science

TYPE Original Research
PUBLISHED 19 November 2024
DOI 10.3389/feart.2024.1491583

OPEN ACCESS

EDITED BY
Yifei Sun,
Taiyuan University of Technology, China

REVIEWED BY
Lei Gao,
Hohai University, China
Zhendong Leng,
Gezhouba Explosive, China

*CORRESPONDENCE
Zhi-wei Ye,
yezhiwei@ncu.edu.cn

RECEIVED 05 September 2024
ACCEPTED 06 November 2024
PUBLISHED 19 November 2024

CITATION
Liu D, Ye Z-w, Xie W-j, Gao J-l, Hu S-t, Li Y and Chen F (2024) Numerical simulation study on the construction of cut off walls using high-pressure jet grouting based on SPH method.
Front. Earth Sci. 12:1491583.
doi: 10.3389/feart.2024.1491583

Numerical simulation study on the construction of cut off walls using high-pressure jet grouting based on SPH method

Da Liu, Zhi-wei Ye*, Wei-jiang Xie, Jiang-lin Gao, Song-tao Hu, Yan Li and Fang Chen

Jiangxi Hydraulic Safety Engineering Technology Research Center, Jiangxi Academy of Water Science and Engineering, Nanchang, China

The optimization of parameters for the construction of cut off walls using high spray method plays a crucial role in improving the permeability stability of hydraulic structures and ensuring the safe operation of water conservancy projects. However, limited by existing research methods, there is currently a lack of systematic research on the influence of construction parameters on the quality of cut off walls. This study fully considers the characteristics of high-speed slurry jet and soil dynamic failure in numerical simulation of the construction of cut off walls using high spray method. Based on the SPH method, a two-dimensional plane strain model of high-pressure jet grouting was established, and the influence of aperture, grouting pressure, and hole spacing on the failure process of soil and the quality of cut off walls is systematically analyzed. The results show that the soil mainly exhibits tensile failure under the continuous action of high-speed cement slurry during the construction of cut off walls using high spray method. Reducing the aperture and grouting pressure, as well as increasing the hole spacing, are not conducive to forming a continuous and dense impermeable wall. Compared to grouting pressure, the influence of aperture and spacing on the quality of cut off walls is more significant. When the aperture is 0.6 m, the grouting pressure is 32 MPa, and the hole spacing is 0.8 m, the quality of cut off walls is great. Finally, the simulation results of this paper were preliminarily verified by combining the construction of cut off walls using high spray method in the flood control project in Luotang Township, Jiangxi Province, China. The findings can provide reference for optimizing the construction parameters of cut off walls using high spray method.

KEYWORDS

cut off wall, high-pressure jet grouting, SPH method, hole spacing, grouting pressure, hole diameter

1 Introduction

The optimization of parameters for the construction of cut off walls using high spray method plays a crucial role in improving the permeability stability of hydraulic structures and ensuring the safe operation of water conservancy projects (Brown and Bruggemann, 2002; Wu et al., 2015; Yu et al., 2015; Heidarzadeh et al., 2019; Wang et al., 2021; Cheng et al., 2022). The high-pressure jet grouting method, also known as the high spray method,

is a construction technique that uses the impact load generated by high-speed slurry jet to destroy the grouted soil, causing the slurry to mix and solidify with soil particles, thereby forming an impermeable wall. Due to its wide applicability, high wall quality, good controllability, and convenient construction, it has been a main method for the construction of cut off walls (Dai et al., 2020; Li et al., 2023; Zhang et al., 2024). Optimizing the high-pressure jet grouting method and improving the construction quality of cut off walls is a hot topic in the anti-seepage treatment of hydraulic engineering.

Numerous scientific researchers and engineering technicians have conducted extensive research on the grouting materials of high-pressure jet grouting, formation mechanisms of cut off walls, and key technical parameters. For grouting materials, Yang (2010) explored the construction process using cement paste as the main grouting material. Wang et al. (2019) found that the seepage control effect and stability of cut off walls formed by using a new non-aqueous reactive polymer material was better than that of the concrete cut off walls. Wu et al. (2023) compared the seepage resistance of three types of grouting materials: the mixture of polymer and cement, the mixture of geopolymer and cement, and the mixture of terracotta, phosphogypsum and cement, and found that the solidified silty soil with high polymer and cement has the best impermeability performance. For the failure mechanism of soil caused by jet flow, Yang (2008) pointed out that high-pressure jet is the main driving force to diffuse the stratum and recombine the coarse particles in the stratum, which also indicates that grouting pressure directly affects the quality of cut off walls. Guo (2021) found that the soil body under the action of jet mainly exhibits splitting failure mainly through indoor model test, and also analyzed the influence of grouting pressure, but the grouting pressure was small. In terms of key technical parameters, Yang et al. (2021) determined parameters such as the spacing of grouting holes, grouting pressure, and lifting velocity based on experiments, providing a reference for the related engineering construction. Huang (2010) analyzed the influence of factors such as nozzle diameter size and quantity, lifting speed, slurry ratio and density, spacing of holes, and wall layout on the quality of cut off walls. In addition, Liu et al. (2022) proposed a large-diameter drilling spraying integrated high-pressure grouting technology through equipment modification and research and development, breaking through the limitations of traditional small-diameter drilling and forming high-quality cut off walls. This provides valuable experience for the application of high-pressure spraying grouting technology in other anti-seepage projects, and indirectly illustrates that drilling diameter can also significantly affect the construction quality of cut off walls. As can be seen from the above, current research on high-pressure jet grouting mainly focuses on model tests and field tests. Although it can provide some reference for related engineering construction, it also faces problems such as high testing costs, long cycles, and limited research content. More specifically, the construction parameters that affect the quality of cut off walls mainly include aperture, grouting pressure, and hole spacing, but currently limited by research methods, there is a lack of systematic research on these construction parameters. In recent years, the continuous emergence of numerical simulation methods has provided ideas for solving this problem. However, the high spray pressure during the construction of cut off walls, the flow characteristics of slurry jets, the impact failure characteristics of soil, and the particle characteristics of soil pose certain challenges for numerical simulation research. Therefore, to facilitate more systematic research, there is an urgent need to explore a numerical simulation method that can better simulate the slurry jet and its dynamic interaction with soil.

The present study fully considered the characteristics of numerical simulation of cut off walls using high spray method, and established a two-dimensional plane strain model of high-pressure jet grouting based on SPH method. The influence of hole diameter, grouting pressure, and hole spacing on soil failure process and quality of cut off walls was systematically analyzed. Combined with the construction test of cut off walls using high spray method in Luotang Township, Jiangxi Province, China, the simulation results of this article were preliminarily verified. The findings can provide reference for optimizing the construction parameters of cut off walls using high spray method.

2 Numerical model of high pressure jet grouting based on SPH method

In the construction of cut off walls using high spray method, the impact failure process of soil under the action of slurry jet is a typical dynamic process. LS-DYNA has significant advantages in simulating the characteristics of impact failure and has been widely used in multiple fields such as water jet (Zhou et al., 2022), rock blasting (Wei et al., 2009), and projectile penetration (Zhang et al., 2023). It supports multiple numerical methods and algorithms, including SPH method, which is suitable for numerical simulation of the construction of cut off walls using high spray method in this paper.

2.1 Introduction to SPH method

SPH algorithm is a computational method used to simulate fluid dynamics, which does not rely on traditional grid (lattice) methods to solve the motion equations of continuous medium, but expresses the spatial and temporal distribution of physical quantities through the interaction between particles and them (Monaghan, 2005). This makes the SPH algorithm particularly suitable for handling large deformations and free surface flow problems, meeting the numerical simulation requirements of this study. During the calculation process, track the motion of each particle from a perspective of Lagrange. The equations of particle motion are usually discretized based on physical laws such as Newton's second law of motion and the principle of conservation of mass.

The SPH algorithm utilizes a weight function called a smoothing kernel to estimate the physical quantities of particles and their spatial derivatives. The kernel function determines the strength of the interaction between particles and typically has a finite support domain, with only neighboring particles having an impact on the current particle. Macro variables are obtained by calculating the integral interpolation of discrete points within the domain. The approximate function of the particle is given by Equation 1

$$f(x) = \int_{\Omega} f(x')W(x - xx', h)dx' \tag{1}$$

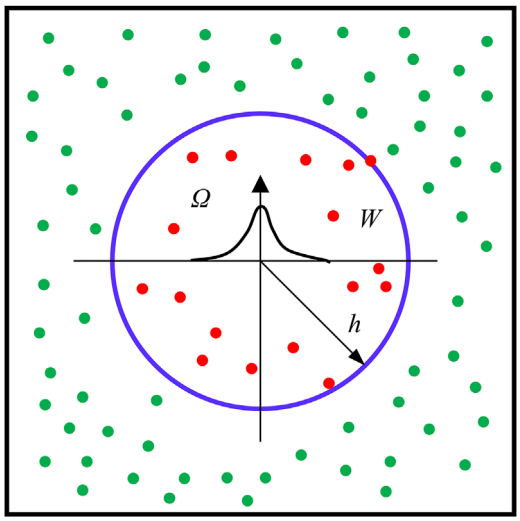

FIGURE 1
Particle approximation method.

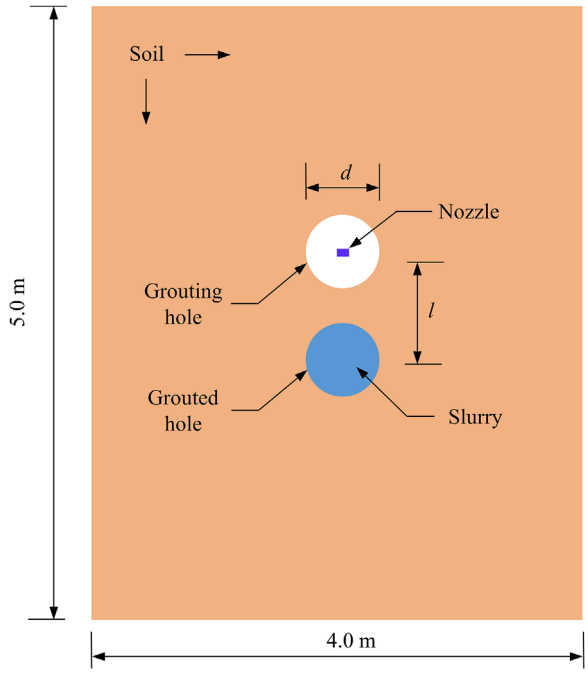

FIGURE 2
High pressure jet grouting model.

where $f(x)$ is a function of the spatial coordinate x, Ω is the support domain for x, x-x' is the distance between particles, h is the smooth length of SPH particles, smooth length varies with time and space, as shown in Figure 1, W (x-x') is the kernel function, defined by the auxiliary function $\theta(x\text{-}x')$, shown in Equation 2:

$$W(x-x',h) = \frac{1}{h(x-x')^d}\theta(x-x') \tag{2}$$

where d is the spatial dimension.

In the SPH method, the particle approximation method is used to write continuous integral equations into discrete equations as shown in Equation 3:

$$f(x) = \sum_{i=1}^{n} \frac{m_i}{\rho_i} \frac{1}{h(x-x')^d}\theta(x-x') \tag{3}$$

where ρ_i is the density of particle i, m_i is the mass of particle i.

The conservation equations of mass, momentum, and energy in the N-S equation based on the SPH method can be found in the literature (Gingold and Monaghan, 1977).

2.2 High pressure jet grouting model

Referring to the construction process of cut off walls using high spray method, which has a better wall formation effect at present (Liu et al., 2022), a two-hole planar model was established, as shown in Figure 2. The overall dimensions of the model are 4 × 5 m^2, and the boreholes are d in diameter and l in spacing. The direction of the grouting hole points in the direction of the preceding grouting hole, which is filled with grout that has not initially set. Fixed constraints were applied around the model. Both soil and slurry were simulated using SPH method.

There are two methods for generating SPH particles in LS-DYNA. One is to directly build the model in the post-processing software LS-PrePost. The other is to first create finite elements in software ANSYS and then import them into LS-PrePost to convert them into SPH particles. This study adopted the second method, which facilitates rapid modeling. In addition, to simulate high-pressure jet grouting, infinite slurry was used to achieve a continuous jet flow of slurry from the nozzle. The method for establishing the high-pressure jet grouting model is shown in Figure 3. To better simulate the impact failure phenomenon of soil body, the mesh in the finite element model was uniformly divided with a size of 1 cm, that is, SPH particle nodes were created with a spacing of 1 cm. Excluding the infinite slurry SPH particles, the total number of SPH particles in the model was 144,270. Three nozzles are simultaneously directed spraying, and the three nozzles are located very close to each other. A simplification is made in the 2D numerical simulation, where the slurry is equated from a point jet to a present jet.

2.3 Material model and parameters

The materials involved in this study mainly include soil and cement slurry. The constitutive model of soil was selected using the MAT-FHWA_SOIL_TITLE model provided by LS-DYNA. This model is suitable for simulating and analyzing the mechanical behavior of soil and has been widely used in numerical simulations of soil blasting seismic dynamic response, soil impact failure under water jet action, and soil cutting. This model modifies the standard Mohr-Coulomb yield surface to a smooth surface, improving the stability of calculations. The yield equation is expressed by Equation 4

$$F = -P\sin\varphi + \sqrt{J_2K(\theta)^2 + AHYP^2\sin^2\varphi} - c\cos\varphi \tag{4}$$

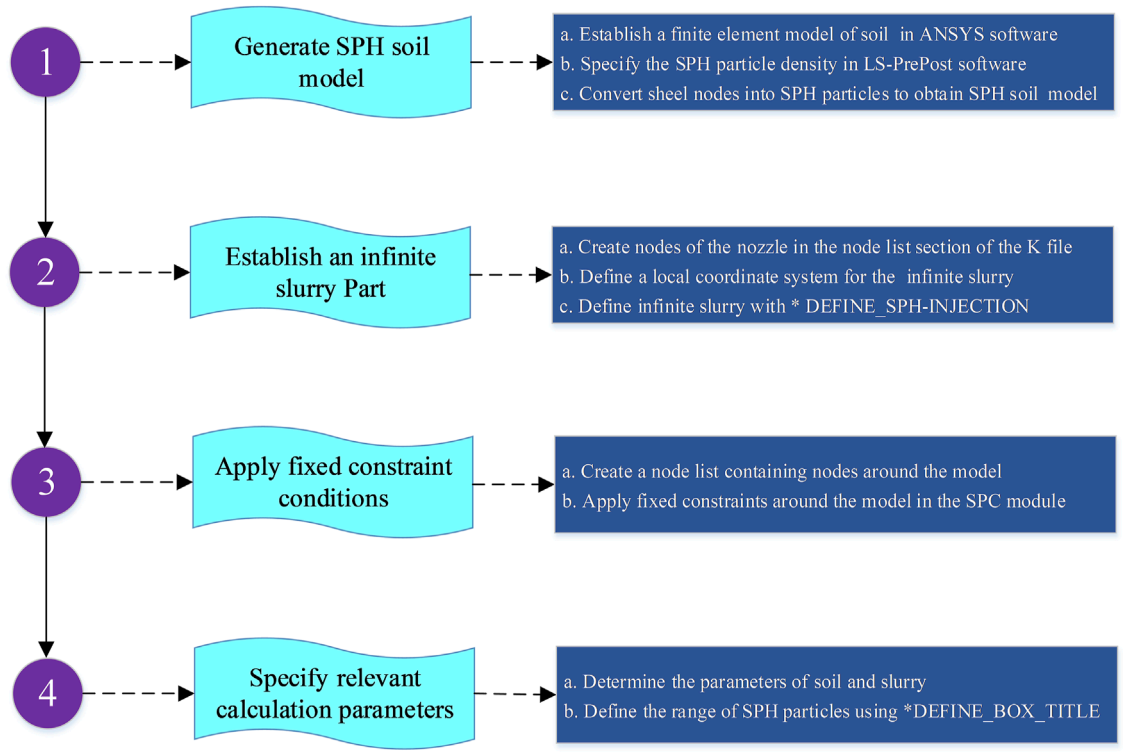

FIGURE 3
Method for establishing high pressure jet grouting model.

where P is the pressure, φ is the internal friction angle, J_2 is the second invariant of the deviatori tensor of stress, $K(\theta)$ is the function of tensor plane angle, c is the cohesive force, AHYP is a parameter for the similarity between the modified Mohr-Coulomb yield surface and the standard Mohr-Coulomb yield surface.

The above model simultaneously considers plastic hardening, plastic softening, strain rate effect, and pore water pressure effect. In addition, it also has the function of element or SPH particle failure. The main parameters controlling the soil mechanics behavior of the model include bulk modulus, shear modulus, soil density, moisture content, friction angle, and cohesion. Based on the parameters of soil in reference (Wu et al., 2024) and relevant explanations in the LS-DYNA keyword manual (Livermore Software Technology Corporation, 2003), the main parameters of soil are determined, as shown in Table 1.

The properties of cement slurry are very complex, and there is no mature material model available in LS-DYNA. This study uses the combination of the empty material model and the related equation of state to simulate cement slurry, which is commonly used to simulate fluid. Specifically, defining the density of 1.5 g/cm^3 and dynamic viscosity of 2 Pa s using the keyword*MATNULL. Referring to the equation of state of the relevant fluid, simulating the properties of cement slurry. It should be noted that the dynamic viscosity of cement slurry will change over time, but considering the continuity of construction, the time interval between the construction of the two grouting hole is relatively short, and the influence of time on the viscosity of cement slurry was ignored in this study.

3 Factors affecting the quality of cut off walls using high spray method

3.1 Calculation conditions

Research shows that the main factors affecting the quality of cut off walls using high spray method are hole diameter, grouting pressure, and hole spacing. Conventionally, the diameter of grouting hole is less than 0.2 m, and the soil-breaking of high-speed slurry is very limited. In recent years, large-diameter grouting holes have gradually been applied due to their good soil-breaking effect. In this paper, grouting holes with diameters of 0.3 mm, 0.4, 0.5, and 0.6 m were selected to study the influence of diameter on grouting quality. The grouting pressure for high-pressure jet grouting is usually 20–40 MPa. The grouting pressures of 24, 28, 32, and 36 MPa were adopted. In numerical simulation, different grouting pressures were achieved by applying different initial velocities of particles, which were estimated based on the formula of small hole shooting flow. The hole spacing was set to 0.8, 1.0, 1.2, and 1.4 m for analysis. The calculation conditions are listed in Table 2.

3.2 Analysis of main influencing factors

Figure 4 shows the variation of the slurry zone between adjacent holes using high-pressure jet grouting method with a hole diameter of 0.6 m in the condition SCI-1. The red area in the figure represents

TABLE 1 Parameters of soil.

Physical quantity	Value	Physical quantity	Value
RO (kg·mm^{-3})	1.95E-06	ECCEN	0.7
NPLOT	3	AN	0
SPGRAV	2.7	ET	0
RHOWAT (kg·mm^{-3})	1.00E-06	MCONT	0.034
VN	1.1	PWD1	0
GAMMAR	0	PWKSK (GPa)	0
INTRMX	10	PWD2	0
K (GPa)	0.00373	PHIRES	0.001
G (GPa)	0.00194	DINT	1.00E-05
PHIMAX (Rad)	0.52	VDFM	3.00E-08
AHYP	1.00E-07	DAMLEV	0.99
COH (GPa)	1.00E-05	EPSMAX	0.8

the grout and the blue area represents the soil. In the figure, the red area represents the slurry while the blue area represents the soil. It is easy to find that the high-speed sprayed cement slurry did not initially cause failure to the soil after acting on the hole wall, but bounced off the hole wall and fell into the hole. Under the continuous action of high-speed cement slurry, radial cracks appeared around the wall of the grouting hole. This is because that the hole wall was subjected to impact load and tended to expand outwards, generating large tensile stress in the circumferential direction of the hole. At the same time, the hole already filled with slurry were subjected to compression, which also generated a certain amount of annular stress, resulting in some radial cracks. The slurry with a certain velocity entered the radial cracks, causing them to extend towards the front grouted hole. Finally, the grouting hole was connected to the front grouted hole to form a continuous cut off wall.

Figure 5 presents the distribution characteristics of slurry between the two holes under different hole diameter conditions. As shown in Figure 5A, when the hole spacing and grouting pressure remained constant, the soil between the small diameter boreholes was thicker, and the guiding effect of the grouted holes on the cracks was not obvious. The soil around the grouting hole was significantly broken, but the soil between the grouting hole and the grouted hole was difficult to break, and the quality of the cut off wall was poor. In Figures 5A–C, the slurry between the two holes was not connected. As the hole diameter increased, the degree of soil failure between the two holes gradually increased, and the area filled with slurry also gradually increased. When the grouting pressure was 32 MPa and the hole spacing is 0.8 m, the slurry could only penetrate the two holes under the condition of a diameter of 0.6 m. At this point, the cut off wall was relatively continuous. The width of the wall is more likely to meet the design requirements. Based on the principle of equivalent area, the average thickness of the wall is 41 cm, as shown in Figure 5D.

Figure 6 presents the distribution characteristics of slurry between the two holes under different grouting pressure conditions. Compared with the influence of the hole diameter on the grouting quality in Figure 5, the influence of the grouting pressure is not significant when it varies between 20–40 MPa. When the hole diameter was 0.6 m and the hole spacing was 0.8 m, the slurry in some areas between the two holes was not connected under the conditions of grouting pressure of 24 or 26 MPa. Correspondingly, the quality of the anti-seepage wall was poor. Under the conditions of grouting pressure of 32 or 36 MPa, although there was some soil wrapped in the slurry between the holes, the slurry and soil mixed together to form a dense and continuous wall. The greater the grouting pressure, the larger the width of the zone of slurry between the holes, and the better the wall quality.

Figure 7 shows the influence of hole spacing on the grouting quality between the two holes. When the grouting pressure was 32 MPa and the hole diameter was 0.6 m, the slurry area between the holes transitioned from a connected state to a non-connected state. When the hole spacing was 0.8 m, the slurry between the holes was connected, as shown in Figure 7A. When the hole spacing was 1.0, 1.2, and 1.4 m, the slurry was not connected, as shown in Figures 7B–D. As the hole spacing increased, the propagation direction of fractures in the soil under the high-speed slurry gradually deviated from the direction of the inter-hole centerline. Moreover, the larger the hole spacing, the greater the deflection angle, which leads to a gradual decrease in the grouting area between the holes and a deterioration in the quality of the cut off wall.

Comparing the distribution of slurry between holes and the average thickness of the wall under different conditions in Figures 5–7, it is found that the influence of hole diameter and spacing on the quality of cut off walls is more significant. Through the above analysis, it can be seen that, if the grouting technology with large diameter and high pressure is used for the construction of cut off walls, the quality of walls is better when the hole diameter is 0.6 m, the grouting pressure is 32 MPa, and the hole spacing is 0.8 m. Reducing the hole diameter and grouting pressure or increasing the hole spacing will lower the quality of cut off walls. Adjusting the hole spacing between holes is an effective method for controlling the quality of cut off walls. The present study provides a method for determining the optimal hole spacing given the hole diameter and grouting pressure, which can provide a reference for optimizing the construction parameters of cut off walls in water conservancy and hydropower projects.

4 Field experiment

Based on the above analysis, field experiments were conducted to test the construction quality of cut off walls using high spray method, relying on the flood control project in Luotang Township, Jiangxi Province, China. The project is located in the lower reaches of the Suichuan River, a tributary of the Ganjiang River, starting from Songyang Village and ending at Zhaitou Village. It is situated on the left bank of the Suichuan River and has a total length of 8.0 km for

TABLE 2 Calculation conditions.

Calculation conditions	Hole diameter (m)	Grouting pressure (MPa)	Hole spacing (m)
SCI-1	0.3、0.4、0.5、0.6	32	0.8
SCI-2	0.6	24、28、32、36	0.8
SCI-3	0.6	32	0.8、1.0、1.2、1.4

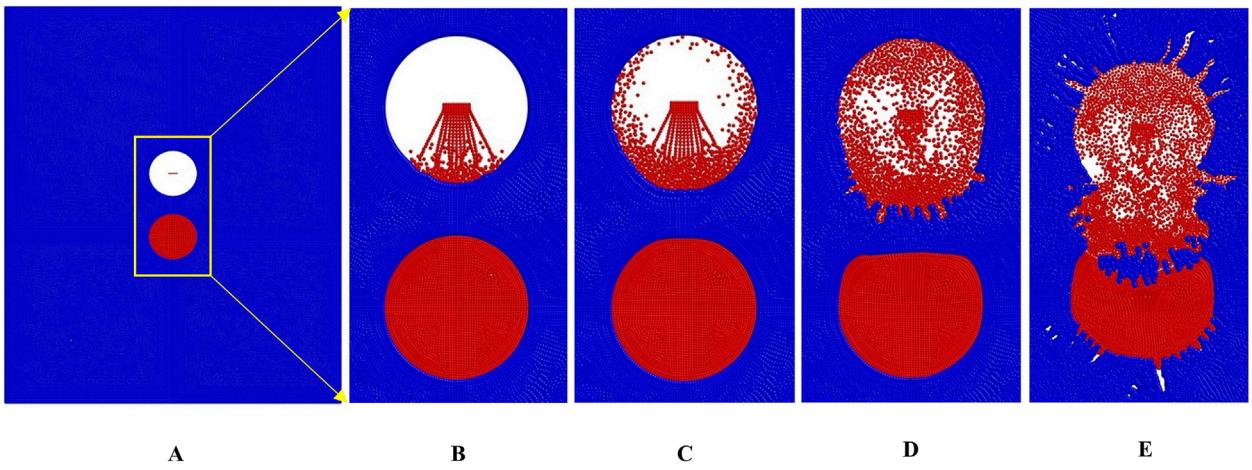

FIGURE 4
The grouting quality under the hole diameter of 0.6 m in the condition SCI-1. **(A)** Initial time. **(B)** 1/5 of the calculation time. **(C)** 2/5 of the calculation time. **(D)** 3/5 of the calculation time. **(E)** Final time.

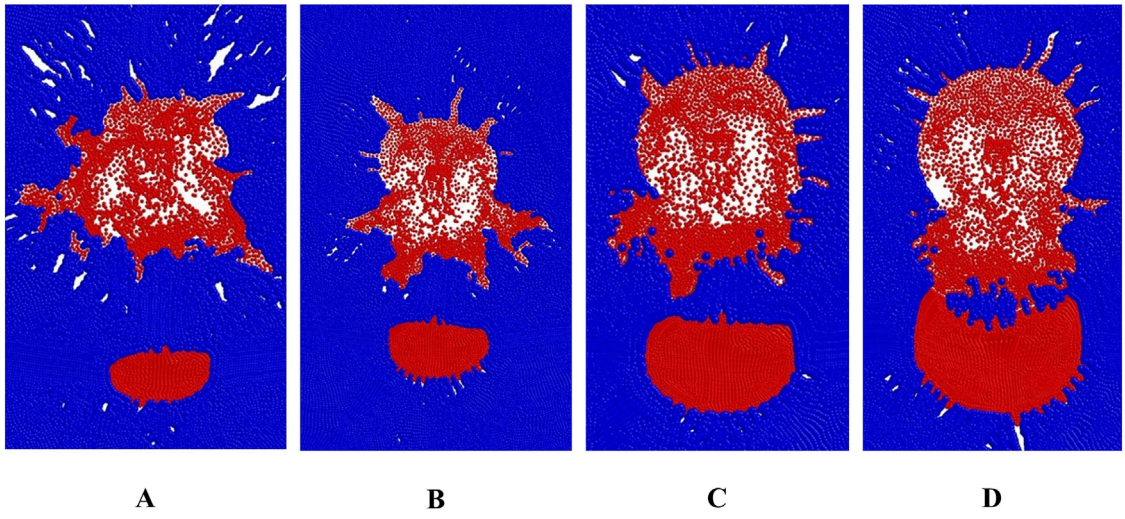

FIGURE 5
The filling area of slurry under different hole diameter conditions **(A)** d = 0.3 m **(B)** d = 0.4 m **(C)** d = 0.5 m **(D)** d = 0.6 m.

river regulation. The foundation of the Songyang embankment in the project location has serious leakage and poor flood resistance, which seriously affects the production and life of the local people and restricts the local economic and social development. Therefore, the main objective of the project is to construct a cut off wall to improve the anti-seepage performance of the embankment foundation.

Through the above numerical simulation, the quality of walls is better when the hole diameter is 0.6 m, the grouting pressure

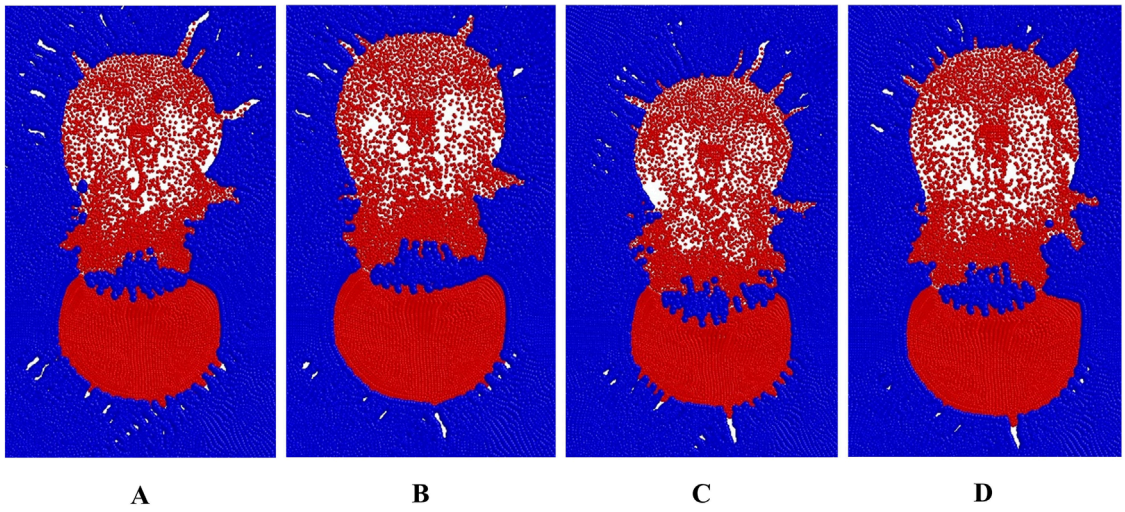

FIGURE 6
The filling area of slurry under different grouting pressure conditions. **(A)** p = 24 MPa. **(B)** p = 28 MPa. **(C)** p = 32 MPa. **(D)** p = 36 MPa.

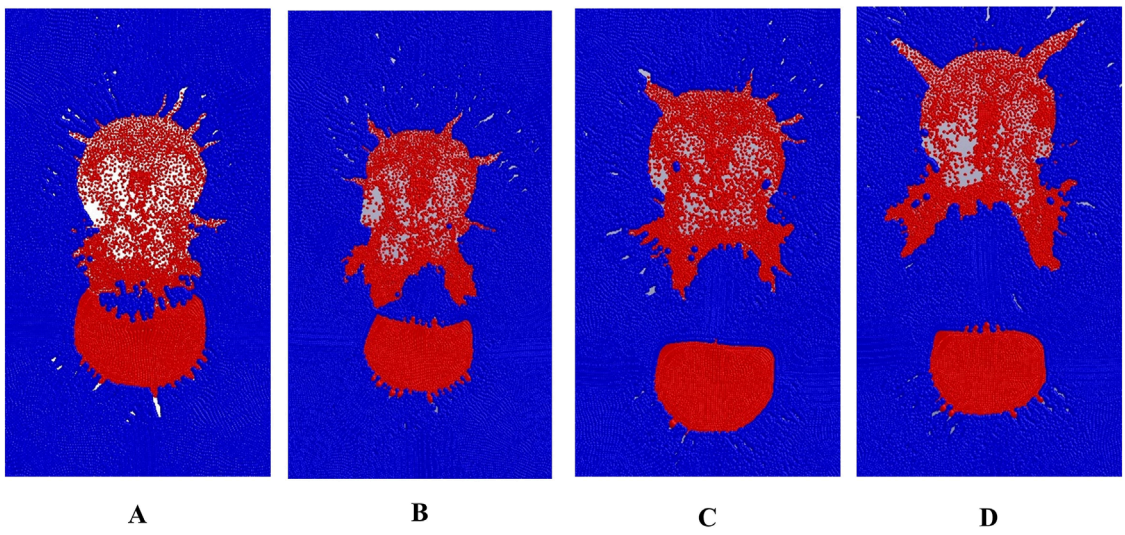

FIGURE 7
The filling area of slurry under different hole spacing conditions. **(A)** l = 0.8 m **(B)** l =1.0 m **(C)** l = 1.2 m **(D)** l = 1.4 m.

is 32 MPa, and the hole spacing is 0.8 m. These parameters were used in the field for the verification test. The method of combining wall excavation detection with core drilling coefficient detection was adopted for the quality inspection and evaluation of cut off walls. Wall excavation was carried out at intervals of 500 m along the wall axis, with each excavation area measuring 3–5 m in length and 2.5–4.0 m in depth. As shown in Figure 8, the cut off wall in the test section was continuous and intact, with no leak spray. By measuring the width of the cut off wall at different locations, the average thickness of the wall was obtained as 38 cm, which is in good agreement with the corresponding wall thickness of 41 cm under the corresponding conditions obtained from the numerical simulation results.

After 28 days of construction, core holes were drilled at 500 m intervals along the axis of the wall. The core drilled samples of the walls in the test section are shown in Figure 9A. The sample core was intact and the surface was smooth. The coefficient of permeability was tested using a SS-2.5 Penetrometer, as shown in Figure 9B. Two core holes were drilled on site, A and B, and three sample cores were taken from each hole to test the permeability coefficient. The core permeability coefficients were listed in Table 3. The average values of permeability coefficient of hole A and hole B were 8.33×10^{-7} cm/s and 9.12×10^{-7} cm/s, respectively, which are less than the design value $(1–9) \times 10^{-6}$ cm/s. Qualitative excavation test results and qualitative core permeability test results verified the reliability of the above numerical simulation results.

A B

FIGURE 8
Wall excavation inspection. **(A)** Test section. **(B)** Wall appearance.

A B

FIGURE 9
Core drilling and permeability coefficient testing equipment. **(A)** Core drilled samples. **(B)** SS-2.5 Penetrometer.

TABLE 3 Core permeability coefficient.

Hole number	Core number	Permeability coefficient (cm/s)	Average permeability coefficient (cm/s)	Design value of permeability coefficient (cm/s)
A	A-1	9.31×10^{-7}	8.33×10^{-7}	$\leq(1–9) \times 10^{-6}$
	A-2	7.47×10^{-7}		
	A-3	8.21×10^{-7}		
B	B-1	9.08×10^{-7}	9.12×10^{-7}	$\leq(1–9) \times 10^{-6}$
	B-2	8.85×10^{-7}		
	B-3	9.45×10^{-7}		

5 Conclusion

The present study established a two-dimensional plane strain model for the simulation of the construction of cut off walls using the high pressure jet grouting based on the SPH method. The influence of hole diameter, grouting pressure and hole spacing on the process of soil failure and the quality of the wall was analyzed systematically. Combined with the construction test of cut off walls using high spray method in Luotang Township, Jiangxi Province, China, the simulation results of this

article were preliminarily verified. The main conclusions are as follows:

(1) The high-speed sprayed cement slurry will not initially cause failure to the soil after acting on the hole wall, but bounce off the hole wall and fell into the hole. Under the continuous action of high-speed cement slurry, radial cracks will appear around the wall of the grouting hole. The slurry with a certain velocity enters the radial cracks, causing them to extend towards the front grouted hole. The grouting hole will be connected to the front grouted hole to form a continuous cut off wall.

(2) As the hole spacing increased, the propagation direction of fractures in the soil under the high-speed slurry gradually deviated from the direction of the inter-hole centerline. The influence of hole diameter and spacing on the quality of cut off walls is more significant. Reducing the hole diameter and grouting pressure or increasing the hole spacing will lower the quality of cut off walls. The quality of walls is better when the hole diameter is 0.6 m, the grouting pressure is 32 MPa, and the hole spacing is 0.8 m.

(3) Relying on the flood control project in Luotang Township, Jiangxi Province, China, the method of combining wall excavation detection with core drilling coefficient detection was adopted for the quality inspection and evaluation of cut off walls. The cut off wall in the test section was continuous and intact, with no leak spray. The average values of permeability coefficient of the two sets of samples are less than the design value. Qualitative excavation test results and qualitative core permeability test results verified the reliability of the above numerical simulation results.

Data availability statement

Data will be made available on request.

Author contributions

DL: Writing–original draft, Writing–review and editing. Z-wY: Resources, Supervision, Validation, Writing–review and editing. W-jX: Software, Writing–review and editing. J-lG: Data curation, Writing–review and editing. S-tH: Methodology, Writing–review and editing. YL: Conceptualization, Writing–review and editing. FC: Visualization, Writing–review and editing.

Funding

The author(s) declare that financial support was received for the research, authorship, and/or publication of this article. The authors declare that financial support was received for the research, authorship, and/or publication of this article. This work is supported by The Water Conservancy Technology Demonstration Project of the Ministry of Water Resources (SF-TJ-202417), the Open Foundation of Jiangxi Hydraulic Safety Engineering Technology Research Center (2022SKSG02), Jiangxi Provincial Department of water resources Foundation (202324YBKT04, 202425TGKT01).

Acknowledgments

The authors wish to express they're thanks to the supporter.

Conflict of interest

The authors declare that the research was conducted in the absence of any commercial or financial relationships that could be construed as a potential conflict of interest.

Publisher's note

References

Brown, A. J., and Bruggemann, D. A. (2002). Arminou Dam, Cyprus, and construction joints in diaphragm cut-off walls. *Geotechnique* 52 (1), 3–13. doi:10.1680/geot.52.1.3.40823

Cheng, H. Z., Li, W. T., Chen, R. P., and Yi, Y. L. (2022). Workability study of sand-bentonite-cement mixtures for construction of two-phase cut-off wall. *Constr. Build. Mater.* 345, 128058. doi:10.1016/j.conbuildmat.2022.128058

Dai, W. K., Liang, L., and Zhang, B. J. (2020). Firefly optimization algorithm for the prediction of uplift due to high-pressure jet grouting. *Adv. Civ. Eng.*, 8833784. doi:10.1155/2020/8833784

Gingold, R. A., and Monaghan, J. J. (1977). Smoothed particle hydrodynamics: theory and application to non-spherical stars. *Mon. Notices R. Astronomical Soc.* 181, 375–389. doi:10.1093/mnras/181.3.375

Guo, H. (2021). *High pressure jet grouting mechanism test and numerical simulation research*. Beijing, China: Beijing Jiaotong University.

Heidarzadeh, M., Mirghasemi, A. A., Niroomand, H., and Eslamin, F. (2019). Construction and performance of the Karkheh dam complementary cut-off wall: an innovative engineering solution. *Int. J. Civ. Eng.* 17 (6B), 859–869. doi:10.1007/s40999-018-0370-4

Huang, B. D. (2010). Discussion on factors influencing quality of high pressure jet grouting diaphragm wall and preventive measures. *Yellow River* 41 (05), 58–61. doi:10.3969/j.issn.1001-4179.2010.05.022

Li, P. P., Huang, X., Lu, F., Qiu, W. E., Liu, H., Li, L. L., et al. (2023). Experimental investigation on the reinforcement of a high-pressure jet grouting pile for an ultra-shallow tunnel in a strongly weathered stratum. *Front. Earth Sci.* 10, 1040461. doi:10.3389/feart.2022.1040461

Liu, D., Xie, W. J., Gao, J. L., Hu, S. T., Chen, M., Li, Y., et al. (2022). Study on the construction method and effects of ipsilateral, multi-nozzle, high-pressure jet grouting cut-off wall. *Sustainability* 14 (16), 10383. doi:10.3390/su141610383

Livermore Software Technology Corporation (2003). *LS-DYNA theoretical manual*. California: Livermore Software Technology Corporation.

Monaghan, J. J. (2005). Smoothed particle hydrodynamics. *Rep. Prog. Phys.* 68 (8), 1703–1759. doi:10.1088/0034-4885/68/8/R01

Wang, F. M., Li, M. J., Fang, H. Y., and Xue, B. H. (2019). Analysis of polymer cut-off wall of Yellow River dyke. *Yellow River* 41 (10), 48–52. doi:10.3969/j.issn.1000-1379.2019.10.009

Wang, K., Li, Z. P., Zheng, H., Xu, X. Z., and He, H. F. (2021). A theoretical model for estimating the water-tightness of jet-grouted cut-off walls with geometric imperfections. *Comput. Geotech.* 138, 104316. doi:10.1016/j.compgeo.2021.104316

Wei, X. Y., Zhao, Z. Y., and Gu, J. (2009). Numerical simulations of rock mass damage induced by underground explosion. *Int. J. Rock Mech. Min. Sci.* 46 (7), 1206–1213. doi:10.1016/j.ijrmms.2009.02.007

Wu, K., Chen, R. G., Gu, H. R., Yuan, J. J., and Qian, X. Q. (2023). Experimental study on seepage control performance of high pressure jet grouting pile using grouting material in water-rich sand layer. *Chin. J. Undergr. Sp. Eng.* 19 (02), 533–540.

Wu, S. H., Lu, Y., Wu, S., Yin, Y. C., Zhang, T., and Yue, Q. J. (2024). Simulation analysis of jet soil-breaking based on arbitrary Lagrange-Euler method. *J. Vib. Shock* 43 (13), 162–171. doi:10.13465/j.cnki.jvs.2024.13.018

Wu, Y. X., Shen, S. L., Yin, Z. Y., and Xu, Y. S. (2015). Characteristics of groundwater seepage with cut-off wall in gravel aquifer. II: numerical analysis. *Can. Geotech. J.* 52 (10), 1539–1549. doi:10.1139/cgj-2014-0289

Yang, S. Q. (2010). Application of paste-slurry and high pressure jet grouting in cofferdam seepage control. *Yangtze River* 41 (24), 58–62. doi:10.16232/j.cnki.1001-4179.2010.24.012

Yang, Y., Zhong, Q. P., Zhang, G. L., and Zhao, X. Y. (2021). Selection and research on key parameters of high pressure jet grouting construction. *Tech. Superv. Water Resour.* 10, 182–185. doi:10.3969/j.issn.1008-1305.2021.10.045

Yang, Z. (2008). *Jet grouting and construction of the mechanism of strengthening anti-technology research*. Central south university.

Yu, X., Kong, X. J., Zou, D. G., Zhou, Y., and Hu, Z. Q. (2015). Linear elastic and plastic-damage analyses of a concrete cut-off wall constructed in deep overburden. *Comput. Geotech.* 69, 462–473. doi:10.1016/j.compgeo.2015.05.015

Zhang, F., Li, J., Deng, Y. F., and Xu, C. L. (2024). Numerical investigation of mixing process of high-pressure jet-cutting clay by water-air coaxial nozzle considering soil rheological properties. *Comput. Geotech.* 165, 105878. doi:10.1016/j.compgeo.2023.105878

Zhang, S. B., Kong, X. Z., Fang, Q., and Peng, Y. (2023). The maximum penetration depth of hypervelocity projectile penetration into concrete targets: experimental and numerical investigation. *Int. J. Impact Eng.* 181, 104734. doi:10.1016/j.ijimpeng.2023.104734

Zhou, X. C., Ma, X. J., Liao, X. Y., Qi, S. W., and Li, H. Y. (2022). Numerical simulation of abrasive water jet impacting porous rock based on SPH method. *Chin. J. Geotech. Eng.* 44 (04), 731–739. doi:10.11779/CJGE202204016

frontiers | Frontiers in Physics

TYPE Original Research
PUBLISHED 25 November 2024
DOI 10.3389/fphy.2024.1502248

OPEN ACCESS

EDITED BY
Yifei Sun,
Taiyuan University of Technology, China

REVIEWED BY
Weng Aihua,
Jilin University, China
XingBo Huang,
Hohai University, China

*CORRESPONDENCE
Xiaoping Fan,
nj_fxp@njtech.edu.cn
Yicheng He,
hyckevin@mail.ustc.edu.cn

RECEIVED 26 September 2024
ACCEPTED 06 November 2024
PUBLISHED 25 November 2024

CITATION
Hu T, Fan X, He Y, Yang L, Yang C, Jiang P, Liu Z, Xia Z, Xu M and Wu Y (2024) Velocity structure of crust and mid-strong earthquake preparation characteristics in the Huoshan region, East China.
Front. Phys. 12:1502248.
doi: 10.3389/fphy.2024.1502248

Velocity structure of crust and mid-strong earthquake preparation characteristics in the Huoshan region, East China

Tiantian Hu[1], Xiaoping Fan[2]*, Yicheng He[3]*, Longshuai Yang[4], Congjie Yang[3], Pengcheng Jiang[1], Zhiwen Liu[1], Ziyan Xia[2], Menghui Xu[2] and Yuhan Wu[2]

[1]Nanjing Shanhai Engineering Technology Co., Ltd., Nanjing, China, [2]College of Transportation Engineering, Nanjing Tech University, Nanjing, China, [3]Jiangsu Earthquake Agency, Nanjing, China, [4]Seismic Safety Assessment Center, East-China Metallurgical Institute of Geology and Exploration, Hefei, China

The Huoshan region, located on the northern margin of the Dabie Orogenic Belt at the junction of the North China Plate and the Yangtze Plate, is one of the most seismically active and concentrated areas in the Dabie Orogenic Belt and adjacent regions. Utilizing the travel time data from 4,427 seismic events observed by 202 stations, we investigated the deep medium structure of the Huoshan region using the double-difference tomography method. The results reveal the medium structure and characteristics of mid-strong earthquake preparation in the region. The crustal medium in the study area exhibits significant lateral heterogeneity. The Dabie Orogenic Belt shows notably high velocity, whereas the North China Plate and the Yangtze Plate display relatively lower velocities. The Tan-Lu Fault Zone exhibits segmentation characteristics; with the crustal medium velocity south of Lujiang being relatively high, north of Jiashan being relatively low, and between Lujiang and Jiashan being intermediate. The epicenters of mid-strong earthquakes are located on the gradient zones of velocity and Poisson's ratio. The source regions of these earthquakes show significant anomalies of high Poisson's ratio and low S-wave velocity, which may indicate the presence of fluids. These anomalies possibly reflect the intrusion of deep materials along the fault zone, which could be the driving force for the preparation of mid-strong earthquakes.

KEYWORDS

Huoshan region, seismogenic environment, double-difference tomography, deep fluids, crustal structure

1 Introduction

The Huoshan region (HSR), located on the northern margin of the Dabie Orogenic Belt (DOB) at the junction of the North China Plate (NCP) and the Yangtze Plate (YP), is one of the most seismically active and concentrated areas within the DOB and its surrounding regions. To date, four earthquakes of magnitude 6 or higher have occurred in Anhui Province, two of which were in the HSR: a magnitude 6 earthquake in 1,652 and a magnitude 6¼ earthquake in 1917. The fine structural characteristics, seismogenic environment, earthquake generation mechanisms,

and earthquake prediction in the HSR have long been key areas of focus for researchers.

In recent years, numerous geophysicists have adopted diverse methodologies to deepen scientific inquiry in the HSR. Through the application of magnetotelluric techniques, Cui et al. (2020) [1] elucidated a three-dimensional electrical structure within the deep HSR. By integrating relocated minor earthquake data, they inferred that small seismic events predominantly arise along structurally weakened zones, with frequent shallow seismicity likely associated with fluid presence in the mid-lower crust, suggesting the region's potential to host moderate to strong earthquakes exceeding magnitude 6. Zhang et al. (2012) [2] employed a multidisciplinary approach combining gravity, magnetics, electromagnetics, and seismology, revealing a deep structural regime along the northern Dabie Mountains characterized by southward subduction of the North China Block and a northward thrust of the North Huaiyang Tectonic Belt (NHTB)—an insight offering profound geological constraints on the collision dynamics between the NCP and South China Plate. Wang et al. (2024) [3] utilized the matched location method to detect small earthquakes in the Huoshan seismic window region, obtaining a more complete earthquake catalog and revealing the relationship between these small earthquakes and the Gushi M3.6 earthquake in 2018 and the Yingcheng M4.9 earthquake in 2019. Ambient noise tomography and body-wave tomography results revealed a widespread low-velocity anomaly in the lower crust to upper mantle beneath the HSR [4–8]. Researchers using double-difference location (LocDD) method have further delineated a concentrated, banded seismic distribution [9, 10], illuminating that the Xiaotian-Mozitan Fault and the Luo'erling-Tudiling Fault jointly govern seismic activity in Huoshan [11]. Focal mechanism analyses yielded fault plane parameters, highlighting a regional stress regime marked by east-west compression and north-south extension [12].

Nonetheless, existing findings remain limited by methodological differences, perspectives, and foundational data variability. Previous large-scale imaging results were limited by the low spatial resolution of the models [5–7, 13], while small-scale imaging primarily focused on the upper crustal velocity structure, lacking constraints on the middle and lower crustal velocity structures [14]. Therefore, conducting detailed studies on the P-wave and S-wave velocity structures and Poisson's ratio in the HSR could provide important seismological constraints for understanding the deep seismogenic environment of the Huoshan earthquake swarm.

In this study, initial P-wave and S-wave arrival data from 4,427 seismic events spanning January 1998 to December 2021 were collected. Utilizing double-difference tomography (TomoDD) method, we constructed a high-resolution three-dimensional model of P-wave and S-wave velocities and Poisson's ratio across the HSR, thereby elucidating the region's crustal medium structure and the characteristics underlying moderate to strong earthquake genesis.

2 Geological background

The study area and its surrounding regions are divided by the NNE-trending Tan-Lu Fault Zone (F1), the near EW-trending Feixi-Hanbaidu Fault (F2), and the NE-trending Huaiyin-Xiangshuikou Fault (F6) into the NCP, the DOB, the YCP, and the Sulu Orogenic Belt. The HSR's geological setting is distinct, located at the southern edge of the northeastern subsidence zone of the Dabie Mountains, near the Anhui-Hubei border. It also lies at the intersection of the DOB and fault F1.The HSR is segmented by several faults, including the NW-trending fault F2, the Meishan - Longhekou Fault (F3) and the Xiaotian-MoziTan Fault (F4), which intersect with the NE-trending Luo'erling-Tudiling Fault (F5) (Figure 1).

Fault F4 serves as a boundary separating the North Dabie Tectonic Belt (NDTB) from the NHTB. This fault is an ancient deep fault zone that has significantly influenced the geomorphology and lithology of the region, with metamorphic rocks predominating to the south and sedimentary rocks to the north. Faults F2 and F3 separate the NHTB and the Lu'an Basin. Fault F2 primarily shows normal fault characteristics, classified as a pre-Quaternary fault, with strong activity during the Mesozoic and early Cenozoic periods. Fault F3 is primarily characterized by extensional tension, with significant tectonic deformation since the Cenozoic era. It mainly exhibits ductile slip activity and is an older fault that remains active today. Fault F5 traverses the NHTB and the Lu'an Basin in a northerly direction, exhibiting strong tectonic activity during the Neotectonic period. The most recent movement of this fault occurred in the Late Pleistocene [15]. Uneven basin-mountain development is observed on both sides of this fault. This unique geological background indicates that the HSR is a tectonic weak point, providing a favorable environment for the generation of tectonic earthquakes. It also suggests that the area is prone to frequent small to mid earthquakes, with large earthquakes being relatively rare [16].

3 Data and methods

3.1 Double-difference tomography method

The TomoDD method is a technique that simultaneously inverts for velocity structures and earthquake source parameters using both absolute and relative travel-time data [17, 18]. This method extends the LocDD method [19]. In the TomoDD method, the model is parameterized using a three-dimensional regular grid, with ray tracing and theoretical travel-time calculation performed using the pseudo-bending method. The inversion process is solved using the damped least squares algorithm [17, 18, 20]. The inversion results can be evaluated using model resolution experiments [21–23], DWS numerical methods or seismic ray density distribution [24], and checkerboard resolution tests [25, 26].

Considering spatial variations in medium velocity structures, TomoDD method employs absolute travel-time data to mitigate errors associated with the assumption of constant velocities between event pairs and stations, leading to more accurate location results. The velocity structure both within and outside the source region, along with the source locations, are determined using differential and absolute travel-time data, respectively [19]. By integrating relative and absolute travel-time data in a joint inversion, it is possible to obtain a more refined three-dimensional velocity structure and precise earthquake locations [27, 28]. In the inversion process, priority is first given to absolute travel-time data to establish absolute earthquake locations and large-scale velocity structures. Subsequently, emphasis is placed on differential travel-time data to

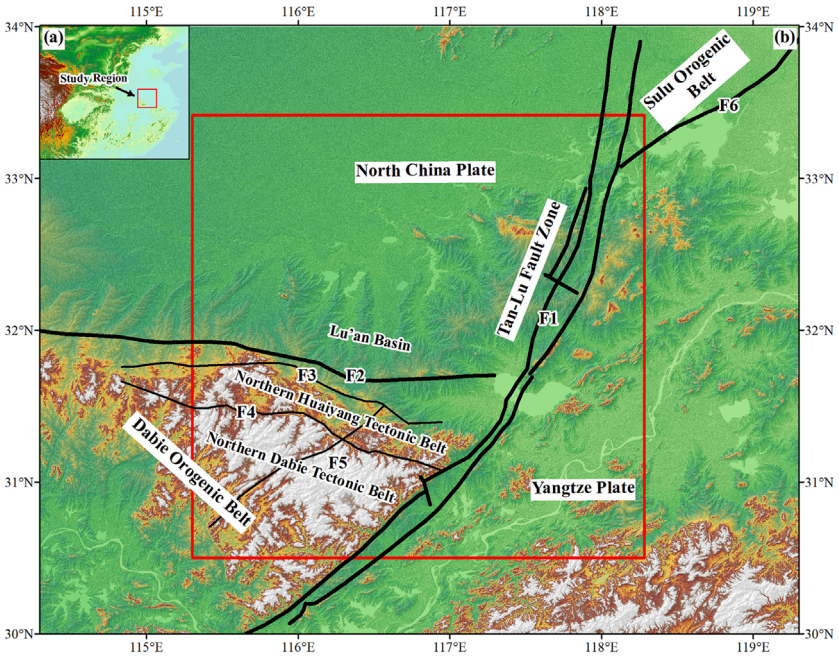

FIGURE 1
Geological structure background map. **(A)** Schematic diagram of the location of the study area, **(B)** Main structural units in and around the study area. The red rectangular box is the research area of this paper, and the black line represents the fault, F1: Tan-Lu Fault Zone, F2: Feixi-Hanbaidu Fault, F3: Meishan-Longhekou Fault, F4: Xiaotian-Mozitan Fault, F5: Luo'erling-Tudiling Fault, F6: Huaiyin - Xiangshuikou Fault.

refine the velocity structure within the source region and achieve precise earthquake localization [17, 18].

This study employs regional-scale the TomoDD method to calculate and obtain a more detailed three-dimensional velocity structure and precise earthquake locations within the study area. It further explores the relationships between geological structures, fault systems, and seismic activity in this area.

3.2 Data

The study area for this paper is defined by the coordinates 30.5°N-33.416°N, 115.3°E–118.283°E. To achieve better seismic ray coverage across the study region, the data collection area was expanded to 29.5°N-34.416°N, 114.3°E–119.283°E. A total of 4,427 earthquake events were collected from January 1998 to December 2021, along with the P- wave and S-wave arrival time data from 202 seismic stations within this extended area. To enhance data quality and achieve more accurate velocity structures and earthquake locations, a rigorous selection of seismic phase data was conducted: (1) Earthquake events recorded by at least five stations were selected; (2) The distance between the earthquake and the station was restricted to no more than 800 km; (3) The maximum distance between earthquake pairs was set at 30 km, with a minimum of 10 km; (4) The required number of phases per earthquake pair ranged from 8 to 120; (5) The maximum number of neighbors for each earthquake was limited to 30. Seismic phase data with significant errors were removed based on the fitted travel-time curves [29]. The travel-time curves before and after data filtering are shown in Figures 2, 3. Ultimately, 4,007 effective earthquake events were selected from the initial 4,427 for joint inversion, yielding 52,465 absolute travel-time data points and 616,425 relative travel-time data points.

Figure 4 displays the distribution of earthquake events and stations after relocation using the TomoDD method. The majority of the relocated events are concentrated at depths of 5–15 km, predominantly within the upper to middle crust, which has significant tectonic implications. A strong correlation is observed between the distribution of small to mid earthquakes and fault structures. The distribution of seismic ray paths within the study area is shown in Figure 5, demonstrating that the study region has good ray path coverage.

3.3 Selection of the initial model and parameters

Tomographic inversion is highly sensitive to the initial model, making the selection of an appropriate model critical. In this study, we incorporated wide-angle reflection data and performed a comprehensive analysis based on the HQ13 artificial seismic sounding velocity profile, alongside the findings of Huang et al. (2011) [30] and Li et al. (2018) [31], to develop the initial 1D P-wave velocity model. The specific parameters are listed in Table 1, with a P-wave to S-wave velocity ratio set at 1.73. In this paper, the model was parameterized using a horizontal grid spacing of 0.25° × 0.25°, with vertical grid nodes set at the depths defined by the initial velocity model.

In the TomoDD method inversion, the solution is derived using the damped least squares algorithm, where smoothing and

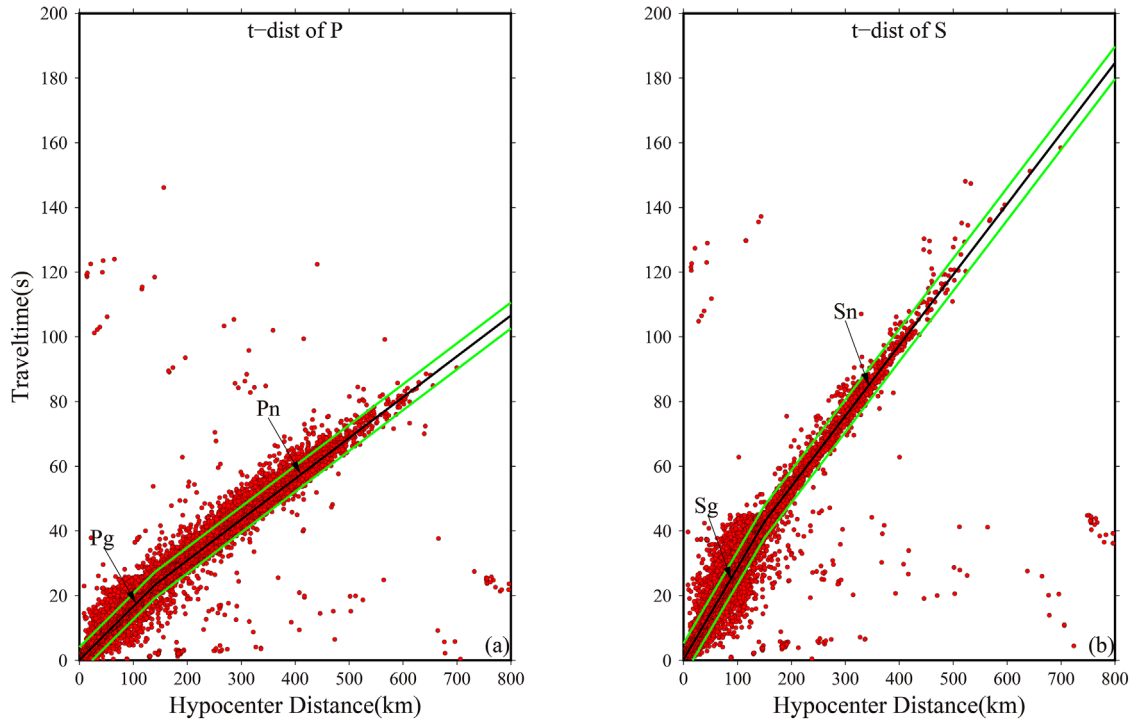

FIGURE 2
Travel-time curves of original data.

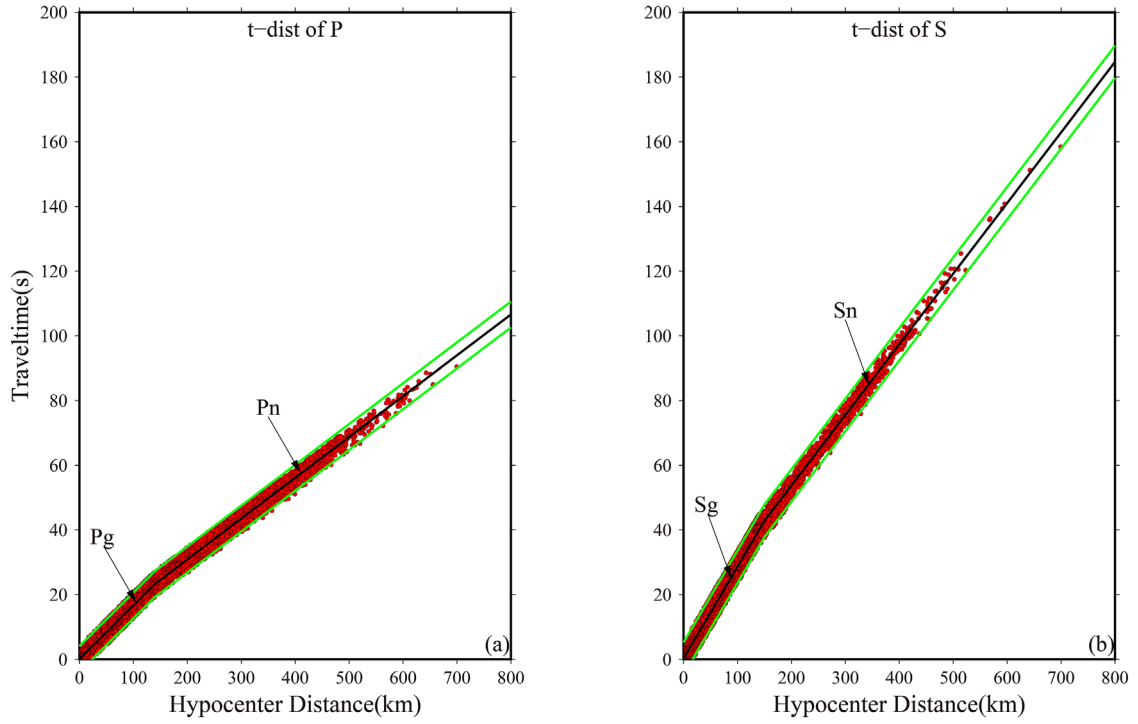

FIGURE 3
Travel-time curves with outliers rejected.

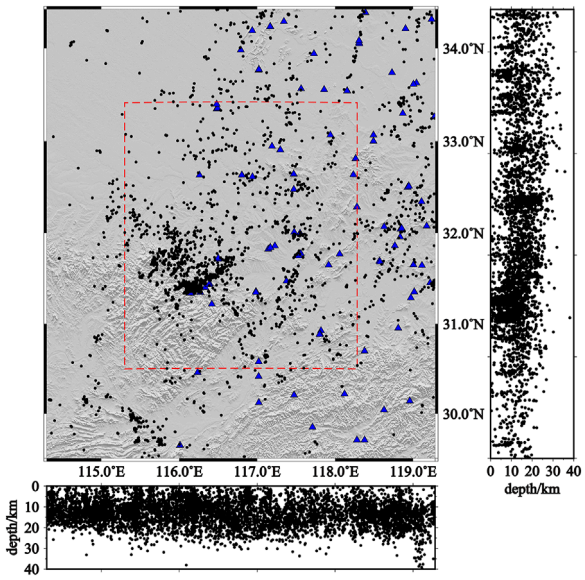

FIGURE 4
Distribution of seismic events and stations after location. The black dots represent the positions of the earthquakes after relocation, the blue triangles indicate the seismic stations, and the red dashed rectangular box outlines the study area.

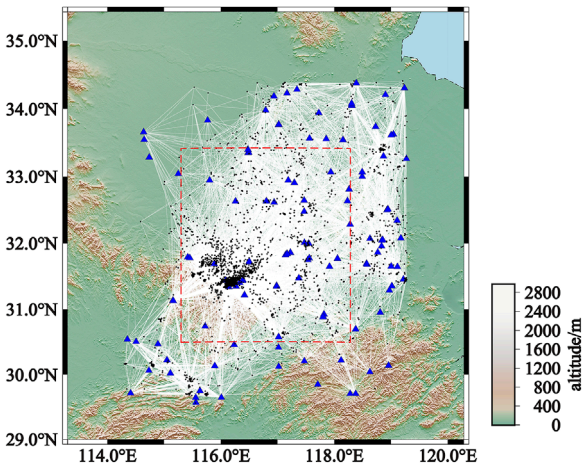

FIGURE 5
Distribution of earthquake, station and ray path. The black dots represent the positions of the earthquakes after relocation, the blue triangles indicate the seismic stations, the red dashed rectangular box outlines the study area, and the white lines depict the seismic ray paths.

damping factors are incorporated to reduce the influence of data errors on the inversion results. These factors play a crucial role in controlling the stability of the inversion process [32]. The smoothing factor constrains the model's slowness, while the damping factor simultaneously constrains both the slowness and the earthquake location parameters. If the smoothing and damping factors are set too low, the solution norm may become excessively large; conversely, if set too high, the data residual norm may increase significantly. In this study, the optimal smoothing and damping factors were determined to be 150 and 500, respectively, using the L-curve method [33, 34].

4 Tomography results

4.1 Model resolution test analysis

In this study, the reliability of the inversion results was evaluated using the checkerboard resolution test [35, 36]. This method involves introducing perturbations to the velocity values of each grid in the initial velocity model to create a perturbed 3D velocity model. The perturbed model is then used to generate synthetic travel times, which are inverted using the TomoDD method with the initial model as a reference. The extent to which the inversion recovers the perturbed model is then assessed. A successful checkerboard test, characterized by alternating positive and negative velocity anomalies, indicates good resolution and high reliability of the inversion results.

In this study, a 5% positive and negative velocity perturbation was applied for the checkerboard test. The results at various depths are presented in Figures 6, 7. As shown, the P-wave and S-wave models demonstrate good recovery at depths of 5–25 km, with high resolution across most areas, except for the northwest corner, where resolution is lower. At a depth of 33.9 km, the resolution is comparatively lower due to sparse seismic activity and reduced ray density. However, the upper mantle at 40 km depth exhibits higher ray density and resolution, as Pn and Sn waves predominantly travel through the uppermost mantle [37]. Overall, the resolution test results indicate good recovery across most regions and depths, confirming the relative reliability of the inversion results.

4.2 Distribution characteristics of velocity and Poisson's ratio

Figures 8–10 display the P-wave and S-wave velocity imaging results, as well as the Poisson's ratio imaging results at various depths within the study area. In these figures, red circles represent historical earthquake epicenters, with the size of the circles indicating earthquake magnitude—the larger the circle, the greater the magnitude. Black line segments denote fault lines. The figures reveal significant lateral heterogeneity in the P-wave and S-wave velocity structures and Poisson's ratio distribution in the crust and upper mantle of the study area. Additionally, the velocity and Poisson's ratio distributions exhibit segmented characteristics along fault F1.

The crust-mantle velocity structures of the DOB, the NCP, and the YP reveal marked lateral heterogeneity. The velocity structure of the middle to upper crust in the study area reveals distinct tectonic features. At depths of 5–10 km (upper crust) (Figures 8A, B), there are pronounced lateral variations in crustal velocity. The DOB displays relatively high velocities, whereas the NCP and the Lower YP exhibit comparatively lower velocities. At depths of 15–25 km (middle to lower crust) (Figures 8C–E, 9C–E), the region

TABLE 1 One-dimensional velocity structure model before and after inversion in the study area.

Depth (km)	−5	0	5	10	15	20	25	33.9	40	60
P-wave velocity (km/s)	1.3	5.14	5.87	5.88	6.05	6.32	6.4	6.41	8.06	8.38

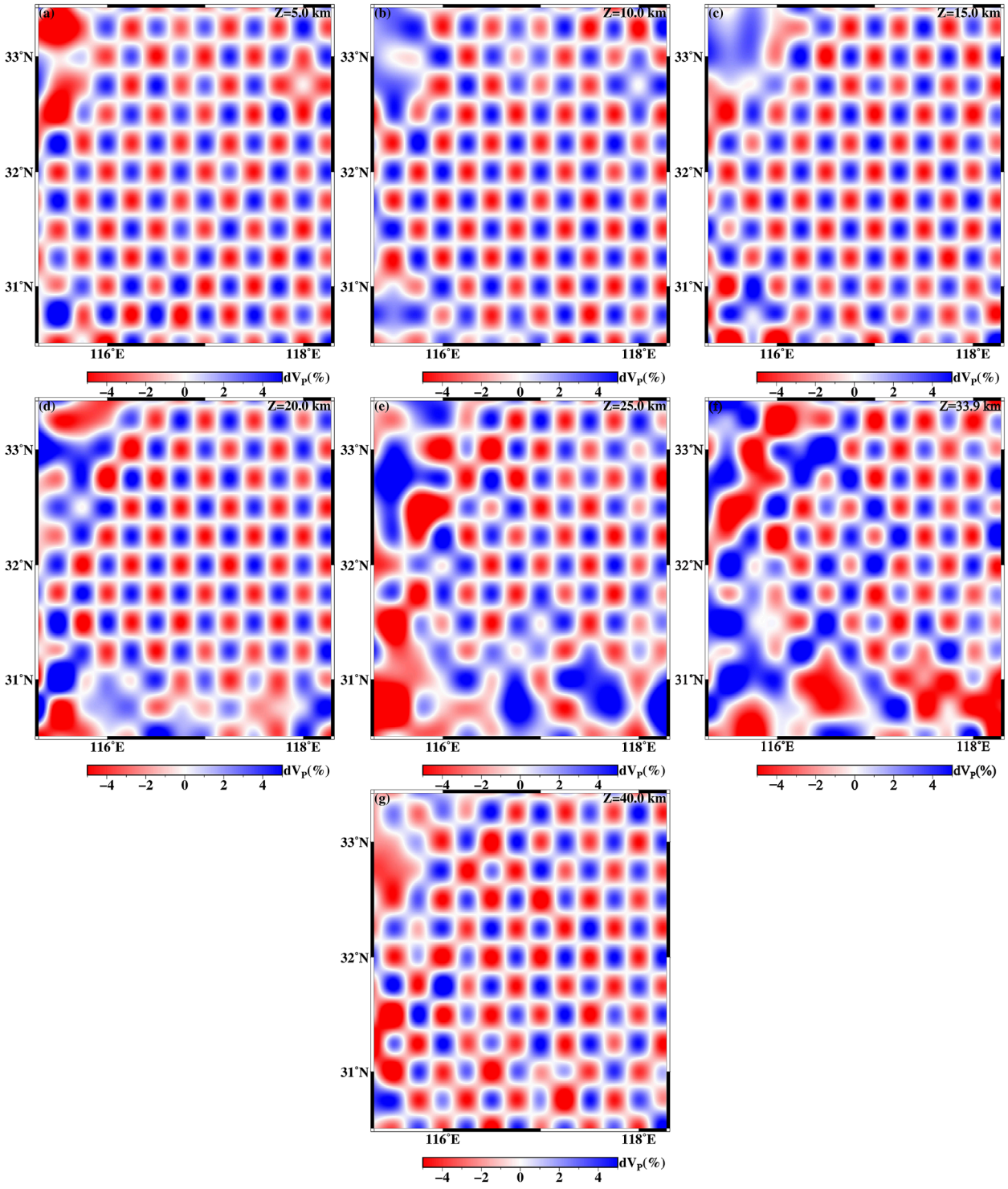

FIGURE 6
P-wave velocity imaging test board. **(A)** 5 km, **(B)** 10 km, **(C)** 15 km, **(D)** 20 km, **(E)** 25 km, **(F)** 33.9 km, **(G)** 40 km.

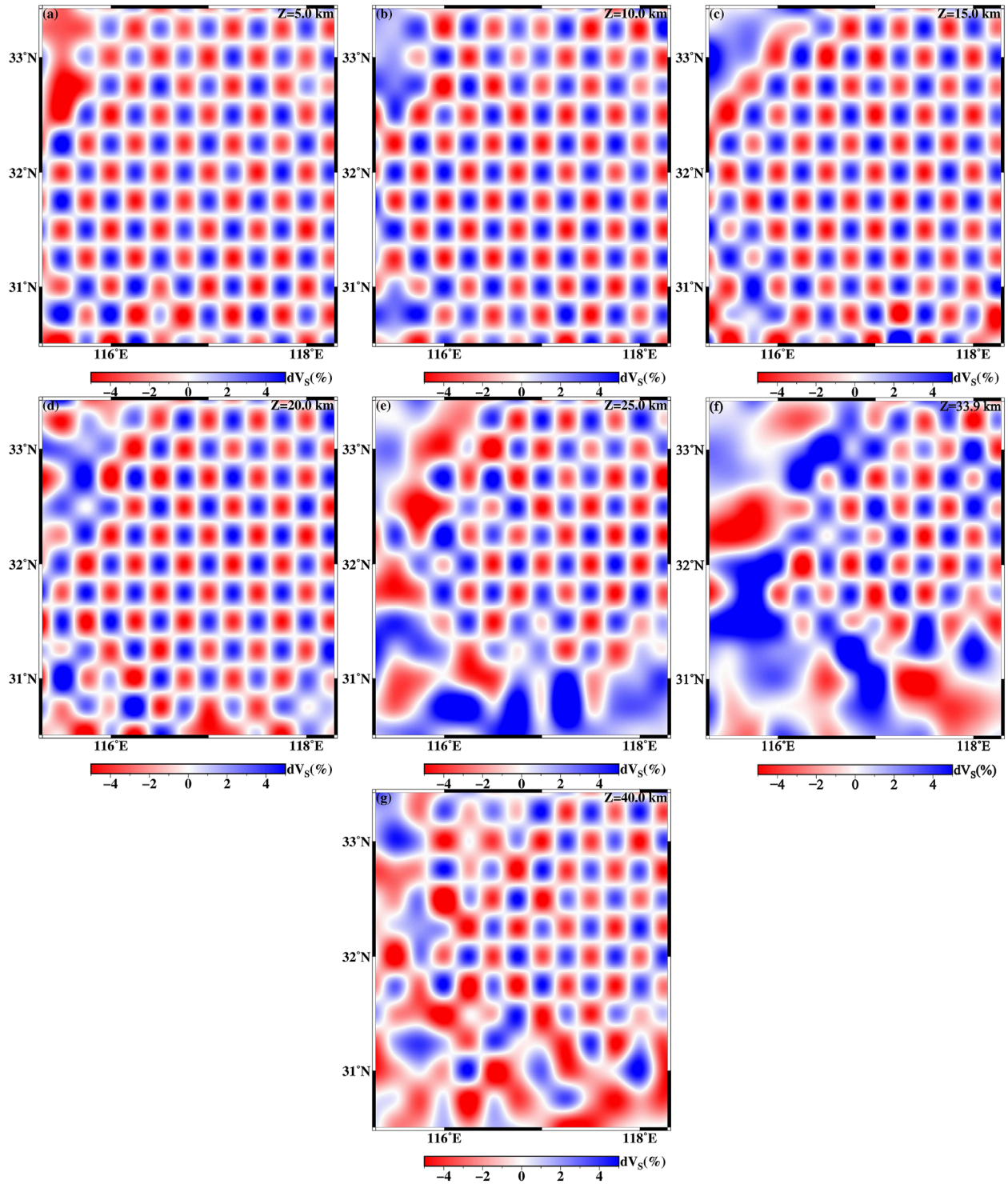

FIGURE 7
S-wave velocity imaging test board. **(A)** 5 km, **(B)** 10 km, **(C)** 15 km, **(D)** 20 km, **(E)** 2 5km, **(F)** 33.9 km, **(G)** 40 km.

of high velocity in the DOB orogen significantly diminishes. Notably, at a depth of 25 km, the S-wave velocity reveals a marked low-velocity zone within the DOB (Figure 9E). Despite this, the overall velocity characteristics in the study area indicate that velocities in the DOB remain higher than those in the NCP and the Lower YP, suggesting a continuity in the velocity structure from the upper to the middle crust.

At depths of 33.9–40 km (lower crust to the upper mantle) (Figures 8F,G, 9F,G), the DOB transitions from a high-velocity to a low-velocity distribution. The NCP displays relatively

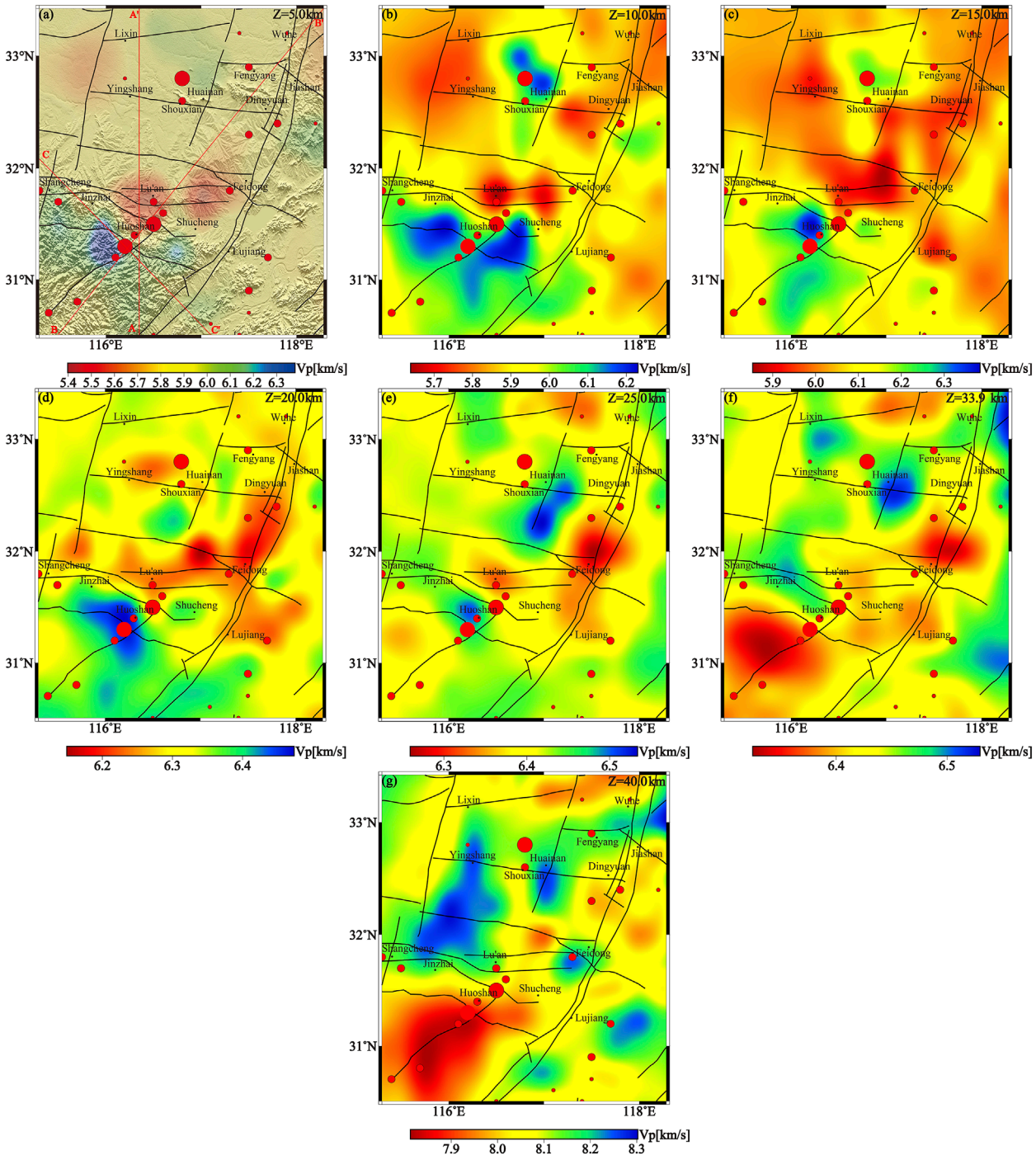

FIGURE 8
P-wave velocity structure imaging results at different depths. ((A) 5 km, **(B)** 10 km, **(C)** 15 km, **(D)** 20 km, **(E)** 25 km, **(F)** 33.9 km, **(G)** 40 km.

high-velocity features compared to the DOB [38], which may be associated with significant thinning and disruption of the lithosphere in the eastern North China Craton due to Pacific Plate subduction since the Mesozoic and Cenozoic eras [39]. Besides the marked velocity differences between tectonic blocks, high and low-velocity anomalies are interspersed within the same block. These variations in velocity structures between and within plates suggest that different geological structures have undergone diverse tectonic evolutionary histories.

Fault F1, extending NNE-SSW across the study area, delineates the boundary between the NCP and the YP. The velocity structure from the upper crust to the top of the upper mantle exhibits pronounced lateral heterogeneity along fault F1 and its surrounding areas. The distribution of P-wave and S-wave velocities along the fault demonstrates a

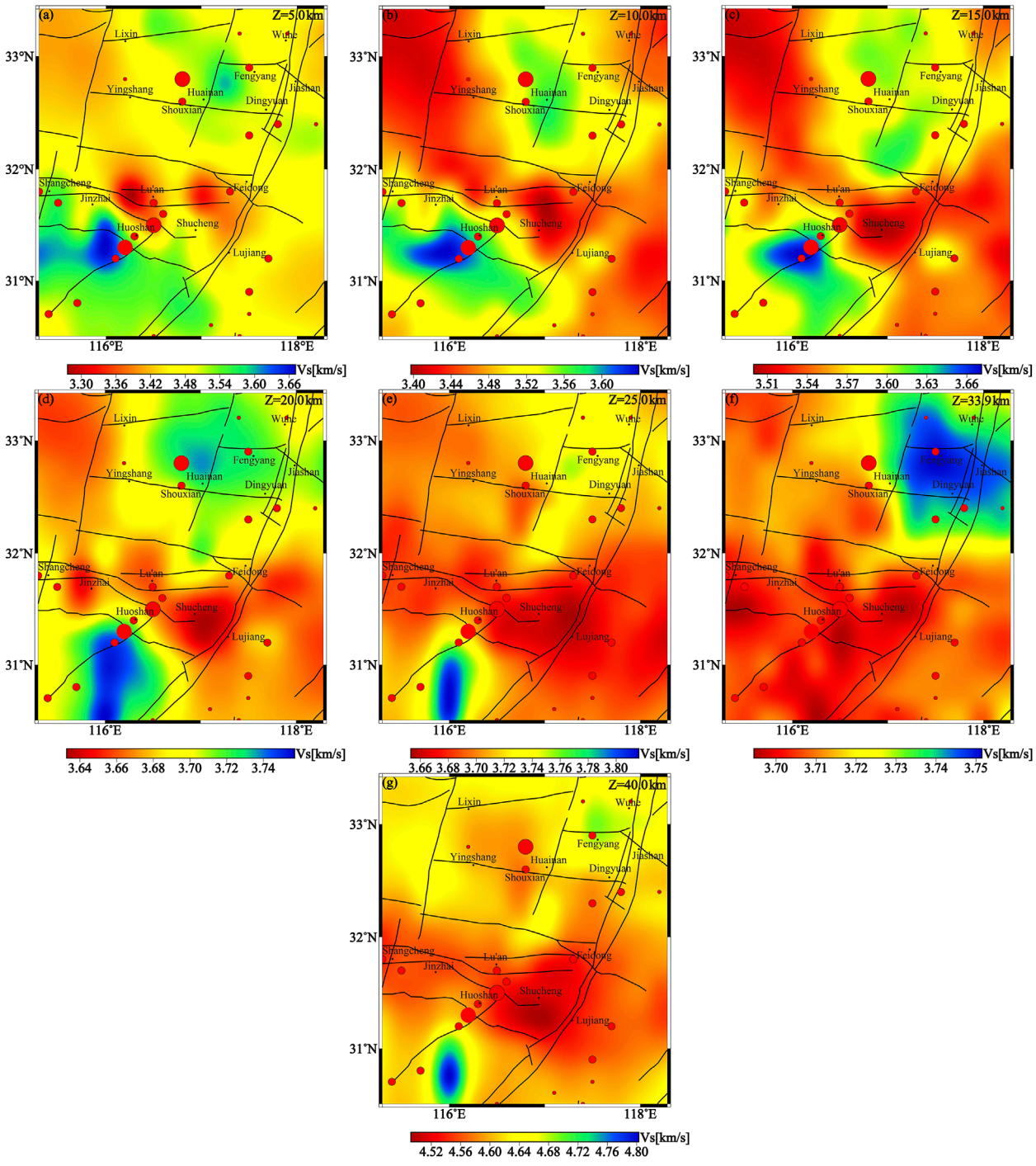

FIGURE 9
S-wave velocity structure imaging results at different depths. **(A)** 5 km, **(B)** 10 km, **(C)** 15 km, **(D)** 20 km, **(E)** 25 km, **(F)** 33.9 km, **(G)** 40 km.

segmented pattern. Specifically, crustal velocities south of Lujiang are relatively high, while those north of Jiashan are relatively low, with the region between Lujiang and Jiashan exhibiting intermediate velocities. These results are consistent with findings from He et al. (2021) [7] based on body wave imaging. The observed segmentation of the crustal and mantle velocity structures along fault F1 is likely associated with its multi-phase tectonic activity and the movement of deep-seated materials [40].

Along the F1 (Figures 8, 9), at a depth of 5 km, the segmentation characteristics of P-wave and S-wave velocities are relatively consistent. At depths of 10–15 km, the segmentation of P-wave velocity becomes more pronounced, with relatively high velocities south of Lujiang, intermediate velocities between Lujiang and

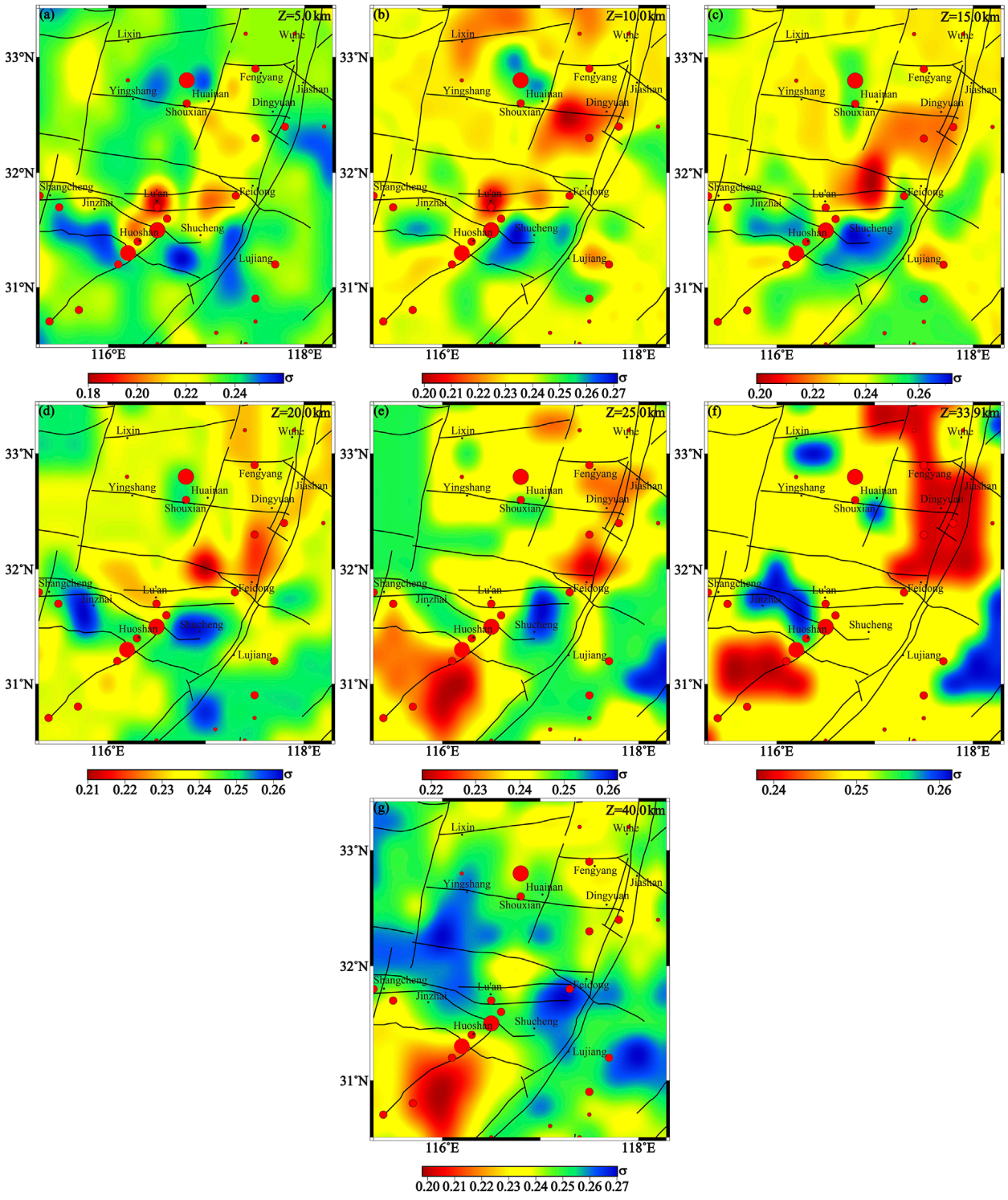

FIGURE 10
Poisson's ratio structure imaging results at different depths. **(A)** 5 km, **(B)** 10 km, **(C)** 15 km, **(D)** 20 km, **(E)** 25 km, **(F)** 33.9 km, **(G)** 40 km.

Jiashan, and relatively low velocities north of Jiashan. In contrast, S-wave velocities show relatively low values in the Feidong to Lujiang segment. At depths of 20–25 km, the velocity is generally higher north of Dingyuan compared to the south. At a depth of 33.9 km, the boundary roughly lies at Feidong, with slightly higher velocities in the Feidong region compared to the south, and more pronounced segmentation in S-wave velocity. At a depth of 40 km, the segmentation of S-wave velocity becomes more distinct, with the segmentation point around Dingyuan, where velocities are slightly higher in the northern segment compared to the south.

The inconsistent distribution characteristics of P-wave and S-wave high-velocity anomalies may be related to the physical properties and the state of the medium within the crust [7]. The surface and subsurface structural morphology of fault F1 exhibits vertical spatial variations, indicating the complexity of its deep and shallow tectonic relationships.

Figures 4, 8 reveal that after relocation, the small to mid earthquakes are predominantly concentrated within the HSR, particularly around the intersection of the NW-trending fault F4 and the NE-trending fault F5. Historical seismic activity is primarily aligned along the NE-trending fault F5 in a banded distribution. The frequent and concentrated seismic activity in the HSR is likely closely related to the unique deep-seated structures in the region. Analyzing the underground velocity structure and Poisson's ratio distribution is an effective method for studying the crustal and mantle medium structures.

The P-wave and S-wave velocities distribution results obtained in this study (Figures 8, 9) reveal significant lateral heterogeneity in the velocity structure of the HSR. At depths of 5–10 km, the NDTB shows high-velocity anomalies in both P-wave and S-wave structures, while the NHTB is located within a transition zone between high and low-velocity anomalies (Figures 8A,B, 9A,B). Faults F4 and F5 transect the high P-wave velocity region (Figures 8A,B, 9A,B), consistent with previous 3D body-wave imaging results [6–8, 13]. At a depth of 10 km, fault F5 is situated within a zone of relatively weak high P-wave velocity between two P-wave high-velocity anomalies (Figure 8B). At 5 km depth, the intersection of faults F4 and F5 is characterized by a weak low S-wave velocity anomaly (Figure 9A), supported by ambient noise tomography results from Li et al. (2023) [14], indicating that the upper crustal fault intersection zone has weak rock physical properties.

At depths of 15–25 km, the high-velocity regions in both the NDTB and the NHTB significantly reduce in size (Figures 8C–E, 9C–E), while the areas of high Poisson's ratio gradually expand (Figures 10C–E). The P-wave low-velocity anomalies are primarily concentrated at a depth of 25 km (Figure 8E), with S-wave low-velocity anomalies extending upwards to 15 km (Figures 9C–E), aligning well with previous body-wave imaging [6, 8] and ambient noise tomography results [4, 5]. At 15 km, the F5 is situated within a weaker P-wave high-velocity zone between two prominent high-velocity anomalies (Figure 8C).

At depths of 33.9–40 km, the extent of low-velocity regions in both P-wave and S-wave structures increases in the NDTB and the NHTB, consistent with large-scale velocity imaging results [4–6, 8, 41]. Fault F4 lies along a P-wave velocity transitional zone, indicating that this fault likely extends deeply, reaching down to the Moho discontinuity.

Poisson's ratio is a vital elastic parameter for elucidating the material composition of Earth's interior, providing an essential basis for understanding earthquake nucleation mechanisms, especially in evaluating the role of crustal fluids in influencing seismic activity [42]. The sensitivity of Poisson's ratio to chemical composition and the nature and degree of fluid content leads to the association of high Poisson's ratio and low velocity anomalies (particularly low Vs.) with the presence of fluids such as water or partial molten materials [43]. Poisson's ratio (σ) for the study region was derived from the calculated P-wave and S-wave velocities using the formula $\sigma = \frac{1}{2}\left\{1 - \left[\left(V_P/V_S\right)^2 - 1\right]^{-1}\right\}$ [7], with distribution results displayed in Figure 10.

At depths of 5–10 km (Figures 10A, B), high Poisson's ratio anomalies align NW along fault F4 on either side of the fault intersection, while low Poisson's ratio anomalies extend NE along fault F5. At a depth of 10 km, east of the fault junction, anomalies in high Poisson's ratio (Figure 10B), high P-wave velocity (Figure 8B), and low S-wave velocity (Figure 9B) are observed, consistent with previous body-wave imaging results [44].

At depths of 15–25 km (Figures 10C–E), high Poisson's ratios are prevalent in the NHTB, while the NDTB transitions from high to lower Poisson's ratios. Fault F4 traverses a marked Poisson's ratio gradient, effectively delineating the structural boundary. Fault F5 lies on a Poisson's ratio gradient only at 15 km depth, implying that this fault may not extend to the middle-lower crust.

At depths of 33.9–40 km (Figures 10F, G), fault F4 is situated within a Poisson's ratio transition zone, suggesting that it acts as a boundary fault separating the NDTB and the NHTB, extending deeply into the Moho [45, 46]. In the northwest sector of the convergence zone between faults F4 and F5, Poisson's ratio is notably elevated compared to the northeast sector of the junction. The low S-wave velocity structure (Figures 9F, G) and heightened Poisson's ratio (Figures 10F, G) on the northwest side extend upwards to approximately 15 km depth (Figures 9C–E and 10C, E), suggesting potential fluid involvement in the mid-to-lower crust of this region [47].

5 Discussionn

5.1 Earthquake, fault and velocity distribution relationship

To more intuitively demonstrate the variation of velocity and Poisson's ratio structures with depth and their relationship to earthquake distribution, this paper selects three vertical profiles (locations shown in Figure 8A): Profile AA' is located between the epicenters of the 1,652 Huoshan M6 earthquake and the 1917 Huoshan M6¼ earthquake; Profile BB' passes through the earthquake cluster at the intersection of faults F4 and F5; and Profile CC' passes through the epicenter of the 1917 Huoshan M6¼ earthquake. The imaging results of P-wave velocity, S-wave velocity, and Poisson's ratio along these profiles are presented in Figures 11–13. In these figures, the solid black lines represent the fault projections in the profiles, inferred from the velocity or Poisson's ratio structures combined with the relocated earthquakes. The red circles indicate the projections of the epicenters of the 1,652 Huoshan M6 earthquake and the 1917 Huoshan M6¼ earthquake on the profiles.

In the AA′ profile (Figure 11), at depths of 5–25 km, high-velocity anomalies for both P-wave and S-wave, along with a high Poisson's ratio, are observed beneath the NDTB and the NHTB, located between faults F4 and F5. Conversely, a weak low-velocity anomaly for P-wave and S-wave velocities and a weak low Poisson's ratio structure are present beneath the NHTB between faults F3

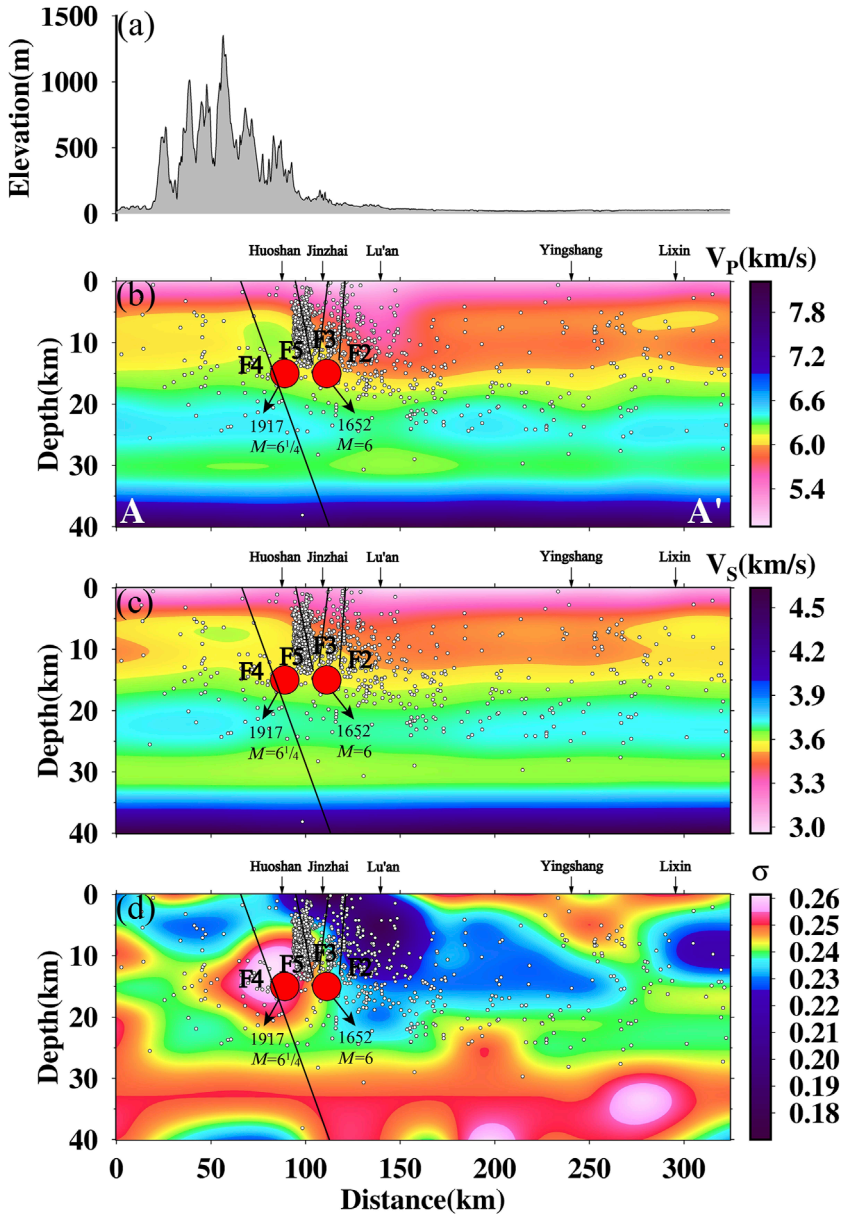

FIGURE 11
Elevation and imaging results along profile AA′, including P-wave, S-wave velocities, and Poisson's ratio. **(A)** Elevation, **(B)** P-wave velocity, **(C)** S-wave velocity, **(D)** Poisson's ratio.

and F5. Additionally, the Lu'an Basin at depths of 5–15 km exhibits low P-wave and S-wave velocities and a low Poisson's ratio anomaly, indicating that the NCP has likely extended beneath the NHTB, north of fault F5. Earthquakes along the AA' profile are primarily concentrated at depths of 5–15 km beneath faults F3 and F5, with the fault F3 acting as a boundary separating the high-velocity and high-Poisson's ratio layers of the orogenic belt in the middle to upper crust from the low-velocity and low-Poisson's ratio layers of the basin.

In the BB′ profile (Figure 12), the NDTB exhibits high-velocity anomalies for both P-wave and S-wave velocities at depths of 5–25 km, while the NHTB shows weak low-velocity anomalies for both P-wave and S-wave velocities. The Lu'an Basin, at depths of 5–15 km, is characterized by low P-wave and S-wave velocities, indicating that the NCP has extended beneath the NHTB, south of fault F3. At depths of 10–25 km beneath the NHTB, the P-wave velocity is relatively high, the S-wave velocity is relatively low, and the Poisson's ratio is elevated, suggesting the presence of fluids in this region [48]. This high Poisson's ratio anomaly is connected to a similar high Poisson's ratio structure below 25 km depth, indicating that fault F4 likely extends down to the upper mantle [49]. This fault represents a typical zone of crustal weakness, providing a conduit for the upwelling of hot material from the mantle. The BB' profile shows a concentration of earthquakes, primarily located beneath fault F4, at depths of 5–15 km. This fault acts as a boundary between the NDTB and the NHTB.

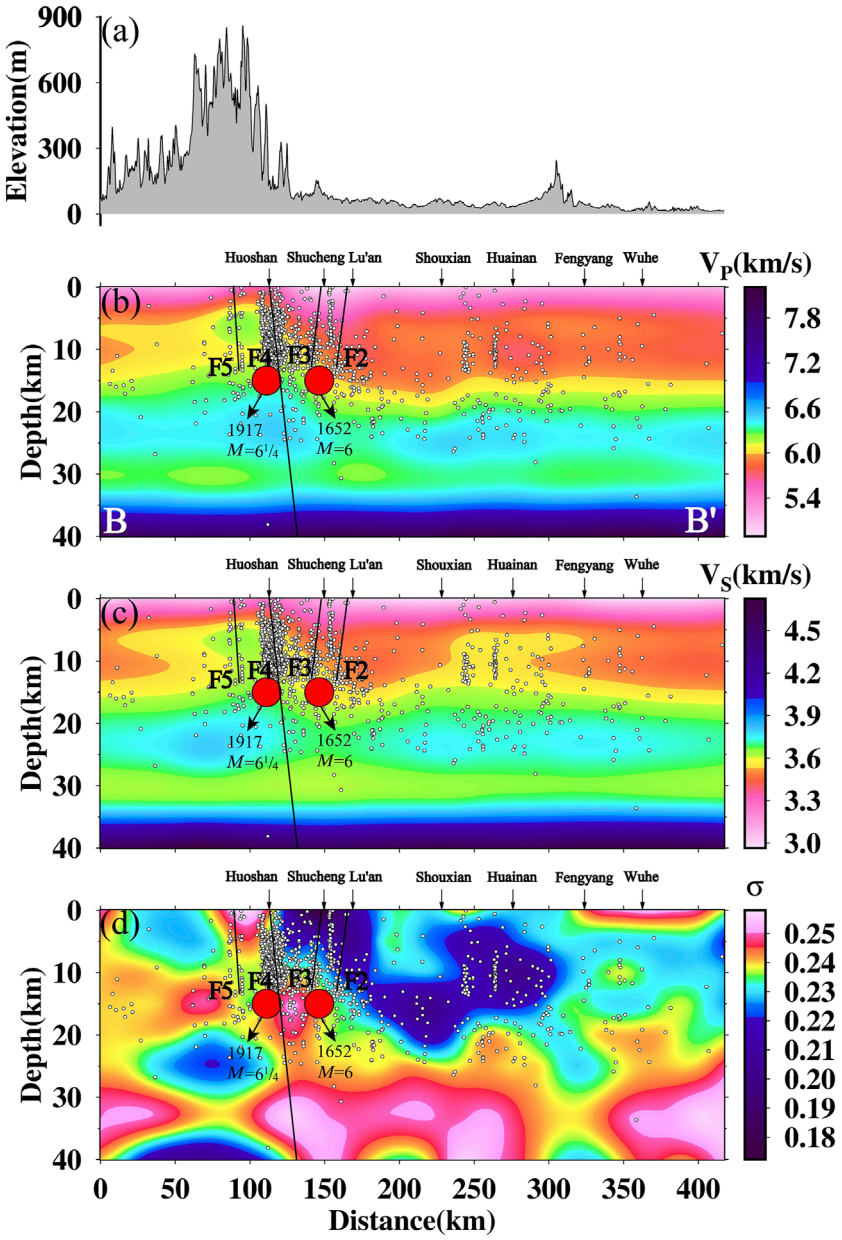

FIGURE 12
Elevation and imaging results along profile BB′, including P-wave, S-wave velocities, and Poisson's ratio. **(A)** Elevation, **(B)** P-wave velocity, **(C)** S-wave velocity, **(D)** Poisson's ratio.

In the CC′ profile (Figure 13), high-velocity anomalies for both P-wave and S-wave velocities, along with high Poisson's ratio structures, are observed beneath the NDTB and the NHTB at depths of 5–25 km. Conversely, at depths of 5–15 km beneath the NCP, low-velocity anomalies for both P-wave and S-wave velocities, along with low Poisson's ratio anomalies, extend southward to the NHTB near fault F3. This suggests that the NCP has intruded beneath the NHTB, south of fault F3. Earthquakes in the CC' profile are predominantly concentrated at depths of 5–15 km beneath fault F5. The relocated seismic events are primarily distributed in this depth range, with smaller earthquakes forming a linear distribution in the vertical direction, well-aligned with the fault structures. The high Poisson's ratio structure beneath fault F4 extends from the lower crust through the upper mantle to the upper crust, indicating that this fault is a deep, major fault cutting through the Moho. Hot mantle material upwells along fault F4, intruding into the middle and upper crust, extending northward beneath fault F3 before tapering off (Figure 13D). The influence of fluid intrusion has resulted in a high concentration of seismic activity within the middle and upper crust between faults F3 and F4 (Figures 4, 13).

In Figures 11–13, the red circles represent the epicenters of the 1,652 Huoshan M6 earthquake and the 1917 Huoshan M6¼

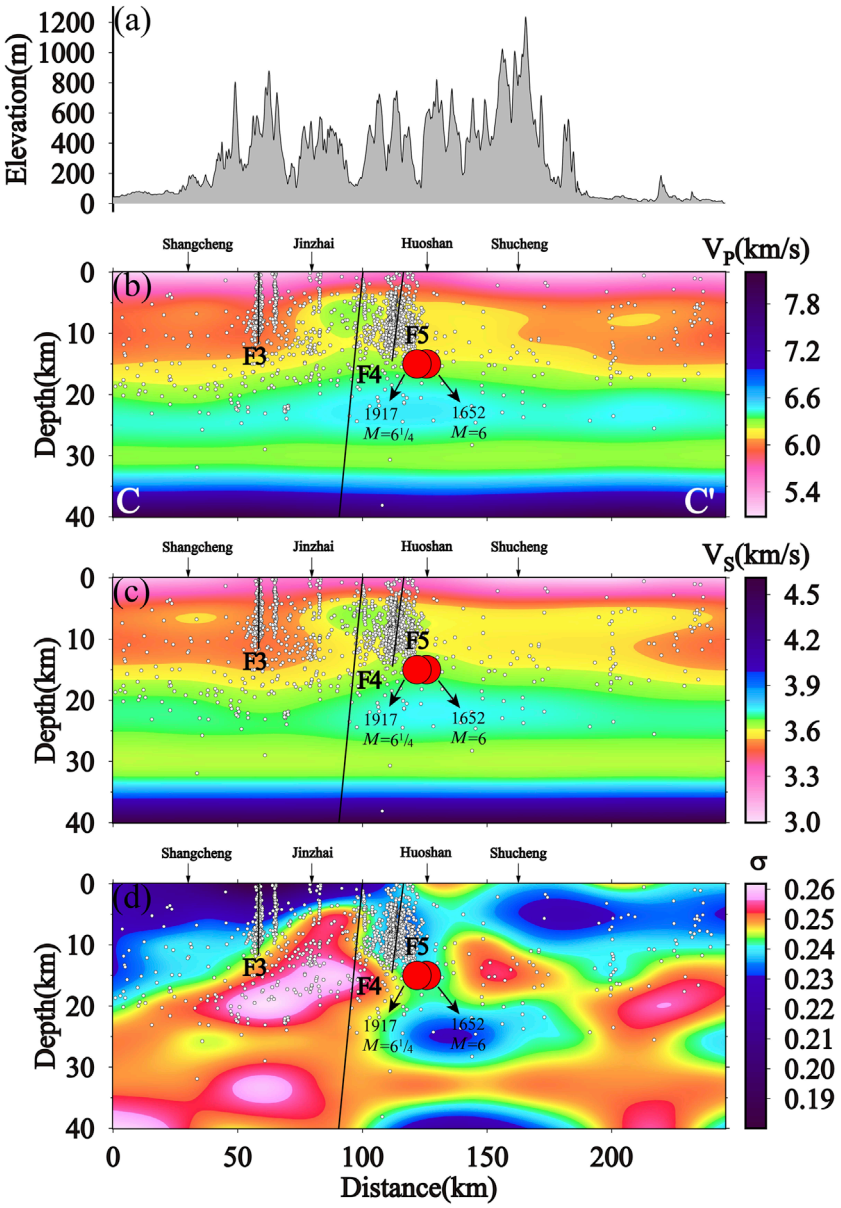

FIGURE 13
Elevation and imaging results along profile CC', including P-wave, S-wave velocities, and Poisson's ratio. **(A)** Elevation, **(B)** P-wave velocity, **(C)** S-wave velocity, **(D)** Poisson's ratio.

earthquake. While the latitude and longitude of these epicenters can be obtained from historical earthquake catalogs, the focal depths are unknown. Based on the velocity-Poisson's ratio structure, the relocation results of small to moderate earthquakes, and fault distribution, we infer that the focal depths of these two earthquakes are around 15 km. The inferred hypocenters are located near the gradient zones of velocity and Poisson's ratio, and closer to structures characterized by high P-wave velocities, low S-wave velocities, and high Poisson's ratios. This is corroborated by magnetotelluric results showing low resistivity and high conductivity in the mid-crust [1], which may indicate the presence of fluids [48]. These anomalous structures suggest that deep material intrusions along the fault zone may serve as a driving force for moderate to strong earthquake development [50], indicating that the Huoshan seismic area has the deep-seated conditions necessary for generating earthquakes of magnitude 6 or greater.

5.2 Analysis of formation of earthquake swarm and deep seismogenic environment

After earthquake relocation, seismic events are particularly concentrated on the northwest side of the intersection between faults F4 and F5 (Figures 4, 8). Under the influence of near east-west horizontal compression and north-south horizontal extensional regional stress, the rock mass along fault F4 is likely to be highly

fractured, forming a tectonically weak zone within the Huoshan Seismic Area. When fault F4 intersects with fault F5, it exploits the pre-existing structural weakness of fault F4, where the fractured zone, influenced by external factors, becomes a region prone to stress release, leading to the concentration of small to mid earthquakes in this area [1]. Small to moderate earthquakes in the region are primarily distributed in the western segment of the intersection between faults F4 and F5. This concentration may be attributed to the gravitational sliding along fault F4 in the NHTB, which predominantly occurs in the western section of the NHTB [46].

Mid to strong earthquakes are primarily located within the tectonically weak zones at fault intersections. For instance, the 1,652 Huoshan M6 earthquake occurred near the intersection of faults F3 and F5, while the 1917 Huoshan M6¼ earthquake was located near the intersection of faults F4 and F5 (Figure 8). The epicenters of these mid to strong earthquakes are situated along zones of velocity and Poisson's ratio gradients within the middle to upper crust (Figures 11, 13). Additionally, beneath these epicenters, there exists a high Poisson's ratio structure extending from the middle and upper crust down to the lower crust and upper mantle. This suggests that high-temperature materials from the deep mantle have upwelled along the fault zones into the middle and upper crust. The strong crust-mantle interaction in this region, with the upwelling fluids, may represent the deep tectonic source for the 1,652 Huoshan M6 earthquake and the 1917 Huoshan M6¼ earthquake [50].

The spatial distribution of the Huoshan earthquake swarm is influenced by underlying deep-seated structures, which require corresponding explanations based on deep structural analyses. Previous research indicates that the deep dynamic background of the Huoshan earthquake swarm is closely related to the subduction interactions among the Tibetan Plateau, the NCP, the YP, and the Pacific Plate [51–53].

On one hand, velocity structures and anisotropy studies [54–57] confirm that tectonic movements at the southeastern margin of the Tibetan Plateau exert near east-west compressive stress on the DOB, resulting in the presence of east-west trending low-velocity material and fast wave directions in the upper mantle beneath the DOB. This may provide a source of fluids for the HSR.

On the other hand, the subduction of the YP beneath the NCP has led to the lithospheric thickening of the DOB. During the post-collision phase, this thickened lithosphere may undergo delamination, allowing asthenospheric material to upwell. The interaction between the upwelling mantle and partial melting of the middle and lower crust generates magma, which intrudes into the overlying crust, cooling to form high-velocity bodies in the middle crust [51, 52].

Additionally, high-velocity subducted slab segments lying flat in the transition zone beneath the Huoshan earthquake swarm, similar to those observed under the North China Craton, suggest that the formation of the Huoshan earthquake swarm is closely related to the westward subduction of the ancient Pacific Plate [58]. The combined influence of upwelling fluids from subduction and low-velocity material extruded from the Tibetan Plateau has made the Huoshan earthquake swarm region a convergence point of multiple deep dynamic processes, leading to the development of tectonic weak zones and consequently inducing seismic activity.

6 Conclusion

Drawing on arrival-time data for initial P-wave and S-wave from 4,427 seismic events recorded between January 1998 and December 2021, this study applies double-difference tomography to generate refined earthquake relocations, P-wave and S-wave velocity models, and Poisson's ratio structures. This methodology significantly enhances the precision of earthquake localization and improves the resolution of velocity inversion. The study integrates the characteristics of velocity, Poisson's ratio distribution, double-difference earthquake location results, and other data to analyze the relationship between regional velocity distribution and geological structures. It also examines the segmented velocity characteristics along fault F1 and investigates the causes of concentrated seismic distribution in the HSR, focusing on the deep seismogenic structures associated with moderate to strong earthquakes. The following results were obtained:

The crustal medium in the study area exhibits significant lateral heterogeneity. The DOB shows notably high velocity values, while the NCP and the YP exhibit relatively low values.

The crustal structure of fault F1 exhibits distinct segmentation, with relatively high velocity values south of Lujian, low values north of Jiashan, and intermediate values in the segment between Lujiang and Jiashan. This segmentation of the crust-mantle structure in fault F1 is related to its multiphase activity and the migration of deep materials.

Relocated seismic events are primarily concentrated in the HSR, particularly around the confluence of the faults F4 and F5. We suggest that, under regional tectonic stress, the active fault F5 exploits the structurally weakened zone created by the earlier fault F4. Deep fluids may migrate upward along these faults, reducing fault strength and encouraging earthquake clustering within this area.

The epicenters of mid-strong earthquakes are located on the gradient zones of velocity and Poisson's ratio. The source regions of these earthquakes show significant anomalies of high Poisson's ratio and low S-wave velocity, which may indicate the presence of fluids. These anomalies may indicate the presence of fluids in the earthquake source regions, suggesting that the intrusion of deep materials along the fault could be the driving force behind the generation of mid to strong earthquakes.

Data availability statement

The original contributions presented in the study are included in the article/supplementary material, further inquiries can be directed to the corresponding authors.

Author contributions

TH: Methodology, Software, Writing–original draft. XF: Conceptualization, Funding acquisition, Writing–review and editing. YH: Supervision, Validation, Writing–review and editing. LY: Data curation, Formal Analysis, Writing–review and editing. CY: Visualization, Writing–review and editing. PJ: Project

administration, Writing–review and editing. ZL: Investigation, Writing–review and editing. ZX: Software, Writing–review and editing. MX: Validation, Writing–review and editing. YW: Validation, Writing–review and editing.

Funding

The author(s) declare that financial support was received for the research, authorship, and/or publication of this article. This study was supported by the National Natural Science Foundation of China (Grant No. 42104099 and 41874051) and Active Fault Detection and Seismic Risk Assessment in Lu'an City.

Conflict of interest

Authors TH, PJ and ZL were employed by Nanjing Shanhai Engineering Technology Co., Ltd.

The remaining authors declare that the research was conducted in the absence of any commercial or financial relationships that could be construed as a potential conflict of interest.

Generative AI statement

The author(s) declare that no Generative AI was used in the creation of this manuscript.

Publisher's note

All claims expressed in this article are solely those of the authors and do not necessarily represent those of their affiliated organizations, or those of the publisher, the editors and the reviewers. Any product that may be evaluated in this article, or claim that may be made by its manufacturer, is not guaranteed or endorsed by the publisher.

References

1. Cui T, Chen X, Zhan Y, Zhao L, Liu Z. Characteristics of deep electrical structure and seismogenic structure beneath Anhui Huoshan earthquake area. *Chin J Geophys (in Chinese)* (2020) 63(01):256–69. doi:10.6038/cjg2019M0458

2. Zhang J, Yang X, Liu C, Zhang L, Li B, Xu Y, et al. The fine deep structure of the northern margin of the Dabie Orogenic Belt from gravity-magnetic-electrical-seismic combination survey. *Chin J Geophys (in Chinese)* (2012) 55(07):2292–306. doi:10.6038/j.issn.0001-5733.2012.07.015

3. Wang X, Zhou D, Li L, Zhang B, Liu J, Li J. Small earthquake detection in huoshan seismic window and its application in earthquake prediction. *Earthquake* (2024) 44(02):135–46. doi:10.12196/j.issn.1000-3274.2024.02.009

4. Luo S, Yao H, Li Q, Wang W, Wan K, Meng Y, et al. High-resolution 3d crustal s-wave velocity structure of the middle-lower yangtze river metallogenic belt and implications for its deep geodynamic setting. *Sci China Earth Sci* (2019) 62:1361–78. doi:10.1007/s11430-018-9352-9

5. Luo S, Yao H, Zhang Z, Bem TS. High-resolution crustal and upper mantle shear-wave velocity structure beneath the central-southern Tanlu Fault: implications for its initiation and evolution. *Earth Planet Sci Lett* (2022) 595:117763. doi:10.1016/j.epsl.2022.117763

6. Cui X, Song X, Xu L, Zhu Y, Li B, Zhang W. Three dimensional crustal P-wave structure beneath the central south segment of the Tanlu Fault Zone determined by local earthquake travel-time tomography. *Terra Nova* (2021) 33(6):613–20. doi:10.1111/ter.12553

7. He Y, Fan X, Zhao Q, Huo Z, Yang C, Zheng L, et al. Segmentation of crustal structure beneath the middle-south segment of tan-Lu Fault Zone. *J Geophys* (2021) 64(09):3164–78. doi:10.6038/cjg2021O0247

8. Sun Y, Wang H, Huang Y, Wang J, Jiang H, He Y, et al. Insight into seismotectonics of the central-south Tanlu Fault in east China from P-wave tomography. *J Asian Earth Sci* (2023) 258:105722. doi:10.1016/j.jseaes.2023.105722

9. Huang X, Yu J, Qi H, Zang B, Xia S, Han C. Precise relocation of small medium earthquakes in Anhui"Huoshan seismic window". *China Earthquake Eng J* (2016) 38(02):236–41+48. doi:10.3969/j.issn.1000-0844.2016.02.0236

10. Zhu H, Lu D, Tao F, Ying Y, Zhou Z, Liu H, et al. Fine location of small and medium earthquakes in Huoshan window based on double difference method. *Sci and Technology Inf* (2020) 18(27):52–5. doi:10.16661/j.cnki.1672-3791.2007-5042-1804

11. Li L, Yao H, Li J, Zhang B, Wang X, Zhou D. High-resolution shallow crustal shear wave velocity structure in Huoshan and its relationship with seismicity. *Seismological Geomagnetic Observation Res* (2022) 43(S1):66–9. doi:10.1360/SSTe-2020-0106

12. Xu X, Wan Y, Meng G, Li X, Liu Z, He J. Study on three seismic fault segments and their sliding properties revealed by clustered seismic events in Huoshan area, Anhui Province. *Chin J Geophys (in Chinese)* (2022) 65(05):1688–700. doi:10.6038/cjg2022P0768

13. Zhang Y, Wang B, Xu T, Yang W, Wang W, Xu Y, et al. Three-dimensional crustal Vp and vs structures beneath the southern segment of the Tan-Lu Fault revealed by active source and earthquake data. *Geophys J Int* (2020) 223(3):2148–65. doi:10.1093/gji/ggaa314

14. Li L, Yao H, Zhang B, Li J, Shu P, Yang Y, et al. High resolution upper crustal velocity and seismogenic structure of the Huoshan "seismic window" in the Dabie orogenic belt. *Front Earth Sci* (2023) 11:1110061. doi:10.3389/feart.2023.1110061

15. Yao D, Liu J, Li J, Zhai H. Seismic activities and structures of the Liu'an-Huoshan seismic risk area. *Seismology Geology* (2003)(02) 211–9.

16. Zhang J, Yao D, Liu D, Shen Y, Shen X, Wang X. Prediction study on mid-long-term seismic risk zone in Anhui Province. In: *Seismological and geomagnetic observation and research* (2006). p. 29–39.

17. Zhang H, Thurber C. Double-Difference Tomography: the method and its application to the hayward fault, California. *Bullseismolsocam* (2003) 93(5):1875–89. doi:10.1785/0120020190

18. Zhang H, Thurber C. Development and applications of double-difference seismic tomography. *Pure and Appl Geophys* (2006) 163(2-3):373–403. doi:10.1007/s00024-005-0021-y

19. Felix W, William L. Ellsworth. A double-difference earthquake location algorithm: method and application to the northern hayward fault, California. *Bull Seismological Soc America* (2000) 90(6):1353–68. doi:10.1785/0120000006

20. Paige CC, Saunders MA. Algorithm 583: lsqr: sparse linear equations and least squares problems. *ACM Trans Math Softw (Toms)* (1982) 8(2):195–209. doi:10.1145/355993.356000

21. Thurber CH. Earthquake locations and three-dimensional crustal structure in the coyote lake area, central California. *J Geophys Res Solid Earth* (1983) 88(B10):8226–36. doi:10.1029/jb088ib10p08226

22. Lei J, Zhao D. Teleseismic evidence for a break-off subducting slab under eastern Turkey. *Earth and Planet Sci Lett* (2007) 257(1-2):14–28. doi:10.1016/j.epsl.2007.02.011

23. Lei J, Zhao D, Su J, Zhang G, Li F. Fine seismic structure under the Longmenshan fault zone and the mechanism of the large Wenchuan earthquake. *Chin J Geophys (in Chinese)* (2009) 52(02):339–45.

24. Hui S, Zhang Y, Li S. Study on the t-D earthquake location method. *Northwest Earthquake J* (2012) 34(01):10–3.

25. Junho U, Clifford T. A fast algorithm for two-point seismic ray tracing. *Bull Seismological Soc America* (1987) 77(3):972–86. doi:10.1785/BSSA0770030972

26. Humphreys E, Clayton RW. Adaptation of back projection tomography to seismic travel time problems. *J Geophys Res Solid Earth* (1988) 93(B2):1073–85. doi:10.1029/JB093iB02p01073

27. Okada T, Umino N, Matsuzawa T, Nakajima J, Uchida N, Nakayama T, et al. Aftershock distribution and 3d seismic velocity structure in and around the focal area of the 2004 mid niigata prefecture earthquake obtained by applying double-difference tomography to dense temporary seismic network data. *Earth, planets and space* (2005) 57(5):435–40. doi:10.1186/BF03351830

28. Yu X, Chen Y, Zhang H. Relocation of earthquakes in Beijing-Tianjin-Tangshan region with double-difference tomography technique. *Acta Seismologica Sinica* (2010) 32(03):257–69.

29. Xin H, Zhang H, Kang M, He R, Gao L, Gao J. High-resolution lithospheric velocity structure of continental China by double-difference seismic travel-time tomography. *Seismological Res Lett* (2019) 90(1):229–41. doi:10.1785/0220180209

30. Huang Y, Li Q, Zhang Y, Sun Y, Bi X, Jin S, et al. Crustal velocity structure beneath the Shandong-Jiangsu-Anhui segment of the Tancheng-Lujiang fault zone and adjacent areas. *Chin J Geophys (in Chinese)* (2011) 54(10):2549–59. doi:10.3969/j.issn.0001-5733.2011.10.012

31. Li X, Zhao Q, Zhu F, Hong M, Wang H. The study of 1d velocity model based on multi-phase joint inversion in jiangsu province. *Earthquake Res China* (2018) 34(02):312–21.

32. Eberhart-Phillips D. Three-dimensional velocity structure in northern California coast ranges from inversion of local earthquake arrival times. *Bullseissocam* (1986) 76(4):1025–52. doi:10.1785/BSSA0760041025

33. Hansen PC. Analysis of discrete ill-posed problems by means of the L-curve. *Siam Rev* (1992) 34(4):561–80. doi:10.1137/1034115

34. O'Leary DP, Hansen PC. The Use of the L-curve in the regularization of discrete ill-posed problems. *SIAM J Scientific Comput* (1993) 14(6):1487–503. doi:10.1137/0914086

35. Zhao D, Hasegawa A, Horiuchi S. Tomographic imaging of P and S wave velocity structure beneath northeastern Japan. *J Geophys Res Solid Earth* (1992) 97(B13):19909–28. doi:10.1029/92JB00603

36. Spakman W, van der Lee S, van der Hilst R. Travel-time tomography of the european-mediterranean mantle down to 1400 km. *Phys Earth Planet Interiors* (1993) 79(1-2):3–74. doi:10.1016/0031-9201(93)90142-V

37. Ma M, Zhao A. Double-difference tomography of crustal P-and S-wave velocity structures beneath north China. *Acta Seismologica Sinica* (2021) 43(01):13–33+136. doi:10.11939/jass.20200062

38. Yao Z, Eric S, Wang C, Ding Z, Chen Y. Asthenospheric upwelling beneath northeastern margin of ordos block: constraints from Rayleigh surface-wave tomography. *Tectonophysics* (2020) 790:228548. doi:10.1016/j.tecto.2020.228548

39. Chen L, Tao W, Zhao L, Zheng T. Distinct lateral variation of lithospheric thickness in the northeastern north China craton. *Earth Planet Sci Lett* (2008) 267(1-2):56–68. doi:10.1016/j.epsl.2007.11.024

40. Li C, Yao H, Yang Y, Luo S, Wang K, Wan K, et al. 3-D shear wave velocity structure in the shallow crust of the Tan-Lu fault zone in Lujiang, Anhui, and adjacent areas, and its tectonic implications. *Earth Planet Phys* (2020) 4(3):1–12. doi:10.26464/epp2020026

41. Lu H, Lei J, Zhao D. Uppermost mantle structure and dynamics of the Tanlu fault zone: new insights from Pn anisotropic tomography. *J Asian Earth Sci* (2024) 268:106170. doi:10.1016/j.jseaes.2024.106170

42. Zhao D, Kanamori H, Negishi H, Wiens D. Tomography of the source area of the 1995 Kobe earthquake: evidence for fluids at the hypocenter? *Science* (1996) 274(5294):1891–4. doi:10.1126/science.274.5294.1891

43. Wang Z, Jin Z, Lin J. Slab melting and arc magmatism behind the Japan Trench: evidence from seismic and thermal structure imaging. *Tectonophysics* (2022) 833:229340. doi:10.1016/j.tecto.2022.229340

44. Ji G, Lei J, Zhao D. Three-dimensional crustal veloeity structure and seismogenic environment arund the Huoshan earthquake swarm. *Seismology Geology* (2024) 46(3):665–85. doi:10.3969/j.issn.0253-4967.2024.03.009

45. Lin W, Michel F, Wang Q. Tectonic evolution of the Dabieshan orogen: in the view from polyphase deformation of the Beihuaiyang metamorphic zone. *Sci China Ser D: Earth Sci* (2005) 48(7):886. doi:10.1360/03YD0306

46. Xiang B, Wang Y, Li C, Zhu G, Shi Y. Evolution of the Xiaotian-Mozitan fault and its implications for exhumation of Dabie HP–UHP rocks. *Prog Nat Sci* (2008) 18(06):713–22. doi:10.1016/j.pnsc.2007.11.020

47. Lei J, Zhao D. Structural heterogeneity of the Longmenshan fault zone and the mechanism of the 2008 Wenchuan earthquake (Ms 8.0). *Geochem Geophys Geosystems* (2009) 10(10). doi:10.1029/2009GC002590

48. Wang Q, Hawkesworth CJ, Wyman D, Chung S-L, Wu F, Li X, et al. Pliocene-Quaternary crustal melting in central and northern Tibet and insights into crustal flow. *Nat Commun* (2016) 7(1):11888. doi:10.1038/ncomms11888

49. Yuan X, Klemperer SL, Teng W, Xiang L, Chetwin E. Crustal structure and exhumation of the Dabie Shan ultrahigh-pressure orogen, eastern China, from seismic reflection profiling. *Geology* (2003) 31:435–8. doi:10.1130/0091-7613(2003)031<0435:csaeot>2.0.co;2

50. Tang Y, Weng A, Yang Y, Li S, Niu J, Zhang Y, et al. Connection between earthquakes and deep fluids revealed by magnetotelluric imaging in Songyuan, China. *Sci China Earth Sci* (2021) 64(1):161–76. doi:10.1007/s11430-019-9633-y

51. Zhao Z, Zheng Y. Remelting of subducted continental lithosphere: petrogenesis of Mesozoic magmatic rocks in the Dabie-Sulu orogenic belt. *Sci China Ser D: Earth Sci* (2009) 52(9):1295–318. doi:10.1007/s11430-009-0134-8

52. Liu S-A, Li S, Guo S, Hou Z, He Y. The Cretaceous adakitic–basaltic–granitic magma sequence on south-eastern margin of the North China Craton: implications for lithospheric thinning mechanism. *Lithos* (2012) 134-135:163–78. doi:10.1016/j.lithos.2011.12.015

53. Liao P, Wang X, Hong D, Li L, Wang J. Dynamic backgrounds of the "huoshan seismic window" and its implications. *Earthquake Res China* (2014) 30(04):534–42.

54. Lei J, Li Y, Xie F, Teng J, Zhang G, Sun C, et al..P Pn anisotropic tomography and dynamics under eastern Tibetan plateau. *J Geophys Res Solid Earth* (2014) 119(3):2174–98. doi:10.1002/2013JB010847

55. Lei J, Zhao D. Teleseismic P-wave tomography and mantle dynamics beneath Eastern Tibet. *Geochem Geophys Geosystems* (2016) 17(5):1861–84. doi:10.1002/2016GC006262

56. Sun A, Zhao D. Anisotropic tomography beneath Northeast Tibet: evidence for regional crustal flow. *Tectonics* (2020) 39(7):e2020TC006161. doi:10.1029/2020TC006161

57. Yu Y, Chen YJ, Feng Y, An M, Liang X, Guo Z, et al.Asthenospheric flow channel from northeastern tibet imaged by seismic tomography between Ordos Block and Yangtze Craton. *Geophys Res Lett* (2021) 48(17):e2021GL093561. doi:10.1029/2021GL093561

58. Huang J, Zhao D. High-resolution mantle tomography of China and surrounding regions. *J Geophys Res Solid Earth* (2006) 111(B9). doi:10.1029/2005JB004066

frontiers | Frontiers in Earth Science

TYPE Original Research
PUBLISHED 09 December 2024
DOI 10.3389/feart.2024.1523656

OPEN ACCESS

EDITED BY
Yifei Sun,
Taiyuan University of Technology, China

REVIEWED BY
Shuangfeng Guo,
Nanjing Tech University, China
Shuang Shu,
Hohai University, China

*CORRESPONDENCE
Yijiang Zhang,
yjzhang@nhri.cn

RECEIVED 11 November 2024
ACCEPTED 26 November 2024
PUBLISHED 09 December 2024

CITATION
Han S, Yu D, Luo H, Li T, Wang Y and Zhang Y (2024) Experimental study on soil improvement by electrochemical injection coupled with anode movement technique. *Front. Earth Sci.* 12:1523656. doi: 10.3389/feart.2024.1523656

Experimental study on soil improvement by electrochemical injection coupled with anode movement technique

Shaoyang Han[1], Daiguang Yu[2], Haidong Luo[2], Tianyi Li[1], Yu Wang[1] and Yijiang Zhang[3]*

[1]College of Civil Engineering, Jiangsu Open University, Nanjing, Jiangsu, China, [2]Nanjing Water Planning and Designing Institute Corp., Ltd, Nanjing, Jiangsu, China, [3]Department of Geotechnical Engineering, Nanjing Hydraulic Research Institute, Nanjing, Jiangsu, China

An improved electroosmotic method which involves coupling anode movement with injection of calcium chloride ($CaCl_2$) solution into soils during the electroosmotic process was proposed in this paper. The laboratory-based experimental study was conducted in a custom-designed test set-up to assess the effectiveness of the proposed method. During the electroosmotic process, the drained water, drainage rate, electric current, electric resistance, power consumption, settlement, and penetration resistance were monitored. The experimental study showed that after treatment, the drainage volume was about 3.5 times that of the pure electroosmotic, 1.6 times that of the electroosmotic process with injection only, and 2.4 times that of the electroosmotic process with anode movement only. Further, electrochemical injection coupled with anode movement can significantly reduce the non-uniform electrochemical changes in the treated samples, resulting in a relatively uniform settlement and considerable cementation area throughout the sample. The results demonstrate that using this method can effectively alleviate anode corrosion, double the voltage gradient and mitigate the electric resistance increase, further enhancing electroosmotic treatment efficiency.

KEYWORDS

electroosmotic process, soil improvement, anode movement, injection, cementation area

1 Introduction

Electroosmosis is a process induced by electricity in which pore water moves from the anode to the cathode along with dissolved electrolytes, resulting in soil drainage and consolidation (Asadi et al., 2013; Pandey et al., 2024). Casagrande (1949) pioneered the use of this phenomenon to strengthen soft soil and improve the geotechnical properties of engineering materials. Since then, several studies followed to explore the characteristics of electroosmotic treatment (Bian et al., 2024; He et al., 2023; Alshawabkeh and Sheahan, 2003).

To enhance the effect of electroosmotic flow, the method of injecting chemical solutions into soil during electroosmotic process was adopted in recent years (Abdullah and Al-Abadi, 2010; Sun et al., 2023). The electroosmotic chemical method takes advantage of the interactions between chemical solutions and soil particles, including cation exchange and particle cementation, under the influence of an electric field

(Martin et al., 2019). By using the electroosmotic chemical method one can inject chemical solutions into soft clay and avoid fracturing, making it a suitable approach for improving low permeability soils (Xue et al., 2018). Numerous solutions have been utilized as the injection materials during electroosmotic process, such as NaCl, KCL, $CaCl_2$ (Chien et al., 2009), aluminum ions (Mohamedelhassan and Shang, 2003), NaOH, and Na_2SiO_3 (Moayedi et al., 2012), $Mg(CH_3COO)_2$, $AgNO_3$ and $ZnSO_4$ (Otsuki et al., 2007), and positively charged SiO_2@Al_2O_3 core-shell nanoparticles (NPs) (Zhang et al., 2017). Injecting chemical solutions during electroosmotic process can increase the soil conductivity at the soil-electrode contact and effectively double the electrical potential transmitted to the soil, thereby improving the performance of electroosmotic consolidation (Chien et al., 2011; Chien et al., 2015). However, it also can be observed from previous studies that the improvements are primarily concentrated in the regions of the anode and cathode (Ou et al., 2009; Chien et al., 2010; Asavadorndeja and Glawe, 2005) despite that injecting chemical solutions during the electroosmotic process can effectively enhance the effectiveness of electroosmotic flow and improve soil strength.

In addition to the inhomogeneous effects, problems such as anode corrosion (Shi et al., 2021a; Liu et al., 2014), high energy consumption (Xiao et al., 2021), potential loss due to increasing contact resistivity (Mohamedelhassan and Shang, 2001; Zhuang and Wang, 2007), and formation of gases (Kalumba et al., 2009), also hinder the widespread application of electroosmotic technique in engineering projects. To overcome the aforementioned issues, a number of technical solutions have been proposed and experimentally studied. Lo et al. (1991) implemented electrode polarity reversal to achieve uniform soil strength between the electrodes. However, after the polarity reversal, the electrode interface resistance increases sharply, resulting in current reduction and low energy efficiency (Tao et al., 2014). Xiao et al. (2021) found that electrokinetic geosynthetics (EKG) electrodes can efficiently alleviate anode corrosion and accumulation of gases during the electroosmotic process. Nonetheless, the EKG electrodes exhibit a greater increase in resistance compared to conventional electrodes. Moreover, Asavadorndeja and Glawe (2005) reported an anode depolarization technique that prevents the formation and migration of hydrogen ions, achieving more uniform strength improvements compared to traditional methods. Peng et al. (2013) adopted a method that combines vacuum preloading and electroosmosis, which significantly and uniformly improved soil strength. However, the practical application of vacuum preloading combined with electroosmotic flow is extremely difficult, as the membrane used in vacuum preloading cannot maintain the tightness of the seal under the electric field conditions (Peng et al., 2015).

The main objective of this paper is to develop an improved method for electroosmotic treatment which could effectively expand the improvement area, decrease the extent of anode corrosion, and enhance the efficiency of the electroosmotic process. The improved electroosmotic method combines anode movement technique with injection of calcium chloride ($CaCl_2$) solution into soils during the electroosmotic process. Treatment effect was investigated through monitoring the main characteristics of soft soils including drained water, drainage rate, electric current, electric resistance, power consumption, settlement, and penetration resistance. For comparison, pure electroosmotic process, electroosmotic process with anode movement technique only and electroosmotic process with injection of calcium chloride ($CaCl_2$) only were also studied.

2 Experimental study

2.1 Experimental apparatus

The test apparatus, as is displayed in Figure 1 in detail, was comprised of an electrokinetic cell and a D.C. power supply device. The electrokinetic cell, made of acrylics, holds a dimension of 440 mm in length, 330 mm in width, 140 mm in height and 10 mm in thickness. Similar to the experiment disposition designed by Chien et al. (2010), tubular stainless steel tubes were used as both electrodes (350 mm apart from each other) and the central tube (a tube at the midpoint between the anode and the cathode, 175 mm away from both electrodes), while the holes were drilled along the surface of the tube for injection (anode and central tube) and draining (cathode) during the electroosmotic process. The D.C. power supply device, which can provide an output voltage of up to 60 V and a current of 5 A, was connected to both the anode and cathode tube for electric supply. A number of drainage holes with a diameter of 3 mm were scattered at the bottom of the cell with a spacing of 10 mm from the cathode. The drainage process could be controlled through a drained tube at the end of the cell during the test.

Five voltage probes were installed on top of the cell to measure the voltage following an organized time interval. In the meantime, the vertical deformation resulting from soil consolidation is monitored by five dial gauges disposed on the top plater. Figure 1 illustrates the specific position of both voltage probes and dial gauges. The measuring cylinder and the multimeter were utilized to monitor of drained water volume and voltage, respectively. In addition, a camera was applied during the electroosmosis tests to investigate the physical behavior of soil-anode interface.

2.2 Materials

The soils used in this study were collected from the Jiangning District of Nanjing, China. The physical properties of the soil were assessed in accordance with the Chinese Standard GB/T 50,123-2019 (Standard for Soil Test Methods) (Chinese Standard GB/T 50123-2019, 2019) and were summarized in Table 1. Based on the Unified Soil Classification System (USCS) (ASTM International Standard D2487-17e1, 2017), the soil was classified as low plasticity clay (CL). Additionally, calcium chloride ($CaCl_2$) solution was employed as the injection material during the electroosmosis process.

2.3 Test procedure

A specified amount of air-dried soil was first mixed with distilled deionized water using a mechanical mixer to reach a water content of 1.5 times the liquid limit. This mixture was then stored

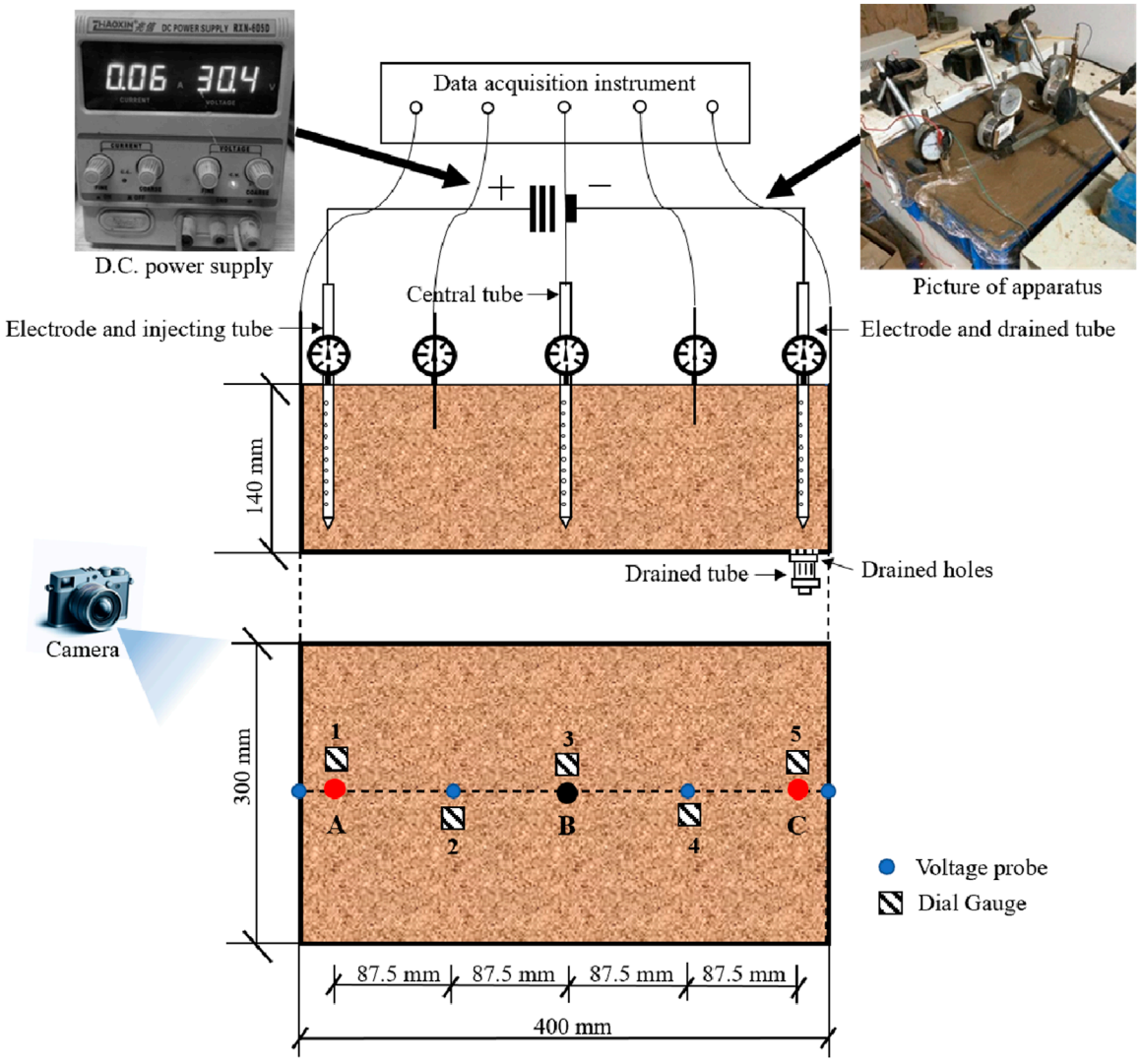

FIGURE 1
Schematic configuration of test apparatus.

TABLE 1 Physical properties of the soil.

Specific gravity (Gs)	Liquid limit (LL)/%	Plastic limit (PL)/%	Plastic index (PI)	USCS classification
2.67	41.8	23.6	18.2	CL

in an airtight container with a sealed lid for 3 days to facilitate moisture equilibration. Subsequently, the prepared soil sample was layered into the electrokinetic cell in five separate layers, allowing for the placement of electrodes and a central tube. A saturated geomembrane was then positioned over the soil surface to create a horizontal flow condition.

A direct current of 30 V was applied to the soil with a voltage gradient of 50 V/m to undertake the electroosmotic process, with each test lasting for 25 h. A total of 140 mL of $CaCl_2$ solution with concentration of 2 mol/L was injected into the anode or the central tube, and water was discharged from the cathode during electroosmotic process. The voltage, current, surface settlement and drained water from the cathode were monitored during the test. The penetrometer resistance of the soil sample was assessed using a specially designed laboratory micro penetrometer, as illustrated in Figure 2. This micro penetrometer featured three dynamometers (I, II, and III) and three probes (A, B, and C). The actual penetration resistance can be obtained by multiplying the recorded reading by the corresponding calibration coefficient, with a measurement accuracy of ±5%. After the experiments, penetrometer resistance values were measured at various locations within the sample, as shown in Figure 2. Data readings were recorded electronically using a digital data logger. A total of four types of test were performed. The procedures for each type of tests are described below.

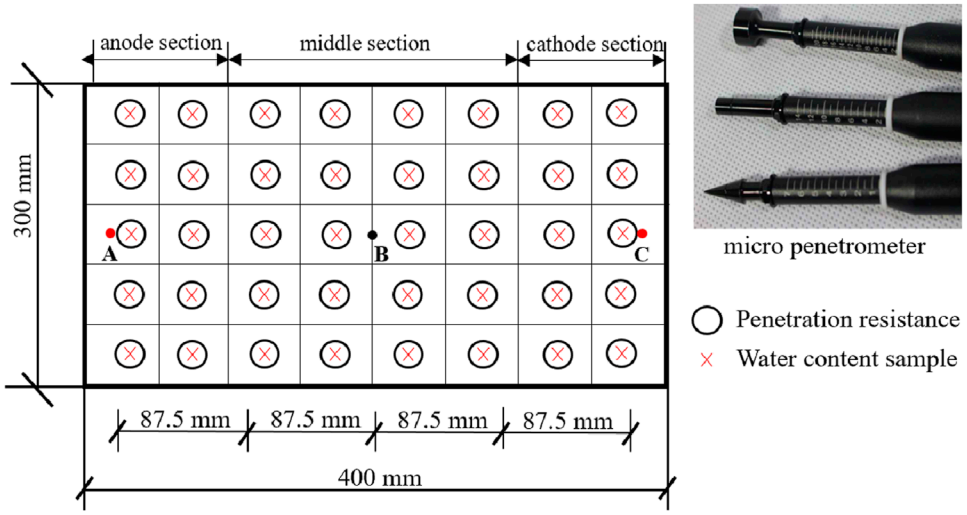

FIGURE 2
Plan view of laboratory penetration resistance tests collection locations.

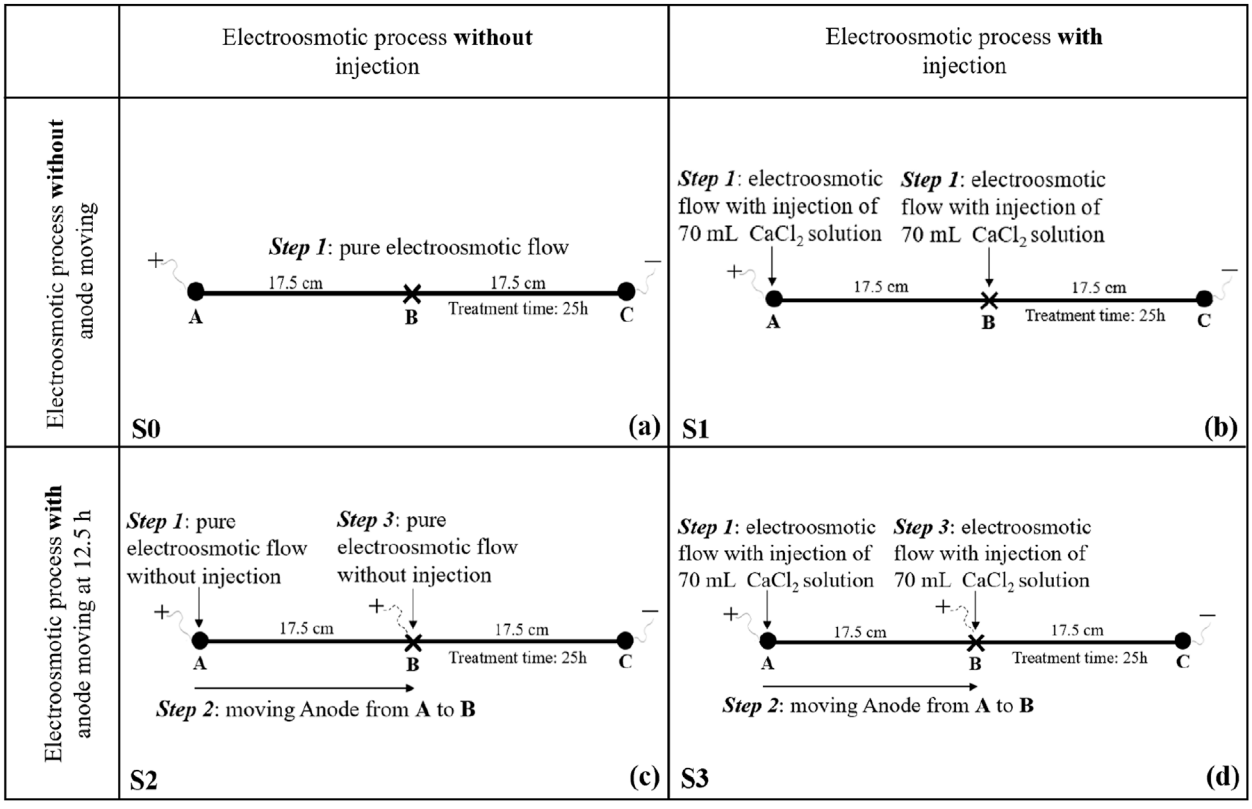

FIGURE 3
Schematic diagram of the tests: **(A)** Test S0, **(B)** Test S1, **(C)** Test S2, and **(D)** Test S3.

Four electroosmotic tests were denoted as S0, S1, S2 and S3 respectively. As presented in Figure 3, S0 refers to pure electroosmotic flow, S1 refers to electroosmotic flow with simultaneous injection through both the anode (Point A) and central tube (Point B), S2 refers to electroosmotic flow with anode movement (from Point A to B) only, and S3 refers to electroosmotic flow with anode movement (from Point A to B) coupled with injection of $CaCl_2$ solution (through Point A followed by Point B). Specifically, for test S1, 70 mL of $CaCl_2$ solution was firstly injected into the anode (Point A) and central tube (Point B) simultaneously

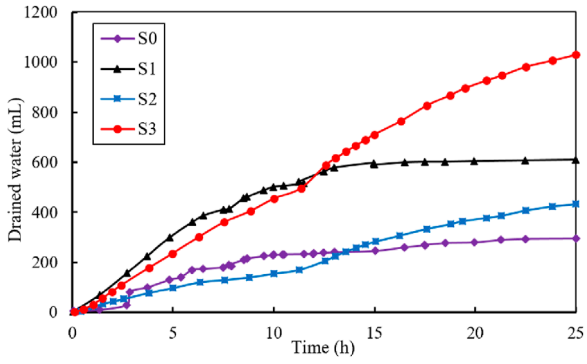

FIGURE 4
Drained water *versus* time during tests.

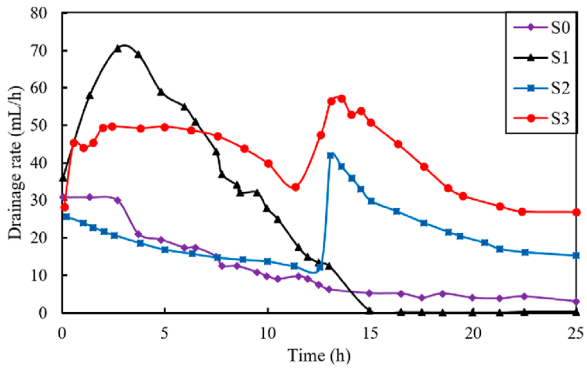

FIGURE 5
Drainage rate *versus* time during tests.

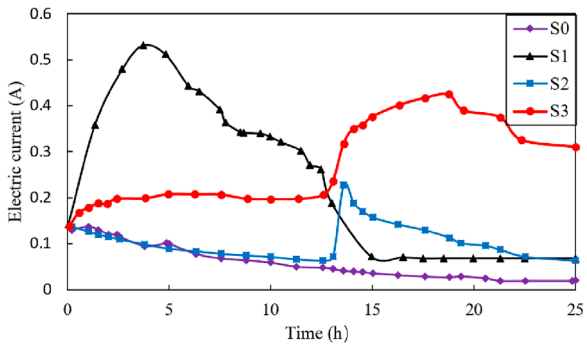

FIGURE 6
Electric current *versus* time during tests.

immediately after powering on, and the electroosmotic process will continue for the whole treatment time of 25 h. For test S2, a pure electroosmotic process was first conducted for 12.5 h, after that the anode was pulled out and moved from Point A to Point B, followed by another 12.5 h of electroosmosis. While for test S3, 70 mL of $CaCl_2$ solution was firstly injected into the anode (Point A) immediately after powering on, then the electroosmotic process will last for 12.5 h. After that, the anode was pulled out and moved from Point A to Point B, and another 70 mL of $CaCl_2$ solution was injected into the anode (Point B), then the electroosmotic process will last for another 12.5 h. A detailed schematic diagram of these four tests are tabulated in Figure 3.

3 Results and discussions

3.1 Drained water and drainage rate

Figure 4 illustrates the variation of drained water (mL) during the electroosmotic process. The total volume of the drained water was 295, 609, 432, and 1030 mL for test S0, S1, S2 and S3, respectively. As shown in the figure, the drainage volume for the S3 test was the largest, approximately 3.5 times that of S0 test, 1.6 times that of the S1 test and 2.4 times that of the S2 test. It is worth noting that for S2 and S3 tests, a turning point in the drainage curve is observed around 12.5 h. In the first 12.5 h, the drainage volume was 170 mL for S2 and 496 mL for S3 test. Following this turning point, the drainage volume increased to 262 and 534 mL for S2 and S3 test, respectively.

Figure 5 shows the drainage rate (mL/h) vs. time (h) during the electroosmotic process. The initial drainage rate for the four tests was approximately 30 mL/h. During electroosmotic process, the drainage rate of S0 exhibited a continuous decrease until it reached a state of stability. For S1 test, the drainage rate initially increased rapidly and reached a peak drainage rate value of 70.6 mL/h at 2.25 h. This was followed by a slow decrease in the next 13–15 h, after which a stable stage was reached. In comparison, both S2 and S3 curves exhibited a subsequent peak around 12.5 h. For the S3 test, the drainage rate increased from 28.5 to 49.4 mL/h in the first 2.5 h, followed by a gradual decrease and a subsequent peak of 57.2 mL/h was reached around 12.5 h. Conversely, the S2 test showed a continuous decrease in drainage rate from 26.0 to 12.4 mL/h in the first 12.5 h and reached its maximum value of 42 mL/h when the anode was moved, followed by a downward trend thereafter. Yoshida (2000) and Burnotte et al., (2004) showed that with the continuous application of a direct current, the electrical contact resistance between the electrodes (mainly the anode) and the soil is considerably increased, leaving an effective voltage gradient too small for significant electroosmotic dewatering. Therefore, it can be concluded that the increase in drainage rate of S2 and S3 during the subsequent 12.5 h was attributed to the movement of the anode, which effectively doubled the voltage gradient, thereby enhancing the drainage capacity of the soil matrix. In contrast, under the same condition of anode movement, S3 exhibited better drainage performance than S2. This is mainly because the injection of $CaCl_2$ solution during the electroosmotic process in S3 will lead to an increase in electric conductivity and hydration of cation, resulting in a better drainage effect.

3.2 Electric current and electric resistance

Figure 6 illustrate the variation of electric current (A) during the electroosmotic process. As noticed in Figure 6, the electric current in S0 test continuously decreased over time. Additionally,

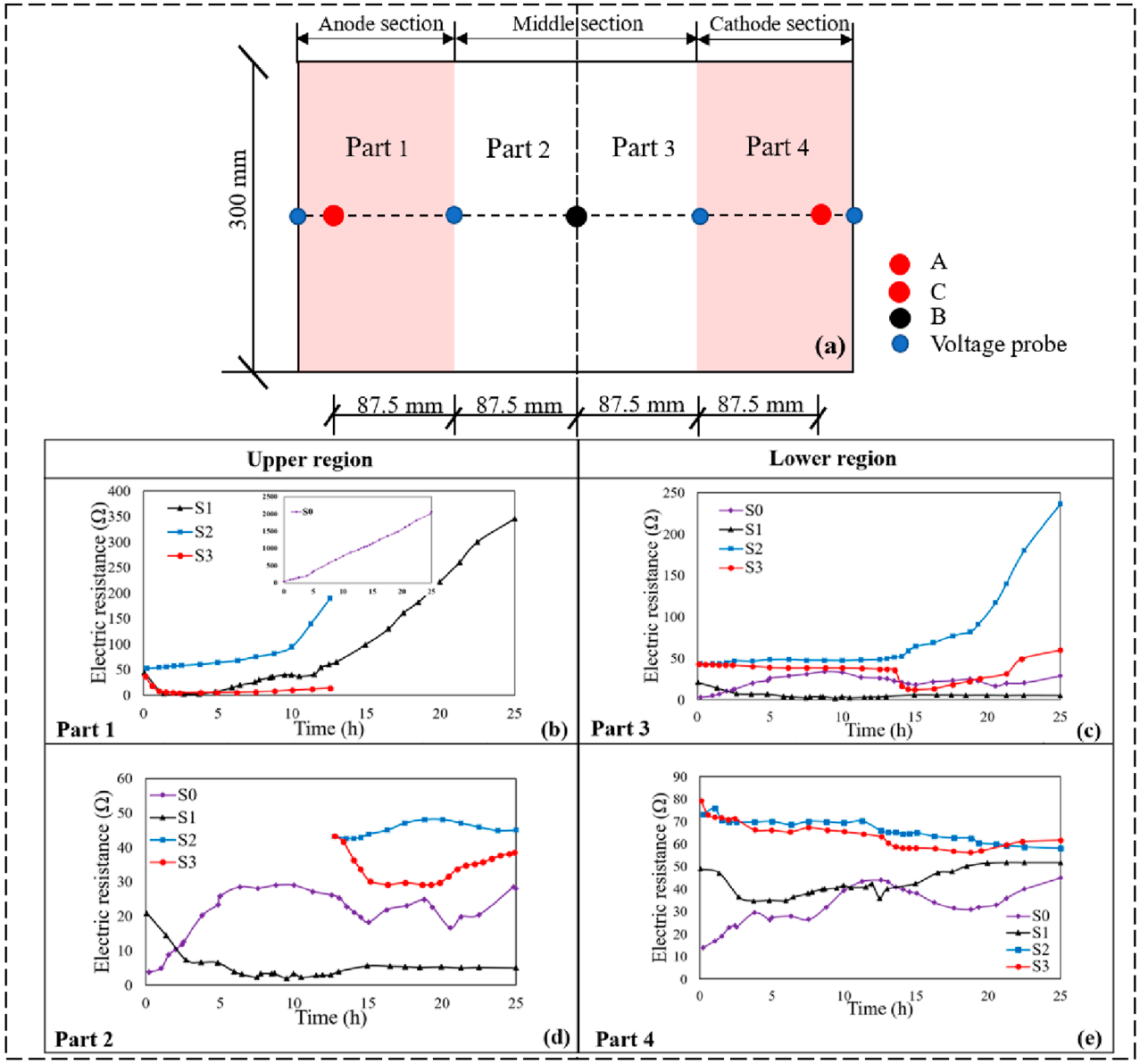

FIGURE 7
Electric resistance *versus* time during tests: **(A)** Schematic diagram of sample segmentation, **(B)** electric resistance of part 1, **(C)** electric resistance of part 3, and **(D)** electric resistance of part 2, and **(E)** electric resistance of part 4.

the electric current of S1 showed a rapid increase to more than 0.5 A due to the presence of salt solution, as well as the desorption and mobilization of ions in the soil matrix. Subsequently, the electric current decreased from 0.53 A to 0.06 A and finally a stable stage was reached. The decrease in electric current can be attributed to two reasons: first, a decline in the gradient of ionic concentration and a partial saturation of charge sites within the clay (Yukselen-Aksoy and Reddy, 2012), and second, anode corrosion and the formation of cracks near the anode area, which caused significant voltage loss and further reduced the electric current (Wu et al., 2015; Shi and Zhao, 2020; Shi et al., 2021b). For S2 and S3 tests, the change in electric current curve was similar to that in drainage rate curve, with a subsequent current peak value of 0.21 A for S2 and 0.42 A for S3 around 12.5 h. This observed increments in drainage efficiency and electric current around 12.5 h of S2 and S3 tests were may be due to fact that the anode being moved during the electroosmotic process. As mentioned, the movement of the anode, coupled with the injection of $CaCl_2$ solution can significantly decrease the power loss and double the voltage, thereby leading to a substantial increase in electric current. In addition, the peak value of electric current of S3, which is twice that of S2, is mainly due to the fact that injection of the $CaCl_2$ solutions.

A plot of electric resistance of the soil with regard to time is presented in Figures 7B–E. To provide a more comprehensive analysis of the electric resistance variations during the electroosmotic process, the changes in electric resistance for

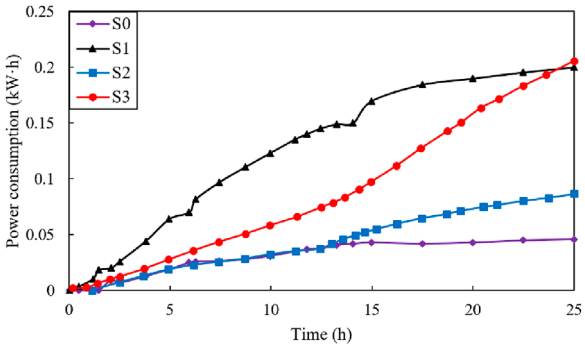

FIGURE 8
Power consumption *versus* time during tests.

TABLE 2 Summary of power consumption after treatment.

Test number	S0	S1	S2	S3
Power consumption (kW·h)	0.05	0.20	0.09	0.21

Part 1 (the soil adjacent to Point A), Part 2 (soil near the left side of the midline/Point B), Part 3 (the soil near the right side of the midline/Point B), and Part 4 (soil adjacent to Point C) were examined, as depicted in Figure 7A. Overall, the soil sample can be delineated into two main regions by the midline: the upper regions, which include Part 1 and Part 2, and the lower regions, which include Part 3 and Part 4.

As illustrated in Figure 7B, the electric resistance of S0 test rapidly increased over time, reaching a value of 1,200 Ω after 25 h in Part 1. In comparison, the electrical resistance of S1 was obviously lower than that of S0 in the same section. This is attributed to the injection of $CaCl_2$ solution, which markedly increased the total ion concentration within the soil matrix, resulting in an increase of current flow and a corresponding decrease in electric resistance. Comparing S1 and S3 tests in Figure 7B, it also can be observed that under the same treatment condition (electroosmotic process with injection of $CaCl_2$ solution), the electric resistance of both tests remained at a relatively low level (below 60 Ω) in the first period of 12.5 h in Part 1. Subsequently, S1 experienced a significant increase in electric resistance, surging from 55 Ω to more than 300 Ω, while the electroosmotic process of S3 was halted due to the movement of the anode. Observing the electric resistance curves in Figure 7C, it can be noted that the electric resistance of S2 increased progressively after 12.5 h. In contrast, under the same conditions of anode movement, the resistance of S3 initially decreased and then experienced a slight increased, while it consistently remained below 55 Ω. Therefore, it can be concluded that injecting of $CaCl_2$ solution coupled with moving the anode can significantly reduce the growth of electric resistance in Part 3. It is also worth noting that the electric resistance in the S2 and S3 tests was slightly higher than that in S0 and S1 within the regions of Parts 2 and 4, with the increase being generally less than 60 Ω, which is considered within an acceptable range for the tested soils. Clearly, the electric resistance was mainly affected in the regions of Parts 1 and 3 because the soil near the anode was more prone to water loss. In addition, water electrolysis and the impervious boundary led to an increase in gas pressure at the anode-soil interface, leading to significant volume shrinkage and cracks in both the Part 1 and Part 3 regions. These shrinkage cracks and gas accumulations substantially elevated the electric resistance, further reducing the electric current. Therefore, coupling anode movement with the injection of calcium chloride ($CaCl_2$) solution during electroosmotic process can effectively prevent the increase in electric resistance, which further enhance the electroosmotic treatment efficiency.

3.3 Power consumption

High power consumption limits the engineering applications of electroosmosis. To evaluate the power consumption of the three tests, the electrical power consumption during the electroosmotic process and the unit drainage energy consumption were calculated and analyzed.

The electrical power consumption, W, can be calculated using:

$$W = \int \frac{V \cdot I \cdot t}{1000} dt$$

Where V is the applied vlotage (V), I is the electric current as a fuction of time (A), and t is the processing time (h).

Figure 8 shows the power consumption (kW·h) vs. time (h) during the electroosmotic process for the three tests. The power consumption after treatment is also presented in Table 2. The final power consumption was 0.05, 0.20, 0.09, and 0.21 kW h for tests S0, S1, S2 and S3, respectively. Analysis of the results from the S1 and S3 tests indicated that moving anode during the electroosmotic process had no significant impact on power consumption. Conversely, the power consumption following the injection of $CaCl_2$ was approximately twice that of the condition without any solution injection. This is mainly because the electroosmotic flow with injection will result in an increase in electric conductivity, thus the power required for the process increases proportionally (Mohamedelhassan and Shang, 2001). Although the power consumed in tests S1 and S3 was slightly greater than that in tests S0 and S2, but the increment is acceptable in the case of the tested soils.

Figure 9 illustrates the variation of unit drainage power consumption (mL/(W·h)) with time during treatment. The unit drainage power consumption, η, was obtained by the volume of drained water (mL) by dividing power consumption (W·h). As shown in the figure, the η of S0 fluctuated around 7 mL/(W·h) over time, while the η of S1 initially increased rapidly, peaking at 2.25 h with a value of 6.1 mL/(W·h). This was followed by a gradual decrease in the next 13–15 h and afterwards a stable stage. The changes in η of S2 and S3 in this study was quite different from those of S0 and S1. In the first 12.5 h, the η for S2 and S3 tests exhibited a similar trend, with minor fluctuations around 8 mL/(W·h) over time. Subsequently, both S2 and S3 experienced a notable reduction in η, with values decreased from 8.0 mL/(W·h) for S2 and 67 mL/(W·h) for S3 to 3.4 mL/(W·h) and 2.3 mL/(W·h), respectively. In summary, the η values for S2 and S3 were consistently higher than that of S1 test throughout the entire electroosmotic process, indicating that S1 test requires more electrical power to discharge the same volume of water.

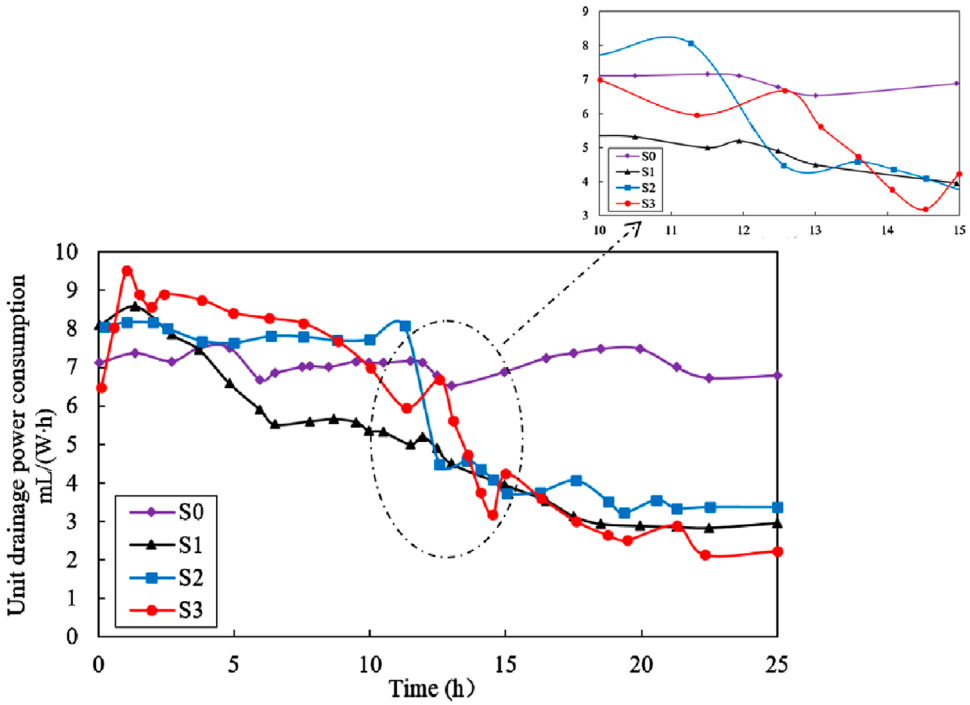

FIGURE 9
Unit drainage power consumption *versus* time during tests.

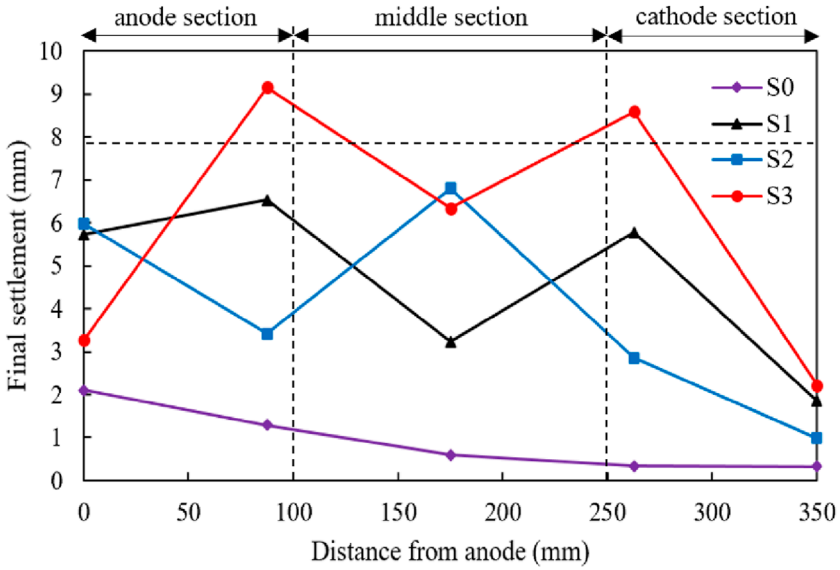

FIGURE 10
Final settlement distribution after treatment.

3.4 Settlement

The final settlement measured at five locations, namely 0, 8.75, 17.5, 26.3 and 35 cm after treating vs. the distance from the anode for four different test procedures are presented in Figure 10. It is not surprising that all the settlements of five locations treated by test S0 keep the lowest, which was consistent with the previously observed lowest drained water among the four tests as shown in Figure 4. It can be readily seen that the settlement near Point A induced by test S1 was close to 6 mm, which is almost twice than that induced by S2 and S3, indicating that keeping the anode at Point A is benefit for the increase of final settlement near Point A. However, throughout the testing area, the settlement induced by S3 always keeps the largest except the observed Point A. To be specific, the final settlements

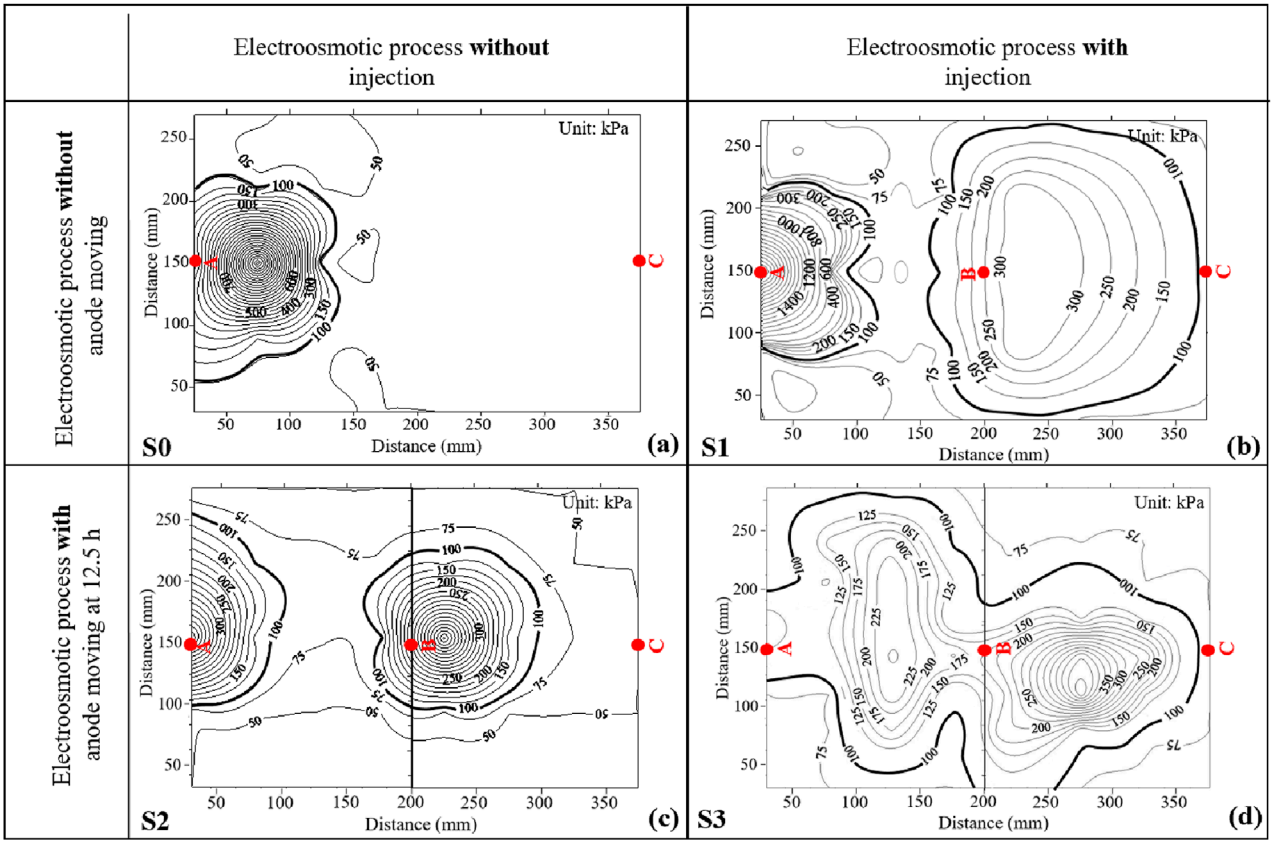

FIGURE 11
Penetration resistance contour plot after treatment: **(A)** S0 (pure electroosmotic flow); **(B)** S1 (electroosmotic flow with injection of $CaCl_2$ solution); **(C)** S2 (electroosmotic flow with anode movement); **(D)** S3 (electroosmotic flow with anode movement coupled with injection of $CaCl_2$ solution).

measured at 8.75 and 26.3 cm away from Point A induced by S3 are 9 and 8.5 mm, 1.5 times than those induced by S1 and triple than those induced by S2. It can be concluded that moving the anode from Point A to B can certainly improve the settlement distribution throughout the whole treating area, especially for the area between Point A and B as well as Point B and C. It is interesting that the final settlement measured at Point B induced by S2 was lower than that induced by S3 and larger than that induced by S1, which means that the improvement on settlement brought by moving the anode from Point A to B is more drastic than that brought by electroosmotic flow with injection. It should also be admitted that the final settlements measured around cathode (Point C) induced by S1, S2 and S3 were close to each other and show not too much improvement compared with S0.

3.5 Penetration resistance

Penetration resistance can describe the strength of soils after electroosmotic treating. Figure 11 shows the contour plots of penetration resistance for the whole treating area after treatment for four tests. The contour plots were generated using Kriging method (Liang et al., 2018), which is a spatial interpolation estimator that is applied to find the best linear unbiased estimate at each location and is determined according to the linear combination of the known values of all sampled locations. The initial penetration resistance for natural samples ranged from 50 to 75 kPa for all the four tests. It is readily seen that Figure 11 can be divided into two categories, i.e., Figures 11A, B present the results for electroosmotic flow without anode moving, while Figures 11C, D present the results for electroosmotic flow with anode moving. It is obvious that the contour lines around Point B induced by S2 and S3 were denser compared with those induced by S1, indicating that moving anode from Point A to B could significantly improve the penetration resistance of soils around Point B. Furthermore, it is apparent that the soils, not only between the anode and the cathode, but also away from the alignment of the anode and the cathode, were significantly improved in S3. It should be noted that the penetration resistance of soils around Point A would be weakened by moving the anode from Point A to B. For example, the peak penetration resistance of soils around Point A treated by S1 was more than 1,400 kPa, while the peak values for S2 and S3 were about 500 kPa and 125 kPa, respectively. However, it has been proved that the area of penetration resistance greater than 100 kPa after treatment could be defined as a cementation area to describe the improvement of electroosmotic treatment, similar to the method used by Chien et al. (2010). It is expected that cementation between soil particles due to the chemical reaction between injected solutions should contribute to a large proportion of the cone resistance when it is greater than 100 kPa.

10.3389/feart.2024.1523656

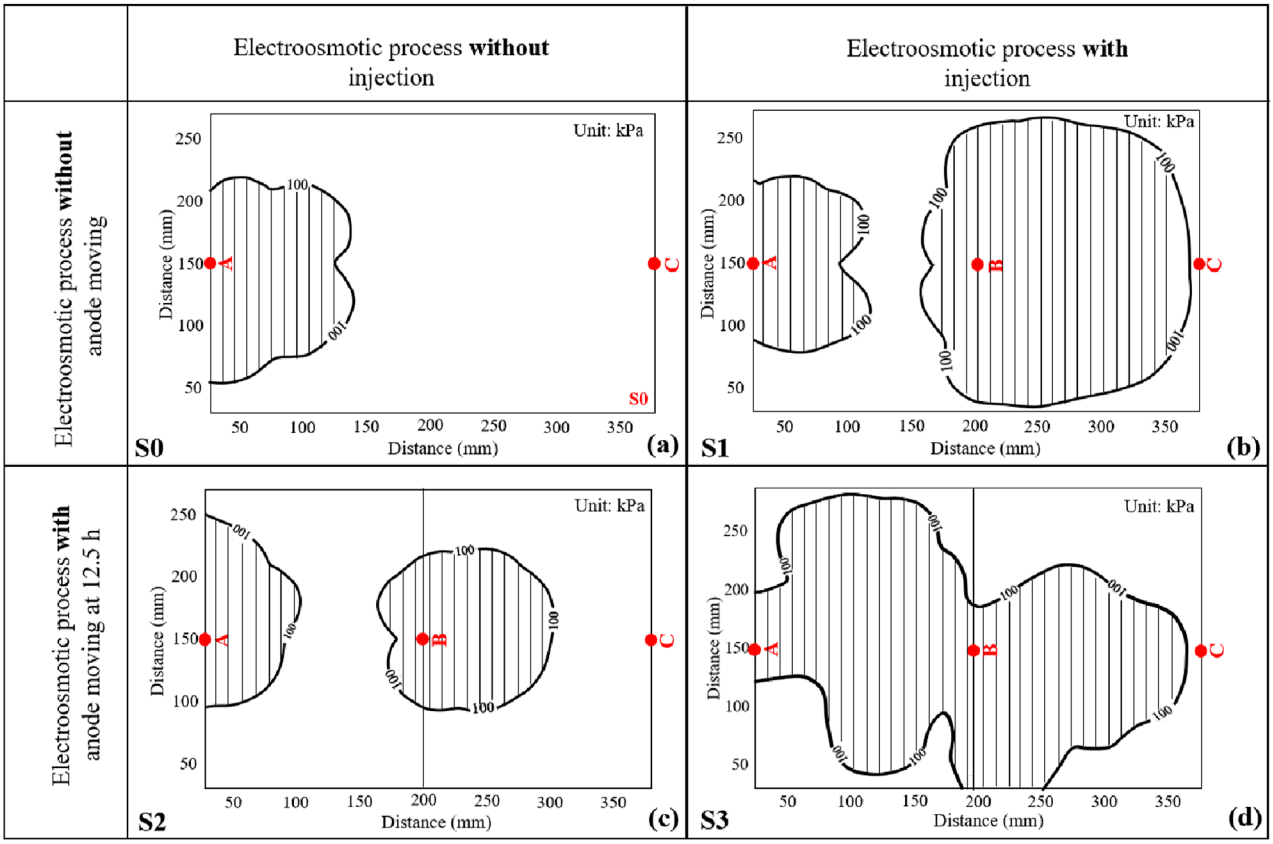

FIGURE 12
Comparison of the cementation area after treatment: **(A)** S0 (pure electroosmotic flow); **(B)** S1 (electroosmotic flow with injection of $CaCl_2$ solution); **(C)** S2 (electroosmotic flow with anode movement); **(D)** S3 (electroosmotic flow with anode movement coupled with injection of $CaCl_2$ solution).

Figure 12 plots the cementation area after treatment for four tests. It was calculated from Figure 12A and c that the cementation area for S0 and S2 were about 18.05% and 26.76% of the whole treating area, respectively. It is also evident that the cementation area in S1 and S3 were larger than that in S0 and S2, accounting for about 62.30% and 63.20% of the total area for S1 and S3, respectively. It is interesting that the cementation area treated by S1 and S3 were very close, the main difference lied in that the cementation area treated by S1 covers most of the area between Point B and C, whereas the cementation area treated by S3 covers most of the area between Point A and B. This is mainly because the injection of $CaCl_2$ solution into Point B was kept during the treatment time for S1, while for S3, $CaCl_2$ solution was injected to Point B only after the abode was moved from Point A to B. This observation indicates that electroosmotic process with anode movement coupled with injection of $CaCl_2$ solution could further improve the homogeneous distribution of the treatment area.

4 Conclusion

In this study, the effect of electroosmotic process with and without anode movement was investigated through laboratory tests. For comparison, pure electroosmotic flow and electroosmotic flow with injection of calcium chloride ($CaCl_2$) were also studied. During the tests, drained water, drainage rate, electric current, electric resistance, power consumption, settlement, and penetration resistance were analyzed to investigate drainage and consolidation behaviors. Based on the results of this study, the following conclusions can be drawn:

(1) The effect of electroosmotic flow can be improved by the injection of $CaCl_2$ solution during electroosmotic process. After electroosmotic flow with injection of $CaCl_2$ solution for a period of 25 h, the total volume of drained water was 609 mL, about 2.06 times that of pure electroosmotic flow without injection. Furthermore, the cementation area after treatment was increased to 62.30% of the entire sample, compared to 18.05% for pure electroosmotic flow.

(2) After pure electroosmotic process with anode movement, the drained water of soil was increased by 46%, compared to anode without movement. The test result also indicates that the electroosmotic process with anode movement can further improve the homogeneous distribution of the treatment area. In the electroosmotic process, the movement of the anode resulted in an approximate 8.71% increase in the cementation area compared to the anode not moving.

(3) After electroosmotic process with anode movement coupled with injection of $CaCl_2$ solution, the drainage volume reached

up to 1,030 mL, approximately 1.6–3.5 times greater than that of other schemes. Additionally, the corresponding cementation area extended to 63.20%, compared to 18.05% for pure electroosmotic flow and 26.76% for electroosmotic flow with anode movement only.

(4) The results found that the electroosmotic process with anode movement coupled with injection of $CaCl_2$ solution was superior to other schemes in this study, which may be a potential technique for the improvement of soft clay.

Data availability statement

The original contributions presented in the study are included in the article/supplementary material, further inquiries can be directed to the corresponding author.

Author contributions

SH: Conceptualization, Data curation, Funding acquisition, Methodology, Validation, Writing–original draft. DY: Conceptualization, Methodology, Writing–review and editing. HL: Conceptualization, Formal Analysis, Writing–review and editing. TL: Funding acquisition, Methodology, Writing–review and editing. YW: Validation, Visualization, Writing–review and editing. YZ: Conceptualization, Data curation, Funding acquisition, Investigation, Writing–review and editing.

Funding

The author(s) declare that financial support was received for the research, authorship, and/or publication of this article. This work was supported by the National Natural Science Foundation of China (No. 52308355, 52309158, 52209166). The financial support from the Foundation of Nanjing Hydraulic Research Institute (NHRI, Grant Number Y323003) and the University Natural Science Foundation of Jiangsu Province (Grant No. 23KJB130004) are also greatly appreciated.

Conflict of interest

Authors DY and HL were employed by Nanjing Water Planning and Designing Institute Corp.

The remaining authors declare that the research was conducted in the absence of any commercial or financial relationships that could be construed as a potential conflict of interest.

Generative AI statement

The author(s) declare that no Generative AI was used in the creation of this manuscript.

Publisher's note

All claims expressed in this article are solely those of the authors and do not necessarily represent those of their affiliated organizations, or those of the publisher, the editors and the reviewers. Any product that may be evaluated in this article, or claim that may be made by its manufacturer, is not guaranteed or endorsed by the publisher.

References

Abdullah, W. S., and Al-Abadi, A. M. (2010). Cationic–electrokinetic improvement of an expansive soil. *Appl. Clay Sci.* 47, 343–350. doi:10.1016/j.clay.2009.11.046

Alshawabkeh, A. N., and Sheahan, T. C. (2003). Soft soil stabilization by ionic injection under electric fields. *Proc. Institution Civ. Eng. - Ground Improv.* 7, 135–144. doi:10.1680/grim.2003.7.4.177

Asadi, A., Huat, B. B. K., Nahazanan, H., and Keykhah, H. A. (2013). Theory of electroosmosis in soil. *Int. J. Electrochem. Sci.* 8, 1016–1025. doi:10.1016/s1452-3981(23)14076-4

Asavadorndeja, P., and Glawe, U. (2005). Electrokinetic strengthening of soft clay using the anode depolarization method. *B Eng. Geol. Environ.* 64, 237–245. doi:10.1007/s10064-005-0276-7

ASTM International Standard D2487-17e1 (2017). *Practice for classification of soils for engineering purposes*. West Conshohocken, PA, U.S: Unified Soil Classification System.

Bian, X. Y., Yang, H. D., Liu, H., Xu, Z. Y., and Zhang, R. J. (2024). Experimental study on the improvement of sludge by vacuum preloading-stepped electroosmosis method with prefabricated horizontal drain. *Geotext. Geomembr.* 52, 753–761. doi:10.1016/j.geotexmem.2024.04.001

Burnotte, F., Lefebvre, G., and Grondin, G. A. (2004). A case record of electroosmotic consolidation of soft clay with improved soil–electrode contact. *Can. Geotech. J.* 41, 1038–1053. doi:10.1139/t04-045

Casagrande, I. L. (1949). Electro-osmosis in soils. *Geotechnique* 1, 159–177. doi:10.1680/geot.1949.1.3.159

Chien, S. C., Ou, C. Y., and Lee, Y. C. (2010). A novel electroosmotic chemical treatment technique for soil improvement. *Appl. Clay Sci.* 50, 481–492. doi:10.1016/j.clay.2010.09.014

Chien, S. C., Ou, C. Y., and Wang, M. K. (2009). Injection of saline solutions to improve the electro-osmotic pressure and consolidation of foundation soil. *Appl. Clay Sci.* 44, 218–224. doi:10.1016/j.clay.2009.02.006

Chien, S. C., Ou, C. Y., and Wang, Y. (2011). Soil improvement using electroosmosis with the injection of chemical solutions: laboratory tests. *Chin. Inst. Eng.* 34, 863–875. doi:10.1080/02533839.2011.591915

Chien, S. C., Teng, F. C., and Ou, C. Y. (2015). Soil improvement of electroosmosis with the chemical treatment using the suitable operation process. *Acta Geotech.* 10, 813–820. doi:10.1007/s11440-014-0319-y

Chinese Standard GB/T 50123-2019 (2019). *Standard for geotechnical testing method*. Beijing, China: Ministry of Housing and Urban-Rural Development of the People's Republic of China.

He, B., Qin, X. H., Zhou, Z. Q., Xu, B., Yu, Sl, Qin, G. L., et al. (2023). Experimental study on composite flocculant-electroosmosis combined with segmented solidification treatment of high-water-content slurry. *Constr. Build. Mater* 400, 132729. doi:10.1016/j.conbuildmat.2023.132729

Kalumba, D., Glendinning, S., Rogers, C., Tyrer, M., and Boardman, D. (2009). Dewatering of tunneling slurry waste using electrokinetic geosynthetics. *J. Environ. Eng.* 135, 1227–1236. doi:10.1061/(asce)0733-9372(2009)135:11(1227)

Liang, C. P., Chen, J. S., Chien, Y. C., Jang, C. S., and Chen, C. F. (2018). Spatial analysis of the risk to human health from exposure to arsenic contaminated groundwater: a kriging approach. *Sci. Total Environ.* 627, 1048–1057. doi:10.1016/j.scitotenv.2018.01.294

Liu, F. Y., Wei, M. I., Zhang, L., and Wang, J. (2014). "Experimental study of the electro-osmosis consolidation of soft clay under anode follow-up," in *Ground improvement and geosynthetics*, 188–197.

Lo, K. Y., Inculet, I. I., and Ho, K. S. (1991). Electroosmotic strengthening of soft sensitive clays. *Can. Geotech. J.* 28, A345–A373. doi:10.1016/0148-9062(91)91244-l

Martin, L., Alizadeh, V., and Meegoda, J. (2019). Electro-osmosis treatment techniques and their effect on dewatering of soils, sediments, and sludge: a review. *Soils Found.* 59, 407–418. doi:10.1016/j.sandf.2018.12.015

Moayedi, H., Kazemian, S., Huat, B. B. K., Mazloomi, K., Niroumand, H., and Daud, N. N. N. (2012). Effect of calcium chloride on the electrokinetic characteristics of organic soil. *Int. J. Electrochem Sci.* 7, 7740–7749. doi:10.1016/s1452-3981(23)15819-6

Mohamedelhassan, E., and Shang, J. Q. (2001). Effects of electrode materials and current intermittence in electro-osmosis. *Proc. Institution Civ. Eng. - Ground Improv.* 5, 3–11. doi:10.1680/grim.5.1.3.39435

Mohamedelhassan, E., and Shang, J. Q. (2003). Electrokinetics-generated pore fluid and ionic transport in an offshore calcareous soil. *Can. Geotech. J.* 40, 1185–1199. doi:10.1139/t03-060

Otsuki, N., Yodsudjai, W., and Nishida, T. (2007). Feasibility study on soil improvement using electrochemical technique. *Constr. Build. Mater* 21, 1046–1051. doi:10.1016/j.conbuildmat.2006.02.001

Ou, C. Y., Chien, S. C., and Wang, Y. G. (2009). On the enhancement of electroosmotic soil improvement by the injection of saline solutions. *Appl. Clay Sci.* 44, 130–136. doi:10.1016/j.clay.2008.12.014

Pandey, B. K., Rajesh, S., and Chandra, S. (2024). Engineering and physicochemical response of soft clay with electrokinetic consolidation process. *Acta Geotech.* 19, 5125–5141. doi:10.1007/s11440-024-02227-w

Peng, J., Xiong, X., Mahfouz, A. H., and Song, E. R. (2013). Vacuum preloading combined electroosmotic strengthening of ultra-soft soil. *J. Cent. South Univ.* 20, 3282–3295. doi:10.1007/s11771-013-1852-9

Peng, J., Ye, H., and Alshawabkeh, A. N. (2015). Soil improvement by electroosmotic grouting of saline solutions with vacuum drainage at the cathode. *Appl. Clay Sci.* 114, 53–60. doi:10.1016/j.clay.2015.05.012

Shi, X. S., Liu, K., and Yin, J. H. (2021b). Effect of initial density, particle shape, and confining stress on the critical state behavior of weathered gap-graded granular soils. *J. Geotech. Geoenviron* 147, 04020160. doi:10.1061/(asce)gt.1943-5606.0002449

Shi, X. S., and Zhao, J. D. (2020). Practical estimation of compression behavior of clayey/silty sands using equivalent void-ratio concept. *J. Geotech. Geoenviron* 146, 04020046. doi:10.1061/(asce)gt.1943-5606.0002267

Shi, X. S., Zhao, J. D., and Gao, Y. F. (2021a). A homogenization-based state-dependent model for gap-graded granular materials with fine-dominated structure. *Int. J. Numer. Anal. Methods* 45, 1007–1028. doi:10.1002/nag.3189

Sun, Z., Zhao, M., Chen, L., Gong, Z., Hu, J., and Ma, D. (2023). Electrokinetic remediation for the removal of heavy metals in soil: limitations, solutions and prospection. *Sci. Total Environ.* 903, 165970. doi:10.1016/j.scitotenv.2023.165970

Tao, Y. L., Zhou, J., Gong, X. N., Chen, Z., and Hu, P. C. (2014). Influence of polarity reversal and current intermittence on electro-osmosis. *Ground Improv. Geosynth.*, 198–208. doi:10.1061/9780784413401.020

Wu, H., Hu, L., and Wen, Q. (2015). Electro-osmotic enhancement of bentonite with reactive and inert electrodes. *Appl. Clay Sci.* 111, 76–82. doi:10.1016/j.clay.2015.04.006

Xiao, F., Guo, K., and Zhuang, Y. F. (2021). Study on electroosmotic consolidation of sludge using EKG. *Int. J. Geosynth. Ground Eng.* 7, 33. doi:10.1007/s40891-021-00273-y

Xue, Z., Tang, X., Yang, Q., Tian, Z., Zhang, Y., and Xu, W. (2018). Mechanism of electro-osmotic chemical for clay improvement: process analysis and clay property evolution. *Appl. Clay Sci.* 166, 18–26. doi:10.1016/j.clay.2018.09.001

Yoshida, H. (2000). Electro-osmotic dewatering under intermittent power application by rectification of A.C. electric field. *J. Chem. Eng. Jpn.* 33, 134–140. doi:10.1252/jcej.33.134

Yukselen-Aksoy, Y., and Reddy, K. R. (2012). Effect of soil composition on electrokinetically enhanced persulfate oxidation of polychlorobiphenyls. *Electrochim Acta* 86, 164–169. doi:10.1016/j.electacta.2012.03.049

Zhang, H., Zhou, G., Zhong, J., Shen, Z., and Shi, X. (2017). Effect of nanomaterials and electrode configuration on soil consolidation by electroosmosis: experimental and modeling studies. *RSC Adv.* 7, 12103–12112. doi:10.1039/c6ra26674f

Zhuang, Y. F., and Wang, Z. (2007). Interface electric resistance of electroosmotic consolidation. *J. Geotechn Geoenviron Eng.* 133, 1617–1621. doi:10.1061/(asce)1090-0241(2007)133:12(1617)

frontiers | Frontiers in Physics

TYPE Original Research
PUBLISHED 12 December 2024
DOI 10.3389/fphy.2024.1514664

OPEN ACCESS

EDITED BY
Yifei Sun,
Taiyuan University of Technology, China

REVIEWED BY
Ting Huang,
Hohai University, China
Lin Yongliang,
Shanghai University, China

*CORRESPONDENCE
Xiaosan Tao,
txs3880@126.com

RECEIVED 21 October 2024
ACCEPTED 26 November 2024
PUBLISHED 12 December 2024

CITATION
Tao X and Gao Z (2024) Permeability behaviour of polyurethane polymer-reinforced granular material with and without clogging.
Front. Phys. 12:1514664.
doi: 10.3389/fphy.2024.1514664

Permeability behaviour of polyurethane polymer-reinforced granular material with and without clogging

Xiaosan Tao* and Zhibing Gao

Jiangsu Earthquake Disaster Risk Mitigation Center (Jiangsu Province Earthquake Engineering Research Institute), Nanjing, China

Polyurethane polymer-reinforced granular material (PPGM) can be used for ground improvement due to its high strength and drainage capacity. However, in engineering practice, clogging may occur that influence the permeability of PPGM. This study makes a laboratory assessment of the permeability of PPGM with and without clogging. It is found that the permeability coefficient of clean PPGM decreases as the content of polyurethane polymer increases, due to the reduction of its porosity and pore constriction size. To account this effect, a modified constriction size formula of PPGM is proposed. With the increase of the extent of clogging, the permeability coefficient of clogged PPGM decreases due to its decrease in the constriction size. A monotonic increase of the permeability coefficient of the mean constriction size of PPGM is found.

KEYWORDS

permeability, polymer, clogging, granular material, constriction size

1 Introduction

The urban surfaces in eastern China are usually covered by hard materials such as asphalt and concrete that provide convenience for public transportation. However, due to the poor permeability of these materials, negative impacts, such as the blockage of underground water supply [1] and urban flooding due to insufficient drainage of heavy rains [2], etc., can be also brought to the city. Therefore, there is an increasing demand for the development and application of pervious materials in urban construction, so that the precipitation in the city can be retained and infiltrated, sometimes turning flood disasters into reliable water resources when necessary [3]. In the past few decades, a variety of pervious materials have been developed [4–6]. For example, the pervious concrete consisting of internal pores was often used in pavement engineering to mitigate the stormwater runoff as well as the potential loss of groundwater recharge [3, 4]. However, the pervious concrete can be vulnerable to temperature which causes freeze-thaws of water in its internal pores that deteriorates the strength and durability of the pavement. Furthermore, the particulate matter, e.g., fines, can also block the internal pores and significantly reduce its permeability, as discussed in Shan, et al. [7] and Yu, et al. [8]. In addition to the pervious concrete, porous asphalt was also successfully applied in different countries, e.g., Switzerland [9] and Spain [10], for constructing the urban surface. However, such kind of permeable asphalt can be

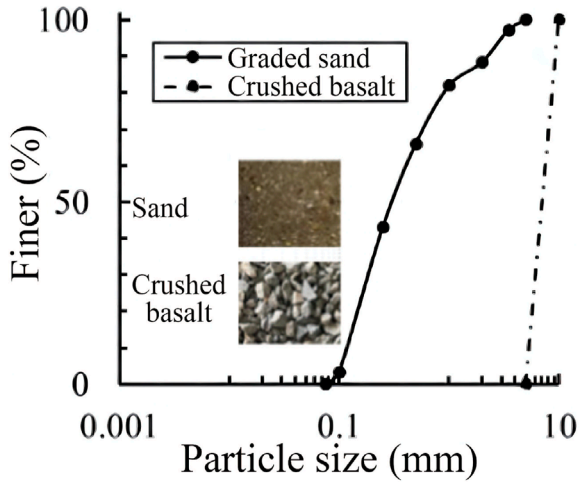

FIGURE 1
Gradations of crushed basalt and sand.

easily corroded by ultraviolet rays in the long run; it is also not resistant to frost due to cracking at low temperatures, which can cause heavy rutting in pavement.

In recent years, granular materials reinforced with polyurethane polymer [11–13] were proposed as an alternative for engineering construction, e.g., railroad foundation and ground improvement that requires a fast drainage of water to avoid potential liquefaction of the base soil caused by dynamic loads. Due to the larger permeable pores among the granular aggregates when compared to the pervious concrete or asphalt, polyurethane polymer-reinforced granular material (PPGM) can have better drainage capacity. Previous studies [12, 14] showed that the inclusion of polyurethane polymer can improve the strength and resilience of the granular material; but, it can also adversely affect the permeability if a high content of polyurethane polymer was used. For better application of the PPGM, further comprehensive studies concerning its permeability performance should be carried out.

This technical note provides a laboratory assessment of the permeability characteristics of PPGM, where the effects of void ratio, content of polyurethane polymer, and clogging on the permeability coefficient of PPGM are investigated.

2 Test material and test program

2.1 Test material

The granular material made of crushed basalt was adopted, where it was uniformly graded between the particle sizes of 5 mm–10 mm, as shown in Figure 1. Its minimum and maximum void ratios were measured to be 0.60 and 0.89, respectively. The permeability coefficient of the gravel was 2.26 cm/s. To investigate the effect of clogging on the permeability behaviour of PPGM, a sand with the gradation shown in Figure 1 was also adopted, where it had a coefficient of uniformity of 3.47, a maximum particle size of 5 mm and a minimum particle size of 0.075 mm. In this experiment, non-foamed polyurethane was used, which mainly consists of two components: component A, the adhesive, and component B, the curing agent, which is prone to oxidation reactions in the air. The polyurethane polymer shown in Figure 2A was produced by mixing the polyol (Figure 2B) and polymethylene polyphenyl isocyanate (Figure 2C), based on a volume ratio of 3:2. Then, the polyurethane polymer was poured into the granular material, based on the contents of 3%, 4%, 5% and 6%, respectively, to produce each PPGM sample tested in this study. The detailed sample preparation steps are as follows: (1) Wash the aggregate thoroughly to remove any surface mud, then allow it to dry; (2) Measure the required amounts of aggregate and polyurethane components A and B according to the design mix and sample volume; (3) Mix polyurethane components A and B thoroughly for about 1 min until they are completely blended; (4) Gradually pour the mixed polyurethane in batches onto the aggregate while stirring, and stop mixing once the surface of the mixture is completely coated with the adhesive; (5) Pack the mixture into the mold in two layers, tamping each layer 15 times, and level the top surface. Once the sample reaches a certain strength (generally after 1 day), demold the sample.

2.2 Test program

The porosity of the PPGM samples with different contents (f_c) of polyurethane polymer were tested by volume-based method. The net weight (m_1) of a PPGM sample was firstly measured; then, it was submerged in into the water and saturated until the air was discharged, after which its weight (m_2) in water was measured again. The porosity (n) of the sample as then calculated as in Equation 1:

$$n = 1 - \frac{m_1 - m_2}{V\rho_w} \tag{1}$$

where V and ρ_w are the volume of the sample and the density of water, respectively. Table 1 lists the porosity of each sample.

The permeability of each PPGM sample was tested under constant water head. As the effect of clogging on the permeability of PPGM should be considered, a modified permeability test instrument instead of the traditional one [15], as schematically shown in Figure 3, was used. The samples were placed in a cylindrical PVC pipe with a diameter of 7.5 cm and a height of 20 cm. Due to the open channels of PPGM connected to the side wall of the test instrument, the water can easily flow through these channels along the side wall, resulting in an inaccurate measurement of the permeability coefficient (k) of PPGM. To resolve this limitation, all the samples were wrapped with the PE plastic wrapper before being placed into the test instrument. To prevent further leakage along the side wall, the contact surface between the wrapper and the side wall of the test instrument was also sealed with vaseline. Then, the tests under constant water head were carried out on PPGM without clogging. The effect of clogging on the permeability of PPGM was carried out by progressively adding sand on the top of the PPGM in the cylindrical PVC pipe. Firstly, the valve was closed and the water level was kept at the target value shown in Figure 3; Secondly, 5 g sand was evenly added to the top of the

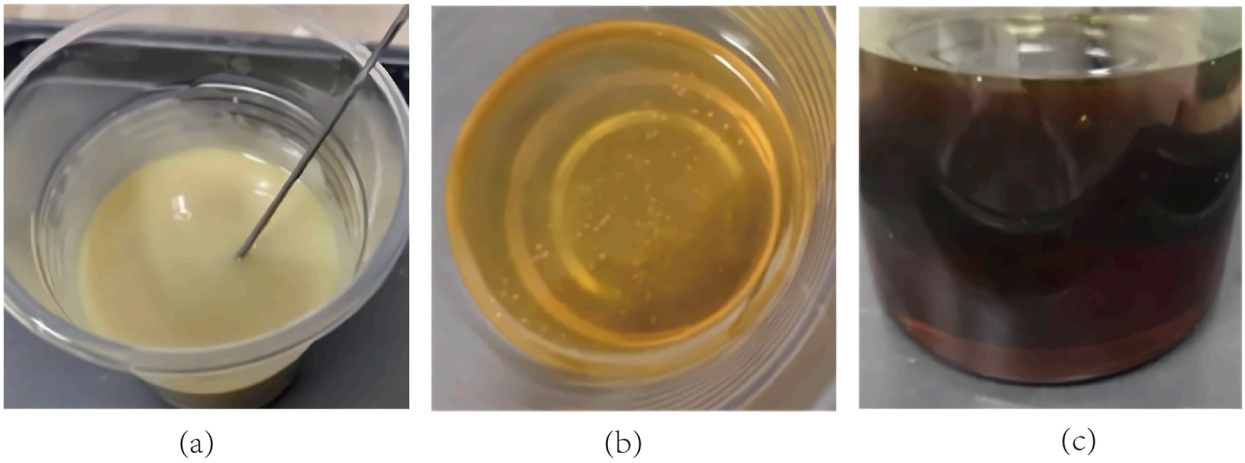

FIGURE 2
(A) Polyurethane polymer, **(B)** Polyol **(C)** Polymethylene polyphenyl isocyanate.

TABLE 1 Properties of test materials.

Sample No.	fc (%)	n	k of unclogged (cm/s)	S35	Sc
1	3	40.23%	2.00	16.71%	79.75%
2	4	36.50%	1.94	17.70%	78.66%
3	5	32.14%	1.88	18.48%	74.69%
4	6	27.85%	1.62	21.01%	64.81%

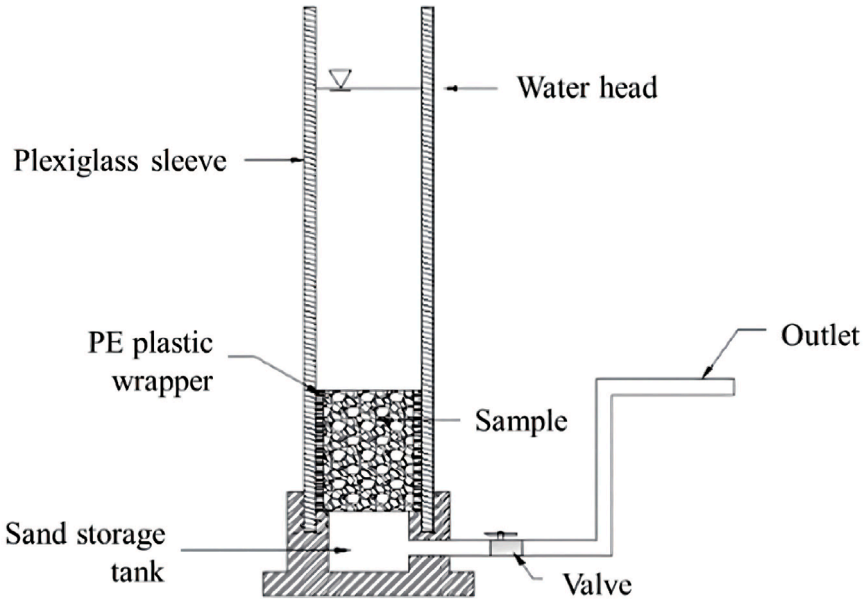

FIGURE 3
Schematic show of the test instrument.

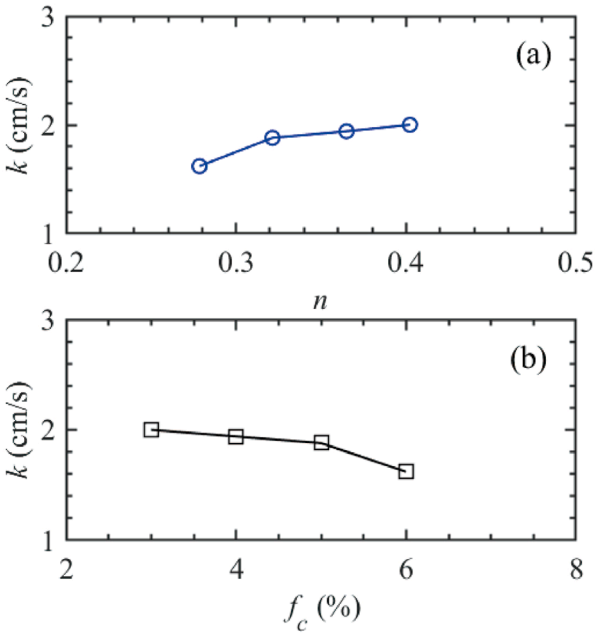

FIGURE 4
Permeability coefficient of clean PPGM: **(A)** Influence of porosity; **(B)** Influence of content of polyurethane polymer.

sample and rested for 1 min; thirdly, switch on the valve, let water and sand particles infiltrate through the PPGM under constant water level; fourthly, measure the permeability and keep record when the data of permeability is stable; repeat the above process for 35 times (N) and stop the test. To evaluate the effect of clogging, an index, called the remaining permeability (S) which measures the remaining capacity for water permeability, is used, as shown in Equation 2:

$$S = \frac{k_i}{k_0} \tag{2}$$

where k_0 is the coefficient of permeability (cm/s) of clean PPGM, k_i is the coefficient of permeability (cm/s) of clogged PPGM after i-th addition of sand.

3 Test results

3.1 Permeability behavior of clean PPGM

Figure 4 shows the coefficient of permeability (k) of PPGM without clogging. It can be found that k increases with an increase of the porosity while it decreases with an increase in the content of polyurethane polymer. This can be attributed to the block or size reduction of the open channels of PPGM caused by increasing the content of polyurethane polymer, which hinders the flow of water through PPGM.

3.2 Permeability behavior of clean PPGM

Figure 5 shows the variation of the permeability of clogged PPGM after adding sand. It can be found that the permeability of PPGM decreases after adding sand. As the amount of sand increases, the extent of clogging increases which results in the reduction of the remain permeability, S. Three stages of the reduction of S can be observed in Figure 5. At first stage, the sand particles infiltrated through the open channels within PPGM and gradually blocked the channels with small constriction size, but most of the channels were still open and the reductions of S is moderate. With the further development of clogging, the permeability of PPGM reached the second stage, where sand particles blocked the majority of flowing channels with different constriction sizes, resulting in a rapid reduction of the permeability and the associated S. With the addition of more sand, the permeability of PPGM became stable and the third stage was reached. At this stage, the infiltration of sand led to a maximum clogging of PPGM. Table 1 also lists the value of S at the end of each test, i.e., S_{35}. A remarkable reduction of the permeability of PPGM induced by clogging was observed. In the experiment, with the addition of sand into the water, some of the sand entered the internal pores of the specimen along with the water flow, while some accumulated on the surface of the specimen. As the amount of sand gradually increased, the accumulation of sand on the specimen's surface also increased. Initially, a small amount of sand accumulated, followed by the majority being covered by a sand layer, leaving only the larger constriction size pores as main permeable channels. Eventually, the entire surface of the specimen was covered by the sand layer. In this experiment, as the amount of sand clogging increased, the permeability coefficient of PPGM with different polyurethane contents (porosity) consistently decreased, and eventually stabilized around 0.37 cm/s.

To further test the permeability of PPGM after clogging, the sand layers at the surface of the PPGM sample were removed. In this case, the loss of permeability was changed from around 16%–21% to around 75%–80%, as shown in Table 1, where S_c indicates the remaining permeability after removing the sand layers at sample surface. This is because the permeability from previous tests takes into account the performances of both the clogged PPGM and the upper sand particles. After removing the cumulated fine particles from the surface of PPGM, the permeability can be partially recovered.

4 Discussions

From the above test results, it can be observed that the permeability of PPGM is influenced by its porosity, particle size (or size distribution), content of polyurethane polymer and clogged particles. However, from the micromechanical perspective, it is the pore constriction that affects the permeability [16, 17]. According to Indraratna, et al. [16], the pore constriction size (D_c) of a granular material can be calculated as in Equation 3:

$$D_c = D_{cD} + P_c(1 - D_c)(D_{cL} - D_{cD}) \tag{3}$$

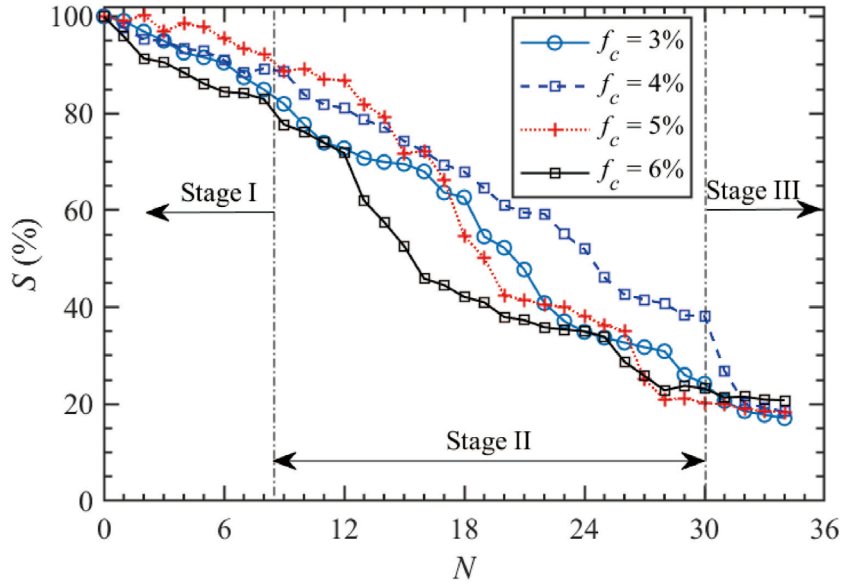

FIGURE 5
Variation of remaining permeability of clogged PPGM with number of times.

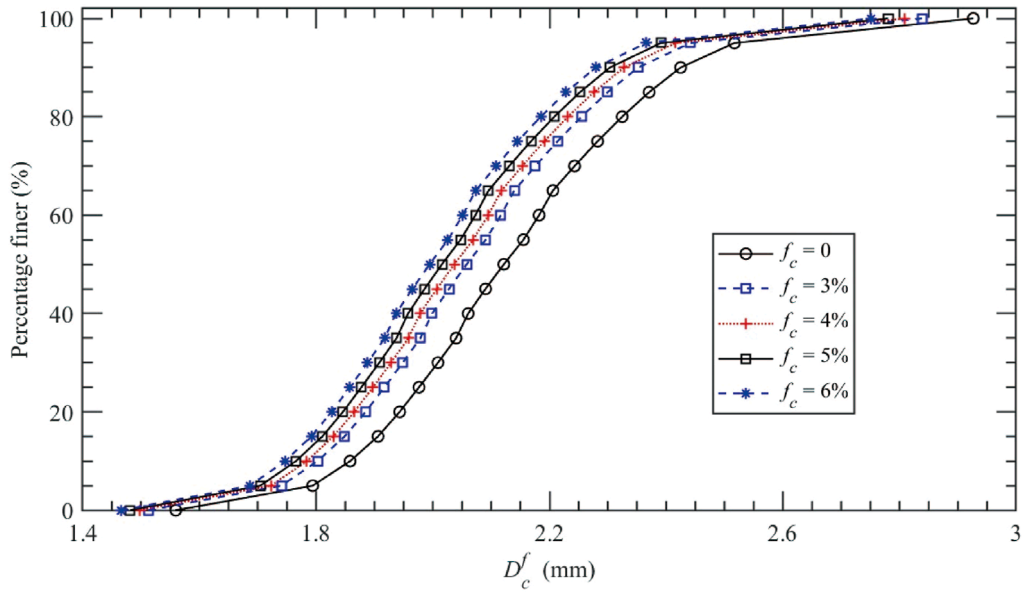

FIGURE 6
The CSD of PPGM with differentf_c.

where D_{cD} and D_{cL} are the constriction sizes of the densest and loosest samples, respectively. Details for calculating D_{cD} and D_{cL} can be found in Indraratna et al. [16], and thus not repeated here for simplicity. P_c is the percentage of the constrictions with sizes finer than D_c; R_d is the relative density of the sample. The constriction size distribution (CSD) of the granular material without adding polyurethane polymer can thus be determined by substituting the measured R_d into Equation 3. However, in this study, as the content of polyurethane polymer increases, the constriction size of PPGM should decrease. To account for the effect of polyurethane polymer, Equation 3 is modified as in Equation 4:

$$D_c^f = (1 - f_c)D_{cD} + (1 - f_c)P_c(1 - R_d)(D_{cL} - D_{cD}) \quad (4)$$

where with the increase of f_c, D_c^f decreases. When $f = 0$, D_c^f corresponds to the constriction size of clean granular material, whilst $f_c = 1$, resulting in $D_c^f = 0$, because all the pore constrictions were sealed by the polyurethane polymer.

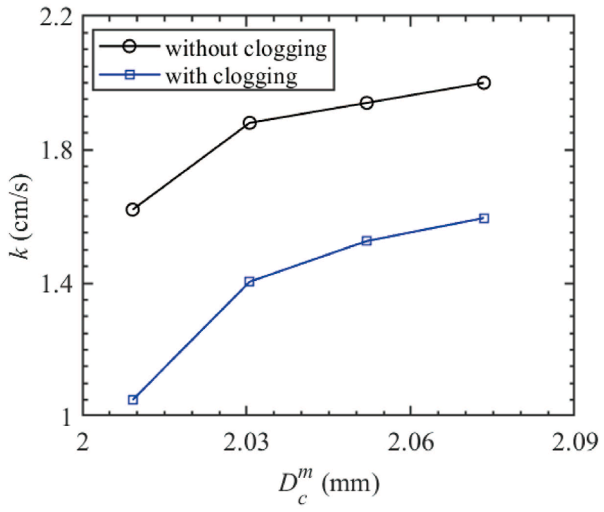

FIGURE 7
Variation of permeability coefficeint with mean constriction size.

Figure 6 shows the CSD of PPGM. Obviously, the greater the content of polyurethane polymer, the smaller the constriction sizes, leading to the decrease of permeability. Indraratna, et al. [16] pointed out that the permeability of granular soil had an explicit relationship with the mean constriction size, D_c^m. D_c^m can be determined from the CSD curve by using the probability of occurrence between two neighbouring constriction sizes, as shown in Equation 5:

$$D_c^m = \frac{\sum_{i=1}^{n} P_{ci} D_{ci}^f}{\sum_{i=1}^{n} P_{ci}} \tag{5}$$

where D_{ci} is the i-th size at the CSD, with the corresponding probability of occurrence (P_{ci}).

Figure 7 shows the variation of the permeability of PPGM with D_c^m. It is found that the permeability coefficient of PPGM without clogging increases with the increasing constriction size. Similarly, the permeability coefficient of the clogged PPGM obtained after removing the cumulated fine particles from the sample surface also increases with the increasing constriction size, but the overall values of the permeability coefficient of clogged PPGMs was smaller than the unclogged ones.

5 Conclusion

The permeability characteristics of a polyurethane polymer-reinforced granular material (PPGM) with and without clogging was evaluated by laboratory test. The main findings of this study can be summarised as:

(1) With the increase of the content of polyurethane polymer or the decrease of the porosity, the permeability coefficient of PPGM decreased, due to the block of internal channels for water flow.
(2) As the extent of clogging increased, the remain permeability (S) of PPGM reduced. Three stages of the reduction of S, including the progressive reduction, rapid reduction and stable state, can be observed.
(3) Clogging would decrease the pore constriction size and thus the permeability of PPGM; an increase of the permeability coefficient with the increasing mean constriction size can be observed.

Data availability statement

The raw data supporting the conclusions of this article will be made available by the authors, without undue reservation.

Author contributions

XT: Conceptualization, Funding acquisition, Investigation, Methodology, Validation, Writing–original draft, Writing–review and editing. ZG: Data curation, Investigation, Methodology, Writing–original draft.

Funding

The author(s) declare that financial support was received for the research, authorship, and/or publication of this article. The authors acknowledge financial support from the National Natural Science Foundation of China (No. 51639002).

Conflict of interest

The authors declare that the research was conducted in the absence of any commercial or financial relationships that could be construed as a potential conflict of interest.

Generative AI statement

The author(s) declare that no Generative AI was used in the creation of this manuscript.

Publisher's note

References

1. Trimble SW. Contribution of stream channel erosion to sediment yield from an urbanizing watershed. *Science* (1997) 278:1442–4. doi:10.1126/science.278.5342.1442

2. Brattebo BO, Booth DB. Long-term stormwater quantity and quality performance of permeable pavement systems. *Water Res* (2003) 37:4369–76. doi:10.1016/S0043-1354(03)00410-X

3. Obla KH. Pervious concrete-An overview. *Indian Concrete J* (2010) 84:9–18.

4. Chandrappa AK, Biligiri KP. Pervious concrete as a sustainable pavement material-Research findings and future prospects: a state-of-the-art review. *Construction Building Mater* (2016) 111:262–74. doi:10.1016/j.conbuildmat.2016.02.054

5. Huang B, Wu H, Shu X, Burdette EG. Laboratory evaluation of permeability and strength of polymer-modified pervious concrete. *Construction Building Mater* (2010) 24:818–23. doi:10.1016/j.conbuildmat.2009.10.025

6. Sahdeo SK, Ransinchung G, Rahul KL, Debbarma S. Reclaimed asphalt pavement as a substitution to natural coarse aggregate for the production of sustainable pervious concrete pavement mixes. *J Mater Civil Eng* (2021) 33. doi:10.1061/(asce)mt.1943-5533.0003555

7. Shan J, Zhang Y, Wu S, Lin Z, Li L, Wu Q. Pore characteristics of pervious concrete and their influence on permeability attributes. *Construction Building Mater* (2022) 327:126874. doi:10.1016/j.conbuildmat.2022.126874

8. Yu F, Guo J, Liu J, Cai H, Huang Y. A review of the pore structure of pervious concrete: analyzing method, characterization parameters and the effect on performance. *Construction Building Mater* (2023) 365:129971. doi:10.1016/j.conbuildmat.2022.129971

9. Isenring T, Koester H, Scazziga I. Experiences with porous asphalt in Switzerland. *Transportation Res Rec* (1990) 41–53.

10. Ruiz A, Alberola R, Pérez F, Sánchez B. Porous asphalt mixtures in Spain. *Transportation Res Rec* (1990) 87–94.

11. Farooq MA, Nimbalkar S. Novel sustainable base material for concrete slab track. *Construction Building Mater* (2023) 366:130260. doi:10.1016/j.conbuildmat.2022.130260

12. Tan H, Yu C, Sun Y. Improved mechanical performance of gravel reinforced by polyurethane polymer adhesive. *J Mater Civil Eng* (2023) 35. doi:10.1061/(asce)mt.1943-5533.0004711

13. Kennedy J, Woodward PK, Medero G, Banimahd M. Reducing railway track settlement using three-dimensional polyurethane polymer reinforcement of the ballast. *Construction Building Mater* (2013) 44:615–25. doi:10.1016/j.conbuildmat.2013.03.002

14. Tan H, Ding B, Chen J. Experimental test on water permeability and clogging characteristic of polymer cemented gravel porous material. *J Waterway Harbor* (2021) 42:775–82.

15. ASTM. *ASTM D2434: standard test method for permeability of granular soils (constant head)*. West Conshohocken, Pennsylvania: ASTM International (2019). p. 3–5. Available from: https://standards.iteh.ai/catalog/standards/cen/50899458-622b-4b86-b3e9-bfa0755bc727/en-14427-2022. (Accessed November 18, 2023).

16. Indraratna B, Nguyen VT, Rujikiatkamjorn C. Hydraulic conductivity of saturated granular soils determined using a constriction-based technique. *Can Geotechnical J* (2012) 49:607–13. doi:10.1139/T2012-016

17. Taylor HF, O'Sullivan C, Sim WW. Geometric and hydraulic void constrictions in granular media. *J Geotechnical Geoenvironmental Eng* (2016) 142. doi:10.1061/(asce)gt.1943-5606.0001547

frontiers | Frontiers in Physics

TYPE Original Research
PUBLISHED 12 December 2024
DOI 10.3389/fphy.2024.1488622

OPEN ACCESS

EDITED BY
Gandhimohan M. Viswanathan,
Federal University of Rio Grande do Norte, Brazil

REVIEWED BY
Junhong Xu,
Nanjing Forestry University, China
Boqi Xiao,
Wuhan Institute of Technology, China

*CORRESPONDENCE
Huiming Tan,
thming@hhu.edu.cn

RECEIVED 30 August 2024
ACCEPTED 18 November 2024
PUBLISHED 12 December 2024

CITATION
Hu X, Li M and Tan H (2024) Exploring mechanical performance of non-foamed polyurethane-bonded gravel and its pile bearing characteristics under embankments: an experimental and numerical approach. *Front. Phys.* 12:1488622. doi: 10.3389/fphy.2024.1488622

Exploring mechanical performance of non-foamed polyurethane-bonded gravel and its pile bearing characteristics under embankments: an experimental and numerical approach

Xin Hu[1], Mengliang Li[2] and Huiming Tan[2]*

[1]Northwest Electric Power Design Institute Co., Ltd. of China Power Engineering Consulting Group, Xi'an, China, [2]College of Harbour, Coastal and Offshore Engineering, Hohai University, Nanjing, China

Pile supported geogrid-reinforced embankment are widely used to treat soft soil. This paper proposes a novel method for reinforcing foundations using non-foamed polyurethane-bonded gravel (NPBG) porous piles. Through triaxial compression tests, the mechanical properties and strength parameters, such as strength and stiffness, of the polyurethane-bonded gravel material are determined. Finite element numerical simulations are then employed to investigate the bearing characteristics of NPBG porous pile under embankment loads. The experimental results indicate that, under the same confining pressure, the strength and stiffness of the NPBG material are significantly higher than those of plain gravel material, while still retaining large pore characteristics. Increasing the polyurethane content enhances the strength and stiffness of the porous material, but the improvement diminishes as the confining pressure increases. A systematic comparative analysis was conducted on the bearing characteristics of NPBG porous pile *versus* concrete pile, cement-mixed pile, and gravel pile under embankment in terms of load sharing ratio and settlement deformation. The permeability coefficient and modulus of the pile significantly influence the dissipation rate of excess pore water pressure in the foundation soil. The NPBGP pile exhibited the fastest consolidation speed, effectively controlling total settlement and reducing the proportion of post-construction settlement of the embankment. Compared to concrete pile and cement-mixed pile, the NPBG porous pile has a lower uniform settlement surface height in embankment, making it suitable for low-height embankment accelerated construction projects.

KEYWORDS

non-foamed polyurethane, gravel pile, porous media, settlement, embankment

1 Introduction

When expressway embankments are built on soft soils, they exert substantial loads over a wide area. Soft clays and other compressible soils frequently experience excessive settlements or fail due to inadequate bearing capacity. A variety of techniques can be used to solve such problems [1]. Pile supported geogrid-reinforced embankment have increasingly been used in the recent years for accelerated construction [2–6]. In this system, piles provide major support for the embankment over soft soils and reduce its settlement. Single or multiple geogrid layer(s) are employed above the piles to enhance the load transfer from soft soils to piles [7–9]. As piles support the majority of the embankment load, soft soils carry reduced pressure, significantly lowering the risk of soil failure and minimizing both total and differential settlements. As a result, accelerated construction becomes possible.

Different pile types can be applied in this system, such as gravel piles [10–12], cement-mixed piles [13–15], and concrete piles [16–18], each exhibiting distinct interaction characteristics with the foundation soil. Gravel piles can replace a portion of the soft soil to enhance bearing capacity, and the porous nature of the pile can create drainage pathways that accelerate soil consolidation. However, since the bearing capacity of gravel piles primarily relies on the constraint provided by the surrounding soil, the total settlement of the foundation remains relatively large when using gravel piles [19]. Cement-mixed piles exhibit significantly higher strength and stiffness compared to gravel piles, while concrete piles offer even greater strength and stiffness, effectively supporting a large portion of the embankment load and helping to reduce total settlement. However, Even with the reduced load on the soft soils, excess pore water pressure would still be generated and then dissipate during and after the construction, and the settlement occurred during the construction of the embankments and increased after the construction. Cement-mixed piles and concrete piles generally lack drainage capability and cannot create drainage pathways in the foundation, resulting in slow drainage consolidation of the foundation soil and often leading to significant post-construction settlement [20]. To achieve both reduced total settlement and post-construction settlement, researchers have found it beneficial to use permeable concrete as the pile material [21–23]. Studies show that permeable concrete piles possess certain strength and stiffness, and compared to stone columns, they enhance both bearing capacity and settlement rate, significantly reducing the development of excess pore pressure in the foundation soil. However, the small and shallow pores characteristic of permeable concrete can lead to clogging, impairing its drainage performance and preventing it from achieving the intended drainage effect [24].

Non-foamed polyurethane-bonded gravel material (NPBG) is formed by mixing non-foamed polyurethane with gravel in a specific proportion. The polyurethane binds the gravel into a cohesive whole while retaining the original interconnected porosity of the gravel particles. This material maintains the excellent permeability of the aggregate gravel while also providing certain strength and stiffness. Researchers have investigated the permeability, thermal stability, strength, stiffness, and durability of NPBG [25, 26], and it has already been applied in pavement engineering [27–29]. However, there is still limited in-depth theoretical research on NPBG, such as the stress-strain relationship considering the effects of confining pressure, particularly the introduction of advanced methods like fractal theory [30] to study the flow characteristics of pore water within the high porosity NPBG porous medium with large pore sizes. Such research will provide important theoretical guidance for the engineering applications of this material.

This study applies the NPBG porous material in the reinforcement of soft soil foundations, proposing a novel NPBG porous pile technology that integrates high bearing capacity with good drainage capability. First, the mechanical properties of NPBG material are investigated through triaxial compression tests to explore the effects of polyurethane content and confining pressure. Subsequently, finite element numerical simulations are conducted to investigate the bearing characteristics of NPBG porous piles under embankment loads. A systematic comparative analysis is performed on the load distribution and settlement deformation characteristics of NPBG piles in relation to concrete piles, cement-mixed piles, and gravel piles. This analysis assesses the applicability of NPBG porous piles in pile supported geogrid-reinforced embankments, providing a reference for their application in practical engineering.

2 Experiment on polyurethane bonded gravel porous material

2.1 Materials

2.1.1 Gravel

The gravel used in this study is basalt, with a particle size of 5–10 mm and angular shape. The specific gravity of the gravel is 2.74, the maximum porosity ratio is 0.89, and the minimum porosity ratio is 0.60.

2.1.2 Non-foam polyurethane

The non-foamed polyurethane is composed of two non-water-reactive monomers: polyol (component A) and polyisocyanurate (component B). Among them, polyol includes polyether polyol, polyester polyol, and polyether-ester. The reaction is initiated with either amine catalyst or metal salt catalyst. The components A and B are mixed in a 3:2 ratio, thoroughly stirred until a white homogenous mixture is formed, and the mixture is homogeneous.

2.2 Sample preparation

To obtain the mechanical properties of NPBG, it is necessary to be cast into a 200 mm high and 100 mm diameter specimen. The gravel used in this study has a dry density of 1.56 g/cm^3 and the corresponding relative compaction ratio is 0.45. Not all coarse-grained soils can be directly tested due to their susceptibility to size effects [31]. In this test, the maximum diameter of the gravel particles in the specimen was no more than 1/10 of the specimen diameter, to reduce the effects of size effects.

Non-foamed polyurethane fully adhered to and completely encapsulated the particles of dried gravel after it was sufficiently mixed with the gravel. Part of the polyurethane slurry filled the voids on the particles due to its fluidity. To ensure that the NPBG materials retain a large amount of voids, we will investigate the improvement of gravel properties under low content levels of polyurethane. Three

FIGURE 1
NPBG samples.

samples were prepared, each with a polyurethane content (W_p) of 2%, 4%, and 6% (defined as the ratio of polyurethane mass to gravel mass). The samples were left in the mold for 3 days after filling and then continue to cure until 7 days before conducting subsequent tests. The step-by-step procedure for preparing the NPBG samples is as follows:

① Wash and dry the surface of the gravel, and then;
② Lubricate the inner wall of the mold with petroleum jelly, and place a transparent plastic sheet tightly against the inner wall of the mold;
③ Weigh the required amount of gravel and pour it into a mixing container;
④ According to the gravel mass, take the designed polyurethane content of component A and component B, mix them together and stir for about 1 min, until the mixture becomes white in color;
⑤ After the polyurethane is prepared, pour it into the gravel evenly in two batches, and start mixing from the time when the surface of the gravel is completely enveloped by the polyurethane liquid. Stop stirring when the surface of the gravel is completely encapsulated;
⑥ Fill the mold with the NPBG mixture in four layers, and level the top surface of the sample before it is left to stand for 3 days.

The specimens after removal from the mold are shown in Figure 1. It can be observed that the polyurethane binds the crushed stones into an integrated whole. Pure gravel specimens were also prepared as a comparison. Pure gravel specimens were filled into the pressure chamber of the testing instrument in four layers, ensuring the relative compaction ratio of 0.45.

2.3 Experiment procedure

The tests were conducted using consolidated drained tests. All samples were encased in a 0.5 mm thick rubber membrane to prevent damage during the test, which could lead to test failure. Before applying axial load, the samples were saturated and a predetermined confining pressure was applied while opening the drainage valve until the samples were consolidated. Four different confining pressures were selected for the tests: 50 kPa, 100 kPa, 200 kPa, and 300 kPa. The axial load was applied at an axial strain rate of 0.2%/min to prevent excessive pore pressure generation during shearing. The tests were terminated when the axial strain of the samples reached 15%. The volume change of the samples was determined by measuring the amount of water expelled from or absorbed into the pressure chamber.

2.4 Mechanical characteristics of NPBG

Figure 2 shows the deviatoric stress-axial strain ($q - \varepsilon_a$) and volumetric strain-axial strain ($\varepsilon_v - \varepsilon_a$) relationship curves for NPBG samples with different polyurethane contents (2%, 4%, 6%) under various confining pressures σ_3. The deviatoric stress is denoted as $q = \sigma_1 - \sigma_3$. For a more intuitive comparison, the figure also includes the result curves for pure gravel samples without added polyurethane. The meaning of the curve numbers in the figure is as follows: for example, S2-50 indicates that the sample has a polyurethane content of 2% and was tested under a confining pressure of 50 kPa.

From the figure, it can be observed that with the increase in confining pressure, the deviatoric stress of the pure gravel samples increases under the same axial strain. At the two lower confining pressures, the samples exhibit less pronounced peak deviatoric stresses, whereas at the two higher confining pressures, no peak stress is observed, showing strain hardening behavior. From the volumetric strain curves, under the two lower confining pressures, the samples initially exhibit volume contraction with increasing axial strain, followed by volume expansion. When the confining pressure increases (≥200 kPa), the samples exhibit shear contraction. This indicates that the confining pressure significantly affects the shear characteristics of the gravel. At lower confining pressures, the resistance to shear forces primarily relies on the interlocking and frictional forces between gravel particles. As the external shear force gradually increases and overcomes the interlocking effect, leading to particle movement, the deviatoric stress reaches its peak. Following this, with an increase in strain, gravel particles begin to slide and rotate under shear forces, and the friction generated during particle movement becomes the main source of resistance to shear forces. At higher confining pressures, the gravel particles experience greater lateral confinement, and the voids between particles gradually decrease. During shear, the friction between particles continues to play a primary role in resisting shear forces, resulting in the deviatoric stress consistently showing a trend of gradual increase with increasing strain.

The NPBG samples exhibit a clear peak in deviatoric stress, showing pronounced strain softening regardless of the polyurethane content and confining pressure conditions. This phenomenon is primarily attributed to the bonding effect of polyurethane, which creates a cohesive strength similar to cohesion between gravel particles. A greater shear force is required to overcome the bonding and interlocking effects between the gravel particles. After reaching the peak deviatoric stress, particle movement gradually occurs, and thereafter, resistance to shear forces relies mainly on the friction between the gravel particles, eventually stabilizing as strain

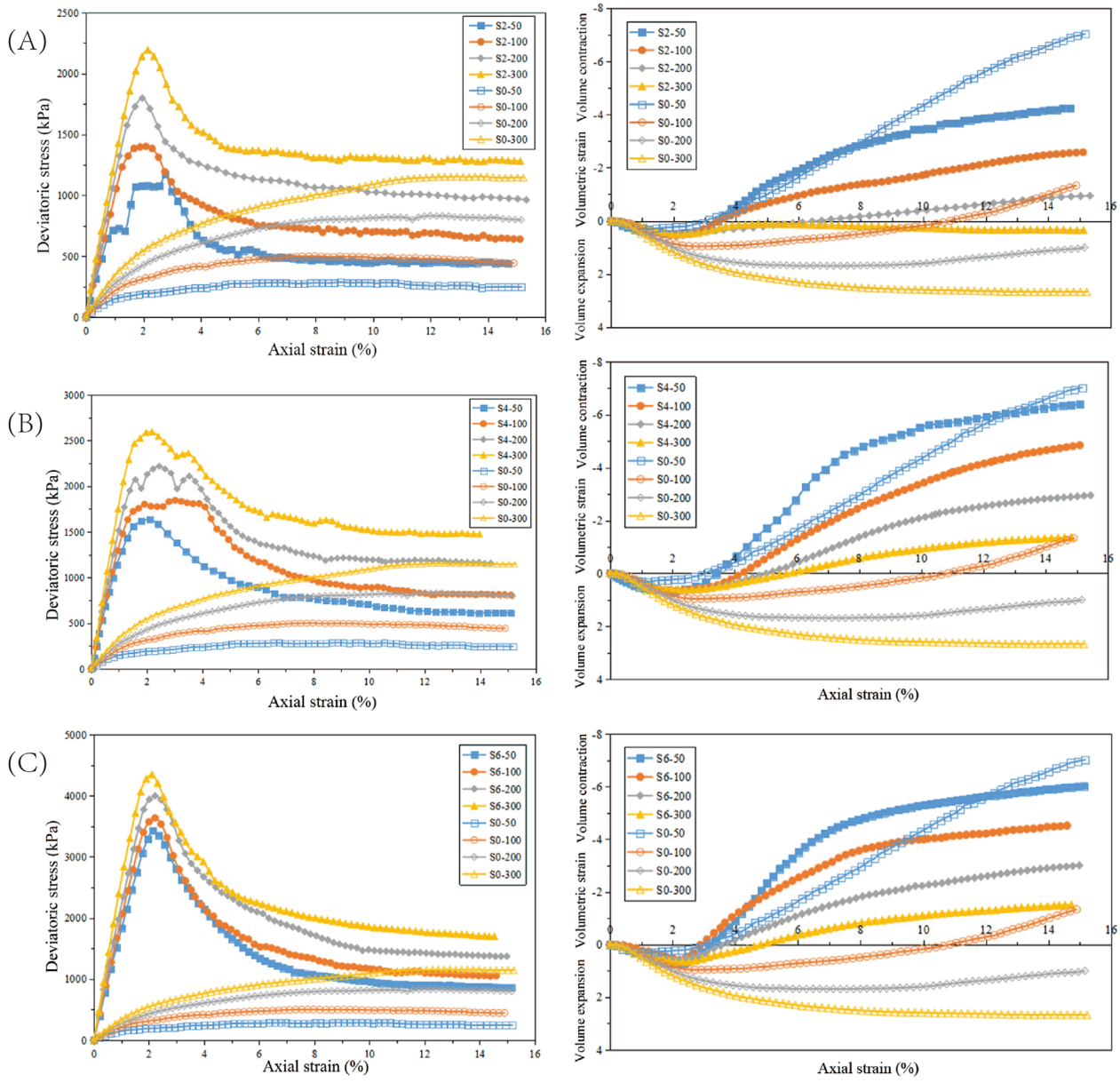

FIGURE 2
(A) The deviatoric stress-axial strain and volumetric strain-axial strain relationship curves for samples with polyurethane contents 2% under various confining pressures. **(B)** The deviatoric stress-axial strain and volumetric strain-axial strain relationship curves for samples with polyurethane contents 4% under various confining pressures. **(C)** The deviatoric stress-axial strain and volumetric strain-axial strain relationship curves for samples with polyurethane contents 6% under various confining pressures.

increases. Under different polyurethane contents and confining pressures, the axial strain corresponding to the peak deviatoric stress is approximately 2.1%. This indicates that the bonding force caused by polyurethane curing is a major factor influencing the increase in shear strength, primarily depending on the strength of the chemical reaction products of polyurethane. Changes in the thickness of the adhesive layer on the gravel surface and the uniformity of contact points between particles due to variations in polyurethane content significantly affect the magnitude of the peak deviatoric stress, but have little impact on the strain value at which the peak occurs. At the same polyurethane content, the peak value increases with the confining pressure. Additionally, there are significant differences in volumetric changes. Only when the polyurethane content is 2% and the confining pressure is 300 kPa do the samples exhibit a tendency for the volume to transition from contraction to expansion during shearing, followed by increased contraction, ultimately resulting in volume contraction. The remaining NPBG samples all undergo volume expansion, and at the same polyurethane content, the amount of expansion decreases with increasing confining pressure.

Observing samples with different polyurethane contents, it can be seen that the sample with a 4% content exhibits a relatively smooth curve near the peak deviatoric stress point, primarily due

to the influence of the polyurethane bonding effect. At higher contents, the bonding effect is strong, and the sample maintains good integrity. After failure, the sample gradually fractures along the shear band, causing a rapid decrease in strength. At lower contents, the bonding effect is generally weaker. As the shear band forms, the bonds between gravel particles continuously fail, and the sample's integrity is compromised, unable to maintain its original strength. However, at a 4% content, due to the inconsistency in the shape and size of the gravel particles, the bonding effect is also uneven. The weaker bonds near the shear band fail first, while the better bonds between particles remain intact, forming "gravel bonded blocks." These blocks typically consist of several gravel particles, have a larger volume, and are less likely to move, which to some extent slows down the failure process of the sample, allowing it to maintain a high strength for some time after reaching the peak deviatoric stress.

To more clearly analyze the effect of polyurethane content on stress-strain behavior, the deviatoric stress-axial strain curves and volumetric strain-axial strain curves of samples under the same confining pressure were plotted, as shown in Figure 3. From the figure, it can be seen that under constant confining pressure, the strength of the samples increases with the increase of polyurethane content; especially when the polyurethane content increases from 4% to 6%, the peak deviatoric stress of the samples increases significantly. In the volumetric strain curves, as the polyurethane content increases from 2% to 6%, the volumetric expansion of the samples gradually increases. Additionally, it can be observed that when the polyurethane content is 2%, the volumetric change trend of the samples is most similar to that of the pure gravel samples. As mentioned earlier, at this content, the gravel particles in the samples disengage due to the failure of polyurethane bonding, and as axial compression increases, the number of detached particles gradually increases. Therefore, in the later stage of compression, the state of the samples is more similar to that of pure gravel samples. It is analyzed that the gravel particles can exhibit interlocking or rotational movement when subjected to shear. The former causes the particles to become more closely packed, resulting in a decrease in sample volume, while the latter has the opposite effect. The confining pressure can suppress the second type of movement. Under higher confining pressures, the gravel becomes more tightly packed, preventing an increase in sample volume. This also explains why the S2-300 sample ultimately exhibits volumetric contraction.

Cohesion and internal friction angle are parameters that represent the shear strength of a material, which can be obtained by plotting the Mohr-Coulomb strength envelope. Figure 4 organizes the Mohr circles and strength envelopes for each group of samples at failure. It can be seen that the envelopes of the failure Mohr circles are essentially straight lines. Therefore, for NBPG materials, their strength can still be described using the Mohr-Coulomb strength criterion, and the strength parameters do not change with varying confining pressures.

The effect of polyurethane content on strength parameters is shown in Figure 5. It can be observed that, compared to pure gravel samples, the cohesion of NPBG increases to varying degrees with the increase in polyurethane content. At a content of 2%, the bonding effect is already significant; when the content increases from 4% to 6%, the cohesion significantly improves, indicating that the 6% polyurethane mixture has the best bonding efficiency. Pure gravel samples also exhibit a small apparent cohesion. Generally, the cohesion of non-cohesive soil is considered to be zero, but the apparent cohesion in gravel is due to the interlocking force generated by the interlocking and embedding of gravel particles under axial load compression, which is fundamentally different from the cohesion of cohesive soil. Furthermore, the internal friction angle of NPBG is also higher than that of pure gravel, although the increase is smaller. As the polyurethane content increases from 2% to 6%, the internal friction angle gradually decreases. The internal friction angle decreases with the increase in polyurethane content, primarily because as the polyurethane content increases, the thickness of the polyurethane covering on the surface of the gravel gradually increases, making the surface smoother and more even. This, to some extent, reduces the interlocking and friction between the gravel particles.

3 Numerical modelling

3.1 Details of the selected case history

To validate the finite element numerical model, this study utilizes an engineering example of a reinforced embankment project as reported by Liu et al. [32]. The cross-sectional diagram of the embankment and soil layers is depicted in Figure 6A. The distribution of soil layers on the site, from top to bottom, includes: 1.5 m of coarse-grained fill soil, 2.3 m of silty clay, 10.2 m of silty clay with silt and sludge, 2 m of loam, and 9 m of sandy silt. The groundwater level is located 1.5 m below the ground surface. The top width of the embankment is 35 m, with a slope ratio (ratio of vertical height to horizontal width) of 1:1.5. The embankment is to be filled to a height of 5.6 m within 55 days, with the graded loading curve shown in Figure 6B. Fly ash is the primary material for embankment filling, and a layer of crushed stone bedding, 0.5 m thick, is placed between the embankment fill and the subgrade soil. In the center of the bedding layer, a geogrid is installed with a strength of 90 kN/m and a maximum allowable strain of 8%. The piles used are cast-in-situ concrete thin-walled pipe piles arranged in a square pattern with a spacing of 3 m. The area replacement ratio is approximately 8.7%. The piles have an outer diameter of 1 m, a wall thickness of 120 mm, and a length of 16 m, with the pile ends placed on the sandy loam layer.

The observation of the pile-supported reinforced embankment utilized a series of instruments including settlement plates, soil pressure cells, and pore pressure gauges. These instruments monitored the settlement of the embankment surface at pile tops and between piles, as well as vertical pressures. Changes in pore water pressures at various depths in the foundation were also recorded. The monitoring began from the start of embankment construction and continued for 180 days.

3.2 Three-dimensional numerical modeling

The study is based on three-dimensional finite element modeling of a pile-supported reinforced embankment test using ABAQUS software, analyzing the load-bearing characteristics of pile-soil interaction during the embankment filling process. Considering the symmetry of the cross-section in this case, half of the embankment

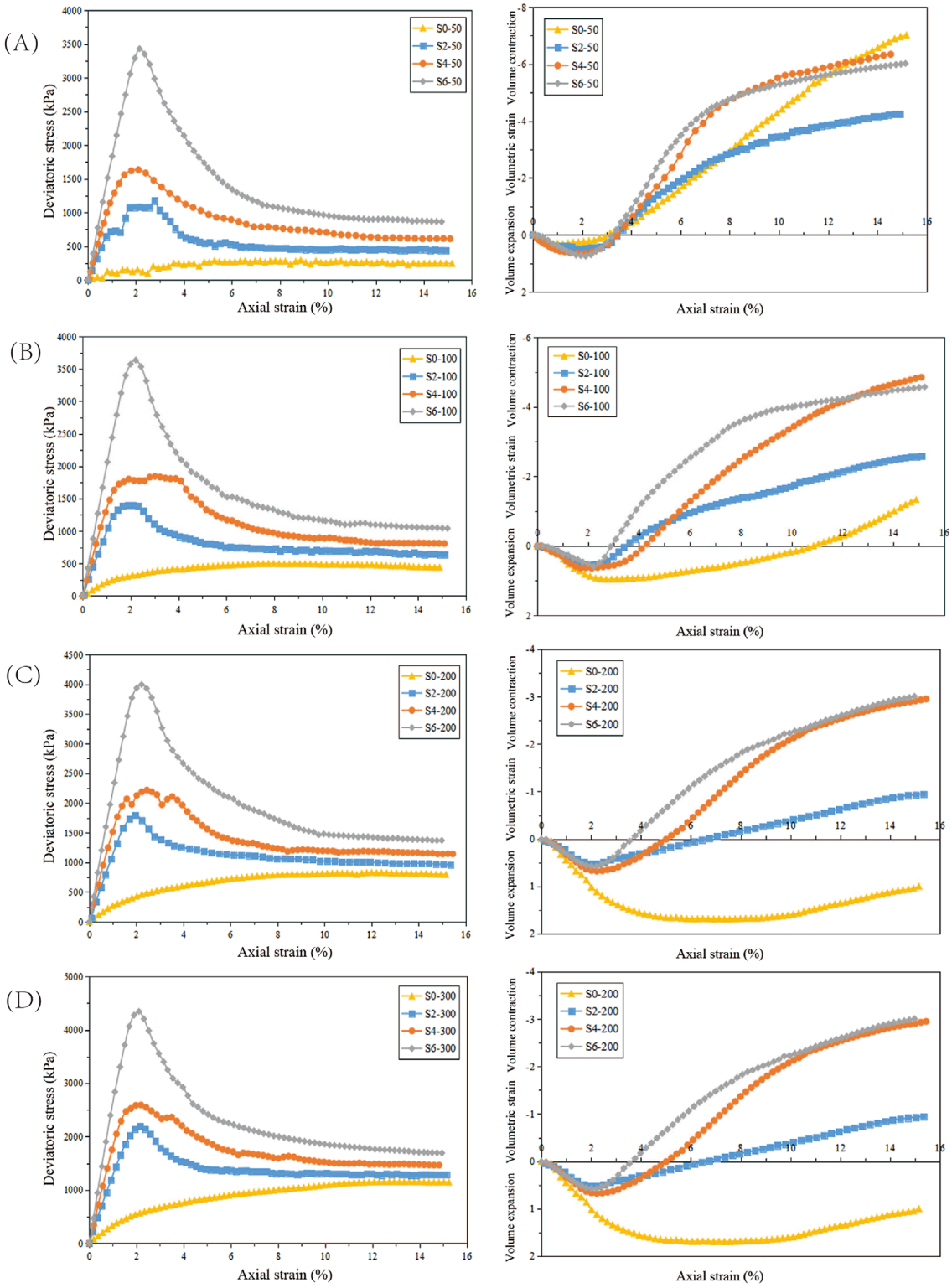

FIGURE 3
(A) The deviatoric stress-axial strain curves and volumetric strain-axial strain curves of samples under the Perimeter pressure 50 kPa. **(B)** The deviatoric stress-axial strain curves and volumetric strain-axial strain curves of samples under the Perimeter pressure 100 kPa. **(C)** The deviatoric stress-axial strain curves and volumetric strain-axial strain curves of samples under the Perimeter pressure 200 kPa. **(D)** The deviatoric stress-axial strain curves and volumetric strain-axial strain curves of samples under the Perimeter pressure 300 kPa.

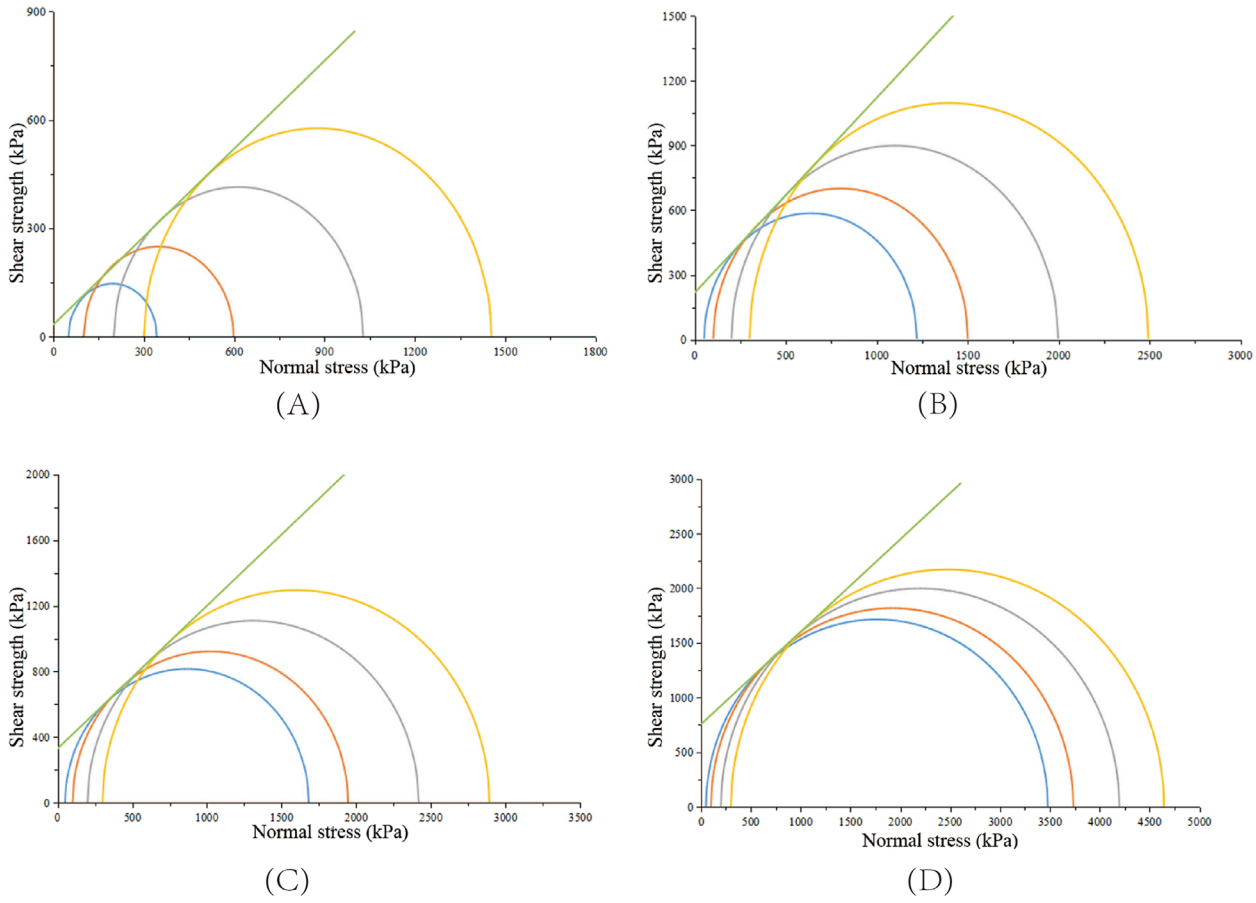

FIGURE 4
(A) The Mohr circles and strength envelopes for gravel of samples at failure. **(B)** The Mohr circles and strength envelopes for polyurethane contents 2% of samples at failure. **(C)** The Mohr circles and strength envelopes for polyurethane contents 4% of samples at failure. **(D)** The Mohr circles and strength envelopes for polyurethane contents 6% of samples at failure.

along the transverse section and one row of piles along the longitudinal direction with half of their surrounding soil were modeled to establish a three-dimensional half-embankment model. The finite element mesh division of the model is shown in Figure 7. The model assumes a foundation depth of 25 m with a rigid impermeable layer assumed below. To mitigate boundary effects, the total width of the analysis area is set to 77.7 m, which is three times the half-width of the embankment base width.

In the FEM model, materials with good drainage capability (e.g., coarse granular fill soil), non-draining materials (e.g., concrete), and materials above the groundwater level that do not require consideration of permeability (embankment fill soil, stone bedding layer) are simulated using 8-node solid elements (C3D8) without considering pore pressure degrees of freedom. The remaining foundation soils are modeled using 8-node coupled solid-fluid elements (C3D8P) to account for stress-pore pressure coupling effects. The geogrid material is simulated using 4-node 3D membrane elements (M3D4). Three types of mesh sizes were used for comparative calculations: a coarse mesh (approximately 25,000 elements), a medium mesh (approximately 50,000 elements), and a fine mesh (approximately 75,000 elements). The relative error of the calculation results was less than 1.4%. Therefore, the medium mesh model was ultimately chosen for the subsequent calculations and analyses in this paper.

3.3 Material models and parameters

In the computational model, the concrete piles are simulated using a linear elastic constitutive model with an elastic modulus of 20 GPa and a Poisson's ratio of 0.2. The interface between piles and soil is modeled using zero-thickness contact elements. The geogrid is also assumed to be a linear elastic material capable of resisting only tension, with a tensile stiffness of 1,180 kN/m and a Poisson's ratio of 0.3. Despite the simplified soil model having limitations, the ideal elastoplastic Mohr-Coulomb model has been successfully applied in many geotechnical studies [33]. The Mohr-Coulomb model can approximate soil behavior similarly to advanced soil models [34]. Therefore, the embankment fill, stone bedding layer, and various layers of subsoil are all simulated using this model. Parameters for each material are summarized in Table 1, with a shear dilation angle set at 0.1°.

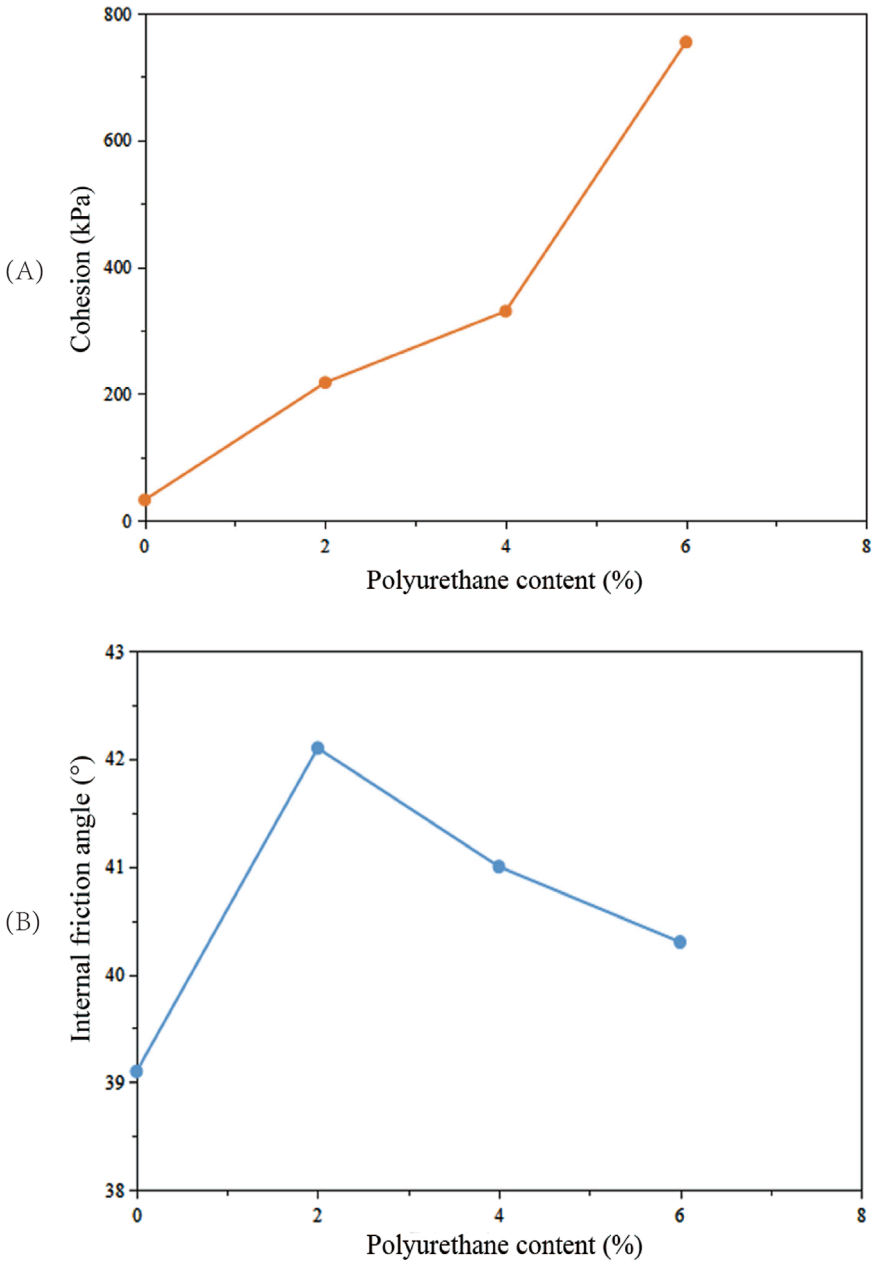

FIGURE 5
(A) The effect of polyurethane content on cohesion. **(B)** The effect of polyurethane content on internal friction.

3.4 Verification of numerical modeling

The comparison between field-measured settlement values and numerical simulation results for the surface settlement variation of composite foundations is shown in Figure 8. Here, S_s represents the settlement of the soil surface between piles, and S_p denotes the settlement at pile tops. From the figure, it can be observed that the computed settlements at pile tops and between piles generally follow the trend of the measured values. The numerical simulation results of this study closely approximate the measured results, with differences in settlement at pile tops and between piles at the end of the observation period (180 days) being 3.4% and 2.6%, respectively. Comparing with Liu's computed results, the differences in pile and soil settlements are 8.3% and 8.9%, respectively, showing relatively close agreement.

The comparison between field-measured soil pressure values and numerical simulation results for the surface of the foundation is shown in Table 2. According to the table, at the end of embankment construction, the computed soil pressure at pile tops in this study is slightly higher than the measured values by 1.2%, and slightly lower than Liu's computed results by 0.3%.

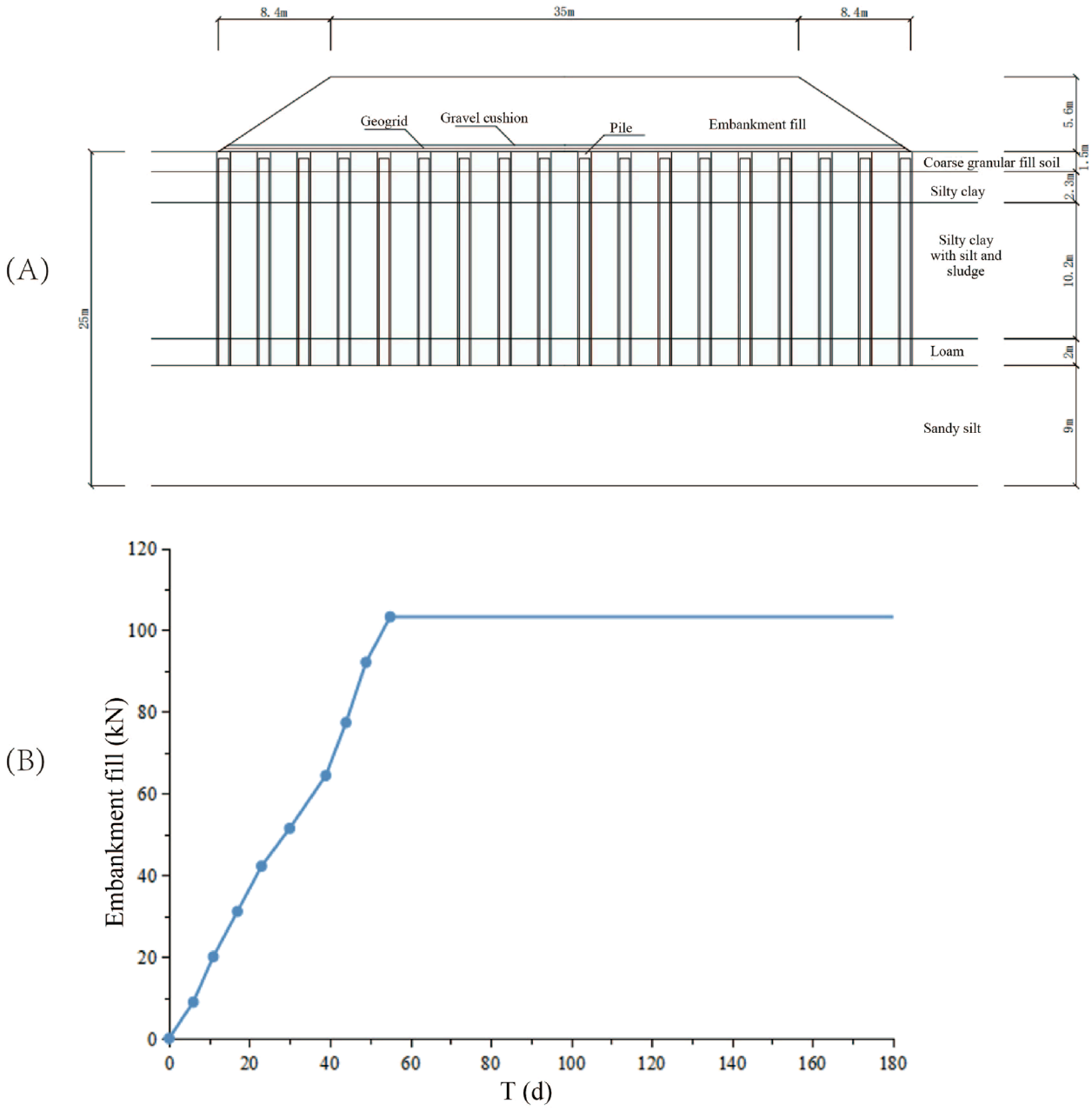

FIGURE 6
(A) The cross-sectional diagram of the embankment. **(B)** The graded loading curve of the embankment.

Meanwhile, at the surface between piles, there is a larger discrepancy between the computed soil pressure values of this study and the measured values, possibly due to some tilting of the soil pressure box between piles during the filling process, resulting in deviations from the actual conditions. Comparing with Liu's computed values shows an error of only 4.0%, indicating relatively close agreement. Therefore, the model calculations in this study are in good agreement with the field measurements, indicating that the numerical model can simulate the actual engineering conditions fairly accurately. The model design is rational, and it exhibits good reliability.

3.5 Comparative modelling procedure

To analyze the working characteristics of NPBG porous piles under the embankment, the aforementioned modeling method was used to establish finite element models for concrete piles, polyurethane gravel piles, cement-mixed piles, and gravel piles. The performance of these four types of piles was compared in terms of ground surface settlement, stress state of piles and soil, and changes in excess pore water pressure in the foundation soil. The study analyzed the role of non-foamed polyurethane gravel piles in foundation reinforcement, highlighting their high bearing capacity

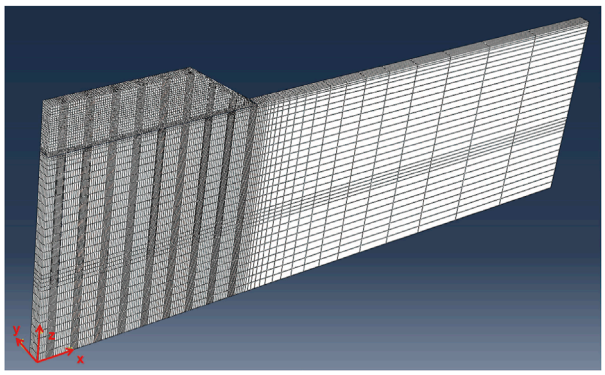

FIGURE 7
The finite element mesh division of the model.

and good drainage properties. For better comparative analysis, the external dimensions and arrangement of the four types of piles were kept the same: the solid pile diameter was 0.65 m, the pile spacing was 1.95 m, and other parameters such as foundation soil and embankment characteristics were consistent with the original numerical model.

The material parameters of the four types of pile bodies are shown in Table 3. The material parameters for the concrete piles are consistent with those mentioned earlier. NPBG with 6% polyurethane content and gravel without polyurethane are selected as the pile body materials for NPBG porous piles and gravel piles, respectively, and these material parameters are determined based on the triaxial test results mentioned above/. The modulus parameters of the NPBG porous pile were determined based on the stress-strain test results of NPBG with 6% polyurethane content under a confining pressure of 100 kPa, specifically using the tangent modulus, and the permeability coefficient of the NPBG porous pile is based on parameters measured in permeability tests [35]. The material parameters for the cement-mixed piles are determined with reference to the literature by Zhu [36]. From the table, it can be observed that compared to concrete piles, the strength and stiffness of the polyurethane gravel piles, cement-mixed piles, and gravel piles are significantly lower. Therefore, it cannot be assumed that these piles remain in an elastic state throughout the loading process, and the Mohr-Coulomb model is adopted for simulation. Additionally, these three types of piles have certain drainage capabilities, so 8-node stress-pore pressure coupled solid elements (C3D8P) are used for simulation. The embankment construction process is the same as described earlier. After the embankment is completed, the foundation soils enter the consolidation phase. Consolidation is considered complete, and the foundation settlement is stabilized when the excess pore water pressure is less than 1 kPa.

4 Results

4.1 Excess pore water pressure

Considering the low permeability coefficient and the weak, easily deformable nature of the silty clay layer, significant excess pore water pressure is expected to accumulate within this soil layer. The excess pore water pressure values are compared at the surface of this layer (at a depth of 4.7 m in the foundation) and at a deeper level (at a depth of 12.1 m in the foundation). Additionally, the changes in excess pore water pressure within the soil layer at the pile tip (at a depth of 20 m in the foundation) are analyzed, a depth beyond the length of the piles.

Figure 9 shows the variation curves of excess pore water pressure at different depths in the subsoil under the middle of the embankment. It can be seen that the excess pore water pressure variations along the depth are different for various piles. From the depth of 4.7 m–12.1 m to 20 m, the peak excess pore water pressure in the concrete pile reinforced foundation gradually increases, while in the cement-mixed pile reinforced foundation, the excess pore water pressure first increases and then decreases.

Concrete piles are impermeable, so the pore water in the soil needs to be discharged from the surface of the foundation soil. At a depth of 4.7 m, the drainage path is short, and the excess pore water pressure dissipates quickly. Correspondingly, at a depth of 12.1 m, the drainage path is longer, and the peak excess pore water pressure increases compared to that at 4.7 m. Additionally, due to the high stiffness of concrete piles, more embankment load is transmitted through the piles to the soil layer at the pile tip, resulting in a higher excess pore water pressure at a depth of 20 m.

In contrast, in the cement-mixed pile reinforced foundation, the soil between the piles bears more of the upper load, generating higher excess pore water pressure at a depth of 12.1 m, while lower excess pore water pressure occurs in the soil layer at the pile tip. Moreover, due to the higher permeability coefficient of the soil at the pile tip, the pore water pressure dissipates relatively quickly, resulting in the maximum excess pore water pressure appearing in the deeper soil between the piles.

The load-bearing behavior of the soil in the NPBG porous pile reinforced foundation is similar to that in the cement-mixed pile reinforced foundation. However, the NPBG porous piles have good drainage capability, allowing pore water to be discharged horizontally through the pile body within the pile length range. As a result, the peak excess pore water pressures at depths of 4.7 m and 12.1 m are both very low. However, at a depth of 20 m, beyond the pile length, the drainage distance increases, and the peak excess pore water pressure slightly increases.

The situation is different for the gravel pile reinforced foundation. In the bearing layer area, the distribution of excess pore water pressure along the depth is similar to that of the NPBG porous pile reinforced foundation. However, unlike the latter, gravel piles are discrete material piles with lower stiffness, leading to a higher load-bearing capacity of the soil between the piles. Therefore, the peak excess pore water pressure in the soil between the piles is significantly higher. Due to the difficulty of transmitting the upper load to the deeper foundation, the excess pore water pressure in the soil layer at a depth of 20 m is significantly reduced compared to that in the soil between the piles.

It can also be observed from the figure that after the construction is completed, the dissipation of excess pore water pressure is a relatively slow process in the cement-mixed pile reinforced foundation and the concrete pile reinforced foundation, whereas in the NPBG porous pile reinforced foundation and the gravel pile

TABLE 1 Soil parameters in FEM numerical model.

Soil layer	Weight density γ (kN/m3)	Elastic modulus E (MPa)	Poisson's ratio ν	Cohesion c' (kPa)	Internal friction angle φ' (°)	Permeability k (m/day)
Embankment fill	18.5	20	0.3	10	30	—
Crushed stone bedding	17.8	20	0.3	10	40	—
Coarse granular fill soil	18.4	7	0.3	15	28	—
Silty clay	19.7	2.5	0.35	28.8	26.5	8.64E-04
Silty clay with silt and sludge	17.3	1.8	0.4	16.1	10	4.32E-04
Loam	20.2	4.4	0.35	20.5	27	4.32E-04
Sandy silt	19.7	70	0.35	26.5	31.1	4.32E-03

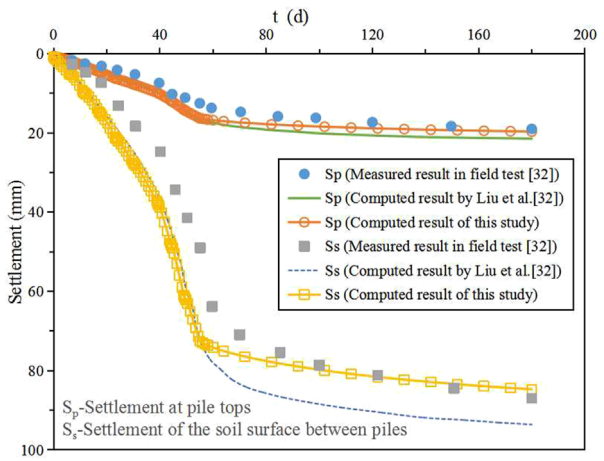

FIGURE 8
The comparison between field-measured settlement values and numerical simulation results for the surface settlement variation of composite foundations.

reinforced foundation, the dissipation occurs more rapidly. This difference is mainly influenced by the drainage capacity of the piles.

Figure 10 shows the variation curves of excess pore water pressure with depth at the toe of the slope. Compared with the excess pore water pressure in the foundation soil at the center of the road, it is not difficult to find that the peak values of excess pore water pressure at various depths at the toe of the slope in both the concrete pile reinforced foundation and the cement-mixed pile reinforced foundation are significantly reduced. This is because the foundation soil at the toe of the slope is subjected to much smaller embankment loads compared to the center of the road. However, in the NPBG porous pile reinforced foundation and the gravel pile reinforced foundation, the excess pore water pressure slightly increases, but the dissipation rate of pore pressure slows down.

The analysis suggests that the foundation soil at the toe of the slope is simultaneously subjected to both vertical and lateral forces, causing the soil to move outward from the embankment and increase the distance between the soil and the piles. This effectively lengthens the drainage path, weakening the effect of the pile's drainage capacity on the soil, making it more difficult for the excess pore water pressure to dissipate. For the NPBG porous pile composite foundation, the excess pore water pressure in the foundation remains at a relatively low level, having little impact on the consolidation time. In contrast, for the gravel pile reinforced foundation, the consolidation time of the foundation soil at the toe of the slope is significantly extended.

The above analysis indicates that the presence of piles with good drainage capacity in the reinforced foundation can effectively promote the dissipation of excess pore water pressure throughout the foundation soil, thereby accelerating the consolidation of the foundation. However, if the piles have low stiffness (such as gravel piles), it can result in the accumulation of larger excess pore water pressures in the foundation, which also slows down the overall consolidation process of the foundation. Only when the piles in the reinforced foundation possess both sufficient stiffness and good drainage capacity can the time required for the reinforced foundation to complete consolidation be most effectively shortened.

According to Rowe's research [37], if an embankment is constructed too quickly on a soft clay foundation, the soil may lose strength due to the accumulation of large excess pore water pressure. Therefore, the embankment construction rate should be controlled within a certain range to avoid insufficient bearing capacity of the foundation soil. For this purpose, a reference indicator, the pore water pressure coefficient B_m, is proposed. It is defined as the ratio of the maximum increment of excess pore water pressure to the increment of vertical total stress. The closer this coefficient is to zero, the better the stability of the foundation during embankment construction. Conversely, the larger the coefficient, the poorer the stability of the foundation.

TABLE 2 The comparison between field-measured soil pressure values and numerical simulation results for the surface of the composite foundation.

Soil pressure	Field-measured values (kPa)	Liu's computed values (kPa)	The calculated results in this paper (kPa)
Soil surface between piles	31.4	58.1	55.8
Pile top	583.6	592.6	590.8

TABLE 3 Pile parameters.

Pile types	Weight density γ(kN/m3)	Elastic modulus E (MPa)	Poisson's ratio ν	Cohesion c' (kPa)	Internal friction angle φ′ (°)	Dilatancy angle ψ(°)	Permeability k (m/day)
Concrete pile	25	20,000	0.2				
NPBG pile	18.9	200	0.3	755	40.3	0.1	3.28
Cement-mixed pile	20	120	0.3	280	25	0.1	4.32E-04
Gravel pile	19.8	15	0.3	1	39	0.1	4.32

In this study, the maximum excess pore water pressure occurs around the time the embankment construction is completed. The increment of vertical total stress is taken as the vertical stress at the surface of the soil between the piles when the construction is finished. The pore water pressure coefficients corresponding to the four types of reinforced foundations are shown in Table 4.

As shown in the table, the pore water pressure coefficients in the concrete pile reinforced foundation and the cement-mixed pile reinforced foundation are at a very high level, especially for the cement-mixed pile reinforced foundation, where the coefficient approaches 1. This indicates that most of the upper load is converted into excess pore water pressure, with a smaller proportion of the load borne by the soil skeleton, which is likely to cause instability in the reinforced foundation. In contrast, the pore water pressure coefficients in the NPBG porous pile reinforced foundation and the gravel pile reinforced foundation are 0.02 and 0.04, respectively, values close to 0. This indicates that the pore pressure can dissipate promptly and that the additional upper load has largely been converted into effective stress within the soil. Thus, if the embankment construction speed is fast, the likelihood of bearing capacity failure is much higher for the concrete pile reinforced foundation and the cement-mixed pile reinforced foundation compared to the NPBG porous pile reinforced foundation and the gravel pile reinforced foundation. From the perspective of the pore water pressure coefficient, a longer construction period should be designed for the former two to ensure the stability of the reinforced foundation. Conversely, even with a continuous embankment construction plan, the pore water pressure coefficient for the latter two can remain very low, making the likelihood of bearing capacity failure quite small. Therefore, for projects requiring continuous embankment construction or with short construction periods, using NPBG porous piles for foundation treatment offers significant advantages over using concrete piles, cement-mixed piles, and gravel piles.

4.2 Settlement

Figures 11A,B show the settlement curves over time for the pile and the soil between piles at the surface of the reinforced foundation. From the figures, it can be seen that during construction, the settlement of both the pile top and the soil surface between piles increases rapidly due to the gradually increasing embankment load. After construction is completed and the embankment load no longer increases, the settlements of the pile top and the soil surface between piles in the NPBG porous pile reinforced foundation and the gravel pile reinforced foundation also almost stop increasing. In the concrete pile reinforced foundation and the cement-mixed pile reinforced foundation, the settlements of the pile top and the soil surface between piles slow down with the consolidation of the foundation soil and eventually stabilize. This indicates that the foundation soils in the NPBG porous pile reinforced foundation and the gravel pile reinforced foundation consolidate quickly, while the concrete pile reinforced foundation and the cement-mixed pile reinforced foundation require a longer consolidation period to achieve settlement stability. Furthermore, regardless of whether it is the settlement at the pile top or the soil surface between piles, the final settlement amounts in ascending order are: concrete pile, NPBG porous pile, cement-mixed pile, and gravel pile. This shows that under the same embankment load, the stiffness of the pile is the main factor determining the final settlement amount of the foundation.

The Figure 11C shows the variation of consolidation degree of the foundation surface with time, providing a more intuitive comparison of the settlement process of reinforced foundations. The consolidation degree is defined as the ratio of settlement at a

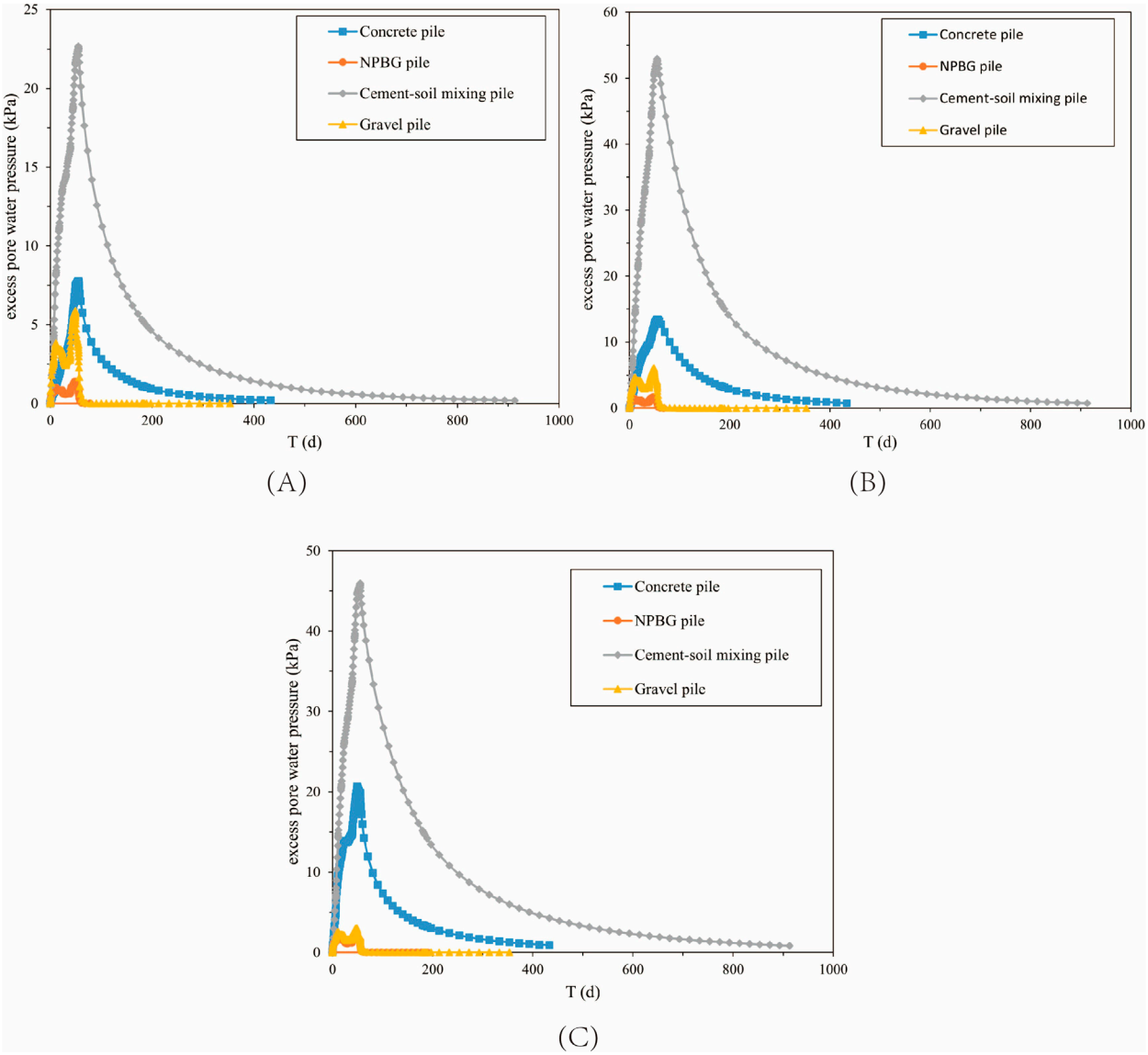

FIGURE 9
(A) The variation curves of excess pore water pressure at 4.7 m in the subsoil under the middle of the embankment. **(B)** The variation curves of excess pore water pressure at 12.1 m in the subsoil under the middle of the embankment. **(C)** The variation curves of excess pore water pressure at 20 m in the subsoil under the middle of the embankment.

certain moment to the final settlement of the foundation surface. The results indicate that due to the lack of drainage capability or weak drainage capability of the concrete pile and cement-mixed pile, these two types of reinforced foundations exhibit lower consolidation degrees at any given moment. In contrast, the NPBG porous pile and gravel pile, which have good drainage capability, show higher consolidation degrees at any given moment. This also demonstrates that the drainage capability of pile bodies in reinforced foundations significantly influences the consolidation speed of the reinforced foundations.

Post-construction settlement refers to the settlement of the embankment from the end of construction until stabilization, which is an important criterion in road embankment design. Excessive post-construction settlement can adversely affect the normal operation of the road. The calculated results of post-construction settlement in this study are shown in Table 5, where the post-construction settlement ratio is defined as the ratio of settlement at the central top of the embankment to the total settlement. Based on the table, it is evident that the embankment supported by NPBG porous piles not only has relatively smaller total settlement at the top of the embankment but also exhibits significantly lower post-construction settlement and post-construction settlement ratio compared to the other three types. While the embankment supported by concrete piles shows the smallest total settlement, its post-construction settlement ratio is relatively high. The embankment supported

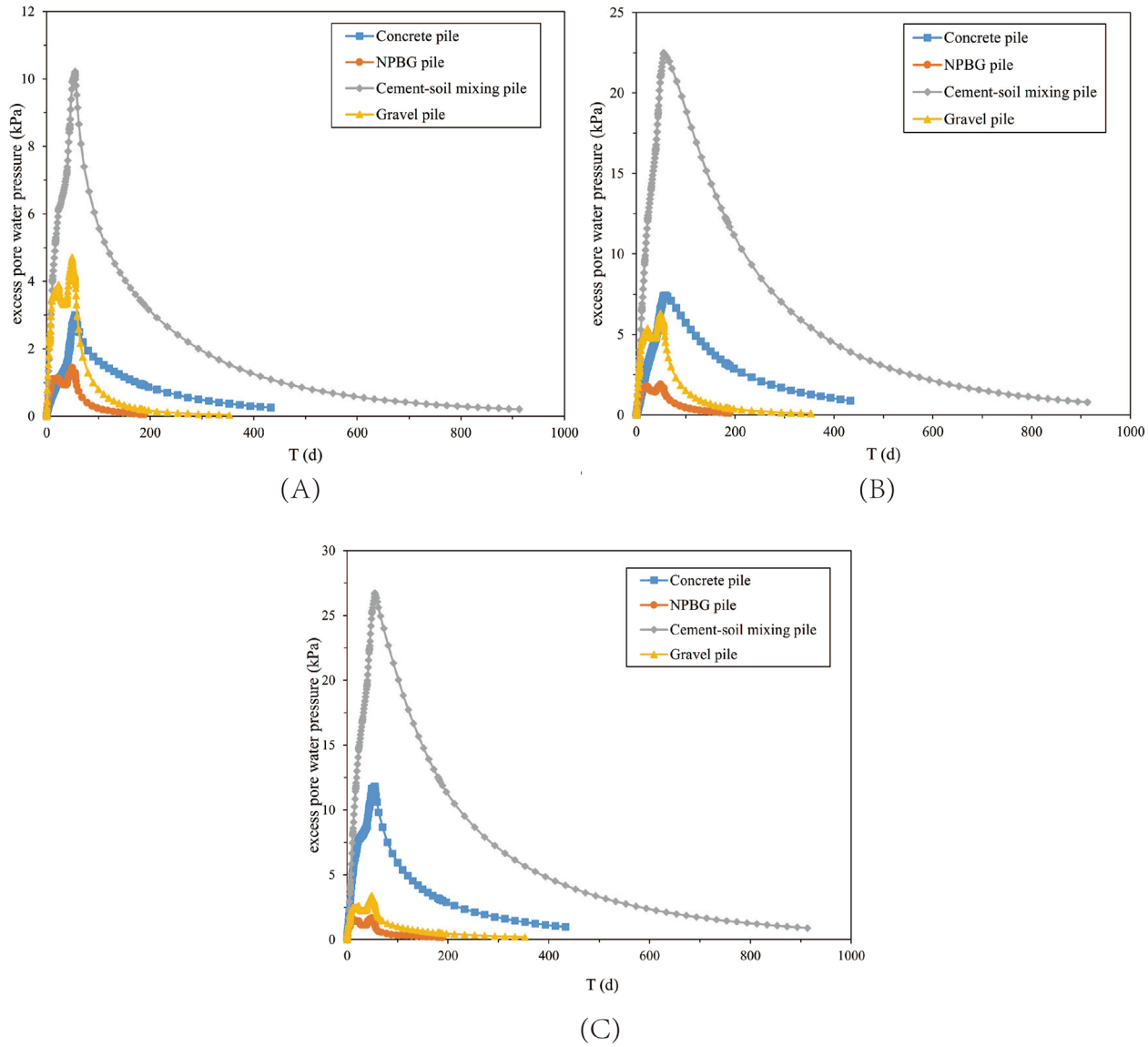

FIGURE 10
(A) Variation curve of excess pore water pressure at 4.7 m depth of foundation soil at the foot of slope. **(B)** Variation curve of excess pore water pressure at 12.1 m depth of foundation soil at the foot of slope. **(C)** Variation curve of excess pore water pressure at 20 m depth of foundation soil at the foot of slope.

TABLE 4 Pore water pressure coefficients.

Pile types	Maximum increment of excess pore water pressure (kPa)	Increment of vertical total stress (kPa)	Pore water pressure coefficient B_m
Concrete pile	13.4	24.4	0.55
NPBG pile	1.0	42.6	0.02
Cement-mixed pile	53.0	57.6	0.92
Gravel pile	4.0	108.3	0.04

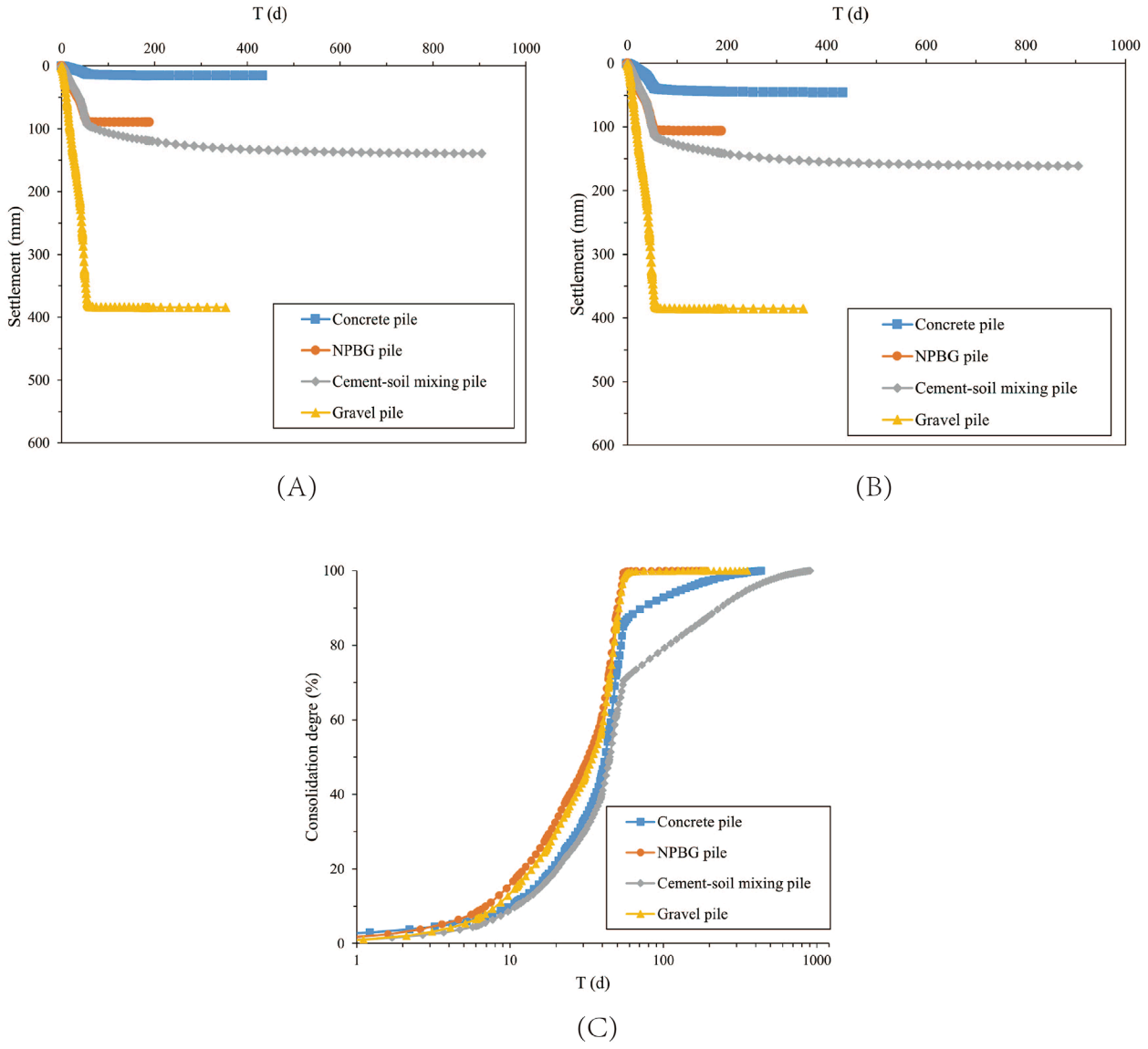

FIGURE 11
(A) The settlement curves over time for the pile. **(B)** The settlement curves over time for the soil between piles at the surface. **(C)** The variation of consolidation degree of the foundation surface with time.

by gravel piles has the largest total settlement, although its post-construction settlement ratio is smaller, the numerical value is larger. The embankment supported by cement-mixed piles has a much larger post-construction settlement and post-construction settlement ratio than the other three types. These results indicate that when the pile has good permeability, more than 95% of the embankment's settlement occurs during construction, which is beneficial for controlling post-construction settlement. Conversely, when the pile has weaker or no permeability, a significant portion of settlement occurs after construction, requiring a longer period for consolidation settlement to stabilize.

Therefore, when piles in reinforced foundations have certain stiffness but poor or weak drainage capabilities (such as concrete piles and cement-mixed piles), it is advantageous for reducing total settlement of the foundation. However, the consolidation rate of the foundation is slower, leading to relatively higher post-construction settlement of the embankment and delaying the time for the embankment to be put into use. On the other hand, when piles in reinforced foundations have good drainage capabilities but lower stiffness (such as gravel piles), the consolidation rate of the foundation is faster, resulting in relatively smaller post-construction settlement of the embankment. However, the total settlement of the foundation increases significantly, often requiring additional fill material to achieve the desired height, thereby increasing construction costs.

However, NPBG porous piles combine certain stiffness with excellent drainage capabilities. Using this type of pile to handle the foundation can effectively control total settlement of the foundation

TABLE 5 The calculated results of post-construction settlement.

Pile types	Total settlement (mm)	Post-construction settlement (mm)	Post-construction settlement ratio (%)
Concrete pile	63.2	5.6	8.9
NPBG pile	122.2	0.9	0.7
Cement-mixed pile	191.9	46.2	24.1
Gravel pile	407.6	8.7	2.1

while significantly reducing post-construction settlement of the embankment. This approach has a notable impact on shortening embankment construction time, reducing costs, and ensuring the normal use of the embankment.

4.3 Pile-soil stress and soil arching effect

Figures 12A,B depict the variation of stress at pile tops and at the surface of the pile-intermediate soil with time, respectively. During the embankment filling process, as the embankment load increases, both the stress at pile tops and at the surface of the pile-intermediate soil gradually increase, with the stress at pile tops increasing much faster than that at the surface of the pile-intermediate soil. After construction is completed, in the concrete pile reinforced foundation and cement-mixed pile reinforced foundation, the stress at pile tops continues to increase but with a smaller rate of increase, while the stress at the surface of the pile-intermediate soil shows a decreasing trend, eventually stabilizing. In contrast, in the NPBG porous pile reinforced foundation and gravel pile reinforced foundation, both the stress at pile tops and at the surface of the pile-intermediate soil remain almost unchanged. From the stable state, it can be concluded that for piles with higher stiffness, the stress at pile tops is higher and the stress at the surface of the pile-intermediate soil is lower. Conversely, for piles with lower stiffness, the stress at pile tops is lower and the stress at the surface of the pile-intermediate soil is higher.

After construction is completed, the decrease in stress at the soil-pile interface can be attributed to the arching effect in soil. Generally, when soil experiences uneven deformation, there exists a shear friction between regions with different deformation extents. This shear friction tends to resist further movement in areas with larger deformations while promoting greater deformation in regions with lesser deformations. Therefore, the differential settlement caused by the varying stiffness between piles and soil modulus is attributed to the arching effect, as illustrated in Figure 12C.

The occurrence of differential settlement causes a downward displacement tendency of the embankment fill above the soil between piles compared to the fill above the pile tops. The embankment fill has a certain shear strength, which results in downward shear stresses acting on the fill above the piles. Through these shear stresses, a portion of the embankment load above the soil between piles transfers to the piles themselves, thereby redistributing the embankment load between piles and the soil between them. This redistribution reduces the load carried by the soil between piles and increases the load carried by the piles, as depicted in Figure 12D. After construction, as the soil continues to consolidate, the settlement of the soil between piles increases, amplifying the differential settlement between piles and soil. This promotes the development of soil arching effects within the embankment, explaining why the stress at the soil-pile interface above the soil between piles gradually decreases after construction in concrete pile reinforced foundations and cement mixed pile reinforced foundations. As discussed earlier, in polyurethane gravel pile reinforced foundations and gravel pile reinforced foundations, the settlement of the foundation soil mainly occurs during the embankment construction period. This indicates that the soil between piles consolidates rapidly during this period, promptly transferring a portion of the load it bears to the pile tops, thus reducing the potential for foundation soil damage.

Figure 13A shows the variation of the pile-to-soil stress ratio in foundations over time. From the information in the figure, it can be seen that due to the soil arching effect, as the height of the embankment increases, the differential settlement between the piles and soil also increases, leading to a gradual increase in the pile-to-soil stress ratio for concrete pile reinforced foundations, NPBG porous pile reinforced foundations, and cement mixed pile reinforced foundations.

However, for gravel pile reinforced foundations, the pile-to-soil stress ratio gradually increases before the embankment height reaches 1.1 m. After the embankment height exceeds 1.1 m, the pile-to-soil stress ratio first decreases rapidly and then gradually stabilizes. This is because the strength of the gravel piles is relatively low, and when the upper load reaches a certain value, the piles are unable to bear additional loads, causing some of the load to transfer to the soil.

After the construction is completed, the pile-to-soil stress ratio continues to increase and eventually stabilizes for concrete pile reinforced foundations and cement mixed pile reinforced foundations. In contrast, the pile-to-soil stress ratio for NPBG porous pile reinforced foundations and gravel pile reinforced foundations remains relatively unchanged.

Figures 13B,C illustrate the variation of additional stress and settlement over time for the soil at the pile end (at a depth of 20 m). It can be observed that at this depth, the NPBG porous pile reinforced foundation experiences the highest additional stress and the most significant settlement. The concrete pile reinforced foundation shows slightly lower values for both, while the gravel pile reinforced foundation has the lowest values. In the cement-mixed pile reinforced foundation, both values are slightly higher than

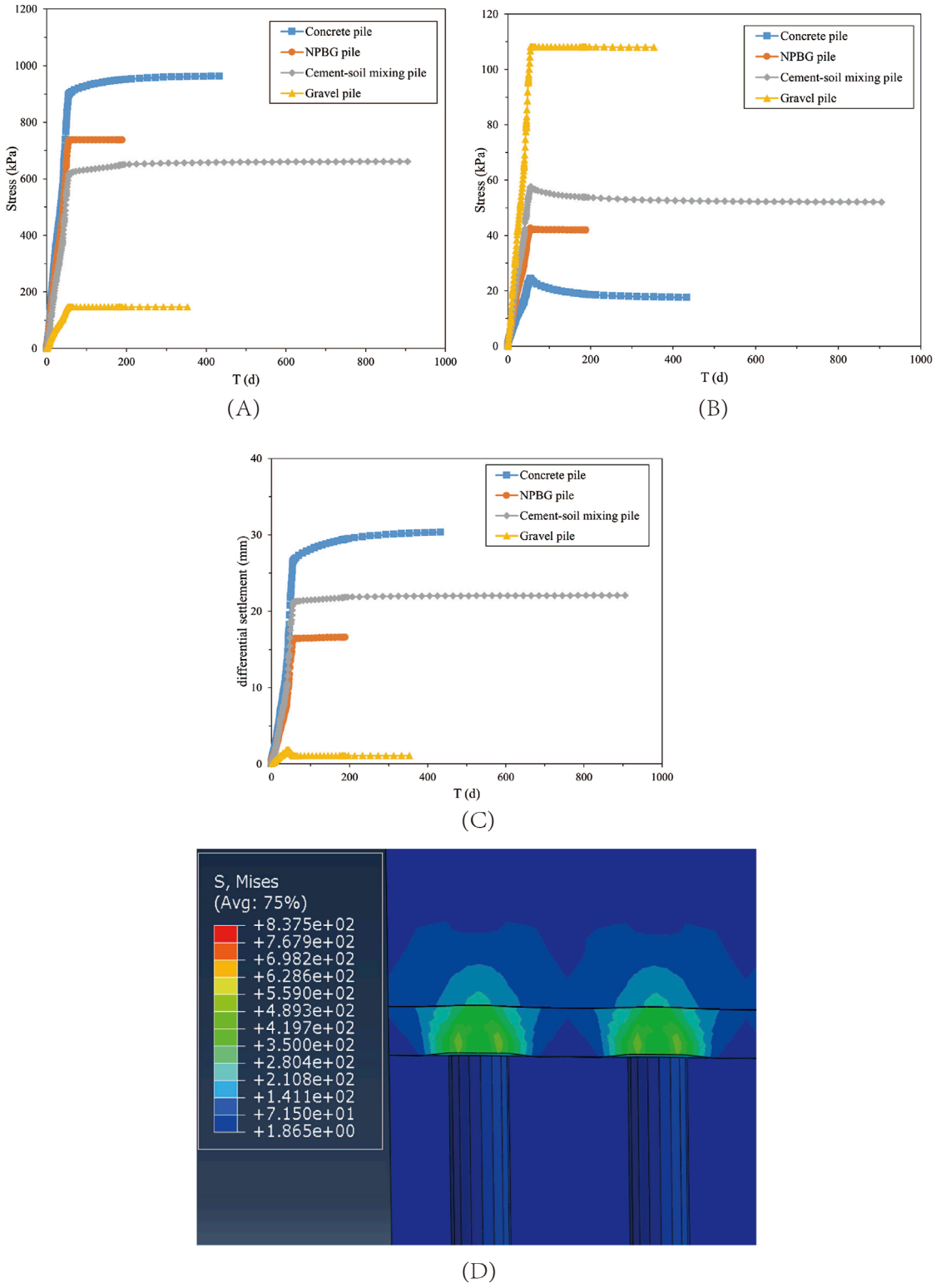

FIGURE 12
(A) The variation of stress at pile tops with time. **(B)** The variation of stress at the surface of the pile-intermediate soil with time. **(C)** The differential settlement caused by the varying stiffness between piles and soil modulus. **(D)** Stress concentration at the top of the pile.

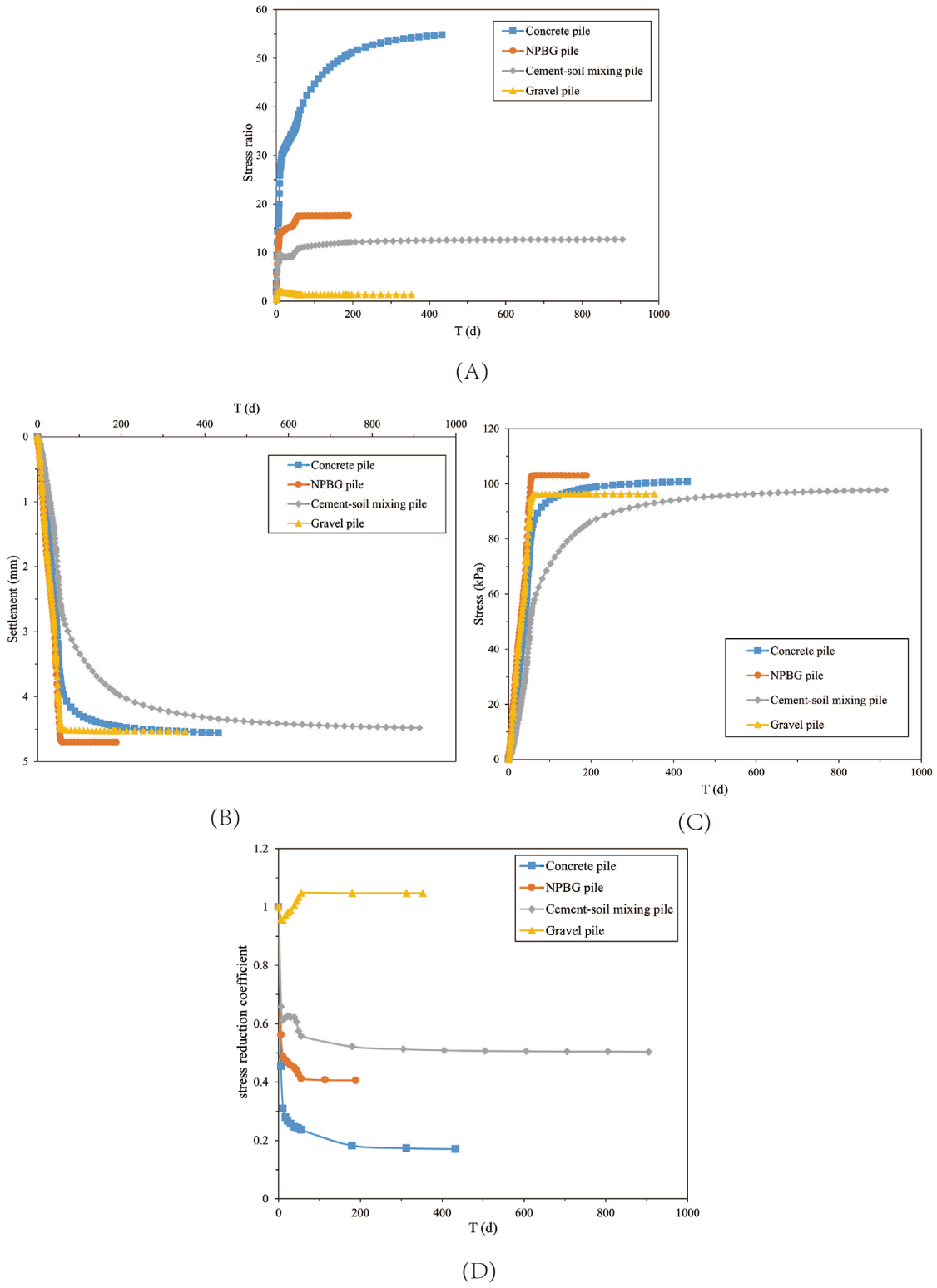

FIGURE 13
(A) The variation of the pile-to-soil stress ratio over time. **(B)** The variation of additional stress over time for the soil at the pile end (at a depth of 20 meters). **(C)** The variation of settlement over time for the soil at the pile end (at a depth of 20 meters). **(D)** The variation curve of the stress reduction coefficient over time.

those in the gravel pile reinforced foundation. This indicates that in the NPBG porous pile reinforced foundation, more embankment load can be transmitted through the piles to the relatively firm soil layer at the pile end, resulting in greater settlement of the pile end soil. Consequently, this reduces the load borne by the soil in the reinforced area, leading to less compression of the soil layers in the reinforced zone and manifesting as smaller differential settlement between the piles and soil on the surface of the foundation.

The degree of development of the soil arching effect is a crucial issue in the design of pile-supported reinforced embankments. This study uses the stress reduction coefficient as an indicator to evaluate the strength of the soil arching effect [32]. The expression for the stress reduction coefficient is shown in Equation 1:

$$S_r = \frac{P_s}{\gamma H_e} \tag{1}$$

where S_r is the stress reduction coefficient; P_s is the stress on the soil between the piles; γ is the unit weight of the embankment fill material; H_e is the height of the embankment fill.

The value of the stress reduction coefficient generally ranges from 0 to 1. When S_r = 0, it indicates that all the embankment load is borne by the piles. Conversely, when S_r = 1, it indicates that no soil arching effect has occurred in the embankment fill, and the pressure on the soil surface between the piles equals the embankment load. Figure 13D compares the variation of the stress reduction coefficient over time for the four types of pile reinforced foundations.

From the figure, it can be seen that the stress reduction coefficient shows varying degrees of decrease at the beginning of the construction, indicating that the soil arching effect starts to act when the differential settlement between the piles and the soil is still small. As mentioned earlier, the NPBG porous pile reinforced foundation exhibits low excess pore pressure values that dissipate quickly post-construction, leading to rapid soil consolidation and stabilization of pile-soil differential settlement. Therefore, compared to the cement-mixed pile reinforced foundation, the stress reduction coefficient for the NPBG porous pile reinforced foundation decreases more rapidly during construction and remains almost unchanged after embankment filling is completed, reaching 0.41.

In contrast, the cement-mixed pile reinforced foundation has a slower soil consolidation rate. As the embankment load increases, the pore water in the soil cannot be discharged promptly, causing a slower transfer of the load from the soil to the piles. The stress reduction coefficient fluctuates around 0.62. After construction is completed, with the gradual dissipation of excess pore pressure, the differential settlement between the piles and the soil continues to increase, leading to a continuous decrease in the coefficient value.

The concrete pile has high stiffness and good load transfer capability, resulting in the reinforced soil bearing less load and developing differential settlement quickly. However, the post-construction consolidation rate of the soil is also slow, resulting in a significant reduction in the stress reduction coefficient both during and after construction. The stress reduction coefficient of the gravel pile reinforced foundation shows a different trend compared to the previous three. It first decreases to 0.95, then increases to 1.05 as the embankment height reaches 1.1 m, and remains stable after construction is completed.

This analysis suggests that the stress reduction coefficient remaining around 1 indicates that the soil arching effect is hardly working, which corresponds to the minimal pile-soil differential settlement (less than 1 mm). When the coefficient exceeds 1, it suggests that due to the uneven settlement of the foundation surface, the settlement is usually greatest in the center and decreases towards the sides. This uneven settlement causes the embankment load not to act vertically on the foundation surface. The load on the adjacent fill material tends to transfer towards the center of the foundation, thereby underestimating the embankment load at that location and resulting in a coefficient value greater than 1.

4.4 Equal settlement plain in embankment

Due to the soil arching effect within the embankment fill, the settlement at the same elevation within the embankment is not uniform. The settlement of the fill within the pile top area is less than that within the pile-interpile soil area, and this phenomenon becomes more pronounced closer to the base of the embankment. As the height of the embankment fill increases, the differential settlement within different positions of the embankment gradually decreases until, at a certain height, there is no differential settlement within the plane. This plane is referred to as the equal settlement plane within the embankment. In engineering design, it is required that the height of the equal settlement plane be lower than the fill height of the embankment; otherwise, the surface will be uneven and unusable.

As shown in Figure 14, from the base of the embankment (z = 25 m) upward, the differential settlement on the same horizontal plane gradually decreases. For the embankment supported by concrete piles, the equal settlement plane is approximately 3.5 m above the base of the embankment. For the embankment supported by NPBG porous piles, the equal settlement plane is about 2 m above the base, while for the embankment supported by cement-mixed piles, it is approximately 5.3 m above the base. The ratios of the equal settlement plane height to the clear spacing between piles are 2.7, 1.5, and 4.1, respectively. In comparison, the use of NPBG porous piles to treat the foundation has a significant effect on reducing the height of the equal settlement plane, which indicates a promising application in projects requiring the construction of low embankments.

4.5 Tension force of geogrid

Figure 15A illustrates the tensile force of the geogrid in the four types of pile reinforced foundations. As shown in the figure, the concrete piles, NPBG porous piles, and cement-mixed piles are bonded material piles with high pile stiffness. Therefore, the maximum geogrid tensile force appears at the edge of the pile, influenced by both the differential settlement between the pile and soil and the deformation of the embankment. For embankments supported by concrete piles and NPBG porous piles, the lateral displacement at the toe of the embankment is relatively small, being 49.0 mm and 47.2 mm, respectively. As a result, the tensile force in the geogrid above the center of the soil between the piles is close to zero. However, the differential settlement between the pile and soil is slightly larger in the concrete pile reinforced foundation, resulting in higher tensile force in the geogrid above the pile. In the cement-mixed pile reinforced foundation, the differential settlement between the pile and soil is significant, and the lateral displacement at the toe of the embankment

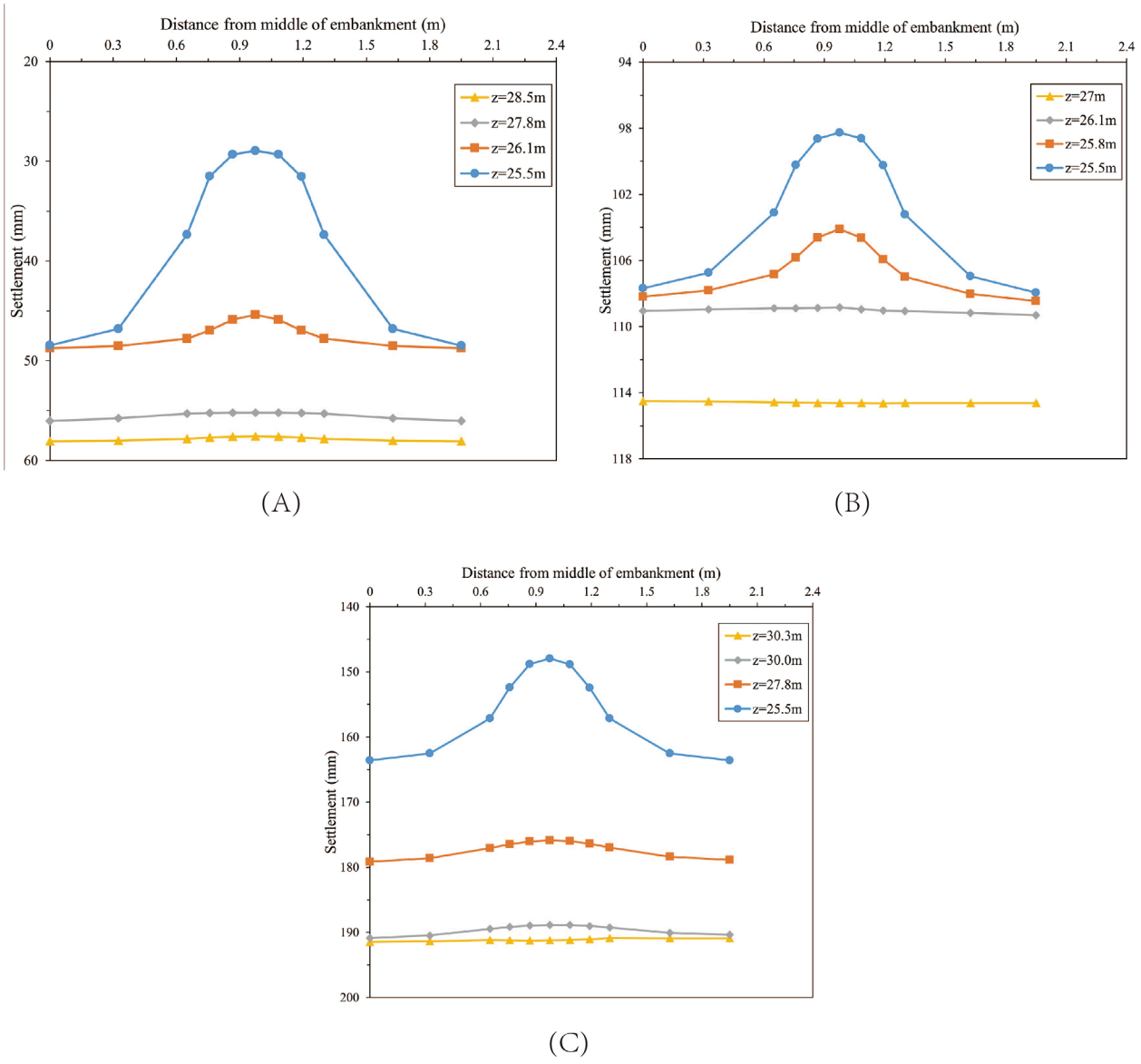

FIGURE 14
(A) Plane settlement at different heights within the embankment supported by concrete piles. **(B)** Plane settlement at different heights within the embankment supported by NPBG porous piles. **(C)** Plane settlement at different heights within the embankment supported by cement-soil mixing piles.

is also large, measuring 79.3 mm. Consequently, the tensile force in the geogrid above the pile is the highest, and there is also a small tensile force in the geogrid above the center of the soil between the piles. The gravel piles are granular material piles and are prone to deformation. Hence, the maximum geogrid tensile force appears above the center of the pile. Although the differential settlement between the pile and soil is small, the lateral displacement at the toe of the embankment is the largest, approximately 98.9 mm. Therefore, the distribution of the geogrid tensile force is relatively uniform, and the tensile force values are at a lower level.

Figures 15B–E shows the vertical stress conditions above and below the geogrid in the four types of pile reinforced foundations. From the figure, it can be seen that the inclusion of the geogrid results in different vertical stress states above and below it. The stress state above the geogrid is mainly caused by the soil arching effect, while the stress below is influenced not only by the soil arching effect but also by the vertical component of the tensile force in the geogrid. This reflects the membrane effect on the vertical stress, which requires some vertical deformation of the reinforcement material to develop. In Figures 15B–E, which represent the three bonded material pile reinforced foundations, the maximum stress above the geogrid occurs near the center of the pile, while below the geogrid, it shifts towards the edge of the pile. This is consistent with the previous description that the maximum tensile force in the geogrid appears at the edge of the pile. Therefore, with the action of the geogrid, the embankment load is more transferred from the soil between the piles to the piles, and it acts relatively uniformly on the top surface of the piles. For the gravel pile reinforced foundation, a similar

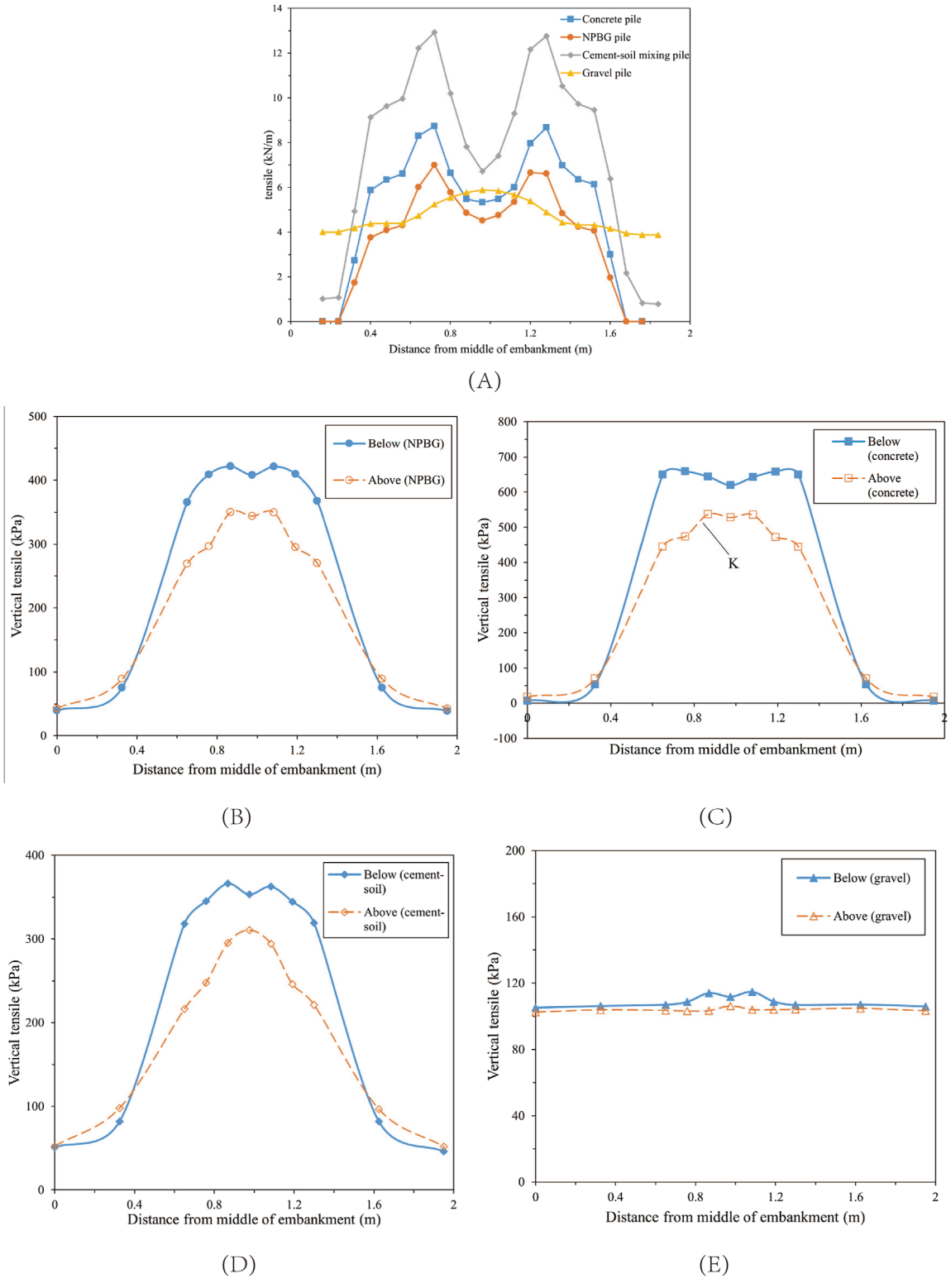

FIGURE 15
(A) Tensile force of the geogrid. **(B)** Vertical stresses above and below geogrids in the embankment supported by concrete piles. **(C)** Vertical stresses above and below geogrids in the embankment supported by NPBG porous piles. **(D)** Vertical stresses above and below geogrids in the embankment supported by cement-soil mixing piles. **(E)** Vertical stresses above and below geogrids in the embankment supported by gravel piles.

pattern is observed, but because the modulus difference between the gravel pile and the foundation soil is not significant, the differential settlement between the pile and soil is small, making the membrane effect less pronounced. Hence, the vertical stress states above and below the geogrid are relatively similar. Comparing the vertical stress at point K on the geogrid (above the pile), the difference in vertical stress between the top and bottom of the geogrid at this point for concrete piles, NPBG porous piles, cement-mixed piles, and gravel piles are 107.2 kPa, 72.0 kPa, 70.9 kPa, and 10.6 kPa, respectively. It can be observed that although the differential settlement between the pile and soil in the NPBG porous pile reinforced foundation is small, resulting in a smaller tensile force in the geogrid, the membrane effect is still significant. Therefore, geogrids with lower tensile strength can be used, reducing construction costs.

5 Conclusion

This paper investigates the application characteristics of NPBG porous new materials in soft soil reinforced pile foundations. Through triaxial compression tests, the stress-strain characteristics and strength parameters of NPBG porous materials were obtained. The effects of polyurethane content, confining pressure, and other factors on the stress-strain characteristics, shear strength, internal friction angle, and cohesion of NPBG were explored. Subsequently, three-dimensional finite element numerical models of four types of pile reinforced foundations—concrete piles, NPBG porous piles, cement-mixed piles, and gravel piles—were established under embankments. The differences among the four pile types were compared in terms of excess pore water pressure, settlement, pile-soil stress, and geogrid stress. The bearing characteristics of the NPBG porous pile were elaborated, with main conclusions as follows:

(1) The triaxial test results show that the stress-strain curve of NPBG porous material exhibits softening characteristics, with the deviator stress reaching its peak at an axial strain of approximately 2.1%. Under shear stress, the material generally shows volumetric expansion. With constant confining pressure, the strength of the sample increases as the polyurethane content increases. The cohesion of NPBG porous material significantly improves with the increase in polyurethane content, although the internal friction angle does not show a noticeable enhancement.

(2) The numerical calculation results indicate that the stiffness and permeability of the piles in foundations significantly affect the dissipation rate of excess pore water pressure in the foundation soil. Compared with concrete piles, cement-mixed piles, and gravel piles, using non-foamed polyurethane gravel piles, which have a combination of certain stiffness and good drainage capability, results in faster consolidation and more efficient dissipation of excess pore water pressure. This improves the stability of the foundation during embankment construction.

(3) The stiffness of the piles determines the total settlement of the foundation, with a higher pile modulus resulting in less foundation settlement. However, the post-construction settlement of the embankment is influenced by both the stiffness and permeability of the piles. Using NPBG porous piles with good permeability allows 95% of the total settlement to occur during the construction period, significantly reducing post-construction settlement. Additionally, when the piles have a higher modulus, the proportion of post-construction settlement is further reduced.

(4) The higher the stiffness of the piles, the greater the pile-soil stress ratio in the foundation, making the soil arching effect more pronounced. However, if the pile strength is insufficient during the loading process, the stress ratio will decrease. The good permeability of NPBG porous piles allows the soil between the piles to share more of the overlying embankment load in a short time, reducing the differential settlement between the piles and the soil. This results in a lower height of the equal settlement plane within the embankment and smaller tensile forces in the geogrid within the cushion layer.

(5) The NPBG porous pile has good stiffness and excellent permeability. Therefore, in the foundation, the NPBG porous pile not only serves as reinforcement but also functions as a drainage channel. This gives the NPBG porous pile reinforced foundation faster consolidation and smaller post-construction settlement, making it highly advantageous for embankment projects involving continuous or rapid filling, as well as low embankment projects.

Data availability statement

The raw data supporting the conclusions of this article will be made available by the authors, without undue reservation.

Author contributions

XH: Data curation, Funding acquisition, Project administration, Resources, Writing–review and editing. ML: Validation, Visualization, Writing–review and editing. HT: Conceptualization, Methodology, Supervision, Writing–original draft.

Funding

The author(s) declare that financial support was received for the research, authorship, and/or publication of this article. The authors acknowledge financial support from the National Science Foundation of China (Nos 52078187 and 51878247) and the Science and Technology Project of Northwest Electric Power Design Institute Co., Ltd. (KC-2022-001).

Conflict of interest

Author XH was employed by Northwest Electric Power Design Institute Co., Ltd. of China Power Engineering Consulting Group.

The remaining authors declare that the research was conducted in the absence of any commercial or financial relationships that could be construed as a potential conflict of interest.

The authors declare that this study received funding from Science and Technology Project of Northwest Electric Power Design Institute Co., Ltd. The funder had the following involvement in the study: data collection and analysis.

Publisher's note

References

1. Magnan J. Methods to reduce the settlement of embankments on soft clay: a review. In: *Proc., vertical-horizontal deformations of foundations and embankments*. ASCE, New York. p. 77–91.

2. Liu KF, Feng WQ, Cai YH, Xu H, Wu PC. Physical model study of pile type effect on long-term settlement of geosynthetic-reinforced pile-supported embankment under traffic loading. *Transportation Geotechnics* (2023) 38:100923. doi:10.1016/j.trgeo.2022.100923

3. Li G, Xu C, Yoo C, Shen P, Wang T, Zhao C. Effect of geogrid reinforcement on the load transfer in pile-supported embankment under cyclic loading. *Geotextiles and Geomembranes* (2023) 51:151–64. doi:10.1016/j.geotexmem.2022.10.004

4. Mangraviti V, Flessati L, di Prisco C. Geosynthetic-reinforced and pile-supported embankments: theoretical discussion of finite difference numerical analyses results. *Eur J Environ Civil Eng* (2023) 27:4337–63. doi:10.1080/19648189.2023.2190400

5. Diao Y, Guo Y, Jia Z, Zheng G, Pan W, Shang D, et al. A simplified method for investigating the bending behavior of piles supporting embankments on soft ground. *Front Struct Civil Eng* (2023) 17:1021–32. doi:10.1007/s11709-023-0952-3

6. Chen T, Zhang G. Centrifuge modeling of pile-supported embankment on soft soil base for highway widening. *Soils and Foundations* (2024) 64:101422. doi:10.1016/j.sandf.2023.101422

7. Han J, Gabr MA. Numerical analysis of geosynthetic-reinforced and pile-supported earth platforms over soft soil. *J Geotechnical Geoenvironmental Eng* (2002) 128:44–53. doi:10.1061/(asce)1090-0241(2002)128:1(44)

8. Van Eekelen SJ, Han J. Geosynthetic-reinforced pile-supported embankments: state of the art. *Geosynthetics Int* (2020) 27:112–41. doi:10.1680/jgein.20.00005

9. Shen P, Xu C, Han J. Geosynthetic-reinforced pile-supported embankment: settlement in different pile conditions. *Geosynthetics Int* (2020) 27:315–31. doi:10.1680/jgein.19.00015

10. Basack S, Indraratna B, Rujikiatkamjorn C, Siahaan F. Modeling the stone column behavior in soft ground with special emphasis on lateral deformation. *J Geotechnical Geoenvironmental Eng* (2017) 143:143. doi:10.1061/(asce)gt.1943-5606.0001652

11. Miranda M, Da Costa A, Castro J, Sagaseta C. Influence of gravel density in the behaviour of soft soils improved with stone columns. *Can Geotechnical J* (2015) 52:1968–80. doi:10.1139/cgj-2014-0487

12. Deb K. A mathematical model to study the soil arching effect in stone column-supported embankment resting on soft foundation soil. *Appl Math Model* (2010) 34:3871–83. doi:10.1016/j.apm.2010.03.026

13. Wu PC, Feng WQ, Yin JH. Numerical study of creep effects on settlements and load transfer mechanisms of soft soil improved by deep cement mixed soil columns under embankment load. *Geotextiles and Geomembranes* (2020) 48:331–48. doi:10.1016/j.geotexmem.2019.12.005

14. Jamsawang P, Phongphinittana E, Voottipruex P, Bergado DT, Jongpradist P. Comparative performances of two- and three-dimensional analyses of soil-cement mixing columns under an embankment load. *Mar Georesources Geotechnology* (2019) 37:852–69. doi:10.1080/1064119X.2018.1504261

15. Wonglert A, Jongpradist P. Impact of reinforced core on performance and failure behavior of stiffened deep cement mixing piles. *Comput Geotechnics* (2015) 69:93–104. doi:10.1016/j.compgeo.2015.05.003

16. Wang A, Zhang D. Lateral response and failure mechanisms of rigid piles in soft soils under geosynthetic-reinforced embankment. *Int J Civil Eng* (2020) 18:169–84. doi:10.1007/s40999-019-00434-1

17. Yu JL, Zhou JJ, Gong XN, Xu RQ, Li JY, Xu SD. Centrifuge study on behavior of rigid pile composite foundation under embankment in soft soil. *Acta Geotechnica* (2021) 16:1909–21. doi:10.1007/s11440-020-01109-1

18. Nunez MA, Briançon L, Dias DC. Analyses of a pile-supported embankment over soft clay: full-scale experiment, analytical and numerical approaches. *Eng Geology* (2013) 153:53–67. doi:10.1016/j.enggeo.2012.11.006

19. Miranda M, Da Costa A. Laboratory analysis of encased stone columns. *Geotextiles and Geomembranes* (2016) 44:269–77. doi:10.1016/j.geotexmem.2015.12.001

20. Wang C, Wang B, Guo P, Zhou S. Experimental analysis on settlement controlling of geogrid-reinforced pile-raft-supported embankments in high-speed railway. *Acta Geotechnica* (2015) 10:231–42. doi:10.1007/s11440-013-0288-6

21. Golait YS, Satyanarayana V, Raju SS. Concept of under reamed cemented stone columns for soft clay ground improvement. *India Geotechnical Conf* (2009) 1:356–60.

22. Ni L, Suleiman MT, Raich A. Pervious concrete pile: an innovation ground improvement alternative. *InGeo-Congress 2013: Stab Perform Slopes Embankments* (2013) III:2051–8.

23. Zhang J, Cui X, Huang D, Jin Q, Lou J, Tang W. Numerical simulation of consolidation settlement of pervious concrete pile composite foundation under road embankment. *Int J Geomechanics* (2016) 16. doi:10.1061/(asce)gm.1943-5622.0000542

24. Huang DW. *Material and performance of pervious concrete pile [dissertation/master's thesis]*. Jinan: SHANDONG UNIVERSITY (2015).

25. Tan H, Yu C, Sun Y. Improved mechanical performance of gravel reinforced by polyurethane polymer adhesive. *J Mater Civil Eng* (2023) 35:35. doi:10.1061/(asce)mt.1943-5533.0004711

26. Liu P, Meng M, Xiao Y, Liu H, Yang G. Dynamic properties of polyurethane foam adhesive-reinforced gravels. *Sci China Technol Sci* (2021) 64:535–47. doi:10.1007/s11431-020-1707-5

27. Foyer G, Oumeraci H. External and internal wave set-up at porous PBA revetments on a sand foundation. *Coastal Eng Proc* (2012) 27. doi:10.9753/icce.v33.structures.27

28. Oumeraci H, Staal T, Pfoertner S, Kudella M, Schimmels S, Verhagen HJ. Hydraulic performance of elastomeric bonded permeable revetments and subsoil response to wave loads. *Coastal Eng Proc* (2011) 22. doi:10.9753/icce.v32.structures.22

29. Wu H, Shu Y, Liu Y. Engineering performance of polyurethane bonded aggregates. *Medziagotyra* (2017) 23:166–72. doi:10.5755/j01.ms.23.2.15798

30. Xiao B, Zhu H, Chen F, Long G, Li Y. A fractal analytical model for Kozeny-Carman constant and permeability of roughened porous media composed of particles and converging-diverging capillaries. *Powder Technology* (2023) 420:118256. doi:10.1016/j.powtec.2023.118256

31. Chen X, Zhang J, Li Z. Shear behaviour of a geogrid-reinforced coarse-grained soil based on large-scale triaxial tests. *Geotextiles and Geomembranes* (2014) 42:312–28. doi:10.1016/j.geotexmem.2014.05.004

32. Liu HL, Ng CW, Fei K. Performance of a geogrid-reinforced and pile-supported highway embankment over soft clay: case study. *J Geotechnical Geoenvironmental Eng* (2007) 133:1483–93. doi:10.1061/(asce)1090-0241(2007)133:12(1483)

33. Huang J, Han J, Oztoprak S. Coupled mechanical and hydraulic modeling of geosynthetic-reinforced column-supported embankments. *J Geotechnical Geoenvironmental Eng* (2009) 135:1011–21. doi:10.1061/(asce)gt.1943-5606.0000026

34. Jiang Y, Han J, Zornberg J, Parsons RL, Leshchinsky D, Tanyu B. Numerical analysis of field geosynthetic-reinforced retaining walls with secondary reinforcement. *Geotechnique* (2019) 69:122–32. doi:10.1680/jgeot.17.P.118

35. Tan HM, Ding BZ, Chen J. Experimental test on water permeability and clogging characteristic of polymer cemented gravel porous material. *J Waterway Harbor* (2021) 42(6):775–82.

36. Zhu WJ. *Study on bearing behavior of composite foundation with nail shaped cement mixing pile in deep soft soil foundation [dissertation/master's thesis]*. Chongqing: Chongqing Jiaotong University (2018).

37. Rowe RK, Soderman KL. Geotextile reinforcement of embankments on peat. *Geotextiles and Geomembranes* (1985) 2:277–98. doi:10.1016/0266-1144(85)90015-9

frontiers | Frontiers in Earth Science

TYPE Original Research
PUBLISHED 12 December 2024
DOI 10.3389/feart.2024.1486831

OPEN ACCESS

EDITED BY
Yifei Sun,
Taiyuan University of Technology, China

REVIEWED BY
Xiangfeng Guo,
South China University of Technology, China
Xiaodong Ni,
Hohai University, China
Li Cheng,
University of Western Australia, Australia
Congyang Yu,
University of Western Australia, Australia, in collaboration with reviewer LC

*CORRESPONDENCE
Leiming Zheng,
zlm0327@hhu.edu.cn

RECEIVED 20 September 2024
ACCEPTED 25 November 2024
PUBLISHED 12 December 2024

CITATION
Zhao Z and Zheng L (2024) Influences of the geogrid-reinforced soil platform on the performance of pile-supported embankment. *Front. Earth Sci.* 12:1486831. doi: 10.3389/feart.2024.1486831

Influences of the geogrid-reinforced soil platform on the performance of pile-supported embankment

Zhihui Zhao[1] and Leiming Zheng[2]*

[1]Suzhou New District Testing Corporation, Suzhou, China, [2]College of Harbour, Coastal and Offshore Engineering, Hohai University, Nanjing, China

Geosynthetic-reinforced pile-supported embankments have seen widespread adoption worldwide in recent years due to their cost-effectiveness and construction efficiency. In this system, the conventional pile cap is replaced by the geogrid-reinforced soil platform (GRSP), which enhances horizontal load transfer to stabilize the embankment. This study investigates the influences of GRSP on the behavior of pile-supported embankments through field testing and numerical computation. The measured results of field testing indicate that a well-compacted GRSP reduces the lateral displacement of the embankment and changes the development of pressures acting on pile and soil. Numerical analysis demonstrates that both soil arching and tensioned membrane effects effectively transfer loads from the soil to the piles, with the tensioned membrane effect typically being more prominent. The characteristics of the GRSP have a significant impact on both effects, with elastic modulus, tensile stiffness, and friction angle being the three most crucial parameters for reducing embankment settlement.

KEYWORDS

pile-supported embankment, reinforced soil platform, geogrid, load transfer, field test, numerical analysis

1 Introduction

A large number of highway embankments are constructed on soft soil, and the geosynthetic-reinforced pile-supported embankments have been increasingly adopted all over the world in the recent years (Liu et al., 2007; 2015; Xing et al., 2014; Esmaeili et al., 2018; Wu et al., 2022; Du et al., 2024) owing to their high cost effectiveness and construction efficiency. In this system, piles (i.e., concrete pile, deep mix column, and stone pile) reinforce the soft soil vertically and are important to impart the loads from the embankment to deeper firm soil (Pham et al., 2004; Stewart et al., 2004; Huang et al., 2009). The geosynthetic-reinforced soil platform (GRSP) enhances horizontal load transfer to stabilize the embankment, and the conventional pile cap is replaced by GRSP, allowing the load between piles to be partially transferred to the pile head (Han J. and Gabr M. A., 2002; Briançon and Simon, 2012; Rowe and Liu, 2015). The GRSP consists of a single or multiple geosynthetic layers (such as geogrid) and soil, with the cohesionless soil being commonly used in practice due to drainage and consolidation of foundation soil under embankment loading. Since the piles bear the majority of the embankment load, the stress on the foundation soil is substantially reduced, leading to a decrease in both vertical and lateral

displacements of the embankment. Consequently, this approach allows for the construction of higher embankments on soft soil. The behavior of geosynthetic-reinforced pile-supported embankment was investigated by model experiments (Blanc et al., 2013; Okyay et al., 2014; Rui et al., 2019; Shen et al., 2020), full-scale field tests (Briançon and Simon, 2012; Zhou et al., 2016; van Eekelen et al., 2020; Terqueux et al., 2023), and numerical simulations (Huang and Han, 2010; Borges and Marques, 2011; Rowe and Liu, 2015; Badakhshan et al., 2020; Ghosh et al., 2021; Khosrojerdi et al., 2018). The performance of load transfer from soft soil to piles has been widely acknowledged as the soil arching effect in embankments (Terzaghi, 1943). Apart from the model proposed by Terzaghi (1936), various methods have been introduced to model the soil arching effect (Xu et al., 2018; Yan et al., 2022; Zhang et al., 2022). However, these models generally ignored the influence of the GRSP and the supporting effect of the foundation soil between piles. In addition to the soil arching effect, the tensioned membrane or stiffened platform effect of the GRSP and the stiffness difference between the pile and soil in foundation are load transfer mechanisms (Han J. and Gabr M. A., 2002). Based on the load transfer mechanisms revealed by field or laboratory testing, many design methods have been proposed, but some of them yield quite different results, especially in the tension force of geosynthetics in the GRSP and the stress reduction ratio (Stewart and Filz, 2005; Chen et al., 2010; Rowe and Liu, 2015).

Several studies have addressed the GRSP, primarily focusing on the role of geosynthetics within the system. Analyses have examined how the stiffness of geosynthetics affects the performance of pile-supported embankments, revealing that geosynthetic properties within the GRSP can significantly influence embankment behavior (e.g., settlement and soil arching) and foundation performance (e.g., load transfer efficiency from the soil to pile and differential settlement between the pile and soil) (Han and Gabr, 2002; Huang and Han, 2010).The distribution of tensile force and strain of geosynthetics was obtained via numerical computation and field testing, revealing that the maximum strain and tensile force occur at the edge of pile heads after the completion of the embankment construction (Han J. and Gabr M. A., 2002; Liu et al., 2007; Huang et al., 2009). Furthermore, the effects of multiple layers of geosynthetic reinforcement on the performance of the pile-supported embankment were discussed via field testing and numerical analysis (Briançon and Simon, 2012; Rowe and Liu, 2015). In addition to the effect of geosynthetics in GRSP, the soil in GRSP also influences the load mechanism. As a result of the penetration of the pile head into the GRSP soil (i.e., gravel), the GRSP soil partially moves to the soil surface surrounding the pile, ensuring that the upper loads act on the foundation soil continuously. The contact surface force between geosynthetics and soil in GRSP is influenced by the tensile force in geosynthetics. In summary, the characteristics of the GRSP have significant influences on the load transfer mechanism of the embankment and foundation.

The objective of this study is to report the influences of GRSP on the performance of the pile-supported embankment, and the effect of the compaction of GRSP materials is studied by comparative field testing. Moreover, based on field testing, parametric studies of GRSP materials, including both soil and geogrid, are conducted via the finite-element analysis. The performances of the pile-supported embankment investigated using the numerical analysis include the stress concentration ratio of pile to soil, soil arching effect, tensioned membrane effect, differential settlement of pile and soil, settlement of the embankment surface, and height of the plane of equal settlement in the embankment and its settlement.

TABLE 1 Soil properties.

Soil layer	Thickness/m	Status	Shear resistance/kPa
Loam	2.0	Plastic	17.4
Muddy clay	8.4	Fluidal plastic	16.5
Sandy loam	3.2	Soft plastic	23.3
Sandy clay	7.4	Plastic	31.4
Silty sand	10.8	Medium dense	39.2

2 Full-scale field test

2.1 Site conditions

The site is located in a suburb of Jiangsu province, China. The soil profile is as follows: there is a 2.0-m-thick loam overlying an 8.4-m-thick deposit of fluidal plastic muddy clay; this deposit overlies soft, plastic, sandy loam of approximately 3.2 m thick. A sandy clay layer of approximately 7.4 m thick lies beneath the soft sandy loam, followed by a deeper layer of medium-density silty sand of approximately 10.8 m thick. The ground water level was 1.2 m high. The soil properties are listed in Table 1.

2.2 Geogrid-reinforced pile-supported highway embankment

The highway embankment is 5.7 m high and 249 m long with a crown width of 35 m. The side slope is 1V: 1.5H. The filling material mainly consists of pulverized fuel ash and clay with the cohesion of 10 kPa, the angle of friction of 26°, and the average unit weight of 18.5 kN/m^3. The cross-sectional view of the testing embankment and the locations of instruments are illustrated in Figure 1.

The embankment is supported by Cast-*in situ* concrete large-diameter pipe (PCC) pile (Liu et al., 2007). The minimum compressive strength of the concrete is 15 MPa. The pipe piles are 16 m in length, the outer diameter of each pile is 1.0 m, and the thickness of the concrete annulus is 120 mm. The pipe piles are arranged in a square pattern at a spacing of approximately three times the pile diameter (3.3 m) from the center to the center of the adjacent piles. The replacement ratio, defined as the percent coverage of the pile annular area over the total foundation area, is 3.1%. A 0.5-m-thick gravel layer is placed on the top of piles, in which two layers of a biaxial polypropylene geogrid are sandwiched. One layer of the geogrid is placed in the middle of the gravel layer, and the other is placed on the top of the gravel layer. The gravel and geogrid form the composite-reinforced bearing

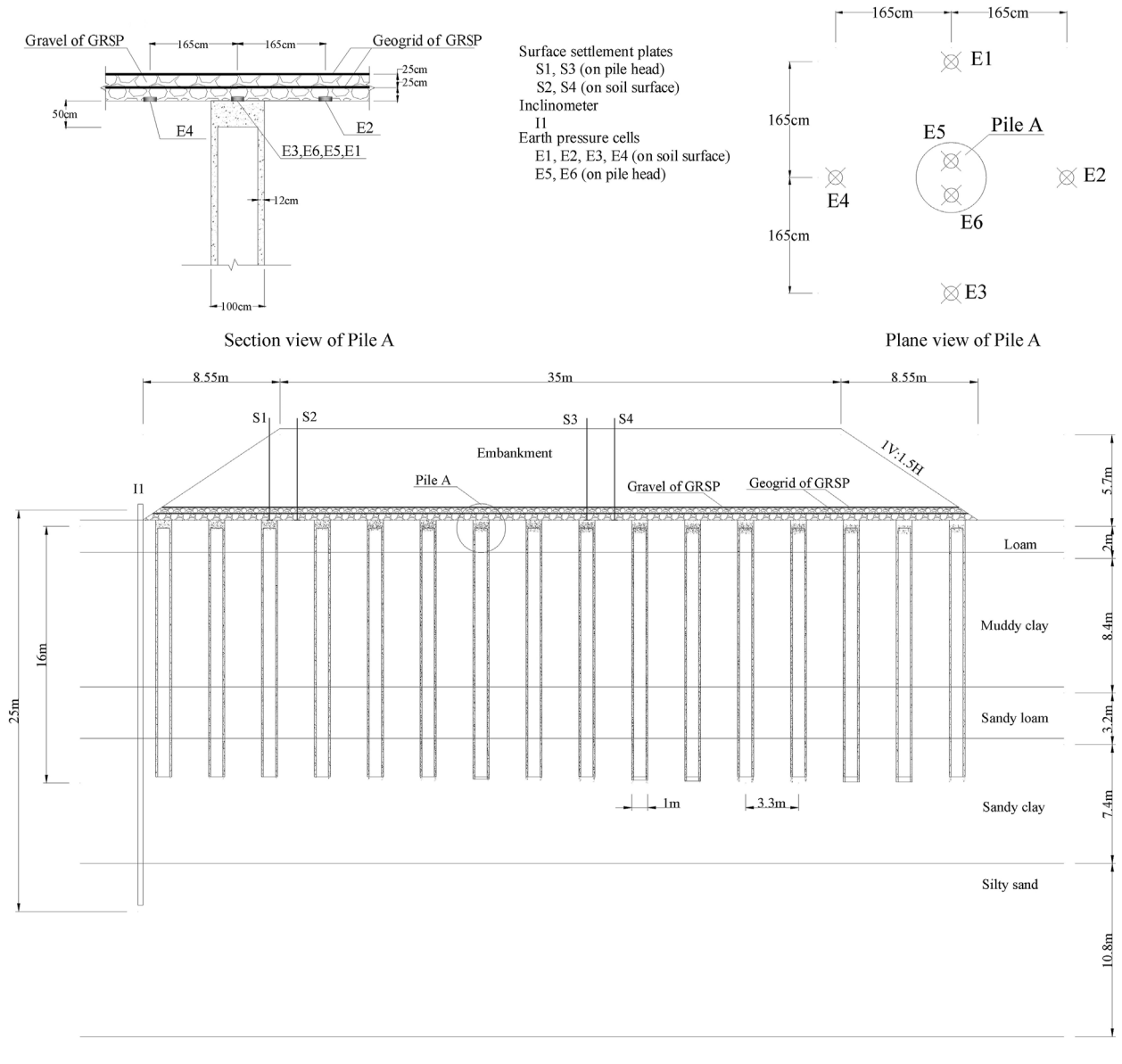

FIGURE 1
Cross-section of the instrumented embankment.

layer between the embankment and pile-reinforced foundation, and the composite-reinforced bearing layer is named GRSP, which is shown in Figure 1. The tensile strength in the longitudinal and latitudinal directions of the geogrid is 90 kN/m, and the natural dry density and the maximum dry density of platform gravel are 1.43 kN/m^3 and 1.87 kN/m^3, respectively. The details of the geogrid-reinforced platform construction are as follows:

First,, a 0.25-m layer of gravel is placed on top of the piles for platform construction, followed by compaction. Next, the first layer of the geogrid is installed. A second 0.25-m layer of gravel is then placed using two different methods for placement: i) spreading and compacting the gravel from the platform center toward both sides using a 4-ton vibratory compactor to achieve a compaction degree of over 90% and ii) placing the gravel from one side to the other without compaction. Finally, the second geogrid layer is installed atop the gravel. These two construction methods for the geogrid-reinforced platform lead to different gravel densities and interaction forces between the geogrid and gravel before embankment filling. The first method (with compaction) produces a higher gravel strength and greater contact force between the geogrid and gravel than the second method (without compaction). For both construction methods, the geogrid was wrapped and anchored back into the platform or embankment over 5 m long at the edges of the embankment.

In order to monitor the performance of the embankment during construction, various instruments were installed *in situ* (Figure 1). The installed instruments are detailed as follows: i) earth pressure cells were used to measure the vertical loads shared by piles and the surrounding soil. Cells measuring load directly on the pile were installed at the pile heads, with a measuring range of 0–1.0 MPa. Additional cells measuring the load carried by the soils were fixed on the surface of

the surrounding soil beneath the GRSP (Figure 1) and measured using portable readout equipment. ii) Four settlement plates were installed at the pile head level, both near the shoulder of the embankment and in the center. One was on the top of the pile, and the other was in the surrounding soil in the middle of the pile spacing. The vertical settlements were monitored using digital level gauges. iii) A vertical inclinometer, 25 m in length, was installed at the embankment toe. All the instruments were installed after the completion of pile construction but before building GRSP and embankment. The field monitoring started with the construction of GRSP and lasted approximately 5 months after the completion of the embankment.

3 Numerical model calibration and parametric study

In order to investigate the influences of GRSP parameters on the performance of the pile-supported embankment, a 2D axisymmetric model was used to simulate the single pile and the surrounding soil with the finite element software PLAXIS. The constitutive models, simulation of construction, and modeling procedures are described below.

The embankment fill, gravel of GRSP, and foundation soils are modeled as linearly elastic, perfectly plastic materials obeying the Mohr–Coulomb failure criteria. The Mohr–Coulomb model requires five parameters: effective cohesion, inner friction angle, dilatancy angle, effective Young's modulus, and Poisson's ratio, as outlined in Table 2. These parameters were derived from the geotechnical investigation report for Yancheng, Jiangsu Province, with the dilatancy angle assumed to be 0°. The pile is modeled as an isotropic linear elastic material with a Young's modulus of 20 GPa and a Poisson's ratio of 0.2. The geogrid in GRSP is modeled as a geogrid element incorporated into the software, which can sustain axial tensile force only, and the tensile stiffness of geogrid is 1,125 kN/m. Furthermore, the interface yield stress is also determined by the Mohr–Coulomb failure criteria, and a reduction factor of 0.7 is applied to the pile–soil contact face and geogrid–gravel contact face, based on the shear strength of GRSP gravel and foundation soil.

The modeling procedure consists of two main steps: to construct initial soil stress field and to model six-staged embankment construction. The staged embankment construction includes six filling steps to the top of the embankment in simulation.

The parametric study on the characteristics of the GRSP was carried out, and the baseline case is the field testing mentioned above. The values of all influencing factors are listed in Table 3. In addition, one parameter was deviated from the baseline case at one time to explore the influences of the specific factor. The variation ranges of all the factors cover the typical range in practice.

TABLE 2 Parameters for FEM analysis.

Material	γ (kN/m^3)	c' (kPa)	φ' (deg)	E(MPa)	ν
Embankment	18.5	10	26	20	0.3
Loam	19.1	20.5	27	35	0.3
Muddy clay	17.9	16.1	10	8	0.3
Sandy loam	1.84	11.9	20	25	0.3
Sandy clay	1.92	28.8	26.5	50	0.3
Silty sand	1.90	26.5	31.1	80	0.3
Gravel	1.78	3	30	30	0.3

Note: γ is the unit weight of soil; c' is the effective cohesion of soil; φ' is the effective friction angle; E is the Young's elastic modulus of soil; ν is the Poisson's ratio.

4 Measured and computed results

4.1 Performance of the geogrid-reinforced soil platform pile-supported embankment

The settlements of the pile and soil are illustrated in Figure 2A. Settlement plates measured the settlements. With the increase in the embankment height, the settlements of both the pile and soil increase, with the similar settlement trends. At the beginning of the embankment filling, the settlements of the pile and soil are quite small, and the settlement rate increases slowly, especially for the pile settlement. As the embankment reaches 2.5–3.0 m high, the settlement rate increases obviously, and the settlement rate of soil is larger than that of piles. The filling height of each step has a significant effect on the settlement rate (i.e., embankment height from 3.7 m to 5.7 m). Following the completion of embankment construction, settlement due to the gradual dissipation of excess pore water pressure accumulated during construction that continued for several months.

Figures 2B, C show the differential settlement and stress ratio of the pile and soil, respectively. The differential settlement obtained by subtracting the pile settlement from the foundation soil surface settlement reflects the deformation of GRSP. The stress ratio of pile to soil, defined as vertical stress acting on the pile head to that on the soil surface, was measured by earth pressure cells. The stress ratio reflects the load redistribution between the pile and soil due to deformation of the GRSP. At the beginning of embankment construction ($H < 1$ m), the settlement of the surrounding soil is small under the low embankment height. Consequently, the vertical stresses of the pile head and soil surface are almost identical, and the vertical stress concentration at the pile head is not obvious. When the embankment is higher than 1 m, soil settlement increases and capacity develops. In terms of the distinct difference of moduli of pile concrete and soil, the settlement of the pile is smaller, resulting in the pile–soil differential settlement. During this period, the effect of the GRSP is induced. The geogrid in the GRSP works as tensile nets between piles, transferring loads from soils to the piles through the tensile force in the geogrid and the friction force between the geogrid and platform gravel. With the embankment up to approximately 3.7 m high, the vertical stress on the soil surface increases slightly, whereas the pile–soil differential settlement and the vertical stress on the pile head increase significantly. During the following construction, the vertical stress on the soil surface and the pile–soil differential settlement is almost unchangeable, whereas the vertical stress on the pile head still increases remarkably. The vertical stress on the pile head became stable after the completion of

TABLE 3 Values of influencing factors of GRSP used.

Item	Parameter	Range of value
Gravel in GRSP	Elastic modulus (MPa)	15, 20, 25, 30*, 50, and 100
	Thickness (cm)	10, 20, 30, 40, and 50*
	Inner friction angle (deg)	10, 15, 20, 25, 30*, 35, and 40
Geogrid in GRSP	Tensile stiffness (kN/m)	600, 900, 1,125*, and 2.250
	Layers and placement	1 (middle), 2 (middle and upper)*, 2 (middle and lower), and 3 (middle, upper and lower)

*values used in the baseline case.

embankment construction, and the stable stress ratio of the pile and soil is 16.5, with the final pile–soil differential settlement of 114 mm.

According to the whole response process of the pile and soil in the construction of the embankment, including settlement and vertical stress, the GRSP plays an important role among the pile, foundation soil, and embankment filling. When the embankment height is less than 1 m, stresses on the pile and soil increase subtly, yet the pile–soil differential settlement is noticeable, which mainly results from the settlement of soil, and the existence of GRSP gravel keeps the surrounding soil carrying the load in the surface subsidence stage. When the embankment height reaches 3.7 m and the tensile force in the geogrid is stimulated gradually due to the increasing pile–soil differential settlement, the stiffness of the geogrid in GRSP limits the load applied on the soil surface and transfers the corresponding load to the pile head, which was reflected from the slight increase in soil stress and the prominent increase in pile stress. When the embankment was built from 3.7 m to 5.7 m, the pile and soil settle as an entirety and pile–soil differential settlement is nearly identical, revealing the stability of the interaction of pile and soil. The additional load at this stage is almost completely carried by pile-supported GRSP, as indicated by the slight increase in soil stress and prominent increase in pile stress, and the continuing soil settlement is mainly caused by the settlement of the pile. The comparison results of the pile–soil differential settlement and the vertical stresses on the pile head and soil surface are illustrated in Figures 2B, C, and the computed results are in a good agreement with the measured values.

Figure 3A displays the development processes of the stress ratio of pile to soil with different GRSP construction methods. The GRSP construction method has a significant influence on the developing mode of the stress ratio of the pile to soil and small influence on the final value of the stress ratio of the pile to soil, which is 17.0 and 16.5, respectively. The stress ratio of the pile to soil with the first type of the GRSP construction method is always larger than that of the second method, and the difference in the stress ratio of pile to soil between the two methods decreases in the whole construction process. With well-compacted GRSP (Method 1), the geogrid tensile force increases distinctly at the early stage and increases slowly at the later stage of embankment construction, owing to the plasticity of the geogrid under large tensile forces. In this study, the main method used for compacting the soil platform on the site is vibratory compaction, with engineering requirements stipulating that the compaction degree must exceed 90%. In contrast, the geogrid tensile force nearly linearly increases for the un-compacted GRSP case (Method 2) during construction.

Figure 3B shows the influences of the GRSP construction method on the horizontal displacement on the foundation surface at the embankment toe. It can be seen that during construction, the horizontal displacement is generally smaller for the well-compacted GRSP compared to the un-compacted GRSP. With the well-compacted GRSP, the final ground surface lateral displacements at the embankment toe are smaller, and the values of lateral displacement are 17.5 mm and 22.5 mm for the embankment with the compacted and un-compacted GRSP, respectively. The larger compaction of GRSP soil benefits both the reduction of embankment horizontal displacement and stability of embankment.

4.2 Load transfer mechanism of geogrid-reinforced compacted

The interactions among piles, foundation soil, embankment fill, and GRSP are schematically explained in Figure 4. Owing to the large stiffness difference between piles and foundation soil, the embankment fill between piles has a tendency to move downward under the self-weight of fill. The movement is partially constrained by the shear resistance (τ) from the fill overlying the piles. The shear resistance transfers the stresses in the embankment, which results in the reduction of the pressure ($\sigma_{a,s}$) acting on the surface of the GRSP between piles and the increase in the pressure ($\sigma_{a,p}$) acting on the surface of GRSP overlying piles. This load transfer mechanism is titled the "soil arching effect" (Terzaghi, 1943). The inner differential settlement in the embankment induced by the differential settlement between the pile and soil varies at different levels of embankment height. To a certain height (h_s), the inner differential settlement is absent due to the shear resistance (τ) from the fill overlying the piles, and a plane of equal settlement (PES) exists (Terzaghi, 1936). In addition to the effect of geosynthetics in GRSP, the soil in GRSP has influences on the load mechanism as well. As a result of the penetration of the pile head into the GRSP soil (i.e., gravel), the GRSP soil partially transfers to the surrounding soil of pile, ensuring that upper loads act on the foundation soil, and the contact surface force between geosynthetics and soil in GRSP is influenced, which affects the tensile force in geosynthetics. In summary, the characteristics of GRSP have significant influences on the load transfer mechanism, including stress concentration on the pile head, soil arching effect of the embankment, tensioned membrane of

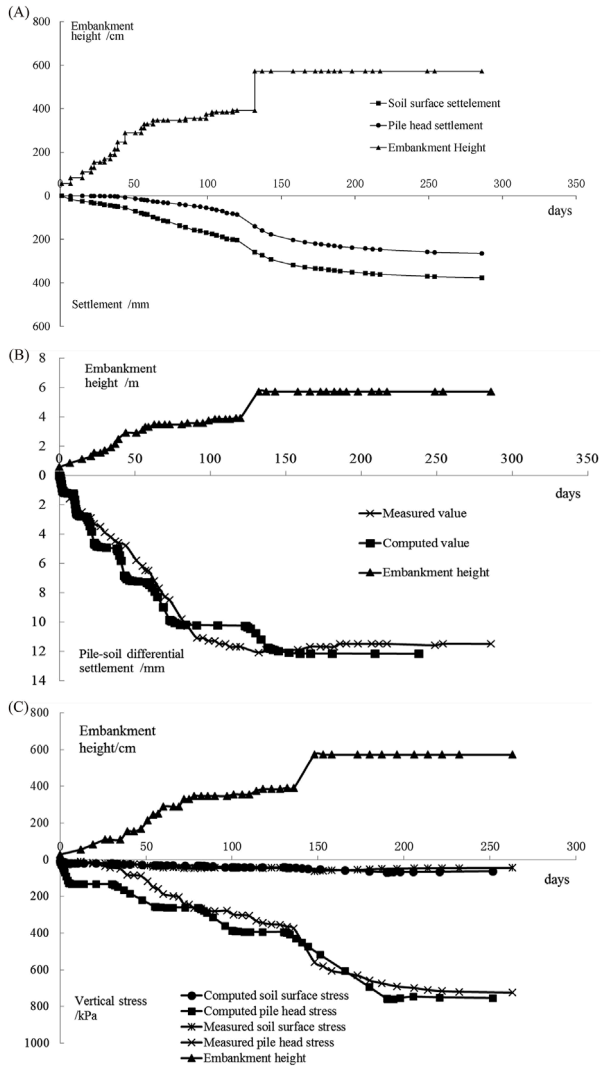

FIGURE 2
(A) Measured settlement of the pile head and soil surface. **(B)** Measured and computed differential settlement of the pile head and soil surface. **(C)** Measured and computed pressure acted on the pile head and soil surface.

geosynthetics, and differential settlement between piles and soil. The effects of GRSP modulus, thickness, shear resistance, and geosynthetic stiffness, layers, and placement will be investigated.

Based on the load transfer mechanism, several coefficients are introduced to discuss the effects of GRSP on the soil arching effect of the embankment, tensioned membrane effect of geosynthetics, and stress concentration of pile, including i) the stress concentration ratio of the pile head to the soil surface (n), which reflects the final load-sharing proportion between the pile and soil due to the soil arching, tensioned membrane effect, and penetration resistance of GRSP; ii) the degree of the soil arching effect (ρ_a), which reflects the stress reduction at the bottom of the embankment fill between piles due to soil arching; iii) the degree of composite effects of soil arching and tensioned membrane ($\rho_{a,m}$), which reflects the stress reduction at the foundation soil surface due to both soil arching and tensioned membrane effects; iv) the degree of the tensioned membrane (ρ_m), which reflects the stress reduction at the foundation soil surface due to the tensioned membrane effect.

The stress concentration ratio of the pile head to the soil surface is defined as Equation 1

$$n = \frac{\sigma_{am,p}}{\sigma_{am,s}}, \tag{1}$$

where $\sigma_{am,p}$ is the applied pressure on the pile head and $\sigma_{am,s}$ is the applied pressure on the soil surface between piles.

The degree of the soil arching effect is given by Equation 2 (as proposed in (McNulty, 1965))

$$\rho_a = \frac{\sigma_{a,s}}{\gamma_f H_f + q_0}, \tag{2}$$

where ρ_a is the soil arching ratio; $\rho_a = 0$ represents the complete soil arching effect, while $\rho_a = 1$ represents no soil arching; $\sigma_{a,s}$ is the applied pressure on the top of the trapdoor in Terzaghi or McNulty's studies (the GRSP surface between piles in this study); γ_f is the unit weight of the embankment fill; H_f is the height of the embankment; and q_0 is the surcharge on the embankment. Furthermore, the degree of load transfer from soil to pile through the soil arching effect can be quantified with $(1\text{-}\rho_a)$.

The degree of composite effects of soil arching and tensioned membrane is given by Equation 3

$$\rho_{a,m} = \frac{\sigma_{am,s}}{\gamma_f H_f + \gamma_c H_c + q_0}, \tag{3}$$

where $\rho_{a,m}$ is the composite effect ratio of soil arching and tensioned membrane; $\rho_{a,m} = 0$ represents the load carried by piles completely, while $\rho_{a,m} = 1$ represents no soil arching and tensioned membrane effects; γ_c is the unit weight of GRSP soil; H_c is the thickness of GRSP. Furthermore, the degree of load transfer from soil to pile through the soil arching and tensioned membrane effects can be quantified with $(1\text{-}\rho_{a,m})$.

The degree of tensioned membrane is defined as Equation 4

$$\rho_m = \rho_a - \rho_{a,m}, \tag{4}$$

where ρ_m is the tensioned membrane ratio, which can quantify the degree of load transfer from the soil to pile through the tension membrane effect and $\rho_m = 1$ represents the complete tensioned membrane effect, while $\rho_a = 0$ represents no tensioned membrane effect.

4.3 Influences of the GRSP modulus on stresses and settlements of pile and soil

4.3.1 Influences of the GRSP modulus on stresses

The degree of the stress concentration from soil to pile is typically evaluated with the stress concentration ratio of the pile head to soil surface (n). The higher the n, the additional loads are transferred to the pile from soil. As shown in Figure 5A, n increases with the increase in the elastic modulus of the GRSP material. As the elastic modulus increases from 15 MPa to 100 MPa, n increases from 10.1 to 18.6. As the elastic modulus of the GRSP increases, its deformation resistance improves, allowing more load

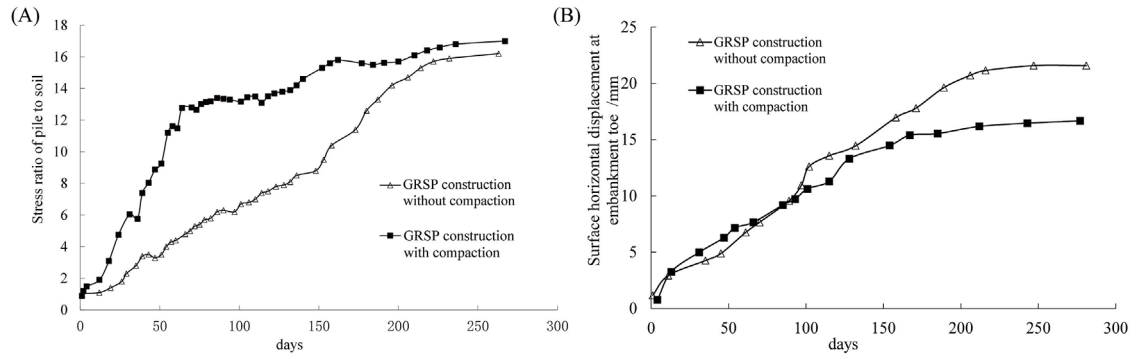

FIGURE 3
(A) Measured stress concentration of the pile and soil with different GRSPs. **(B)** Measured lateral displacement of the ground surface at the embankment toe.

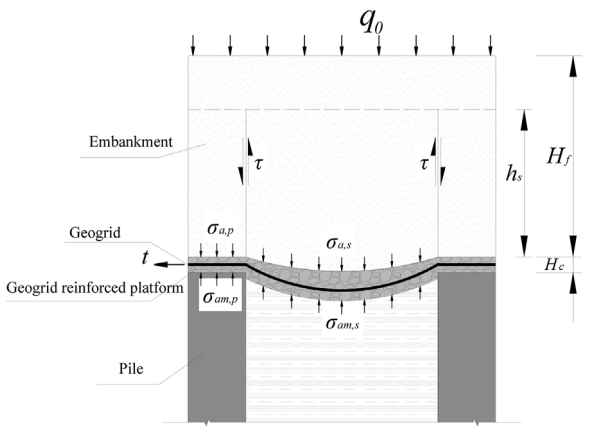

FIGURE 4
Load transfer mechanisms of GRSP in the pile-supported embankment.

to be effectively transferred to the piles, with the GRSP functioning as a deformed beam between the piles.

Except for the stress concentration ratio, the load transfer mechanisms are affected at different degrees owing to the variety of the GRSP modulus, as presented in Figure 5B. With the increase in the GRSP material modulus, the soil arching ratio (ρ_a) and tensioned membrane ratio (ρ_m) increase, while the composite soil arching and tensioned membrane ratio ($\rho_{a,m}$) decrease. As the elastic modulus increases from 15 MPa to 100 MPa, ρ_a increases from 0.75 to 0.84, ρ_m increases from 0.33 to 0.58, and $\rho_{a,m}$ decreases from 0.42 to 0.25. The increase in ρ_a reflects the weakening of the soil arching effect in the embankment, which results in less loads transferred to the pile, but the corresponding increase in ρ_m implies the enhancement of the tensioned membrane effect of GRSP, which leads to additional loads transferred to the pile. The two opposite tendencies mutually affect the load transfer between the pile and soil. Then, the decrease in $\rho_{a,m}$ also shows the composite effect of soil arching, and tensioned membrane is strengthened, which results in the increase in pile–soil stress concentration ratio and loads acted on pile, as mentioned above. Therefore, the increase in the GRSP modulus helps to transfer additional loads to pile heads. Furthermore, the influence of the GRSP modulus on the tensioned membrane effect is more notable than that on the soil arching effect. The increases in ρ_m and ρ_a are 77.1% and 12%, respectively, as the elastic modulus increases from 15 MPa to 100 MPa.

4.3.2 Influences of the GRSP modulus on settlements

As shown in Figure 5C, the elastic modulus of GRSP affects the settlements of the pile and soil, including the differential settlement of the pile and soil, the settlement of the embankment surface, the height of the plane of equal settlement (PES) h_s in the embankment, and the settlement of PES. The settlement results of different moduli are normalized based on the case of the GRSP modulus of 15 MPa. All the settlements decrease with the increase in the GRSP modulus. Due to the increase in the GRSP modulus, the deformation of GRSP decreases, causing reduction in pile–soil differential settlement. The decrease in the differential settlement of pile and soil is prominent, and the maximum reduction is estimated to be 24% within the variation range of the GRSP modulus. The settlements of the embankment surface and PES also decrease, with the maximum reductions of 9.2% and 9.8%, respectively. The influence of the GRSP modulus on the height of PES h_s is relatively small, especially when it exceeds 25 MPa, with a maximum reduction of 5.1% in this analysis. The lowering of the height of PES h_s demonstrates the decrease in the inner differential settlement in the embankment and the weakening of the soil arching effect, as illustrated in Figure 5B.

4.4 Influences of GRSP thickness on stresses and settlements of pile and soil

4.4.1 Influences of GRSP thickness on stresses

Figure 6A presents the stress concentration ratio of the pile head to the soil surface versus the thickness of GRSP. Clearly, the stress concentration ratio of pile to soil linearly increases with an increase in the thickness of GRSP in this analysis. In other words, the stress concentration ratio of pile to soil increases with an increase in the thickness of GRSP. This result can be explained that when

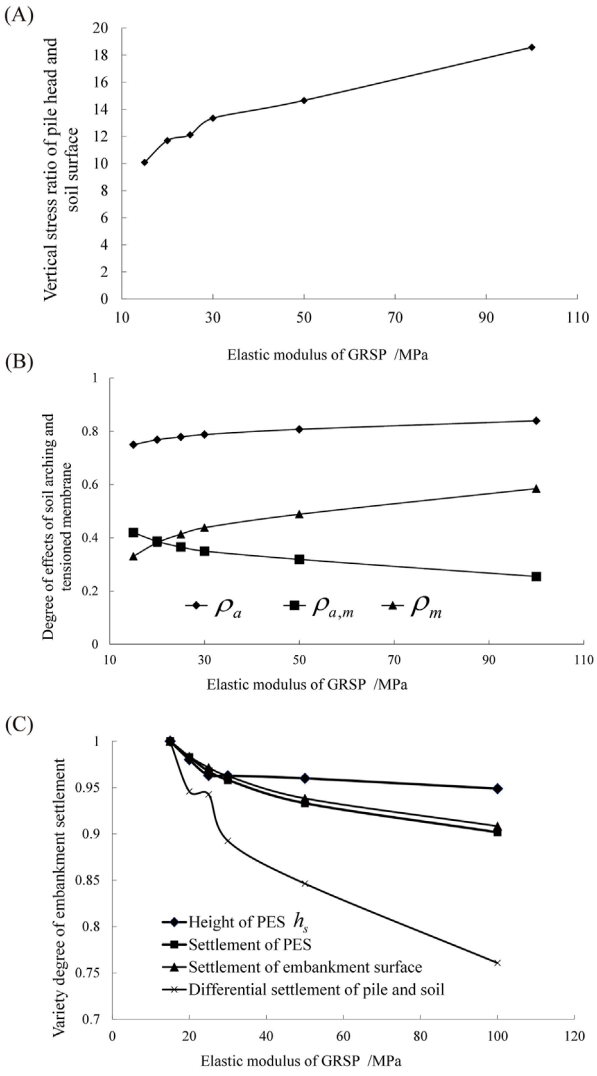

FIGURE 5
(A) Influence of the elastic modulus of GRSP on the stress concentration ratio of pile to soil (*n*). **(B)** Influence of the elastic modulus of GRSP on the effects of soil arching and tensioned membrane. **(C)** Influence of the elastic modulus of GRSP on embankment settlements.

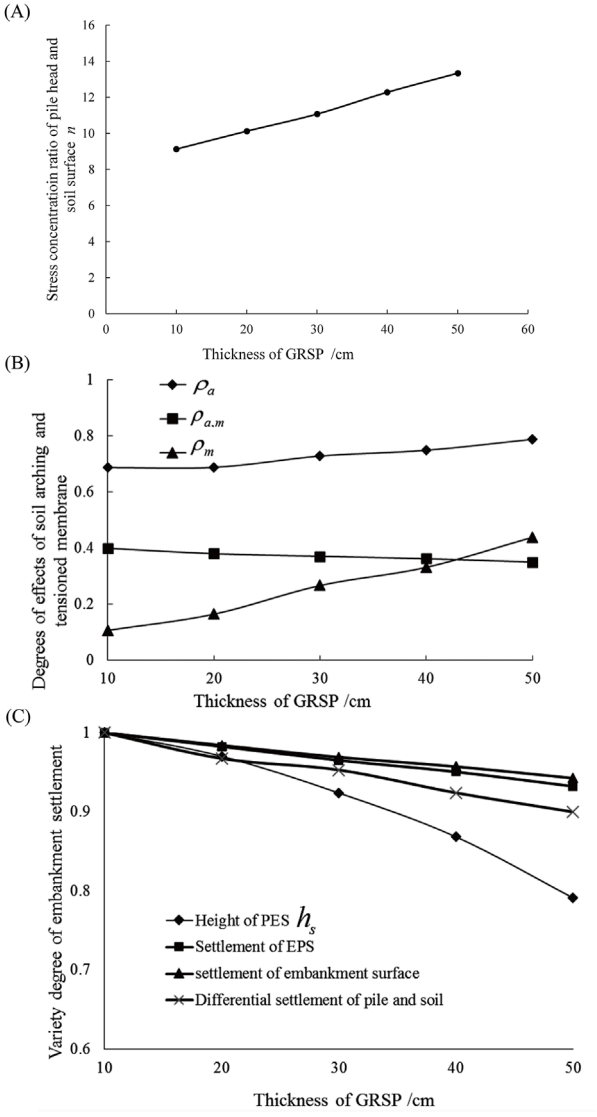

FIGURE 6
(A) Influence of the thickness of GRSP on the stress concentration ratio of pile to soil (*n*). **(B)** Influence of the thickness of GRSP on the effects of soil arching and tensioned membrane. **(C)** Influence of the thickness of GRSP on embankment settlements.

the GRSP is thicker, the deformation resistance of GRSP can be strengthened, which is similar to the increase in the GRSP modulus mentioned above, and more stresses can be transferred to piles through GRSP. As the thickness increases from 10 cm to 50 cm, the stress concentration ratio increases by 46.5% from 9.1 to 13.4.

The different degrees of effects of soil arching and tensioned membrane are plotted against the GRSP thickness in Figure 6B. Consistent with the stress concentration ratio, the thicker the GRSP, the higher the soil arching ratio (ρ_a) and tensioned membrane ratio (ρ_m). However, the composite soil arching and tensioned membrane ratio ($\rho_{a,m}$) decreases with an increase in GRSP thickness. As the GRSP thickness increases from 10 cm to 50 cm, ρa increases from 0.69 to 0.79; ρm increases from 0.11 to 0.44, and $\rho_{a,m}$ decreases from 0.40 to 0.35. The increase in ρ_a reflects the decreases in the soil arching effect in the embankment, which causes less loads transferred to the pile, but the correlating increase in ρ_m shows the enhancement of the tensioned membrane effect of GRSP, which results in additional loads transferred to the pile. The two opposite tendencies affect the load transfer between the pile and soil together. The ultimate adjustments of soil arching and tensioned membrane induce additional loads applied to piles, which is reflected by the decrease in $\rho_{a,m}$. Therefore, the increase in GRSP thickness benefits in transfer of additional loads to pile heads. Moreover, ρ_a, ρ_m, and $\rho_{a,m}$ nearly linearly vary with the increase in GRSP thickness, and the influence on the tensioned membrane effect is more pronounceable than that on the soil arching effect. The increases in ρ_m and ρ_a are 0.33 and 0.10, respectively, as the elastic modulus increases from 10 cm to 50 cm.

4.4.2 Influence of GRSP thickness on settlements

Figure 6C demonstrates the influence of GRSP thickness on the settlements of pile and soil, including the differential settlement of pile and soil, the settlement of the embankment surface, the height of the plane of equal settlement (PES) h_s in the embankment, and the settlement of PES. The settlement results of different thicknesses are normalized based on the case of 10-cm-thick GRSP. With the increase in GRSP thickness, the settlements of pile and soil all decrease at different rates. The influence on the height of PES h_s is greater than that of the other settlements, with a maximum reduction of 20.9% within the variation range of the GRSP thickness in this analysis. The enhanced deformation resistance of GRSP resulting from the increase of thickness causes the reduction of h_s and the improvement of the stress concentration ratio of pile and soil, as discussed in the previous section. The lowering of the height of PES h_s demonstrates the reduction in inner differential settlement in the embankment and the weakening of soil arching effect, as illustrated in Figure 6B. Additionally, on account of the different varying rates of the height of PES h_s and soil arching ratio ρ_a within the varying range of the GRSP thickness, the increasing compression of GRSP with the increase in the thickness also plays an important role on the reduction rate of h_s. The differential settlement of pile and soil also decreases with the increase in the GRSP thickness, with a maximum reduction of 10% in this analysis. The influence of the GRSP modulus on the settlement of the embankment surface and the settlement of PES is relatively small, with the maximum reductions of 5.7% and 6.8%, respectively.

4.5 Influence of GRSP shear resistance on stresses and settlements of pile and soil

4.5.1 Influence of GRSP shear resistance on stresses

The shear resistance of the GRSP material (i.e., friction angle and cohesion) is expected to affect the performance of the pile and soil. In practical applications, gravel or sand is commonly used as the GRSP material due to its effectiveness in dissipating excess pore water pressure within the soil. Consequently, the variation in cohesion is minimal, and the effect of GRSP material cohesion is disregarded in this analysis. However, the influence of the friction angle of the GRSP material is analyzed as below.

As shown in Figure 7A, the friction angle of the GRSP material influences the stress concentration ratio of the pile head to the soil surface. Noticeably, the stress concentration ratio of pile to soil linearly increases with an increase in the friction angle of the GRSP material. In other words, it is effective to increase the stress concentration ratio of pile to soil when the friction angle of the GRSP material increases. The results can be explained by the fact that the larger friction angle induced the higher shear resistance and more loads were transferred to the pile head from soil, which is the same as that of the increase in GRSP modulus or thickness. When the friction angle increases from 10°to 40°, the stress concentration ratio increases from 10.1 to 14.7.

The different degrees of effects of soil arching and tensioned membrane versus friction angle are illustrated in Figure 7B. Consistent with the stress concentration ratio, with the increase in the friction angle, both the soil arching ratio (ρ_a) and the tensioned membrane ratio (ρ_m) also increase. Nevertheless, the increased friction angle induces the decrease in composite soil arching and tensioned membrane ratio ($\rho_{a,m}$). As the GRSP friction angle increases from 10° to 40°, ρ_a increases from 0.77 to 0.79, ρ_m increases from 0.03 to 0.50, and $\rho_{a,m}$ decreases from 0.43 to 0.34. The increase in ρ_a reflects the decrease in the soil arching effect, which causes less loads transferred to the pile, but the correlating increase in ρ_m shows the enhancement of the tensioned membrane effect of GRSP, which results in additional loads transferred to the pile. The two opposite tendencies affect the load transferring between the pile and soil, and the final adjustment of the two effects induced additional loads applied on the pile, which is reflected by the decrease in $\rho_{a,m}$. Hence, the increase in the GRSP friction angle

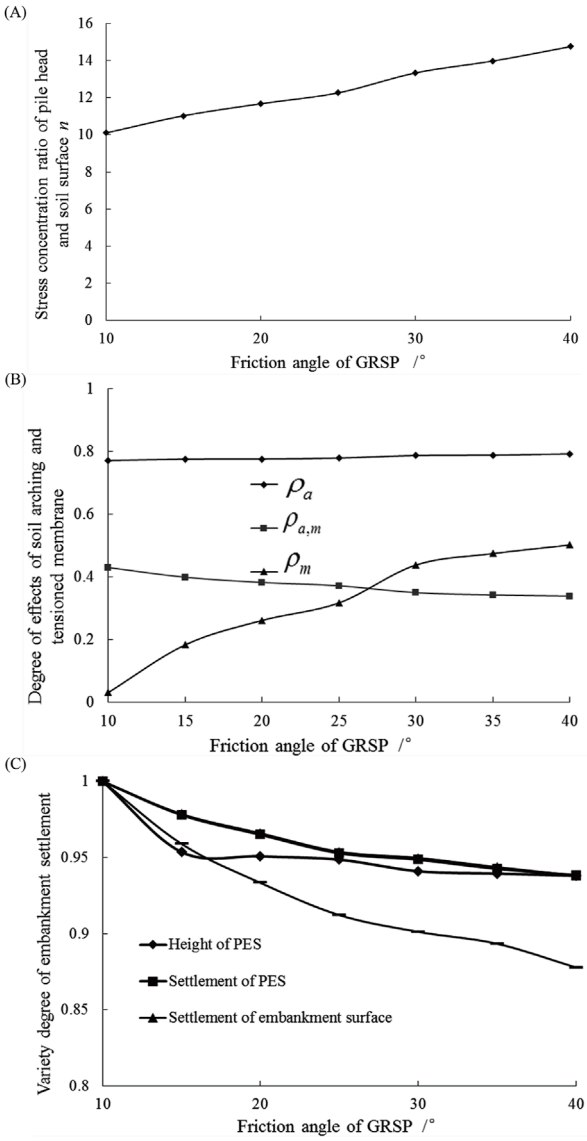

FIGURE 7
(A) Influence of friction angles of GRSP on the stress concentration ratio of pile to soil (*n*). **(B)** Influence of friction angles of GRSP on the effects of soil arching and tensioned membrane. **(C)** Influence of friction angles of GRSP on embankment settlements.

displays the benefit for transferring additional loads to the pile. Furthermore, the influence on the tensioned membrane effect is more noticeable than that on the soil arching effect. The increases in ρ_m and ρ_a are approximately 0.47 and 0.02, respectively, as the angle friction increases from 10° to 40°.

As shown in Figure 7C, the friction angle of the GRSP material has effects on the settlements of the pile and soil, including the differential settlement of the pile and soil, the settlement of the embankment surface, the height of the plane of equal settlement (PES) h_s in the embankment, and the settlement of PES. The settlement results of different friction angles are normalized based on the case of the 10° GRSP friction angle. All the settlements decrease with the increase in the friction angle of GRSP. Due to the increase in the GRSP friction angle, the shear resistance of GRSP increases, causing the reduction in the shear deformation of GRSP and the pile–soil differential settlement. The decrease in the differential settlement of pile and soil is apparent, with the maximum reduction estimated at 12.2% within the variation range of the GRSP friction angle. The settlements of embankment surface and PES also decrease, with the maximum reductions of 6.18% and 6.15%, respectively. The reduction in the height of PES h_s is maximum 6.19% in this analysis, and the influence is even smaller as the friction angle of GRSP exceeds 15°. The lowering of the height of PES h_s presented the decrease in inner differential settlement in embankment, which is consistent with the weakening of the soil arching effect, as illustrated in Figure 7B.

4.6 Influence of geogrid tensile stiffness on stresses and settlement of pile and soil

4.6.1 Influence of geogrid tensile stiffness on stresses

Figure 8A demonstrates the stress concentration ratio of the pile head and soil surface versus the tensile stiffness of the geogrid. Clearly, the stress concentration ratio of the pile to soil increased significantly with an increase in the tensile stiffness of the geogrid in GRSP. In other words, the stress concentration ratio of the pile to soil can be improved by increasing the tensile stiffness of the geogrid. This result is in good agreement with the findings obtained by Han and Gabr (2002). It can be explained that when the tensile stiffness of the geogrid is higher, the deformation resistance of the GRSP is enhanced. This effect is similar to the impact of other physical or mechanical parameters of the GRSP mentioned earlier, such as increased elastic modulus, thickness, and shear resistance, enabling greater load transfer to the piles through the GRSP between them. As the tensile stiffness increases from 300 kN/m to 2,250 kN/m, the stress concentration ratio increases by 58.9% from 10.4 to 16.5.

The influences of geogrid tensile stiffness on the effects of soil arching and tensioned membrane are plotted in Figure 8B. Consistent with the stress concentration ratio, the higher the tensile stiffness of the geogrid, the larger the soil arching ratio (ρ_a) and tensioned membrane ratio (ρ_m). However, the composite soil arching and tensioned membrane ratio ($\rho_{a,m}$) decreases with an increase in the geogrid tensile stiffness. As the geogrid tensile stiffness increases from 300 kN/m to 2,250 kN/m, ρ_a increases from 0.73 to 0.83, ρ_m increases from 0.32 to 0.48, and $\rho_{a,m}$ decreases from 0.40 to 0.32. The increase in ρ_a reflects the weakening of the soil arching effect in the embankment, causing less loads to be transferred to the pile, but the correlating increase in ρ_m showed the enhancement of the tensioned membrane effect of GRSP, resulting in additional loads being transferred to the pile. The two opposite tendencies affected the load transfer between the pile and soil mutually. The crucial adjustment of soil arching and tensioned membrane induces additional loads applied on the pile, which is reflected by the decrease in $\rho_{a,m}$. Therefore, the increase in geogrid tensile stiffness greatly benefits the transfer of additional loads to pile heads. Moreover, the ρ_a, ρm, and $\rho_{a,m}$ vary at different rates, and the influence on the tensioned membrane effect was more pronounceable than that on the soil arching effect. The increases in

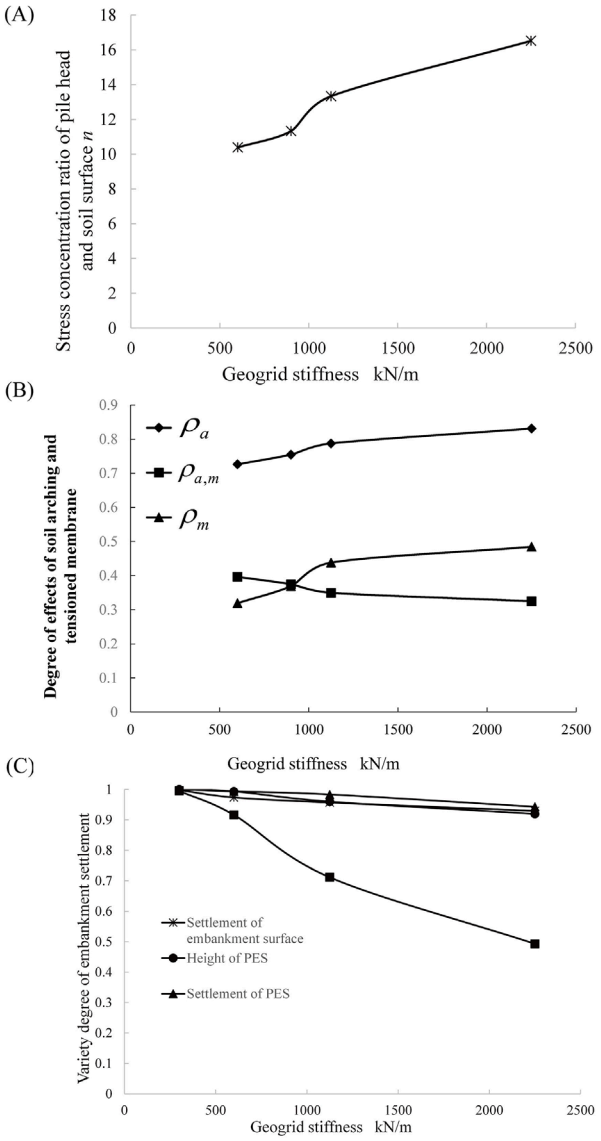

FIGURE 8
(A) Influence of tensile stiffness of the geogrid on the stress concentration ratio of pile to soil (*n*). **(B)** Influence of tensile stiffness of the geogrid on the effects of soil arching and tensioned membrane. **(C)** Influence of tensile stiffness of the geogrid on embankment settlements.

ρ_m and ρ_a are approximately 0.17 and 0.1, respectively, as the geogrid tensile stiffness increases from 300 kN/m to 2,250 kN/m.

4.6.2 Influence of geogrid tensile stiffness on settlements

As illustrated in Figure 8C, the tensile stiffness of the geogrid also has an influence on the settlements of pile and soil, including the differential settlement of pile and soil, the settlement of the embankment surface, the height of the plane of equal settlement (PES) h_s in the embankment, and the settlement of PES. The settlement results of different tensile stiffness are normalized based on the case of 300 kN/m tensile stiffness of the geogrid. All the settlements decrease with the increase in the geogrid tensile stiffness. Due to the increase in tensile stiffness, the deformation resistance of GRSP increases, which induces the reduction of the deformation of GRSP and the pile–soil differential settlement. The decrease in the differential settlement of pile and soil is significant, with the maximum reduction estimated to be 50.5% within the variation range of the geogrid tensile stiffness. The settlements of embankment surface and PES also decrease, with the maximum reductions of 6.9% and 5.7%, respectively. The reduction of the height of PES h_s is maximum 8.1% in this analysis. The lowering of the height of PES h_s shows the decrease in the inner differential settlement in the embankment and agrees well with the weakening of the soil arching effect as discussed earlier.

4.7 Influences of geogrid layers and placement on stresses and settlements of pile and soil

4.7.1 Influence of geogrid layers and placement on stresses

Figure 9A presents the stress concentration ratio of the pile head to the soil surface versus the geogrid layers and placement. The stress concentration ratio of the pile to soil increases with the increase in the geogrid layers and the lowering placement of the geogrid in GRSP. In other words, the stress concentration ratio of the pile to soil is strengthened by increasing the layers of the geogrid and lowering the placement elevation of the geogrid in GRSP. These results can be explained by the fact that when the geogrid layers increase or the placement elevation of geogrid reduce, the deformation resistance of GRSP under pile penetration is strengthened, which was similar to the increase in the geogrid tensile stiffness, and additional loads can be transferred to piles through GRSP between piles. As the geogrid layers increase from single layer to triple layers, the stress concentration ratio increases by 11% from 12.8 to 14.2. When one of the geogrid layers is shifted from the top of GRSP to the bottom in the double layer cases, the stress concentration ratio increases slightly from 13.3 to 13.6 at an approximately 2.2% increasing rate.

The different degrees of effects of soil arching and tensioned membrane versus geogrid layers and placement are illustrated in Figure 9B. Consistent with the stress concentration ratio, the more the geogrid layers, the larger the soil arching ratio (ρ_a) and tensioned membrane ratio (ρ_m). However, the composite soil arching and tensioned membrane ratio ($\rho_{a,m}$) decreases with an increase in geogrid layers. As the geogrid layers increase from single layer to triple layers, the increase in ρ_a is slight from 0.77 to 0.78, ρ_m increases distinctly from 0.26 to 0.45, and $\rho_{a,m}$ decreases from 0.42 to 0.34. The slight increase in ρ_a reflects the weakening of the soil arching effect in the embankment owing to the increase in geogrid layers, whereas the corresponding increase in ρ_m shows the enhancement of the tensioned membrane effect of GRSP, which results in additional loads transferred to the pile. With the mutual effects of soil arching and tensioned membrane, the additional loads are transferred to piles, which were reflected by the decrease in

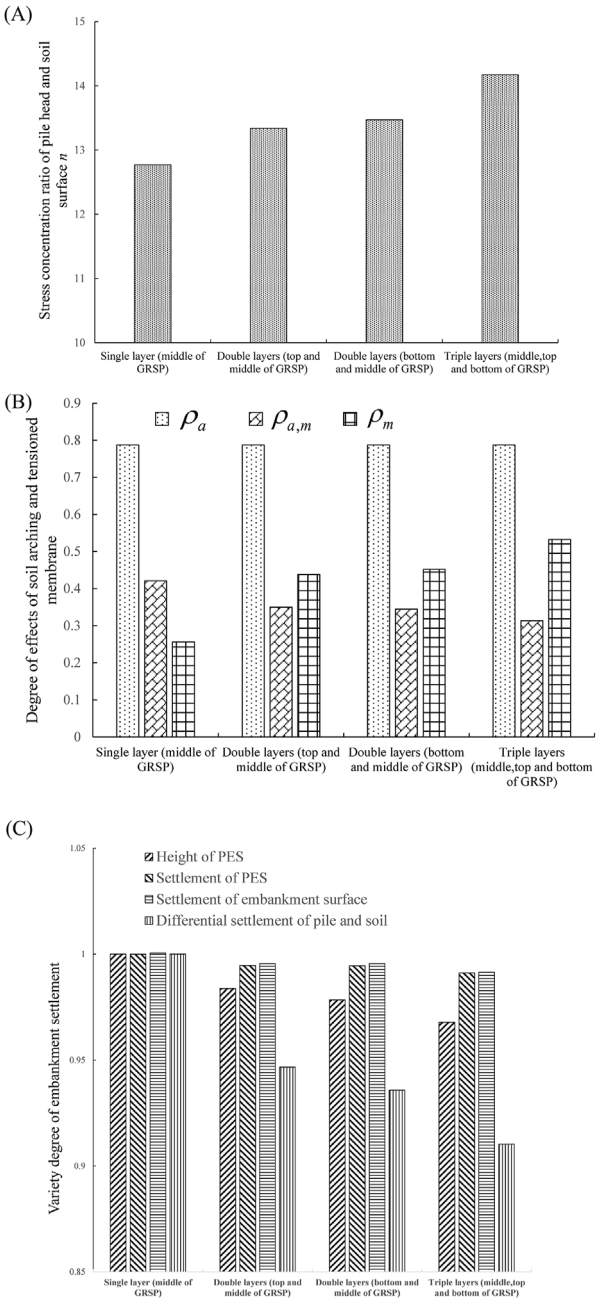

FIGURE 9
(A) Influence of layer and placement of the geogrid in GRSP on the stress concentration ratio of pile to soil (*n*). **(B)** Influence of the layer and placement of the geogrid in GRSP on the effects of soil arching and tensioned membrane. **(C)** Influence of the layer and placement of the geogrid in GRSP on embankment settlements.

$\rho_{a,m}$ directly. Therefore, the increase in geogrid layers benefits the transfer of the loads to pile heads. Moreover, the placement of the geogrid with the same layers influences the soil arching and tensioned membrane as well at a certain degree. As one of the geogrid layer is shifted from the top of GRSP to the bottom in the double layer cases, ρ_a inappreciably increases from 0.787 to 0.788, ρ_m increases distinctly from 0.44 to 0.45, and $\rho_{a,m}$ decreases from 0.65 to 0.64 in this analysis. Hence, the influences of the placement of the geogrid on the effects of soil arching and tensioned membrane are practically ignorable.

4.7.2 Influence of geogrid layers and placement on settlements of pile and soil

As shown in Figure 9C, the layers and placement of the geogrid in GRSP affect the settlements of pile and soil, including the differential settlement of the pile and soil, the settlement of the embankment surface, the height of the plane of equal settlement (PES) h_s in the embankment, and the settlement of the PES. The settlement results of different layer quantity and placement are normalized based on the case of the single layer of the geogrid in the middle of GRSP. All the settlements decrease at different degrees, with the increase in the quantity of the geogrid layer. Due to the increase in geogrid layers, the deformation resistance of GRSP increases, resulting in the reduction in the deformation of GRSP and the pile–soil differential settlement. The decrease in the differential settlement of the pile and soil is apparent, with the maximum reduction estimated to be 9.0% within the variation range of the geogrid in this analysis. The settlements of the embankment surface and PES also decrease slightly, with the maximum reductions of 0.91% and 0.88%, respectively. The reduction in the height of PES h_s is maximum 3.2% in this analysis. The lowering of the height of PES h_s results in the reduction of inner differential settlement in the embankment, which is consistent with the weakening of the soil arching effect, as illustrated in Figure 9B. As for the influences of geogrid placement, the settlements of soil and piles are affected negligibly. As one of the geogrid layer is shifted from the top of GRSP to the bottom in the double layer cases, the pile–soil differential settlement slightly decreases from 0.95 to 0.93, the height of PES h_s decreases inappreciably from 0.98 to 0.97, and the settlements of the embankment surface and PES are almost unchanged, which are approximately 0.995 and 0.994, respectively.

5 Discussion

The influences of various factors of GRSP on the stress concentration ratio of pile to soil, soil arching effect, tensioned membrane effect, differential settlement of pile and soil, settlement of embankment surface, and height of PES in embankment and its settlement are summarized below.

According to the definitions of the composite ratio of soil arching and tensioned membrane effects ($\rho_{a,m}$), the degree of load transfer from soil to pile through the two effects can be quantified with (1-$\rho_{a,m}$). In the 22 cases of numerical computations, the values of 1-$\rho_{a,m}$ are approximately 0.55–0.75, which reflects that most load of the embankment is transferred to the piles, and the soil arching and tensioned membrane effects are effective and efficient to reduce the load applied on ground soil. However, the parametric studies also

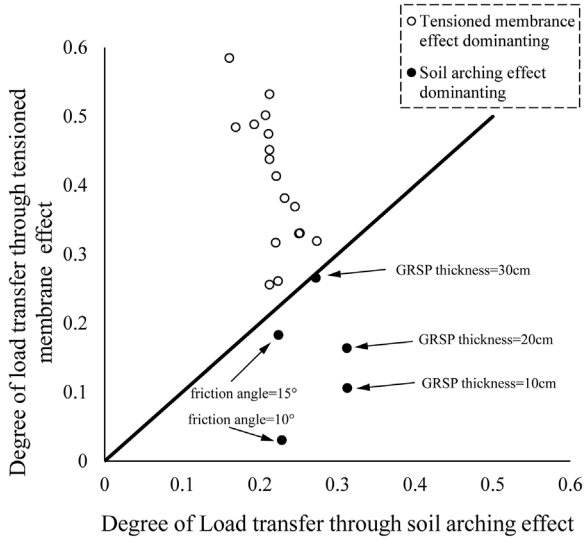

FIGURE 10
Load transfer degrees with the effects of soil arching and tensioned membrane.

reveal that the major role of load transfer is varied in different cases. Similarly to (1-$\rho_{a,m}$), the degree of load transfer through the soil arching effect and tensioned membrane effect can be quantified with (1-ρ_a) and ρ_m, respectively. Figure 10 presents the degree of load transfer through the tensioned membrane effect ρ_m versus the degree of load transfer through the soil arching effect (1-ρ_a), and the straight line in figure means the equivalent efficiency of the two effects in load transfer. Clearly, the tensioned membrane effect of GRSP mostly plays the principal role in the transfer of load from soil to piles in the 22 computation cases. The degrees of load transfer through the soil arching effect are approximately 20%–25% mostly, and the degrees of load transfer through the tensioned membrane effect are mainly larger than 30%, with some cases exceeding 50%. However, in the five cases located to the right of the straight line, it is observed that smaller friction angles and reduced GRSP thickness emphasize the dominant role of the soil arching effect in load transfer. Overall, except in the scenarios characterized by smaller friction angles and thinner GRSP layers, the tensioned membrane effect of the GRSP generally plays a more significant role in transferring loads from the embankment soil to the piles.

Various factors of the GRSP, including elastic modulus, thickness, friction angle, tensile stiffness, and the number of geogrid layers, all have positive effects. Increasing these factors facilitates greater load transfer from the soil to the piles and reduces embankment settlement. However, increases in various GRSP factors lead to different load transfer processes. For example, the increase in these influencing factors shows negative effects on soil arching and positive effects on the tensioned membrane effect. The influencing degree of each influencing factor has been introduced to evaluate the variation degree of investigated performance parameters, such as the stress concentration ratio of pile and soil, soil arching effect, tensioned membrane effect, differential settlement of pile and soil, settlement of embankment surface, and the height of PES in the embankment and its settlement. The influencing degree

TABLE 4 Degrees of influencing factors.

GRSP factor	n	ρ_a	ρ_m	$\rho_{a,m}$	S_d	S_e	h_s	S_{PES}
Modulus	63.4	11.4	58.0	47.3	26.6	9.5	5.3	10.3
Thickness	31.7	13.5	117.1	13.3	10.6	5.9	22.9	7.0
Friction angle	37.3	2.7	149.7	24.5	13.2	6.4	6.5	6.4
Tensile stiffness of the geogrid	47.6	13.8	41.0	19.7	64.5	7.1	8.3	5.8
Layers of the geogrid	10.4	0	67.6	29.9	9.4	0.9	3.3	0.9
Placement of the geogrid	1.0	0	3.0	1.5	1.2	0	0.5	0

Note: n is the stress concentration ratio of pile to soil; ρ_a is the soil arching ratio; ρ_m is the tensioned membrane ratio; $\rho_{a,m}$ is the composite ratio of soil arching and tensioned membrane; S_d is the differential settlement of soil and pile; S_e is the settlement of embankment surface; h_s is the height of plane of equal settlement (PES) in embankment; S_{PES} is the settlement of PES.

is defined as the ratio of the maximum variation of the performance parameter to the mean value of the performance parameter. As an example, the stress concentration ratios of pile to soil for the GRSP elastic modulus equal to 15, 20, 25, 30, 50, and 100 MPa are 10.1, 11.7, 12.1, 13.5, 14.7, and 18.6, respectively. The maximum variation of the stress concentration ratio of pile to soil within the variation range in this analysis is 18.6–10.1 = 8.5, and the mean value of the stress concentration ratio of the pile and soil is (10.1+11.7+12.1+13.5+14.7+18.6)/6 = 13.45. Hence, the degree of influence of the GRSP elastic modulus on the stress concentration ratio of the pile to soil is calculated as (8.5/13.45)×100% = 63.2%. The calculated degree of influence for each factor on each investigated performance parameter is listed in Table 4.

According to the results shown in Table 4, the elastic modulus of GRSP has significant influences on the performance of the pile-supported embankment, especially on the stress concentration ratio of pile to soil, the composite soil arching and tensioned membrane ratio, the settlement of the embankment surface, and PES. The thickness of GRSP affected the height of PES and tensioned membrane ratio notably, compared to other factors, and the influence of the larger compression value for thicker GRSP should be taken into account. The friction angle of the GRSP material influences the tensioned membrane ratio significantly as well. The tensile stiffness of the geogrid has a significant impact on the soil arching ratio and the differential settlement of soil and pile. The influence of the geogrid layer on the tensioned membrane ratio is noticeable. The influence of geogrid placement on the performance of the pile-supported embankment is practically negligible. The settlement of the embankment surface and the stress concentration ratio of pile to soil are the important controlling indexes in practice; thus, the elastic modulus, tensile stiffness, and friction angle can be considered the three most important design parameters among the discussed influencing factors.

6 Conclusion

Based on the field monitoring and numerical parametric studies on the influences of GRSP on the performances of pile-supported embankment, the following conclusions can be drawn:

(1) By comparing field observation results of the embankment sections with different GRSPs, it is found that the compaction of the GRSP material affects the developing process of the stress concentration ratio of pile to soil, as well as the lateral displacement of the embankment. If the GRSP material is well compacted, the stress concentration ratio of the pile to soil increases distinctly at the early stage of embankment construction, and the lateral displacement becomes smaller compared to the un-compacted case.

(2) In reference to the definition of the soil arching ratio (ρ_a), the composite ratio of soil arching and tensioned membrane ($\rho_{a,m}$) and the tensioned membrane ratio of GRSP (ρ_m) are introduced to quantify the loading effect of GRSP, according to the load transfer mechanisms of the pile-supported embankment.

(3) A number of factors of GRSP influence not only the results of load transfer between pile and soil (i.e., the stress concentration ratio of pile to soil and the settlement of embankment surface) but also the process of load transfer (i.e., soil arching ratio, tensioned membrane ratio, and the differential settlement of pile and soil). The soil arching and tensioned membrane effects effectively reduce the load applied on the ground soil, with the tensioned membrane effect of GRSP typically playing a predominant role in transferring loads from soil to piles compared to the soil arching effect.

(4) With an increase in the GRSP factor (elastic modulus, thickness, friction angle, tensile stiffness, and layers of the geogrid), the load transferred to piles increases, and all the corresponding settlements decrease at different degrees. However, the soil arching effect in the embankment and the tensioned membrane effect in the GRSP exhibit opposite trends: the soil arching effect is diminished, while the tensioned membrane effect is enhanced.

(5) Using embankment surface settlement and the stress concentration ratio between piles and soil as key control indices, the elastic modulus, tensile stiffness, and friction angle of the GRSP are identified as the three most critical design parameters. Specifically, based on our case studies, we recommend using materials with higher elastic modulus and greater friction angles, such as well-compacted sand or gravel, as the soil platform. Additionally, incorporating high-strength

geogrids as reinforcement in the GRSP is advised to effectively reduce the overall settlement of the embankment. However, beyond these three parameters, the placement of geogrids within the GRSP has a negligible impact on the performance of the pile-supported embankment.

Data availability statement

The original contributions presented in the study are included in the article/Supplementary Material; further inquiries can be directed to the corresponding author.

Author contributions

ZZ: data curation, investigation, methodology, software, and writing–original draft. LZ: conceptualization, supervision, and writing–review and editing.

Funding

The author(s) declare that financial support was received for the research, authorship, and/or publication of this article. The authors acknowledge financial support from the National Science Foundation of China (No. 51890912).

Conflict of interest

Author ZZ was employed by Suzhou New District Testing Corporation.

The remaining author declares that the research was conducted in the absence of any commercial or financial relationships that could be construed as a potential conflict of interest.

The reviewer XN declared a shared affiliation with the author LZ to the handling editor at the time of review.

Publisher's note

All claims expressed in this article are solely those of the authors and do not necessarily represent those of their affiliated organizations, or those of the publisher, the editors, and the reviewers. Any product that may be evaluated in this article, or claim that may be made by its manufacturer, is not guaranteed or endorsed by the publisher.

References

Badakhshan, E., Noorzad, A., Bouazza, A., Zameni, S., and King, L. (2020). A 3D-DEM investigation of the mechanism of arching within geosynthetic-reinforced piled embankment. *Int. J. SOLIDS Struct.* 187, 58–74. doi:10.1016/j.ijsolstr.2019.03.035

Blanc, M., Rault, G., Thorel, L., and Almeida, M. (2013). Centrifuge investigation of load transfer mechanisms in a granular mattress above a rigid inclusions network. *Geotext. Geomembr.* 36, 92–105. doi:10.1016/j.geotexmem.2012.12.001

Borges, J. L., and Marques, D. O. (2011). Geosynthetic-reinforced and jet grout column-supported embankments on soft soils: numerical analysis and parametric study. *Comput. Geotech.* 38, 883–896. doi:10.1016/j.compgeo.2011.06.003

Briançon, L., and Simon, B. (2012). Performance of pile-supported embankment over soft soil: full-scale experiment. *J. Geotech. Geoenvironmental Eng.* 138, 551–561. doi:10.1061/(ASCE)GT.1943-5606.0000561

Chen, R. P., Xu, Z. Z., Chen, Y. M., Ling, D. S., and Zhu, B. (2010). Field tests on pile-supported embankments over soft ground. *J. Geotech. Geoenvironmental Eng.* 136, 777–785. doi:10.1061/(ASCE)GT.1943-5606.0000295

Du, W., Nie, R., Qi, Y., Ruan, B., and Mo, F. (2024). Investigation on the static performance of geogrid reinforced aeolian sand railway embankment: field test and discrete element simulation. *Geotext. Geomembr.* 52, 736–752. doi:10.1016/j.geotexmem.2024.03.012

Esmaeili, M., Naderi, B., Neyestanaki, H. K., and Khodaverdian, A. (2018). Investigating the effect of geogrid on stabilization of high railway embankments. *Soils Found.* 58, 319–332. doi:10.1016/j.sandf.2018.02.005

Ghosh, B., Fatahi, B., Khabbaz, H., Nguyen, H. H., and Kelly, R. (2021). Field study and numerical modelling for a road embankment built on soft soil improved with concrete injected columns and geosynthetics reinforced platform. *Geotext. Geomembr.* 49, 804–824. doi:10.1016/j.geotexmem.2020.12.010

Han, J., and Gabr, M. A. (2002). Numerical analysis of geosynthetic-reinforced and pile-supported earth platforms over soft soil. *J. Geotech. Geoenvironmental Eng.* 128, 44–53. doi:10.1061/(ASCE)1090-0241(2002)128:1(44)

Huang, J., and Han, J. (2010). Two-dimensional parametric study of geosynthetic-reinforced column-supported embankments by coupled hydraulic and mechanical modeling. *Comput. Geotech.* 37, 638–648. doi:10.1016/j.compgeo.2010.04.002

Huang, J., Han, J., and Oztoprak, S. (2009). Coupled mechanical and hydraulic modeling of geosynthetic-reinforced column-supported embankments. *J. Geotech. Geoenvironmental Eng.* 135, 1011–1021. doi:10.1061/(ASCE)GT.1943-5606.0000026

Khosrojerdi, M., Qiu, T., Xiao, M., and Nicks, J. (2018). Numerical investigation on the performance of geosynthetic-reinforced soil piers under axial loading: 3rd international foundation congress and equipment expo 2018: developments in earth retention, support systems, and tunneling, IFCEE 2018. *Geotech. Spec. Publ. 2018-March*, 99–108. doi:10.1061/9780784481608.010

Liu, H., Kong, G., Chu, J., and Ding, X. (2015). Grouted gravel column-supported highway embankment over soft clay: case study. *Can. Geotech. J.* 52, 1725–1733. doi:10.1139/cgj-2014-0284

Liu, H. L., Ng, C. W. W., and Fei, K. (2007). Performance of a geogrid-reinforced and pile-supported highway embankment over soft clay: case study. *J. Geotech. Geoenvironmental Eng.* 133, 1483–1493. doi:10.1061/(ASCE)1090-0241(2007)133:12(1483)

McNulty, J. (1965). An experimental study of arching in sand. Available at: https://api.semanticscholar.org/CorpusID:108153817.

Okyay, U. S., Dias, D., Thorel, L., and Rault, G. (2014). Centrifuge modeling of a pile-supported granular earth-platform. *J. Geotech. Geoenvironmental Eng.* 140, 04013015. doi:10.1061/(ASCE)GT.1943-5606.0001004

Pham, H. T. V., Suleiman, M. T., and White, D. J. (2004). Numerical analysis of geosynthetic-rammed aggregate pier supported embankments. *Geotech. Eng. Transp. Proj.*, 657–664. doi:10.1061/40744(154)52

Rowe, R. K., and Liu, K.-W. (2015). Three-dimensional finite element modelling of a full-scale geosynthetic-reinforced, pile-supported embankment. *Can. Geotech. J.* 52, 2041–2054. doi:10.1139/cgj-2014-0506

Rui, R., Han, J., van Eekelen, S. J. M., and Wan, Y. (2019). Experimental investigation of soil-arching development in unreinforced and geosynthetic-reinforced pile-supported embankments. *J. Geotech. Geoenvironmental Eng.* 145, 04018103. doi:10.1061/(ASCE)GT.1943-5606.0002000

Shen, P., Xu, C., and Han, J. (2020). Geosynthetic-reinforced pile-supported embankment: settlement in different pile conditions. *Geosynth. Int.* 27, 315–331. doi:10.1680/jgein.19.00015

Stewart, M. E., and Filz, G. M. (2005). "Influence of clay compressibility on geosynthetic loads in bridging layers for column-supported embankments," in *Contemporary issues in foundation engineering* (Austin, Texas, United States: American Society of Civil Engineers), 1–14. doi:10.1061/40777(156)8

Stewart, M. E., Navin, M. P., and Filz, G. M. (2004). Analysis of a column-supported test embankment at the I-95/Route 1 interchange. *Geotech. Eng. Transp. Proj.*, 1337–1346. doi:10.1061/40744(154)123

Terqueux, C., Racinais, J., Briançon, L., Pantet, A., and Gotteland, P. (2023). "Full scale experiment of a geosynthetic-reinforced piled embankment," in *Geosynthetics: leading the way to a resilient planet* (London: CRC Press).

Terzaghi, K. (1936). Stress distribution in dry and in saturated sand above a yielding trap-door. Available at: https://api.semanticscholar.org/CorpusID:132913229.

Terzaghi, K. (1943). *Theoretical soil mechanics*. John Wiley and Sons.

van Eekelen, S. J. M., Venmans, A. a. M., Bezuijen, A., and van Tol, A. F. (2020). Long term measurements in the Woerden geosynthetic-reinforced pile-supported embankment. *Geosynth. Int.* 27, 142–156. doi:10.1680/jgein.17.00022

Wu, D., Luo, C., Gao, Z., Li, D., and Xu, C. (2022). Effect of different reinforced load transfer platforms on geosynthetic-reinforced pile-supported embankment: centrifuge model test. *KSCE J. Civ. Eng.* 26, 630–649. doi:10.1007/s12205-021-0623-7

Xing, H., Zhang, Z., Liu, H., and Wei, H. (2014). Large-scale tests of pile-supported earth platform with and without geogrid. *Geotext. Geomembr.* 42, 586–598. doi:10.1016/j.geotexmem.2014.10.005

Xu, C., Wu, D., Song, S., and Liu, B. (2018). "Centrifuge model tests of basal reinforcement effects on geosynthetic-reinforced pile-supported embankment," in *Proceedings of geoshanghai 2018 international conference: ground improvement and geosynthetics*. Editors L. Li, B. Cetin, and X. Yang (Singapore: Springer-Verlag Singapore Pte Ltd), 279–287. doi:10.1007/978-981-13-0122-3_31

Yan, M., Song, X., Xiao, H., Guo, S., Zhang, H., and Chango, I. V. L. (2022). Analysis of load transfer in geosynthetic-reinforced pile-supported embankments. *2022 16TH IEEE Int. Conf. SIGNAL Process. (ICSP2022)* 1, 354–358. doi:10.1109/ICSP56322.2022.9965213

Zhang, X., Zhuang, Y., Hu, S., and Dong, X. (2022). A simplified method for assessing the serviceability performance of geosynthetic reinforced and pile-supported embankment. *Geotext. Geomembr.* 50, 1214–1229. doi:10.1016/j.geotexmem.2022.08.006

Zhou, M., Liu, H., Chen, Y., and Hu, Y. (2016). First application of cast-in-place concrete large-diameter pipe (PCC) pile-reinforced railway foundation: a field study. *Can. Geotech. J.* 53, 708–716. doi:10.1139/cgj-2014-0547

frontiers | Frontiers in Earth Science

TYPE Original Research
PUBLISHED 06 January 2025
DOI 10.3389/feart.2024.1518849

OPEN ACCESS

EDITED BY
Huiming Tan,
Hohai University, China

REVIEWED BY
Geng Jiabo,
Jiangxi University of Science and Technology, China
Zhiwei Ye,
Nanchang University, China

*CORRESPONDENCE
Xianzhou Lyu,
lyuxianzhou0608@sdust.edu.cn

RECEIVED 29 October 2024
ACCEPTED 09 December 2024
PUBLISHED 06 January 2025

CITATION
Deng Q, Fu H, Wang J, An X and Lyu X (2025) Macro-meso failure mechanism and strength criterion of frozen weakly cemented sandstone under triaxial unloading. *Front. Earth Sci.* 12:1518849. doi: 10.3389/feart.2024.1518849

Macro-meso failure mechanism and strength criterion of frozen weakly cemented sandstone under triaxial unloading

Qinghai Deng[1], Hao Fu[1], Junchao Wang[2], Xiaobiao An[1] and Xianzhou Lyu[1]*

[1]College of Earth Science and Engineering, Shandong University of Science and Technology, Qingdao, China, [2]Longshou Mine of Jinchuan Group Co., Ltd., Jinchuan, China

Introduction: In the excavation engineering of tunnels and mines in the western cold region, the unloading failure zone is mainly caused by stress release. This study aimed to investigate the deformation and failure mechanism of frozen weakly cemented sandstone (FWCS) when the initial principal stress σ_3 was 3, 6, or 10 MPa.

Methods: A conventional triaxial compression test and a triaxial unloading test with an unloading rate of 0.05 MPa/s were carried out. Based on the experimental data and mathematical analysis methods, the non-linear criterion was constructed and analyzed. The microfracture characteristics of the damaged surface were studied by scanning electron microscopy (SEM).

Results: The results show that compared with conventional triaxial compression and room temperature triaxial compression tests, the strength and plastic deformation characteristics of FWCS during unloading were significantly weakened, with transverse deformation and volume strain increased, showing obvious dilatancy characteristics. Unloading reduced the cohesion of FWCS, increased the internal friction angle, and increased the risk of rock failure. Macroscopic and microscopic analysis revealed the failure mechanism of FWCS. The unloading stress ratio was introduced to establish relationships. A non-linear criterion based on the Mohr–Coulomb strength criterion was established, with the power function strength criterion being more accurate in describing the failure of FWCS.

Discussion: This study provides valuable insights into the mechanical properties and failure mechanism of FWCS under unloading conditions, which is beneficial for the excavation engineering of tunnels and mines in the western cold region.

KEYWORDS

frozen weakly cemented sandstone, loading-unloading, confining pressure unloading, failure mechanism, strength criterion

1 Introduction

Weakly cemented soft rock (WCSR) is a general name for a type of soft rock widely distributed in Western China. There are many types of WCSRs, which have different mechanical properties, but they have common characteristics such as poor cementation, low strength, easy disintegration in water, susceptibility to softening, and extremely unstable mechanical properties (Chen et al., 2018; You et al., 2018; Hadi and Ali, 2018). Their extremely weak mechanical characteristics pose many challenges to engineering practices, and it is easy to induce engineering disasters if they are not properly mitigated (Cai and Zou, 2020; Liu J. S. et al., 2020; Lyu et al., 2019). Artificial freezing is widely utilized for the reinforcement of weakly cemented strata, which can improve strength, deformation resistance, and impermeability (Bai et al., 2020; Wang L. et al., 2020). The excavation and support of frozen rock mass is actually a process of loading and unloading, and the stress state of rock mass changes (Vazaios et al., 2019; Li et al., 2019). When disturbed by underground excavation, WCSR is unloaded, and its strength characteristics are obviously different from those of rock under loading conditions. If the research results on the strength of WCSR unloading are not accurately distinguished, potential risks may arise in guiding weakly consolidated soft rock engineering involving excavation and unloading, potentially leading to accidents and disasters. Therefore, it is highly significant to investigate the loading and unloading mechanical properties of WCSR and establish a failure criterion for the design and stability analysis of underground engineering involving weakly cemented rock.

In recent years, some scholars have studied the loading–unloading mechanical characteristics of frozen weakly cemented soft rock (FWCSR). Shan et al. (2016) pointed out that the ultimate strength of FWCSR under confining pressure unloading before the peak is lower than the peak strength in conventional triaxial tests; the lower the temperature, the smaller the deformation of the specimen caused by confining pressure unloading. Tensile failure is dominant in the specimen at the same time, and confining pressure unloading accelerates the axial compression and lateral expansion of the rock. Furthermore, the lateral expansion is much larger than the axial compression, which is positively correlated with the initial confining pressure (Dong et al., 2018). The ultimate bearing strength of rock under confining pressure unloading is positively related to the unloading rate, and brittle failure occurs at a high unloading rate, while plastic failure characteristics, including creep deformation, are observed at a low unloading rate, presenting an overall splitting failure form. With a decrease in the freezing temperature, the number of acoustic emission (AE) counts decreases, and the peak of AE energy increases. The peak of AE energy is positively correlated with the initial confining pressure and unloading rate (Liu, 2020; Liu et al., 2021). Other scholars have studied the mechanical properties of FWCSR using the cyclic loading–unloading tests, and the results show the energy-driven unloading process significantly affects the stress–strain evolution and failure characteristics of frozen soft rock. The peak strength increases under low confining pressure and decreases under high confining pressure. The elastic modulus first increases and then decreases with an increase in deviatoric stress (Li et al., 2018).

At present, the research on the loading–unloading mechanical properties of WCSR at room temperature is relatively sufficient (Zhao G. Y. et al., 2015; Fan et al., 2018; Wang et al., 2021); however, the loading–unloading mechanical properties of FWCSR are not sufficient, and the meso-failure mechanisms are not clear. Accordingly, several scholars have conducted qualitative analyses of mineral composition, micro-structure, and disintegration mechanisms of rocks using techniques including X-ray diffraction, scanning electron microscopy (SEM), and other microscopic observation methods. Research suggests that lithology, crystal structure, grain morphology, cement type, and clay mineral content are the key factors influencing the mechanical properties and failure mechanisms of rock (Zhao et al., 2023). Current research primarily aims to elucidate the microscopic influence of porosity on the strength of FWCSR (Qu et al., 2023). In our previous studies on the failure mechanisms of FWCSR (Liu et al., 2023; Lyu et al., 2024), we have identified a correlation between macroscopic failure characteristics and the development of microscopic fracture patterns. However, the macro and micro failure mechanisms of FWCSR under the unloading path are unclear and require further study.

Rock strength criterion has strong specificity. The strength criterion between different rocks is seriously affected by diagenesis, stress state, and internal structure (Yang et al., 2019), and only by constructing the strength criterion under the unloading path can the ultimate stress state of rock failure be better described. Many scholars have investigated different types of rocks. They pointed out that the non-linear Mohr strength criterion can be used as the strength criterion of rock failure in conventional triaxial loading–unloading tests (Wang et al., 2010; Zhao Y. C. et al., 2015; Zhou, 2020), and the linear Mohr–Coulomb strength criterion can be used as the strength criterion of rock failure in true triaxial loading–unloading tests (Liu S. et al., 2020; Feng et al., 2021; Lu et al., 2021). However, the current research mainly focuses on common rocks, and few reports present the research on the strength criterion of WCSR. Research on the strength criterion of FWCSR under loading–unloading tests is scarce, leading to a lack of applicable strength criterion for rock failure in engineering practice.

In this paper, the triaxial unloading test of FWCS is carried out, the stress–strain evolution under unloading conditions is obtained, and its mechanical characteristics are analyzed. The meso-failure mechanism of rock is analyzed using the FEI Quanta 450 field emission scanning electron microscope. Based on the experimental data, three non-linear strength criteria of FWCS are established, and the strength criterion is evaluated using the ordinary least squares. It is expected that the findings of this study can provide theoretical guidance for underground engineering in frozen weakly cemented strata.

2 Test overview

2.1 Specimen preparation

The weakly cemented sandstone specimens used in this paper were taken from the same area of weakly cemented strata in Mengcun, Xi'an. They are symmetrical, no cracks, fewer impurities, and good integrity. The specimen is a cylinder of Φ50 mm × 100 mm. The non-parallelism of the two ends of the specimen is

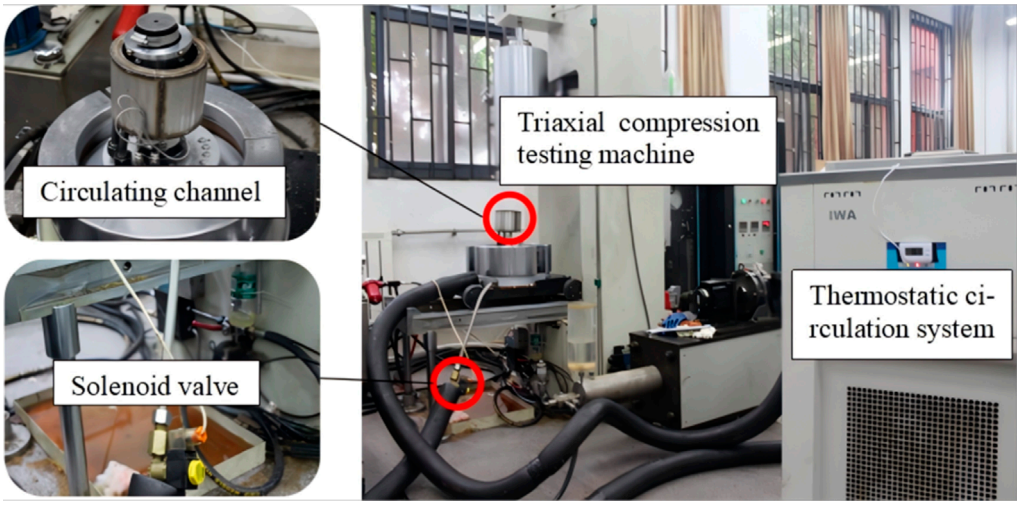

FIGURE 1
TAW-2000 low temperature triaxial test system.

controlled within 0.05 mm, the diameter error is not more than 0.3 mm, and the angle between the normal line of the end face and the axis of the specimen is not more than 0.25° (GB/T 50266-99, 2013).

2.2 Test scheme

First, the sandstone specimens were placed in the DWX low-temperature freezing test chamber at −10°C for 48 h and then taken out for the next test step. The TAW-2000 constant temperature triaxial test system is selected to conduct the test, as shown in Figure 1. The initial confining pressures of triaxial unloading (σ_3, σ_2=σ_3) were set at three levels: 3, 6, and 10 MPa. In addition, the conventional triaxial test is also conducted with the same confining pressures (3, 6, and 10 MPa) and loading rates for comparative analysis.

During the excavation of artificial frozen ground, stress redistribution leads to an increase in circumferential stress and a decrease in radial stress. Based on this, the triaxial unloading test program is designed, which mainly comprises three stages: (1) increase the confining pressure σ_3 to the predetermined value (3, 6 ,and 10 MPa) with a loading rate of 0.05 MPa/s; (2) increase the axial pressure σ_1 to 70~80% of the peak strength with a loading rate of 0.02 mm/min through displacement control (the strength is greater than the uniaxial compressive strength); and (3) decline the confining pressure with a rate of 0.05 MPa/s and increase the axial pressure with a rate of 0.02 mm/min through displacement control until sample failure. The stress path diagram is shown in Figure 2.

The thermostatic circulation system was turned on to maintain the temperature at −10°C during the test. After the test, FEI Quanta 450 Field Emission Scanning Electron Microscope was used to scan the meso-structure of the FWCS fracture surface. Subsequently, the meso-structure of rock specimens was observed and analyzed.

3 Test results and analysis

3.1 Stress–strain curve and analysis

The stress–strain (axial, lateral, and bulk) curves of FWCS subjected to various initial confining pressures are depicted in Figure 3 during conventional triaxial compression tests.

Under various confining pressures, the stress–strain curves of FWCS manifest distinct elastic–plastic phases. As the confining pressure increases, the elastic stage gradually shortens, while the plastic stage gradually prolongs. Correspondingly, the principal stress difference increases when the volume strain of the rock sample changes from compression to expansion. The turning point stress difference increases from 50 MPa at an initial confining pressure of 3 MPa to 68 MPa at a confining pressure of 10 MPa. Under low confining pressure, the dilatancy of FWCS is notable. Under high confining pressure, the expansion phenomenon is relatively minor. This is because microfractures are more prone to develop in weakly consolidated sandstones with lower confining pressure, leading to an increase in volume. However, at higher confining pressure, the development of microcracks is restricted, resulting in a relatively small expansion phenomenon. With the growth of confining pressure, the yield strength of weakly cemented sandstone gradually decreases, and the yield strain gradually increases. The elastic modulus and Poisson's ratio of FWCS also vary under different confining pressures.

Triaxial unloading deviatoric stress–strain (axial, lateral, and volumetric) curves of FWCS with different initial confining pressures are shown in Figure 4.

FWCS, under various confining pressures, exhibits distinct brittle failure characteristics. As the test proceeds, the axial and lateral strain increase, and the body strain shifts from positive to negative. Before unloading, sandstone undergoes an elastic–plastic stage, during which the main fracture is gradually closed and compressed, and the secondary fracture forms in the plastic stage.

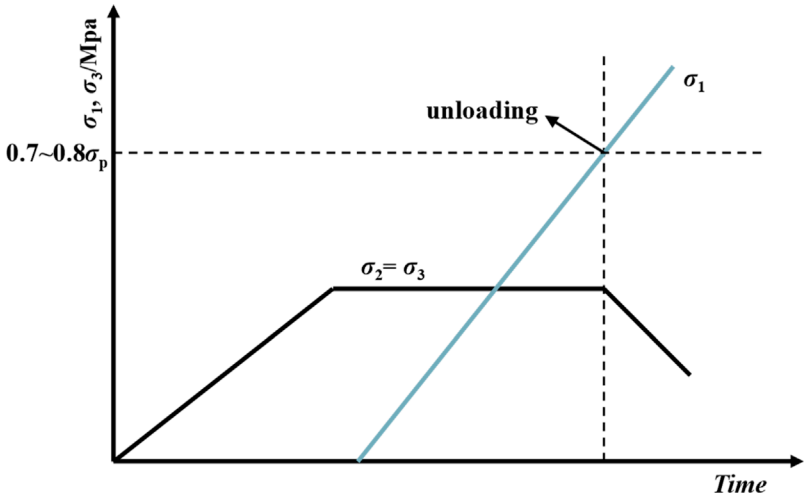

FIGURE 2
Stress path diagram.

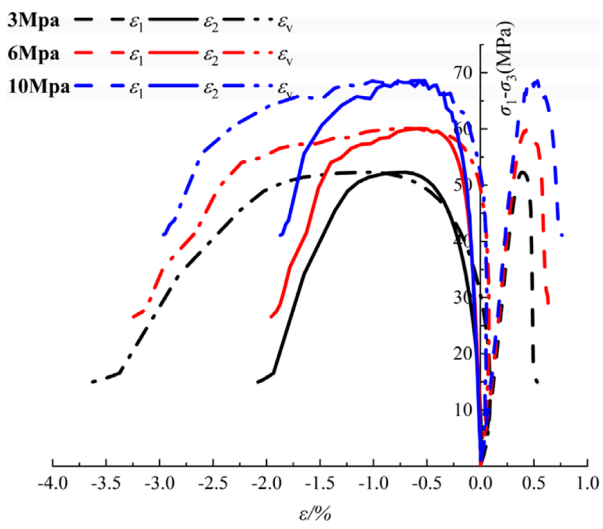

FIGURE 3
Conventional triaxial compressive stress–strain curve of FWCS.

The lateral strain increases rapidly, and the bulk strain decreases. The higher the confining pressure is, the more pronounced the inhibitory effect on secondary cracks becomes. At the onset of unloading, axial, lateral, and volumetric strains all present different "inflection points," with those of lateral strain and volumetric strain being more evident. The lateral and bulk strain curves are relatively prominent, and the lower the confining pressure, the more conspicuous the decrease. Additionally, the lateral deformation of the rock sample increases rapidly at the beginning of confining pressure relief, and the bearing capacity of the rock sample decreases sharply when its strength exceeds the peak value of the principal stress difference. Taking the initial confining pressure of 6 MPa as an example, when the peak value of the principal stress difference is exceeded, the principal stress difference decreases directly from 48 MPa to 13 MPa, and the corresponding lateral strain value increases from −0.5% to −1.8%. The volume strain value increases from −0.4% to −2.6%, and the dilatation characteristics of rock samples are notable, indicating that the confining pressure relief of the unloading shaft before the peak accelerates the deformation and failure of rock samples. With axial loading and unloading of the confining pressure, the deviational stress gradually increases and reaches the ultimate bearing strength, the higher the initial confining pressure, the greater the ultimate bearing strength. Subsequently, the stress decreases significantly, the deviational stress decreases rapidly, the rock sample softens rapidly, the bearing capacity decreases rapidly, and the expansion volume continues to increase. After the peak strain, the rock sample loses its bearing capacity. The higher the residual confining pressure, the greater the inhibitory effect on the propagation of secondary cracks, the smaller the peak strain, and the greater the residual strength.

The stress–strain (axial and bulk) curves of conventional triaxial compression tests and triaxial unloading confining pressures of FWCS under different initial confining pressures are shown in Figure 5.

The stress–strain (axial) curve of FWCS under the conventional triaxial compression test and triaxial unloading test at different initial confining pressures shows a consistent trend during the initial densification stage.

Under conventional triaxial conditions, with increases in the initial confining pressure, the axial strain values increase, respectively, from 0.38%, 0.47%, 0.55%–0.52%, 0.69%, and 0.77%. The volume strain values increase, respectively, from −0.75%, −0.2%, −0.15% to −3.68%, −3.25%, and −3.1%. Additionally, with the increase in axial stress, the stress–strain relationship of the rock turns non-linear, and the axial curve begins to bulge and tends to be horizontal. The main reason for non-linear deformation is the formation and development of micro-cracks in the rock. Meanwhile, the lateral strain increases rapidly and dominates, causing the rock to expand.

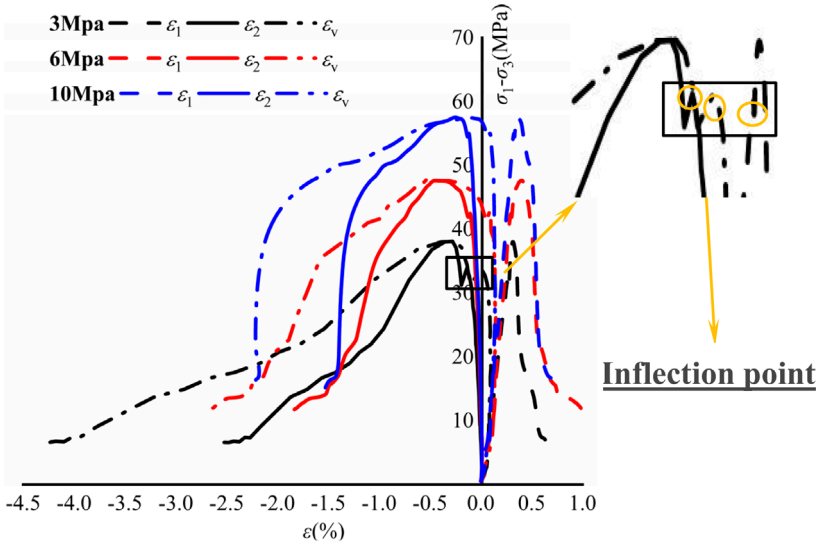

FIGURE 4
Triaxial unloading deviatoric stress–strain curve of FWCS.

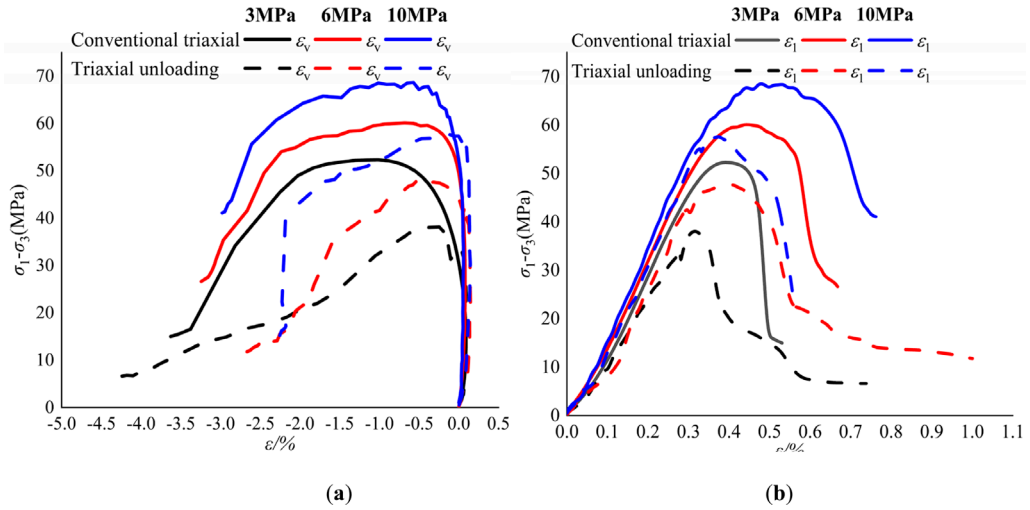

FIGURE 5
Stress–strain (axial and bulk) curves of conventional triaxial compression tests and triaxial unloading confining pressures: **(A)** Stress–strain (bulk) curve and **(B)** stress–strain (axial) curve.

Under the triaxial unloading confining pressure condition, the strain curve of the rock sample exhibits a stress decrease with a small amplitude, and the axial strain of the rock sample does not vary significantly. This occurs because when the confining pressure is released, the control mode switches to maintain displacement, which, in turn, reduces the axial pressure and the principal stress difference of the rock sample. The lower the initial confining pressure, the more pronounced the stress decrease in the stress–strain curve. During the unloading stage, as the confining pressure continuously decreases, the deviatoric stress increases again. Although the axial strain remains essentially unchanged, a slight reduction in the confining pressure leads to a rapid increase in the volumetric strain. The confining pressure continues to decrease until the rock sample exceeds the peak point. At this stage, the bearing capacity of the rock sample decreases rapidly, the rock sample expands vigorously along the unloading direction, the rock sample strain surges, and the axial strain values increase, respectively, from 0.33%, 0.43%, 0.35%–0.72%, 1%, and 0.6%. The volumetric strain values increase, respectively, from −0.25%, −0.5%, 0.1% to −4.4%, −2.75%, and −2.25%. The rock samples expanded sharply along the unloading direction, and the brittle failure characteristics were more pronounced than those of conventional loading tests. When the peak strain is reached, the rock sample loses its bearing capacity.

TABLE 2 Deformation parameters under various stress paths of FWCS.

	Peak stress /MPa		Strain at unloading/%		Strain at time of failure/%	
	σ_p	σ_3	ε_1	ε_3	ε_1	ε_3
Conventional triaxial	55.29	3	—	—	0.46	−1.24
	66.11	6	—	—	0.57	−1.40
	78.53	10	—	—	0.61	−1.16
Triaxial unloading	43.5	3	0.28	−0.19	0.33	−0.48
	58.1	6	0.30	−0.19	0.42	−0.50
	78.0	10	0.36	−0.21	0.38	−0.26

3.2 Analysis of the failure strength characteristics of triaxial unloading

According to the above analysis, in the loading state, the stress of the rock gradually increases to its peak strength and failure occurs, while in the unloading process, the deviational stress of the rock does not reach its peak strength. In order to quantitatively analyze the influence of triaxial unloading on the strength characteristics of FWCS, Mohr-Coulomb strength criterion was used to determine the strength parameters, and the obtained results were shown in Table 1. Among them, the peak strength level of rock failure during unloading is expressed by the ultimate bearing strength σ_p.

It can be observed from the data in Table 1 that the strength of FWCS along three axial confining paths under different initial confining pressures shows an obvious confining effect. The confining amounts under 3 MPa, 6 MPa, and 10 MPa confining pressures are 53.6%, 44.2%, and 44.9%, respectively. According to the state of residual stress, the residual stress of the rock sample under the triaxial unloading path is the smallest, which indicates that the plastic deformation of the rock sample under this path is larger..

Compared with the conventional triaxial compression tests, the cohesion of the triaxial unloading rock sample decreases by approximately 27%, while the internal friction angle increases by approximately 5.1%. The greater the cohesion, the stronger the tensile resistance of the rock; the greater the internal friction angle, the stronger the shear resistance of the rock and, the more stable the rock.

3.3 Analysis of the deformation characteristics of triaxial unloading

In order to quantitatively analyze the deformation characteristics of rock samples under triaxial loading, the axial and volumetric strain data of each initial confining pressure of FWCS under different stress paths are shown in Table 2.

It can be observed from Table 2 that the axial and lateral strains of rock samples under the unloading stress path are smaller than those under the loading stress path, indicating a reduction in the deformation resistance of rocks. Moreover, it is observed that as the initial confining pressure decreases, the axial strain of rock samples during conventional triaxial failure increases, while the lateral strain during both triaxial unloading and conventional triaxial failure decreases. In terms of triaxial unloading, it is noted that the applied peak axial stress does not reach the ultimate strength capacity of rocks. Additionally, lower initial confining pressures result in smaller applied peak axial stresses and reduced susceptibility to failure for rock samples. As confinement progresses, internal cracks within rock samples fully develop, leading to larger lateral strains.

3.4 Macro-meso failure mechanism of weakly cemented sandstone under triaxial unloading

3.4.1 Macro-failure characteristics

The failure characteristics of rock have an obvious correlation with the stress path, and the failure forms of different stress paths are different. The macro-failure patterns of weakly cemented sandstone in triaxial unloading and conventional triaxial are shown in Figure 6.

As shown in Figure 6, there is a main fracture and no incomplete fracture on the surface of the specimen in the triaxial unloading test. The rock specimen exhibits shear failure as the dominant mode, with the shear characteristics being more obvious. When the initial confining pressure is 3 MPa, the main fracture penetrates both ends of the rock specimen. As the initial confining pressure increases, the main fracture no longer penetrates both ends of the rock specimen, and the left and right parts of the main fracture surface are obviously dislocated. Similar to the conventional triaxial test, a large amount of rock powder and a small amount of rock fragments are attached to the main fracture surface, but the rock powder and rock fragments in the triaxial unloading test are more than those in the conventional triaxial test. The higher the initial confining pressure, the more rock powder and rock fragments on the fracture surface. The reason for this phenomenon is that during the continuous axial loading process, the confining pressure decreases, which is equivalent to the lateral tension applied to the rock specimen; as the lateral inhibition to the rock specimen

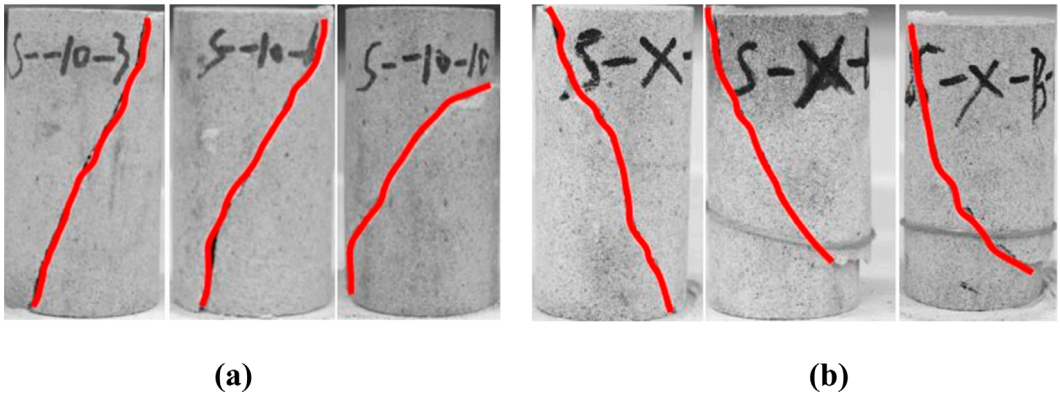

FIGURE 6
Macro-failure characteristics of FWCS: **(A)** conventional triaxial and **(B)** triaxial unloading.

weakens, the friction between particles decreases, making it easier for the particles on the fracture surface to fall off. Furthermore, the expansion phenomenon gradually intensifies as the lateral inhibition weakens. Similar to the conventional triaxial test, the angle between the main fracture surface and the axis of the rock specimen increases with the initial confining pressure. However, under the same initial confining pressure, the angle between the main fracture surface and the axis of the rock specimen in the triaxial unloading test is smaller than that in the conventional triaxial test, and the brittle failure characteristics of rock in the triaxial unloading test are more pronounced than those observed in the conventional triaxial test.

In the triaxial unloading test, the corresponding maximum principal stress σ_1 increases continuously, and the minimum principal stress σ_3 decreases continuously due to continuous axial loading and lateral unloading. According to the Mohr–Coulomb yield criterion, the center of Mohr's circle is $(\sigma_1+\sigma_3)/2$, and the radius is $(\sigma_1-\sigma_3)/2$. As shown in Figure 7, because the unloading rate of the confining pressure is less than the axial loading rate, the center of Mohr's circle gradually shifts to the right. However, the radius of Mohr's circle increases rapidly. Thus, the yield limit is reached quickly, and the rock specimen showed brittle tensile-shear failure. The higher the initial confining pressure, the greater the residual confining pressure and the stronger the inhibition effect on the lateral deformation of the rock specimen. Therefore, the higher the initial confining pressure, the less obvious the tensile failure characteristics of the rock specimens.

3.4.2 Meso-failure characteristics

The deformation and failure of rock materials are products of microcrack evolution (Wang S. et al., 2020). From the point of view of fracture mechanics, the formation of macroscopic failure surfaces of rock is mainly due to the drive of external load and the generation and expansion of internal cracks and their interaction. The meso-fracture morphology can qualitatively reflect the meso-failure mechanism of rock (Fu et al., 2022; Wu et al., 2020; Niu et al., 2021). Typical fractures under different paths are shown in Figure 8.

As shown in Figure 8, the meso-fracture morphology of triaxial unloading and conventional triaxial have some similarities, showing areas that are locally flat and locally rough, and because of the existence of the primary pores, cracks, and the shear slide friction of the rock specimen, some particles fall off and break, creating local unevenness and causing the rock particles to attach to the surface.

For triaxial unloading, when the initial confining pressure is 3 MPa, the meso-fracture of FWCS is mainly intergranular, with localized transgranular fractures. Because of the low confining pressure, the pores inside the rock are relatively large, resulting in shear slip cracks, with shear failure characteristics being obvious. Shedding particles and debris are present in the main crack, and a few cracks are perpendicular to the main crack, indicating that tensile failure in the main crack is accompanied by shear failure during unloading. When the initial confining pressure is 6 MPa, many intergranular fractures are randomly distributed around the main crack; these intergranular fractures only produce cracks due to the longitudinal adhesion of some particles. Some particles fall off and fill the main crack due to the weak longitudinal bonding force between particles, and there are transgranular fractures in some places. The tensile failure characteristics still exist. When the initial confining pressure is 10 MPa, intergranular fractures are clearly visible, higher pressure aggravates the particles falling off. A transgranular fracture refers to a fracture mode in which the crack spreads through the grain inside the crystal in the form of tearing. A intergranular fracture is a type of the fracture mode in which the crack expands along the grain boundary when the material is fractured. Several cracks are perpendicular to the main fracture surface, indicating that during unloading, tensile failure within the main fracture surface transitions to shear failure. This further confirms a shear-dominated, shear-tensile combined failure mechanism. Under low magnification, a "Basin" structure appears locally, with numerous pieces of debris of different sizes. Under high magnification, a step pattern can be clearly observed, the width of the main crack increases, corresponding to the dislocation of the fracture surface, while secondary cracks are not developed, and the tensile failure characteristics are not obvious.

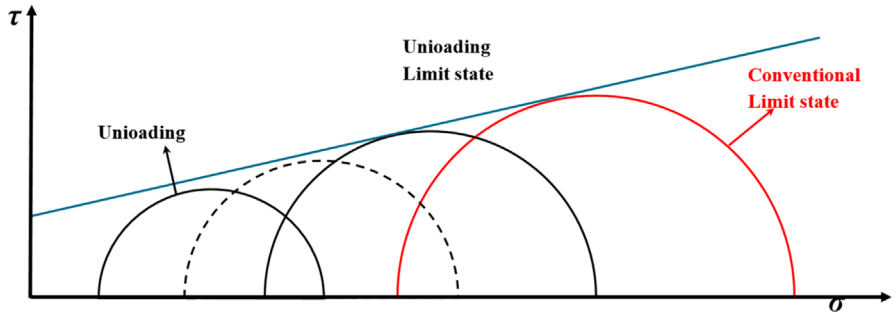

FIGURE 7
Triaxial unloading stress state diagram.

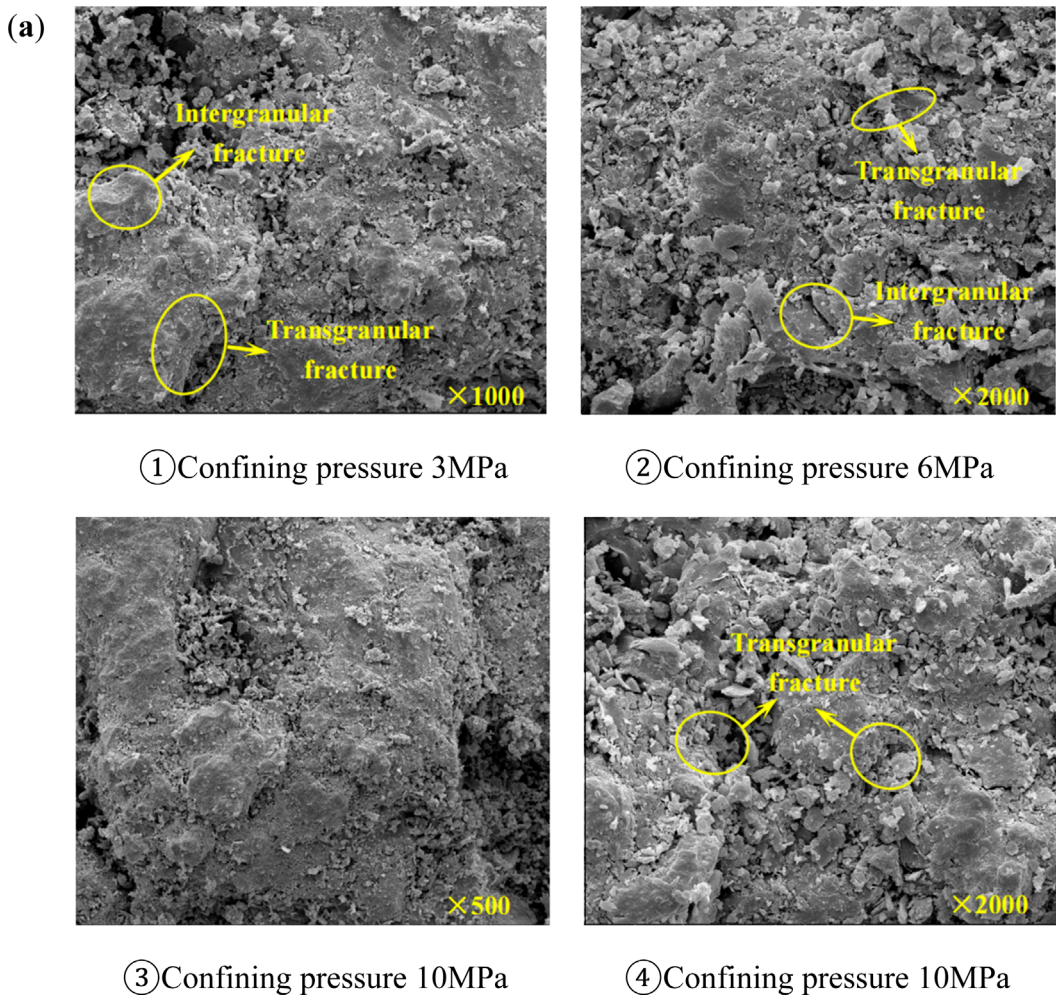

FIGURE 8
(Continued).

With an increase in the initial confining pressure, the tensile failure characteristics of rock specimens gradually weaken. The transgranular failure effect also gradually weakens except for the main crack, and the amount of rock debris and rock particles increase gradually. In addition, there are some differences between triaxial unloading and conventional triaxial tests. Under the same (initial) confining pressure, the size of debris and particles attached to the conventional triaxial meso-surface is smaller than that in the triaxial unloading test. As the confining pressure decreases, the interlocking and cementation strength

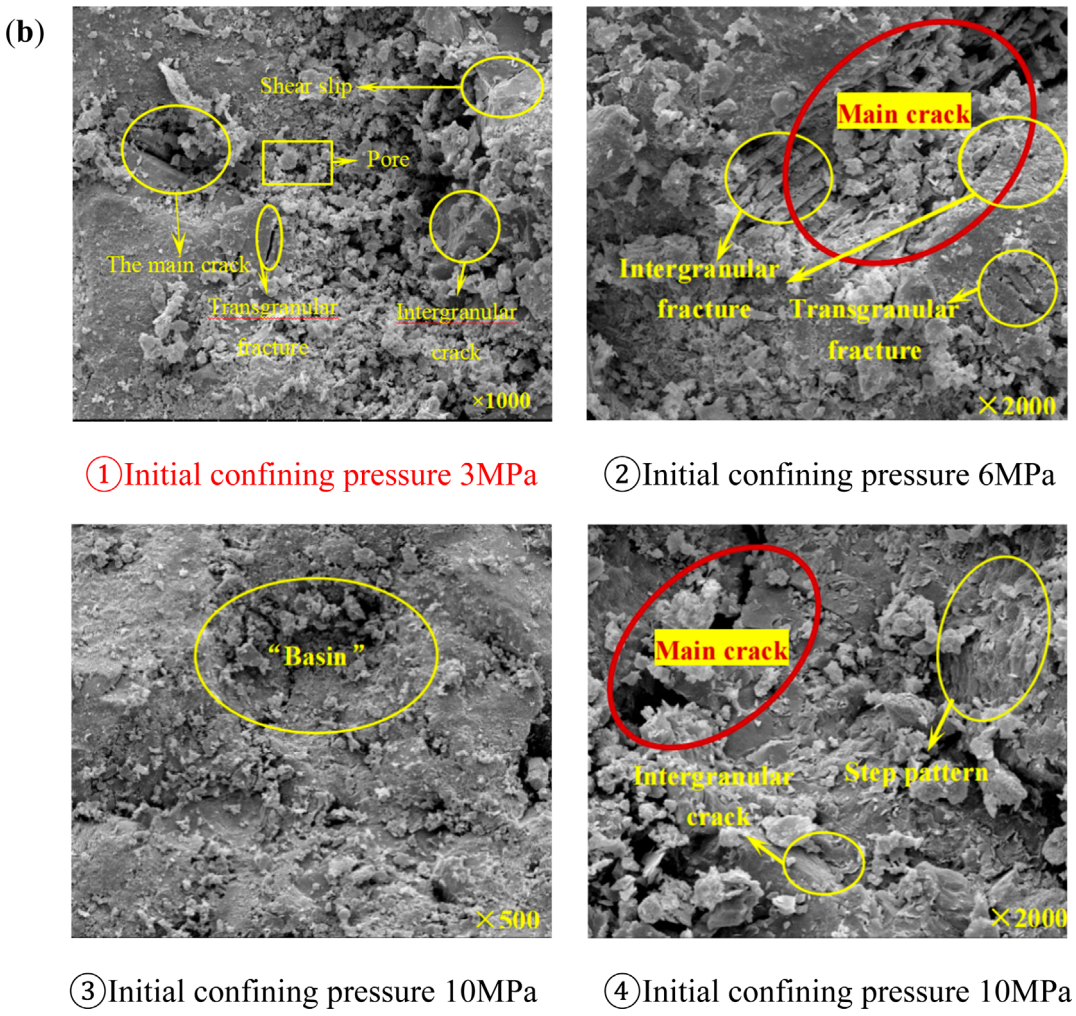

FIGURE 8
(Continued). Meso-fracture morphology of FWCS: **(A)** conventional triaxial and **(B)** triaxial unloading.

between particles weakens, making it more prone to large rock debris spalling. Furthermore, no main cracks are found on the conventional triaxial meso-surface, while unloading causes the meso-structure to be more prone to large-scale, connected failures.

Combined with the macro-failure analysis, the rock samples under triaxial unloading show a tensile-shear failure form under low initial confining pressure in a macro-view, which gradually transforms into shear-tensile failure as the confining pressure increases. This indicates that the shear failure is closely related to the transgranular fracture of rock, while the tensile failure is closely related to the intergranular fracture. After unloading to a certain extent, when the shear-tensile stress in the rock sample exceeds the maximum tensile stress that the rock particle bonding and the ice crystal itself and the contact surface can withstand, cracks commence and spread gradually. At this point, lateral deformation increases rapidly, which eventually leads to the brittle failure of the rock sample. The mesoscopic rock debris corresponds to the rock powder and fragments found on the macro-fracture surface.

4 Triaxial unloading strength characteristics and criterion of frozen weakly cemented sandstone

4.1 Triaxial unloading strength characteristics of frozen weakly cemented sandstone

The stress value of FWCS is shown in Table 3.

As shown in Table 3, $\sigma_u < \sigma_p$, which proves that confining pressure unloading reduces the bearing capacity of rock, making rock specimens more susceptible to destruction (Hu et al., 2022); this defines the unloading stress ratio λ_i. This is shown in Equation 1.

$$\lambda_i = \frac{\sigma_{i|u}}{\sigma_{i|c}} \times 100\% \, (i = 1, 3), \tag{1}$$

where λ_i, $\sigma_{i|u}$, and $\sigma_{i|c}$ are the unloading stress ratio, principal stress of triaxial unloading of rock failure, and principal stress of conventional triaxial of rock failure, respectively; when subscript i is 1, it represents the maximum principal stress, and when i is 3,

10.3389/feart.2024.1518849

TABLE 1 Conventional triaxial compression test and triaxial unloading confining pressure strength characteristic value of FWCS.

	Peak stress /MPa		Unloading stress /MPa		Failure stress /MPa		Residual stress /MPa		Cohesive force/MPa	Internal friction angle/(°)
	σ_p	σ_3	σ_1	σ_3	σ_1	σ_3	σ_1	σ_3	c	φ
Conventional triaxial	55.29	3	—	—	51.94	3	16.20	3	9.88	39
	66.11	6	—	—	60.04	6	25.49	6		
	78.53	10	—	—	75.77	10	41.98	10		
Triaxial unloading	43.5	3	33.85	3	38.13	1.39	6.60	1.39	7.23	41
	58.1	6	42.48	6	47.71	3.35	12.05	3.35		
	78.0	10	55.28	10	57.73	5.51	15.93	5.51		

(Note: Peak stress is the ultimate stress state in the triaxial compression test. Unloading stress, failure stress, and residual stress are the stress states of unloading, destruction, and residual stage in the triaxial unloading test, respectively).

TABLE 3 Stress value of FWCS.

Peak stress/MPa		Unloading stress/MPa		Failure stress/MPa		Residual stress/MPa	
σ_p	σ_3	σ_1	σ_3	σ_u	σ_3	σ_1	σ_3
43.5	3	33.85	3	38.13	1.39	6.60	1.39
58.1	6	42.48	6	47.71	3.35	12.05	3.35
78.0	10	55.28	10	57.73	5.51	15.93	5.51

TABLE 4 Unloading stress ratio of FWCS.

Unloading stress ratio	Initial confining pressure/MPa		
	3	6	10
λ_1	87.66%	82.17%	74.01%
λ_3	46.33%	55.83%	55.10%

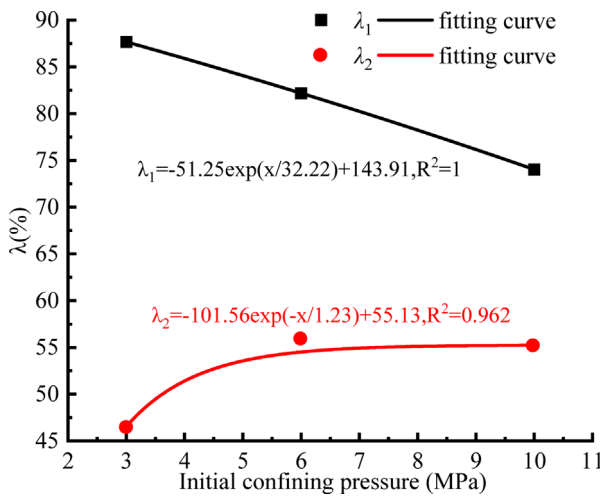

FIGURE 9
Unloading stress ratio of FWCS.

it represents the minimum principal stress. The unloading stress ratio under different initial confining pressures can be obtained, as shown in Table 4.

The data in Table 4 are plotted and fitted to obtain Figure 9.

It can be observed that there is an exponential function relationship between the initial confining pressure and the unloading stress ratio. According to the fitting relationship, as the initial confining pressure increases, the maximum principal stress of unloading decreases, and the minimum principal stress ratio of unloading increases.

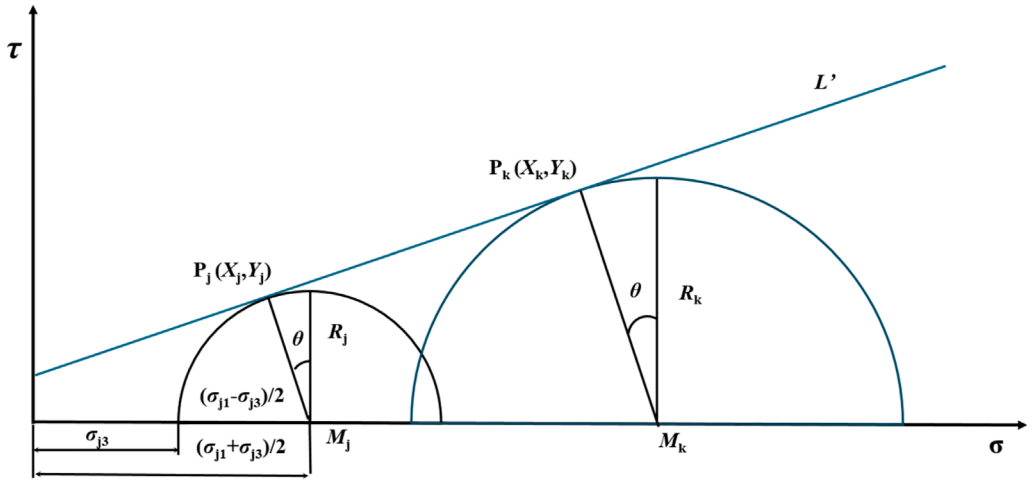

FIGURE 10
Common tangent and tangent point coordinates of arbitrary two Mohr's circles.

For FWCS, the following relationship exists.

$$\begin{cases} \sigma_u = \sigma_p\left[51.25\exp\left(\sigma_{3|i}/32.22\right)+143.91\right] \\ \sigma_{3|r} = \sigma_{3|i}\left[101.56\exp\left(\sigma_{3|i}/1.23\right)+55.13\right] \end{cases}. \tag{2}$$

Extending Equation 2 to other types of FWCSR, we obtain

$$\begin{cases} \sigma_u = \sigma_p\left[A\exp\left(\sigma_{3|i}/B\right)+C\right] \\ \sigma_{3|r} = \sigma_{3|i}\left[D\exp\left(-\sigma_{3|i}/E\right)+F\right] \end{cases}. \tag{3}$$

In Equations 2, 3, σ_u is the ultimate triaxial unloading bearing strength; σ_p is the peak strength of conventional triaxial loading; $\sigma_{3|r}$ and $\sigma_{3|i}$ are triaxial unloading residual confining pressure and initial confining pressure, respectively; *A, B, C, D, E,* and *F* are the parameters related to the test, respectively.

4.2 Triaxial unloading strength criterion of frozen weakly cemented sandstone

Assuming that the maximum principal stress is σ_{i1} and the corresponding minimum principal stress is σ_{i3} when rock failure occurs, the abscissa of the center and the radius of any Mohr's circle are as follows in Equation 4:

$$\begin{cases} M_i = (\sigma_{i1}+\sigma_{i3})/2 \\ R_i = (\sigma_{i1}-\sigma_{i3})/2 \end{cases}, \tag{4}$$

where M_i and R_i are the abscissa of the center and the radius of any Mohr's circle, respectively. Two Mohr's circles and their common tangent should be drawn as shown in Figure 10.

In Figure 10, P_j (X_j, Y_j) and P_k (X_k, Y_k) are tangent points on any two non-nested Mohr's circles and L' is the common tangent. According to the geometric relationship, Equation 5 can be written as follows:

$$\begin{cases} X_j = M_j - R_j\sin\theta, Y_j = R_j\cos\theta \\ X_k = M_k - R_k\sin\theta, Y_k = R_k\cos\theta \end{cases}. \tag{5}$$

Among them,

$$\sin\theta = \frac{R_k - R_j}{M_k - M_j}. \tag{6}$$

Equation 5 can be written as

$$\begin{cases} X_j = M_j - R_j\dfrac{R_k-R_j}{M_k-M_j}, Y_j = R_j\cos\left(\arcsin\dfrac{R_k-R_j}{M_k-M_j}\right) \\ X_k = M_k - R_k\dfrac{R_k-R_j}{M_k-M_j}, Y_k = R_k\cos\left(\arcsin\dfrac{R_k-R_j}{M_k-M_j}\right) \end{cases}. \tag{7}$$

Combining Equations 6, 7, in the case of obtaining two groups of maximum and minimum principal stresses when rock specimens are destructed, the inclination angle, tangent point coordinates, and the expression of common tangent line can be obtained. Assuming that there are k $(k \geq 2)$ groups of Mohr's circles, the number of common tangent points on any two Mohr's circles can be obtained as shown in Equation 8.

$$N = 2C_k^2 = k(k-1), \tag{8}$$

where N and C are the number of common tangent points on any two Mohr's circles and combination operation symbol, respectively. Assuming the fitting relationship of the strength envelope for the triaxial unloading test of the FWCS is an n-order polynomial, it can be expressed as the Equation 9

$$\psi(X) = \zeta_0 + \zeta_1 X + \zeta_2 X^2 + \cdots + \zeta_n X^n = \sum_{i=1}^{n}\zeta_n X^n, \tag{9}$$

where ψ represents the shear stress τ, X represents the principal stress σ, and ζ_i (i=1, 2, 3, … , n) is the regression coefficient. According to the least-squares principle (Zeng, 2018),

$$J(\zeta_0,\zeta_1,\zeta_2,\ldots,\zeta_n) = \sum_{j=1}^{N}\left[\sum_{i=0}^{n}\left(\zeta_i X_j^i - Y_j\right)\right]. \tag{10}$$

Solving partial derivative of Equation 10,

$$\frac{\partial J}{\partial \zeta_i} = 2\sum_{j=1}^{N}\left[\sum_{i=0}^{n}\left(\zeta_i X_j^i - Y_j\right)X_j^i\right] = 0, i = 1,2,3,\ldots,n. \tag{11}$$

Let

$$\begin{cases} l_{ab} = \sum_{j=1}^{N} X_j^a X_j^b \\ q_a = \sum_{j=1}^{N} X_j^a Y_j \end{cases} \quad a, b = 0, 1, 2, \ldots, n. \tag{12}$$

Combining Equations 11, 12, it is expressed in the matrix form as follows:

$$\begin{bmatrix} \zeta_0 \\ \zeta_1 \\ \vdots \\ \zeta_n \end{bmatrix} = \begin{bmatrix} q_0 \\ q_1 \\ \vdots \\ q_n \end{bmatrix} \begin{bmatrix} l_{00} & l_{01} & \cdots & l_{0n} \\ l_{10} & l_{11} & \cdots & l_{1n} \\ \vdots & \vdots & \ddots & \vdots \\ l_{n0} & l_{n1} & \cdots & l_{nn} \end{bmatrix}^{-1}. \tag{13}$$

The envelope curve of any n-order polynomial can be fitted by Equation 13. Based on the data in Table 1, all the tangent points of Mohr's circles of the three sets of rock specimens are calculated as follows:

$$\begin{bmatrix} (6.72, 12.82) & (6.43, 12.53) \\ (10.06, 16.15) & (9.70, 15.78) \\ (13.87, 20.12) & (13.42, 19.66) \end{bmatrix}. \tag{14}$$

For the triaxial unloading test of FWCS, the non-linear Mohr–Coulomb strength criterion such as power function type, parabolic function type, and logarithmic function type are used for fitting.

4.2.1 Power function strength criterion

The fitting expression of the single parameter power function strength criterion can be expressed as the Equation 15 (Zhang and Yu, 2020)

$$\psi(X) = \zeta_0 + \zeta_1 X^{0.75}. \tag{15}$$

Let $X^{0.75}$=K; after the linear transformation of the matrix (Equation 14), ζ_0 = 2.69 and ζ_1 = 2.41 can be obtained according to the method described in Section 4.2. So, the power function strength criterion expression can be expressed as the Equation 16

$$\tau = 2.69 + 2.41\sigma^{0.75}. \tag{16}$$

4.2.2 Parabolic function strength criterion

Referring to the single parameter parabolic strength criterion (Bieniawski, 1974), the fitting expression of the parabolic function strength criterion can be expressed as the Equation 17

$$X = \zeta_0 + \zeta_1 \psi(X) + \zeta_2 \psi^2(X). \tag{17}$$

After the linear transformation of the matrix (Equation 14), ζ_0 = −7.359, ζ_1 = 1.175, and ζ_2 = −0.00598 can be obtained according to the method described in Section 4.2. Thus, the parabolic function strength criterion expression can be expressed as the Equation 18

$$\sigma = -0.00598\tau^2 + 1.175\tau - 7.359. \tag{18}$$

TABLE 5 Standard deviation and mean square deviation of non-linear strength criterion fitting curve.

Strength criterion	$\hat{S}$			SD
	3 MPa	6 MPa	10 MPa	
Power function	0.089	0.156	0.089	0.116
Parabolic function	0.195	0.205	0.213	0.204
Logarithmic function	0.170	0.728	0.219	0.450

4.2.3 Logarithmic function strength criterion

The fitting expression of the logarithmic function strength criterion can be expressed as the Equation 19 (Shi et al., 2015)

$$\psi(X) = \zeta_0 + \zeta_1 \ln X. \tag{19}$$

Let ln$X$ = W, after the linear transformation of the matrix (14), ζ_0 = −5.99 and ζ_1 = 9.80 can be obtained according to the method described in Section 4.2. Thus, the logarithmic function strength criterion expression can be expressed as the Equation 20

$$\tau = 9.80 \ln \sigma - 5.99. \tag{20}$$

4.2.4 Strength criterion evaluation

The standard deviation SD of the fitting envelope is used to evaluate the error of the strength criterion. The standard deviation calculation formula can be expressed as the Equation 21

$$SD = \sqrt{\frac{\sum_{j=1}^{N} (Y_j - \hat{Y}_j)^2}{N}}, \tag{21}$$

where Y_j, $\hat{Y}_j$, and N are the vertical ordinate of the tangent point of common tangent, the vertical ordinate corresponding to the abscissa of the tangent point in each strength criterion fitting curve, and the total number of tangent points, respectively. To determine the reliability of the test data, the mean square error $\hat{S}$ of all tangent points on any Mohr's circle can be calculated as follows in Equation 22:

$$\hat{S} = \sqrt{\frac{\sum_{i=1}^{n} (Y_i - \hat{Y}_i)^2}{n}}, \tag{22}$$

where Y_i, $\hat{Y}_i$, and n are the vertical ordinate of the tangent point of common tangent, the vertical ordinate corresponding to the abscissa of the tangent point in each strength criterion fitting curve, and the total number of tangent points on any Mohr's circle, respectively. The test data are proved reliable if $\hat{S} < 1.8\ SD$ (Guo et al., 2020). The standard deviation SD and mean square error $\hat{S}$ of the non-linear strength criterion fitting curve are shown in Table 5.

It can be observed from Table 5 that three non-linear strength criteria satisfy $\hat{S} < 1.8\ SD$, which proves that the test data are

very reliable. In the case of confining pressure of 3 MPa, the mean square error of the logarithmic function is slightly smaller than that of parabolic function. In other cases, given standard deviation or mean square error, the power function is the smallest, the parabolic function is the second, and the logarithmic function is the largest, which indicates that the power function strength criterion is the best criterion for the triaxial unloading failure of FWCS.

5 Conclusion

In this paper, the triaxial unloading test is carried out with FWCS as the research object. The stress–strain evolution of FWCS under triaxial unloading is clarified, and the macro-meso failure mechanism of FWCS under triaxial unloading is revealed. The strength criterion of FWCS is constructed and optimized by the least squares method, and the following conclusions are obtained:

(1) The axial, lateral, and volumetric strains bend to different degrees because of confining pressure unloading. The stress–strain curve is no longer smooth, and the lateral expansion and volume expansion are obvious. The larger the initial confining pressure, the smaller the peak strain, and the greater the ultimate bearing strength and residual strength. Compared with the conventional loading peak strength, the higher the initial confining pressure, the greater the difference between the ultimate bearing strength and the peak strength.

(2) The meso-failure of the specimen is mainly characterized by intergranular and transgranular fractures, with the intergranular fracture being dominant, and there are a lot of particles and rock debris on the meso-fracture surface. The lower the initial confining pressure, the more obvious the transgranular fracture and the tensile characteristics. With an increase in the initial confining pressure, transgranular fractures gradually decreased, tensile characteristics weakened, and debris and particles on the meso-fracture surface gradually increased. Under the condition of low initial confining pressure, the mesoscopic tensile failure characteristics make the specimen show tensile-shear failure, and the main fracture penetrates both ends of the rock specimen. With an increase in the initial confining pressure, the mesoscopic tensile characteristics weaken, so the macro-failure of the rock gradually transforms into shear-tensile failure, and rock debris and particles are macroscopically manifested as rock powder and rock fragments.

(3) With an increase in the initial confining pressure, the unloading maximum principal stress ratio decreases and the unloading minimum principal stress ratio increases. The relations between σ_u, σ_p, $\sigma_{3|i}$, and $\sigma_{3|r}$ are constructed, and the applicability of the power function, parabolic function, and logarithmic function strength criterion for triaxial unloading of FWCS is analyzed. The results show that the power function strength criterion can best reflect the triaxial unloading mechanical properties of frozen weakly cemented sandstone.

Data availability statement

The original contributions presented in the study are included in the article/Supplementary Material; further inquiries can be directed to the corresponding author.

Author contributions

QD: project administration, supervision, validation, writing–original draft, and writing–review and editing. HF: conceptualization, data curation, methodology, supervision, validation, writing–original draft, and writing–review and editing. JW: data curation, project administration, writing–original draft, and writing–review and editing. XA: software, supervision, validation, visualization, and writing–review and editing. XL: data curation, formal analysis, supervision, validation, and writing–review and editing.

Funding

The author(s) declare that no financial support was received for the research, authorship, and/or publication of this article.

Acknowledgments

The authors wish to acknowledge the support of the Department of College of Earth Science and Engineering of the Shandong University of Science and Technology and the Longshou Mine of Jinchuan Group Co.

Conflict of interest

Author JW was employed by Longshou Mine of Jinchuan Group Co., Ltd.

The remaining authors declare that the research was conducted in the absence of any commercial or financial relationships that could be construed as a potential conflict of interest.

Generative AI statement

The author(s) declare that no Generative AI was used in the creation of this manuscript.

Publisher's note

References

Bai, Y., Shan, R. L., Ju, Y., Wu, Y. X., Sun, P. F., and Wang, Z. N. (2020). Study on the mechanical properties and damage constitutive model of frozen weakly cemented red sandstone. *Cold. Reg. Sci. Technol.* 171, 102980. doi:10.1016/j.coldregions.2019.102980

Bieniawski, Z. T. (1974). Estimating the strength of rock materials. *J. S. Afr. I. Min. Metall.* 74, 312–320.

Cai, J. L., and Zou, W. (2020). Triaxial compressive failure characteristics and constitutive model study of jurassic-cretaceous weakly cemented sandstone. *Adv. Civ. Eng.* 2020, 8812575. doi:10.1155/2020/8812575

Chen, Z. Q., He, C., Dong, W. J., Ma, G. Y., Pan, X. Y., and Pei, C. Y. (2018). Physico-mechanical properties and its energy damage evolution mechanism of the Jurassic and Cretaceous argillaceous sandstone in Northern Xinjiang. *Rock. Soil. Mech.* 39, 2873–2885. doi:10.16285/j.rsm.2018.0212

Dong, X. H., Yang, G. S., Tian, J. F., Rong, T. L., Jia, H. L., and Liu, H. (2018). Characteristics of deformation properties of frozen sandstone under lateral unloading condition. Rock. *Soil. Mech.* 39, 2518–2526. doi:10.16285/j.rsm.2017.1299

Fan, G. W., Chen, M. W., Zhang, D. S., Wang, Z., Zhang, S. Z., Zhang, C. G., et al. (2018). Experimental study on the permeability of weakly cemented rock under different stress states in triaxial compression tests. *Geofluids* 2018, 1–9. doi:10.1155/2018/9035654

Feng, F., Chen, S. J., Wang, Y. J., Huang, W. P., and Han, Z. Y. (2021). Cracking mechanism and strength criteria evaluation of granite affected by intermediate principal stresses subjected to unloading stress state. *Int. J. Rock. Mech. Min. Sci.* 143, 104783. doi:10.1016/j.ijrmms.2021.104783

Fu, X. D., Du, Y. X., Sheng, Q., Zhang, Z. P., and Huang, J. H. (2022). Influences of water on the microstructure and mechanical behavior of the Xigeda formation. *Bull. Eng. Geol. Environ.* 81, 72. doi:10.1007/s10064-022-02567-5

GB/T 50266-99 (2013). Standard for test methods of engineering rock mass. Available at: https://www.codeofchina.com/standard/GBT50266-2013.html (Accessed October 1, 2013).

Guo, B. H., Wang, L., Li, Y. Z., and Chen, Y. (2020). Triaxial strength criteria in Mohr stress space for intact rocks. *Adv. Civ. Eng.* 2020, 8858363. doi:10.1155/2020/8858363

Hadi, A., and Ali, M. (2018). The influence of mean grain size on unconfined compressive strength of weakly consolidated reservoir sandstones. *J. Petrol. Sci. Eng.* 171, 63–70. doi:10.1016/j.petrol.2018.07.029

Hu, X. Z., Li, Q. B., Wu, Z. M., and Yang, S. T. (2022). Modelling fracture process zone width and length for quasi-brittle fracture of rock, concrete and ceramics. *Eng. Fract. Mech.* 259, 108158. doi:10.1016/j.engfracmech.2021.108158

Li, T., Ma, Y. J., Liu, B., Sheng, H. L., and He, P. (2018). Strength characteristics and elastic modulus evolution of frozen gray sandstone under cyclic loading. *J. China. Coal. Soc.* 43, 2438–2443. doi:10.13225/j.cnki.jccs.2018.0482

Li, X. B., Chen, Z. H., Weng, L., and Li, C. J. (2019). Unloading responses of pre-flawed rock specimens under different unloading rates. *T. nonferr. Metal. Soc.* 29, 1516–1526. doi:10.1016/s1003-6326(19)65059-4

Liu, J., Lyu, X., Liu, Y., and Zhang, P. (2023). Energy evolution and macro-micro failure mechanisms of frozen weakly cemented sandstone under uniaxial cyclic loading and unloading. *Cold Reg. Sci. Technol.* 214, 103947. doi:10.1016/j.coldregions.2023.103947

Liu, J. S., Jing, H. W., Meng, B., Wang, L. G., Yang, J. J., and Zhang, X. F. (2020). A four-element fractional creep model of weakly cemented soft rock. *Bull. Eng. Geol. Environ.* 79, 5569–5584. doi:10.1007/s10064-020-01869-w

Liu, S. (2020). *Experimental study on mechanical properties of Cretaceous frozen sandstone under lateral unloading*. Xi'an: Xi'an university of science and technology.

Liu, S., Yang, G. S., Dong, X. H., Shen, Y. J., and Liu, H. (2021). Mechanical characteristics of frozen sandstone under lateral unloading: an experimental study. *Adv. Civ. Eng.* 2021, 6653294. doi:10.1155/2021/6653294

Liu, S., Zhu, Q. Z., and Shao, J. F. (2020). Deformation and mechanical properties of rock: effect of hydromechanical coupling under unloading conditions. *Bull. Eng. Geol. Environ.* 79, 5517–5534. doi:10.1007/s10064-020-01824-9

Lu, W. B., Zhu, Z. D., He, Y. X., and Que, X. C. (2021). Strength characteristics and failure mechanism of a columnar jointed rock mass under uniaxial, triaxial, and true triaxial confinement. *Rock. Mech. Rock. Eng.* 54, 2425–2439. doi:10.1007/s00603-021-02400-7

Lyu, X., Du, J., Fu, H., Lyu, D., and Wang, W. (2024). Macro-micro behaviors and failure mechanism of frozen weakly cemented mudstone. *J. Rock. Mech. Geotech. Eng.* 16 (4), 1337–1347. doi:10.1016/j.jrmge.2023.06.024

Lyu, X. Z., Zhao, Z. G., Wang, X. J., and Wang, W. M. (2019). Study on the permeability of weakly cemented sandstones. *Geofluids* 2019, 1–14. doi:10.1155/2019/8310128

Niu, C. Y., Zhu, Z. M., Zhou, L., Li, X. H., Ying, P., Dong, Y. Q., et al. (2021). Study on the microscopic damage evolution and dynamic fracture properties of sandstone under freeze-thaw cycles. *Cold. Reg. Sci. Technol.* 191, 103328. doi:10.1016/j.coldregions.2021.103328

Qu, Y., Yang, G., Xi, J., Ni, W., Ding, X., and Wu, B. (2023). Mechanical properties and energydissipation mechanism of frozen coarse-grained and medium-grained sandstones. *J. Cent. South Univ.* 30 (6), 2018–2034. doi:10.1007/s11771-023-5344-2

Shan, R. L., Yang, H., Zhang, J. X., Guo, Z. M., and Zhao, D. H. (2016). Mechanical properties of saturated red sandstone of Meilinmiao mine under loading and unloading at negative temperatures. *J. Min. Saf. Eng.* 33, 924–931.

Shi, X. C., Cai, W. Q., Meng, Y. F., Li, G., and Li, J. X. (2015). Wellbore stability analysis based on a new strength criterion. *J. Nat. Gas. Sci. Eng.* 27, 1005–1015. doi:10.1016/j.jngse.2015.09.050

Vazaios, I., Vlachopoulos, N., and Diederichs, M. S. (2019). Assessing fracturing mechanisms and evolution of excavation damaged zone of tunnels in interlocked rock masses at high stresses using a finite-discrete element approach. *J. Rock. Mech. Geotech.* 11, 701–722. doi:10.1016/j.jrmge.2019.02.004

Wang, B., Zhu, J. B., Wu, A. Q., and Liu, X. H. (2010). Experimental validation of nonlinear strength property of rock under high geostress. *Chin. J. Rock Mech. Eng.* 29, 542–548.

Wang, L., Su, H. M., Chen, S. G., and Qin, Y. (2020). Nonlinear dynamic constitutive model of frozen sandstone based on weibull distribution. *Adv. Civ. Eng.* 2020, 6439207. doi:10.1155/2020/6439207

Wang, S., Xu, W., Yan, L., Feng, X.-T., Xie, W.-C., and Chen, H. (2020). Experimental investigation and failure mechanism analysis for dacite under true triaxial unloading conditions. *Eng. Geol.* 264, 105407. doi:10.1016/j.enggeo.2019.105407

Wang, Z. K., Li, W. P., and Hu, Y. B. (2021). Experimental study on mechanical behavior, permeability, and damage characteristics of Jurassic sandstone under varying stress paths. *Bull. Eng. Geol. Environ.* 80, 4423–4439. doi:10.1007/s10064-021-02214-5

Wu, Z. J., Ji, X. K., Liu, Q. S., and Fan, L. F. (2020). Study of microstructure effect on the nonlinear mechanical behavior and failure process of rock using an image-based-FDEM model. *Comput. Geotech.* 121, 103480. doi:10.1016/j.compgeo.2020.103480

Yang, G. S., Wei, Y., Shen, Y. J., Wang, L., Liu, H., Dong, X. H., et al. (2019). Mechanical behavior and strength forecast model of frozen saturated sandstone under triaxial compression. *Chin. J. Rock Mech. Eng.* 38, 683–694. doi:10.13722/j.cnki.jrme.2018.1417

You, S., Ji, H. G., Wang, T., and Song, Z. Y. (2018). Thermal and mechanical coupling effects on permeability of weakly cemented sandstone. *Emerg. Mate. Res.* 7, 100–108. doi:10.1680/jemmr.16.00082

Zeng, B. (2018). *Study on mechanical characteristics and constitutive model of red sandstone during axial unloading-tensile under confining pressure*. Chongqing: Chongqing University.

Zhang, J., and Yu, J. H. (2020). Parameter resolution of estimation method for linear regression models. *Acta. Math. Sci.* 40, 1381–1392.

Zhao, G. Y., Dai, B., Dong, L. J., and Yang, C. (2015). Experimental research on mechanical characteristics and strength criterion of rock under triaxial unloading tests under different stress paths. *Rock. Soil. Mech.* 36, 3121–3127+3149. doi:10.16285/j.rsm.2015.11.011

Zhao, Y. C., Yang, T. H., Xiao, F. K., Wang, H., Liu, G., Zheng, X., et al. (2015). The variation law of plastic strain energy of weak cemented sandstone under cyclic loading in western China. *J. China. Coal. Soc.* 40, 1813–1819. doi:10.13225/j.cnki.jccs.2014.1192

Zhao, Z., Liu, H., Gao, X., and Feng, Y. (2023). Meso-macro damage deterioration of weakly cemented red sandstone under the coupling effect of high-humidity and uniaxial loading. *Eng. Fail. Anal.* 143, 106911. doi:10.1016/j.engfailanal.2022.106911

Zhou, X. X. (2020). *Study on mechanical characteristics of rock unloading crushing under high stress*. Shenyang: Shenyang Jianzhu University.

frontiers | Frontiers in Physics

TYPE Original Research
PUBLISHED 29 January 2025
DOI 10.3389/fphy.2024.1526223

OPEN ACCESS

EDITED BY
Huiming Tan,
Hohai University, China

REVIEWED BY
Zhiwei Ye,
Nanchang University, China
Junhong Xu,
Nanjing Forestry University, China

*CORRESPONDENCE
Zheng Zhou,
zhougeohhu@foxmail.com

RECEIVED 11 November 2024
ACCEPTED 27 December 2024
PUBLISHED 29 January 2025

CITATION
Chen X, Zhou Z, Zhu Y, Pu S, Zhang D and Li E (2025) Evaluating seismic stability of reinforced soil slopes using the limit equilibrium method: influence of geosynthetic strength indicators. *Front. Phys.* 12:1526223. doi: 10.3389/fphy.2024.1526223

Evaluating seismic stability of reinforced soil slopes using the limit equilibrium method: influence of geosynthetic strength indicators

Xin Chen[1], Zheng Zhou[2]*, Yuming Zhu[3], Shikun Pu[2], Dengke Zhang[2] and Erbing Li[2]

[1]School of Civil Engineering, Suzhou University of Science and Technology, Suzhou, Jiangsu, China, [2]State Key Laboratory of Disaster Prevention and Mitigation of Explosion and Impact, Chinese People's Liberation Army Engineering University, Nanjing, Jiangsu, China, [3]College of Civil and Transportation Engineering, Hohai University, Nanjing, Jiangsu, China

Seismic stability of soil slopes is a critical issue within engineering geology, with a particular emphasis on understanding how geosynthetic strength indicators influence the stability of reinforced slopes. This paper employs the limit equilibrium method, in conjunction with the log spiral curve model, to evaluate the seismic stability of reinforced soil slopes considering varying pullout strength indicators. The proposed method is verified by comparing with a same case in the corresponding reference. Then, effects of the non-uniform pullout strength distribution on the seismic reinforcement of slopes is revealed theoretically by changing parameters such as slope angles, friction angles of fill soils, and design length of geosynthetics. The results indicated that when lengths of the geosynthetics are reduced, the seismic yield accelerations calculated using the ultimate bearing capacity is significantly smaller than that obtained using the ultimate pullout strength. It is suggested that the nonuniform pullout strength distribution should be taken into consideration to ensure the stability of slopes under seismic actions. Additionally, this study provides new perspectives and methods for the theoretical study and engineering application of geosynthetic reinforcement techniques.

KEYWORDS

soil slopes, seismic stability, limit equilibrium method, pullout strength of geosynthetics, log spiral curve model

1 Introduction

The seismic stability of soil slopes is a critical concern in geotechnical earthquake engineering. Among the various techniques for stabilizing slopes, soil reinforcement, particularly with geosynthetics, is widely recognized as a cost-effective and efficient method [1–5]. Consequently, understanding the behavior of reinforced soil slopes under seismic loading is essential for improving design and performance.

Research conducted post the 1999 Chi-Chi earthquake highlighted that reinforced soil structures outperformed those without reinforcement. Subsequent evaluations of seismic designs have been conducted through earthquake case studies and laboratory tests [6, 7]. Research by Perez and Holtz [8] revealed that reinforcement spacing, and length

significantly influence the yield acceleration of reinforced slopes, while [9] identified embankment density and reinforcement stiffness as key factors in seismic performance. Laboratory studies showed that reinforced soil slopes exhibit higher natural frequencies than unreinforced slopes [10]. Hazari et al. [11] further confirmed, through laboratory and numerical studies, that soil reinforcement reduces both deformations and acceleration response, with geogrids being identified as one of the best reinforcements for slope stabilization [12]. Further, shaking table tests by Huang et al. [13] underscored the critical importance of reinforcement tensile strength in determining yield acceleration, while Zeng et al. [14] conducted large-scale tests to analyze pullout forces and methods to enhance geogrid reinforcement performance.

Yazdandoust [15] determined the equivalent seismic coefficients for pseudo-static analysis of reinforced soil structures based on shaking table tests, comparing them with current specifications. Patra and Shahu [16] conducted a pseudo-static analysis of a reinforced soil wall, examining the effects of horizontal seismic coefficients, backfill properties, and wall geometry. Sarbishei and Fakher [17] proposed a new dynamic model using the pseudo-static method and the horizontal slice method, estimating acceleration distribution along the wall height by applying the principle of minimum potential energy. To address the limitations of the pseudo-static method, Steedman and Zeng [18] introduced the pseudo-dynamic method in 1990, offering a more accurate representation of earthquake dynamics. Basha and Babu [19] applied this method to optimize the design of reinforced soil structures under bi-directional sinusoidal waves. Yan et al. [20] used the pseudo-dynamic method with limit analysis to assess the stability of reinforced soil slopes during earthquakes, incorporating dynamic variations in anchor cable axial forces, which yielded a larger dynamic safety coefficient and smaller variation compared to methods that ignore these variations. Ruan and Sun [21] employed the pseudo-dynamic method to calculate the safety factor for reinforced soil walls under seismic conditions.

Many reinforced soil slopes have failed under earthquake-induced vibrations in recent years, with pullout failures being particularly common [22, 23]. Current specifications [24, 25] often do not account for the impact of pullout failures on the internal stability of reinforced soil slopes. Moreover, the distribution of reinforcement pullout resistance during seismic events is non-uniform, complicating stability evaluations. This paper introduces a seismic stability evaluation method for reinforced soil slopes, incorporating the limit equilibrium and log-spiral failure mechanisms and accounting for varying pullout resistance indices. Case studies validate the proposed method, and the effects of reinforcement arrangement, pullout strength distribution, and total pullout resistance on seismic yield acceleration and overall stability are analyzed.

2 Reinforcement evaluation method and verification

The limit equilibrium method posits that soil behaves as an ideal rigid-plastic material, verifying its assumptions against a defined failure surface. In the assessment calculations for reinforced soil slopes, it is assumed that both the soil and

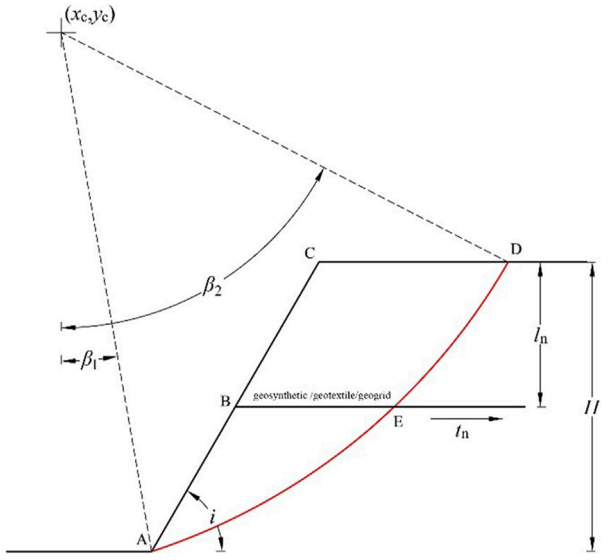

FIGURE 1
A slope model based on log spiral slip surface.

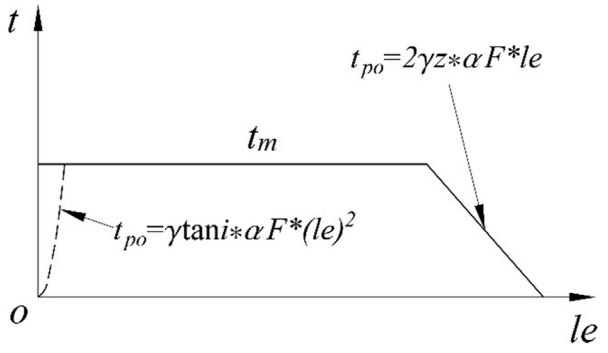

FIGURE 2
The resistance strength along the length of geosynthetic material.

geosynthetics reach a limit state. This international mainstream method is widely used in engineering applications due to its ease in establishing calculation models and considering the resistance strength provided by each layer of geosynthetics. Here, a rotational failure mechanism is adopted, assuming that the slope sliding surface is a logarithmic spiral curve. Based on the limit equilibrium method, the soil slope reinforced with geosynthetics satisfies the moment equilibrium condition for the sliding body. In Figure 1, a calculation model for geosynthetic-reinforced slopes is established considering varies geosynthetics strength indices. This section focuses on the basic theoretical explanation and derivation using a single-layer reinforced soil slope.

The equation of the log spiral curve can be expressed as:

$$r = Ae^{-\beta\psi},\ \psi = \tan(\varphi) \tag{1}$$

in which r represents the distance from the rotation center to any point on the sliding surface, A is the log spiral curve constant, β is

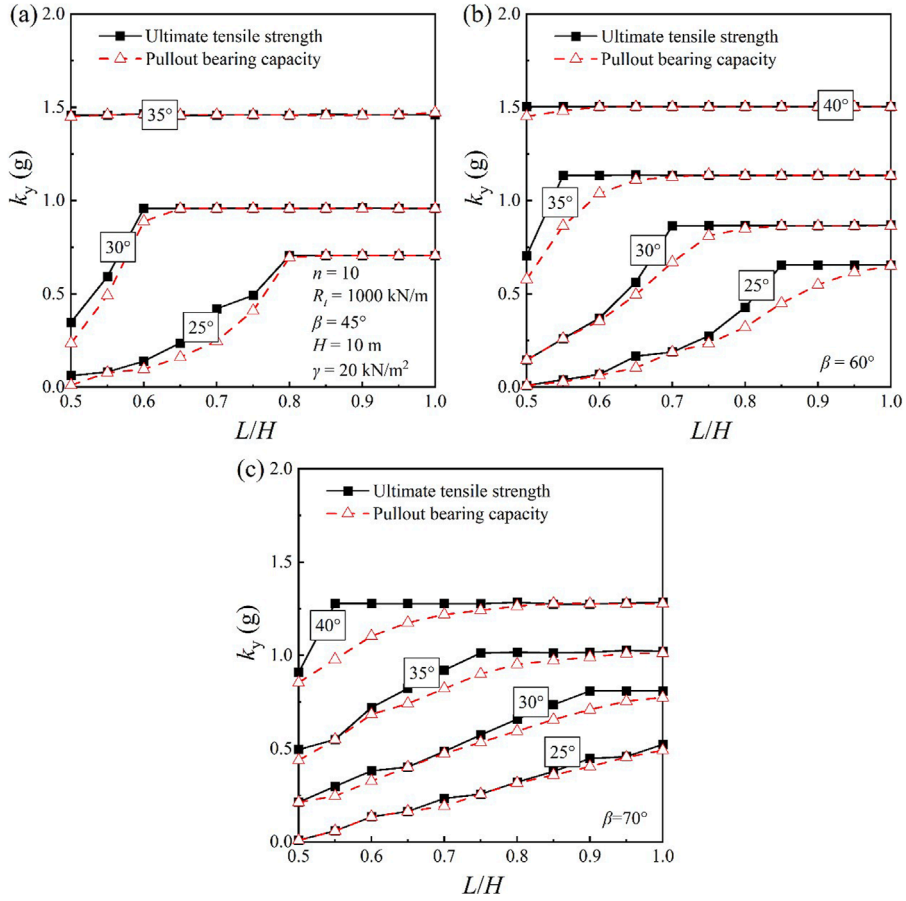

FIGURE 3
Yield accelerations obtained from different geosynthetic material properties. ((**A**) β=45°; (**B**) β=60°; (**C**) β=70°).

the rotation angle from the rotation center to any point on the sliding surface, and φ is the internal friction angle of the soil.

According to Equation 1, the coordinates of any point on the sliding surface can be expressed as:

$$\begin{cases} x = x_c + Ae^{-\psi\beta}\sin\beta \\ y = y_c - Ae^{-\psi\beta}\cos\beta \end{cases} \tag{2}$$

Given the known angles β_1 and β_2, the coefficient A and the rotation center c coordinate expressions in Equation 2 can be obtained as follows (Equations 3, 4):

$$A = \frac{H}{e^{-\psi\beta_1}\cos\beta_1 - e^{-\psi\beta_2}\cos\beta_2} \tag{3}$$

$$\begin{cases} x_c = -Ae^{-\psi\beta_1}\sin\beta_1 \\ y_c = Ae^{-\psi\beta_1}\cos\beta_1 \end{cases} \tag{4}$$

If the slope reaches a limit equilibrium state under the gravity and horizontal seismic force, the equilibrium equation can be obtained:

$$M_w + kM_s = M_c + M_t \tag{5}$$

In Equation 5, M_w is the moment of the soil's gravity on the sliding surface, M_s is the moment of the horizontal seismic force (pseudo-static method), M_c is the resisting moment provided by the soil's shear strength, and M_t is the moment of the geosynthetics' resistance strength, respectively.

The moment M_w can be obtained by subtracting the moments M_2 and M_3 of gravities of triangles OCA and OCD from the moment M_1 of sector OAD. The expression can be written as:

$$M_w = M_1 - M_2 - M_3 \tag{6}$$

And the expressions for M_1, M_2, and M_3 in Equation 6 are shown below:

$$\begin{cases} M_1 = \dfrac{\gamma A^3}{3(1+9\psi^2)}\left[(\cos\beta_1 + 3\psi\sin\beta_1)e^{-3\psi\beta_1} - (\cos\beta_2 + 3\psi\sin\beta_2)e^{-3\psi\beta_2}\right] \\ M_2 = \dfrac{\gamma A}{6}e^{-\psi\beta_1}\dfrac{H}{\sin i}\sin\left(\dfrac{\pi}{2} - i + \beta_1\right)(H\cot i - 2x_c) \\ M_3 = \dfrac{\gamma A}{6}\cos\beta_2 e^{-\psi\beta_2}\left(x_c + A\sin\beta_2 e^{-\psi\beta_2} - H\cot i\right)\left(H\cot i + A\sin\beta_2 e^{-\psi\beta_2} - x_c\right) \end{cases} \tag{7}$$

By substituting the results in Equation 7 into Equation 6, the moment M_w can be obtained. The moment of the external force provided by the horizontal seismic acceleration can be expressed as:

$$M_s = M_{s1} - M_{s2} - M_{s3} \tag{8}$$

In Equation 8, M_{s1}, M_{s2}, and M_{s3} are expressed as:

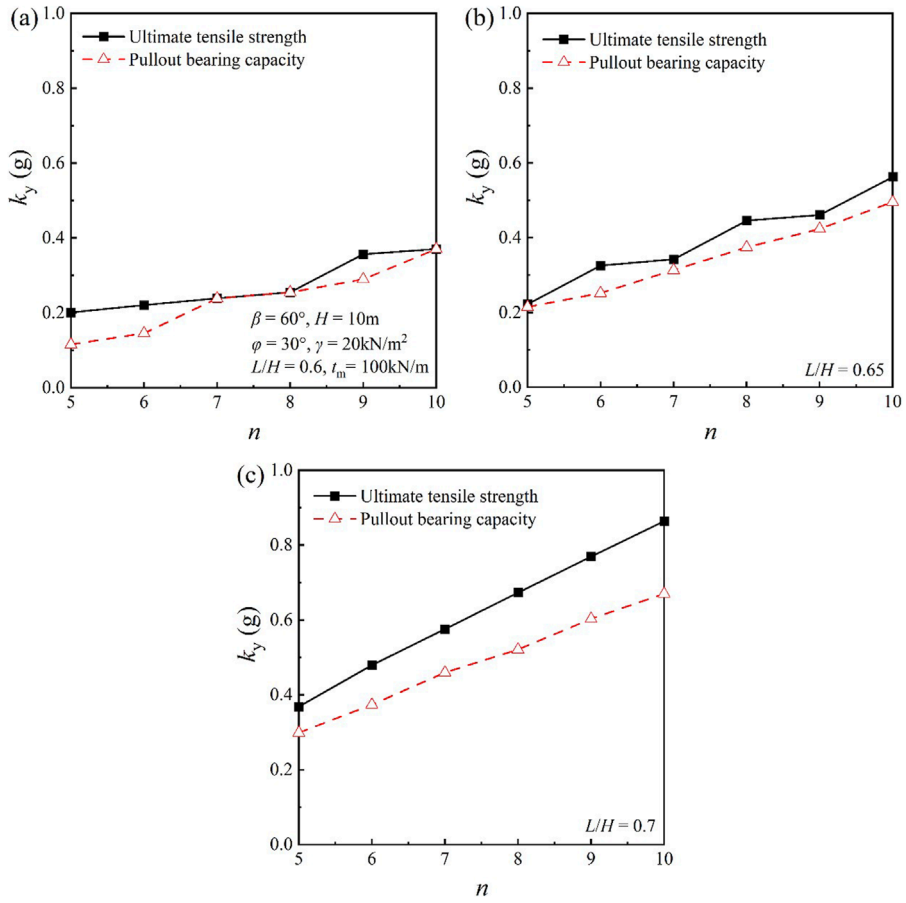

FIGURE 4
Yield accelerations of different layer designs with the same strength for a single layer. (**(A)** L/H=0.6; **(B)** L/H=0.65; **(C)** L/H=0.7).

$$\begin{cases} M_{s1} = \dfrac{\gamma A^3}{3(1+9\psi^2)}\left[(\sin\beta_2 - 3\psi\cos\beta_2)e^{-3\psi\beta_2} - (\sin\beta_1 - 3\psi\cos\beta_1)e^{-3\psi\beta_1}\right] \\ M_{s2} = \dfrac{\gamma A}{6}e^{-\psi\beta_1}\dfrac{H}{\sin i}\sin\left(\dfrac{\pi}{2} - i + \beta_1\right)(2y_c - H) \\ M_{s3} = \dfrac{\gamma A^2}{3}e^{-2\psi\beta_2}\cos^2\beta_2\left[x_c + Ae^{-\psi\beta_2}\sin\beta_2 - H\cot i\right] \end{cases} \tag{9}$$

Similarly, the moment M_s can be obtained by substituting the results in Equation 9 into Equation 8

Following the assumption of the log spiral curve sliding surface, the normal stress σ and the shear stress component $\sigma\tan(\varphi)$ on the sliding surface are directed towards the rotation center. Therefore, only the anti-slip effect of the shear stress component c needs to be considered when calculating the moment M_c. The expression of M_c is given in Equation 10 below.

$$M_c = -\frac{cA^2}{2\psi}\left(e^{-2\psi\beta_2} - e^{-2\psi\beta_1}\right) \tag{10}$$

The expression for the moment M_t provided by each layer of geosynthetics is shown in Equation 11:

$$M_t = \sum t_n(y_c - H + l_n) \tag{11}$$

where t_n is the pullout resistance provided by the geosynthetics.

In the past reinforced design and verification, the geosynthetics' ultimate resistance strength t_m is often used for calculation. But in actual applications, the actual pullout bearing capacity of the geosynthetics is not uniformly distributed from the front to the back end as shown in Figure 2. Due to the front-end pullout force of the geosynthetics with measures such as overturning and packaging, this paper only takes into consideration the characteristic of the reduction of the pullout bearing capacity at the end of the reinforcement geosynthetics.

In Figure 2, the envelope composed of the geosynthetics' ultimate tensile strength t_m and the bearing capacity t_{po} is the maximum envelope that can be provided by each point of the geosynthetics. When the sliding surface and the distribution of the geosynthetics are known, the position where the sliding surface passes through the geosynthetics can be determined through geometric relationships. And the maximum pullout force that the corresponding geosynthetics can provide in that case can be confirmed through the function t_n. F^* in Figure 2 is the pullout resistance coefficient, i.e., the interface friction coefficient, and α is the nonlinear distribution effect coefficient considering the interaction between the geosynthetics and the soil. The function t_n can be expressed as in Equation 12:

$$t_n = t(x_n, y_n) \tag{12}$$

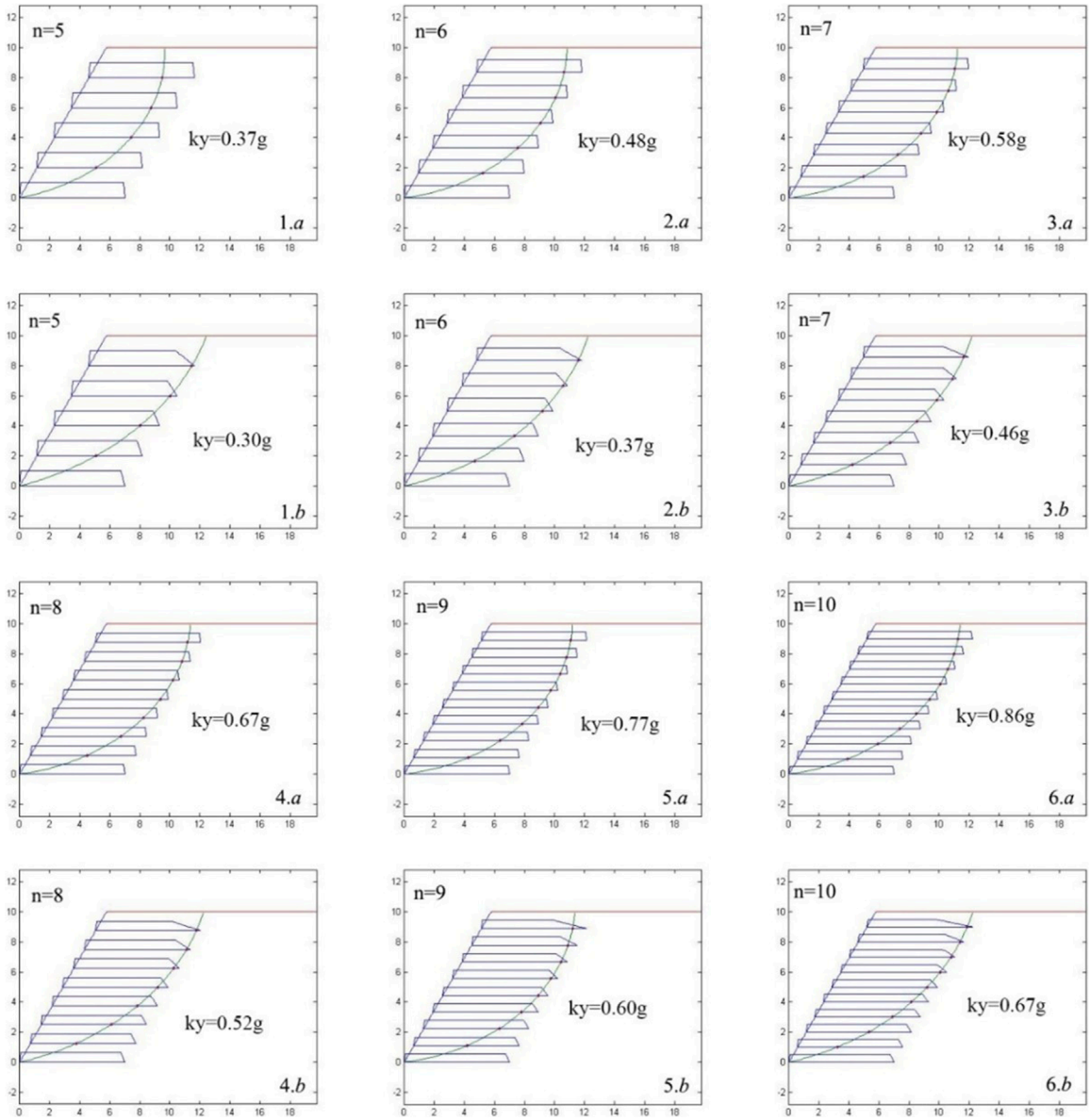

FIGURE 5
Slip surfaces of different layer designs with the same strength for a single layer (L/H = 0.7).

By combining the position y_n of the geosynthetics with the log spiral surface equation, the specific position where the sliding surface passes through the corresponding geosynthetic can be obtained to determine the maximum pullout force. The following is the corresponding set of equations:

$$\begin{cases} y_n = H - l_n \\ \begin{cases} x_n = x_c + Ae^{-\psi\beta}\sin\beta \\ y_n = y_c - Ae^{-\psi\beta}\cos\beta \end{cases} \end{cases} \tag{13}$$

Substituting the above derived Equation 13 into Equation 5, the expression for theyield acceleration k under the corresponding state can be obtained as shown in Equation 14:

$$k = \frac{M_c + M_t - M_w}{M_s} \tag{14}$$

Similarly, the safety factor Fs under static conditions can be given in Equation 15:

$$Fs = \frac{M_c + M_t}{M_w} \tag{15}$$

Here, an example from Ling et al. [26] is used to verify the limit equilibrium method employed in this paper. The example model is a reinforced soil slope that is 6 m high with a slope ratio of 1:1, with a unit weight γ of 20 kN/m^3 and a designed internal friction angle φ of 30°. According to the charts in Ling et al. [26], the total pullout resistance required from the geosynthetics in the reinforced zone is 32.4 kN/m. This strength is evenly distributed across the design tensile strength of each layer of geosynthetics, assuming uniform pullout strength at all points along the geosynthetics. The lengths of the geosynthetics L are 0.7 times the height H. By

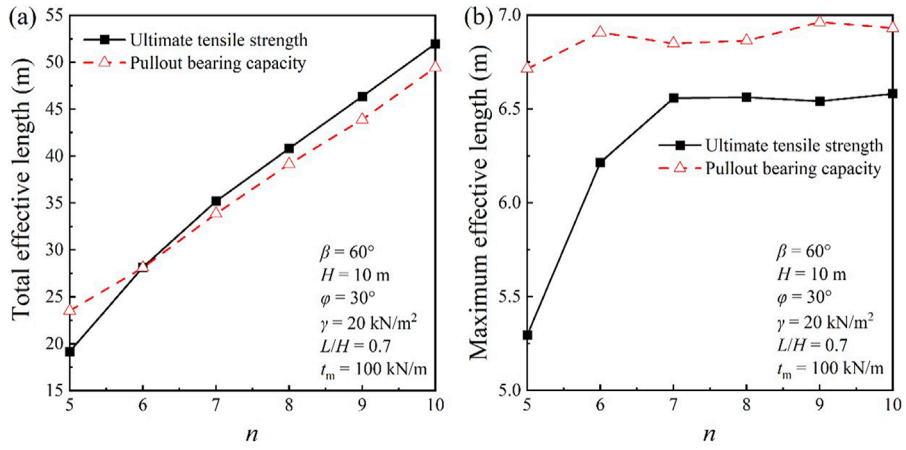

FIGURE 6
(A) Total effective length; **(B)** Maximum effective length.

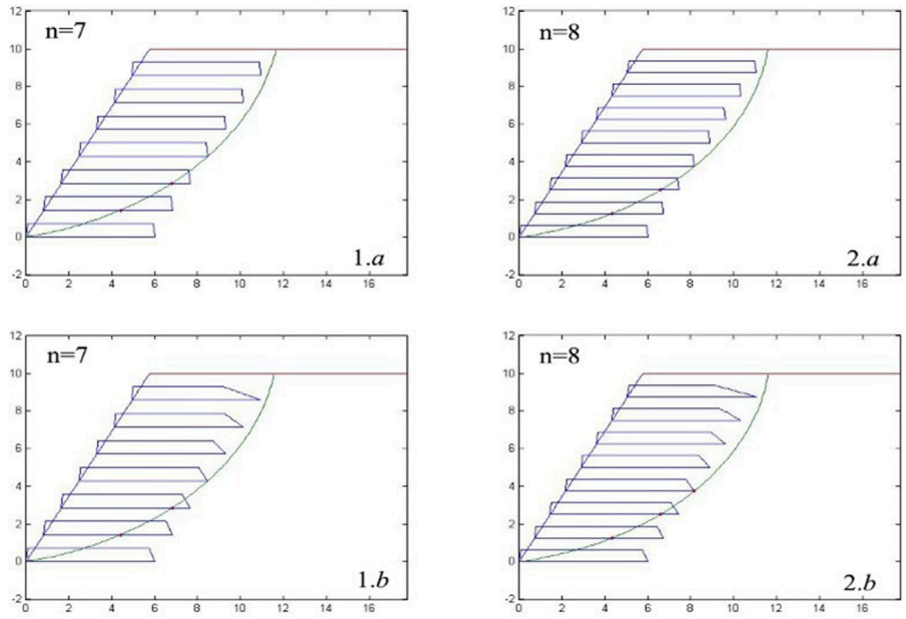

FIGURE 7
The slip surface for cases with the same yield acceleration.

inputting the aforementioned parameters into the limit equilibrium method used in this section, the safety factor F_s of 1.02 is obtained, indicating that the method and algorithm program used in this paper are valid.

3 Seismic stability review results of the reinforced soil slope

Building on the above verification, and employing the seismic yield acceleration of the reinforced soil slope as a key metric, this study analyzes how the end decay of geosynthetics' pullout strength impacts seismic stability across varying slope angles and soil fill conditions. This paper takes a reinforced soil slope with a height of 10 m as the basic model, with slope angles β of 45°, 60°, and 70°, and internal friction angles φ of the fill soil being 25°, 30°, 35°, and 40°. The designed ultimate pullout strength of a single geosynthetic is 100 kN/m, and there are 10 geosynthetics uniformly distributed within the slope. By using the proposed calculation method, the corresponding seismic yield accelerations for the slope under different design lengths of the geosynthetics are calculated, and the results are shown in the Figure 3.

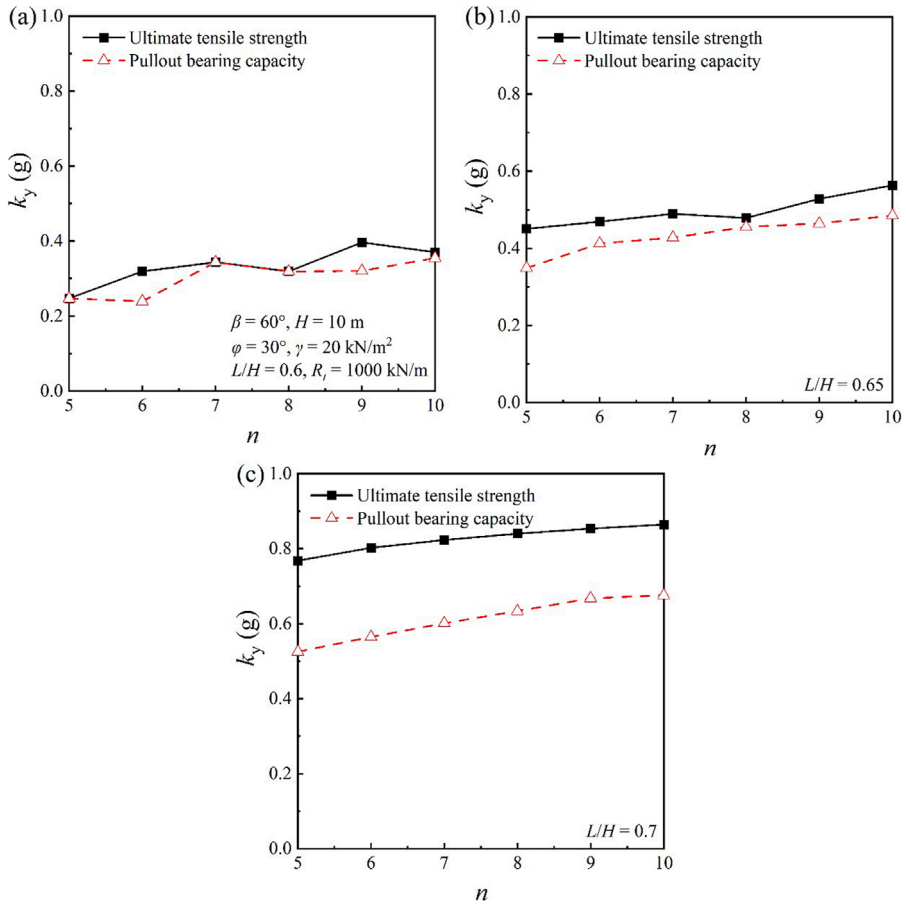

FIGURE 8
Yield accelerations of different layer designs with the same total strength. ((**A**) L/H=0.6; (**B**) L/H=0.65; (**C**) L/H=0.7).

It can be seen in Figure 3 that the seismic yield accelerations of the reinforced slope remain constant and are not affected by the distribution characteristics of the geosynthetics' pullout strengths when the geosynthetics are sufficiently long. But when the length is reduced, in some cases, using the bearing capacity ultimate pullout strength index for calculation may result in a significantly smaller seismic yield acceleration. Based on the calculation results of the various models, and considering the design length range of geosynthetics as L/H = 0.6 to 0.7, it is known that for the reinforced soil slope model with an internal friction angle φ of 30° and a slope angle of 60°, the decay of the pullout strength at the end of the geosynthetics has the greatest effect on the seismic yield acceleration. Therefore, this model is selected to analyze the effect of different numbers of geosynthetics on the seismic yield acceleration, under the conditions of controlling the total and the single pullout strength. The critical slip surface of the reinforced soil slope under different numbers of geosynthetics when L/H = 0.7 is shown in Figure 4, where the rectangle or trapezoid above the geosynthetics indicates the distribution of pullout strength at the corresponding point, with different indices showing different distributions, and the slip surface passing through the geosynthetics is marked with red dots.

3.1 Effect of different indices when the pullout strength of a single geosynthetic is consistent

From Figure 4, one can find that under the condition of controlling the pullout strength of a single geosynthetic to be consistent, reducing the number of layers results in an obvious downward trend in the seismic yield acceleration. This means that reducing the arrangement of geosynthetics may decrease the seismic stability of the slope. Meanwhile, considering the decay of the pullout strength at the end of the geosynthetic, i.e., using the pullout bearing capacity for calculation and analysis, will yield a smaller result for the seismic yield acceleration compared to using only the geosynthetic's ultimate pullout strength for calculation. That is, using the geosynthetic's ultimate pullout strength for the seismic stability review of reinforced soil slopes will overestimate the seismic stability of the slopes. In this case, when L/H = 0.7, the difference between using the pullout bearing capacity limit and using the ultimate pullout strength is the most significant.

Figure 5 presents the critical slip surfaces of the reinforced soil slope calculated using the ultimate bearing capacity and the ultimate pullout strength of the geosynthetic, for different numbers of layers

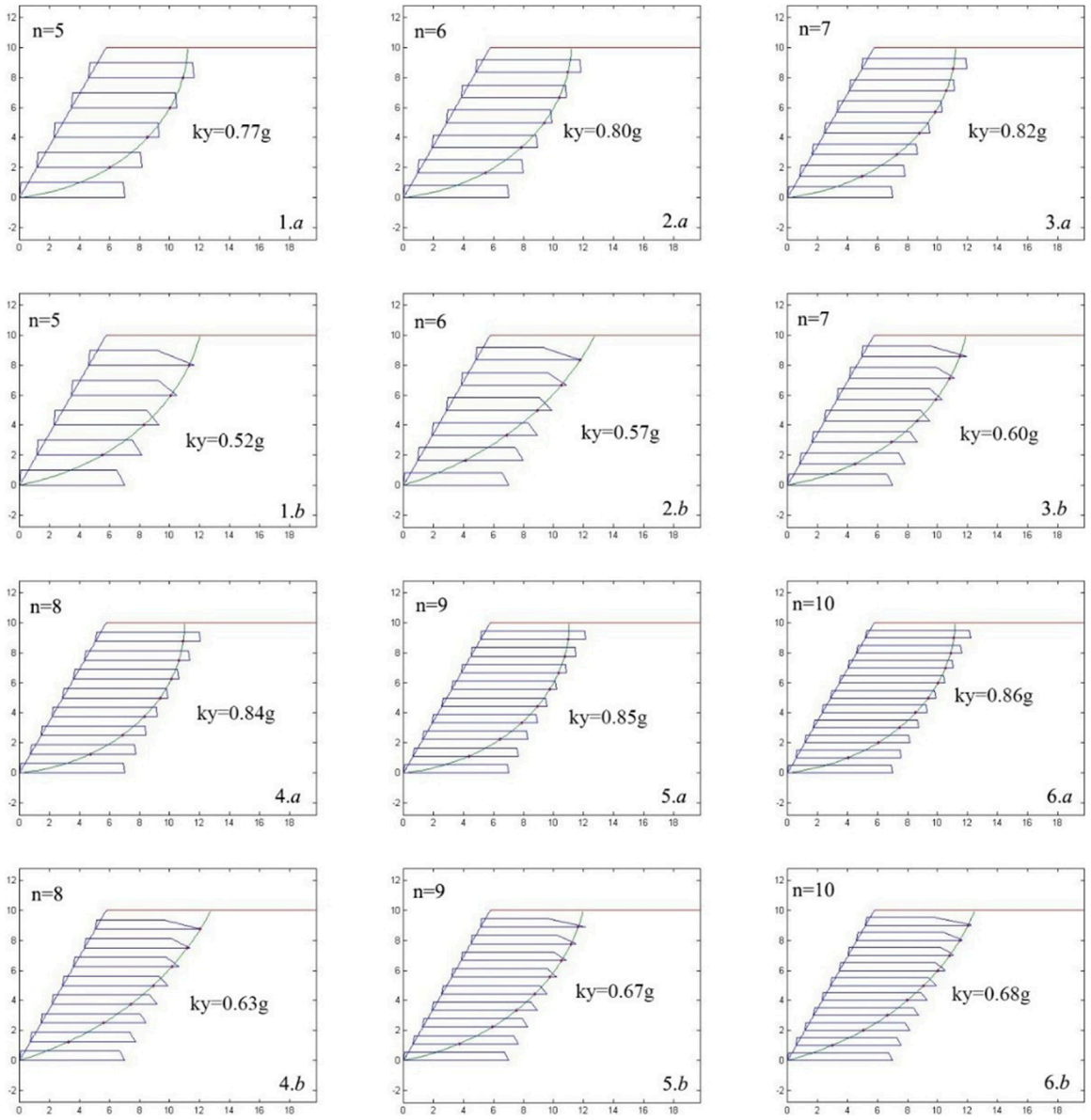

FIGURE 9
Slip surfaces of different layer designs with the same total strength(L/H = 0.7).

when L/H = 0.7. For the same number of layers, due to the decay of the pullout force at the end of the geosynthetic, the critical slip surface calculated using the ultimate bearing capacity is closer to the end of the geosynthetic compared to that calculated using the ultimate pullout strength. For different numbers of layers, the upper parts of the slip surface generally pass through the end of the upper geosynthetic.

To quantify the differences in the slip surfaces, this paper defines the total length of geosynthetics within the slip surface and the maximum single length as the effective total length and maximum effective length of geosynthetics, respectively. Figure 6 shows the effective total length and maximum effective length for corresponding lengths of each model in Figure 5. It can be seen from Figure 6 that when the number of layers is constant, the difference in the effective total length verified by the two indicators is small, but the difference in the maximum effective length is obvious. The maximum effective length verified by the ultimate bearing capacity is close to the designed length (7 m). When the number of layers is between 7 and 10, the maximum effective strength verified by the ultimate pullout strength is about 6.5 m, which is about 0.3 m less than that verified by the ultimate bearing capacity. As the number decreases below 7, the significant increase in the difference is most pronounced, where the discrepancy between the two indicators is 1.5 m at 5 layers.

For the case when L/H = 0.6, where the same seismic yield acceleration is obtained using both the ultimate bearing capacity and the ultimate pullout strength, Figure 7 presents the corresponding slip surfaces. It can be observed that when n = 7 or 8, the shapes

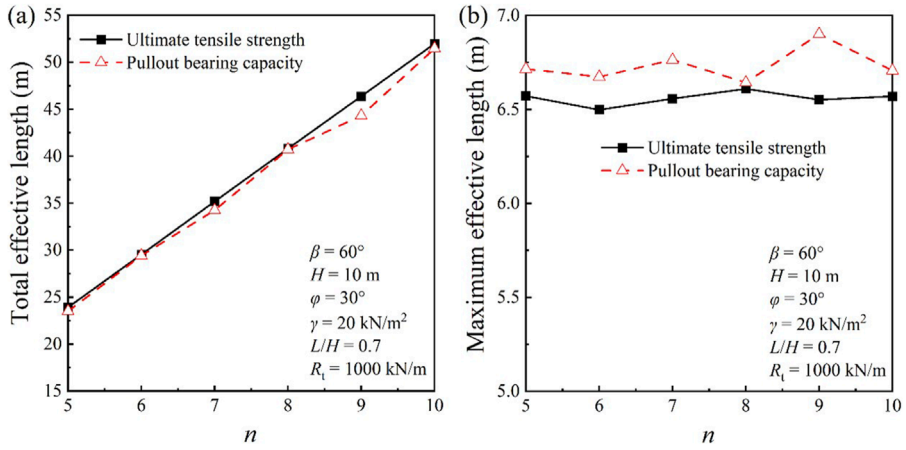

FIGURE 10
(A) Total effective length; **(B)** Maximum effective length.

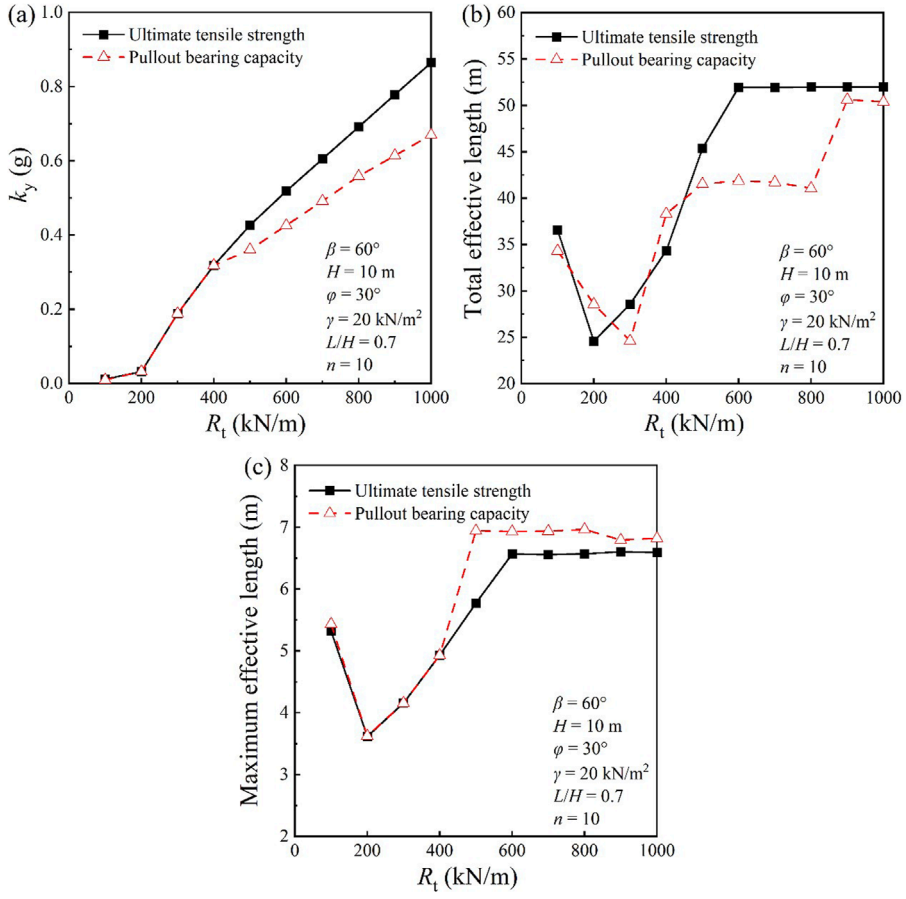

FIGURE 11
(A) Yield accelerations of different strength; **(B)** Total effective length; **(C)** Maximum effective length.

of the slip surfaces are identical, and they pass through the same position of the geosynthetic without being in the decay region at the end of the geosynthetic. Therefore, if the pullout force is provided by the ultimate pullout strength, the yield acceleration calculated by the proposed method is consistent. This indicates that the differences in results caused by the two indicators need to be considered for specific design lengths, that is, specific engineering cases must be analyzed to determine whether they need to be taken into account.

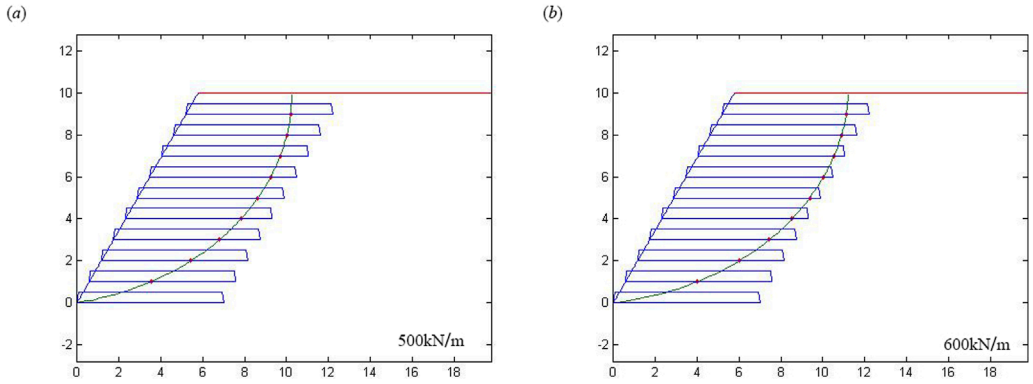

FIGURE 12
(A) The slip surfaces of slopes with Rt = 500 kN/m; **(B)** The slip surfaces of slopes with Rt = 600 kN/m.

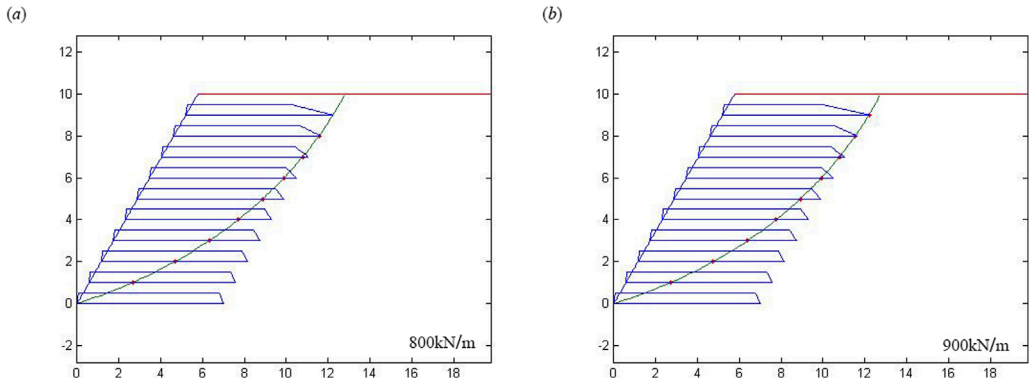

FIGURE 13
(A) The slip surfaces of slopes with Rt = 800 kN/m; **(B)** The slip surfaces of slopes with Rt = 900 kN/m.

3.2 Effect of different indices when the total pullout strength is consistent

It can be seen from Figure 8 that a slower decreasing trend of the seismic yield acceleration of the slope occurs under the condition of maintaining consistent total pullout strength of the geosynthetics and reducing the number of layers. Meanwhile, the seismic yield acceleration using the ultimate bearing capacity for calculation is smaller compared to the results obtained by using the ultimate pullout strength. This means that using the ultimate pullout strength to verify the seismic stability of reinforced soil slopes will overestimate the seismic stability of the slopes. In this case, when L/H = 0.7, the difference between the results obtained using the two indicators is the most significant. When the length is 0.6H, and n = 7 or 8, the seismic yield acceleration calculated using the two indicators is consistent. Similar to the case of the ultimate pullout force of a single geosynthetic, the corresponding slip surfaces are identical, the positions where the slip surfaces pass through are the same, and the pullout strengths that the geosynthetic can provide at the corresponding positions are consistent.

Figure 9 presents the critical slip surfaces of reinforced soil slopes calculated using the ultimate bearing capacity and the ultimate pullout strength for different numbers of layers when L/H = 0.7. It can be seen that the positions that slip surfaces obtained using the ultimate bearing capacity pass through the upper geosynthetic is further-back. Figure 10 also provides the effective total length and maximum effective length corresponding to each model in Figure 9. It can be seen from Figure 10 that when the number of layers is constant, the effective total length verified by the two indicators is almost the same, and the difference in the maximum effective length is obviously less than the results obtained by controlling the ultimate pullout strength of a single geosynthetic. Moreover, the change in the number of layers has a smaller effect on the maximum effective length. The average result obtained from the ultimate pullout strength is 6.55 m, and that obtained using the ultimate bearing capacity is 6.78 m, with a difference of 0.23 m.

3.3 Effect of different indices when the arrangement is consistent

When the strength of a single geosynthetic is consistent with the total strength, the effect of the two indicators is mainly reflected in

the difference in seismic acceleration. And changing the number of layers has little effect on the shape and size of the slip surface. Here a reinforced soil slope model with an internal friction angle φ of 30° and a slope angle of 60° is selected, with a geosynthetic design length of L/H = 0.7 and the layer number n = 10, to reveal the effect of different indicators on the seismic yield acceleration by changing the total pullout force.

In Figure 11, the seismic yield acceleration obtained from the verification using the two indicators increases linearly with the increase in total pullout force within the range of 500–1,000 kN/m. The seismic yield acceleration obtained from the verification using the ultimate pullout strength is greater than that obtained using the ultimate bearing capacity. The maximum effective length obtained from the verification using the ultimate bearing capacity is greater than that corresponding to the ultimate pullout strength, and the effective total length obtained from the verification using the ultimate bearing capacity is less than that corresponding to the ultimate pullout strength indicator.

In Figure 12, using the ultimate pullout strength for verification, effects of the total pullout force on the maximum effective length and effective total length are negligible at levels more than 600 kN/m. However, an obvious reduction in these lengths is observed when the total pullout force drops to 500 kN/m. Figure 12 also displays the slip surfaces for total pullout forces of 500 and 600 kN/m. The comparison reveals that the slip surface area decreases substantially and a noticeable reduction emerges in both the effective total length and the maximum effective length at Rt = 500 kN/m.

In Figure 13, using the ultimate bearing capacity for verification, changes in total pullout force have a minor effect on the maximum effective length. As the total pullout force Rt decreases to 800 kN/m, the effective total lengths drop noticeably from 50 m to 42 m, and the maximum effective lengths increase slightly from approximately 6.75 m to about 6.9 m. Figure 13 also shows the slip surfaces for total pullout forces of 800 kN/m and 900 kN/m. It is evident that the slip surface does not intersect the first layer, leading to a marked decrease in the effective total length at Rt = 800 kN/m.

4 Discussion

4.1 Merits of the proposed method

The method presented in this paper, which integrates the limit equilibrium method with the log spiral failure mechanism, offers several distinct merits that enhance our understanding and assessment of the seismic stability of reinforced soil slopes. Firstly, it provides a more sophisticated and realistic representation of slope failure modes under seismic conditions compared to traditional planar failure models. The log spiral curve acknowledges the rotational component of slope failures, which is often observed in practice but frequently overlooked in simpler models.

Secondly, this approach accounts for the variable pullout strength along geosynthetic reinforcements, which is a critical factor in the seismic performance of reinforced soil structures. This consideration allows for a more nuanced evaluation of the actual field conditions, where uniform distribution of reinforcement strength is rarely achieved.

Thirdly, the method's applicability is broad, not confined to specific soil types or geosynthetic materials, thus offering a versatile tool for geotechnical engineers across a range of projects. It also leads to more informed design recommendations that can improve the seismic resilience of geosynthetic-reinforced soil structures.

4.2 Limitations of the proposed method

Despite its merits, this method is not without limitations. The complexity inherent in the log spiral failure mechanism requires detailed input data and a deep understanding of the soil-geosynthetic interaction, which may pose challenges for practitioners in various engineering settings.

The method also relies on several assumptions, including the rigid-plastic behavior of soil and the idealized log spiral failure surface, which can introduce approximation errors into the analysis. The precision of slope stability assessments is sensitive to the accuracy of input parameters, such as the internal friction angle of soil and the pullout strength of geosynthetics. Uncertainties in these parameters can lead to variations in the outcomes of slope stability evaluations.

5 Conclusion

This paper presents a thorough analysis of the seismic stability of reinforced soil slopes, utilizing both the limit equilibrium method and the log spiral curve model. The conclusion mainly revolves around the following key points:

5.1 Effects of pullout strength indicators of geosynthetics

The pullout strength indicators of geosynthetics have a significant effect on the seismic stability of reinforced soil slopes. The seismic yield accelerations calculated using the ultimate bearing capacity are noticeably smaller than that obtained using the ultimate pullout strength particularly as the length of the reinforcement is reduced. This suggests that the distribution characteristics of the actual pullout strength of geosynthetics should be fully considered in seismic design.

5.2 Optimization of reinforcement layout and layering

This paper discusses the effect of different layouts and layer numbers on slope stability. The results show that reducing the number of layers decreases the seismic stability of the slope, while a reasonable layout of geosynthetics can enhance the seismic performance of the slope. This provides theoretical support for the optimized layout of geosynthetics in engineering practice.

5.3 Guidance for seismic reinforcement design

The results have significant guiding implications for the seismic reinforcement design of reinforced soil slopes. By considering the nonuniform distribution of pullout strengths, the stability of the slope under seismic action can be more accurately assessed, and more effective reinforcement measures can be formulated.

Although this paper provides valuable insights, there are still some limitations. For example, the simplification of model assumptions and the uncertainty of parameters may affect the accuracy of the results. Future research can improve the precision and applicability of the evaluation method by considering more influencing factors and more complex models.

Data availability statement

The original contributions presented in the study are included in the article/supplementary material, further inquiries can be directed to the corresponding author.

Author contributions

XC: Formal Analysis, Funding acquisition, Investigation, Software, Supervision, Writing–original draft. ZZ: Conceptualization, Data curation, Formal Analysis, Methodology, Software, Validation, Writing–review and editing. YZ: Data curation, Formal Analysis, Validation, Writing–original draft. SP: Methodology, Software, Writing–review and editing. DZ: Methodology, Resources, Writing–review and editing. EL: Methodology, Supervision, Validation, Writing–review and editing.

Funding

The author(s) declare that financial support was received for the research, authorship, and/or publication of this article. This research was funded by the National Natural Science Foundation of China, grant number 52208361, 52278420; and the Natural Science Foundation of Jiangsu Province, grant number BK20220638.

Conflict of interest

The authors declare that the research was conducted in the absence of any commercial or financial relationships that could be construed as a potential conflict of interest.

The handling editor HT declared a shared affiliation with the author YZ at the time of review.

Generative AI statement

The author(s) declare that no Generative AI was used in the creation of this manuscript.

Publisher's note

References

1. Zhang F, Zhu Y, Chen Y, Yang S. Seismic effects on reinforcement load and lateral deformation of geosynthetic-reinforced soil walls. *Front Struct Civil Eng* (2021) 15(4):1001–15. doi:10.1007/s11709-021-0734-8

2. Fan C, Liu X, Zhang Y, An X, Liu H. Centrifuge shaking table tests on tiered reinforced soil retaining walls subjected to the excitations of near-field ground motions. *Geotextiles and Geomembranes* (2024) 52(4):343–54. doi:10.1016/j.geotexmem.2023.12.001

3. Ren F, Huang Q, Zhang F, Wang G. Numerical study on seismic performance of tiered reinforced soil retaining walls. *Soil Dyn Earthquake Eng* (2024) 181:108672. doi:10.1016/j.soildyn.2024.108672

4. Shu S, Ge B, Wu Y, Zhang F. Probabilistic assessment on 3D stability and failure mechanism of undrained slopes based on the kinematic approach of limit analysis. *Int J Geomechanics* (2023) 23(1):06022037. doi:10.1061/(asce)gm.1943-5622.0002635

5. Shu S, Ge B, Wu Y, Zhang F. Reliability analysis of excavated slopes in undrained clay. *Front Struct Civil Eng* (2023) 17(11):1760–75. doi:10.1007/s11709-023-0018-6

6. Bathurst RJ, Hatami K, Alfaro MC. Geosynthetic-reinforced soil walls and slopes—seismic aspects. In: *Geosynthetics and their applications*. Thomas Telford Publishing (2002). p. 327–92.

7. Yünkül K, Gürbüz A. Determination of shear stress-shear strain behavior of polymeric geostrip reinforced MSE wall. *Geotextiles and Geomembranes* (2024) 52(2):184–95. doi:10.1016/j.geotexmem.2023.10.002

8. Perez A, Holtz RD. Seismic response of reinforced steep soil slopes: results of a shaking table study. In: *Geotechnical engineering for transportation projects* (2004). p. 1664–72.

9. Nova-Roessig L, Sitar N. Centrifuge model studies of the seismic response of reinforced soil slopes. *J Geotechnical Geoenvironmental Eng* (2006) 132(3):388–400. doi:10.1061/(asce)1090-0241(2006)132:3(388)

10. Lin YL, Leng WM, Yang GL, Li L, Yang JS. Seismic response of embankment slopes with different reinforcing measures in shaking table tests. *Nat Hazards* (2015) 76:791–810. doi:10.1007/s11069-014-1517-5

11. Hazari S, Ghosh S, Sharma RP. Experimental and numerical study of soil slopes at varying water content under dynamic loading condition. *Int J Civil Eng* (2020) 18:215–29. doi:10.1007/s40999-019-00439-w

12. Jana K, Hazari S, Ghosh S. Experimental and numerical studies of three-layered unreinforced and geosynthetic-reinforced soil slopes. *Innovative Infrastructure Solutions* (2021) 6:41–29. doi:10.1007/s41062-020-00408-6

13. Huang L, He W, Hou Y, Liu D, Wang B, Zhu J, et al. Seismic behavior of flexible geogrid wrap-reinforced soil slope. *Adv Civil Eng* (2021) 2021(1):8833662. doi:10.1155/2021/8833662

14. Zeng WX, Liu FY, Ying MJ. Cyclic response of stereoscopic geogrid–sand interface under static and cyclic loading. *Geosynthetics Int* (2023) 1–14. doi:10.1680/jgein.23.00009

15. Yazdandoust M. Assessment of horizontal seismic coefficient for three different types of reinforced soil structure using physical and analytical modeling. *Int J Geomechanics* (2019) 19(7):04019070. doi:10.1061/(asce)gm.1943-5622.0001344

16. Patra S, Shahu JT. Pseudo-static analysis of reinforced soil wall based on pasternak model. *Indian Geotechnical J* (2020) 50(2):252–60. doi:10.1007/s40098-019-00400-7

17. Sarbishei S, Fakher A. Energy-based horizontal slice method for pseudo-static analysis of reinforced walls. *Geosynthetics Int* (2012) 19(5):370–84. doi:10.1680/gein.12.00023

18. Steedman RS, Zeng X. The influence of phase on the calculation of pseudo-static earth pressure on a retaining wall. *Geotechnique* (1990) 40(1):103–12. doi:10.1680/geot.1990.40.1.103

19. Basha BM, Babu GS. Reliability assessment of internal stability of reinforced soil structures: a pseudo-dynamic approach. *Soil Dyn Earthquake Eng* (2010) 30(5):336–53. doi:10.1016/j.soildyn.2009.12.007

20. Yan M, Xia Y, Liu T, Bowa VM. Limit analysis under seismic conditions of a slope reinforced with prestressed anchor cables. *Comput Geotechnics* (2019) 108:226–33. doi:10.1016/j.compgeo.2018.12.027

21. Ruan XB, Sun SL. Seismic stability of reinforced soil walls under bearing capacity failure by pseudo-dynamic method. *J Cent South Univ* (2013) 20:2593–8. doi:10.1007/s11771-013-1773-7

22. Kitamoto Y, Abe H, Shimomura H, Morishima H, Taniguchi Y. Rapid and strengthened repair construction for a seriously damaged railway embankment during violent earthquakes. In: *Proc. Of 8th international conference on geosynthetics* (2006). p. 861–4.

23. Kuwano J, Miyata Y, Koseki J. Performance of reinforced soil walls during the 2011 Tohoku earthquake. *Geosynthetics Int* (2014) 21(3):179–96. doi:10.1680/gein.14.00008

24. FHWA. *Design and construction of mechanically stabilized earth walls and reinforced soil slopes-Volume I, Federal Highway Administration Publication No. FHWA-NHI-10-243*. Washington, DC, USA: US Department of Transportation (2009).

25. AASHTO. *LRFD bridge design specifications*. 6th ed. Washington, DC: AASHTO (2012).

26. Ling HI, Leshchinsky D, Chou NN. Post-earthquake investigation on several geosynthetic-reinforced soil retaining walls and slopes during the Ji-Ji earthquake of Taiwan. *Soil Dyn Earthquake Eng* (2001) 21(4):297–313. doi:10.1016/s0267-7261(01)00011-2

frontiers | Frontiers in Physics

TYPE Brief Research Report
PUBLISHED 26 February 2025
DOI 10.3389/fphy.2025.1522240

OPEN ACCESS

EDITED BY
Sanjay Shrawan Nimbalkar,
University of Technology Sydney, Australia

REVIEWED BY
Zeeshan Asghar,
Prince Sultan University, Saudi Arabia
Gan Feng,
Sichuan University, China
Yifei Gong,
Hohai University, China

*CORRESPONDENCE
Shu Yang,
matrixwho@stu.xju.edu.cn
Shuaikang Li,
17799703263@163.com

RECEIVED 04 November 2024
ACCEPTED 06 February 2025
PUBLISHED 26 February 2025

CITATION
Gu J, Wang J, He M, Yang S and Li S (2025) Research on relaxation characteristics of columnar jointed basalts of deep foundation in hydropower station.
Front. Phys. 13:1522240.
doi: 10.3389/fphy.2025.1522240

Research on relaxation characteristics of columnar jointed basalts of deep foundation in hydropower station

Jinjian Gu[1], Jianxin Wang[1], Mingjie He[1], Shu Yang[2]* and Shuaikang Li[2]*

[1]PowerChina Huadong Engineering Corporation, Hangzhou, China, [2]College of Civil Engineering and Architecture, Xinjiang University, Urumqi, China

The columnar basalt is a widely distributed in Southwestern China with different types. The first type of columnar jointed basalt is distributed below the elevation of 665 m on the left bank and 590 m on the right bank of the arch dam foundation. Micro-fissures are prevalent within the columns, with gently dipping structural surfaces and an intermittent mosaic structure despite poor overall integrity. The structure is easy to relax after unloading, and the acoustic wave of rock mass is obviously reduced. The control of relaxation deformation of columnar joint basalt is a key problem of hydropower exploration. Based on the structural of columnar jointed basalt, this paper analyzed the relaxation characteristics of columnar jointed basalt.

KEYWORDS

hydropower exploration, columnar joint basalt, intermittent mosaic structure, relaxation characteristics, treatment measures

1 Introduction

In recent years, with the rise of the concept of green ecological development in the world, the development and utilization of clean energy has become one of the indispensable means in the world. Hydropower is a globally recognized clean, high-quality and flexible renewable energy power. All countries in the world give priority to hydropower development, and the western developed countries basically completed their hydropower resource development tasks in the 1980 s. Large and medium-sized hydropower projects also have comprehensive utilization functions such as flood control, disaster reduction, water supply, shipping, irrigation, tourism, and breeding, and have become the most important infrastructure for economic and social development in various countries [1–4]. Hydropower development is not only the need to promote the development of new energy, optimize the energy structure, and reduce carbon emissions, but also the need to realize the comprehensive utilization of water resources, disaster prevention and mitigation, and ecological protection. Therefore, the Chinese government attaches great importance to hydropower development and continues to incorporate hydropower development tasks into the national development plan [5, 6].

In hydropower construction, dams are the most common hydropower infrastructure [7]. China's hydropower station construction is world-renowned [8–14]. The main facility of a hydroelectric power station is the construction of the dam, which is usually located in an unpopulated and difficult terrain. Therefore, dam foundation excavation is an important construction link in water conservancy projects and is the focus of quality control in water conservancy construction. In this paper, the relaxation characteristics of columnar jointed basalt after excavation of the foundation are investigated. At the same time, the treatment measures for the relaxation of columnar jointed basalt are explored.

The Baihetan Hydropower Station's 289m-high arch dam features a massive structure and complex dam foundation geology. Columnar jointed basalt, characterized by 2–3 m long columns with diameters of 13–25 cm and micro-cracks forming 5 cm-sized fragments, is distributed below 665 m on the left bank and 590 m on the right. This rock mass relaxes easily after excavation, making the study of its relaxation characteristics and treatment measures crucial for the dam foundation's stability [15].

2 Method

2.1 Structural classification and distribution of columnar jointed basalt

The basalts in the area exhibit diverse lithologies, strong heterogeneity, well-developed structural planes, and significant unloading characteristics. Columnar jointed basalts are irregular, with varying column sizes and lengths, primarily pentagonal or quadrilateral cross-sections, and lack the regular finger structure typically formed by double diffusion and convection. Instead, they result from magma cooling and contraction [16]. Based on geological conditions and dam foundation evaluation requirements, columnar joints are classified into three categories.

(1) The density of columnar joints is relatively high, and most of them are not cut into a complete column. The length of the column is generally 2~3 m, and the diameter is 13–25 cm. It is about 5 cm.
(2) The columnar joints develop irregularly and are not cut into a complete column. The length of the column is generally between 0.5 and 2.0 m, and the diameter is 25–50 cm. The micro-cracks in it are relatively developed, but they bite each other and are not completely cut. The block size is 10 cm about.
(3) The columnar joints develop irregularly and are not cut into a complete cylinder. The cylinder is thick, with a length ranging from 1.5 to 5 m and a diameter of 0.5–2.5 m. The cutting is incomplete and the chimera is tight.

Among them, the first type of columnar jointed basalt has the characteristics of high wave velocity, high integrity coefficient, small block size, well-developed cracks, small crack spacing, and tightly embedded rock blocks. It is neither a sub-blocky structure nor a fragmented structure. and mosaic structures, but have a unique structure outside the specification standard. Therefore, it is classified into the category of mosaic structure and named as the subcategory of "columnar mosaic structure". The joint distribution of the first type of columnar joint basalts is shown in Figure 1. $P_2\beta_3^3$, $P_2\beta_4^1$ and $P_2\beta_6^1$ layers of columnar jointed basalts are mainly distributed in the dam foundation, and the specific distribution. The $P_2\beta_3^3$ sublayer is distributed in the riverbed and the low-elevation dam foundation on both banks, and the columnar joints are the most developed, which is the focus of the dam foundation rock mass research.

2.2 *In-situ* experiment test

Two main *in situ* test, namely, rigid bearing plate method and acoustic borehole testing method are used in this study as shown in Figure 2. Rigid bearing plate test is used to get the deformation modulus, while acoustic borehole test is employed to get the reduction of seismic velocity.

2.2.1 Rigid bearing plate method

2.2.1.1 Experiment procedure

In the rigid pressure plate test, a Φ504.6 mm, 60 mm thick pressure plate with a surface area of 2000 cm^2 is used. A 3200 kN jack and a 60 MPa high-pressure rubber hose connect to a manual or electric oil pump for loading. Four mechanical micrometers are symmetrically fixed to measuring rods embedded in concrete as reference points. Pressurization follows a step-by-step approach with five pressure levels: 2.0 MPa, 4.0 MPa, 6.0 MPa, 8.0 MPa, and 10.0 MPa, applied in single steps, with a maximum pressure of 10.0 MPa. The test adheres to geological standards and specifications.

To measure rock deformation, four measurement points are symmetrically arranged around the pressure plate, each equipped with a micrometer. Loading begins only after ensuring instrument stability, confirmed by consistent readings across three consecutive checks. Upon loading, an initial reading is taken immediately, followed by readings every 10 min. The criterion for deformation stability is that the ratio of the difference between two consecutive readings of the 4 μm to the difference between the initial reading at the current pressure level and the final reading at the previous level must remain within 5% per hour. After the loading process, pressure is gradually released in steps. When the pressure reaches zero, an immediate reading is recorded, followed by additional readings every 10 min until the experiment concludes.

2.2.1.2 Deformation modulus computation

The total deformation and elastic deformation of the rock mass are determined by averaging the measurements from the 4 μm. The deformation modulus and elastic modulus of the rock mass are subsequently calculated using the following formulas:

$$E = \frac{\pi}{4} \times \frac{\left(1-\mu^2 PD\right)}{W} \tag{1}$$

Where, the parameters include the Poisson's ratio of the rock mass (μ), unit pressure(P), diameter of the pressure plate(D), and the measured deformation of the rock mass(W). When total deformation values are substituted into the formulas, the resulting modulus(E) represents the deformation modulus (E_0). Conversely, when elastic deformation values are substituted, the calculated modulus represents the elastic modulus.

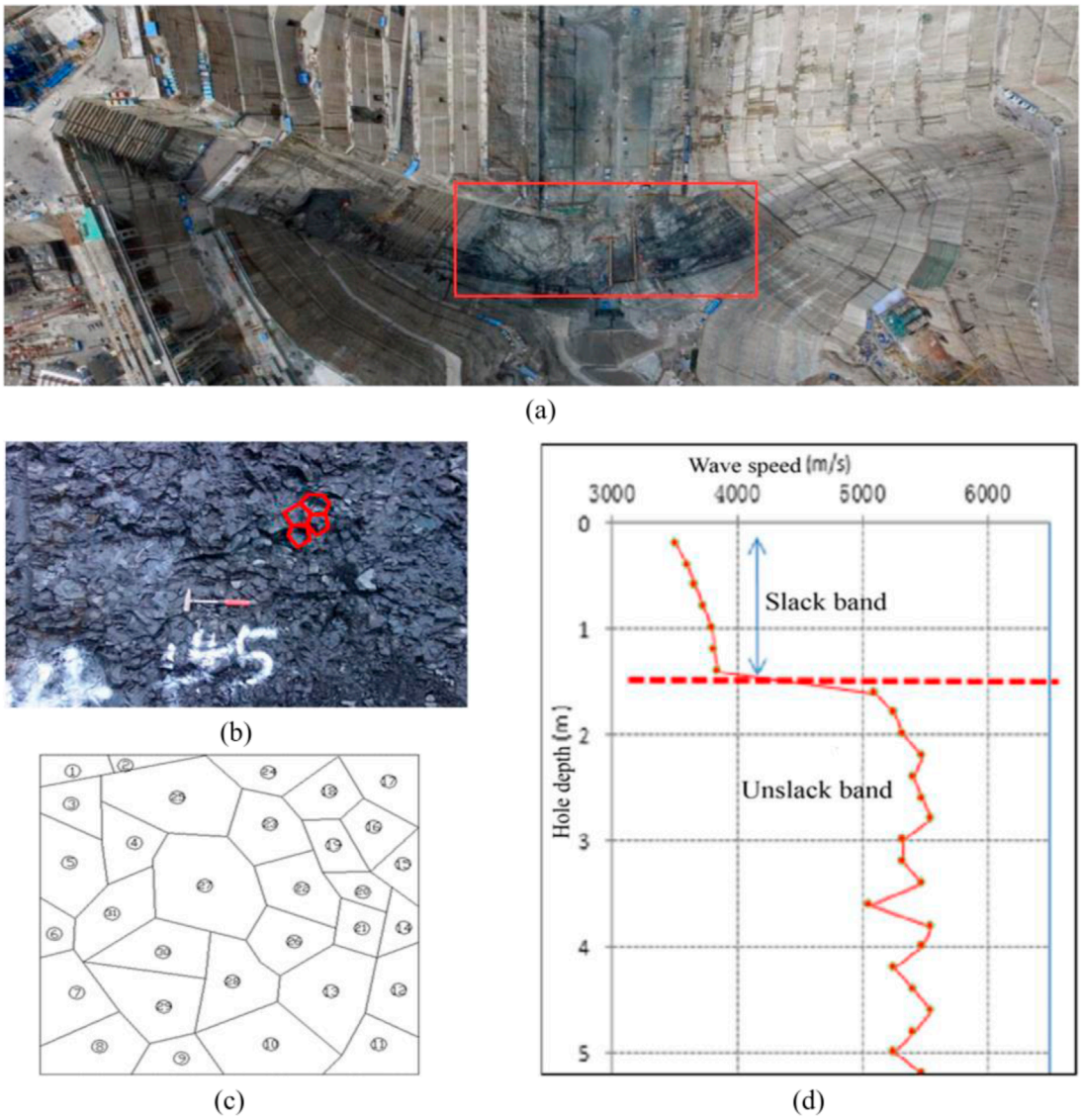

FIGURE 1
(A) Baihetan hydropower station infrastructure **(B)** The image of the first type of columnar joint basalt; **(C)** The geological sketch of the columnar joint basalt; **(D)** Typical graph of wave speed distribution in relaxed rock mass.

2.2.2 Acoustic borehole testing method

2.2.2.1 Basic theory

A Yanhai RS-ST01C non-metallic acoustic detector was used for single-hole acoustic wave tests with a single-transmit, dual-receive configuration. The probe transmits acoustic waves, received by two transducers, and the propagation velocity is calculated from the time difference and known transducer spacing. This velocity provides insights into rock mass properties, failure surfaces, and structural integrity. Measurements are taken every 20 cm from top to bottom, with the test conducted before the rock deformation test.

To determine the acoustic velocity of the rock mass along the borehole wall, the time difference of the acoustic waves traveling from various measurement points to the two receiving transducers is extracted from the original acoustic wave record. The acoustic velocity of the rock mass is then calculated by dividing the distance between the transducers by this time difference, as expressed in the following formula:

$$\Delta t = |t_1 - t_2| \tag{2}$$

$$v_p = \frac{L}{\Delta t} \times 10^6 \tag{3}$$

Where, t_1, t_2 represent the first arrival times of the same excitation signal at each of the two receiving transducers, respectively. The time difference between these arrivals, denoted as Δt is measured in microseconds (μs). The spacing between the two receiving transducers, L is fixed at 0.2 m (m). The speed of sound in the rock mass, represented as v_p, is then calculated in meters per second (m/s) using this time difference and the known distance between transducers.

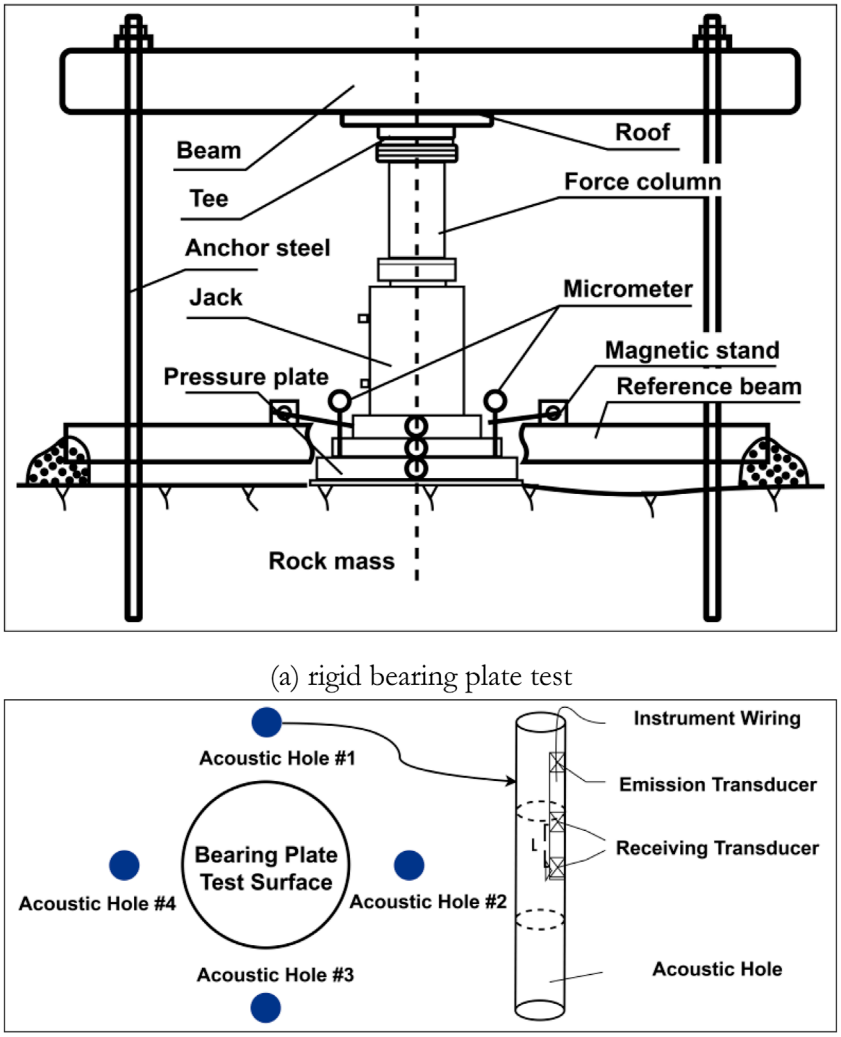

FIGURE 2
Experiment test used in this study. **(A)** Rigid bearing plate test. **(B)** acoustic borehole test.

2.2.2.2 Evaluation of the relaxation effect

Assuming the original wave velocity of the rock mass (v_0) is known, the wave velocity (v_w) is then measured again after the surface of the rock mass is excavated, resulting in a reduced wave velocity. To quantify the change between these two wave velocity values, a wave velocity change coefficient (η)can be defined.

$$\eta = 1 - \frac{v_\omega}{v_0} \tag{4}$$

According to the Technical Specifications for Construction of Rock Foundation Excavation Engineering of Hydraulic Structures, it is stipulated that when the wave velocity change coefficient (η) of the excavated rock mass is less than or equal to 10%, excavation is considered to have no impact on rock mass quality. Conversely, when η exceeds 15%, the rock mass quality is regarded as being significantly affected by the excavation. If η falls between these two values, excavation is considered to have only a minor impact on the quality of the rock mass.

3 Results

3.1 Physical and mechanical parameters of columnar jointed basalt

There is anisotropy in the columnar joint basalt structure, and there is a certain difference in the deformation modulus perpendicular to the direction parallel to the columnar joints [17–19]. In order to study the deformation modulus of columnar joint basalt in different directions, Baihetan Project conducted a series of on-site *in situ* tests, which can better reflect the natural characteristics of the rock mass. The *in situ* test mainly adopts the rigid bearing plate test, and the load direction is divided into horizontal direction and vertical direction [20, 21].

In the *in situ* pressure plate test at Baihetan, the deformation modulus of III1 rock mass ranges from 9–11 GPa horizontally and 7–9 GPa vertically, while for III2 rock mass, it ranges from 7–9 GPa horizontally and 5–7 GPa vertically. Vertical deformation modulus

is significantly lower than horizontal, with vertical-to-horizontal ratios of 0.8 for III_1 and 0.75 for III_2, indicating pronounced anisotropy.

3.2 Structural and mechanical properties of columnar basalt after relaxation

There must be relaxation after excavation of columnar jointed basalt. The relaxed rock mass needs to be used as the foundation of high arch dams. It is necessary to study the characteristics of columnar jointed basalt after relaxation.

The Maxwell model can be used to describe the properties of rocks that exhibit instantaneous deformation, steady creep, and relaxation. Next, the relaxation phenomenon of rocks is explained based on the physical concept of the model. The Maxwell model is a viscoelastic body composed of a spring and a damper connected in series.

(1) Constitutive equation

$$\sigma = \sigma_1 = \sigma_2 \tag{5}$$

$$e = \varepsilon_1 + \varepsilon_2 \tag{6}$$

Due to:

$$\dot{\varepsilon_1} = \frac{1}{k}\sigma \tag{7}$$

$$\dot{\varepsilon_2} = \frac{1}{\eta}\sigma \tag{8}$$

Therefore:

$$\dot{\varepsilon} = \frac{1}{k}\sigma + \frac{1}{\eta}\sigma \tag{9}$$

(2) Creep equation

Under a constant load σ ($\sigma = \sigma_0$), since $d\sigma/dt = 0$, the constitutive equation simplifies to:

$$\dot{\varepsilon} = \frac{1}{\eta}\sigma_0 \tag{10}$$

Solving this differential equation gives:

$$\varepsilon = \frac{1}{\eta}\sigma_0 t + C \tag{11}$$

Where C is the integration constant. Using the initial conditions to solve for C, when $t = 0$, $\varepsilon = \varepsilon_0 = \frac{\sigma_0}{k}$, Thus, $C = \sigma_0/k$,Substituting C into the above equation, the creep equation for the Maxwell model is obtained as:

$$\varepsilon = \frac{1}{\eta}\sigma_0 t + \frac{\sigma_0}{k} \tag{12}$$

From the equation, it can be seen that the model exhibits instantaneous strain and that the strain gradually increases with time. This model represents steady-state creep.

(3) Relaxation equation

To maintain a constant strain ε, $\dot{\varepsilon} = 0$, and the constitutive equation becomes:

$$\frac{1}{k}\sigma + \frac{1}{\eta}\sigma = 0 \tag{13}$$

Solving this equation yields:

$$-\frac{k}{\eta}t = \ln\sigma + C \tag{14}$$

Where C is the integration constant. Using the initial condition, at $t = 0$, $\sigma = \sigma_0$ (σ_0 is the instantaneous stress), we find $C = -\ln\sigma_0$. Substituting C into the equation gives:

$$-\frac{k}{\eta}t = \ln\sigma - \ln\sigma_0 = \ln\frac{\sigma}{\sigma_0} \tag{15}$$

Thus,

$$\sigma = \sigma_0 e^{-\frac{k}{\eta}t} \tag{16}$$

From this equation, it can be observed that as t increases, σ gradually decreases. In other words, when the strain is constant, the stress decreases over time, a mechanical phenomenon known as relaxation.

From the physical concept of the model, relaxation can be understood as follows: at $t = 0$, the viscous element cannot deform instantaneously, so only the elastic element undergoes deformation. However, as time progresses, the viscous element gradually deforms under the action of the spring. As the damper elongates, the spring gradually contracts, leading to a reduction in stress within the spring. This is the essence of relaxation.

Long-term observations were conducted on columnar joint basalt to analyze its structural and mechanical properties after relaxation. Following the excavation of a simulated test hole in March 2011, geological points were observed again in June 2015, with comparison photos recorded. Observations from March to July 2015 at the dam foundation revealed no significant changes in rock mass structure, though surface rock blocks became more prone to detachment. After 4 years and 3 months, the relaxed layer at the dam base site stabilized, with slight surface weathering and discoloration but no significant opening of columnar joints or microfractures, maintaining a columnar mosaic structure.

To assess the mechanical properties of the relaxed layer of columnar joint basalt at the Baihetan dam foundation (650–660 m elevation), 11 rigid bearing plate tests were conducted. Results show the deformation modulus of the relaxed layer is 4–6 GPa, slightly lower than the 5–7 GPa of the unrelaxed rock mass. While the deformation modulus has deteriorated, the rock mass structure remains intact, and the mechanical properties of the relaxed and unrelaxed rock masses are largely comparable.

3.3 Determination of relaxation property in columnar jointed basalt

Due to the dense joints of columnar joint basalt, the relaxation effect is more obvious after excavation and unloading, the columnar

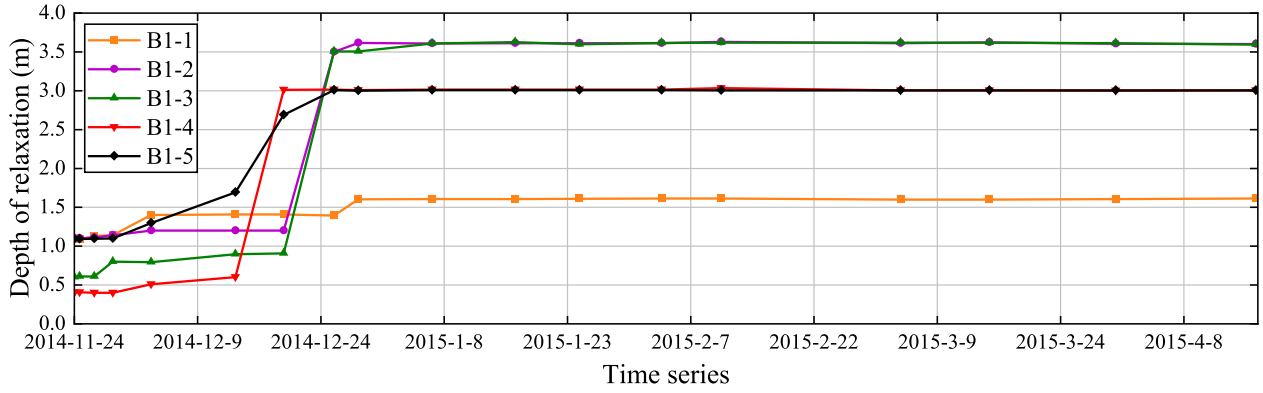

FIGURE 3
Variation of relaxation depth in dam foundation excavation test area.

TABLE 1 Average wave velocity values of rock bodies within 1 m depth in columnar joints.

Category	Rock type grade	η ≤ 10%		10%<η ≤ 15%		η>15%	
		Count	Proportion	Count	Proportion	Count	Proportion
First type of columnar jointed basalt	III1	13	43.3%	3	10.0%	10	33.3%
	III2	---	---	1	3.3%	3	10.0%
Cryptocrystalline basalt	III1	2	33.3%	2	33.3%	---	---
	III2	2	33.3%	---	---	---	---
Breccia Lava	III1	3	33.3%	1	11.1	3	33.3%
	III2	---	---	---	---	2	22.2%

joints of the surface rock mass open, the transverse micro-cracks gradually appear, and the sound wave velocity of the rock mass decreases, especially in the surface layer where the ground stress is high.

As shown in Table 1, for the First Type of Columnar Jointed Basalt, the proportion of rocks with a wave velocity variation coefficient η>15% is 43.3%, 10%<η ≤ 15% is 13.3%, and η<10% is 43.3%. Therefore, excavation has a relatively large impact on the quality of the First Type of Columnar Jointed Basalt. The cryptocrystalline basalt has all wave velocity variation coefficients η below 15%, indicating that excavation has only a slight impact on the quality of cryptocrystalline basalt. For breccia lava, the proportion of rocks with a wave velocity variation coefficient η ≤ 10% is 33.3%, 10%<η ≤ 15% is 11.1%, and η>15% is 55.6%, Thus, excavation has a greater impact on the quality of breccia lava, with more than half of the rocks affected by excavation.

4 Discussion

The first type of columnar jointed basalt, characterized by dense joints and developed transverse micro-cracks, easily relaxes after excavation and unloading. Thus, its relaxation characteristics are a key focus in the foundation treatment of the Baihetan Dam. Extensive acoustic detection tests have been conducted in exploration tunnels, simulation test tunnels, diversion tunnels, and dam foundation test areas to systematically study these characteristics.

Comparing the factors affecting the relaxation depth of columnar joint basalt such as size effect, time effect and *in situ* stress, the specific effects are as follows.

4.1 Size effect

Comparing the excavation size and the average relaxation layer thickness, the thickness of the columnar joint basalt relaxation layer basically increases with the increase of the excavation size. When the excavation size is larger, the influence on the relaxation layer thickness decreases [22].Unloading relaxation exhibits a certain size effect, specifically manifested as follows: for smaller sizes, the relaxation depth increases with the size, while for larger sizes, the relaxation depth no longer increases. Fault zones have a certain impact on rock mass relaxation, particularly at the leading edge of the fault zone, where localized shear deformation occurs.

4.2 Time effect

Statistics show that the stable time of the relaxed layer is roughly between 25 days and 46 days, and the stable time tends to prolong with the expansion of the excavation surface. The change process of the rock mass excavation relaxation depth measured by the acoustic inspection hole in the dam foundation excavation test area is shown in Figure 3 below. The relaxation depth gradually increases with time, and the relaxation depth reaches a stability about 40 days after excavation, with less variation later on [23].

4.3 *In-situ* stress effect

Comparing the test results of the observation section of $3^{\#}$ and $4^{\#}$ diversion tunnels, the relaxation depth of $4^{\#}$ diversion tunnel with higher *in situ* stress is 5.2–7.7 m, which is significantly higher than that of $3^{\#}$ diversion tunnel at 2.5–3.0 m. The higher the *in situ* stress, the greater the unloading rebound deformation, and the greater the stress relaxation [24].

5 Conclusion and prospect

The relaxation and deformation control of columnar jointed basalt foundations is crucial for super-high hydropower projects. This study investigates the structural and relaxation characteristics of columnar jointed basalt through various tests and proposes comprehensive control measures, including thick-layer protection, grouting consolidation, deep anchorage, and precise blasting. These measures effectively limit the relaxation depth to levels comparable to conventional rock masses, meeting the requirements for super-high hydropower stations.

This paper combines extensive monitoring data with experimental research to explore the deformation and strength characteristics of unloaded columnar jointed basalt, deepening the understanding of its mechanical properties. However, further research is needed to address shortcomings, including detailed studies of intact columnar jointed basalt alongside the relaxation layer. Integrating findings from other research units at the dam site will provide a more comprehensive understanding of columnar jointed basalt.

Data availability statement

The original contributions presented in the study are included in the article/supplementary material, further inquiries can be directed to the corresponding authors.

Author contributions

JG: Conceptualization, Software, Writing–original draft, Writing–review and editing. JW: Formal Analysis, Writing–original draft, Writing–review and editing. MH: Methodology, Writing–original draft, Writing–review and editing. SY: Visualization, Writing–original draft, Writing–review and editing. SL: Data curation, Supervision, Writing–original draft, Writing–review and editing.

Funding

The author(s) declare that financial support was received for the research, authorship, and/or publication of this article. This study is supported by the Fund for Less Developed Regions of the National Natural Science Foundation of China (Grant No. 52068066), the Fund for Less Developed Regions of the National Natural Science Foundation of China (Grant No. 52368052), and the National Science Fund for Distinguished Young Scholars of Xinjiang Uygur Autonomous Region (Grant No. 2022D01E32).

Conflict of interest

Authors JG, JW, and MH were employed by PowerChina Huadong Engineering Corporation.

The remaining authors declare that the research was conducted in the absence of any commercial or financial relationships that could be construed as a potential conflict of interest.

Generative AI statement

The author(s) declare that no Generative AI was used in the creation of this manuscript.

Publisher's note

References

1. Li X-z., Chen Z-j., Fan X-c., Cheng Z. Hydropower development situation and prospects in China. *Renew Sustainable Energy Rev* (2018) 82:232–9. doi:10.1016/j.rser.2017.08.090

2. Bartle A. Hydropower potential and development activities. *Energy policy* (2002) 30(14):1231–9. doi:10.1016/s0301-4215(02)00084-8

3. Moran EF, Lopez MC, Moore N, Müller N, Hyndman DW. Sustainable hydropower in the 21st century. *Proc Natl Acad Sci* (2018) 115(47):11891–8. doi:10.1073/pnas.1809426115

4. Egré D, Milewski JC. The diversity of hydropower projects. *Energy policy* (2002) 30(14):1225–30. doi:10.1016/s0301-4215(02)00083-6

5. Chang X, Liu X, Zhou W. Hydropower in China at present and its further development. *Energy* (2010) 35(11):4400–6. doi:10.1016/j.energy.2009.06.051

6. Sun X, Wang X, Liu L, Fu R. Development and present situation of hydropower in China. *Water Policy* (2019) 21(3):565–81. doi:10.2166/wp.2019.206

7. Zarfl C, Lumsdon AE, Berlekamp J, Tydecks L, Tockner K. A global boom in hydropower dam construction. *Aquat Sci* (2015) 77:161–70. doi:10.1007/s00027-014-0377-0

8. Tang H, Wasowski J, Juang CH. Geohazards in the three gorges reservoir area, China–lessons learned from decades of research. *Eng Geology* (2019) 261:105267. doi:10.1016/j.enggeo.2019.105267

9. Sun G, Yang Y, Jiang W, Zheng H. Effects of an increase in reservoir drawdown rate on bank slope stability: a case study at the Three Gorges Reservoir, China. *Eng Geology* (2017) 221:61–9. doi:10.1016/j.enggeo.2017.02.018

10. Niu C, Wang Q, Chen J, Zhang W, Xu L, Wang K. Hazard assessment of debris flows in the reservoir region of wudongde hydropower station in China. *Sustainability* (2015) 7(11):15099–118. doi:10.3390/su71115099

11. Li B, Xu N, Dai F, Gu G, Ke W. Microseismic monitoring and stability analysis for the large-scale underground caverns at the Wudongde hydropower station. *Bull Eng Geology Environ* (2020) 79:3559–73. doi:10.1007/s10064-020-01777-z

12. Zhang Z, Xu W, Wang W, Wang R. Triaxial creep tests of rock from the compressive zone of dam foundation in Xiangjiaba Hydropower Station. *Int J Rock Mech Mining Sci* (2012) 50:133–9. doi:10.1016/j.ijrmms.2012.01.003

13. Zhang S-l., Zhu Z-h., Qi S-c., Hu Y, Du Q, Zhou J. Deformation process and mechanism analyses for a planar sliding in the Mayanpo massive bedding rock slope at the Xiangjiaba Hydropower Station. *Landslides* (2018) 15:2061–73. doi:10.1007/s10346-018-1041-x

14. Zhao Y, Wang X, Zhang X, Jia Z, Zeng X, Zhang H. Rock borehole shear tests in dam foundation of Xiangjiaba hydropower station. *J Rock Mech Geotechnical Eng* (2012) 4(4):360–6. doi:10.3724/sp.j.1235.2012.00360

15. Shi A, Tang M, Zhou Q. Research of deformation characteristics of columnar jointed basalt at Baihetan hydropower station on Jinsha river. *Chin J Rock Mech Eng* (2008) 27(10):2079–86.

16. Ni S, He S, Chen Y. The failure modes, failure mechanisms and countermeasures of columnar jointed basalt rock mass. *Chin J Rock Mech Eng* (2016) 35(S1):3064–75. doi:10.13722/j.cnki.jrme.2015.0006

17. Di SJ, Zheng WT, Zhang JK. Back analysis on mechanical deformation parameters of columnar jointed rock mass [C]. *Proc Appl Mech Mater* (2011). doi:10.4028/www.scientific.net/AMM.55-57.1947

18. Kelsall PC, Case JB, Chabannes CR. Evaluation of excavation-induced changes in rock permeability. *Int J Rock Mech Mining Sci and Geomechanics Abstr* (1984) 21(3):123–35. doi:10.1016/0148-9062(84)91530-4

19. Pusch R, Stanfors R. The zone of disturbance around blasted tunnels at depth. *Int J Rock Mech Mining Sci* (1992) 29(5):447–56. doi:10.1016/0148-9062(92)92629-q

20. Fan Q, Wang Z, Xu J, Zhou M, Jiang Q, Li G. Study on deformation and control measures of columnar jointed basalt for baihetan super-high arch dam foundation. *Rock Mech And Rock Eng* (2018) 51(8):2569–95. doi:10.1007/s00603-017-1378-9

21. Carlson SR, Young RP. Acoustic emission and ultrasonic velocity study of excavation-induced micro-crack damage at the Underground Research Laboratory. *Int J Rock Mech Mining Sci Geomechanics Abstr* (1993) 30(7):901–7. doi:10.1016/0148-9062(93)90042-c

22. Wentang Z, Weiya X, Yu N. Scale effect and anisotropy of deformation modulus of closely jointed basaltic mass. *J Eng Geology* (2010) 18(4):559–65.

23. Pei S, Feng X, Zhang J. Time-dependent relaxation characteristics of columnar jointed basalts in high-slope dam foundation during excavation. *Rock Soil Mech* (2018) 39(10):3743–54. doi:10.16285/j.rsm.2018.0153

24. Peng W, Wang-bing H, Gang S. Size effect and *in-situ* stress influence of columnar jointed basalt relaxation zone. *Chin J Geotechnical Eng* (2018) 40(1):139–46. doi:10.11779/CJGE201801014

frontiers | Frontiers in Earth Science

TYPE Original Research
PUBLISHED 12 March 2025
DOI 10.3389/feart.2025.1544660

OPEN ACCESS

EDITED BY
Huiming Tan,
Hohai University, China

REVIEWED BY
Siyuan Zhao,
Sichuan University, China
Kun Fang,
Hong Kong University of Science and Technology, Hong Kong SAR, China

*CORRESPONDENCE
Hao Wen,
wenha0@yeah.net

RECEIVED 13 December 2024
ACCEPTED 17 February 2025
PUBLISHED 12 March 2025

CITATION
Wang D and Wen H (2025) Dynamic response and damage evolution characteristics of uniform rocky slopes with unstable rock masses based on shaking table tests.
Front. Earth Sci. 13:1544660.
doi: 10.3389/feart.2025.1544660

Dynamic response and damage evolution characteristics of uniform rocky slopes with unstable rock masses based on shaking table tests

Dong Wang[1] and Hao Wen[2]*

[1]China Railway Eryuan Engineering Group Co. Ltd, Chengdu, China, [2]College of Civil Engineering, Southwest Jiaotong University, Chengdu, China

Seismic activities often trigger catastrophic events including collapses and rockfalls on rocky slopes. This research endeavors to understand the dynamic behavior and damage modes in uniform rocky slopes with unstable rock masses. To achieve this objective, the paper constructs a physical model of uniform rocky slope with unstable rock mass and performs triaxial loading shaking table tests. Subsequently, the seismo-dynamic responses and associated damage modes of the slope are scrutinized, and the initiation and deformation mechanisms of the hazardous rock are revealed. Further, we obtained the marginal spectral energy evolution characteristics of measurement points of both the unstable rock and bedrock. This deciphers the damage evolution characteristics of the weak structural plane. The results indicate that there are distinct elevation and surface amplification effects within the rock slopes, which systematically lessened with increasing seismic intensity. The vertical deformation of unstable rock mass is more sensitive to high seismic intensity. The seismic-induced initiation process of unstable rock masses is split into three stages: trailing edge tension cracking, sliding damage of structural planes, and a complete failure of structural plane shear capacity. It is also established that the Hilbert and marginal spectra effectively identified the damage process of unstable rock masses containing weak structural planes.

KEYWORDS

HHT transformation, shaking table tests, marginal spectrum, rocky slope, unstable rock mass

1 Introduction

Numerous slopes vary in complexity and steepness in the mountainous regions, posing significant threats to transportation, housing, and public buildings along the routes (Huang, 2011; Tang et al., 2010; Zheng et al., 2023). Collapses and rockfalls are important manifestations of the destruction of rocky slopes (Kusak, 2019; Macciotta et al., 2014; Moos et al., 2022; Yang et al., 2023; Zhan et al., 2022). Recent years have seen growing attention in the engineering community toward slope safety, leading to substantial research progress in understanding landslides, collapses, and other disasters under static conditions (Cheng et al., 2017; Istiyanti et al., 2021; Yang et al., 2022; Yun et al., 2023; Zhao et al., 2019), as well as advancements in slope protection engineering (Jiang et al., 2022; Wei et al., 2024).

However, the western region is adjacent to the seismically active Qinghai-Tibet Plateau, characterized by numerous faults and fault zones, which predispose the area to frequent earthquakes (Ren et al., 2018). These seismic events significantly contribute to triggering collapses and rockfalls in the weathered rock layers of these slopes (Oswald et al., 2021; Valagussa et al., 2014; Zheng et al., 2022). Consequently, it becomes imperative to examine how rocky slopes, particularly those with unstable rock masses, behave and potentially fail when subjected to seismic activity. Such research could advance early detection of post-earthquake rockfall initiation and enhance the seismic resilience of slope engineering.

Under seismic loads, rocky slopes undergo elevation amplification effects, which directly affects the weak structural interfaces within the rock mass due to the bedrock's thrust, causing surface cracking (Alfaro et al., 2012; Song et al., 2020). In this scenario, the slope acts as the disturbance object, the rock mass represents the impacted object, and the structural surfaces serve as the transmission medium. It can be seen that the triggering factor for rock mass sliding during seismic events is the structural surface's load-bearing capacity failure post-seismic activity. Current scholarly work has yielded significant findings concerning the seismic stability of rocky slopes, focusing on risk assessment (Deng et al., 2020; Jeong et al., 2024; Yeznabad et al., 2021), multi-source coupling (Li et al., 2023; Martino et al., 2022), numerical analysis (Bouckovalas and Papadimitriou, 2005; Li H. et al., 2017), theoretical analysis (Zhang et al., 2022), and anchor destruction (Jia et al., 2024; Lin et al., 2017; Liu et al., 2016). Centrifuge modeling and shaking table tests are extensively utilized to examine the cumulative damage and failure mechanisms of seismic rocky slopes (Fang et al., 2023b; Song et al., 2021). Theoretical approaches such as acceleration response (Lin et al., 2017), Fourier transform spectrum (Li L.-Q. et al., 2017; Li et al., 2018), Hilbert-Huang Transform (HHT) (Fan et al., 2016), and transfer functions (Yang, 2013) are applied to investigate the gradual damage and instability of rocky slopes. Nonetheless, these studies predominantly focus on the seismic damage behavior of rocky slopes, with little consideration given to secondary disasters such as collapses and rockfalls triggered by the failure of rocky slopes with unstable rock masses. Microseismic signals are widely used in studying seismic rockfalls due to their effectiveness in providing information about surface processes (Feng et al., 2021). They serve as an efficient tool for early warning and localization of rockfalls. However, they are susceptible to disruption by external environmental factors and can be costly to implement. The seismic destruction of such slopes represents a complex dynamic coupling system (Chen et al., 2023), where the energy transfer between the slope and unstable rock, along with the condition of structural surfaces, is essential for evaluating rock stability. Furthermore, most research relies on uniaxial shaking table tests, neglecting multi-directional seismic forces' impact, which results in a gap with reality and an incomplete simulation of the seismic interaction between bedrock and unstable rocks.

To reveal the dynamic coupling mechanism of rock slopes and unstable rock mass systems, as well as the seismic damage behavior and damage evolution characteristics of weak structural planes, this paper simulates the dynamic behavior of uniform rocky slopes under seismic action using triaxial shake table tests, with a unstable rock mass containing weak structural planes set at the top of the slope. Analysis of monitored acceleration and displacement data reveals the initiation mechanism of the unstable rock mass. Utilizing the HHT method revealed the extent of damage to weak structural surfaces and the energy transfer dynamics. The results provide valuable insights for advancing engineering practices in rocky slope management.

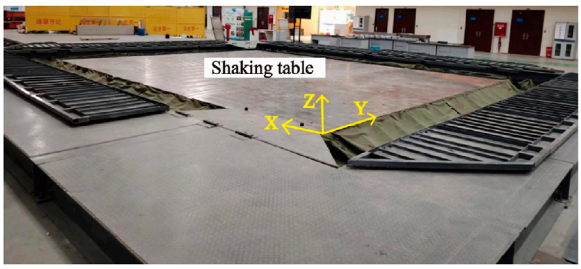

FIGURE 1
Schematic diagram of shaking table.

2 Experimental study

2.1 Test equipment

The rock slope model featuring an unstable rock mass underwent shaking table tests at Southwest Jiaotong University. The table has size of eight by 10 m and supports a maximum load of 160 tons (see Figure 1). The system functions over a frequency range spanning 0.1–50 Hz, allowing it to replicate a broad spectrum of seismic loads across three dimensions and six degrees of freedom. It can achieve a peak horizontal acceleration of ±1.2 g and horizontal travel of up to 800 mm along the X and Y-axes.

2.2 Modeling

Materials that mimic the properties of soil or rock have been extensively utilized in physical modeling experiments to study slope dynamics. In shaking table tests for slopes, it is essential to maintain similarity between the prototype and the model. Due to the substantial geometric dimensions of actual slope engineering, achieving correspondence across all parameters within a single similarity system is challenging. This study establishes a similarity system utilizing 17 independent physical quantities commonly employed in shaking table tests. The model is constructed based on Buckingham's π theorem and similarity theory (Yue et al., 2024). This theorem states that if phenomena are similar, the relationship describing various parameters can be transformed into a functional relationship between similarity criteria, and the functional relationship of the similarity criteria should be the same. Through analysis and organization, 17 independent physical quantities involved in this experiment are selected to establish a similarity system. These physical quantities must satisfy Equation 1:

$$f(L, \gamma, g, \varphi, E, \mu, c, v_s, A, T_d, \omega, \theta, s, V, a, \sigma, \varepsilon) = 0 \quad (1)$$

Taking physical dimensions L, volumetric weight γ, and gravity acceleration g as control parameters, the similarity

TABLE 1 Similarity ratio of the model.

No.	Parameters	Scale factor
1	Physical dimension, L	$C_L = 30$
2	Volumetric weight, γ	$C_\gamma = 1$
3	Gravitational acceleration, g	$C_g = 1$
4	Internal friction angle, φ	$C\varphi = 1$
5	Dynamic modulus of Elasticity, E	$C_E = C_\gamma C_L = 30$
6	Dynamic Poisson's ratio, μ	$C_\mu = 1$
7	Cohesion, c	$C_c = C_\gamma C_L = 30$
8	Shear wave velocity, V_s	$C_{Vs} = C_L^{0.5} = 5.477$
9	Input acceleration, A	$C_A = 1$
10	Duration, T_d	$C_{Td} = C_L^{0.5} = 5.477$
11	Frequency, ω	$C_\omega = C_L^{-0.5} = 0.18$
12	Linear displacement, s	$C_s = C_L = 30$
13	Angular displacement, θ	$C_\theta = 1$
14	Strain, ε	$C_\varepsilon = 1$
15	Stress, σ	$C_\sigma = C_\gamma C_L = 30$
16	Response velocity, V	$C_V = C_L^{0.5} = 5.477$
17	Response acceleration, a	$C_a = 5.477$

TABLE 2 Physic-mechanical parameters of materials.

Lithology	Density (g/cm^3)	Cohesion (kPa)	Internal friction angle (°)
Rock mass	2.2	20.01	36.6
Weak intercalation	1.8	0.95	27.65

relationships among various physical quantities are established as shown in Table 1.

To simulate the rock mass for the study, a blend was selected comprising barite powder, quartz sand, gypsum, water, and glycerin, with a weight ratio of 31:60:20:10:1. For the simulation of weak structural planes, a blend consisting of loess, river sand, and water in a weight ratio of 4:7:1 was employed (Fan et al., 2025). In mixed material construction, manual compaction is performed every 20 cm to ensure uniformity and density. To verify the compaction effect, density measurements of the compacted soil samples are taken at various locations using a ring knife after each layer is compacted. Table 2 provides the mechanical parameters for both the model materials and the structural surfaces.

FIGURE 2
Rigid model box.

To accommodate the size and loading constraints of the shake table, a specially designed and constructed rigid model box was used for the tests, as depicted in Figure 2. Robust bolts firmly attached the box to the table, facilitating the efficient transfer of seismic waves to the internal slope model. This model had dimensions of 2.9 m in length, 1.0 m in width, and 2.3 m in height. To observe the slope's dynamic response to different seismic forces, triaxial acceleration sensors and displacement sensors were strategically positioned along its central cross-section through the monitoring points marked on the foam boards on both sides of the model box. The location and side view of the model, as well as the sensor positions, are illustrated in Figure 3. The triaxial acceleration sensors had a measurement range of $\pm 2g \cdot s^{-2}$ and sensitivity of $42mV/m \cdot s^{-2}$, while the displacement sensors had a range of $50cm$ and sensitivity of $0.0195mV/mm$. All sensors operated at a sampling rate of 1,000 Hz. In rock slope studies, the boundary condition is often considered a semi-infinite medium. As vibration waves propagate through the slope, they gradually attenuate, dissipating energy through radiation and damping. Polyethylene foam boards are used to reduce vibrational energy from boundary reflections, simulating the actual slope conditions of a "non-reflective" or "free field." Within the model enclosure, a 10 cm thick layer of polyethylene foam acted as a padding to absorb and reduce the energy of vibrations caused by boundary reflections.

2.3 Test conditions

Based on the ATC-63 standards (Council, 2009), at least three seismic records, either artificial or actual, should be used for time-history analysis in shaking table tests. For this test, the seismic events selected as models were the typical Wolong, EL Centro, and Kobe earthquakes. These seismic waves were adjusted based

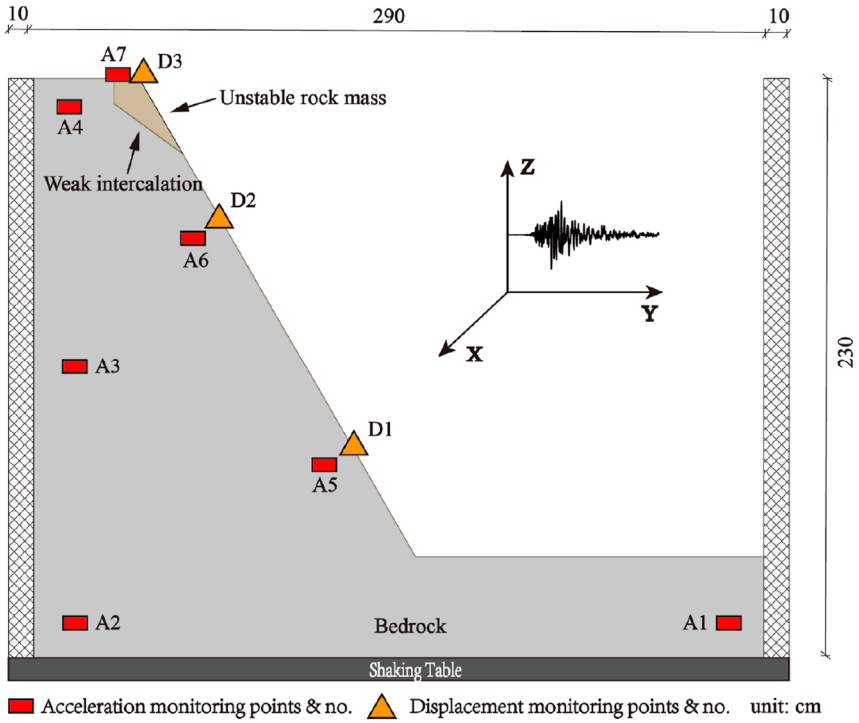

FIGURE 3
Sensors arrangement and model side view.

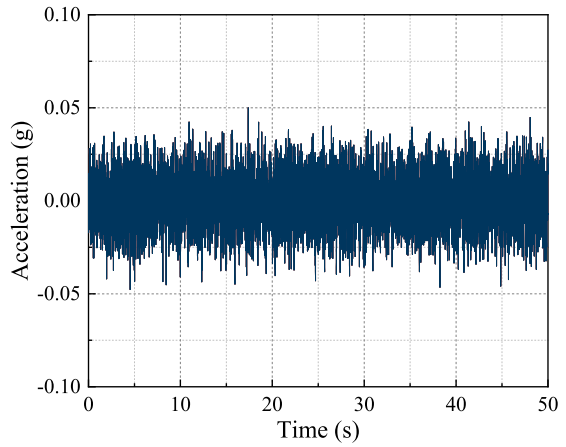

FIGURE 4
White noise time history curve.

on a time similarity ratio. After the adjustment, the durations for the Wolong, EL Centro, and Kobe seismic waves were reduced to approximately 36 s, 8 s, and 8 s, respectively. The seismic waves were applied in three different directions. Before application, each wave was normalized to achieve a peak amplitude of 0.1 g and subjected to baseline correction. Furthermore, varying vibration amplitudes were adjusted to mimic different seismic intensities. Before each seismic loading, the test model was subjected to frequency scanning using white noise to provide data for subsequent studies on how the rock-soil mass of slopes evolves in terms of damage following an earthquake. The selected white noise signal had low energy and frequency bandwidth (covering the resonant frequency band of the slope model at least three times). Specifically, the signal exhibited a vibration acceleration of 0.05 g and was characterized by a dominant frequency range spanning 0–150 Hz, as depicted in Figure 4. The sequence for applying the seismic waves is detailed in Table 3, while the time history curves and spectral characteristics of normalized waves in the X direction are depicted in Figure 5.

3 Dynamic response characterization

3.1 Accelerated response

The dynamic characteristics of slopes during seismic processes can be reflected by acceleration signals. To better understand the acceleration response of rocky slopes internally and on the surface at various depths along the free surface direction (X direction), two sets of monitoring points (A2, A3, A4) and (A5, A6, A4) under seismic excitation were selected for analysis, as depicted in Figure 6. Within the rock slope, elevational and surface amplification effects are apparent, and these effects intensify as the slope's height increases. Moreover, as seismic intensity rises, the acceleration amplification effects at different depths gradually weaken and tend to equilibrium.

Wave effects such as reflection, transmission, and waveform transformation on the slope surface or interface can result in local acceleration distortion on the slope surface. Consequently, single-point acceleration values do not adequately represent the vibration

TABLE 3 Seismic wave loading sequence.

No.	Amplitude (g)			Excitation signal	No.	Amplitude (g)			Excitation signal	No.	Amplitude (g)			Excitation signal
	X	Y	Z			X	Y	Z			X	Y	Z	
1	0.05	0.05	0.05	WN	10	0.4			KB	19	0.8	0.48	0.48	EL
2	0.1			KB	11	0.4	0.24	0.24	EL	20	0.8	0.56	0.72	WL
3	0.1	0.06	0.06	EL	12	0.4	0.28	0.36	WL	21	0.05	0.05	0.05	WN
4	0.1	0.07	0.09	WL	13	0.05	0.05	0.05	WN	22	1.0			KB
5	0.05	0.05	0.05	WN	14	0.6			KB	23	1.0	0.6	0.6	EL
6	0.2			KB	15	0.6	0.36	0.36	EL	24	1.0	0.7	0.9	WL
7	0.2	0.12	0.12	EL	16	0.6	0.42	0.54	WL	25	0.05	0.05	0.05	WN
8	0.2	0.14	0.18	WL	17	0.05	0.05	0.05	WN					
9	0.05	0.05	0.05	WN	18	0.8			KB					

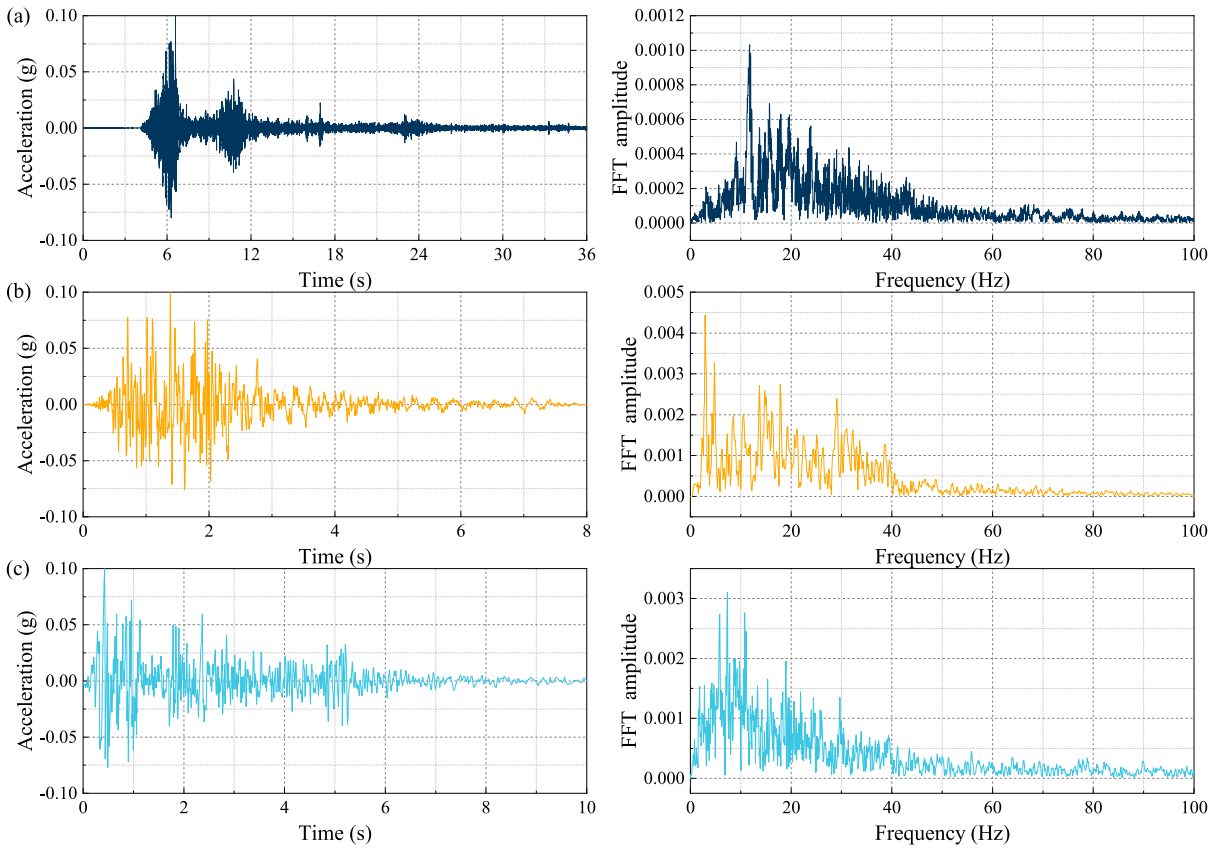

FIGURE 5
Acceleration curve and its spectral characteristics of normalized input waveforms in X-direction. **(A)** WL wave; **(B)** KB wave; **(C)** ELwave.

response of the slope. To effectively examine the dynamic response of rocky slopes with unstable rock masses, it is vital to create contour maps illustrating the peak acceleration amplification factors during seismic events. The 0.8gKB wave condition resulted in a rock mass failure; therefore, for clarity and appropriate comparison, the KB seismic wave is employed as a case study in the paper. Utilizing data

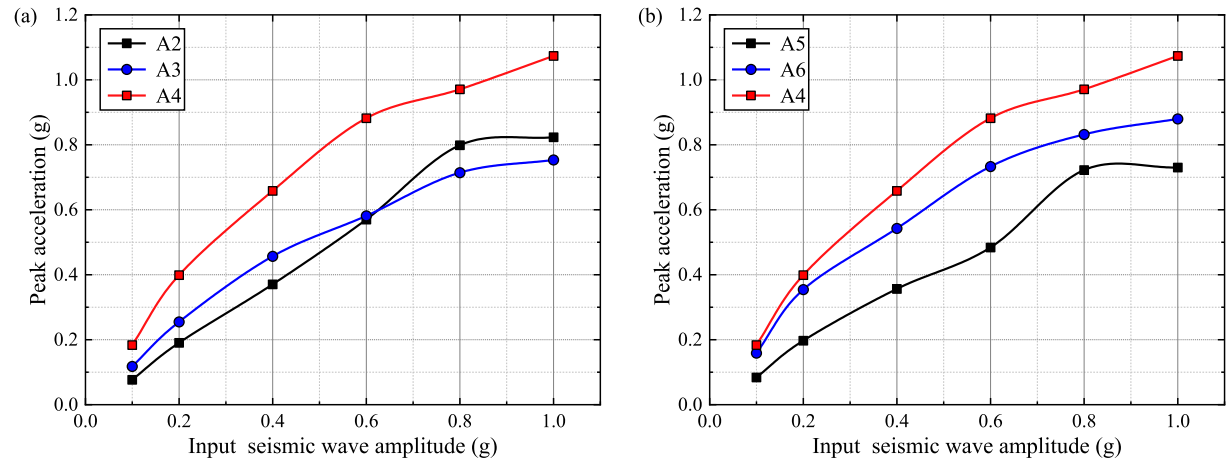

FIGURE 6
Evolutionary characteristics of acceleration response at different depths. **(A)** Measurement points A2, A3 and A4; **(B)** Measurement points A5, A6 and A4.

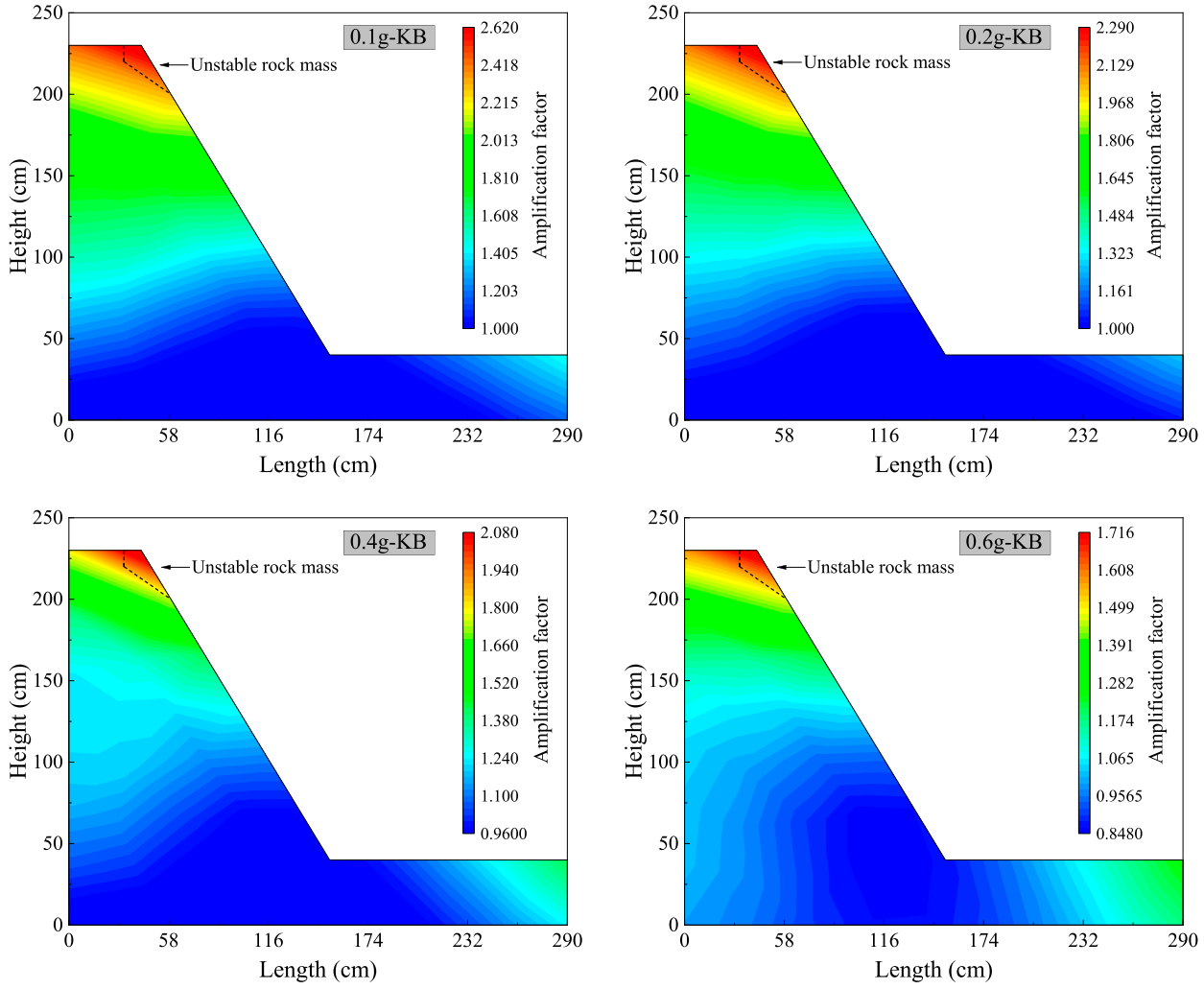

FIGURE 7
Contour maps of peak acceleration amplification factors in X-direction.

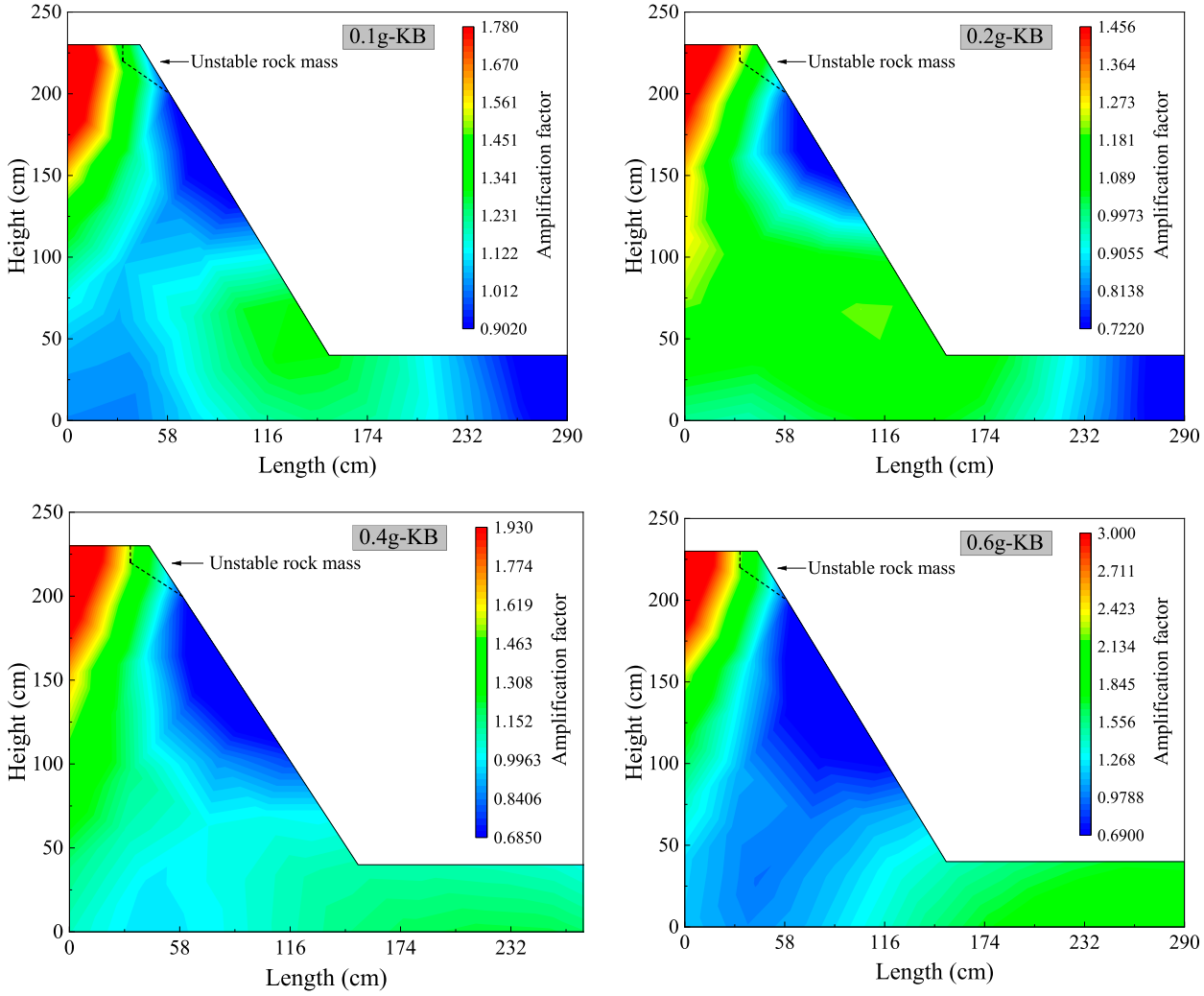

FIGURE 8
Contour maps of peak acceleration amplification factors in Z-direction.

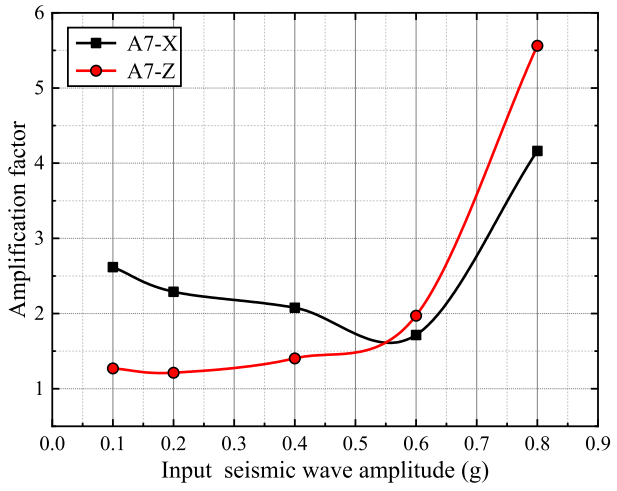

FIGURE 9
Evolution of the amplification factor for unstable rock mass.

from seven effective triaxial acceleration sensors from the model test, contour maps of peak acceleration amplification factors have been presented in Figures 7, 8. In these figures, the X-direction denotes the slope surface's free direction, while the Z-direction indicates its vertical orientation (see Figure 3).

As seismic intensity increases, the vibration amplification region of rocky slopes expands from its top toward its interior. This expansion demonstrates that the plastic zone within the slope mass enlarges with increased seismic intensity. Under different seismic intensities, the peak acceleration exhibits significant elevation amplification effects, but the vibration field in two directions shows obvious differences. At low seismic intensities, the amplification of acceleration is more significant in the direction parallel to the free surface of the slope-rock mass system compared to the vertical direction. In contrast, during high-intensity seismic events, the amplification behavior is reversed, with the vertical direction experiencing greater acceleration amplification than the free surface direction. Figure 9 illustrates the amplification factors within the rock mass, depicting how these factors evolve with increasing

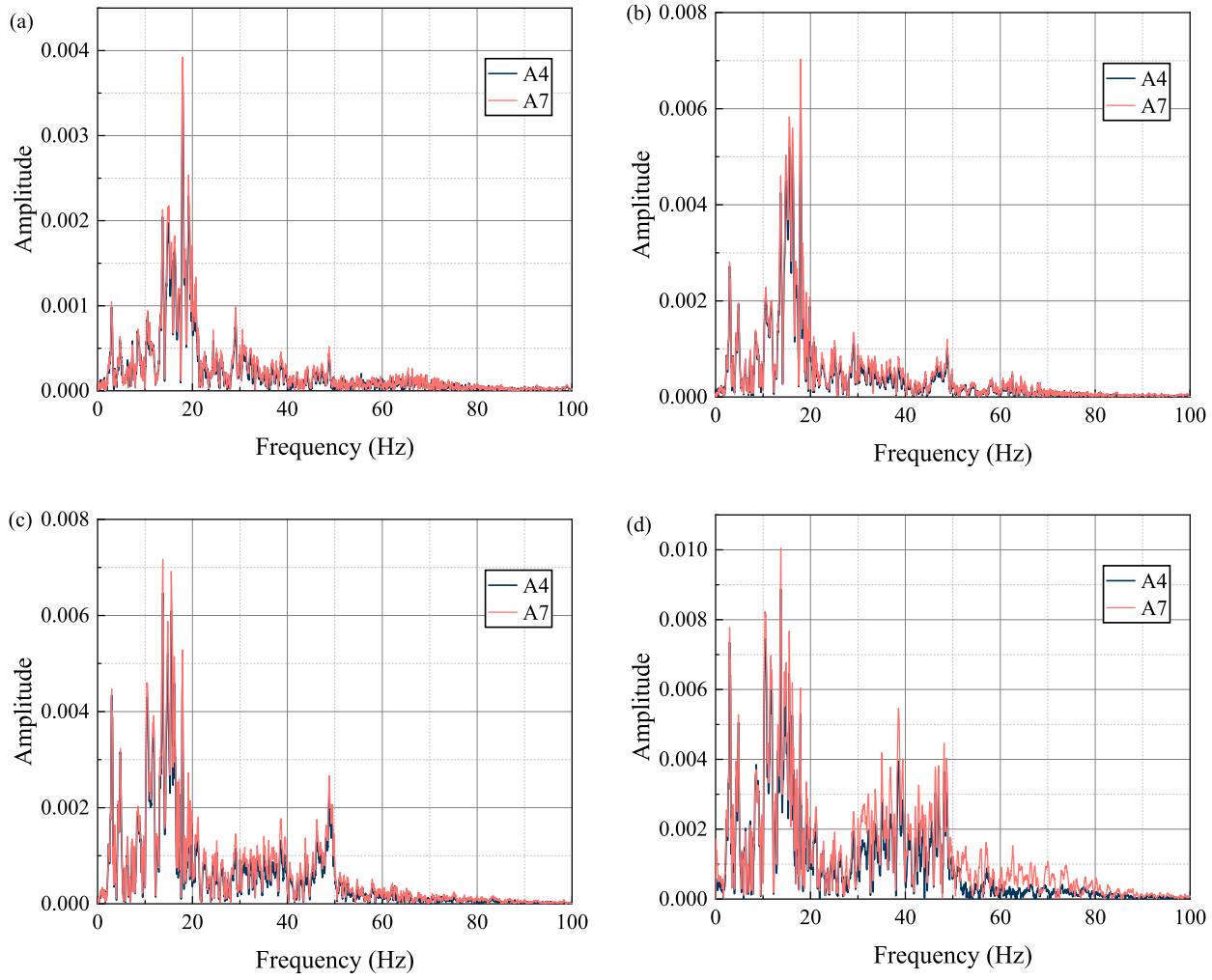

FIGURE 10
Fourier spectrum evolution of A4 and A7 measurement points under seismic loading. **(A–D)** represent the input 0.1 g, 0.2 g, 0.4 g, and 0.6 g KB seismic waves respectively.

seismic intensity. As seismic intensity escalates, the amplification factor at point A7 shows a rise in the Z direction while it diminishes in the X direction, indicating that vertical deformations of the rock mass are more sensitive to higher seismic intensities. Strong vertical vibrations are critical indicators of damage to the fragile structural planes in rocky slopes and unstable rock masses.

3.2 Fourier spectrum evolution

To investigate the evolution of the Fourier spectrum characteristics of unstable rock masses and bedrock under various seismic intensities, this study analyzes the acceleration data recorded at the free surface at points A4 and A7, which flank the weak interface. Figure 10 illustrates the pertinent results. When peak seismic accelerations reach 0.1 and 0.2g, the fourier spectra of the unstable rock masses and bedrock are nearly identical, each displaying a distinct single peak. However, as seismic intensity increases to 0.4g, this single peak transforms into multiple peaks, with point A7 exhibiting notably higher amplitudes than point A4. This multi-peak pattern intensifies further with a seismic intensity of 0.6 g. These observations suggest that at lower seismic intensities, the bedrock-interface-unstable rock mass system behaves as a cohesive unit, undergoing collective movement with minimal damage at the weak interface. The sliding mass, in turn, attenuates high-frequency wave components while accentuating low-frequency components. Once the seismic intensity reaches 0.4g, the unstable rock mass undergoes substantial sliding and internal disruption. This results in a scattering effect as seismic waves traverse the interface, generating derived waves and a complex wave field that manifests as the observed multi-peak phenomena.

3.3 Deformation response

The evolution curves of displacement increments monitored on the surface of the slope model under three seismic wave

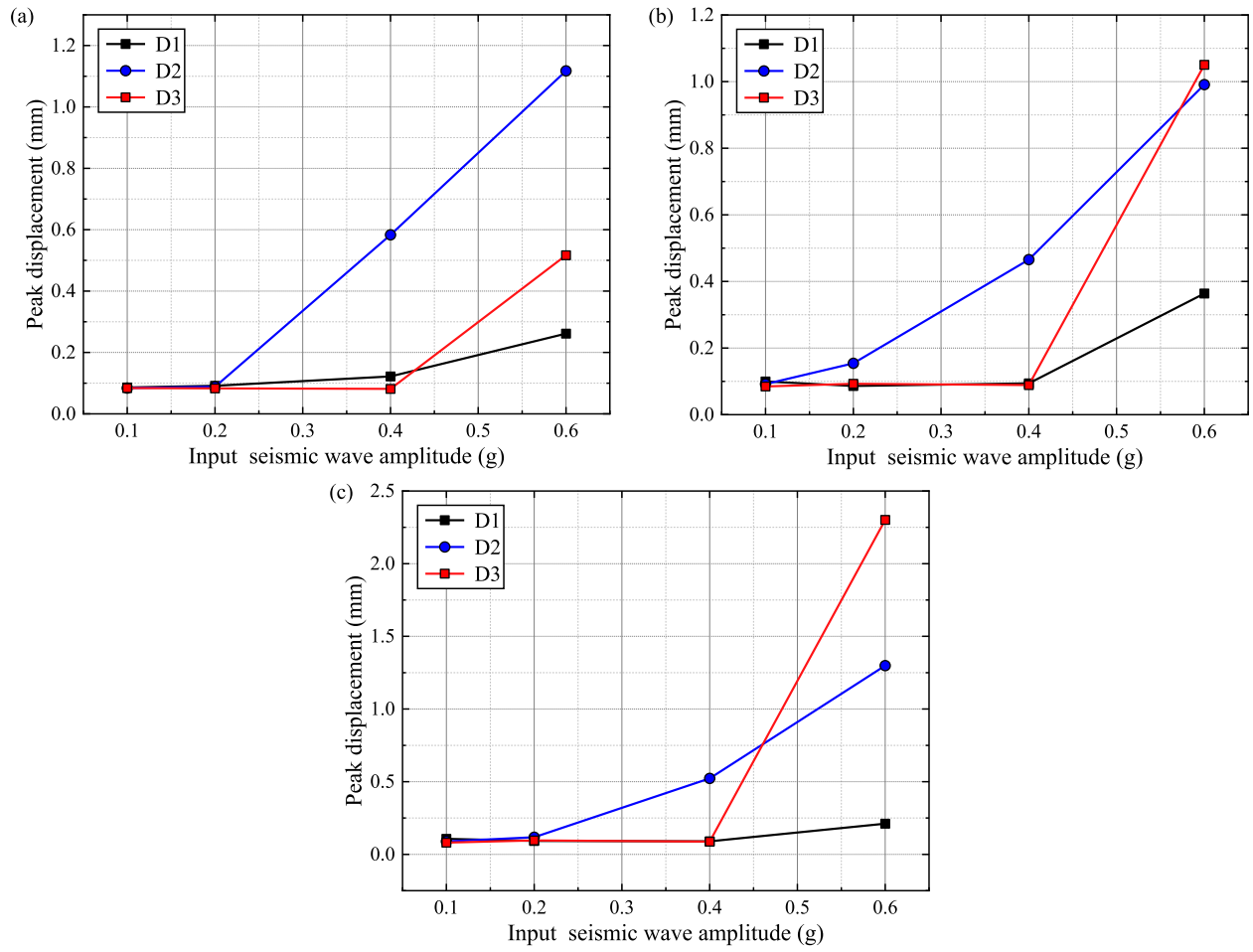

FIGURE 11
Evolution of displacement increment. **(A–C)** are the KB seismic wave, El seismic wave, and WL seismic wave respectively.

conditions are plotted in Figure 11. These increments reflect the slope's permanent damage and deformation characteristics. Under these conditions, displacement increments at monitoring point D2 become pronounced starting from a seismic intensity of 0.4g, marking the development of elastoplastic zones in the slope's upper region. In contrast, monitoring point D3 mainly notes displacement increments under a 0.6 g seismic wave, indicating substantial damage to the structural planes within the unstable rock mass. Therefore, it is deduced that noticeable slope damage initiates at a seismic intensity level of 0.4g, with significant cracking and propagation of the weak structural planes becoming apparent at a seismic intensity of 0.6 g.

The time-history curve of slope surface displacement measurement points under a loading condition before rockfall (input of 0.6 g WL seismic wave) is plotted, as shown in Figure 12. Significant increments in displacement are recorded at all three points, with the least displacement at the slope's toe (monitoring point D1). Notably, peak displacement occurs in the slope's middle to rear part (monitoring point D2), where the unstable rock mass exhibits the most substantial permanent displacement. This observation suggests that the initial phases of seismic activity introduce cumulative damage to the structural planes within the unstable rock mass.

4 Mechanism of initiation and damage of unstable rock mass

4.1 Rockfall initiation process

Figure 13 depicts the triaxial acceleration time-history curves for the brief fall duration of the unstable rock mass under a 0.8 g seismic event. The acceleration curves show marked deviations from the initial waveform, including a pronounced increase in amplitude. Before the collapse, the acceleration in the X-direction spikes to 1.6 g. This suggests that the rock mass has lost intimate contact with the underlying bedrock and that the weak structural planes are heavily compromised, disrupting waveform transmission through the rock mass. Figure 14 provides real-time imagery capturing the onset of instability in the rock mass, taken with an industrial-grade camera, while Figure 15 presents the corresponding displacement time-history curve. Under the influence of the 0.8 g KB seismic

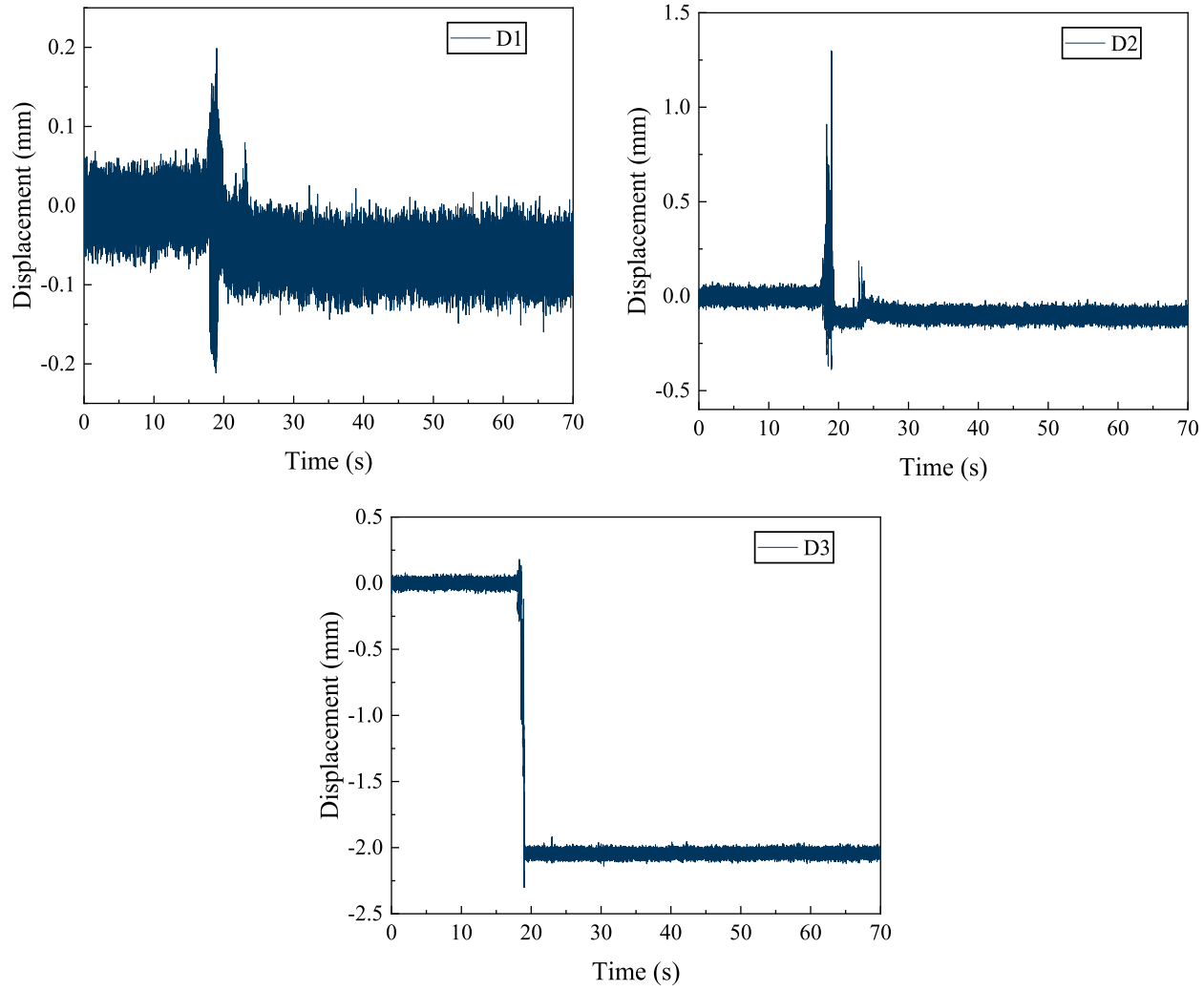

FIGURE 12
Displacement time-course curve with input 0.6 g WL seismic wave.

wave, the initiation of the rock mass can primarily be divided into three stages: (1) Rear edge cracking: e previous 17 seismic events, the rear edge structural surface accumulated minor damage, which closed after the earthquakes ended. Under a horizontal seismic force of 0.8 g KB wave, the rear edge structural surface of the rock mass was the first to fail (during the 26.5s–27.3s period), resulting in approximately 4 mm of horizontal displacement. During this stage, the acceleration amplitude in the X direction peaked at 1.67 g. (2) Structural plane sliding damage: The significant horizontal displacement of the unstable rock mass rapidly led to the failure of the shear resistance at the bottom structural surface, causing the rock mass to slide (during the 27.3s–28.2s period). During this stage, the unstable rock mass experienced approximately 80 mm of horizontal displacement, and the acceleration amplitude in the X direction stabilized. (3) Total loss of shear capacity in structural planes: The bottom structural surface completely failed, losing its load-bearing capacity and resulting in the failure of the unstable rock mass. During this stage, 56 mm of deformation occurred within 0.4 s.

4.2 Damage identification of structural plane of unstable rock mass

The Hilbert-Huang Transform is a commonly acknowledged technique for analyzing vibration signals, providing an effective depiction of the spectral features of seismic responses. It has been utilized by several researchers for structural damage identification. The HHT analysis method is primarily composed of two fundamental steps: Empirical Mode Decomposition (EMD) and Hilbert Spectrum Analysis (HSA) (Diao et al., 2021; Hamdi et al., 2013). The method unfolds in the following steps:

(1) From the monitored signal $x(t)$, identify the upper envelope $X_{max}(t)$ and lower envelope $X_{min}(t)$ by pinpointing the local extreme points. Subtract the mean $m_1(t)$ of these envelopes from $x(t)$ to generate a new sequence $h_1(t)$. Assess if $h_1(t)$ meets the Intrinsic Mode Function (IMF) criteria. If it does, designate $h_1(t)$ as the first IMF component. If not, substitute $h_1(t)$ with $x(t)$ and repeat until an IMF component is isolated.

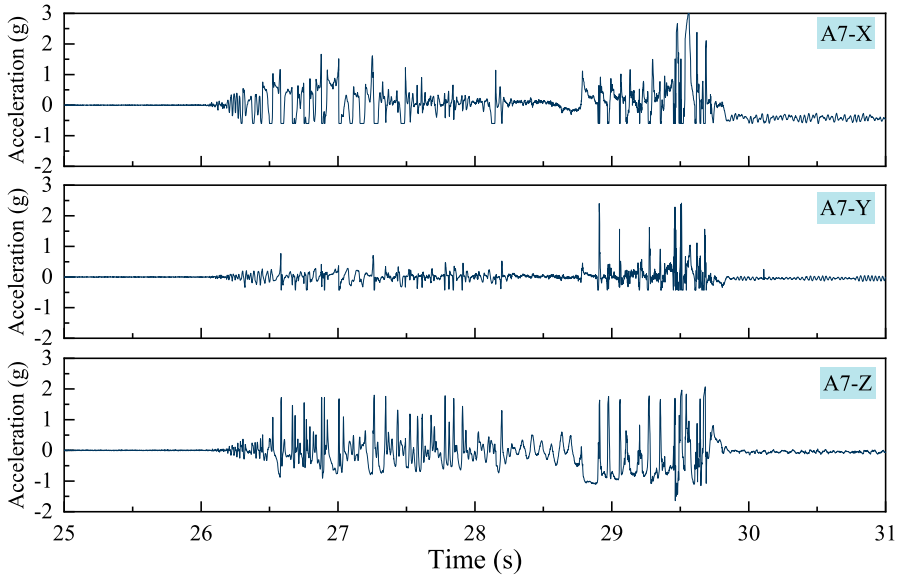

FIGURE 13
Acceleration time-history curves for the fall process of the unstable rock mass.

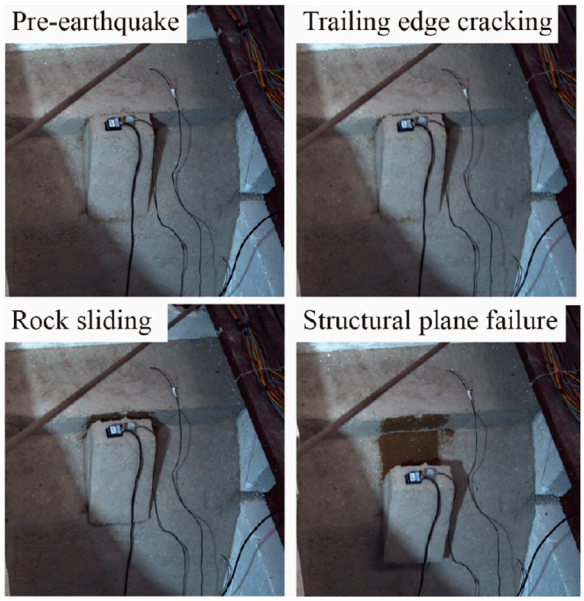

FIGURE 14
Record of unstable rock mass initiation.

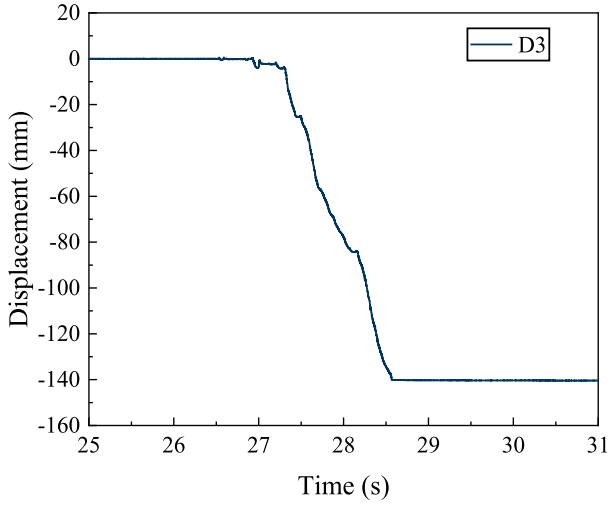

FIGURE 15
Time-displacement response curve of the unstable rock mass with input 0.8 g KB seismic wave.

(2) Subtract this IMF component from $x(t)$ and treat the resultant sequence as the new original sequence. Continue to isolate subsequent IMF components until the residual sequence $R_n(t)$ either becomes a monotonic function or decreases beneath a predefined threshold, culminating the process.

(3) Apply the convolution of the IMF component $h_1(t)$ with $1/(\pi t)$ as in Equation 2:

$$H[h(t)] = \frac{1}{\pi} P_v \int_{-\infty}^{+\infty} \frac{x(\tau)}{t-\tau} d\tau \tag{2}$$

Where P_v represents the Cauchy principal value; $x(\tau)$ represents each order of IMF component; τ represents frequency.

In the amplitude-time plane, the original signal can be expressed as Equation 3.

$$H(w,t) = \mathrm{Re} \sum_{j=1}^{n} a_j(t) e^{i \int \omega_j(t) dt} \omega(t) \tag{3}$$

In the equation, n represents the number of IMF components; $a_j(t)$ and $\omega(t)$ respectively represents the instantaneous amplitude and frequency of IMF components.

The HHT offers a significant advantage by minimizing the fitting errors of the Fourier transform. This capability allows

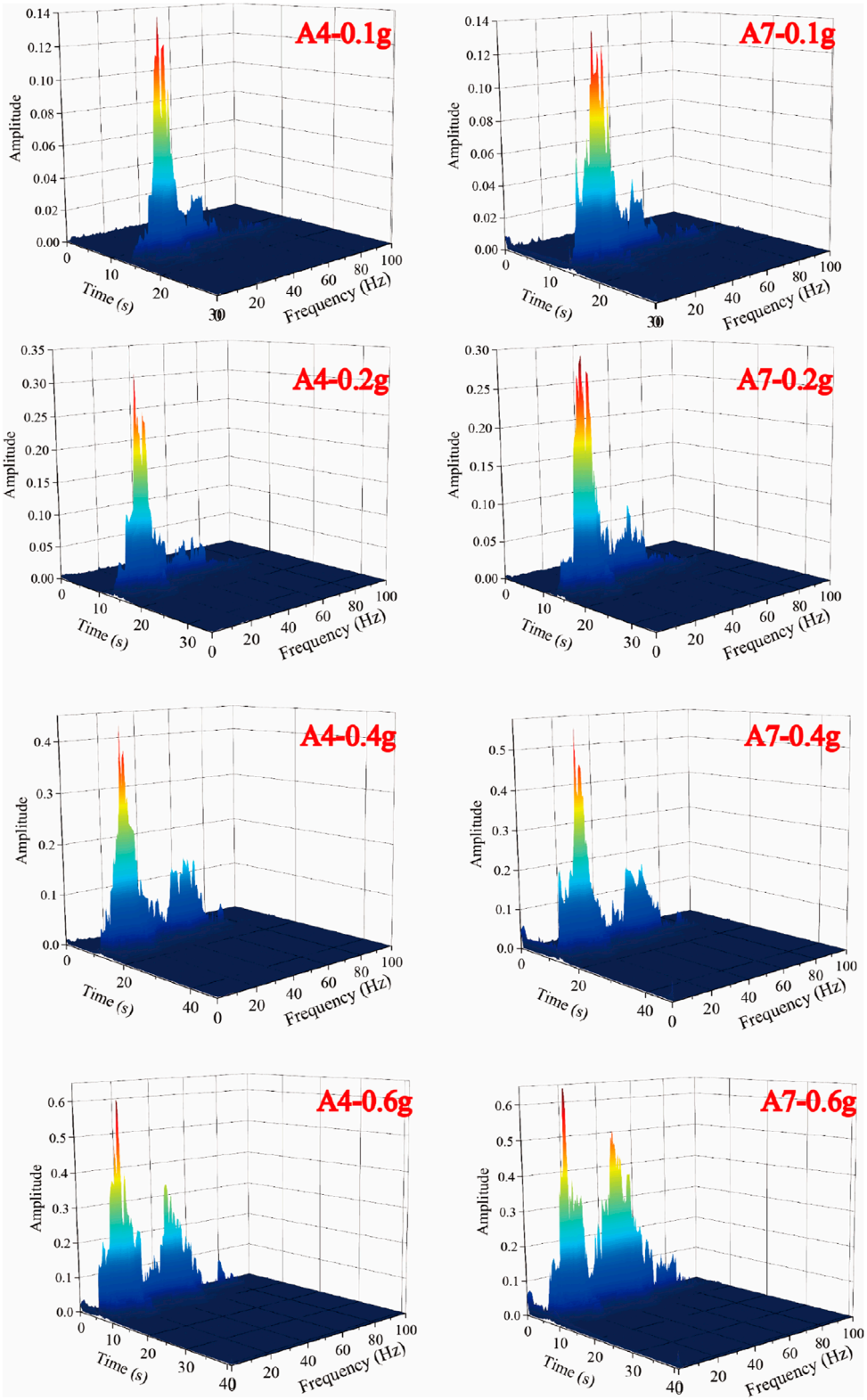

FIGURE 16
Hilbert spectrum of slope A4/A7 monitoring point with input KB seismic wave.

it to overcome the time-frequency correspondence challenges dictated by the Heisenberg uncertainty principle (Yue et al., 2024). HHT is especially effective for examining sudden signals, offering detailed insights into both the time-domain and frequency-domain responses observed during structural vibrations. Consequently, deploying the HHT method to investigate seismic responses in

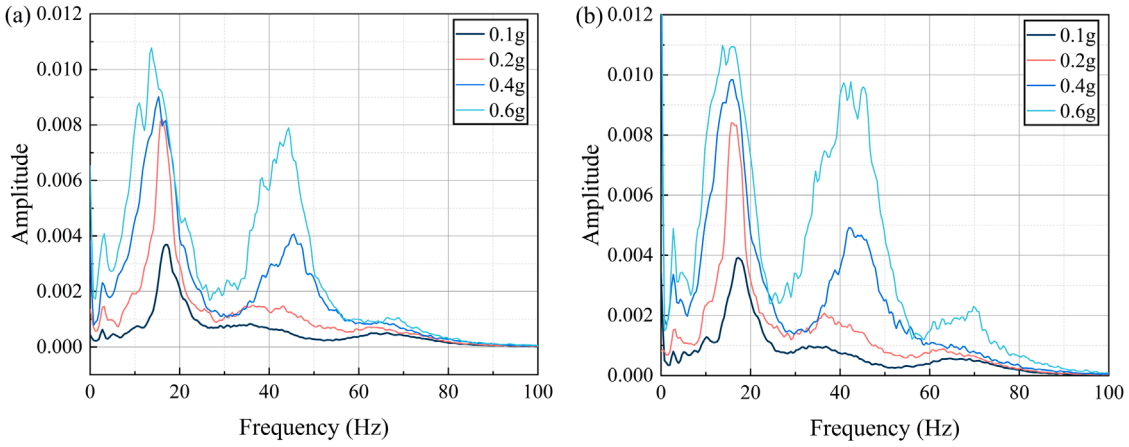

FIGURE 17
Marginal spectral curves. **(A)** A4 Monitoring point **(B)** A7 Monitoring point.

slopes can provide a more accurate representation of the evolving damage state in rock masses.

This study focuses on recognizing the damage patterns in the structural plane of unstable rock masses. By selecting monitoring points A4 and A7 as representative examples, the acceleration data oriented toward the free surface is analyzed using the HHT. This analysis is illustrated in Figure 16. The resulting Hilbert spectrum predominantly exhibits energy concentration across two frequency bands: low frequency (10–20 Hz) and high frequency (30–45 Hz), with the peak amplitudes chiefly within the low-frequency range. At an acceleration of 0.1g, the peak magnitudes corresponding to both the bedrock and the unstable rock mass are congruent, suggesting no apparent damage to the slope or rock mass, as corroborated by Section 3's analysis. At 0.2 g acceleration, the bedrock's peak amplitude surpasses that of the unstable rock mass, although both exhibit relatively subdued energy distributions in both frequency bands compared to the unstable rock mass, indicating damage to the weak structural planes. At 0.4 g, there is a marked escalation in energy distribution across both frequency bands, and the amplitude of the Hilbert Spectrum for the rock mass far exceeds that of the bedrock. At this time, both the slope and the rock mass experience a certain degree of damage. Concurrently, a decreasing trend in the dominant seismic energy frequency band within the unstable rock mass indicates diminished shear resistance along the weak structural planes. At 0.6 g, similar peak amplitudes are observed for the bedrock and the unstable rock mass, but the latter displays a pronounced increase in high-frequency energy.

The marginal spectrum assesses how much each frequency contributes to a signal's total energy over its entire duration. The marginal spectrum traits derived from the Hilbert spectrum in Figure 16 are illustrated in Figure 17. When seismic waves travel through a slope, any damage at a specific location can lead to disrupted energy transmission, causing significant fluctuations and anomalies in the marginal spectrum. This behavior is reflected in the marginal spectrum characteristics of an unstable rock mass. Both the slope and the unstable rock mass primarily release energy in the low-frequency range. As the seismic intensity increases, displacement occurs between the bedrock and the unstable rock mass. The wave impedance of weak structural surfaces increases, amplifying low-frequency vibrations and attenuating high-frequency vibrations. This makes it difficult for high-frequency energy to transfer to the rock mass, resulting in the rock mass having less high-frequency energy than the bedrock. An increase in shear failure points lowers the main frequency band of the unstable rock mass. A reduction in low-frequency vibrations combined with an increase in high-frequency energy serves as critical indicators of impending failure along weak structural planes.

5 Discussion and limitations

Based on the method proposed by Fang et al. (2023b), a summarized protocol of the physical model tests is provided in Table 4, which directly presents the brief and essential information from the tests. Nevertheless, despite careful planning and execution, this study has limitations. The homogeneity of the materials used in the shaking table experiments may lead to idealized results that do not fully simulate actual site characteristics. Additionally, cost constraints limited the number of comparative tests. Factors such as the slope of weak structural surfaces and material strength may affect the outcomes. The potential impact of bedrock damage and cracking on unstable rock masses introduces further uncertainty.

Nevertheless, the findings provide valuable insights for assessing slope stability in engineering. Strong vertical acceleration can indicate damage to weak structural planes and unstable rock masses. Seismic damage also correlates with shifts in energy and frequency, aiding in the multi-field information monitoring of landslide deformation and failure (Fang et al., 2023a).

6 Conclusion

This study reveals the seismic damage patterns and dynamic response characteristics of uniform rocky slopes containing unstable rock masses through triaxial shaking table tests. The principal conclusions are:

TABLE 4 Summarized protocol of the test.

Test aim		Dynamic response and failure performance of uniform rocky slope-unstable rock system			
Basic	Classification	Rocky slope	Container	Composition	Steel plates, angles and channels
	Triggers	Earthquake		Size	Length: 3.1 m, Width: 1.2 m, Height: 2.5 m
				Preparation	Compaction
Slope model	Angle	60°	Weak structural plane	Angle	36°
	Material	Mixture of barite powder, quartz sand, gypsum, water, and glycerin		Material	Mixture of loess, river sand, and water
	Properties	Density: 2.2 g/cm^3; Cohesion: 20.01kPa; Internal friction angle: 36.6°		Properties	Density: 1.8 g/cm^3; Cohesion: 0.95 kPa; Internal friction angle: 27.65°
Monitoring tools	Acceleration sensors	Tritial acceleration	Test condition	Test cases	25
	Displacement sensor	Deformation		Test variable	Seismic wave types and amplitudes
	Industrial Camera	Image Record			
Main test observations					
①	Elevation and surface amplification effects are evident within the rock slope, and these effects intensify as the slope's height increases. The vertical deformation of unstable rock masses exhibits heightened sensitivity to elevated seismic intensities				
②	The unstable rock mass is initiated under the input 0.8 gKB seismic wave condition, and the initiation process can be summarized into three distinct stages				

(1) Within a rock slope, both elevation and surface amplification effects are notably significant, with their prominence escalating as the slope's elevation rises. However, as seismic intensity grows, the acceleration amplification effect diminishes over time and eventually reaches a point of stabilization.
(2) The vertical deformation of unstable rock masses exhibits heightened sensitivity to elevated seismic intensities. Strong vertical acceleration shaking can serve as a key signal for damage to the weak structural planes of rock slopes and unstable rock masses. At lower seismic intensities, the acceleration amplification is notably more significant in the horizontal direction along the free surface compared to the vertical direction.
(3) The initiation process of unstable rock masses under seismic events is categorized into three stages based on experimental observations. Rear edge cracking: Horizontal seismic forces precipitate the initial failure of the rear structural planes, leading to notable horizontal displacement; Structural plane sliding damage: Excessive horizontal movement causes the rapid degradation of shear resistance along the lower structural planes, resulting in the rock mass sliding; Total loss of shear capacity in structural planes: A comprehensive failure of the load-bearing capability of the lower structural planes leads to the falling of the rock mass.
(4) Hilbert spectrum and marginal spectrum effectively identify the structural plane damage process of unstable rock masses. Energy distribution in rock slopes and unstable rock masses mainly concentrates within two frequency bands: 10–20 Hz and 30–45 Hz. Under low seismic intensity, the contact between the bedrock and unstable rock mass is relatively intact, and the Hilbert spectrum and the marginal spectrum exhibit comparable characteristics. Under high seismic intensity, there is significant energy loss that results in pronounced fluctuations and sudden changes within the marginal spectrum. This serves as an indicator of damage to structural planes. A notable reduction in low-frequency vibration frequencies, coupled with a rise in high-frequency vibration energy, are crucial signals pointing to the failure of these structural planes.

Data availability statement

The original contributions presented in the study are included in the article/supplementary material, further inquiries can be directed to the corresponding author.

Author contributions

DW: Conceptualization, Funding acquisition, Writing–original draft. HW: Writing–review and editing.

Funding

The author(s) declare that financial support was received for the research, authorship, and/or publication of this article. This research was financially supported by the China Railway Group Limited

Science and Technology Research and Development Program (2022-Major-01).

Conflict of interest

Author DW was employed by China Railway Eryuan Engineering Group Co. Ltd.

The remaining author declares that the research was conducted in the absence of any commercial or financial relationships that could be construed as a potential conflict of interest.

The authors declare that this study received funding from China Railway Group Limited R&D Program (2022-Major-01). The funder had the following involvement in the study: decision to publish.

Generative AI statement

The author(s) declare that no Generative AI was used in the creation of this manuscript.

Publisher's note

All claims expressed in this article are solely those of the authors and do not necessarily represent those of their affiliated organizations, or those of the publisher, the editors and the reviewers. Any product that may be evaluated in this article, or claim that may be made by its manufacturer, is not guaranteed or endorsed by the publisher.

References

Alfaro, P., Delgado, J., García-Tortosa, F. J., Giner, J. J., Lenti, L., López-Casado, C., et al. (2012). The role of near-field interaction between seismic waves and slope on the triggering of a rockslide at Lorca (SE Spain). *Nat. Hazards Earth Syst. Sci.* 12, 3631–3643. doi:10.5194/nhess-12-3631-2012

Bouckovalas, G. D., and Papadimitriou, A. G. (2005). Numerical evaluation of slope topography effects on seismic ground motion. *Soil Dyn. Earthq. Eng.* 25, 547–558. doi:10.1016/j.soildyn.2004.11.008

Chen, H., Zhu, H., and Zhang, L. (2023). Rock slope stability analysis incorporating the effects of intermediate principal stress. *Rock Mech. Rock Eng.* 56, 4271–4289. doi:10.1007/s00603-023-03277-4

Cheng, X. S., Zheng, G., Diao, Y., Huang, T. M., Deng, C. H., Nie, D. Q., et al. (2017). Experimental study of the progressive collapse mechanism of excavations retained by cantilever piles. *Can. Geotechnical J.* 54, 574–587. doi:10.1139/cgj-2016-0284

Council, A. T. (2009). Quantification of building seismic performance factors.

Deng, Z., Liu, X., Liu, Y., Liu, S., Han, Y., Liu, J., et al. (2020). Model test and numerical simulation on the dynamic stability of the bedding rock slope under frequent microseisms. *Earthq. Eng. Eng. Vib.* 19, 919–935. doi:10.1007/s11803-020-0604-8

Diao, Y., Jia, D., Liu, G., Sun, Z., and Xu, J. (2021). Structural damage identification using modified Hilbert–Huang transform and support vector machine. *J. Civ. Struct. Health Monit.* 11, 1155–1174. doi:10.1007/s13349-021-00509-5

Fan, G., Zhang, J., Wu, J., and Yan, K. (2016). Dynamic response and dynamic failure mode of a weak intercalated rock slope using a shaking table. *Rock Mech. Rock Eng.* 49, 3243–3256. doi:10.1007/s00603-016-0971-7

Fan, J., Yang, C., Yue, M., Luo, J., Lian, J., and Wei, P. (2025). Dynamic response of rock landslides and avalanche debris flows impacting flexible barriers based on shaking table tests. *Soil Dyn. Earthq. Eng.* 188, 109078. doi:10.1016/j.soildyn.2024.109078

Fang, K., Miao, M., Tang, H., Jia, S., Dong, A., An, P., et al. (2023a). Insights into the deformation and failure characteristic of a slope due to excavation through multi-field monitoring: a model test. *Acta Geotech.* 18, 1001–1024. doi:10.1007/s11440-022-01627-0

Fang, K., Tang, H., Li, C., Su, X., An, P., and Sun, S. (2023b). Centrifuge modelling of landslides and landslide hazard mitigation: a review. *Geosci. Front.* 14, 101493. doi:10.1016/j.gsf.2022.101493

Feng, L., Intrieri, E., Pazzi, V., Gigli, G., and Tucci, G. (2021). A framework for temporal and spatial rockfall early warning using micro-seismic monitoring. *Landslides* 18, 1059–1070. doi:10.1007/s10346-020-01534-z

Hamdi, S. E., Le Duff, A., Simon, L., Plantier, G., Sourice, A., and Feuilloy, M. (2013). Acoustic emission pattern recognition approach based on Hilbert–Huang transform for structural health monitoring in polymer-composite materials. *Appl. Acoust.* 74, 746–757. doi:10.1016/j.apacoust.2012.11.018

Huang, R. (2011). Mechanisms of large-scale landslides in China. *Bull. Eng. Geol. Environ.* 71, 161–170. doi:10.1007/s10064-011-0403-6

Istiyanti, M. L., Goto, S., and Ochiai, H. (2021). Characteristics of tuff breccia-andesite in diverse mechanisms of landslides in Oita Prefecture, Kyushu, Japan. *Geoenvironmental Disasters* 8, 4. doi:10.1186/s40677-021-00176-0

Jeong, S., Moon, M., and Kim, D. (2024). Seismic wave amplification characteristics in slope sections of various inclined model grounds. *Appl. Sciences-Basel* 14, 9014. doi:10.3390/app14199014

Jia, J., Gao, X., Bao, X., Xiang, X., Zhang, L., and Tu, B. (2024). Dynamic stability analysis method of anchored rocky slope considering seismic deterioration effect. *Sci. Rep.* 14, 7014. doi:10.1038/s41598-024-57413-3

Jiang, X., Qian, Y., Yang, H., Xiao, Z., Fan, W., Zhu, Y., et al. (2022). Model test studies on slope supported by bamboo anchor and timber frame beam. *Geotechnical Geol. Eng.* 40, 4327–4344. doi:10.1007/s10706-022-02157-y

Kusak, M. (2019). Key issues in 3D rockfall modeling, natural hazard and risk assessment for rockfall protection in Hrensko (Czechia). *Acta Geodyn. Geomaterialia*, 393–408. doi:10.13168/agg.2019.0033

Li, H., Liu, Y., Liu, L., Liu, B., and Xia, X. (2017a). Numerical evaluation of topographic effects on seismic response of single-faced rock slopes. *Bull. Eng. Geol. Environ.* 78, 1873–1891. doi:10.1007/s10064-017-1200-7

Li, L.-q., Ju, N.-p., Zhang, S., and Deng, X.-x. (2017b). Shaking table test to assess seismic response differences between steep bedding and toppling rock slopes. *Bull. Eng. Geol. Environ.* 78, 519–531. doi:10.1007/s10064-017-1186-1

Li, L.-q., Ju, N.-p., Zhang, S., Deng, X.-x., and Sheng, D. (2018). Seismic wave propagation characteristic and its effects on the failure of steep jointed anti-dip rock slope. *Landslides* 16, 105–123. doi:10.1007/s10346-018-1071-4

Li, Z., Yin, C., Tan, Z., Liu, X., Li, S., and Zhang, X. (2023). Rainfall-seismic coupling effect induced landslide hazard assessment. *Nat. Hazards* 118, 2123–2152. doi:10.1007/s11069-023-06084-w

Lin, Y.-l., Li, Y.-x., Yang, G.-l., and Li, Y. (2017). Experimental and numerical study on the seismic behavior of anchoring frame beam supporting soil slope on rock mass. *Soil Dyn. Earthq. Eng.* 98, 12–23. doi:10.1016/j.soildyn.2017.04.008

Liu, X., Liu, Y., He, C., and Li, X. (2016). Dynamic stability analysis of the bedding rock slope considering the vibration deterioration effect of the structural plane. *Bull. Eng. Geol. Environ.* 77, 87–103. doi:10.1007/s10064-016-0945-8

Macciotta, R., Martin, C. D., and Cruden, D. M. (2014). Probabilistic estimation of rockfall height and kinetic energy based on a three-dimensional trajectory model and Monte Carlo simulation. *Landslides* 12, 757–772. doi:10.1007/s10346-014-0503-z

Martino, S., Marmoni, G. M., Fiorucci, M., Ceci, A. F., Discenza, M. E., Rouhi, J., et al. (2022). Role of antecedent rainfall in the earthquake-triggered shallow landslides involving unsaturated slope covers. *Appl. Sciences-Basel* 12, 2917. doi:10.3390/app12062917

Moos, C., Bontognali, Z., Dorren, L., Jaboyedoff, M., and Hantz, D. (2022). Estimating rockfall and block volume scenarios based on a straightforward rockfall frequency model. *Eng. Geol.* 309, 106828. doi:10.1016/j.enggeo.2022.106828

Oswald, P., Strasser, M., Hammerl, C., and Moernaut, J. (2021). Seismic control of large prehistoric rockslides in the Eastern Alps. *Nat. Commun.* 12, 1059. doi:10.1038/s41467-021-21327-9

Ren, J., Xu, X., Zhang, S., Yeats, R. S., Chen, J., Zhu, A., et al. (2018). Surface rupture of the 1933 M 7.5 Diexi earthquake in eastern Tibet: implications for seismogenic tectonics. *Geophys. J. Int.* 212, 1627–1644. doi:10.1093/gji/ggx498

Song, D., Chen, Z., Ke, Y., and Nie, W. (2020). Seismic response analysis of a bedding rock slope based on the time-frequency joint analysis method: a case study from the middle reach of the Jinsha River, China. *Eng. Geol.* 274, 105731. doi:10.1016/j.enggeo.2020.105731

Song, D., Liu, X., Huang, J., Zhang, Y., Zhang, J., and Nkwenti, B. N. (2021). Seismic cumulative failure effects on a reservoir bank slope with a complex geological structure considering plastic deformation characteristics using shaking table tests. *Eng. Geol.* 286, 106085. doi:10.1016/j.enggeo.2021.106085

Tang, H., Jia, H., Hu, X., Li, D., and Xiong, C. (2010). Characteristics of landslides induced by the great Wenchuan earthquake. *J. Earth Sci.* 21, 104–113. doi:10.1007/s12583-010-0008-1

Valagussa, A., Frattini, P., and Crosta, G. B. (2014). Earthquake-induced rockfall hazard zoning. *Eng. Geol.* 182, 213–225. doi:10.1016/j.enggeo.2014.07.009

Wei, Z., Li, Y., Dong, J., Cao, S., Ma, W., Wang, X., et al. (2024). The identification and influence factor analysis of landslides using SBAS-InSAR technique: a case study of Hongya Village, China. *Appl. Sciences-Basel* 14, 8413. doi:10.3390/app14188413

Yang, C. (2013). *Study on seismic dynamic characters of rock slopes and system including formation mechanism of landslides, stability discrimination of slope and assement of harzard scope of landslide for slope of bedrock and overburden layer. (Ph.D. thesis)*. Southwest Jiaotong University.

Yang, H., Xing, B., He, J., Jiang, H., and Cheng, Q. (2022). The formation mechanism and failure mode of a talus slope induced by rockfalls in Nayong County, Southwest China. *Front. Earth Sci.* 10, 973528. doi:10.3389/feart.2022.973528

Yang, Y., Zhang, Y., Teng, Z., Liu, P., and Qiao, L. (2023). Study on movement characteristics and numerical simulation of high-altitude rockfall in babao mountain in China. *Front. Earth Sci.* 11. doi:10.3389/feart.2023.1281364

Yeznabad, A. F., Molnar, S., and El Naggar, M. H. (2021). Probabilistic solution for the seismic sliding displacement of slopes in Greater Vancouver. *Soil Dyn. Earthq. Eng.* 140, 106393. doi:10.1016/j.soildyn.2020.106393

Yue, M., Qu, L., Zhou, S., Wu, D., Chen, Z., and Wen, H. (2024). Dynamic response characteristics of shaking table model tests on the gabion reinforced retaining wall slope under seismic action. *Geotext. Geomembranes* 52, 167–183. doi:10.1016/j.geotexmem.2023.10.001

Yun, L., Zhang, X., Zheng, Y., Wang, D., and Hua, L. (2023). Enhance the accuracy of landslide detection in UAV images using an improved mask R-CNN model: a case study of sanming, China. *Sensors* 23, 4287. doi:10.3390/s23094287

Zhan, J., Yu, Z., Lv, Y., Peng, J., Song, S., and Yao, Z. (2022). Rockfall hazard assessment in the Taihang grand canyon scenic area integrating regional-scale identification of potential rockfall sources. *Remote Sens.* 14, 3021. doi:10.3390/rs14133021

Zhang, H., Wu, Y., Huang, S., Zheng, L., and Miao, Y. (2022). Analysis of flexural toppling failure of anti-dip rock slopes due to earthquakes. *Front. Earth Sci.* 9, 831023. doi:10.3389/feart.2021.831023

Zhao, X., Hu, K., Burns, S. F., and Hu, H. (2019). Classification and sudden departure mechanism of high-speed landslides caused by the 2008 Wenchuan earthquake. *Environ. Earth Sci.* 78, 125. doi:10.1007/s12665-019-8083-9

Zheng, B., Song, S., Cheng, X., Niu, R., Cheng, X., Ruan, H., et al. (2023). The influence of coal mining subsidence on the movement and deformation of loess slope in the loess gully area of Northern Shaanxi. *Front. Earth Sci.* 11. doi:10.3389/feart.2023.1273389

Zheng, L., Wu, Y., Zhu, Z., Ren, K., Wei, Q., Wu, W., et al. (2022). Investigating the role of earthquakes on the stability of dangerous rock masses and rockfall dynamics. *Front. Earth Sci.* 9. doi:10.3389/feart.2021.824889

frontiers | Frontiers in Earth Science

TYPE Original Research
PUBLISHED 19 March 2025
DOI 10.3389/feart.2025.1554812

OPEN ACCESS

EDITED BY
Yifei Sun,
Taiyuan University of Technology, China

REVIEWED BY
Yue Yao,
Jiangsu Open University, China
Liu Zhenghao,
Tongji University, China

*CORRESPONDENCE
Wenwei Li,
✉ 180804010002@hhu.edu.cn

RECEIVED 03 January 2025
ACCEPTED 11 February 2025
PUBLISHED 19 March 2025

CITATION
Yan Q, Peng B, Li W, Wang B, Zuo J, Lv G and Wang T (2025) Low-carbon stabilization of expansive soils using cement kiln dust and calcium carbide slag: mechanisms and performance.
Front. Earth Sci. 13:1554812.
doi: 10.3389/feart.2025.1554812

Low-carbon stabilization of expansive soils using cement kiln dust and calcium carbide slag: mechanisms and performance

Qiangzhen Yan[1], Bo Peng[1], Wenwei Li[2,3]*, Baotian Wang[4], Jinyu Zuo[4], Guangdong Lv[5] and Tongzhang Wang[6]

[1]Environmental Branch, Gansu Institute of Engineering Geology, Lanzhou, China, [2]School of Civil Engineering, Shandong University, Jinan, China, [3]Jiangsu Hanjian Group Co., Ltd., Yangzhou, China, [4]Laboratory of Ministry of Education for Geomechanics and Embankment Engineering, Hohai University, Nanjing, China, [5]Water Conservancy Civil Engineering College, Tibet Agriculture and Animal Husbandry University, Nyingchi, China, [6]Jiangsu Hehai Engineering Technology Co., Ltd., Nanjing, China

In response to the environmental challenges posed by conventional expansive soil stabilization methods, this study investigates the low-carbon potential of industrial by-products—cement kiln dust (CKD) and calcium carbide slag (CCS)—as sustainable stabilizers. A comprehensive series of laboratory tests, including compaction tests, free swelling rate measurements, unconfined compressive strength (UCS) evaluations, and scanning electron microscopy (SEM) analyses, were conducted on expansive soil samples treated with varying dosages in both single and binary formulations. The results indicate that the binary system significantly outperforms individual stabilizers; for example, a formulation containing 10% CKD and 9% CCS achieved a maximum dry density of 1.64 g/cm^3, reduced the free swelling rate to 22.7% at 28 days, and reached a UCS of 371.3 kPa. SEM analysis further revealed that the enhanced performance is due to the synergistic formation of hydration products—namely calcium silicate hydrate (C-S-H) and calcium aluminate hydrate (C-A-H)—which effectively fill interparticle voids and reinforce soil structure. These findings demonstrate that the dual mechanism, combining rapid early-stage hydration from CCS with sustained long-term strength development from CKD, offers a cost-effective and environmentally sustainable alternative to traditional stabilizers for expansive soils.

KEYWORDS

expansive soil, cement kiln dust, calcium carbide slag, soil stabilization, microstructural analysis, sustainable construction materials

1 Introduction

Soil instability poses critical challenges to geotechnical engineering, manifesting in diverse forms such as slope failures (Song et al., 2024), foundation subsidence (Shan et al., 2022), and vibration-induced structural damage (Liu et al., 2024). Among these issues, expansive soils represent a particularly problematic category of geomaterials due to their propensity for significant volumetric changes in response to moisture variations. These volumetric fluctuations can lead to severe infrastructure distress, including

cracking, uneven settling, and reduced service life (Abbas et al., 2023; Ye et al., 2023; Laporte et al., 2023; Sarker et al., 2023). In Jiangsu Province, China, expansive soils underlie a range of important slope engineering projects, where repeated slope instabilities pose severe risks to transportation corridors, embankments, and other critical structures. Historically, civil engineers have relied on cement and lime as primary stabilizing agents to mitigate these deleterious volume-change effects (Wei et al., 2023; Zada et al., 2023). While undeniably effective in controlling soil swelling and improving load-bearing capacity, these conventional stabilizers pose critical challenges in the modern era due to their carbon-intensive production processes (Syed et al., 2023; Zhang et al., 2023). Their reliance on substantial energy inputs and fossil fuel combustion has generated mounting concern from environmental stakeholders, regulators, and project owners seeking to align construction operations with contemporary sustainability directives. Consequently, identifying low-carbon alternatives that retain or exceed the efficacy of traditional methods has emerged as a central focus in soil improvement science, reflecting the broader movement toward climate-responsive infrastructure development (Chen et al., 2021; Miraki et al., 2022). In this context, the search for innovative soil stabilization methodologies that reduce carbon emissions while maintaining or enhancing performance has become increasingly urgent.

In response to the escalating challenges posed by global climate change, the pursuit of low-carbon and environmentally sustainable construction materials has become a pressing objective within the civil engineering domain (Fatima et al., 2023; Hassan et al., 2023). Indeed, the cement industry alone is estimated to contribute approximately 7%–8% of global CO_2 emissions, with the production of one tonne of ordinary Portland cement typically releasing about 0.8–0.9 tonnes of CO_2 (Habert et al., 2020). Lime production also involves energy-intensive calcination processes that contribute significantly to greenhouse gas emissions. This urgent imperative arises from the need to reduce overall carbon output, conserve natural resources, and promote circular economy practices. Accordingly, the development and deployment of novel soil improvement strategies that embrace low-carbon stabilizers have gained significant traction in geotechnical research and practice. In particular, employing industrial by-products for soil stabilization can simultaneously meet performance requirements for strength and durability while minimizing environmental footprints. Moreover, the integration of such waste-derived binders into soil improvement processes not only enhances mechanical properties but also contributes to reduced raw material consumption, thereby enabling more responsible use of natural resources. Consequently, this approach to soil stabilization represents a vital step forward in realizing sustainable resource management practices at both local and global scales (Dang et al., 2021; Barman and Dash, 2022; Tiwari et al., 2021).

Within this conceptual framework, the utilization of industrial waste products as alternative stabilizers has garnered growing attention, driven by the dual imperatives of enhancing performance and promoting environmental sustainability. Generally, these waste-derived materials contribute to soil stabilization through one or more primary mechanisms: pozzolanic reactions (Zheng et al., 2023), cementitious binding (Al-Adhadh et al., 2024), and/or alkaline activation (Syed et al., 2022). By leveraging such mechanisms, researchers not only address the swelling and strength limitations of expansive soils but also advance circular economy principles by repurposing by-products otherwise destined for landfills.

Among these materials, fly ash stands out for its prominent pozzolanic properties. As a voluminous by-product of coal combustion, fly ash contains substantial quantities of silica and alumina that can react with calcium in soil or other binders to form cementitious hydrates, thereby refining the pore structure and improving load-bearing capacity (Mahedi et al., 2020; Chen et al., 2022). In contrast, steel slag (Wu et al., 2021) and ground granulated blast furnace slag (GGBS) (Al-Saedi and Sabbar, 2024; Zhao et al., 2023) exhibit both latent hydraulic and pozzolanic characteristics: they can harden in the presence of water and/or supplementary alkalis, thus enhancing soil stiffness and mitigating volumetric instability (Muthukkumaran and Anusudha, 2020; Mustafayeva et al., 2024). Meanwhile, materials with inherently high calcium oxide (CaO) content—such as cement kiln dust (CKD) and calcium carbide slag (CCS)—contribute significantly to alkaline activation. By elevating the soil's pH, these high-lime residues foster flocculation of clay particles and promote the formation of additional hydration products. CKD, collected as fine particulates during cement production, is rich in silica, alumina, and CaO, enabling robust pozzolanic interactions and the generation of calcium silicate hydrates (Wei et al., 2023; Attah et al., 2021; Almuaythir and Abbas, 2023; Al-Bakri et al., 2022). CCS, derived from acetylene production, also contains elevated levels of CaO, creating conditions conducive to accelerated formation of cementitious compounds (Chu et al., 2023; Gong et al., 2022; Wang et al., 2024).

Despite the proven utility of each waste material in isolation, research exploring combined or binary stabilizer formulations—particularly involving CKD and CCS—remains relatively limited. Consequently, deeper insights into optimal dosage strategies, specific reaction pathways, and attendant improvements in soil performance are needed. The present study therefore undertakes a comprehensive investigation of expansive soil stabilization using CKD and CCS, both individually and in combination, to elucidate these stabilization mechanisms more fully. Through a multi-pronged experimental approach encompassing compaction tests, free swelling rate assessments, unconfined compressive strength (UCS) measurements, and scanning electron microscopy (SEM) analyses, this study aims to illuminate how best to harness the synergistic potential of CKD and CCS for expansive soil improvement. The findings not only provide robust technical guidance on deploying these by-products as low-carbon stabilizers but also underscore the broader sustainability benefits of industrial waste reutilization in geotechnical applications.

2 Materials and methods

2.1 Materials

The primary experimental materials used in this study include expansive soil, cement kiln dust, and calcium carbide slag (as shown in Figure 1), all of which were collected and prepared

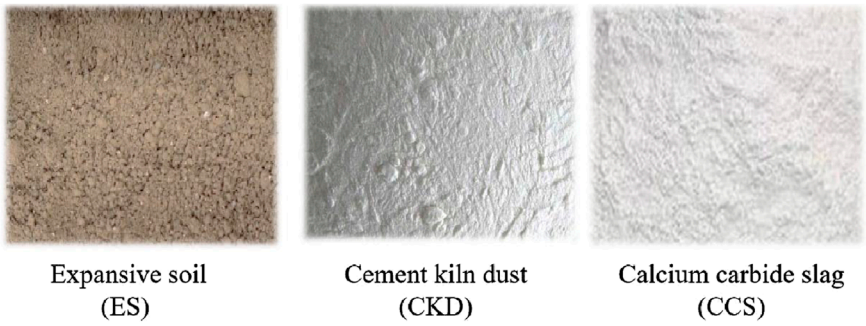

FIGURE 1
Materials used in this study.

TABLE 1 Basic properties of expansive soil used.

Free expansion rate δ_{ef} (%)	Natural dry density p (g/cm^3)	Optimum moisture content ω_{op} (%)	Maximum dry density ρ_d (g/cm^3)	Plastic limit ω_L (%)	Liquid limit ω_P (%)	Plasticity index IL (%)	Specific gravity Gs
52	1.42	18.9	1.55	23.6	51.2	27.6	2.72

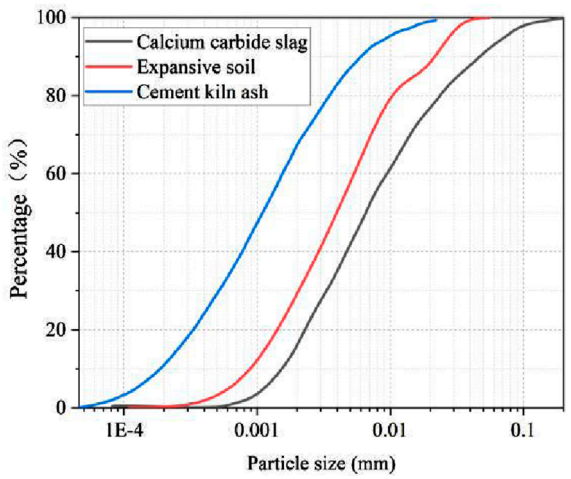

FIGURE 2
The gradation curves for cement kiln dust, calcium carbide slag, and expansive soil.

TABLE 2 Chemical compositions of the cement kiln ash.

Chemical composition	Content/%
Cao	51.95
SiO_2(%)	21.86
Al_2O_3(%)	4.23
Fe_2O_3(%)	4.76
MgO (%)	3.20
Others (%)	14

under strictly controlled conditions. The expansive soil used in this study was collected from a landslide in Gaochun District, Nanjing, Jiangsu Province, China. The soil is regarded as waste soil in the local engineering project due to the high uncertainty and hazard. The basic properties were tested by field density test, compaction test, liquid-plastic limit test and specific gravity test according to the "Standard for Geotechnical Testing Methods" (GB/T50123-2019) (Ministry of Construction P.R.China, 2019). The values obtained were summarized in Table 1, and the gradation curve was shown in Figure 2.

Cement kiln dust (CKD) is an industrial waste product derived from the cement production process, with primary chemical components including calcium oxide (CaO), silicon dioxide (SiO_2), and aluminum oxide (Al_2O_3), as well as small amounts of alkali oxides and sulfates. Cement kiln dust exhibits pozzolanic activity, with fine particles that can fill soil pores, thus improving the soil structure. The cement kiln dust used for the experiment was sourced from a cement plant in Henan Province, with its main components and parameters shown in Table 2.

Calcium carbide slag (CCS) is a by-product generated during the production of acetylene, primarily composed of calcium hydroxide ($Ca(OH)_2$), and has a strong alkalinity. The calcium carbide slag can undergo a hydration reaction with silicates and aluminates in the soil, producing calcium silicate hydrate (C-S-H) and calcium aluminate hydrate (C-A-H), thus improving the strength and stability of the soil. The calcium carbide slag used in the experiment

TABLE 3 Details of the stabilized soil samples.

Experiment number	Group	Cement kiln dust content/%	Calcium carbide slag content/%
CG-0/0[a]	Control group (CG)	0	0
BSS-5/6[b]	Binary Stabilizer System (BSS)	5	6
BSS-5/9		5	9
BSS-5/12		5	12
BSS-10/6		10	6
BSS-10/9		10	9
BSS-10/12		10	12
BSS-15/6		15	6
BSS-15/9		15	9
BSS-15/12		15	12
SSS-K5[c]	Single Stabilizer System (SSS)	5	0
SSS-K10		10	0
SSS-K15		15	0
SSS-C6[d]		0	6
SSS-C9		0	9
SSS-C12		0	12

[a]CG-0/0 indicates the Control Group with 0% CKD, and 0% CCS.
[b]BSS-x/y refers to the Binary Stabilizer System, where x% CKD, is combined with y% CCS (e.g., BSS-5/6 has 5% CKD +6% CCS).
[c]SSS-Kx denotes the Single Stabilizer System with only CKD, at x% (e.g., SSS-K10, has 10% CKD, and 0% CCS).
[d]SSS-Cy denotes the Single Stabilizer System with only CCS, at y% (e.g., SSS-C9, has 0% CKD, and 9% CCS).

was obtained from a chemical plant in Hunan Province, with a $Ca(OH)_2$ content of 93.00%.

2.2 Experiment methods

2.2.1 Experimental design

This investigation systematically evaluates the modification mechanisms of expansive soil matrices by utilizing cement kiln dust (CKD) and calcium carbide slag (CCS) as stabilizing agents. To facilitate clear comparisons across different formulations, the experimental program is organized into four main categories, as summarized in Table 3: (1) a control group with no stabilizer addition (CG-0/0), (2) a CKD-only series (SSS-K) at three dosage levels, (3) a CCS-only series (SSS-C) at three dosage levels, and (4) a set of binary stabilizer series (BSS) with combined CKD and CCS additions.

In the CKD-only (SSS-K) series, CKD is incorporated at concentrations of 5%, 10%, and 15%, where hydration reactions facilitate the formation of calcium silicate hydrate (C-S-H) and calcium aluminate hydrate (C-A-H). Similarly, the CCS-only (SSS-C) series includes CCS at concentrations of 6%, 9%, and 12%, wherein its principal constituent, calcium hydroxide (Ca(OH)2), suppresses expansion and enhances strength through reactions with soil minerals. The mono-component stabilizer configurations (i.e., SSS-K and SSS-C) enable a systematic evaluation of individual stabilizer efficacy, whereas the binary stabilizer series (BSS) assesses potential synergistic enhancements to both mechanical properties and dimensional stability when CKD and CCS are used in combination. Establishing CG-0/0 as the control baseline allows quantitative assessment of stabilizer-induced performance improvements.

A multi-parameter experimental methodology—encompassing compaction tests, free swelling rate measurements, unconfined compressive strength (UCS) evaluations, and scanning electron microscopy (SEM) analyses—was adopted to capture both macroscopic and microstructural changes. By comparing different stabilizer dosages and single/binary combinations, this study elucidates the impact of CKD and CCS on critical engineering parameters, such as compressive strength and swelling behavior, thereby informing optimal dosage strategies.

2.2.2 Experimental method

In order to comprehensively evaluate the mechanical properties and swelling characteristics of cement kiln dust and calcium carbide slag-modified expansive soil, this study

conducted several laboratory tests, including compaction tests, unconfined compressive strength tests, free swelling rate tests, and microstructure analysis. The following are the specific methods of each test:

2.2.2.1 Compaction test

In this study, the sample preparation process for expansive soil first requires determining the optimum moisture content and maximum dry density for each dosage through compaction tests. These parameters are essential to ensure the optimal compaction of soil samples during preparation, thereby ensuring the accuracy of the test results. The compaction test was conducted according to the "Standard for Geotechnical Testing Methods" (GB/T50123-2019) (Ministry of Construction P.R.China, 2019), using the heavy compaction method. Samples with different combinations of cement kiln dust and calcium carbide slag contents were compacted in layers to determine the optimum moisture content and maximum dry density for each mix ratio.

2.2.2.2 Free swelling rate test

This study investigated the variations in expansive properties of modified expansive soil through free swelling rate tests, conducted in accordance with the "Standard for Soil Test Methods" (GB/T50123-2019) (Ministry of Construction P.R.China, 2019). Initially, the central portion was extracted from the cured unconfined compression specimens, air-dried, and subsequently pulverized to pass through a 0.5 mm sieve. A 50 g sample was then collected for the swell ratio test. During the experimental procedure, the specimen was placed in a cylindrical vessel with dimensions of 100 mm in height. Deionized water was gradually introduced until the water level was flush with the soil specimen surface. After a 24-h immersion period, the expansion height was measured to calculate the free swelling rate, thereby evaluating the changes in expansive properties of the modified soil. The free swelling rate was calculated using the Equation 1:

$$\text{Free swelling rate} = \left(\Delta H / H_0\right) \times 100\% \quad (1)$$

Where ΔH represents the change in specimen height after swelling, and H_0 denotes the initial height of the specimen.

2.2.2.3 Unconfined compressive strength test

This study evaluated the strength performance of the modified soil using unconfined compressive strength tests, which were conducted according to the "Specifications for Highway Subgrade Testing" (JTG E40-2007) (Ministry of Transport P.R. China, 2007), using a WDW-10E electronic universal testing machine to measure compressive strength. The preparation of the specimens followed the mix design plan, using a static compaction method to form cylindrical specimens with a diameter of 50 mm and a height of 100 mm, with a compaction degree of 96% of the maximum dry density. The molded specimens were sealed and placed in a standard curing chamber, maintained at a temperature of 23°C ± 2°C and a relative humidity of over 95%. The curing periods were set at 7, 14, and 28 days. After the curing period, the specimens were removed from the curing chamber, placed on the testing machine, and loaded at a constant rate of 1 mm/min until failure, with the failure load being recorded.

The unconfined compressive strength (UCS) is calculated by Equation 2:

$$UCS = P/A \quad (2)$$

Where P is the maximum load at failure, and A is the cross-sectional area of the specimen.

2.2.2.4 Microstructural analysis

This research employed Scanning Electron Microscopy (SEM) technology to analyze the microstructure of soil modified with cement kiln dust and calcium carbide slag, aiming to investigate the modification mechanisms. As a high-resolution microscopic imaging technique, SEM can reveal detailed information about particle morphology, pore distribution, and cementitious material formation within the soil matrix, which is crucial for understanding the microstructural and mechanical properties of modified materials. In the experimental procedure, small specimens were first extracted from the failure surface of unconfined compression test samples. These specimens underwent drying treatment followed by gold coating to prevent charging effects during electron beam scanning. Subsequently, observations were conducted using a HITACHI SU8010 high-resolution scanning electron microscope, obtaining three-dimensional morphological and compositional information through secondary electron and backscattered electron imaging. The SEM images clearly illustrated the distribution of cementitious materials between particles, changes in pore structure, and the formation of microscopic connection networks in the modified soil samples.

Through the aforementioned experimental methods, this study systematically analyzed the individual and combined modification effects of cement kiln dust and calcium carbide slag, evaluated their effectiveness in improving the strength and expansive characteristics of expansive soil, and revealed the modification mechanisms from a microscopic perspective.

3 Results and analysis

3.1 Compaction characteristics

Building on the preliminary soil characterizations from Section 2, this subsection analyzes how varying CKD and CCS contents affect the compaction behavior of expansive soils. Figures 3, 4 depict the maximum dry density (MDD) and optimal moisture content (OMC) for each mix ratio, revealing systematic variations in compaction characteristics as cement kiln dust (CKD) and calcium carbide slag (CCS) contents change.

Compared to the control group (MDD = 1.55 g/cm^3, OMC = 18.6%), single-stabilizer systems (SSS) show notable improvements in compaction parameters. Specifically, a 5% CKD addition (SSS-K5) reduces the OMC to 18.2% and increases the MDD to 1.62 g/cm^3, while 6% CCS (SSS-C6) achieves an OMC of 18.3% and an MDD of 1.63 g/cm^3. These enhancements are attributable to reduced free water demand and improved compaction efficiency. The stabilizers occupy voids within the soil matrix and generate cementitious hydration products (e.g., calcium silicate hydrate), effectively refining the pore structure and facilitating densification.

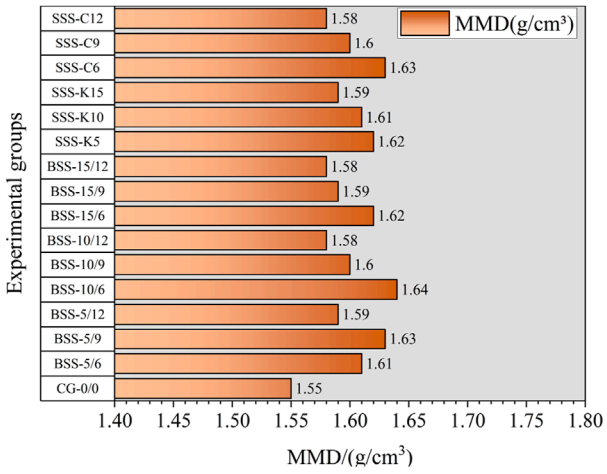

FIGURE 3
Maximum dry density (MMD) for each mix ratio.

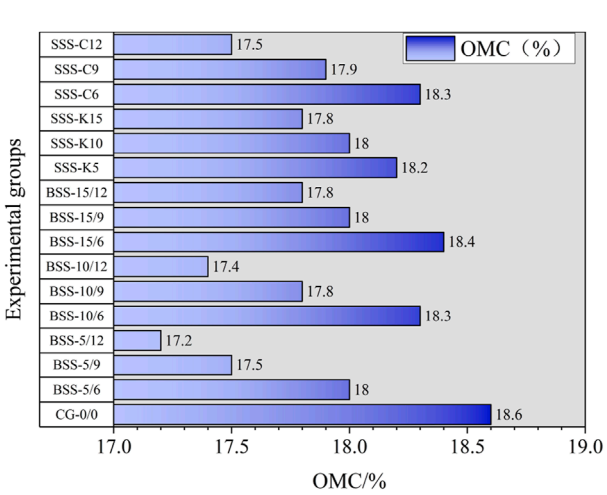

FIGURE 4
Optimal moisture content (OMC) for each mix ratio.

Comparisons between single- (SSS) and binary-stabilizer systems (BSS) illustrate that binary additions generally yield superior compaction performance at intermediate dosage levels. For instance, the BSS-5/9 configuration realizes an OMC of 17.5% and an MDD of 1.63 g/cm^3, a net increase of 0.08 g/cm^3 over the control. This outcome underscores the synergistic effect arising from simultaneously adding CKD and CCS, whereby accelerated hydration kinetics and enhanced void-filling contribute to improved matrix consolidation. Relative to corresponding single-stabilizer mixes (e.g., 5% CKD only or 9% CCS only), the binary formulation exhibits appreciably higher density and reduced moisture demand, demonstrating the robust synergistic mechanisms that underpin BSS performance.

At higher stabilizer concentrations, however, the incremental gains in maximum dry density appear to diminish. Although the BSS-15/12 configuration achieves an OMC of 17.8% and an MDD of 1.58 g/cm^3, it does not surpass certain intermediate formulations—such as BSS-10/6, which reaches an MDD of 1.64 g/cm^3. These findings suggest that excessive stabilizer content may impede uniform inter-particle distribution and introduce saturation-like effects that inhibit additional compaction benefits. In contrast, intermediate-dosage configurations (e.g., BSS-10/6) strike a favorable balance between material input and achievable densification, thereby offering an optimal cost–performance ratio. Collectively, these observations highlight the importance of targeted CKD–CCS proportions in achieving both enhanced compaction and economic efficiency when stabilizing expansive soils.

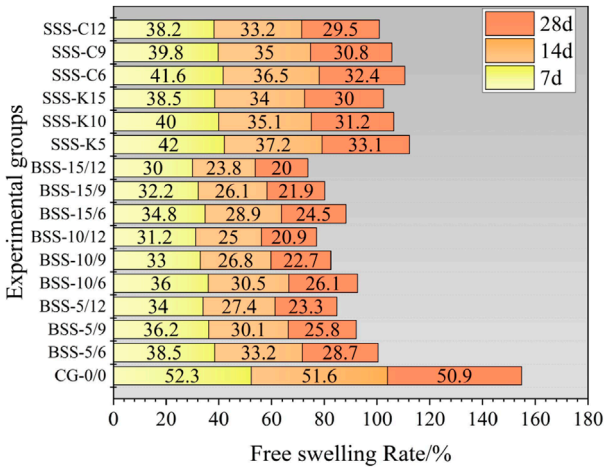

FIGURE 5
Changes in free swelling rate for different stabilized samples.

3.2 Free swelling rate analysis

Following the compaction analysis in Section 3.1, this subsection focuses on the influence of different CKD and CCS dosages on the free swell behavior of expansive soils. Figure 5 delineates the temporal evolution of free swelling rate parameters across diverse stabilizer configurations throughout prescribed curing time of 7, 14, and 28 days. Empirical analysis demonstrates that progressive elevation in stabilizer concentrations, specifically cement kiln dust (CKD) and calcium carbide slag (CCS), manifests in substantial attenuation of free swell characteristics in modified expansive soil matrices. Moreover, the binary stabilizer system (BSS) exhibits markedly superior expansiveness suppression efficacy relative to monolithic stabilizer configurations (SSS). Specifically, the BSS-5/6 configuration yielded an initial free swelling rate of 38.5% at 7-day curing duration, subsequently exhibiting progressive reduction to 28.7% at 28-day maturation, representing a substantial diminution of 22.2 percentage points relative to control specimens (CG-0/0). Further optimization through elevated CCS incorporation, as manifested in the BSS-5/12 configuration, demonstrated enhanced performance characteristics, yielding an initial free swelling rate of 34.0% at 7-day curing duration, followed by significant reduction to 23.3% at 28-day maturation, corresponding to a marked decrease of 27.6 percentage points comparative to control specimens.

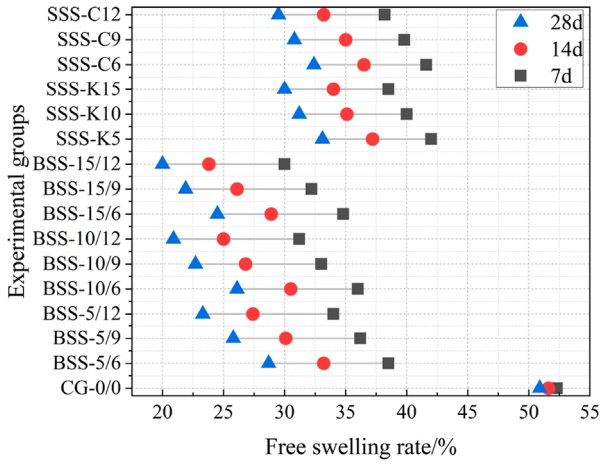

FIGURE 6
Changes in free swelling rate with curing times.

The BSS configuration manifests dual physicochemical functionality through C-S-H and C-A-H generation, facilitating concurrent void space occupation and matrix stability enhancement, thereby achieving significant expansiveness suppression. The BSS-10/9 configuration demonstrated superior performance characteristics, exhibiting an expansion coefficient reduction to 22.7% at 28-day curing duration, representing decrements of 10.3 and 28.2 percentage points relative to 7-day measurements and CG-0/0 specimens, respectively. In contrast, the SSS configurations exhibited marginally diminished efficacy, with SSS-K10 and SSS-C9 yielding expansion coefficients of 31.2% and 30.8%, respectively, at 28-day maturation. Despite demonstrable improvements through single stabilizer incorporation, the singular physicochemical mechanisms manifested constrained effectiveness, failing to achieve the synergistic inhibitory phenomena characteristic of binary systems.

Figure 6 shows the changes in free swelling rate with curing times. The temporal evolution of free swell characteristics exhibits significant attenuation concurrent with curing duration extension, particularly pronounced in BSS configurations where expansion coefficient reduction demonstrates progressive enhancement. Initial modifications manifest at 7-day curing duration, exemplified by BSS-10/9 configuration yielding an expansion coefficient of 33.0%, corresponding to a 19.3 percentage point reduction relative to CG-0/0 specimens. Subsequent maturation to 14-day duration facilitates enhanced pore structure modification through progressive hydration product development, yielding further reduction to 26.8%. Terminal measurements at 28-day curing duration demonstrate optimized stabilization of reaction products, manifesting in an expansion coefficient of 22.7%, representing a substantial decrement of 10.3 percentage points relative to 7-day measurements.

The modification efficacy of BSS configurations exhibits progressive enhancement concurrent with curing duration extension. Specifically, the BSS-15/12 configuration demonstrates significant performance optimization at 14-day maturation, manifesting a free swelling rate reduction to 20.0%, corresponding to a 10 percentage point decrement relative to 7-day measurements, thereby validating the enhanced stabilizer reactivity under prolonged curing conditions. Furthermore, elevated BSS configurations, exemplified by BSS-15/12, exhibit superior expansiveness suppression, achieving a 32.3 percentage point reduction at 28-day maturation relative to SSS configurations.

The synergistic incorporation of stabilizing agents in BSS configurations demonstrates markedly enhanced expansiveness suppression efficacy comparative to SSS configurations, particularly pronounced at intermediate to elevated dosages under extended curing durations. Progressive matrix densification and stability enhancement manifest through systematic pore structure modification via hydration product evolution. While SSS configurations demonstrate measurable expansiveness suppression, their limited physicochemical modification mechanisms yield comparatively diminished efficacy. Empirical analysis indicates that BSS-10/9 configuration achieves optimal performance parameters, manifesting an expansion ratio of 22.7% at 28-day maturation, thereby establishing an optimal equilibrium between economic considerations and modification efficacy for practical engineering applications.

3.3 Strength characteristics

This section presents a detailed analysis of unconfined compressive strength (UCS) under varying curing conditions, elucidating how binary stabilizer systems (BSS) exploit potential synergistic interactions between cement kiln dust (CKD) and calcium carbide slag (CCS) to offer insights into optimal dosage strategies for expansive soil stabilization. Figure 7 shows the changes in UCS with different curing times for different stabilized samples. Within the binary stabilizer matrix, the mechanistic characteristics and performance parameters of CCS and CKD exhibit distinctive temporal variations across curing durations. Empirical analysis elucidates that CCS functions primarily as an activation agent, wherein incremental dosage elevation manifests in accelerated early-stage strength development. The SSS-C series demonstrates systematic strength enhancement correlating with concentration gradients, specifically yielding 7-day strength parameters of 111.8 kPa, 129.2 kPa, and 141.3 kPa for SSS-C6, SSS-C9, and SSS-C12 configurations, respectively. This phenomenon correlates with the enhanced reactivity of CaO components within CCS matrices during soil modification processes. The formation of ettringite, C-S-H gel, and associated hydration products facilitates concurrent enhancement of initial bonding strength and significant attenuation of plasticity and shrinkage characteristics in expansive soil matrices. While this reaction mechanism demonstrates superior early-stage activation efficacy, the long-term strength development contribution exhibits limitations, exemplified by the SSS-C12 configuration achieving merely 171.8 kPa at 28-day maturation. This temporal evolution pattern indicates stabilization of CCS reactivity in terminal stages, with primary efficacy manifesting in early-stage strength enhancement mechanisms.

In contrast to CCS behavior, CKD exhibits progressive strength enhancement characteristics, particularly pronounced during terminal curing phases. Empirical data demonstrates systematic strength optimization correlating with elevated CKD

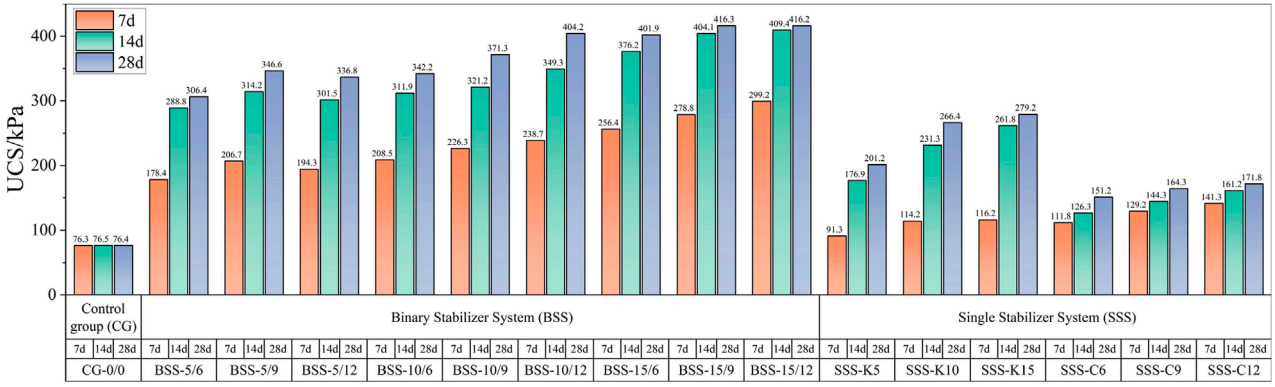

FIGURE 7
Changes in UCS with different curing times for different stabilized samples.

concentrations at 14-day and 28-day maturation intervals. The BSS-10/6 configuration manifests strength parameters of 208.5 kPa, 311.9 kPa, and 342.2 kPa at 7-day, 14-day, and 28-day intervals, respectively, reflecting the sustained hydration kinetics of CKD components. This phenomenon correlates with secondary hydration mechanisms of free calcium oxide, silicates, and aluminates, facilitating progressive matrix densification through C-S-H gel and ettringite formation.

For CKD concentrations ≤10%, optimal strength enhancement manifests in configurations approximating unity CKD:CCS ratios, effectively leveraging early-stage CCS activation concurrent with terminal-stage CKD strength development. The BSS-10/9 and BSS-10/12 configuration exemplifies this optimization. BSS-10/9 yielding progressive strength evolution of 226.3 kPa, 321.2 kPa, and 371.3 kPa across respective curing intervals. CKD concentrations exceeding 10% manifest primarily in early-stage strength enhancement with constrained terminal-stage optimization. The BSS-15/6 configuration yields 256.4 kPa at 7-day maturation, substantially exceeding BSS-10/6 (208.5 kPa); however, terminal strength parameters (401.9 kPa versus 342.2 kPa) demonstrate limited incremental benefit. This phenomenon correlates with accelerated early-stage hydration kinetics at elevated CKD concentrations, culminating in reaction saturation during terminal phases due to comprehensive pore structure modification through C-S-H and ettringite formation.

To systematically evaluate the synergistic efficacy of binary CKD-CCS configurations on expansive soil compressive strength characteristics, this investigation introduces a novel quantitative parameter: the Synergistic Enhancement Factor (SEF). This metric facilitates comprehensive analysis of performance parameters across diverse binary configurations throughout prescribed curing durations, enabling quantitative assessment of BSS efficacy relative to corresponding SSS configurations. The mathematical formulation for SEF determination is expressed as Equation 3:

$$SEF = \Delta\sigma_{BBS} / \Delta\sigma_{SSS-K} + \Delta\sigma_{SSS-C} \quad (3)$$

where:

$\Delta\sigma_{BBS}$ (Combined Strength Increase). This term represents the net improvement in unconfined compressive strength (UCS) realized by the binary stabilizer system (i.e., CKD + CCS used together) compared to the untreated control sample. Physically, it embodies the total effect of both stabilizers acting in tandem, including any additional hydration products or enhanced particle bonding resulting specifically from the interaction of CKD and CCS within the soil matrix.

$\Delta\sigma_{SSS-K}$ (CKD-Only Strength Increase). This parameter captures the individual contribution of cement kiln dust (CKD) as if it were used alone at the same or comparable dosage. In other words, it is the UCS gain relative to the control group when only CKD is applied, reflecting phenomena such as pozzolanic reactions, C-S-H gel formation, and pore structure refinement attributable solely to CKD.

$\Delta\sigma_{SSS-C}$ (CCS-Only Strength Increase). Analogous to ΔSSS-K, this term indicates how much calcium carbide slag (CCS) alone improves the UCS. Its physical significance lies in the early-stage activation potential of CCS, driven by its $Ca(OH)_2$ or CaO content, and the resultant hydration products that form independently of CKD.

A broader comparative examination of SEF trends, (as shown in Figure 8), taking into account both performance and cost-effectiveness, strengthens the conclusion regarding optimal CKD–CCS formulations. Within the lower-CKD category (CKD ≤10%), BSS-5/6 maintains a notable advantage in early-age strength gain, as evidenced by its SEF peak of 2.02 at 7 days—a value exceeding that of BSS-5/9 and BSS-5/12—and remains competitive at 28 days (1.15). Although some higher-CKD formulations—such as BSS-15/6—can achieve even higher SEF values at 7 days, the relatively larger total stabilizer content increases material costs without providing proportionally greater long-term strength improvements. Indeed, while BSS-15/6 achieves a 7-day SEF of 2.39, its 28-day value (1.17) suggests diminishing returns, underscoring its lower cost-effectiveness compared to BSS-5/6 in contexts where both performance and economic factors must be balanced.

In the higher-CKD range (CKD >10%), the SEF trends similarly indicate that BSS-10/9 offers a more attractive balance between short-term efficiency and sustained long-term performance, thereby favorably impacting material costs relative to higher-dosage formulations. For example, BSS-10/9 attains an SEF of 1.65 at 7 days

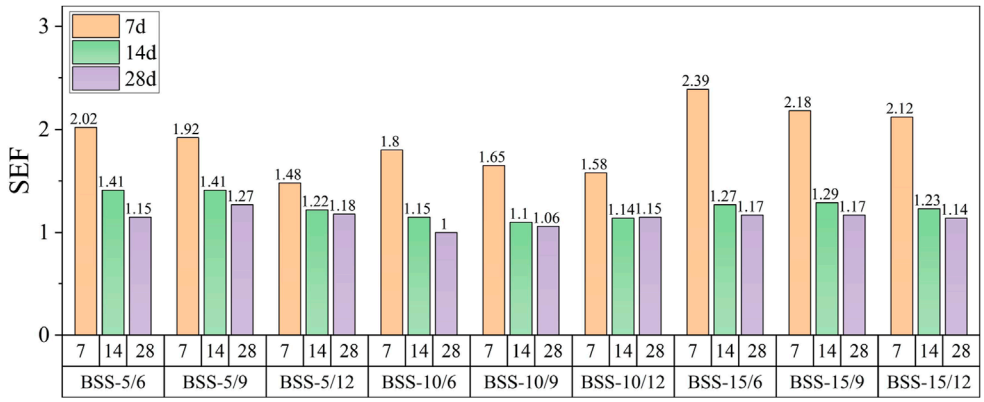

FIGURE 8
Changes in SEF with different curing times for different stabilized samples.

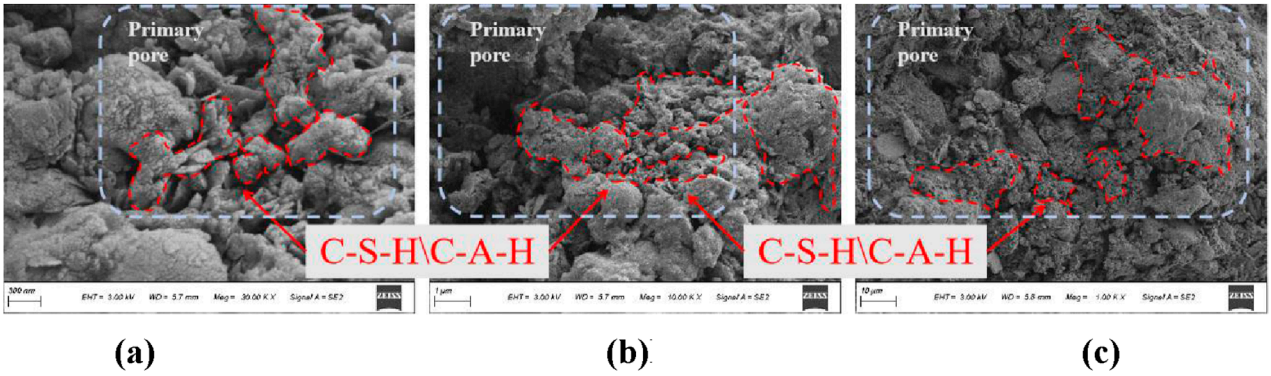

FIGURE 9
The SEM results for BSS-5/6 and BBS-5/10 samples. **(A)** BSS-5/6 (scanning area 1) **(B)** BSS-5/6 (scanning area 2) **(C)** BBS-5/10 (scanning area 1).

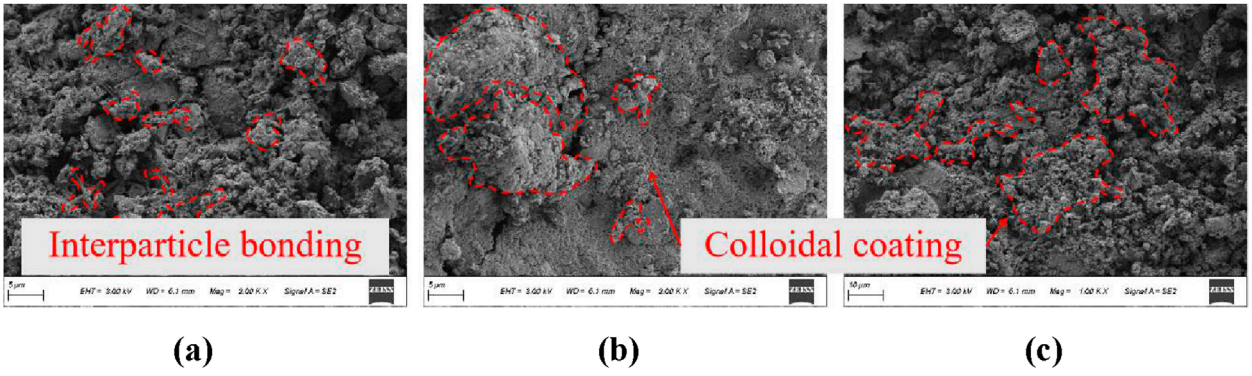

FIGURE 10
The SEM results for BSS-10/9 and BBS-15/12 samples. **(A)** BSS-10/9 (scanning area 1) **(B)** BSS-10/9 (scanning area 1) **(C)** BBS-15/12 (scanning area 2).

and 1.10 at 14 days, effectively balancing early and terminal strength enhancement. By contrast, configurations such as BSS-15/6, despite their high early SEF, exhibit reduced performance gains at extended curing intervals and elevate stabilizer dosage requirements, leading to heightened material expenditures with no commensurate increase in long-term strength. Consequently, BSS-10/9 emerges as the most suitable choice in higher-CKD scenarios when cost-effectiveness and consistent strength development over time are prioritized, complementing the lower-CKD optimum (BSS-5/6) for rapid early gains in expansive soil stabilization.

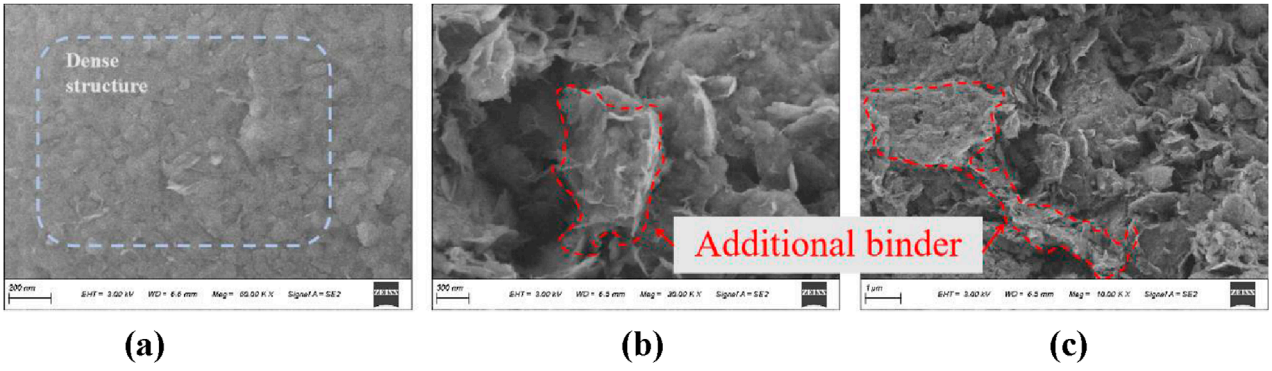

FIGURE 11
The SEM results for high magnification. **(A)** BSS-10/9 (scanning area 3) **(B)** BSS-15/12 (scanning area 1) **(C)** BBS-15/12 (scanning area 2).

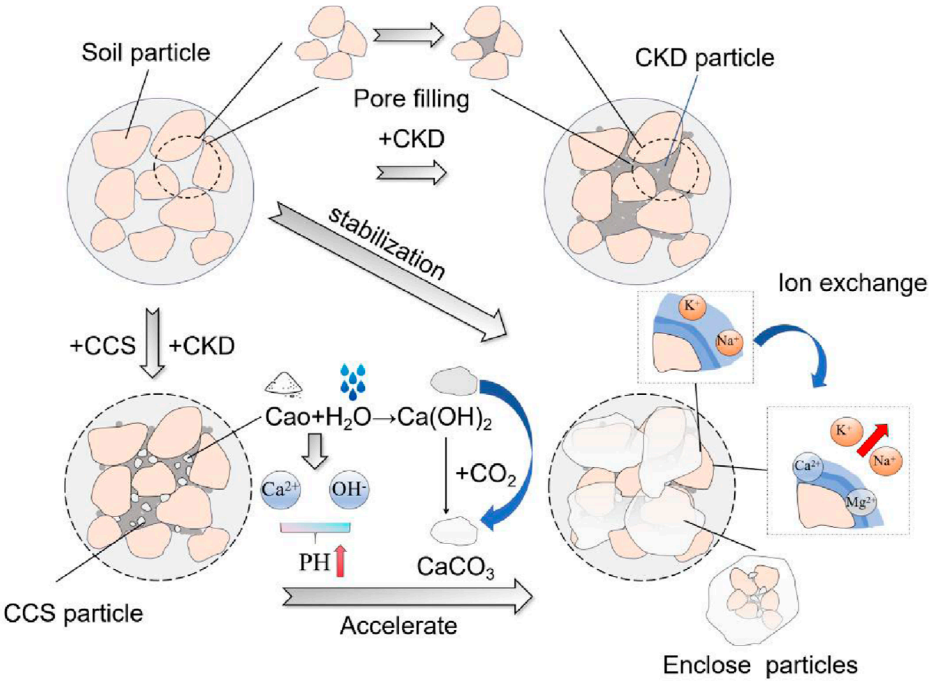

FIGURE 12
The mechanism of stabilizing expansive soil by composite action of CKD and CCS.

3.4 Scanning electron microscopy analysis

As shown in Figure 9, the scanning electron micrographs (SEM) of the cement kiln dust (CKD)–calcium carbide slag (CCS) stabilized expansive soil reveal a pronounced decrease in interparticle voids and the emergence of dense particle clusters. These observations underscore the formation of hydration products, particularly calcium silicate hydrate (C-S-H) and calcium aluminate hydrate (C-A-H), which fill pore spaces and integrate soil grains into cohesive aggregations. Additionally, the fine particles of CKD can physically occupy voids within the soil matrix, reinforcing the densification process alongside the chemical reactions. The resultant microstructure is more compact than that of the untreated control samples, aligning with the elevated maximum dry density (MDD) and reduced free swelling rate recorded in the laboratory tests. By occupying previously unfilled pore spaces, these newly formed cementitious phases effectively limit water infiltration and the attendant volumetric expansion, a phenomenon corroborated by the substantial decrease in free swelling rates observed across various stabilizer configurations.

Figure 10 also illustrate the development of robust interparticle bonding in the binary stabilizer systems, especially at intermediate stabilizer dosages such as BSS-10/6 or BSS-10/9. The synergy between CKD and CCS fosters progressive pozzolanic reactions involving CaO, SiO2, and Al2O3, generating semi-crystalline and amorphous gel phases that coat the soil grains and reinforce

interparticle contact areas. This morphological connectivity reduces stress concentrations under load, thus enhancing unconfined compressive strength (UCS) at both early (7-day) and later (28-day) curing stages. In contrast, higher stabilizer contents can produce a dense, albeit unevenly distributed matrix that may not sustain continued strength gains due to localized agglomeration and diminished reactivity. The BSS-15/12 configuration, for example, appears less effective in the long term despite an initially dense structure, underscoring the importance of balancing stabilizer supply with the soil's reactive capacity.

As shown in Figure 11, Closer examination at high magnification provides further evidence that carefully calibrated CKD–CCS ratios optimize the extent and distribution of hydration products. In intermediate-dosage mixtures, microcracks are minimized and pore networks are effectively sealed, preventing excessive water ingress and associated swelling. This refined pore structure likewise contributes to improved particle interlocking and a more efficient transfer of loads through the modified soil matrix. Conversely, higher stabilizer concentrations may yield a form of "saturation" effect in which additional binder cannot interact uniformly with soil particles, limiting further gains in microstructural refinement. Consequently, the enhanced cohesion and reduced porosity observed in intermediate-dosage binary systems correlate strongly with both the notable increases in UCS and the mitigated swelling behavior, ultimately confirming that these formulations strike a more favorable balance between cost-effectiveness and long-term performance in expansive soil stabilization.

4 Discussion on the mechanisms of CKD-CCS in soil stabilization

The binary stabilizer system comprising cement kiln dust (CKD) and calcium carbide slag (CCS) demonstrates superior modification efficacy through synergistic physicochemical mechanisms (as shown in Figure 12) in expansive soil matrices. The primary modification mechanism encompasses concurrent physical densification and chemical transformation processes, wherein fine-grained CKD particles facilitate optimal void space occupation while CCS components establish conducive alkaline conditions for secondary pozzolanic reactions. This dual-mechanism approach manifests in systematic enhancement of matrix properties, evidenced by elevated maximum dry density (1.64 g/cm^3 in BSS-10/6) and accelerated strength development (226.3 kPa at 7-day curing in BSS-10/9). Comparative analysis with conventional stabilizers reveals distinctive advantages: the rapid dissolution of CCS-derived CaO establishes immediate strength development through C-A-H formation, demonstrating superior early-stage performance compared to traditional lime stabilization, while the progressive generation of C-S-H gel structures through CKD components facilitates sustained strength enhancement, achieving optimal parameters (371.3 kPa) at 28-day curing. This synergistic interaction, quantified by elevated Synergistic Enhancement Factor (1.65), significantly exceeds the combined individual effects of constituent stabilizers and traditional pozzolanic materials.

The microstructural evolution in CKD-CCS modified matrices provides fundamental validation for the observed macroscopic performance enhancement while demonstrating significant environmental and economic advantages. The progressive development of cementitious compounds facilitates systematic reduction in expansion characteristics, achieving minimal free swelling rate (22.7%) at 28-day maturation in BSS-10/9 configurations - a marked improvement over conventional lime stabilization methodologies. The comprehensive particle encapsulation and enhanced matrix densification manifest in superior durability characteristics, evidenced by sustained strength development during extended curing periods. This represents particular advantages over single-component stabilizers, wherein limited modification mechanisms often result in incomplete matrix transformation. Furthermore, as industrial by-products, both CKD and CCS represent cost-effective alternatives to traditional stabilizers while simultaneously facilitating productive utilization of waste materials. The demonstrated performance characteristics, coupled with these sustainability advantages, establish CKD-CCS stabilization as an optimal methodology for expansive soil modification in practical engineering applications, achieving superior technical performance while advancing sustainable construction practices.

5 Conclusion

This study systematically examined the feasibility of using cement kiln dust (CKD) and calcium carbide slag (CCS) as stabilizers for expansive soil, focusing on compaction characteristics, swelling behavior, unconfined compressive strength (UCS), and microstructural evolution. Based on the experimental findings and analyses, several key conclusions can be drawn:

(1) Compared with the control group (MDD = 1.55 g/cm^3), binary CKD–CCS blends produced higher maximum dry density. BSS-10/6 attained 1.64 g/cm^3. The addition of CKD and CCS reduced the optimal moisture content by occupying soil pores and facilitating early-stage hydration reactions.

(2) Binary stabilizers suppressed volumetric expansion relative to untreated soil. BSS-10/9 decreased the free swelling rate to 22.7% at 28 days. Higher CCS contents (9%–12%) combined with moderate CKD levels led to greater swelling reduction than single-stabilizer systems.

(3) Unconfined compressive strength (UCS) tests indicated substantial gains under CKD–CCS stabilization. BSS-10/9 achieved 226.3 kPa at 7 days and 371.3 kPa at 28 days. The Synergistic Enhancement Factor (SEF) for certain binary formulations exceeded 1.5, indicating that CKD and CCS together outperform individual stabilizers.

(4) SEM analysis confirms CKD–CCS synergy in expansive soils, as hydration products (C-S-H, C-A-H) fill voids and strengthen particle bonds. Moderate dosages optimize pozzolanic reactions for higher density and reduced swelling, whereas excessive content yields diminishing returns due to uneven binder distribution.

(5)BSS-10/9 demonstrated a balanced improvement in densification, swelling control, and UCS, highlighting the low-carbon, cost-effective potential of CKD–CCS blends for stabilizing expansive soil.

Data availability statement

The original contributions presented in the study are included in the article/supplementary material, further inquiries can be directed to the corresponding author.

Author contributions

QY: Conceptualization, Writing–review and editing, Formal Analysis, Funding acquisition, Writing–original draft. BP: Funding acquisition, Writing–original draft, Writing–review and editing, Investigation, Project administration, Validation, Visualization. WL: Project administration, Writing–review and editing, Conceptualization, Resources. BW: Supervision, Writing–review and editing. JZ: Data curation, Visualization, Writing–review and editing. GL: Project administration, Writing–review and editing. TW: Data curation, Writing–review and editing.

Funding

The author(s) declare that financial support was received for the research, authorship, and/or publication of this article. This work was supported by Science and Technology Project of Natural Resources Department of Gansu Province (Major Project, 24JRRA800), 2024 Jiangsu Province construction system research project (2024ZD052), and Xizang Civil water Conservancy and electric power Engineering Technology Research center open project (XZA202405CHP2008B).

Conflict of interest

Author WL was a postdoctoral fellow at Jiangsu Hanjian Group Co., Ltd. Author TW was employed by Jiangsu Hehai Engineering Technology Co., Ltd.

The remaining authors declare that the research was conducted in the absence of any commercial or financial relationships that could be construed as a potential conflict of interest.

Generative AI statement

The author(s) declare that no Generative AI was used in the creation of this manuscript.

Publisher's note

References

Abbas, M. F., Shaker, A. A., and Al-Shamrani, M. A. (2023). Hydraulic and volume change behaviors of compacted highly expansive soil under cyclic wetting and drying. *J. Rock Mech. Geotechnical Eng.* 15 (2), 486–499. doi:10.1016/j.jrmge.2022.05.015

Al-Adhadh, A. R., Daud, N. N. N., Yusuf, B., and Al-Rkaby, A. H. (2024). Supplementary cementitious materials in sandy soil improvement: a review. *J. Build. Pathology Rehabilitation* 9 (2), 138. doi:10.1007/s41024-024-00496-2

Al-Bakri, A. Y., Ahmed, H. M., and Hefni, M. A. (2022). Cement Kiln Dust (CKD): potential beneficial applications and eco-sustainable solutions. *Sustainability* 14 (12), 7022. doi:10.3390/su14127022

Almuaythir, S., and Abbas, M. F. (2023). Expansive soil remediation using cement kiln dust as stabilizer. *Case Stud. Constr. Mater.* 18, e01983. doi:10.1016/j.cscm.2023.e01983

Al-Saedi, M., and Sabbar, A. S. (2024). Treatment of expansive soils with slag: a review study. *Soil Mech. Found. Eng.* 60 (6), 574–580. doi:10.1007/s11204-024-09931-5

Attah, I. C., Okafor, F. O., and Ugwu, O. O. (2021). Optimization of California bearing ratio of tropical black clay soil treated with cement kiln dust and metakaolin blend. *Int. J. Pavement Res. Technol.* 14, 655–667. doi:10.1007/s42947-020-0003-6

Barman, D., and Dash, S. K. (2022). Stabilization of expansive soils using chemical additives: a review. *J. Rock Mech. Geotechnical Eng.* 14 (4), 1319–1342. doi:10.1016/j.jrmge.2022.02.011

Chen, R., Congress, S. S. C., Cai, G., Duan, W., and Liu, S. (2021). Sustainable utilization of biomass waste-rice husk ash as a new solidified material of soil in geotechnical engineering: a review. *Constr. Build. Mater.* 292, 123219. doi:10.1016/j.conbuildmat.2021.123219

Chen, Y., Huang, Y., Wu, M., and Wang, S. (2022). Fly ash/paraffin composite phase change material used to treat thermal and mechanical properties of expansive soil in cold regions. *J. Renew. Mater.* 10 (4), 1153–1173. doi:10.32604/jrm.2022.018856

Chu, C., Zhan, M., Feng, Q., Deng, Y., Li, D., Zha, F., et al. (2023). Expansive soil modified by iron tailing sand and calcium carbide slag as subgrade material. *Environ. Dev. Sustain.* 25 (9), 10393–10410. doi:10.1007/s10668-022-02498-x

Dang, L. C., Khabbaz, H., and Ni, B. J. (2021). Improving engineering characteristics of expansive soils using industry waste as a sustainable application for reuse of bagasse ash. *Transp. Geotech.* 31, 100637. doi:10.1016/j.trgeo.2021.100637

Fatima, B., Alshameri, B., Hassan, W., Maqsood, Z., Jamil, S. M., and Madun, A. (2023). Sustainable incorporation of Plaster of Paris kiln dust for stabilization of dispersive soil: a potential solution for construction industry. *Constr. Build. Mater.* 397, 132459. doi:10.1016/j.conbuildmat.2023.132459

Gong, X., Zhang, T., Zhang, J., Wang, Z., Liu, J., Cao, J., et al. (2022). Recycling and utilization of calcium carbide slag-current status and new opportunities. *Renew. Sustain. Energy Rev.* 159, 112133. doi:10.1016/j.rser.2022.112133

Habert, G., Miller, S. A., John, V. M., Provis, J. L., Favier, A., Horvath, A., et al. (2020). Environmental impacts and decarbonization strategies in the cement and concrete industries. *Nat. Rev. Earth and Environ.* 1 (11), 559–573. doi:10.1038/s43017-020-0093-3

Hassan, W., Alshameri, B., Jamil, S. M., Maqsood, Z., Haider, A., and Shahzad, A. (2023). Incorporating potassium-rich waste material in a sustainable way to stabilize dispersive clay: a novel practical approach for the construction industry. *Constr. Build. Mater.* 400, 132717. doi:10.1016/j.conbuildmat.2023.132717

Laporte, S., Eichhorn, G., Kingswood, J., Siemens, G., and Beddoe, R. (2023). Physical modelling of climate-soil-infrastructure interactions of paved roadways constructed in expansive soil. *Transp. Geotech.* 43, 101126. doi:10.1016/j.trgeo.2023.101126

Liu, Z., Ma, X., Chi, J., Chen, Y., and Wang, C. (2024). Centrifuge model tests and numerical simulation on ground-borne vibration propagating and vibration reduction scheme for tunnel inner structure. *Tunn. Undergr. Space Technol. incorporating Trenchless Technol. Res.* 153, 105996. doi:10.1016/j.tust.2024.105996

Mahedi, M., Cetin, B., and White, D. J. (2020). Cement, lime, and fly ashes in stabilizing expansive soils: performance evaluation and comparison. *J. Mater. Civ. Eng.* 32 (7), 04020177. doi:10.1061/(asce)mt.1943-5533.0003260

Ministry of Construction P.R.China (2019). *GB/T 50123-2019 Standard for soil test method*. Beijing: China Planning Press.

Ministry of Transport P.R. China (2007). *JTG E40-2007 Test methods of soils for highway engineering*. Beijing: China communication press.

Miraki, H., Shariatmadari, N., Ghadir, P., Jahandari, S., Tao, Z., and Siddique, R. (2022). Clayey soil stabilization using alkali-activated volcanic ash and slag. *J. Rock Mech. Geotechnical Eng.* 14 (2), 576–591. doi:10.1016/j.jrmge.2021.08.012

Mustafayeva, A., Moon, S.-W., Satyanaga, A., and Kim, J. (2024). Enhancing mechanical properties of expansive soil through BOF slag stabilization: a sustainable alternative to conventional methods. *Minerals* 14, 1145. doi:10.3390/min14111145

Muthukkumaran, K., and Anusudha, V. (2020). Study on behavior of copper slag and lime–treated clay under static and dynamic loading. *J. Mater. Civ. Eng.* 32 (8), 04020230. doi:10.1061/(asce)mt.1943-5533.0003259

Sarker, D., Apu, O. S., Kumar, N., Wang, J. X., and Lynam, J. G. (2023). Sustainable lignin to enhance engineering properties of unsaturated expansive subgrade soils. *J. Mater. Civ. Eng.* 35 (8), 04023259. doi:10.1061/jmcee7.mteng-15008

Shan, Y., Huang, A., Qin, X., Zhou, S., and Zhou, X. (2022). Long-term *in-situ* monitoring on foundation settlement and service performance of a novel pile-plank-supported ballastless tram track in soft soil regions. *Transp. Geotech.* 36, 100821. doi:10.1016/j.trgeo.2022.100821

Song, J., Lu, Z., Pan, Y., Ji, J., and Gao, Y. (2024). Investigation of seismic displacements in bedding rock slopes by an extended Newmark sliding block model. *Landslides* 21 (3), 461–477. doi:10.1007/s10346-023-02170-z

Syed, M., GuhaRay, A., and Goel, D. (2022). Strength characterisation of fiber reinforced expansive subgrade soil stabilized with alkali activated binder. *Road Mater. Pavement Des.* 23 (5), 1037–1060. doi:10.1080/14680629.2020.1869062

Syed, M., GuhaRay, A., and Raju, S. (2023). Subgrade strength performance behavior of alkali-activated binder and cement stabilized expansive soil: a semifield study. *J. Mater. Civ. Eng.* 35 (10), 04023329. doi:10.1061/jmcee7.mteng-15580

Tiwari, N., Satyam, N., and Puppala, A. J. (2021). Strength and durability assessment of expansive soil stabilized with recycled ash and natural fibers. *Transp. Geotech.* 29, 100556. doi:10.1016/j.trgeo.2021.100556

Wang, H., Jiang, M., Cao, B., Wang, F., and Xu, J. (2024). Stabilized/solidified chlorine saline soils with ground granulated blast furnace slag and calcium carbide residue. *Constr. Build. Mater.* 449, 138490. doi:10.1016/j.conbuildmat.2024.138490

Wei, J., Wei, J., Huang, Q., Zainal Abidin, S. M. I. B. S., and Zou, Z. (2023). Mechanism and engineering characteristics of expansive soil reinforced by industrial solid waste: a review. *Buildings* 13 (4), 1001. doi:10.3390/buildings13041001

Wu, Y., Qiao, X., Yu, X., Yu, J., and Deng, Y. (2021). Study on properties of expansive soil improved by steel slag powder and cement under freeze-thaw cycles. *KSCE J. Civ. Eng.* 25 (2), 417–428. doi:10.1007/s12205-020-0341-6

Ye, W., Gao, C., Liu, Z., Wang, Q., and Su, W. (2023). A Fuzzy-AHP-based variable weight safety evaluation model for expansive soil slope. *Nat. Hazards* 119 (1), 559–581. doi:10.1007/s11069-023-06130-7

Zada, U., Jamal, A., Iqbal, M., Eldin, S. M., Almoshaogeh, M., Bekkouche, S. R., et al. (2023). Recent advances in expansive soil stabilization using admixtures: current challenges and opportunities. *Case Stud. Constr. Mater.* 18, e01985. doi:10.1016/j.cscm.2023.e01985

Zhang, C., Wang, W., Zhu, Z., Shao, L., Wan, Y., and Zhang, Y. (2023). Mechanical and microscopic properties of cement composite expansive soil with graphene oxide: ecofriendly modification material. *Int. J. Geomechanics* 23 (6), 04023071. doi:10.1061/ijgnai.gmeng-8574

Zhao, G., Yan, D., Ren, G., Zhu, Z., Wu, T., Ding, S., et al. (2023). Influence of ground granulated blast furnace slag on the dispersivity and mechanical property of dispersive soil. *Constr. Build. Mater.* 409, 134036. doi:10.1016/j.conbuildmat.2023.134036

Zheng, X., Liu, K., Gao, S., Wang, F., and Wu, Z. (2023). Effect of pozzolanic reaction of zeolite on its internal curing performance in cement-based materials. *J. Build. Eng.* 63, 105503. doi:10.1016/j.jobe.2022.105503

frontiers | Frontiers in Earth Science

TYPE Original Research
PUBLISHED 29 April 2025
DOI 10.3389/feart.2025.1519602

OPEN ACCESS

EDITED BY
Yifei Sun,
Taiyuan University of Technology, China

REVIEWED BY
Zhengzheng Cao,
Henan Polytechnic University, China
Tola Garo Shaka,
Adama Science and Technology University, Ethiopia

*CORRESPONDENCE
Xiangsen Gao,
2016006@sdipct.edu.cn

RECEIVED 30 October 2024
ACCEPTED 31 March 2025
PUBLISHED 29 April 2025

CITATION
Lei Y, Wang J, Zhu Z, Li M, Zhao X, Gao X and Zhang M (2025) Influence of borehole trajectory and pressure on the characteristics of drilling induced fractures.
Front. Earth Sci. 13:1519602.
doi: 10.3389/feart.2025.1519602

Influence of borehole trajectory and pressure on the characteristics of drilling induced fractures

Yushun Lei[1], Jiayu Wang[1], Zihan Zhu[1], Muyuan Li[1], Xinwei Zhao[1], Xiangsen Gao[1,2]* and Mingming Zhang[3]

[1]Shandong Institute of Petroleum and Chemical Technology, Dongying, China, [2]School of Geoscience, China University of Petroleum, Qingdao, China, [3]Sinopec Research Institute of Petroleum Engineering Co., Ltd., China Petroleum and Chemical Corporation, Beijing, China

Research on the identification and classification of drilling-induced fractures plays a critical role in clarifying the mechanisms of wellbore instability and drilling fluid loss, while also supporting the analysis of imaging logging data and reservoir evaluation. In this study, a prediction model for the occurrence of drilling induced fractures is established by using linear elastic wellbore stress model combined with the tensile failure criterion of wellbore surrounding rock. The influences of engineering parameters, specifically borehole trajectory and bottom-hole pressure, on the distribution of principal stresses around the wellbore, as well as the angle between drilling-induced fractures and the borehole axis are investigated. The findings reveal that the induced fractures exhibit a highly organized pattern, typically forming at 180° intervals with a nearly symmetrical, downward-diffusing arrangement. This pattern provides a solid theoretical basis for the identification and classification of these fractures. In addition, under low bottom-hole pressure, the well tends to form feather-shaped induced fractures. As the pressure of the liquid column increases, the angle between these fractures and the borehole axis decreases while their length expands, eventually evolving into a "J"-shaped fracture. Accurate detection and identification of such induced fractures are crucial for reliably interpreting fracture networks and evaluating reservoirs in unconventional oil and gas fields.

KEYWORDS

bottom hole pressure, breakout pressure, drilling induced fracture, fracture occurrence, engineering parameter

1 Introduction

Natural fractures in the formation significantly contribute to borehole instability and drilling fluid losses. Triaxial mechanical tests on fractured rocks indicate that the stress required to reinitiate failure along these pre-existing fracture surfaces is 43%–55% lower than that for intact core samples (Bai, 2020; Dong et al., 2025; Fengjiao et al., 2023; Fontoura et al., 2002; Guan and Sheng, 2017; Huang et al., 2019; Li, 2020). Due to the lower tensile strength of natural fractures compared to the rock's tensile strength, natural fractures tend to open preferentially under certain conditions, thereby controlling the spatial characteristics of fracture propagation (Qin, 2006; Al-Ajmi and Zimmerman, 2006; Ewy, 1999; Lee et al., 2012; He et al., 2015; Setiawan and Zimmerman, 2018). Improving

the understanding of fractures is beneficial for further research on reservoir evaluation, geological understanding, and reservoir knowledge across various geological historical periods (Liu et al., 2016; Liu et al., 2018; Lu et al., 2020; Moos et al., 2003; Noohnejad et al., 2021; Qiu et al., 2011; Sheng et al., 2006). Current methods for analyzing natural fractures in formations often lack precision (Sheng et al., 2017; Sheng et al., 2018; Tabatabaee et al., 2018; Wei et al., 2013; Wen, 2012; Wu et al., 2024; Wen, 2012). In contrast, imaging logging offers an intuitive two-dimensional visualization of the borehole wall, providing a reliable foundation for accurately identifying and extracting geological features—such as rock structure, stratification, pore networks, and fractures—which in turn leads to superior geological interpretations (Singh et al., 2019; Chen et al., 2015; Liu et al., 2016; Zhou et al., 2018; Lu et al., 2013; Økland and Cook, 1998; Zhang, 2013; Amadei, 2012). In reservoir evaluation, it is crucial to more accurately and effectively identify effective fractures and discern and eliminate the influence of drilling-induced fractures (Zhang et al., 2021b; Zhang et al., 2023; Zhao et al., 2020Ai, 2015Al-Ajmi and Al-Harthy, 2010). Due to the strong heterogeneity of the Ordovician carbonate rocks in the Shunbei oil and gas field, the diversity of reservoir space types, and the varying shapes of fractures, detecting and identifying fractures are particularly challenging (Wu et al., 2024; Xia, 2018; Zhang et al., 2017; Zhang et al., 2021a). Therefore, the correct identification of induced fractures is essential (Huang et al., 2012; Liu et al., 2016; Ebrahimi et al., 2020; Denney, 2005; Udegbunam et al., 2013; Ma et al., 2021; Chen et al., 2019).

In the realm of borehole stability, Lee et al. (2012) proposed a wellbore stability model for formations with anisotropic strength and predicted collapse positions in different drilling directions. He et al. (2015) explored the impact of water content on weak planes and wellbore stability by developing a model that accounts for these planes. Their comparison of slip failure along weak planes versus shear failure in intact rock revealed that cross-dip wells are less stable than up-dip or down-dip wells in a strike-slip stress regime, and that higher water content leads to increased collapse pressure. Setiawan and Zimmerman (2018) introduced a transversely isotropic well stress model for shale reservoirs, employing a three-dimensional Mogi-Coulomb criterion to assess borehole collapse pressure while considering the effects of weak surface structures on rock strength. Singh et al. (2019) presented an analytical solution for wellbore stability in rock masses exhibiting elastic-perfectly plastic and elastic-brittle behavior using a 3D failure criterion. Their findings indicate that the plastic zone predicted by the Mogi-Coulomb criterion is about 13%–20% smaller than that estimated by the Mohr-Coulomb criterion, with intermediate principal stress contributing to improved wellbore stability and wellbore column pressure significantly affecting the plastic zone radius. Additionally, Chen et al. (2015) together with Ding et al. (2018) developed a model for wellbore stability that incorporates multiple weak planes, demonstrating that when more than four such planes are present, the collapse pressure is predominantly controlled by these features and increases gradually. Liu et al. (2016) developed a wellbore stress distribution model in a transversely isotropic formation drilled at an arbitrary angle to the weak planes. They studied both controllable factors (internal pressure, dipping angle, and dipping direction) and uncontrollable factors (weak planes occurrence and *in situ* stress), concluding that a proper lower critical mud weight is essential for ensuring wellbore stability. Zhou et al. (2018) investigated how rock elastic transverse isotropy influences pore pressure distribution and seepage stresses, emphasizing that anisotropic seepage in shales with bedding and fractures requires a lower internal critical mud weight than that applied at the borehole wall. Similarly, Lu et al. (2013) found that porous flow in shale formations exacerbates wellbore instability, with the critical mud weight highly sensitive to the presence of weak planes. Økland and Cook (1998) showed through thick-walled cylinder tests that wells drilled within 15° of the bedding-parallel direction are particularly unstable, necessitating a higher mud density to prevent losses. Borehole stability analysis typically begins by calculating the stress tensor on the wellbore wall after drilling, followed by applying a strength criterion to compare principal stresses with rock strength. Zhang (2013) noted that when weak bedding planes are present, the maximum slip failure direction deviates from the minimum stress direction, and the overlap of shear failure in intact rock with sliding failure along weak planes enlarges unstable areas. Although Lu et al. (2013) also observed that porous flow in fractured formations further undermines stability, their study did not consider elastic anisotropy and natural fractures in bedding. Static stability models often overlook the hydraulic effects of drilling fluids on pore pressure and rock failure. To address this, Kanfar et al. (2015) developed a time-dependent numerical model that incorporates the transverse isotropy of shales, revealing significant differences in pore pressure compared to isotropic models and leading to different critical mud pressure recommendations, despite not accounting for thermal and chemical gradients. Higgins et al. (2008) further demonstrated that models including anisotropy capture subtle stress variations more accurately, which is crucial for well completion decisions. Additionally, Dokhani et al. (2016) incorporated the interaction between aqueous fluids and clay minerals into their model, treating shale as an isotropic medium with strength anisotropy defined by an extended Jaeger's criterion and a bedding plane angle (β) relative to the maximum principal stress. Given the finely laminated structure, natural fractures, low permeability, and cation exchange capacity of shales, it is essential to account for the combined effects of natural fractures and bedding planes on near-wellbore stresses. Finally, Huang et al. (2012) analyzed stress distributions around boreholes in layered rocks with water-based drilling fluids, highlighting the critical roles of borehole inclination, hydraulic conductivity, and water activity in determining a safe mud pressure window.

Both domestic and international scholars have extensively studied fracture identification, highlighting that each fracture type possesses unique features that significantly affect oil and gas exploration and production. During drilling, fractures are typically classified as natural or induced based on their origin (Gao et al., 2021; Gao et al., 2024). Currently, imaging logging is the most precise method for detecting fractures, providing images that reveal a broad spectrum of geological events as well as drilling-induced disturbances on the wellbore. Drilling-induced tensile fractures are formed under the influence of ground stress during the drilling process and occur simultaneously with the drilling operation. These fractures typically develop parallel to the wellbore, appearing symmetrically at 180° intervals. Drilling-induced tensile fractures occur only when there is a significant disparity in horizontal stresses, and they usually extend less than

1 cm into the surrounding formation. If the bottom-hole pressure is maintained below the minimum principal stress, these fractures will not propagate further, thereby preventing drilling fluid loss. Unlike natural fractures, induced fractures form as a result of stress changes during drilling, following predictable patterns that can be modeled under different operating conditions.

Research on predicting the initiation locations and morphologies of drilling-induced fractures around wellbores remains limited. A thorough understanding of the mechanisms behind fracture formation and propagation is essential for ground stress inversion, determining optimal drilling fluid density windows, and optimizing the particle size distribution of sealing materials. This knowledge also aids in classifying fracture types and precisely determining their orientations from imaging logging data, which is critical for reliable reservoir evaluation. Consequently, this study develops a prediction model for drilling-induced fractures, investigating the impact of engineering parameters such as wellbore trajectory and borehole pressure on fracture characteristics. It further provides quantitative criteria to assess the effectiveness of drilling fluid leak prevention and plugging strategies based on these fracture features.

2 Drilling-induced fractures prediction model

2.1 Coordinate transformation

To determine the stress distribution characteristics around the wellbore, it is first necessary to transform the *in situ* stresses into the global coordinate system. As illustrated in Figure 1, X_G-Y_G-Z_G represents the global coordinate system, where X_G points north, Y_G points east, and Z_G is vertical. X_S-Y_S-Z_S represents the *in situ* stress coordinate system, corresponding to the maximum horizontal stress, minimum horizontal stress, and vertical stress, respectively. To transform the *in situ* stresses into the global coordinate system, three coordinate transformations are required. First Step, rotate the global coordinate system around the Z_G axis by an angle α_1, resulting in the X′-Y′-Z′ coordinate system. Second Step, rotate the X′-Y′-Z′ coordinate system around the Y′ axis by an angle β_1, yielding the X″-Y″-Z″ coordinate system. Third Step, rotate the X″-Y″-Z″ coordinate system around the X″ axis by an angle β_1. This series of transformations converts the X_G-Y_G-Z_G coordinate system into the X_s-Y_s-Z_s coordinate system. This transformation process enables the accurate determination of the stress distribution around the wellbore in relation to the global geographic orientation.

Based on geometric knowledge, a transformation matrix R_1 is established, as shown in Equation 1,

$$R_1 = \begin{bmatrix} \cos\alpha_1\cos\beta_1 & \sin\alpha_1\cos\beta_1 & -\sin\beta_1 \\ \cos\alpha_1\sin\beta_1\sin\gamma_1 - \sin\alpha_1\cos\gamma_1 & \sin\alpha_1\sin\beta_1\sin\gamma_1 + \cos\alpha_1\cos\gamma_1 & \cos\beta_1\sin\gamma_1 \\ \cos\alpha_1\sin\beta_1\cos\gamma_1 - \sin\alpha_1\sin\gamma_1 & \sin\alpha_1\sin\beta_1\cos\gamma_1 + \cos\alpha_1\sin\gamma_1 & \cos\beta_1\cos\gamma_1 \end{bmatrix} \tag{1}$$

Using the stress tensor σ_G to represent the components of stress in the global coordinate system and σ_S to represent the components of stress in the stress coordinate system, the transformation relationship between them can be expressed as shown in Equation 2,

$$\sigma_G = R_1^T \sigma_S R_1 \tag{2}$$

Where $\sigma_S = [\sigma_H, 0, 0; 0, \sigma_h, 0; 0, 0, \sigma_v]$, σ_H represents the maximum horizontal stress, measured in MPa; σ_h represents the minimum horizontal stress, measured in MPa; and σ_v represents the vertical stress, measured in MPa.

After transforming the stress into the global coordinate system, it should be further transformed into the wellbore coordinate system for analysis. The transformation relationship between the global coordinate system (GCS) and the wellbore coordinate system (BCS) is shown in Figure 2, where X_B-Y_B-Z_B represents the wellbore coordinate system, α_2 represents the angle between the wellbore inclination and the true north direction, usually referred to as the wellbore azimuth angle; β_2 represents the angle between the wellbore axis and the vertical direction, typically referred to as the well deviation angle. Using σ_B to represent the stress tensor in the wellbore coordinate system, according to the study by Lee et al. (2012), the transformation relationship between σ_B and σ_G is expressed as shown in Equation 3,

$$\sigma_B = R_2 \sigma_G R_2^T \tag{3}$$

The transformation matrix R_2 is represented as shown in Equation 4.

$$R_2 = \begin{bmatrix} \cos\alpha_2\cos\beta_2 & \sin\alpha_2\cos\beta_2 & \sin\beta_2 \\ \sin\alpha_2 & \cos\alpha_2 & 0 \\ \cos\alpha_2\sin\beta_2 & \sin\alpha_2\sin\beta_2 & \cos\beta_2 \end{bmatrix} \tag{4}$$

2.2 Wellbore stress distribution

The representation of stress tensors around the wellbore in polar coordinates is more convenient. Therefore, after transforming the stress from the global coordinate system to the wellbore coordinate system, the stress tensor σ_B, i.e., $[\sigma_x, \sigma_y, \sigma_z, \tau_{xy}, \tau_{xz}, \tau_{yz}]$, needs to be further transformed into polar coordinates. Due to the disturbance of the original stress state by drilling through the formation, the stress redistributes around the wellbore and creates stress concentration effects. According to Biot's effective stress theory, the equation for the effective stress around the wellbore at any inclination angle is expressed as shown in Equation 5,

$$\begin{cases} \sigma_r = \dfrac{(\sigma_x+\sigma_y)}{2}\left(1-\dfrac{r_w^2}{r^2}\right) + \dfrac{(\sigma_x-\sigma_y)}{2}\left(1-4\dfrac{r_w^2}{r^2}+3\dfrac{r_w^4}{r^4}\right)\cos 2\theta \\ \qquad +\tau_{xy}\left(1-4\dfrac{r_w^2}{r^2}+3\dfrac{r_w^4}{r^4}\right)\sin 2\theta + P_w\dfrac{r_w^2}{r^2} - \alpha P_p \\ \sigma_\theta = \dfrac{(\sigma_x+\sigma_y)}{2}\left(1+\dfrac{r_w^2}{r^2}\right) - \dfrac{(\sigma_x-\sigma_y)}{2}\left(1+3\dfrac{r_w^4}{r^4}\right)\cos 2\theta \\ \qquad +\tau_{xy}\left(1+3\dfrac{r_w^4}{r^4}\right)\sin 2\theta - P_w\dfrac{r_w^2}{r^2} - \alpha P_p \\ \sigma_z = \sigma_{zz} - 2\nu\left(\sigma_x-\sigma_y\right)\dfrac{r_w^2}{r^2}\cos 2\theta - 4\nu\tau_{xy}\dfrac{r_w^2}{r^2}\sin 2\theta - \alpha P_p \\ \tau_{r\theta} = \left[\dfrac{(\sigma_x+\sigma_y)}{2}\sin 2\theta + \tau_{xy}\cos 2\theta\right]\left(1+2\dfrac{r_w^2}{r^2}-3\dfrac{r_w^4}{r^4}\right) \\ \tau_{rz} = \left[\tau_{yz}\sin\theta + \tau_{xz}\cos\theta\right]\left(1-\dfrac{r_w^2}{r^2}\right) \\ \tau_{\theta z} = \left[-\tau_{xz}\sin\theta + \tau_{yz}\cos\theta\right]\left(1+\dfrac{r_w^2}{r^2}\right) \end{cases} \tag{5}$$

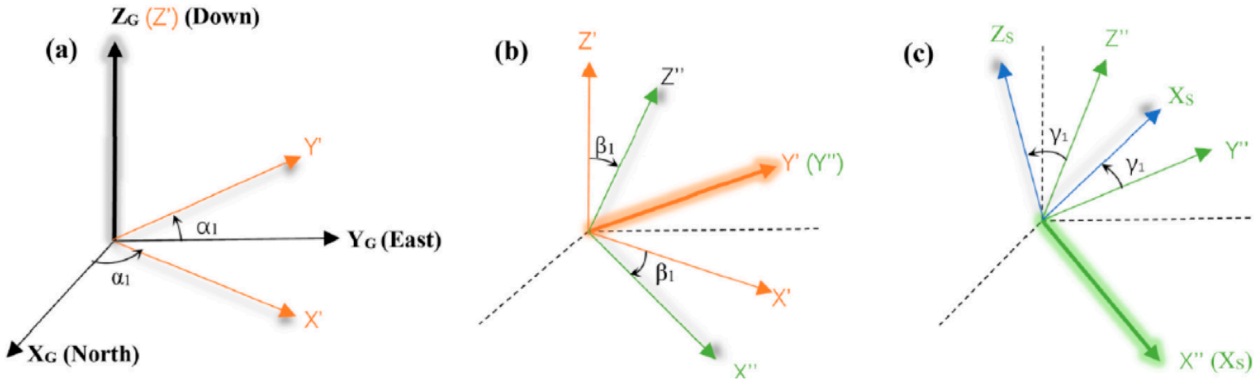

FIGURE 1
Three steps of the transformation between the global coordinate system (GCS) and the *in situ* stress coordinate system (ICS) **(a)** rotation about the Z_G axis **(b)** rotation about the Y′ axis **(c)** rotation about the X″ axis.

In the equation, r_w represents the wellbore radius, measured in meters; r represents the distance from any point around the wellbore to the wellbore axis, measured in meters; P_w represents the bottomhole fluid column pressure, measured in MPa; Pp represents the pore pressure of the formation, measured in MPa; θ represents the azimuth angle around the wellbore, i.e., the angle, measured in degrees, from a point around the wellbore rotating clockwise to the X_b coordinate axis; α represents the Biot's effective stress coefficient, which ranges from 0 to 1 and is dimensionless.

Once the stress distribution around the wellbore is determined, these values must be incorporated into rock strength criteria to evaluate the formation's stability. Because these criteria are typically expressed in terms of principal stresses, the wellbore stresses need to be transformed accordingly. Equation 6 shows how to convert stresses from polar coordinates into principal stresses,

$$\begin{cases} \sigma_i = \sigma_r \\ \sigma_j = (\sigma_\theta + \sigma_z)/2 + \sqrt{(\sigma_\theta + \sigma_z)^2 + 4\tau_{\theta z}^2}/2 \\ \sigma_k = (\sigma_\theta + \sigma_z)/2 - \sqrt{(\sigma_\theta + \sigma_z)^2 + 4\tau_{\theta z}^2}/2 \end{cases} \tag{6}$$

The relative magnitudes of the three principal stresses at any point around the wellbore vary with changes in the bottomhole fluid column pressure. To accurately distinguish between the three principal stresses around the wellbore, substitute the expression $\sigma_i, \sigma_j, \sigma_k$ obtained from Equation 6 into Equation 7,

$$\begin{cases} \sigma_1 = \max(\sigma_i, \sigma_j, \sigma_k) \\ \sigma_3 = \min(\sigma_i, \sigma_j, \sigma_k) \\ \sigma_2 = \sigma_i + \sigma_j + \sigma_k - \sigma_1 - \sigma_3 \end{cases} \tag{7}$$

2.3 Induced fracture orientation determination

To differentiate between types of tensile failure in the wellbore wall, it is necessary to quantitatively analyze the relationship between the three principal stresses around the wellbore. Additionally, it is important to compare the minimum principal stress around the wellbore with the tensile strength of the rock, as shown in Equation 8,

$$\sigma_3 \le -\sigma_t \tag{8}$$

When σ_r equals σ_3 and Equation 8 holds true, drilling-induced fractures occur around the wellbore. If the hydrostatic pressure exceeds the formation pressure, it may lead to drilling fluid loss. The relationship between the angle of induced fractures and the well axis stress is expressed as shown in Equation 9,

$$\tan 2\omega = \frac{2\tau_{\theta z}}{\sigma_z - \sigma_\theta} \tag{9}$$

In which, ω represents the angle between the drilling-induced fractures and the wellbore axis, measured in degrees, as shown in Figure 3. This angle represents the orientation between the maximum principal stress around the wellbore and the wellbore axis. By incorporating *in situ* stress, wellbore trajectory, and fluid column pressure, the principal stresses at different points around the wellbore can be determined. This enables the identification of tensile failure types and the calculation of the angle at each point relative to the wellbore axis, ultimately predicting the morphology of drilling-induced fractures under these conditions.

It is worth noting that this study assumes the formation rock to be a linear elastic medium and does not consider the effects of temperature, fluid interactions, chemical influences, or formation exposure time on the stress distribution around the wellbore. Additionally, given the characteristics of rock being strong in compression but weak in tension, as well as the natural development of fractures, it is generally assumed that cracks will form when the rock experiences tensile stress.

2.4 Model verification

Based on the MATLAB 2022a platform, a wellbore-induced fracture prediction model was developed and implemented. To

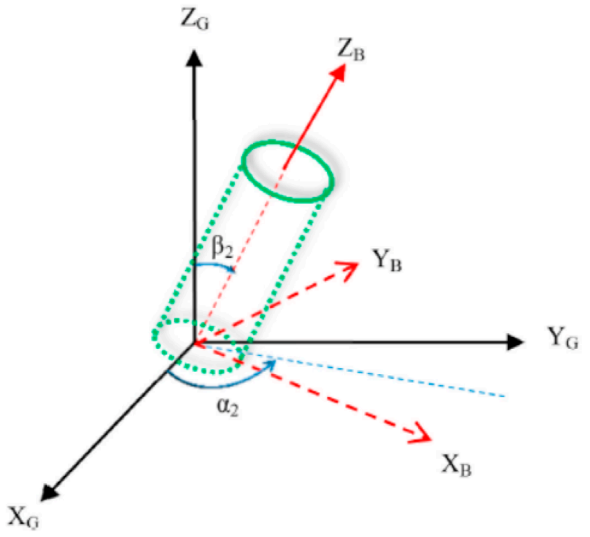

FIGURE 2
Transformation between global coordinate system (GCS) and borehole coordinate system (BCS).

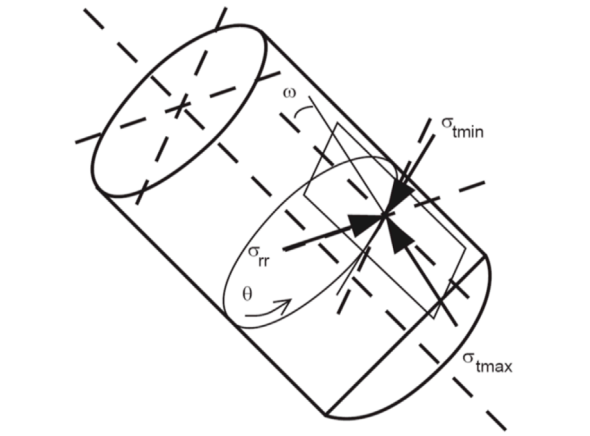

FIGURE 3
The angle between the minimum principal stress acting on the borehole wall and the borehole axis in any trajectory (Zoback, 2007).

verify the accuracy of the program, the data from Table 1 was used as input for the model. The program was then employed to calculate the circumferential, radial, and vertical stresses around a vertical wellbore. The results were compared with those obtained using Equation 5 to ensure the correctness of the developed program.

The circumferential, radial, and vertical stresses on the wellbore wall of a vertical well, as calculated using the program developed in this study, are shown in Figure 4. Similarly, for a vertical well in the direction of the minimum horizontal *in situ* stress, the calculation process and results for wellbore circumferential stress, based on Equation 5, are presented in Equation 10,

$$\begin{cases} \sigma_r = \dfrac{\sigma_H + \sigma_h}{2} \times 0 + \dfrac{\sigma_H - \sigma_h}{2} \times 0 \times \cos 2\theta + 0 \times 0 \times \sin 2\theta + P_w \\ \quad \times 1 - P_p = 5\text{MPa} \\ \sigma_\theta = \dfrac{(\sigma_H + \sigma_h)}{2} \times 2 - \dfrac{(\sigma_H - \sigma_h)}{2} \times 4 \cos 2\theta + 0 \times 4 \sin 2\theta - P_w \\ \quad \times 1 - P_p = 35\text{MPa} \\ \sigma_z = \sigma_v - 2\nu(\sigma_H - \sigma_h) \times 1 \times \cos 2\theta - 4\nu \times 0 \times 1 \\ \quad \times \sin 2\theta - \alpha P_p = 25\text{MPa} \end{cases} \tag{10}$$

Comparing the results obtained from Equation 5 with those shown in Figure 4 reveals a perfect match, confirming the accuracy of the developed model and calculation program, including the coordinate transformation equations and principal stress calculations.

3 Results and analysis

Based on this model, the study further explores the effects of different wellbore trajectories and fluid column pressures on the principal stresses around the wellbore, the initiation angle of induced fractures, and their occurrence. The variation patterns of wellbore principal stresses and induced fracture orientations with changes in wellbore trajectory and fluid column pressure are discussed in the following sections.

3.1 The impact of wellbore trajectory

This study investigates the locations and morphologies of drilling-induced fractures in a normal fault environment. Assuming a fluid column pressure of 50 MPa in the wellbore, the remaining parameters from Table 1 are used to analyze the effects of borehole trajectory and pressure on the characteristics of drilling-induced fractures. Utilizing the drilling-induced fracture prediction model established in this study and inputting the parameters from Table 1, the variation trends of the principal stresses on the wellbore wall and the angles between induced fractures and the wellbore axis along the circumferential angle of the wellbore are depicted in Figure 5–20. The dual vertical axes in the diagrams respectively quantify two critical parameters: the left axis measures principal stress magnitudes, while the right axis (purple crosses) tracks angular deviation between drilling-induced fractures and the wellbore axis. Rock mechanics analysis reveals these fractures initiate when tangential stress at the borehole wall exceeds the tensile strength threshold. Specifically, fracture propagation commences as the minimum principal stress transitions from compressive to tensile domain, a fundamental principle derived from tensile failure criteria in wellbore stability studies.

From Figure 5a, it can be observed that the first and second principal stresses around the wellbore do not vary with the circumferential angle. The third principal stress reaches its maximum value in the direction of minimum horizontal *in situ* and its minimum value in the direction of maximum horizontal

TABLE 1 Inputting parameters.

Vertical *in situ* stress/MPa	Horizontal maximum *in situ* stress/MPa	Horizontal minimum *in situ* stress/MPa	Pore pressure/ MPa	Fluid column pressure in well/MPa	有效应力系数/ 无量纲	Poisson' ratio/无量纲	Tensile strength/ MPa	Diameter/ cm
50	40	30	25	30	1	0.22	0	15.24

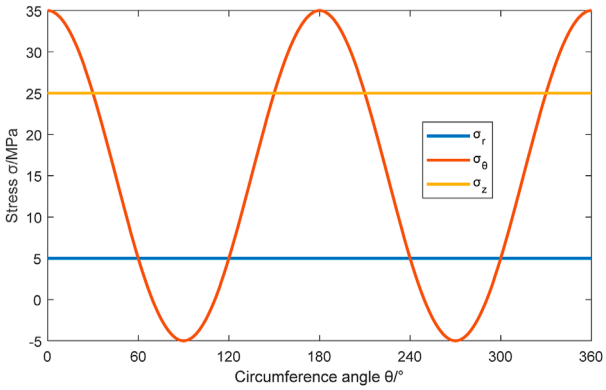

FIGURE 4
Stresses around wellbore wall for vertical well.

in situ. The angle ω between induced fractures and the wellbore axis remains 0 throughout. This indicates that a vertical fracture is generated in the direction of maximum horizontal *in situ*, as depicted in Figure 5b.

Maintaining the drilling direction constant, but varying the well deviation angle, the wellbore's principal stresses, the angle between induced fractures and the wellbore axis, and the induced fracture orientations for well deviation angles of 30°, 60°, and 90° are illustrated in Figures 6–8, respectively. The mechanical response exhibits distinct patterns across different well orientations. At βb = 30° deviation, circumferential stress analysis shows dual stress minima at 90°/270° azimuths. Stress state transition initiates fracture development with maintained near-orthogonal fracture-wellbore alignment (θ ≈ 90°), producing characteristic feather-textured fracture patterns as documented in Figures 6a,b. Notably, increasing deviation to β_b = 60° induces comprehensive tensile transformation (σ_{min}<0 throughout azimuths), driving θ fluctuations exceeding 60°. This mechanically governed instability generates multi-axial fracture intersections shown in Figures 7a,b, demonstrating progressive complexity with inclination angle. The horizontal well configuration (β_b = 90°) presents polar stress minima at 0°/180° positions. Theta maintains perfect coaxial alignment (θ≡0°) during wellbore rotation, forming vertically oriented fracture planes that bisect the borehole circumference (Figures 8a,b). This orientation-dependent fracture geometry evolution follows fundamental principles of anisotropic stress redistribution in inclined boreholes.

Keeping the wellbore azimuth angle at 30° and varying the well deviation angle to 0°, 30°, 60°, and 90°, the principal stresses around the wellbore, induced fractures, and their angles with the wellbore axis are depicted in Figures 9–12. When the well deviation angle β_b = 0°, the minimum principal stress around the wellbore reaches its minimum values at 60° and 240° around the wellbore. The angle between induced fractures and the wellbore axis remains 0°, resulting in two vertical fractures at positions 60° and 240° around the wellbore. For a well deviation angle of β_b = 30°, the minimum principal stress around the wellbore transitions to tensile stress in the range of 0°–108° and 181°–289° around the wellbore. Mechanical analysis reveals pronounced angular instability in fracture trajectory deviation (Δθ>45°), yielding distinctive hooked fracture geometries. This bifurcation pattern, encompassing both J-type curvature and mechanical fishhook configurations, arises from critical stress anisotropy conditions documented in Figures 10a,b. The observed morphological bifurcation demonstrates fundamental fracture path selection mechanisms governed by near-wellbore stress tensor reconfiguration. With a well deviation angle of β_b = 60°, the minimum principal stress around the wellbore transitions to tensile stress in the ranges of 0°–82°, 163°–262°, and 323°–360° around the wellbore. Similar to the previous case, the angle between induced fractures and the wellbore axis undergoes significant variations, resulting in induced fracture orientations resembling "J-shaped" fractures. The induced fractures exhibit inflection points at 60° and 240°, forming more pronounced "J-shaped" fractures, as depicted in Figures 11a,b. In horizontal well configurations (β_b = 90°), fracture trajectory angularity demonstrates constrained variability (Δθ<10°), manifesting hybrid fracture morphologies that bridge classical feather-textured patterns and mechanical "fishhook" configurations. This transitional morphology emerges from the unique stress coupling effects inherent to horizontal borehole geometries.

Maintaining the wellbore azimuth angle at 60°, the variations in principal stresses around the wellbore and induced fracture orientations with respect to the circumferential angle for well deviation angles of 0°, 30°, 60°, and 90° are illustrated in Figures 13–16. The mechanical response exhibits systematic dependence on wellbore orientation relative to *in situ* stress fields. In vertical wells (β_b = 0°), coaxial alignment with the principal *in situ* stress orientation induces fracture propagation vectors parallel to the borehole axis through geomechanical coupling. At intermediate inclinations (β_b = 30°,60°), stress anisotropy intensification during tensile state transition triggers angular instability (Δθ>30°), forming characteristic J-curvature fractures through stress-dependent path selection mechanisms, as quantitatively verified in Figure 10b. Conversely, horizontal wells (β_b = 90°) demonstrate constrained trajectory deviation (Δθ<10°) under compressive-tensile stress

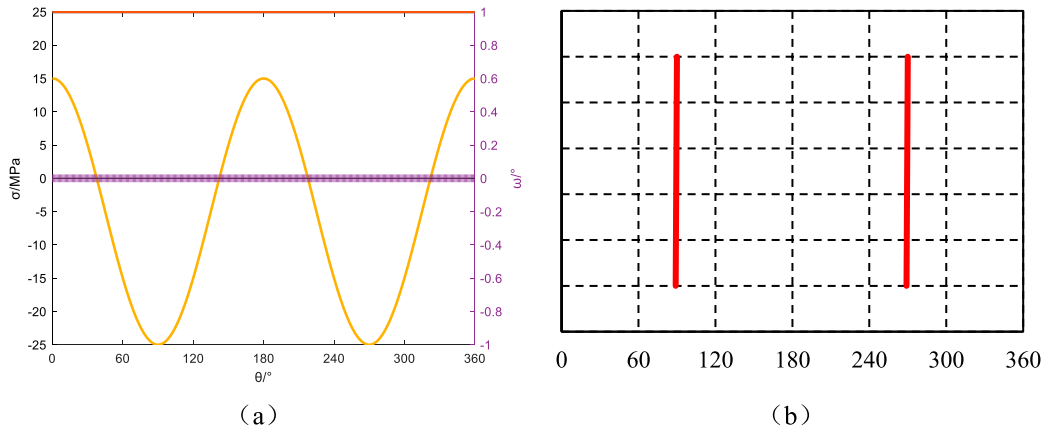

FIGURE 5
Azimuth angle αb = 0°, Well inclination angle βb = 0°: Principal stresses around the wellbore, induced fractures, and their angles relative to the wellbore axis. **(a)** Principal stress and induced fracture angle, **(b)** Induced fracture.

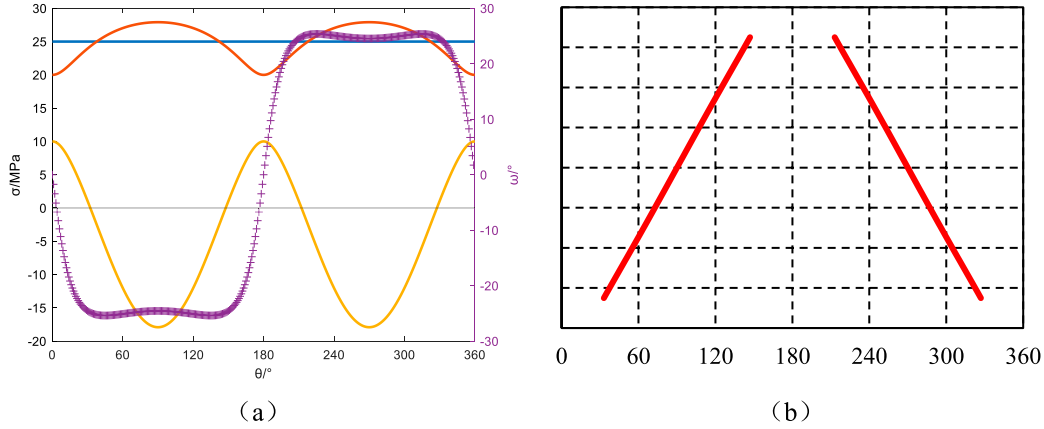

FIGURE 6
Azimuth angle αb = 0°, Well inclination angle βb = 30°: Principal stresses around the wellbore, induced fractures, and their angles relative to the wellbore axis. **(a)** Principal stress and induced fracture angle, **(b)** Induced fracture.

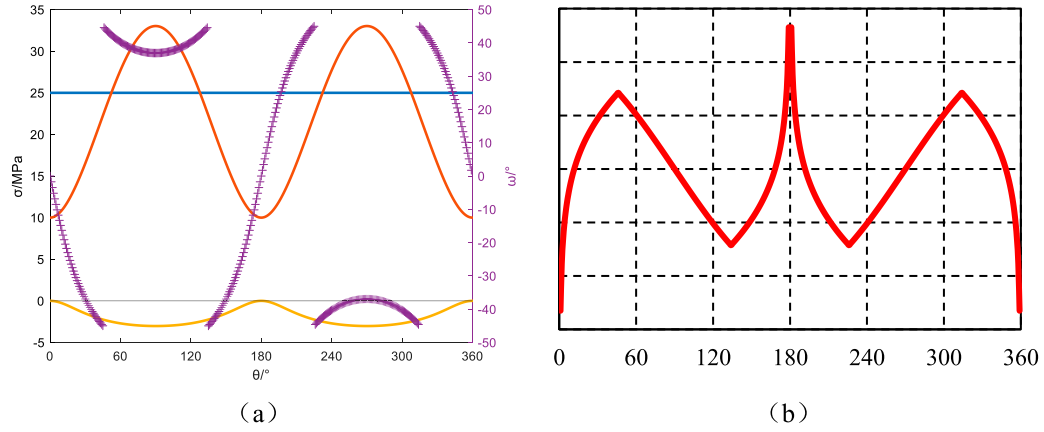

FIGURE 7
Azimuth angle αb = 0°, Well inclination angle βb = 60°: Principal stresses around the wellbore, induced fractures, and their angles relative to the wellbore axis. **(a)** Principal stress and induced fracture angle, **(b)** Induced fracture.

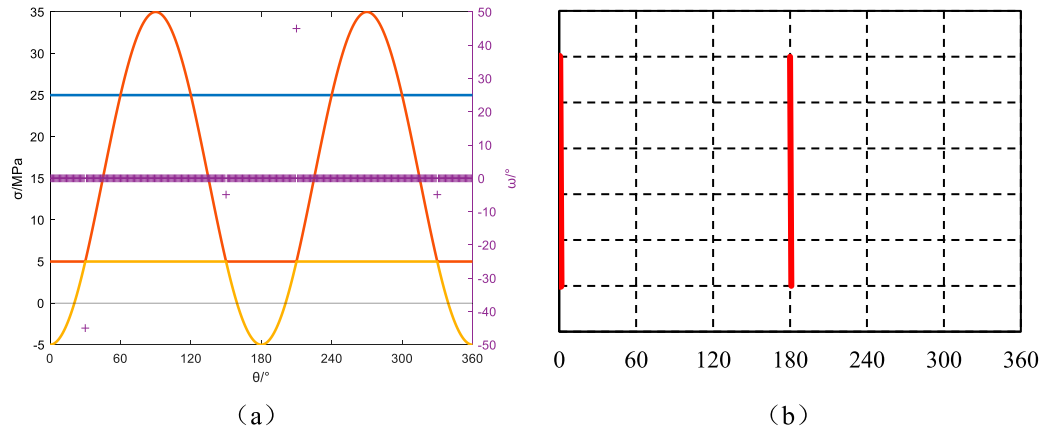

FIGURE 8
Azimuth angle αb = 0°, Well inclination angle βb = 90°: Principal stresses around the wellbore, induced fractures, and their angles relative to the wellbore axis. **(a)** Principal stress and induced fracture angle, **(b)** Induced fracture.

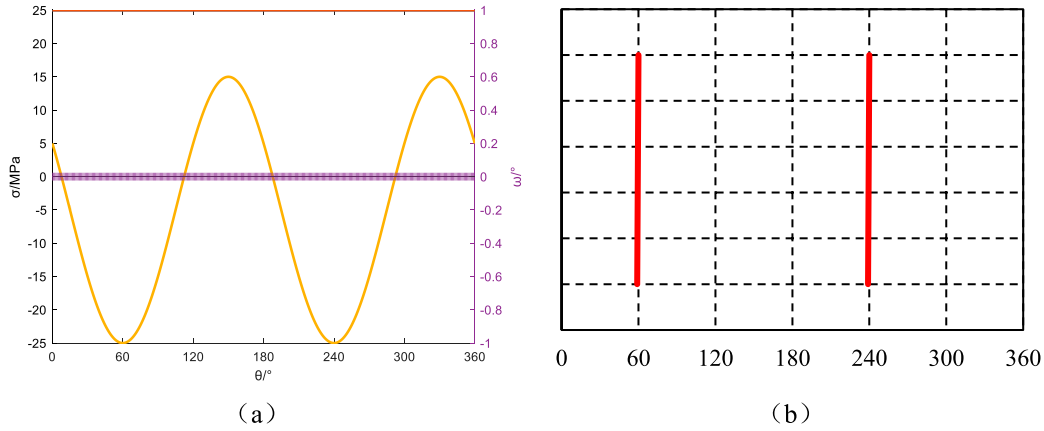

FIGURE 9
Azimuth angle αb = 30°, Well inclination angle βb = 0°: Principal stresses around the wellbore, induced fractures, and their angles relative to the wellbore axis. **(a)** Principal stress and induced fracture angle, **(b)** Induced fracture.

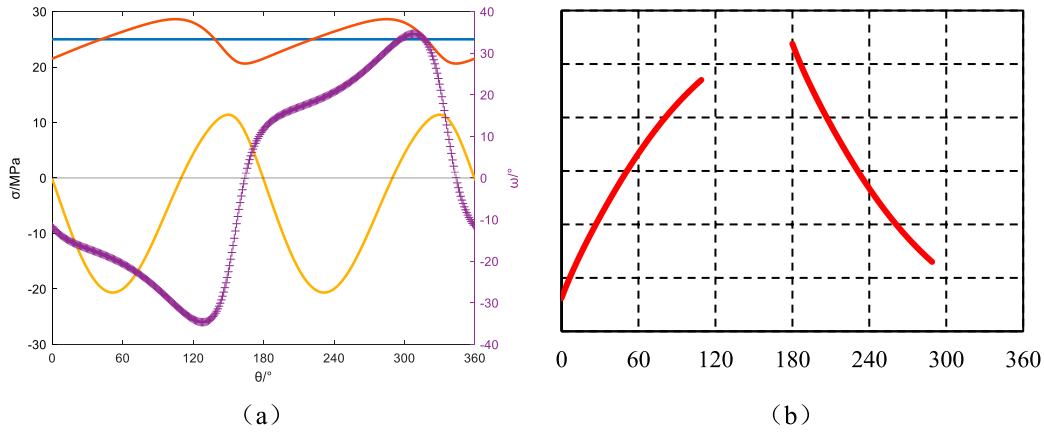

FIGURE 10
Azimuth angle αb = 30°, Well inclination angle βb = 30°: Principal stresses around the wellbore, induced fractures, and their angles relative to the wellbore axis. **(a)** Principal stress and induced fracture angle, **(b)** Induced fracture.

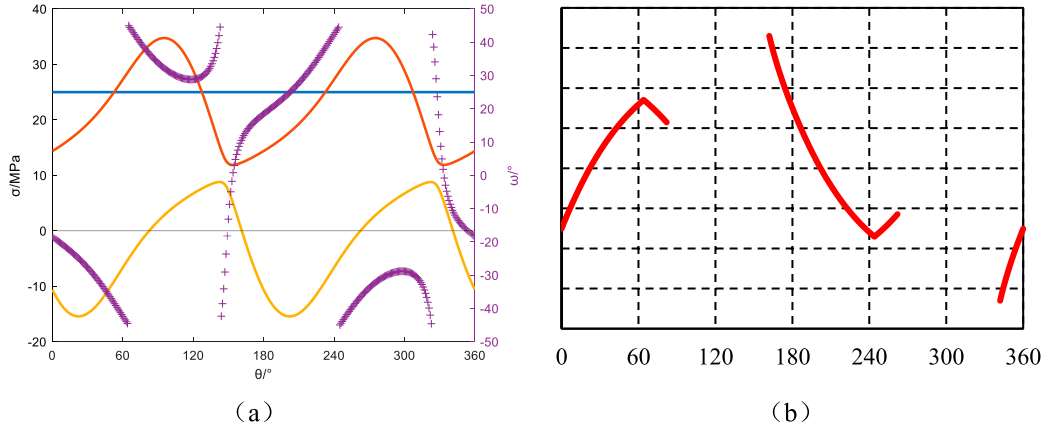

FIGURE 11
Azimuth angle αb = 30°, Well inclination angle βb = 60°: Principal stresses around the wellbore, induced fractures, and their angles relative to the wellbore axis. **(a)** Principal stress and induced fracture angle, **(b)** Induced fracture.

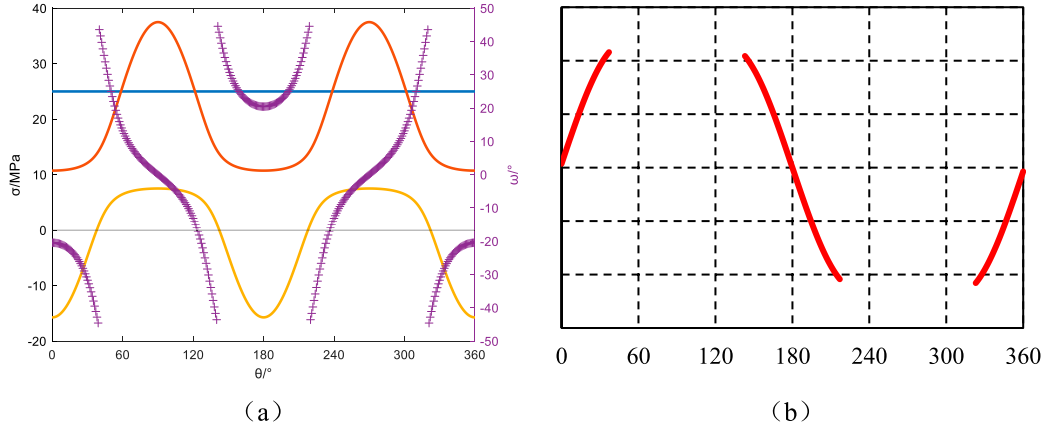

FIGURE 12
Azimuth angle αb = 30°, Well inclination angle βb = 90°: Principal stresses around the wellbore, induced fractures, and their angles relative to the wellbore axis. **(a)** Principal stress and induced fracture angle, **(b)** Induced fracture.

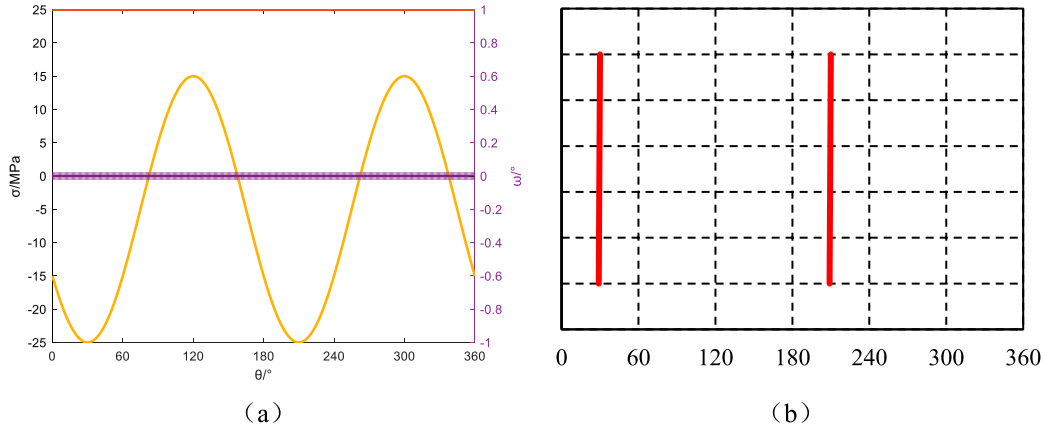

FIGURE 13
Azimuth angle αb = 60°, Well inclination angle βb = 0°: Principal stresses around the wellbore, induced fractures, and their angles relative to the wellbore axis. **(a)** Principal stress and induced fracture angle, **(b)** Induced fracture.

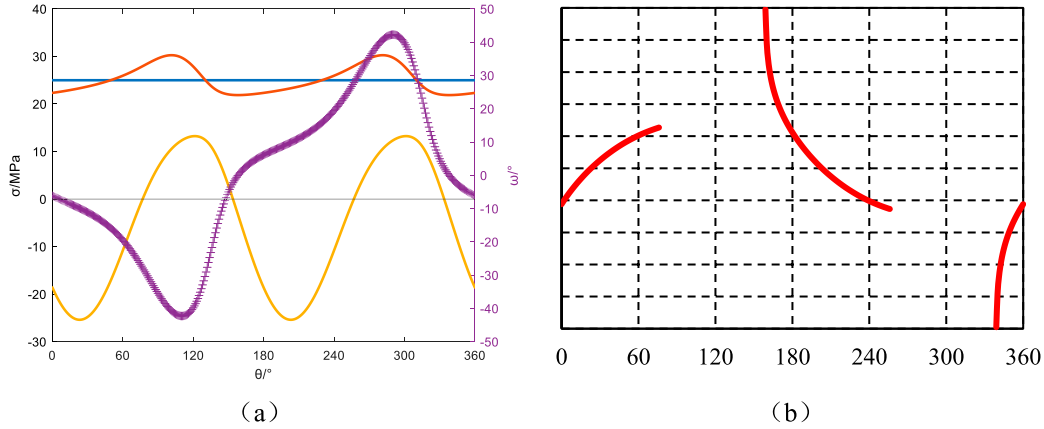

FIGURE 14
Azimuth angle αb = 60°, Well inclination angle βb = 30°: Principal stresses around the wellbore, induced fractures, and their angles relative to the wellbore axis. **(a)** Principal stress and induced fracture angle, **(b)** Induced fracture.

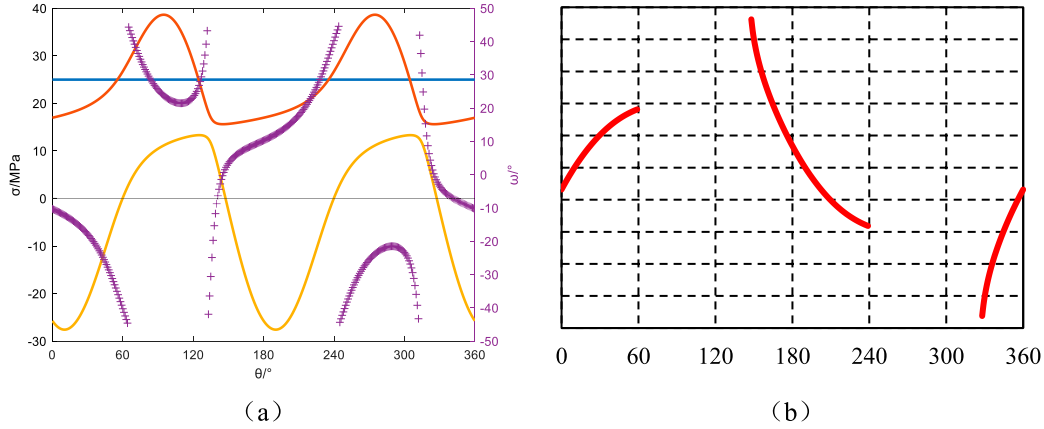

FIGURE 15
Azimuth angle αb = 60°, Well inclination angle βb = 60°: Principal stresses around the wellbore, induced fractures, and their angles relative to the wellbore axis. **(a)** Principal stress and induced fracture angle, **(b)** Induced fracture.

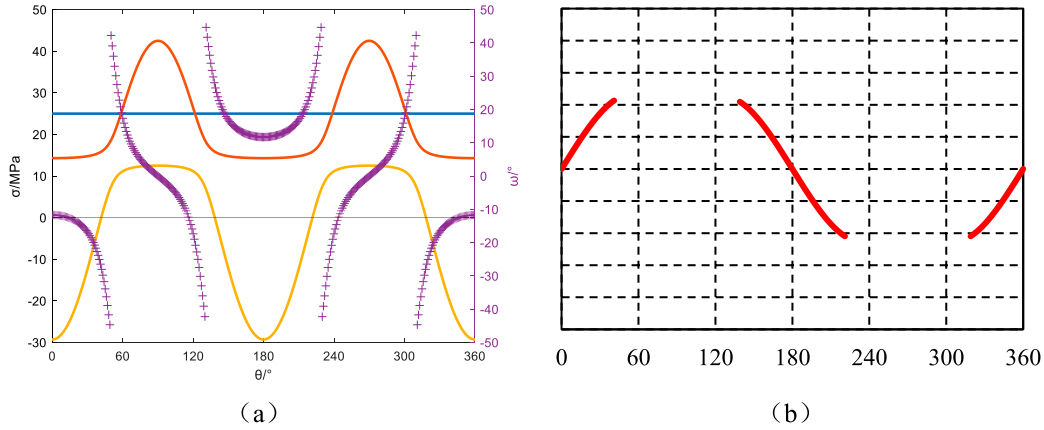

FIGURE 16
Azimuth angle αb = 60°, Well inclination angle βb = 90°: Principal stresses around the wellbore, induced fractures, and their angles relative to the wellbore axis. **(a)** Principal stress and induced fracture angle, **(b)** Induced fracture.

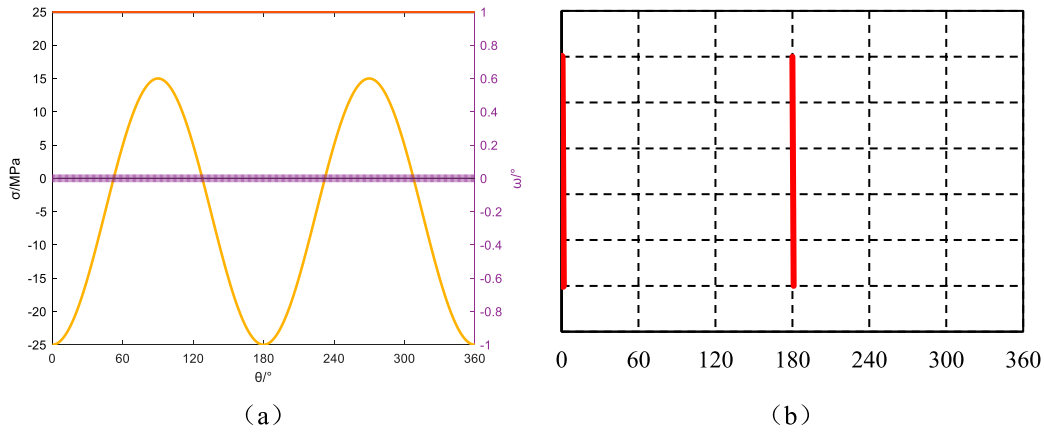

FIGURE 17
Azimuth angle αb = 90°, Well inclination angle βb = 0°: Principal stresses around the wellbore, induced fractures, and their angles relative to the wellbore axis. **(a)** Principal stress and induced fracture angle, **(b)** Induced fracture.

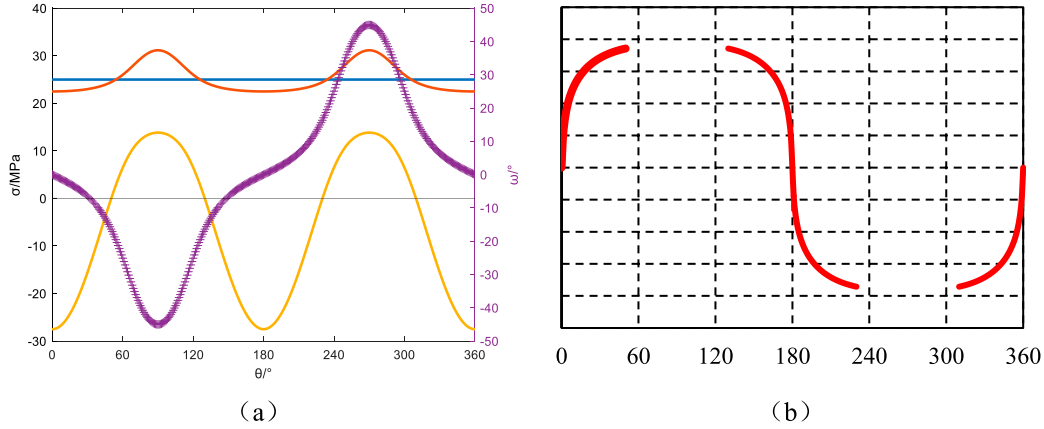

FIGURE 18
Azimuth angle αb = 90°, Well inclination angle βb = 30°: Principal stresses around the wellbore, induced fractures, and their angles relative to the wellbore axis. **(a)** Principal stress and induced fracture angle, **(b)** Induced fracture.

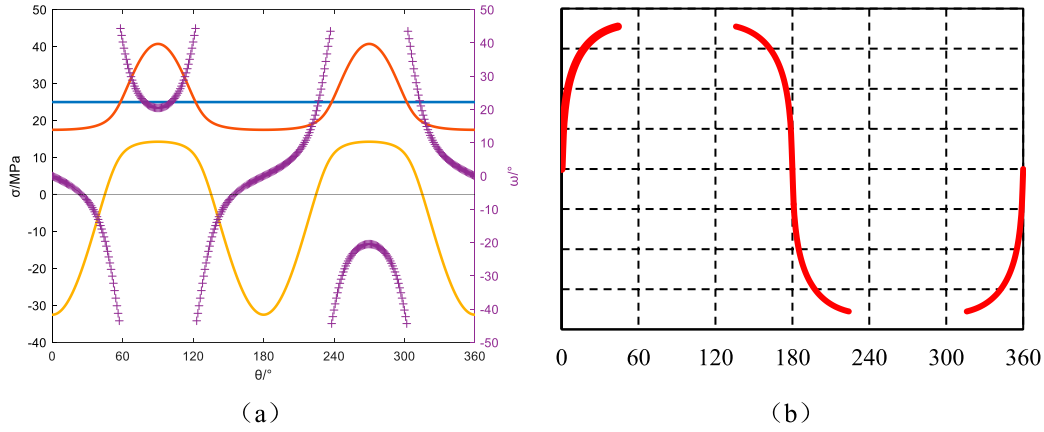

FIGURE 19
Azimuth angle αb = 90°, Well inclination angle βb = 60°: Principal stresses around the wellbore, induced fractures, and their angles relative to the wellbore axis. **(a)** Principal stress and induced fracture angle, **(b)** Induced fracture.

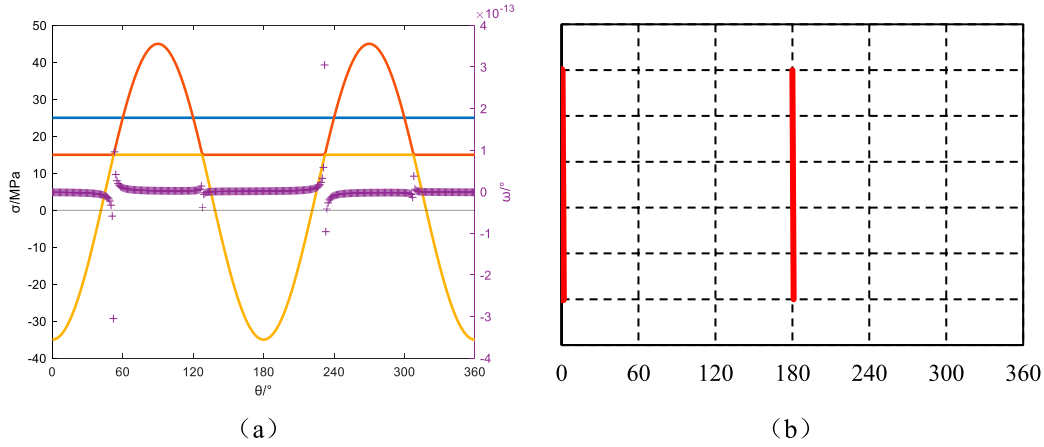

FIGURE 20
Azimuth angle αb = 90°, Well inclination angle βb = 90°: Principal stresses around the wellbore, induced fractures, and their angles relative to the wellbore axis. **(a)** Principal stress and induced fracture angle, **(b)** Induced fracture.

tensor reconfiguration. This transitional regime produces hybrid fracture architectures blending feather-textured discontinuities with incipient hook-shaped geometries, reflecting progressive stress decoupling in high-angle completions.

The wellbore azimuth angle is 90°, and the well deviation angles are 0°, 30°, 60°, and 90°. The principal stresses around the wellbore and the induced fracture orientations for these angles are depicted in Figures 17–20. In stress-aligned well configurations, the borehole axis maintains strict parallelism with principal *in situ* stress orientations: vertical stress correspondence at βb = 0° (Figures 17a,b) and maximum horizontal stress alignment at β_b = 90° (Figures 20a,b). This geometric optimization induces dual fracture initiation with perfect coaxial propagation through stress-controlled failure mechanisms. The resultant fracture planes exhibit diametric symmetry with exact 180° phasing, forming textbook hydraulic fracture patterns through geomechanical resonance. When the well deviation angles are 30° (Figures 18a,b) and 60° (Figures 19a,b) , the minimum principal stress around the wellbore reaches its minimum value at the circumferential angles of 0° and 180°. When the minimum principal stress transitions to tensile stress, the angle between induced fractures and the wellbore axis is close to 0° at the 0° (Figures 17a,b) and 180° (Figures 20a,b) positions, exhibiting minimal variation. As the circumferential angle increases, the variation becomes more significant, resulting in induced fracture orientations resembling sine curves, as predicted in Figures 18b, 19b. This makes them easily mistaken for natural fractures.

When analyzing the induced fractures around the wellbore formed by different trajectories, it is evident that if the wellbore axis is parallel to any principal *in situ* stress direction, such that no shear stress is induced around the wellbore, the angle between the induced fractures and the wellbore axis will remain at 0°. As a result, two symmetrically distributed fractures parallel to the wellbore axis are typically produced. When the variation in the angle between the induced fractures and the wellbore axis is within 10°, feather-like fractures appear. Once this angular variation exceeds 10°, "J-shaped" fractures are formed. Furthermore, when the angle between the induced fractures and the wellbore axis approaches 0° at the minimum principal stress extremum around the wellbore and then changes sharply either increasing or decreasing, the fractures tend to follow an approximately sine-curve pattern. Moreover, the induced fractures usually occur in pairs symmetrically arranged at 180° intervals.

3.2 The impact of bottomhole fluid column pressure

Bottomhole fluid column pressure is one of the most direct, effective, and controllable measures to maintain wellbore stability. It directly determines complex scenarios such as erosion or shear collapse of the wellbore wall and loss of drilling fluid. The authors studied the influence of bottomhole fluid column pressure on the development of drilling-induced fractures. The induced fracture orientations of a wellbore with azimuth angle α_b = 0° and well deviation angle β_b = 30° under different bottomhole pressures are illustrated in Figure 21. Analysis indicates that feather-like fractures are consistently formed under various bottomhole pressures. As the bottomhole fluid column pressure rises, the angle between the drilling-induced fractures and the wellbore axis progressively diminishes, while the length of these induced fractures gradually increases. The induced fractures are symmetrically distributed within the wellbore, with a spacing of 180° between them.

The variations in drilling-induced fracture orientations of a wellbore with azimuth angle α_b = 30° and well deviation angle β_b = 30° under different bottomhole pressures are depicted in Figure 22. Analysis indicates that feather-like fractures are consistently formed under various bottomhole pressures. As the bottomhole fluid column pressure rises, the angle between the drilling-induced fractures and the wellbore axis progressively diminishes, while the length of these induced fractures gradually increases. The induced fractures are symmetrically distributed within the wellbore, with a spacing of 180° between them.

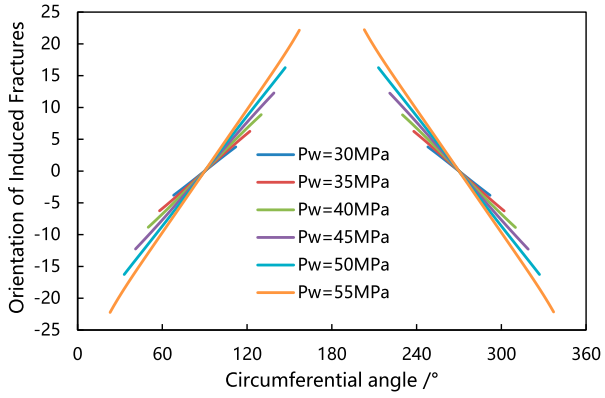

FIGURE 21
The orientation angle α_b = 0°, inclination angle β_b = 30°, and the orientation of induced fractures during directional drilling changes with the variation of bottom hole pressure.

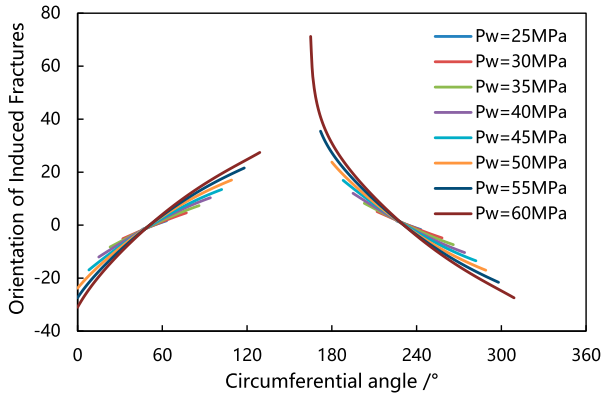

FIGURE 22
The azimuth angle α_b = 30°, inclination angle β_b = 30°, and the orientation of induced fractures in the wellbore change with variations in bottom hole pressure.

4 Conclusion

The identification and classification research of drilling-induced fractures is of great significance for clarifying the mechanisms of wellbore instability and drilling fluid loss, analyzing imaging logging data, and reservoir evaluation. This study adopts a linear elastic per-wellbore stress model and combines it with the tensile failure criterion of the wellbore surrounding rock to establish a predictive model for the occurrence of drilling-induced fractures around the wellbore. The influence of different engineering parameters such as wellbore trajectories and bottomhole pressures on the distribution of principal stresses around the wellbore, the angle and occurrence of drilling-induced fractures relative to the wellbore axis has been investigated. The main conclusions of this study are as follows, Drilling-induced fractures result from the combined effects of *in situ* stresses and engineering disturbances. They have a close relationship with *in situ* stresses and typically occur in pairs symmetrically arranged at 180° intervals. This organized arrangement provides a solid basis for identifying and classifying drilling-induced fractures, distinguishing them from natural fractures. When the wellbore axis is parallel to any principal *in situ* stress direction, with no shear stress induced around the wellbore, the angle between the drilling-induced fractures and the wellbore axis remains 0°. Consequently, two symmetrically distributed fractures parallel to the wellbore axis are usually formed. Feather-like fractures occur when the variation in the angle between the drilling-induced fractures and the wellbore axis is within 10°. When this variation exceeds 10°, "J-shaped" fractures are formed. Fractures approximately follow a sine curve when the angle between the drilling-induced fractures and the wellbore axis approaches 0° at the minimum principal stress extremum around the wellbore and then changes sharply either increasing or decreasing. With relatively low bottomhole pressure, feather-like drilling-induced fractures occur in the wellbore. As the pressure of the fluid column inside the well increases, the angle between the drilling-induced fractures and the wellbore axis gradually decreases, resulting in an increase in fracture length. Eventually, they transform into "J-shaped" fractures.

In reservoir evaluation, it is very important to more accurately and effectively identify effective fractures and distinguish and exclude the influence of drilling-induced fractures. Especially for unconventional reservoirs with strong heterogeneity, diverse types of storage spaces, and various fracture morphologies, the detection and identification of fractures are particularly difficult. Therefore, the correct identification of induced fractures is particularly important. The predictive model for the occurrence of drilling-induced fractures established in this paper can help reasonably and correctly interpret effective fractures in unconventional reservoirs and reservoir evaluation.

Data availability statement

The original contributions presented in the study are included in the article/supplementary material, further inquiries can be directed to the corresponding author.

Author contributions

YL: Conceptualization, Data curation, Formal Analysis, Funding acquisition, Investigation, Methodology, Project administration, Resources, Software, Supervision, Validation, Visualization, Writing – original draft, Writing – review and editing. JW: Conceptualization, Data curation, Formal Analysis, Funding acquisition, Investigation, Methodology, Project administration, Resources, Software, Supervision, Validation, Visualization, Writing – original draft, Writing – review and editing. ZZ: Conceptualization, Data curation, Formal Analysis, Funding acquisition, Investigation, Methodology, Project administration, Resources, Software, Supervision, Validation, Visualization, Writing – original draft, Writing – review and editing. ML: Conceptualization, Data curation, Formal Analysis, Funding acquisition, Investigation, Methodology, Project administration, Resources, Software, Supervision, Validation, Visualization,

Writing – original draft, Writing – review and editing. XZ: Conceptualization, Data curation, Formal Analysis, Funding acquisition, Investigation, Methodology, Project administration, Resources, Software, Supervision, Validation, Visualization, Writing – original draft, Writing – review and editing. XG: Conceptualization, Data curation, Formal Analysis, Funding acquisition, Investigation, Methodology, Project administration, Resources, Software, Supervision, Validation, Visualization, Writing – original draft, Writing – review and editing. MZ: Conceptualization, Data curation, Formal Analysis, Funding acquisition, Investigation, Methodology, Project administration, Resources, Software, Supervision, Validation, Visualization, Writing – original draft, Writing – review and editing.

Funding

The author(s) declare that financial support was received for the research and/or publication of this article. This paper is supported by the team construction project of the young innovative talents inducing and cultivating program of Shandong Province "Research and Innovation Team of Complex Oil and Gas Well Drilling Engineering" (Grant No. 2019035).

Conflict of interest

Author MZ was employed by Sinopec Research Institute of Petroleum Engineering Co., Ltd., China Petroleum and Chemical Corporation.

The remaining authors declare that the research was conducted in the absence of any commercial or financial relationships that could be construed as a potential conflict of interest.

Generative AI statement

The author(s) declare that no Generative AI was used in the creation of this manuscript.

Publisher's note

References

Ai, E. (2015). *Research on early warning theory and method of wellbore instability in shale*. Xian, Shanxi: Xi'an Shiyou University Master's thesis.

Al-Ajmi, A., and Zimmerman, R. (2006). A new 3D stability model for the design of non-vertical wellbores. *Eng. and Technol. Environ. Eng.*

Al-Ajmi, A. M., and Al-Harthy, M. H. (2010). Probabilistic wellbore collapse analysis. *J. Petroleum Sci. Eng.* 74 (3-4), 171–177. doi:10.1016/j.petrol.2010.09.006

Amadei, B. (2012). "Rock anisotropy and the theory of stress measurements,", 2. Springer Science and Business Media. doi:10.1007/978-1-4615-1633-4

Bai, G. (2020). Optimization method for drilling fluid density design in Wei 202,204 shale gas well area. *Drill. Fluid and Complet. Fluid* 37 (2), 196–201.

Chen, P., Ma, T., and Xia, H. (2015). A collapse pressure prediction model for horizontal shale gas wells with multiple weak planes. *Nat. Gas. Ind. B* 2 (1), 101–107. doi:10.1016/j.ngib.2014.12.003

Chen, Y., Deng, C., and Ma, T. (2019). Reliability theory-based evaluation method for wellbore instability risk. *Nat. Gas. Ind.* 39 (11), 97–104.

Denney, D. (2005). Safe operating window: wellbore stability is more than just fluid density. *J. petroleum Technol.* 57 (09), 69–71. doi:10.2118/0905-0069-jpt

Ding, Y., Luo, P., Liu, X., and Liang, L. (2018). Wellbore stability model for horizontal wells in shale formations with multiple planes of weakness. *J. Nat. Gas Sci. Eng.*, S187551001830043X. doi:10.1016/j.jngse.2018.01.029

Dokhani, V., Yu, M., and Bloys, B. (2016). A wellbore stability model for shale formations: accounting for strength anisotropy and fluid induced instability. *J. Nat. Gas Sci. Eng.* 32, 174–184. doi:10.1016/j.jngse.2016.04.014

Dong, Z., Tian, S., Xue, H., Lu, S., Liu, B., Erastova, V., et al. (2025). A novel method for automatic quantification of different pore types in shale based on SEM-EDS calibration. *Mar. Petroleum Geol.* 173, 107278. doi:10.1016/j.marpetgeo.2024.107278

Ebrahimi, M. A., Ahmadi, M., and Ameri, M. J. (2020). Application of unconditional simulation methods for quantifying the uncertainties in mud window design of gas reservoirs based on 3-dimensional mechanical earth modeling. *J. Nat. Gas Sci. Eng.* 76, 103186. doi:10.1016/j.jngse.2020.103186

Ewy, R. T. Wellbore-stability predictions by use of a modified lade criterion (1999). *Spe Drill. and Complet.*, 14(2):85–91. doi:10.2118/50671-PA

Fengjiao, W., He, X., Liu, Y., Meng, X., and Liu, L. (2023). Mechanism of low chemical agent adsorption by high pressure for hydraulic fracturing-assisted oil displacement technology: a study of molecular dynamics combined with laboratory experiments. *Langmuir* 39 (46), 16628–16636. doi:10.1021/acs.langmuir.3c02634

Fontoura, S. A. B., Holzberg, B. B., Teixeira, É. C., and Frydman, M. (2002). "Probabilistic analysis of wellbore stability during drilling," in *SPE/ISRM rock mechanics conference* (OnePetro).

Gao, R., Bai, D., Yu, B., Tai, Y., Meng, X., and Zhang, W. (2024). Ground fracturing of multi-strata for strong ground pressure control in extra-thick coal seams with hard roofs: numerical simulation and case study. *Eng. Fract. Mech.* 303, 110129. doi:10.1016/j.engfracmech.2024.110129

Gao, R., Kuang, T., Meng, X., and Huo, B. (2021). Effects of ground fracturing with horizontal fracture plane on rock breakage characteristics and mine pressure control. *Rock Mech. Rock Eng.* 54 (6), 3229–3243. doi:10.1007/s00603-020-02294-x

Guan, Z. C., and Sheng, Y. N. (2017). Study on evaluation method for wellbore stability based on uncertainty analysis. *J. Appl. Sci. Eng.* 20 (4), 453–457. doi:10.1080/13321349.2017.1373419

He, S., Wei, W., Zhou, J., Zhen, H., and Ming, T. (2015). A model for analysis of wellbore stability considering the effects of weak bedding planes. *J. Nat. Gas Sci. and Eng.* 27 (part_P2), 1050–1062. doi:10.1016/j.jngse.2015.09.053

Higgins, S. M., Goodwin, S. A., Bratton, T. R., and Tracy, G. W. (2008). "Anisotropic stress models improve completion design in the Baxter Shale," in *SPE annual technical conference and exhibition* (Richardson, TX, United States: Society of Petroleum Engineers (SPE)).

Huang, L., Yu, M., Miska, S. Z., Takach, N. E., and Bloys, J. B. (2012). "Parametric sensitivity study of chemo-poro-elastic wellbore stability considering transversely isotropic effects in shale formations," in *SPE Canadian unconventional Resources conference* (Richardson, TX, United States: Society of Petroleum Engineers).

Huang, Y., Sheng, Y., Guan, Z., Luo, M., Li, W., and Deng, W. (2019). Quantitative risk evaluation of wellbore stability in Yingqiong Basin. *Fault-Block Oil and Gas Field* 26 (3), 380–384.

Lee, H., Ong, S. H., Azeemuddin, M., and Goodman, H. (2012). A wellbore stability model for formations with anisotropic rock strengths. *J. Petroleum Sci. Eng.* 96, 109–119. doi:10.1016/j.petrol.2012.10.011

Li, W. (2020). *Analysis and risk assessment of wellbore stability based on uncertainty of lithology parameters*. East China: China University of Petroleum.

Liu, M., Jin, Y., Lu, Y., Chen, M., Hou, B., Chen, W., et al. (2016). A wellbore stability model for a deviated well in a transversely isotropic formation considering poroelastic effects. *Rock Mech. Rock Eng.* 49 (9), 3671–3686. doi:10.1007/s00603-016-1019-8

Liu, X., Yi, R., Zhou, X., and Wang, R. (2018). "Application of Bayesian network method in optimal completion of gas wells," in *Proceedings of the 2018 national natural gas academic annual conference (04 engineering Technology)*.

Lu, Y., Xiao, X., Zhao, L., Jin, Y., and Chen, M. (2020). Influence of temperature on the stability of wellbore in ultra-deep fractured formations. *Drill. Fluid and Complet. Fluid* 37 (2), 160–167.

Lu, Y. H., Chen, M., Jin, Y., Ge, W. F., An, S., and Zhou, Z. (2013). Influence of porous flow on wellbore stability for an inclined well with weak plane formation. *Petroleum Sci. Technol.* 31 (6), 616–624. doi:10.1080/10916466.2010.520912

Ma, T., Zhang, Y., Qiu, Y., Liu, Y., and Chen, P. (2021). Risk assessment method for inclined wellbore instability based on reliability theory. *Acta Pet. Sin.* 42 (11), 1486–1498.

Moos, D., Peska, P., Finkbeiner, T., and Zoback, M. (2003). Comprehensive wellbore stability analysis utilizing quantitative risk assessment. *J. Petroleum Sci. Eng.* 38(3-4): 97–109. doi:10.1016/s0920-4105(03)00024-x

Noohnejad, A., Ahangari, K., and Gosht asbi, K. (2021). Integrated mechanical earth model and quantitative risk assessment to successful drilling. *J. Petroleum Explor. Prod.* 11 (1), 219–231. doi:10.1007/s13202-020-01043-7

Økland, D., and Cook, J. M. (1998). "Bedding-related borehole instability in high-angle wells," in *SPE/ISRM rock mechanics in petroleum engineering* (Richardson, TX, United States: Society of Petroleum Engineers).

Qin, J. (2006). Identification of drilling induced fractures using imaging logging technology. *Inn. Mong. Petrochem. Ind.* 32 (10), 116–117.

Qiu, K., Chen, M., and Jin, Y. (2011). Collapse pressure model of wellbore based on statistical damage. *Rock Soil Mech.* 32 (7), 2029–2033.

Setiawan, N. B., and Zimmerman, R. W. (2018). Wellbore breakout prediction in transversely isotropic rocks using true-triaxial failure criteria. *Int. J. Rock Mech. Min. Sci.* 112, 313–322. doi:10.1016/j.ijrmms.2018.09.022

Sheng, Y., Guan, Z., Luo, M., Li, W., and Ju, R. (2018). Sensitivity analysis of wellbore stability reliability random variables based on Monte Carlo method. *Drill. and Prod. Technol.* 40 (1), 14–19.

Sheng, Y., Guan, Z., Xu, Y., Wang, Q., and Zhang, B. (2017). Discussion on uncertainty analysis method of wellbore stability problems. *Fault-Block Oil and Gas Field* 24 (6), 847–850.

Sheng, Y., Reddish, D., and Lu, Z. (2006). *Assessment of uncertainties in wellbore stability analysis[M]//Modern trends in geomechanics*. Berlin, Heidelberg: Springer, 541–557.

Singh, A., Rao, K. S., and Ayothiraman, R. (2019). An analytical solution to wellbore stability using Mogi-Coulomb failure criterion. *J. Rock Mech. Geotechnical Eng.* 11, 1211–1230. doi:10.1016/j.jrmge.2019.03.004

Tabatabaee, M. S. S., Nikolaev, N., and Khormali, A. (2018). "A comprehensive uncertainty assessment of wellbore stability models," in *Saint petersburg 2018: innovations in geosciences and time for breakthrough*, 44298.

Udegbunam, J. E., Fjelde, K. K., Arild, Ø., Ford, E., and Lohne, H. P. (2013). Uncertainty-based approach for predicting the operating window in UBO well design. *SPE Drill. and Complet.* 28 (04), 326–337. doi:10.2118/161997-PA

Wei, K., Guan, Z., Liao, H., Shi, Y., and Liu, Y. (2013). Evaluation method of wellbore instability risk. *J. China Univ. Petroleum Ed. Nat. Sci.* 37 (2), 62–66.

Wen, Q. (2012). *Research on risk assessment of complex geological drilling systems in deep wells based on soft computing theory Doctoral dissertation*. East China: Qingdao: China University of Petroleum.

Wu, W., Wang, T., Bai, J., Liu, J., Wang, X., Xu, H., et al. (2024). Failure characteristics and cooperative control strategies for gob-side entry driving near an advancing working face: a case study. *Processes* 12, 1398. doi:10.3390/pr12071398

Xia, P. (2018). *Impact fracture law and safety analysis of bare-eye wellbore in shale gas well Master's thesis*. East China: China University of Petroleum.

Zhang, J. (2013). Borehole stability analysis accounting for anisotropies in drilling to weak bedding planes. *Int. J. Rock Mech. and Min. Sci.* 60 (2), 160–170. doi:10.1016/j.ijrmms.2013.01.012

Zhang, M., Fan, X., Zhang, Q., Yang, B., Zhao, P., Yao, B., et al. (2021a). Influence of multi-planes of weakness on unstable zones near wellbore wall in a fractured formation. *J. Nat. Gas Sci. Eng.* 93, 104026. doi:10.1016/j.jngse.2021.104026

Zhang, M., Fan, X., Zhang, Q., Yang, B., Zhao, P., Yao, B., et al. (2021b). Parametric sensitivity study of wellbore stability in transversely isotropic medium based on poly-axial strength criteria. *J. Petroleum Sci. Eng.* 197, 108078. doi:10.1016/j.petrol.2020.108078

Zhang, M., Li, D., Liu, J., Zhang, D., Zhang, Y., and Cui, K. (2023). The modification of Mohr-Coulomb criteria based on shape function and determination method of undetermined parameters. *Mech. Mater.* 185, 104772. doi:10.1016/j.mechmat.2023.104772

Zhang, M. M., Liang, L. X., and Liu, X. J. (2017). Analysis of the influence of different rock shear failure criteria on wellbore collapse pressure. *Chin. J. Rock Mech. Eng.* 36 (S1), 3485–3491.

Zhao, L., Wang, Q., Guo, Z., Fang, C., and Cao, H. (2020). Evaluation of wellbore stability in laminated shale formations based on finite collapse width. *Sci. Technol. Rev.* 38 (11), 122–130. doi:10.16651/j.cnki.issn0253-2778.2020.11.027

Zhou, J., He, S., Tang, M., Huang, Z., Chen, Y., Chi, J., et al. (2018). Analysis of wellbore stability considering the effects of bedding planes and anisotropic seepage during drilling horizontal wells in the laminated formation. *J. Petroleum Sci. Eng.* 170, 507–524. doi:10.1016/j.petrol.2018.06.034

Zoback, M. D. (2007). *Reservoir geomechanics*. Cambridge University Press. doi:10.1017/CBO9780511535596

frontiers | Frontiers in Physics

TYPE Original Research
PUBLISHED 02 July 2025
DOI 10.3389/fphy.2025.1597946

OPEN ACCESS

EDITED BY
Yifei Sun,
Taiyuan University of Technology, China

REVIEWED BY
Emad Awad,
Alexandria University, Egypt
Markus Heß,
Technical University of Berlin, Germany

*CORRESPONDENCE
Bo Zhang,
xiaobotd@126.com

RECEIVED 22 March 2025
ACCEPTED 19 June 2025
PUBLISHED 02 July 2025

CITATION
Qiu L and Zhang B (2025) Reflection and transmission of P-wave incident obliquely at the interface between an elastic solid and a fluid-saturated porous medium: a comprehensive study via the model of soil mechanics.
Front. Phys. 13:1597946.
doi: 10.3389/fphy.2025.1597946

Reflection and transmission of P-wave incident obliquely at the interface between an elastic solid and a fluid-saturated porous medium: a comprehensive study via the model of soil mechanics

Lijun Qiu[1,2] and Bo Zhang[2,3]*

[1]Institute of Geophysics, China Earthquake Administration, Beijing, China, [2]School of Civil Engineering, Hebei University of Architecture, Zhangjiakou, China, [3]Hebei Innovation Center of Transportation Infrastructure in Cold Region, Hebei University of Architecture, Zhangjiakou, China

Introduction: A model of soil mechanics is used to study the problem of reflection and transmission of an obliquely incident plane P-waveon a discontinuous interface. Based on the propagation theory of elastic waves in an elastic solid and a fluid-saturated porous medium, the propagation analysis model of P-wave incident obliquely at the interface of such media is established.

Methods: The theoretical formulas of reflection coefficients of P- and SV-waves and the transmission coefficients of P_1-, P_2-, and SV-waves are obtained in terms of the boundary conditions of the interface between an elastic solid and a saturated two-phase medium. Furthermore, the derived formulas in this paper are reduced to the reflection and transmission problems of P-wave incident on two different single-phase media to verify their correctness. Finally, numerical investigations are carried out on the variations of the reflection and transmission coefficients with the incident angle for various boundary conditions, wave frequency, and material characteristics (i.e., dynamic permeability coefficient, porosity, and Poisson's ratio).

Results: It is shown that the effects of incident angles, boundary conditions, wave frequency, and material characteristics on the reflection and transmission coefficients cannot be ignored.

Discussion: These conclusions are of guiding significancefor theoretical research of soil dynamics and engineering seismic exploration.

KEYWORDS

saturated two-phase medium, elastic solid, model of soil mechanics, dispersion equation, boundary conditions, reflection coefficients, transmission coefficients

1 Introduction

The reflection and transmission of elastic waves at discontinuous interfaces have always been an important subject of soil dynamics, which is of considerable interest in various fields such as soil dynamics, geotechnical engineering, earthquake engineering, geophysics, and so on. The interface between an ordinary elastic solid and a fluid-saturated porous medium

is one of the important research branches. For the two-phase medium, due to the existence of pore water in the soil frame, its mechanical properties become very complex, which leads to the problem of wave propagation being much more complicated than that of a single-phase medium [1, 2]. The lower crust can be approximately treated as a single-phase medium, and the upper crust can be regarded as a saturated two-phase medium when the earthquake wave propagates outward from the seismic hypocenter to the surface [3]. Hence, when the seismic wave travels towards the surface, it will encounter the interface between elastic and two-phase medium and show complicated reflection and transmission characteristics.

It is well known that Biot first revealed the existence of three body waves in a two-phase medium, i.e., the fast P_1-wave, the slow P_2-wave, and the S-wave. The three body waves are dispersed and attenuated, the speed and attenuation of which are affected by the frequency and the properties of saturated soil materials [4, 5]. All of the above laid the foundation for the theoretical study of wave propagation in a fluid-saturated porous medium. Since then, more and more researchers studied various aspects of wave propagation in such medium. The P_2-wave with strong dispersion and high attenuation characteristics was successively confirmed through experiments by Plona [6] and Berryman [7]. Following the Biot model, many scholars established different two-phase medium models, including the Zienkiewicz model [8, 9], the Men Fu-lu model [10, 11], the model of soil mechanics [12], and the theory of mixture [13]. Chen and Liao [14] compared the first four models and theoretically explained that the model of soil mechanics is a special case of the Biot model, which has the advantage of the clear physical meaning of modeling parameters.

Gutenberg [15] was the first to study the reflection and transmission of elastic waves incident at the interface between different semi-infinite solid media. After that, numerous researchers made use of the Biot model to investigate the reflection and transmission of elastic waves on the interface between an elastic solid and a fluid-saturated porous medium. The problem of reflection and transmission of elastic waves from one elastic solid to another porous medium was simply examined by Geertsma and Smit [16]. Then, Deresiewicz and Rice [17] derived the expressions for amplitude ratios and phase shifts of the displacements for the P-wave traveling from an elastic solid into a porous medium. However, both publications were confined to a special case of normal incidence. Hajra and Mukhopadhyay [18] considered the obliquely incident seismic waves (P- and SV-waves) across the interface between an elastic solid and a fluid-saturated porous medium and calculated the amplitude and energy ratios for all reflected and refracted waves theoretically and numerically in the absence of dissipation. Sharma and Gogna [19] and Vashisth et al. [20] also studied the reflection and refraction of P- and SV-waves at the interface between an elastic solid and a fluid-saturated porous solid. Unlike Ref. [18], Sharma and Gogna [19] considered the dissipation caused by liquid viscosity. Among them, Hajra and Mukhopadhyay [18] and Sharma and Gogna [19] assumed the interface in welded contact, but Vashisth et al. [20] provided that the boundary is a loosely bonded interface, introduced a bonding constant ψ and stated that the smooth (ψ = 0) and welded interfaces (ψ = 1) are the special cases. Zhao et al. [3, 21] deduced the reflected and transmitted coefficients in the cases of seismic waves (P- and SV-waves) propagating from the elastic solid to the liquid-saturated porous solid (considering the energy dissipation) and P_1-wave traveling through the liquid-saturated porous solid to the elastic solid (free of the energy dissipation). Ye et al. [22] presented the expressions of reflection and refraction coefficients when the S-wave propagates from fluid-saturated soil to elastic soil and analyzed the dependence on the incident angle, wave frequency, and interface drainage condition. The concept of homogeneous pore fluid was applied to the Biot model to simulate the partially saturated soil. Based on this, the reflection and transmission of P- and SV-waves propagating from an elastic solid to partially saturated soil were investigated by Yang [23, 24] and Yang and Sato [25, 26]. Similarly, Li [27] analyzed the reflection and transmission when the P_1-wave in the partially saturated soil was incident on the elastic solid. And they all explained the effect of water saturation on the reflection and transmission. Xu and Xia [28] also studied the reflection and transmission of the incident plane P_1-wave from the nearly saturated soil to the elastic soil, but the model used was the governing equation of nearly saturated soil. Following Fillunger's model, Kumar et al. [29] discussed the reflection and transmission of waves on the interface between a fluid-saturating incompressible porous medium and an elastic medium. Moreover, the reflection and refraction problem of elastic waves from an elastic solid to other different soil was also widely studied, such as a transversely isotropic liquid-saturated porous medium [30, 31], a double porosity medium [32], an unsaturated medium [33, 34], a swelling porous half-space [35], porous solid saturated with-two immiscible viscous fluids [36, 37], a saturated frozen soil medium [38, 39], and water [40–42], etc. Recently, this wave propagation can be extended to other distinct media [43, 44].

Since Chinese scholar Men proposed the model of soil mechanics, quite a few researchers have also used it to study the wave propagation characteristic in a two-phase medium from theoretical [45–52] and practical views [53–56]. Among them, it is worth mentioning that Chen and Men [54] and Cui [53] presented a new method to understand the mechanism of soil liquefaction. Chen [45] and Chen et al. [46] analyzed the near-field wave motions combining the transmitting boundary. Recently, Xiao et al. [50] investigated the propagation and attenuation characteristics of Rayleigh waves in ocean sites. A preliminary analysis of the characteristics of wave propagation in the infinite and finite saturated medium based on the model of soil mechanics has been conducted by Zhang et al. [51] and Zhang and Qiu [52]. The results showed that the frequency and soil properties significantly shaped the velocity and attenuation coefficient of the three body waves. For this reason, these parameters are bound to affect the reflection and transmission of each wave incident upon the interface between an elastic solid and a fluid-saturated porous medium.

2 Theory of wave propagation

2.1 Elastic solid medium

For the homogeneous isotropic elastic solid, the equation of motion in vector form can be written as [57, 58].

$$(\lambda' + \mu')\nabla(\nabla \cdot \boldsymbol{u}') + \mu\Delta\boldsymbol{u}' = \rho\ddot{\boldsymbol{u}}' \tag{1}$$

Where, λ' and μ' are the Lame's constants. $\boldsymbol{u}'$ and $\ddot{\boldsymbol{u}}'$ are the displacement and acceleration vectors in the elastic solid, respectively. ρ is the mass density of an elastic solid. Δ denotes the Laplace operator, and $\Delta = \nabla^2$. ∇ is the Hamilton operator.

To gain a deeper understanding of plane wave solutions of Equation 1, we assume the direction of wave propagation lies in the x-z plane. Then, we consider a Helmholtz resolution of the displacement $\boldsymbol{u}'$, which may be the sum of the gradient of scalar potential ϕ' (for P-wave) and the curl of vector potential $\boldsymbol{\psi}'$ (for SV-wave), namely, $\boldsymbol{u}' = \nabla\phi' + \nabla \times \boldsymbol{\psi}'$. For the two-dimensional motion (i.e., P-SV system), the potential functions of P- and SV-waves only contribute to the displacement components in the x and z directions, not to the displacement component in the y direction, so they are independent of y and depend only on x, z, and time t, i.e., $\phi' = \phi'(x,z,t)$, and $\boldsymbol{\psi}' = (0, \psi'(x,z,t), 0)$. Hence, the displacement components u_x' and u_z', the normal stress σ_{zz}', and shear stress σ_{xz}' are described by

$$\begin{cases} u_x' = \dfrac{\partial\phi'}{\partial x} - \dfrac{\partial\psi'}{\partial z} \\ u_z' = \dfrac{\partial\phi'}{\partial z} + \dfrac{\partial\psi'}{\partial x} \end{cases} \tag{2a}$$

$$\begin{cases} \sigma_{zz}' = \lambda'\nabla^2\phi' + 2\mu'\left(\dfrac{\partial^2\phi'}{\partial z^2} + \dfrac{\partial^2\psi'}{\partial x\partial z}\right) \\ \sigma_{xz}' = 2\mu'\dfrac{\partial^2\phi'}{\partial x\partial z} + \mu'\left(\dfrac{\partial^2\psi'}{\partial x^2} - \dfrac{\partial^2\psi'}{\partial z^2}\right) \end{cases} \tag{2b}$$

2.2 Fluid-saturated porous medium

Provided that the liquid phase is an ideal fluid, the solid phase is isotropic and elastic, and the solid particles with infinite compression modulus are in point contact. In the model of soil mechanics proceeding as in Men [12], Xiao [50], Zhang [51], and Zhang and Qiu [52], the field equations for a liquid-saturated porous medium are written as follows.

$$\begin{cases} \mu\Delta\boldsymbol{u} + (\lambda+\mu)\nabla(\nabla\cdot\boldsymbol{u}) + (1-n)\nabla p_f + [B](\dot{\boldsymbol{U}} - \dot{\boldsymbol{u}}) = \rho_1\ddot{\boldsymbol{u}} \\ n\nabla p_f - [B](\dot{\boldsymbol{U}} - \dot{\boldsymbol{u}}) = \rho_2\ddot{\boldsymbol{U}} \\ (1-n)\nabla\cdot\boldsymbol{u} + n\nabla\cdot\boldsymbol{U} - \dfrac{n}{E_w}p_f = 0 \end{cases} \tag{3}$$

where $\boldsymbol{u}$, $\dot{\boldsymbol{u}}$, and $\ddot{\boldsymbol{u}}$ correspond to the displacement, velocity, and acceleration of the solid, respectively, and $\boldsymbol{U}$, $\dot{\boldsymbol{U}}$, and $\ddot{\boldsymbol{U}}$ those of the fluid. ρ_1 and ρ_2 are the mass of solid and liquid per unit volume, separately, with $\rho_1 = (1-n)\rho_s$ and $\rho_2 = n\rho_w$. ρ_s denotes the mass density of the solid and ρ_w that of the liquid. n is the porosity. p_f represents the true pore pressure. λ and μ (i.e., shear modulus) are the Lame's constants, in which $\lambda = Ev/((1+v)(1-2v))$ and $\mu = E/2(1+v)$. v is the Poisson's ratio. E is the Young's modulus of the solid phase. $[B]$ is a third-order diagonal matrix concerning the dissipation coefficients, of which the diagonal elements $b = b_x = b_y = b_z = n^2/k$. k (Unit: m^3 s/kg) refers to the dynamic permeability coefficient, and $k = K/\rho_w g$, in which K (Unit: m/s) is the permeability coefficient corresponding to Darcy's law and g is the gravitation acceleration. E_w is the pore fluid bulk modulus.

Similar to the single-phase medium, to gain the plane wave solutions of a saturated two-phase medium, the Helmholtz decomposition is considered, and the displacement vectors of the solid phase $\boldsymbol{u}$ (liquid phase $\boldsymbol{U}$) can be the sum of the gradient of a scalar potential ϕ_s (ϕ_w) and the curl of a vector potential $\boldsymbol{\psi_s}$ ($\boldsymbol{\psi_w}$).

$$\begin{cases} \boldsymbol{u} = \nabla\phi_s + \nabla\times\boldsymbol{\psi_s} \\ \boldsymbol{U} = \nabla\phi_w + \nabla\times\boldsymbol{\psi_w} \end{cases} \tag{4}$$

Plugging Equation 4 into Equation 3, we can get the wave equations of potentials in the following form [48].

$$\begin{cases} \rho_1\ddot{\phi}_s - (\lambda+2\mu)\Delta\phi_s = p_f - \rho_2\ddot{\phi}_w \\ \rho_1\ddot{\boldsymbol{\psi}}_s - \mu\Delta\boldsymbol{\psi}_s = -\rho_2\ddot{\boldsymbol{\psi}}_w \\ np_f - [B](\dot{\phi}_w - \dot{\phi}_s) - \rho_2\ddot{\phi}_w = 0 \\ \rho_2\ddot{\boldsymbol{\psi}}_w + [B](\dot{\boldsymbol{\psi}}_w - \dot{\boldsymbol{\psi}}_s) = 0 \\ (1-n)\Delta\phi_s + n\Delta\phi_w - \dfrac{n}{E_w}p_f = 0 \end{cases} \tag{5}$$

Similarly, the potentials in the solid phase $\phi_s = \phi_s(x,z,t)$, and $\boldsymbol{\psi_s} = (0, \psi_s(x,z,t), 0)$. The potentials in the liquid phase $\phi_w = \phi_w(x,z,t)$, and $\boldsymbol{\psi_w} = (0, \psi_w(x,z,t), 0)$, in the xz plane. The relations of the displacement components in the solid and liquid phases (u_x, u_z, U_x, and U_z) and the stresses (σ_{zz}, σ_{xz}, and p_f) with potentials are given by

$$\begin{cases} u_x = \dfrac{\partial\phi_s}{\partial x} - \dfrac{\partial\psi_s}{\partial z} \\ u_z = \dfrac{\partial\phi_s}{\partial z} + \dfrac{\partial\psi_s}{\partial x} \end{cases} \tag{6a}$$

$$\begin{cases} U_x = \dfrac{\partial\phi_w}{\partial x} - \dfrac{\partial\psi_w}{\partial z} \\ U_z = \dfrac{\partial\phi_w}{\partial z} + \dfrac{\partial\psi_w}{\partial x} \end{cases} \tag{6b}$$

$$\begin{cases} \sigma_{zz} = \left(\lambda + \dfrac{1-n}{n}E_w\right)\nabla^2\phi_s + 2\mu\left(\dfrac{\partial^2\phi_s}{\partial z^2} + \dfrac{\partial^2\psi_s}{\partial x\partial z}\right) + E_w\nabla^2\phi_w \\ \sigma_{xz} = 2\mu\dfrac{\partial^2\phi_s}{\partial x\partial z} + \mu\left(\dfrac{\partial^2\psi_s}{\partial x^2} - \dfrac{\partial^2\psi_s}{\partial z^2}\right) \\ p_f = \dfrac{1-n}{n}E_w\nabla^2\phi_s + E_w\nabla^2\phi_w \end{cases} \tag{6c}$$

Then, assume that the plane harmonic wave solutions of the potentials are as follows.

$$\begin{cases} \phi_s = A_s e^{i(\omega t - \boldsymbol{k_P}\cdot\boldsymbol{r})} \\ \phi_w = A_w e^{i(\omega t - \boldsymbol{k_P}\cdot\boldsymbol{r})} \\ \psi_s = B_s e^{i(\omega t - \boldsymbol{k_S}\cdot\boldsymbol{r})} \\ \psi_w = B_w e^{i(\omega t - \boldsymbol{k_S}\cdot\boldsymbol{r})} \end{cases} \tag{7}$$

where A_s and A_w are the amplitudes of P-wave in the solid and liquid phases, B_s and B_w those of S-wave. $i = \sqrt{-1}$. $\boldsymbol{r}$ is the location vector. ω denotes the circular frequency of a wave. $\boldsymbol{k_P}$ and $\boldsymbol{k_S}$ are the wave vectors of P- and SV-waves, which indicate the propagation directions of waves. k_P and k_S are the magnitudes (wave numbers). t represents the travel time.

Substituting Equation 7 into Equation 5 provides the characteristic equations of elastic waves [51, 52]. By introducing four variables (A, B, C, and D), the characteristic equations can be reduced to

$$\mathrm{A}\left(\frac{k_P}{\omega}\right)^4 - \mathrm{B}\left(\frac{k_P}{\omega}\right)^2 + \mathrm{C} = 0 \tag{8a}$$

$$\mathrm{D}\left(\frac{k_S}{\omega}\right)^2 + \mathrm{C} = 0 \tag{8b}$$

where $A = \frac{(\lambda+2\mu)nE_w}{\rho_1\rho_2}$, $B = \left[\frac{\lambda+2\mu}{\rho_1} + \frac{nE_w}{\rho_2} + \frac{(1-n)^2E_w}{n\rho_1}\right] - \frac{ib}{\omega\rho_1\rho_2}\left(\lambda+2\mu+\frac{E_w}{n}\right)$, $C = 1 - \frac{ib}{\omega}\left(\frac{1}{\rho_1}+\frac{1}{\rho_2}\right)$, and $D = \frac{ib\mu}{\omega\rho_1\rho_2} - \frac{\mu}{\rho_1}$.

Equations 8a and 8b constitute a general solution of Equation 3. In an unbounded two-phase medium, the phase velocities and attenuation coefficients can be easily extracted from Equations 8a, 8b [51, 52].

3 The reflection and transmission of interface induced by P-wave

As shown in Figure 1, to illustrate in detail the two-dimensional reflection-refraction problem, we set up a Cartesian coordinate system (x, z), with the x-axis as the horizontal direction, and the z-axis as the vertical direction. For convenience, the interface is chosen horizontally, i.e., the plane $z = 0$, and the direction of z is positive into the fluid-saturated porous medium. As a result, the upper half-space ($z < 0$) is an elastic solid, and the lower half-space ($z > 0$) is a two-phase medium. Let a plane harmonic P-wave with an angular frequency ω originate in the elastic solid and be incident obliquely at the interface at an angle θ_{IP}. For this situation, there will be two refracted compressive (P_1- and P_2-waves) waves and one refracted SV-wave in the semi-infinite porous medium, together with reflected P- and SV-waves in the semi-infinite elastic medium. All the waves generated at the interface travel with the frequency of the incident P-wave. And the angles of refraction for P_1-, P_2-, and SV-waves are θ_{T1}, θ_{T2}, and θ_{TS}, the reflection angles are θ_{RP} and θ_{RS} for reflected P- and SV-waves.

According to Snell's law, the relations between the angles of incidence, reflection, and refraction can be expressed by

$$\frac{C_P}{\sin\theta_{IP}} = \frac{C_P}{\sin\theta_{RP}} = \frac{C_S}{\sin\theta_{RS}} = \frac{V_{P1}}{\sin\theta_{T1}} = \frac{V_{P2}}{\sin\theta_{T2}} = \frac{V_S}{\sin\theta_{TS}} \tag{9}$$

where C_P and C_S are the velocities of P- and SV-waves in the elastic solid. V_{P1}, V_{P2}, and V_S are the velocities of P_1-, P_2-, and SV-waves in the two-phase medium. From Equation 9, the angle of reflection (θ_{RP}) equals the angle of incidence (θ_{IP}) for the P-wave. In addition, if the wave velocities and the angle of incidence (θ_{IP}) are given, the angles of reflection and refraction (i.e., θ_{RS}, θ_{T1}, θ_{T2}, and θ_{TS}) can be calculated.

3.1 Wave potentials in the elastic solid

For the elastic solid in the region $z < 0$, the reflected P- and SV-waves are generated when the P-wave propagates from an elastic solid to a saturated porous medium. The wave potentials of P- and SV-waves in the elastic solid, ϕ' and ψ', are given by Equation 10. The plane wave solutions of wave potentials (ϕ' and ψ') can be expressed by Equations 11a–11c.

$$\begin{cases} \phi' = \phi^I + \phi^R \\ \psi' = \psi^R \end{cases} \tag{10}$$

$$\phi^I = A^I \exp\left[i\left(\omega t - k_x^I x - k_z^I z\right)\right] \tag{11a}$$

$$\phi^R = A^R \exp\left[i\left(\omega t - k_x^I x + k_z^I z\right)\right] \tag{11b}$$

$$\psi^R = B^R \exp\left[i\left(\omega t - k_x^R x + k_z^R z\right)\right] \tag{11c}$$

where ϕ^I is the potential of the incident P-wave, which travels in the $+x$ and $+z$ directions, and A^I corresponds to the amplitude. ϕ^R and ψ^R are the potentials of the reflected P- and SV-waves, which travel in the $+x$ and $-z$ directions, and A^R and B^R are the amplitudes. k_x^I and k_z^I represent the components of the wave number along the x-direction and z-direction, respectively, for the incident P-wave. k_x^R and k_z^R are the components of the wave number in the x and z directions for the reflected SV-wave.

3.2 Wave potentials in the fluid-saturated porous medium

For the fluid-saturated porous medium in the domain $z > 0$, part of the incident P-wave is converted into three transmitted P_1-, P_2-, and SV-waves. The potentials in the solid phase (ϕ_s and ψ_s), and the potentials in the liquid phase (ϕ_w and ψ_w) are given by the expression (Equation 12). The plane wave solutions of potentials for each transmitted wave in the solid and liquid phases are written by

$$\begin{cases} \phi_s = \phi_{s1}^T + \phi_{s2}^T \\ \phi_w = \phi_{w1}^T + \phi_{w2}^T \\ \psi_s = \psi_s^T \\ \psi_w = \psi_w^T \end{cases} \tag{12}$$

$$\begin{cases} \phi_{s1}^T = A_{s1}^T \exp\left[i\left(\omega t - k_{1x}^T x - k_{1z}^T z\right)\right] \\ \phi_{w1}^T = A_{w1}^T \exp\left[i\left(\omega t - k_{1x}^T x - k_{1z}^T z\right)\right] \end{cases} \tag{13a}$$

$$\begin{cases} \phi_{s2}^T = A_{s2}^T \exp\left[i\left(\omega t - k_{2x}^T x - k_{2z}^T z\right)\right] \\ \phi_{w2}^T = A_{w2}^T \exp\left[i\left(\omega t - k_{2x}^T x - k_{2z}^T z\right)\right] \end{cases} \tag{13b}$$

$$\begin{cases} \psi_s^T = B_s^T \exp\left[i\left(\omega t - k_{sx}^T x - k_{sz}^T z\right)\right] \\ \psi_w^T = B_w^T \exp\left[i\left(\omega t - k_{sx}^T x - k_{sz}^T z\right)\right] \end{cases} \tag{13c}$$

where ϕ_{s1}^T, ϕ_{s2}^T, and ψ_s^T are the refracted P_1-, P_2-, and SV-waves potentials in the solid phase, and ϕ_{w1}^T, ϕ_{w2}^T, and ψ_w^T are those in the liquid phase. A_{s1}^T, A_{s2}^T, and B_s^T are the amplitudes corresponding to the transmitted P_1-, P_2-, and SV-waves in the solid phase, and A_{w1}^T, A_{w2}^T, and B_w^T those in the liquid phase. k_{1x}^T, k_{1z}^T, k_{2x}^T, k_{2z}^T, k_{sx}^T, and k_{sz}^T are the components of wave numbers in the x and z directions, in which the indices 1, 2, and s denote P_1, P_2, and SV waves, and the superscript T represents refraction. In terms of the negative sign before each wave number, all transmitted waves propagate along the $+x$ and $+z$ directions.

Given the geometric relationship of wave vectors, the wave vectors and their components for various waves fulfill Equation 14. In addition, the apparent velocity along the interface (i.e., $z = 0$) is the same. Hence, the horizontal components of the wave vector for all mode waves are the same as shown in Equation 15.

$$\begin{cases} \left(k_x^I\right)^2 + \left(k_z^I\right)^2 = \left(k^I\right)^2 \\ \left(k_x^R\right)^2 + \left(k_z^R\right)^2 = \left(k^R\right)^2 \\ \left(k_{1x}^T\right)^2 + \left(k_{1z}^T\right)^2 = \left(k_1^T\right)^2 \\ \left(k_{2x}^T\right)^2 + \left(k_{2z}^T\right)^2 = \left(k_2^T\right)^2 \\ \left(k_{sx}^T\right)^2 + \left(k_{sz}^T\right)^2 = \left(k_s^T\right)^2 \end{cases} \tag{14}$$

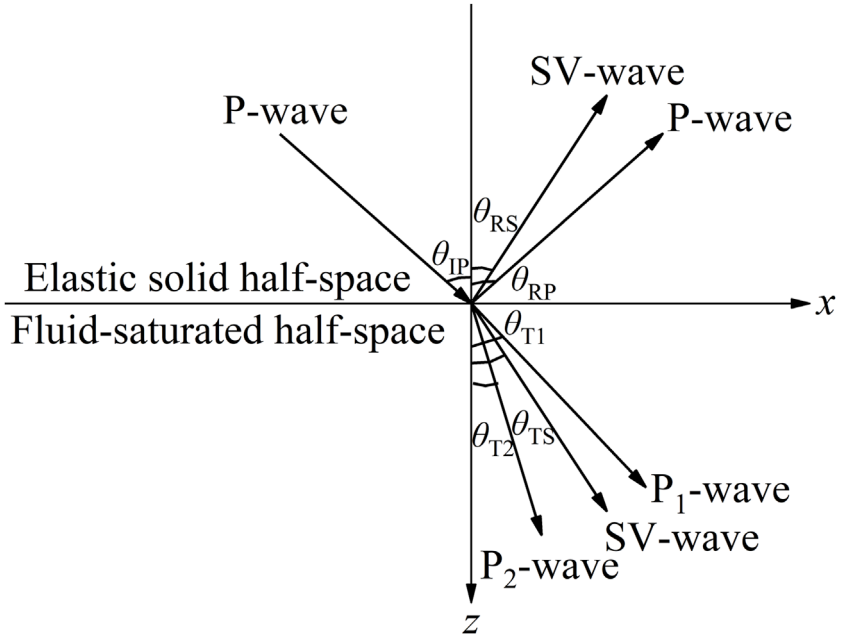

FIGURE 1
Reflection and transmission of an incident P-wave at the interface between the monophasic and two-phase media.

$$k_x^{\mathrm{I}} = k_x^{\mathrm{R}} = k_{1x}^{\mathrm{T}} = k_{2x}^{\mathrm{T}} = k_{sx}^{\mathrm{T}} \tag{15}$$

For the liquid-saturated medium, it can be seen from Equations 8a, 8b that the amplitude ratios of potentials in Equations 13a–c can be determined as

$$\delta_1 = \frac{A_{\mathrm{w1}}^{\mathrm{T}}}{A_{\mathrm{s1}}^{\mathrm{T}}} = \frac{\left(\lambda + 2\mu + \frac{1-n}{n}E_{\mathrm{w}}\right)\left(k_1^{\mathrm{T}}\right)^2 - \rho_1\omega^2}{\rho_2\omega^2 - E_{\mathrm{w}}\left(k_1^{\mathrm{T}}\right)^2} \tag{16a}$$

$$\delta_2 = \frac{A_{\mathrm{w2}}^{\mathrm{T}}}{A_{\mathrm{s2}}^{\mathrm{T}}} = \frac{\left(\lambda + 2\mu + \frac{1-n}{n}E_{\mathrm{w}}\right)\left(k_2^{\mathrm{T}}\right)^2 - \rho_1\omega^2}{\rho_2\omega^2 - E_{\mathrm{w}}\left(k_2^{\mathrm{T}}\right)^2} \tag{16b}$$

$$\delta_{\mathrm{s}} = \frac{B_{\mathrm{w}}^{\mathrm{T}}}{B_{\mathrm{s}}^{\mathrm{T}}} = \frac{\mu\left(k_{\mathrm{s}}^{\mathrm{T}}\right)^2 - \rho_1\omega^2}{\rho_2\omega^2} \tag{16c}$$

3.3 Boundary conditions and solutions

3.3.1 Boundary conditions

When the P-wave travels from the single-phase medium to the two-phase medium, the reflection and transmission will occur at the interface (say, $z = 0$). For this situation, the boundary conditions will make a difference to the propagation characteristics of waves, namely the unknown amplitudes A^{R}, B^{R}, $A_{\mathrm{s1}}^{\mathrm{T}}$, $A_{\mathrm{s2}}^{\mathrm{T}}$, and $B_{\mathrm{s}}^{\mathrm{T}}$. On the assumption of the existence of welded contact between two semi-infinite media, we consider two boundary conditions: (a) Open-pore boundary (see expressions (28) to (32) in Philippacopoulos [59]) and (b) Sealed-pore boundary (expressions (19) in Hajra and Mukhopadhyay [18] and Deresiewicz and Skalak [60]). More specifically, the boundary conditions are the continuity of stress and displacement components along the interface. Besides, in case (a), the pore fluid can flow freely into the permeable elastic solid, but in case (b), the flow of fluid (i.e., the relative fluid displacement) is restricted. Consequently, the two different boundary conditions are shown as

$$\begin{cases} \sigma_{ij|z=0^+} = \sigma'_{ij|z=0^-} \\ u_{i|z=0^+} = u'_{i|z=0^-} \\ p_{f|z=0^+} = 0 \end{cases} \tag{17a}$$

$$\begin{cases} \sigma_{ij|z=0^+} = \sigma'_{ij|z=0^-} \\ u_{i|z=0^+} = u'_{i|z=0^-} \\ u_{z|z=0^+} - U_{z|z=0^+} = 0 \end{cases} \tag{17b}$$

where the subscripts i and j (=x and z) denote the components in the x and z directions. $\sigma_{ij|z=0^+}$ and $\sigma'_{ij|z=0^-}$ are the total stresses (e.g., normal and shearing stresses) of the fluid-saturated porous medium and elastic solid, respectively. $u_{i|z=0^+}$ is the displacement component of the soil skeleton in a two-phase medium at the interface, and $u'_{i|z=0^-}$ that of a single-phase medium at the interface. $p_{f|z=0^+}$ represents the pore pressure at the interface.

3.3.2 Reflection and transmission coefficients

Without loss of generality, set the amplitude of the incident P-wave (A^{I}) equal to unity. After the introduction of Equations 2a, 2b, 6a–6c, together with Equations 14, 15, 16a–16c, through Equations 17a, 17b, we can get the set of equations for the determination of the amplitude ratios (i.e., $A^{\mathrm{R}}/A^{\mathrm{I}}$, $B^{\mathrm{R}}/A^{\mathrm{I}}$, $A_{\mathrm{s1}}^{\mathrm{T}}/A^{\mathrm{I}}$,

A_{s2}^{T}/A^{I}, and B_{s}^{T}/A^{I}) under permeable and impermeable boundaries in the matrix form as

$$[S_{P-SV}]\left\{A^{R},B^{R},A_{s1}^{T},A_{s2}^{T},B_{s}^{T}\right\}^{T}=\left\{\lambda'\left(k^{I}\right)^{2}+2\mu'\left(k_{z}^{I}\right)^{2},2\mu'k_{x}^{I}k_{z}^{I},k_{x}^{I},k_{z}^{I},0\right\}^{T} \tag{18a}$$

$$\left[\overline{S}_{P-SV}\right]\left\{A^{R},B^{R},A_{s1}^{T},A_{s2}^{T},B_{s}^{T}\right\}^{T}=\left\{\lambda'\left(k^{I}\right)^{2}+2\mu'\left(k_{z}^{I}\right)^{2},2\mu'k_{x}^{I}k_{z}^{I},k_{x}^{I},k_{z}^{I},0\right\}^{T} \tag{18b}$$

where $[S_{P-SV}]$ and $\left[\overline{S}_{P-SV}\right]$ are the 5 × 5 matrices, which represent permeable and impermeable boundaries respectively, and the elements of the matrices are given in the Appendix. The unknown quantities A^{R}, B^{R}, A_{s1}^{T}, A_{s2}^{T}, and B_{s}^{T} can be solved as the amplitude reflection and transmission coefficients at the plane interface.

4 Degenerate validation of solutions

4.1 Validation of degenerate formulas

Set the mass density of liquid $\rho_{w}=0$ and the bulk modulus of liquid $E_{w}=0$. The analytical formulas in this paper can revert to the classical problem of P-wave incident at the interface between two diverse elastic solids. For this situation, the amplitude ratios of liquid- and solid-phase $\delta_{1}=0$, $\delta_{2}=0$, and $\delta_{s}=0$. The wave vectors of the refracted P_{1}- and P_{2}-waves are equal, namely, $k_{1}^{T}=k_{2}^{T}$ and $k_{1z}^{T}=k_{2z}^{T}$. The velocities of refracted P- and SV-waves $V_{P}=\sqrt{(\lambda+2\mu)/\rho_{s}}$, $V_{S}=\sqrt{\mu/\rho_{s}}$, when the two-phase medium degenerates to a single-phase medium. The potential amplitude of the refracted P-wave is equivalent to the sum of the amplitudes of P_{1}- and P_{2}-waves, namely, $A_{s}^{T}=A_{s1}^{T}+A_{s2}^{T}$. The formula (Equation 18a) or (Equation 18b) may reduce to

$$\begin{cases}\mu\left(\dfrac{V_{P}^{2}}{V_{S}^{2}}\left(k_{1}^{T}\right)^{2}-2\left(k_{1x}^{T}\right)^{2}\right)A_{s}^{T}+2\mu k_{sx}^{T}k_{sz}^{T}B_{s}^{T}=\mu'\left(\dfrac{C_{P}^{2}}{C_{S}^{2}}\left(k^{I}\right)^{2}-2\left(k_{x}^{I}\right)^{2}\right)\\ \quad\times\left(A^{I}+A^{R}\right)-2\mu'k_{x}^{R}k_{z}^{R}B^{R}\\ 2\mu k_{1x}^{T}k_{1z}^{T}A_{s}^{T}+\mu\left(\left(k_{sx}^{T}\right)^{2}-\left(k_{sz}^{T}\right)^{2}\right)B_{s}^{T}=2\mu'k_{x}^{I}k_{z}^{I}\left(A^{I}-A^{R}\right)\\ \quad+\mu'\left(\left(k_{x}^{R}\right)^{2}-\left(k_{z}^{R}\right)^{2}\right)B^{R}\\ k_{1x}^{T}A_{s}^{T}-k_{sz}^{T}B_{s}^{T}=k_{x}^{I}\left(A^{I}+A^{R}\right)+k_{z}^{R}B^{R}\\ k_{1z}^{T}A_{s}^{T}+k_{sx}^{T}B_{s}^{T}=k_{z}^{I}\left(A^{I}-A^{R}\right)+k_{x}^{R}B^{R}\end{cases} \tag{19}$$

After some simplification, Equation 19 can degenerate into a classical problem in that the P-wave travels from an elastic solid to another one (see expressions (3-45) and (3-46) in [1]). It is interesting to unravel that the reflection and transmission between different elastic solids is a special case in this paper.

4.2 Validation of numerical analysis

To explain the correctness of the formulas graphically, the computed results of Equation 19 are compared with those of Pujol [57]. The parameters of the incident and transmitted media are as follows: $\lambda'=44.006$, $\mu'=43.729$, $\rho'=3.16$, $\lambda=13.32$, $\mu=13.34$ and $\rho_{s}=2.5$ (see in ref. [57]). Figure 2 depicts the variation of reflection and refraction coefficients with the incident angle when the P-wave propagates from one elastic solid to another.

From Figure 2, the calculated results of Equation 19 coincide with those shown by Pujol [57]. In a word, the case of P-wave traveling from an elastic solid to another one is a special case of ours, and it is sufficient to demonstrate the rationality and correctness of the formulas derived in this article.

5 Numerical results and discussion

In this section, we consider a model consisting of a fluid-saturated medium in welded contact with the elastic solid. The plane harmonic P-wave propagates through the elastic solid and becomes incident at the interface. The Gauss elimination method is used to calculate Equations 18a, 18b, then we obtain the amplitude ratios. Numerical examples are carried out to investigate the effects of boundary conditions, incident wave frequency, and properties of the saturated two-phase medium (i.e., the dynamic permeability coefficient k, the porosity n, and the Poisson's ratio v) on the reflection and transmission coefficients. The physical parameters of the two-phase medium are taken from Refs. [1, 22] and listed in Table 1, together with the single-phase medium.

Figures 3–7 depict the variation of reflection and transmission coefficients in the form of amplitude computed as described in Equations 18a, 18b with incident angle under diverse conditions, i.e., boundary drainage, wave frequency, permeability coefficient, porosity, and Poisson's ratio. It is found that the amplitudes of the reflected and refracted waves depend significantly on the angle of incidence, and the nature of dependence is quite different. When the incident P-wave strikes the interface perpendicularly, no reflected or transmitted SV-wave is generated, i.e., the reflection and transmission coefficients of the SV-wave are zero. At the same time, the amplitudes of transmitted P_{1}- and P_{2}-waves arrive at the largest values in this case. When the incident P-wave is at grazing incidence (i.e., the incident angle approaches 90°), there is only a reflected compressional P-wave whose reflection coefficient is 1.0. In addition, for transmitted P_{1}- and P_{2}-waves, the amplitudes decrease gradually when the angle of incidence (θ_{IP}) increases from 0° to 90°. The amplitudes of reflected and transmitted SV-waves increase with an increase in the incident angle before reaching their maximum values and thereafter, decrease and approach their minimum values. However, the effect of the incident angle on the amplitude of the reflected P-wave is quite complex, which will be explained in specified sections.

5.1 The influence of boundary drainage

When the P-wave propagates from the elastic solid to the two-phase medium, the boundary conditions for the interface will play a key role in the reflection and transmission of seismic waves. To study in greater detail the dependence of the reflection and transmission coefficients on the boundary drainage, we select two different boundary conditions (i.e., permeable or impermeable interface). In our calculations, the soil parameters are taken from Table 1, and the wave frequency of the incident wave $f=100$ Hz. Figure 3 describes the reflection and transmission coefficients as a function of incident angle at permeable and impermeable interfaces.

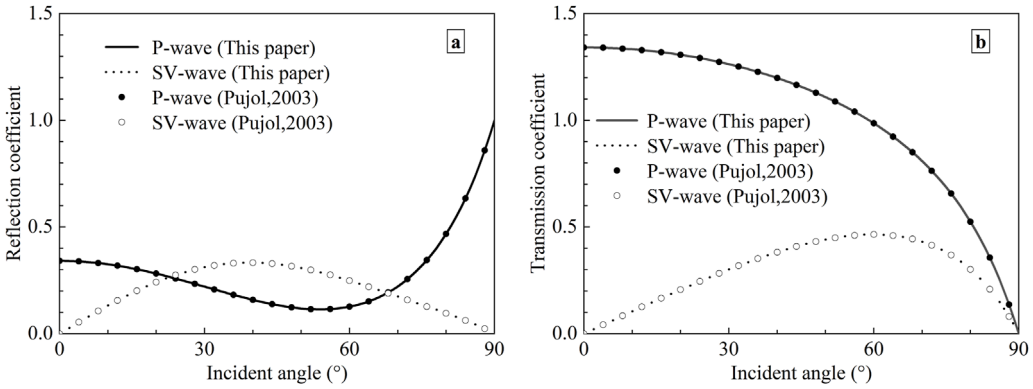

FIGURE 2
Variation of the amplitude reflection and transmission coefficients with the incident angle for two diverse elastic solids. **(a)** Reflection coefficients; **(b)** Transmission coefficients.

TABLE 1 Material properties of single- and two-phase media.

λ' (Pa)	μ' (Pa)	ρ' (kg m^{-3})	λ (Pa)	μ (Pa)	ρ_s (kg m^{-3})	ρ_w (kg m^{-3})	n	E_w (Pa)	ν	K (m^3 s/kg)
2.51×10^9	2.32×10^9	1,900	2.61×10^7	2.61×10^7	2,650	1,000	0.27	2.0×10^9	0.25	1.0×10^{-7}

It is shown in Figure 3 that whether the interface is drained or not, the reflection and transmission coefficients are affected significantly by the incident angle. The variation of reflection and transmission coefficients of other waves exhibits the same trend with the incident angle under diverse interfaces, except for the reflected P-wave. However, the actual values of reflection and transmission coefficients differ appreciably for the two types of interfaces considered. For the reflected SV-wave, the reflection coefficient in the permeable interface is much larger than that in the impermeable interface. For the transmitted SV-wave, the amplitude in the permeable interface is larger than that in the impermeable interface before reaching 79°; thereafter, the amplitude in the permeable interface is less than that in the impermeable interface. What's more, the transmission coefficient of P_2-wave under undrained conditions is much smaller than the corresponding one under drained conditions, while the P_1-wave has the reverse regularity. The relative fluid displacement with respect to the soil skeleton is taken to be zero, which causes the difficulty of generating of P_2-wave. It is enough to show that when the interface is permeable, we must pay attention to the P_2-wave, which cannot be ignored because of its slow velocity and fast attenuation, otherwise it may lead to the problem of instability in numerical calculations.

5.2 The influence of wave frequency

The results in Section 5.1 are obtained at a special frequency of 100 Hz. To investigate the effect of frequency on the reflection and transmission coefficients, three typical frequencies (i.e., f = 1, 10, and 1,000 Hz) are added to the numerical calculations, and the properties of the medium are taken from Table 1. The characteristic frequency of the saturated medium $f_c = n/2\pi k\rho_f$ = 430 Hz, which is defined by Biot [4, 5]. According to the results of Yang [23], the reflection and transmission coefficients for the permeable interface exhibit a large dispersion in the low-frequency range (i.e., $f/f_c \leq 0.1$). All wave frequencies in this study are below 1,000 Hz, which covers the common frequencies used in seismic and acoustic fields [33]. Given that mentioned above, the boundary is assumed to be permeable. The variation of the computed reflection and transmission coefficients with the incident angle of the P-wave is shown in Figure 4.

For all the cases of wave frequency under consideration, the reflection and transmission coefficients of all waves are affected significantly by it. The transmission coefficient of P_1-wave (P_2-wave) decreases (increases) with the increasing frequency. For the reflected SV wave, the amplitude increases with an increase in frequency. For the transmitted SV-wave, the amplitude increases with a rise in frequency if the incident angle $\theta_{IP} < 76°$, while the impact of frequency becomes less significant if the incident angle $\theta_{IP} > 76°$. However, for the reflected P-wave, when the frequency f = 1, 10, and 100 Hz, the reflected P-wave extinguishes at a specific angle of incidence. Under the case that f = 1 Hz (10 Hz), the two special angles are 23° and 83° (43° and 77°). If the frequency f = 100 Hz, the corresponding angles are 61° and 67°.

5.3 The influence of dynamic permeability coefficient

Since the fluid flows in the two-phase medium, it is instructive to investigate the effect of the dynamic permeability coefficient on the reflection and transmission coefficients. In calculations, the properties of the media are taken from Table 1, except for the

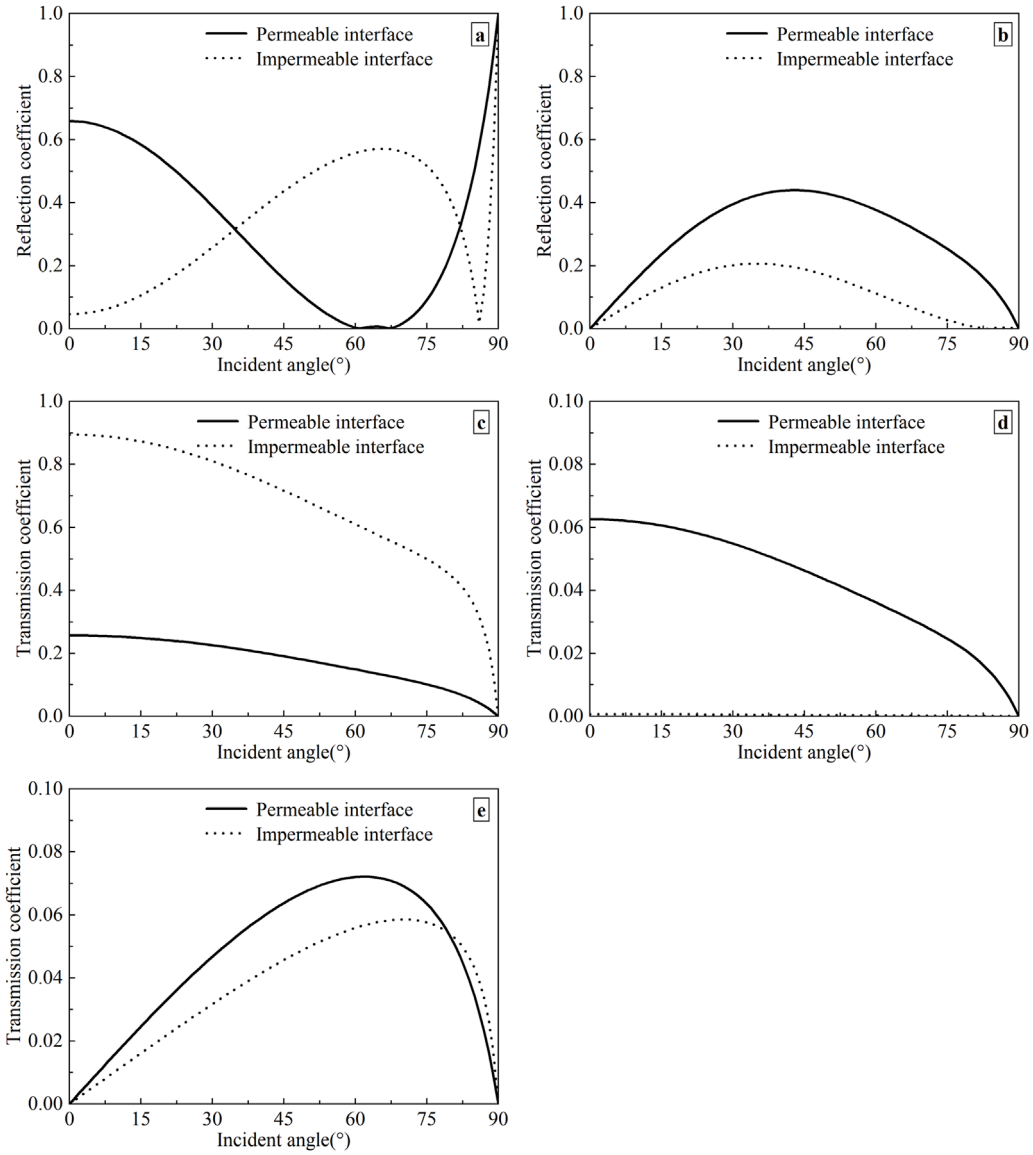

FIGURE 3
Variation of reflection and transmission coefficients with the incident angle under different drainage conditions. **(a)** Reflected P-wave; **(b)** Reflected SV-wave; **(c)** Transmitted P_1-wave; **(d)** Transmitted P_2-wave; **(e)** Transmitted SV-wave.

dynamic permeability coefficient. The frequency of the incident P-wave is 100 Hz, and the interface is assumed to be permeable. The reflection and transmission coefficients as a function of incident angle for four cases of dynamic permeability coefficient (i.e., k = 1.0 × 10^{-9}, 1.0 × 10^{-8}, 1.0 × 10^{-7}, and 1.0 × 10^{-6} m^3 s/kg) are shown in Figure 5.

As shown in Figure 5, the reflection and transmission coefficients of all waves vary with the dynamic permeability coefficient. For the reflected SV-wave and transmitted P_2-wave, the higher the dynamic permeability coefficient is, the larger the amplitude is. Whereas for the transmitted P_1-wave, the higher the dynamic permeability coefficient is, the smaller the amplitude is. In addition, the transmission coefficient of the SV-wave increases with a rise in the dynamic permeability coefficient before the incident angle reaches 76°. Thereafter, the dynamic permeability coefficient has little effect on the transmission coefficient of SV-wave. For the reflected P-wave, when the dynamic permeability coefficient k = 1.0 × 10^{-9}, 1.0 × 10^{-8}, and 1.0 × 10^{-7} m^3 s/kg, there are special angles that make the reflected SV-wave exist, and the reflected P-wave disappear. Also, different permeability coefficients correspond to different angles of incidence. If k = 1.0 × 10^{-9} m^3 s/kg (1.0 × 10^{-8} m^3 s/kg), the two special angles are 23° and 83° (43° and 77°). If k = 1.0 × 10^{-7} m^3 s/kg, the corresponding angles are 61° and 67°.

By comparing Figure 5 with Figure 4, it is obvious that the reflection and transmission coefficient curves are the same when the product of the permeability coefficient k and frequency ω is equal. The reason is that when $k\omega$ takes the same value, the velocities of the two-phase medium do not change [51]. If the wave velocities of the two-phase medium remain constant, the reflection and transmission coefficients are also fixed values.

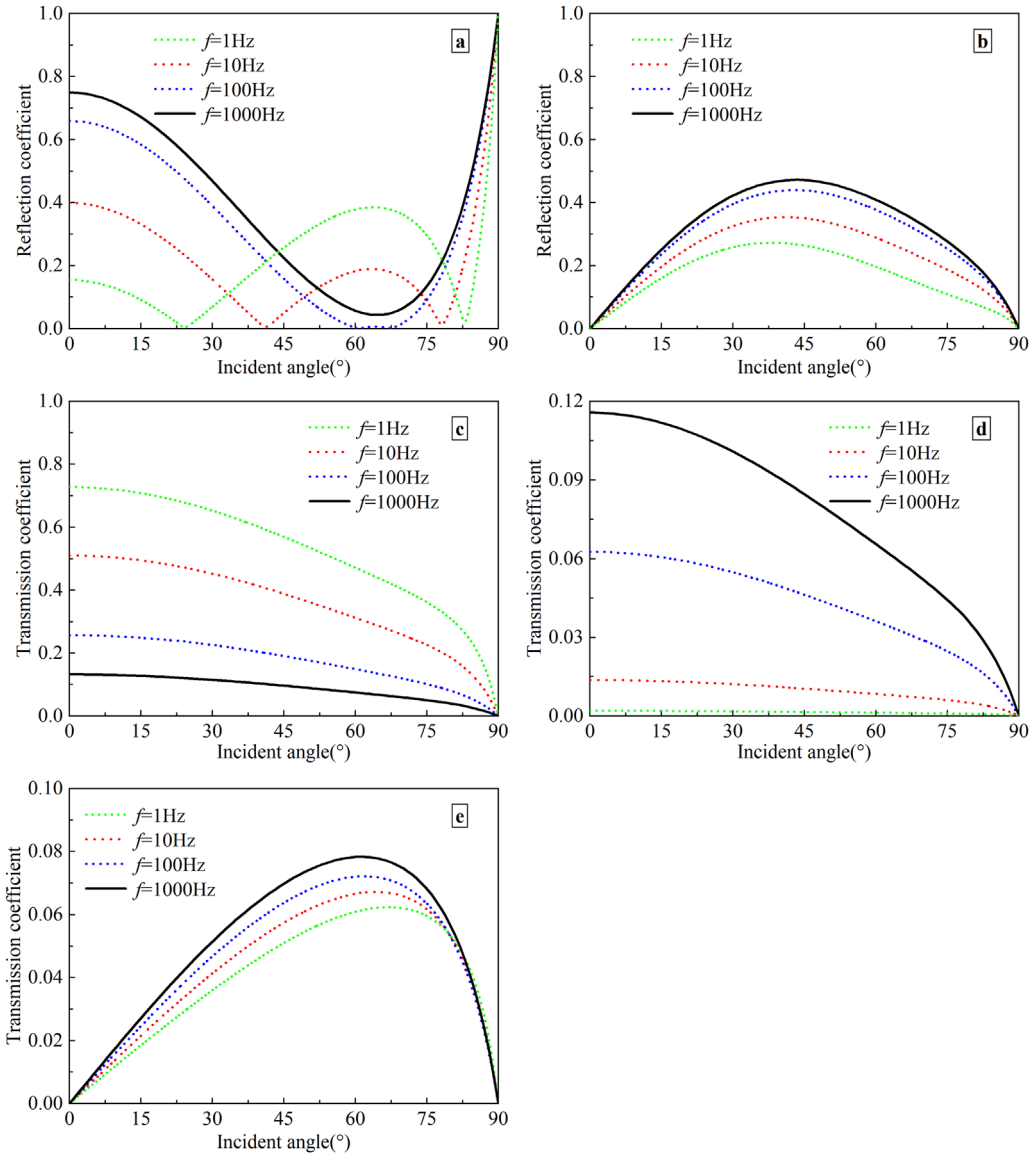

FIGURE 4
Variation of reflection and transmission coefficients with the incident angle at different frequencies. **(a)** Reflected P-wave; **(b)** Reflected SV-wave; **(c)** Transmitted P_1-wave; **(d)** Transmitted P_2-wave; **(e)** Transmitted SV-wave.

To explain the influence of the dynamic permeability coefficient and frequency on the reflection and transmission coefficients, we introduce a non-dimensional frequency ratio f/f_c $(=\rho_w k\omega/n)$. In calculations, the incident angle of the P-wave is taken to be 30°, and the boundary is assumed to be permeable. The physical parameters of media are taken from Table 1. Figure 6 shows the variation of reflection and transmission coefficients with the non-dimensional frequency ratio.

From Figure 6, it can be observed that the reflection and transmission coefficients are dispersive, namely, frequency-dependent. And all coefficients are affected by frequency, even in a very low frequency range. Moreover, the reflection and transmission coefficients depend on the function of frequency-permeability product.

5.4 The influence of porosity

The porosity is an important property in the fluid-saturated porous medium, which concerns the soil structure. To analyze the effect of porosity, the porosity n is taken to be 0.2, 0.3, 0.4, and 0.5, respectively. The other physical parameters of media remain constant as listed in Table 1. The wave frequency f = 100 Hz, and the interface is permeable. Figure 7 depicts the angle-dependent reflection and transmission coefficients for the above four values of porosity.

As observed in Figure 7, it is worth noting that the porosity has a slight influence on the reflection and transmission coefficients. The variation of transmission coefficients for P_1- and P_2-waves with porosity is gentle. The reflection and transmission coefficients of the

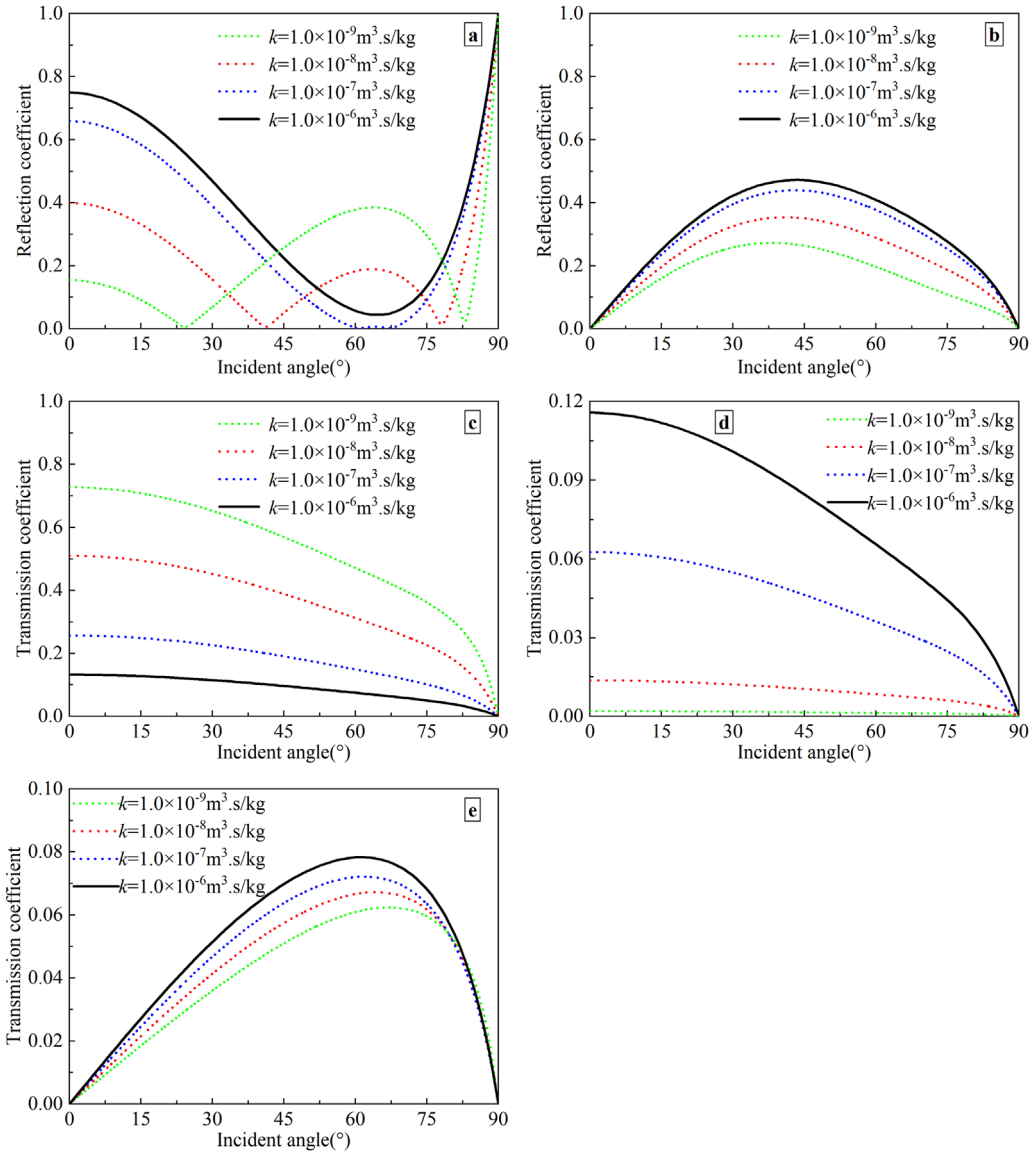

FIGURE 5
Variation of reflection and transmission coefficients with the incident angle for different values of dynamic permeability coefficient. **(a)** Reflected P-wave; **(b)** Reflected SV-wave; **(c)** Transmitted P_1-wave; **(d)** Transmitted P_2-wave; **(e)** Transmitted SV-wave.

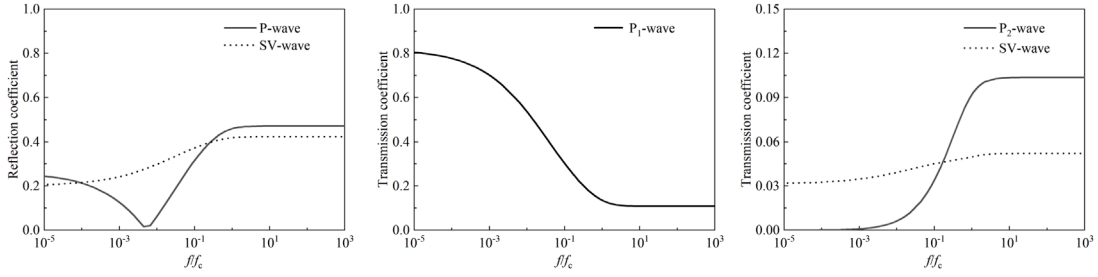

FIGURE 6
Variation of reflection and transmission coefficients with the non-dimensional frequency ratio.

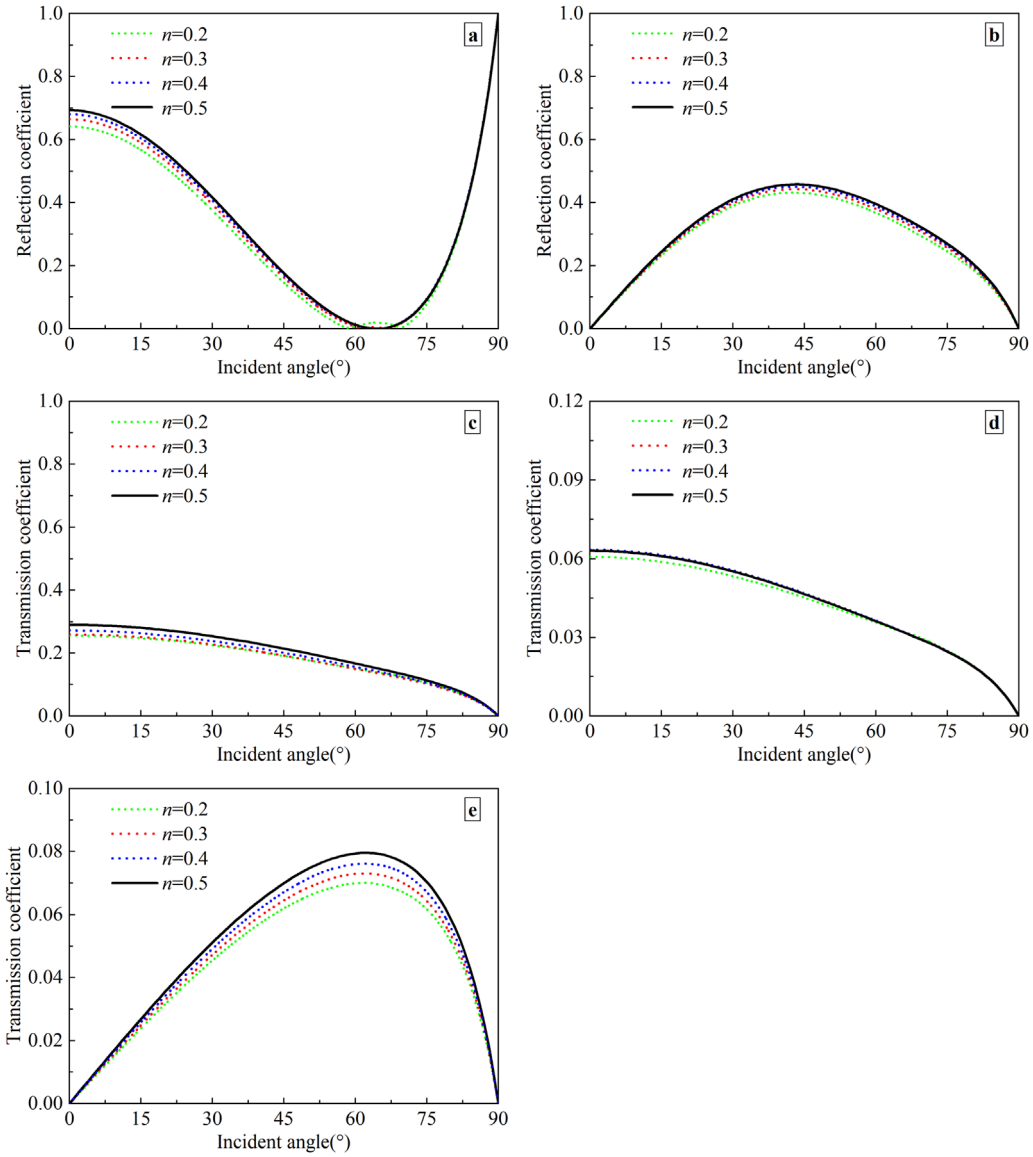

FIGURE 7
Variation of reflection and transmission coefficients with the incident angle under different porosities. **(a)** Reflected P-wave; **(b)** Reflected SV-wave; **(c)** Transmitted P_1-wave; **(d)** Transmitted P_2-wave; **(e)** Transmitted SV-wave.

SV-wave increase with a rise in porosity. For the reflected P-wave, there are two zero values, i.e., the incident angles $\theta_{IP} = 58°$ and 72°, when the porosity $n = 0.2$.

5.5 The influence of Poisson's ratio

The Poisson's ratio, one of the characteristic parameters in the two-phase medium, reflects the deformation characteristics of the soil. To investigate the effects of Poission's ratio on the reflection and transmission coefficients, the parameters of the soil remain invariable as listed in Table 1, except for Poission's ratio. The wave frequency $f = 100$ Hz, and the interface is permeable. The variation of reflection and transmission coefficients with the incident angle of the P-wave is depicted in Figure 8.

As described in Figure 8, the effects of the Poisson's ratio on the reflection and transmission coefficients of each wave are more obvious than those of the porosity in the previous Section 5.4. The transmission coefficients of P_1- and P_2-waves increase as the Poisson's ratio increases at the same angle of incidence. While the transmission coefficients of SV-wave decrease with the increase in Poisson's ratio if $\theta_{IP} < 68°$, thereafter the Poisson's ratio has little impact on it. The reflection coefficient of the SV-wave decreases with increasing Poisson's ratio. For the reflected P-wave, when the Poisson's ratio $v = 0.3$ and 0.4, there are special angles that make the reflected SV-wave exist, and the reflected P-wave disappears. Also,

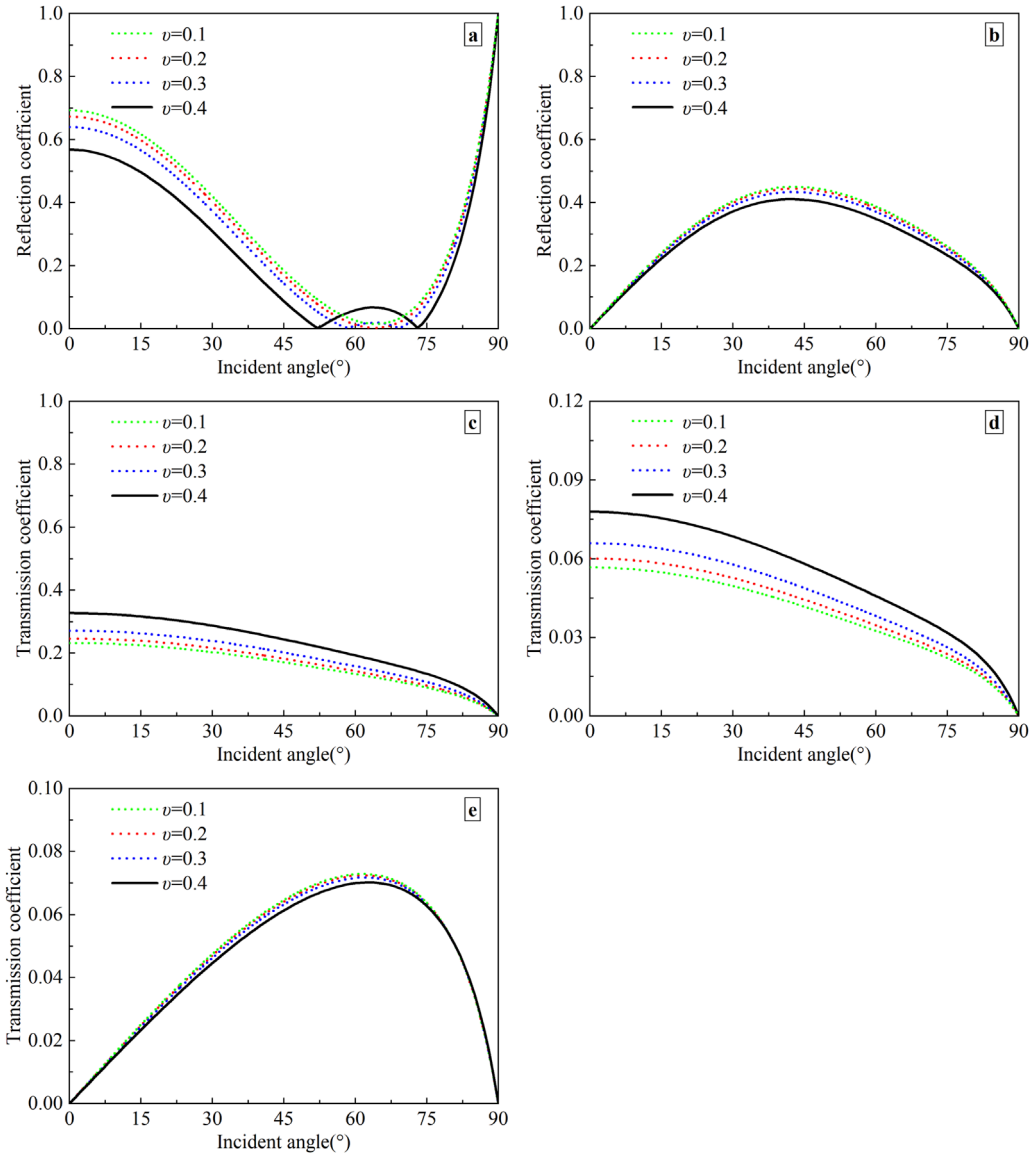

FIGURE 8
Variation of reflection and transmission coefficients with the incident angle under different Poisson's ratios. **(a)** Reflected P-wave; **(b)** Reflected SV-wave; **(c)** Transmitted P_1-wave; **(d)** Transmitted P_2-wave; **(e)** Transmitted SV-wave.

different Poisson's ratios correspond to different angles of incidence. When the Poisson's ratio $\upsilon = 0.3$ (0.4), the two special angles are 58° and 68° (52° and 73°).

6 Conclusion

Based on the model of soil mechanics proposed by Men [12], the reflection and transmission of a plane harmonic P-wave traveling from an elastic solid to the fluid-saturated porous media are investigated. The analytical expressions for the reflection and transmission coefficients have been derived for permeable and impermeable boundaries. Numerical calculations are performed to analyze the dependence of reflection and transmission coefficients on the incident angle, boundary drainage, wave frequency, and material properties (dynamic permeability coefficient, porosity, and Poisson's ratio). Some useful results are obtained as follows: (1) The incident angle has a great influence on the reflection and transmission coefficient of each wave. When the angle of incidence θ_{IP} = 0°, the reflected and transmitted SV-waves disappear, and the transmission coefficients of P_1- and P_2-waves reach the largest values. Moreover, when the angle of incidence θ_{IP} = 90°, there is only a reflected P-wave, with which the reflection coefficient is 1.0. (2) The interface flow condition has a great impact on the reflection and transmission coefficients. (3) The reflection and transmission coefficients are dispersive and depend on the product of frequency and permeability. (4) The physical parameters of the two-phase medium (dynamic

permeability coefficient, porosity, and Poisson's ratio) have different influences on the reflection and transmission coefficients of waves.

Hence, it is interesting to study the propagation characteristics of elastic waves at the interface between the elastic solid and the two-phase medium. It is hoped that this paper may be useful in the theoretical and observational studies of wave propagation in the liquid-saturated porous medium. At last, it can be extended to study the reflection and transmission of elastic waves at other various boundaries, e.g., the porous medium/the porous medium [61, 62], the water/porous medium [63, 64], and ocean sediment [65, 66], etc.

Data availability statement

The original contributions presented in the study are included in the article/supplementary material, further inquiries can be directed to the corresponding author.

Author contributions

LQ: Writing – original draft, Writing – review and editing, Software, Data curation, Validation. BZ: Supervision, Conceptualization, Writing – review and editing, Funding acquisition, Writing – original draft, Methodology.

Funding

The author(s) declare that financial support was received for the research and/or publication of this article. This research work was supported by the Science Research Project of Hebei Education Department, QN2025419, BZ.

Acknowledgments

The authors would like to thank the Science Research Project of Hebei Education Department (Grant No. QN2025419) for funding the work presented in this paper.

Conflict of interest

The authors declare that the research was conducted in the absence of any commercial or financial relationships that could be construed as a potential conflict of interest.

Generative AI statement

The author(s) declare that no Generative AI was used in the creation of this manuscript.

Publisher's note

References

1. Wu S. *Wave propagation in soils*. Beijing: Science Press (1997). p. 62–84. [in Chinese].

2. Yang J, Wu S, Cai Y. Characteristics of propagation of elastic waves in saturated soils. *J Vib Eng* (1996) 9(02):128–37. doi:10.16385/j.cnki.issn.1004-4523.1996.02.011

3. Zhao C, Gao F, Zeng Q. The reflection and transmission of plane waves on an interface between solid and liquid-filled porous solid with dissipation of energy. *Chin J Rock Mech Eng* (1996) 15(s1):470–5. (in Chinese).

4. Biot MA. Theory of propagation of elastic waves in a fluid-saturated porous solid. I. Low-frequency range. *J Acoust Soc Am* (1956) 28(2):168–78. doi:10.1121/1.1908239

5. Biot MA. Theory of propagation of elastic waves in a fluid-saturated porous solid. II. Higher frequency range. *J Acoust Soc Am* (1956) 28(2):179–91. doi:10.1121/1.1908241

6. Plona TJ. Observation of a second bulk compressional wave in a porous medium at ultrasonic frequencies. *Appl Phys Lett* (1980) 36:259–61. doi:10.1063/1.91445

7. Berryman JG. Confirmation of Biot's theory. *Appl Phys Lett* (1980) 37:382–4. doi:10.1063/1.91951

8. Zienkiewicz OC, Chang CT, Bettess P. Drained, undrained, consolidating and dynamic behavior assumptions in soils. *Geotechnique* (1980) 30(4):385–95. doi:10.1680/geot.1980.30.4.385

9. Zienkiewicz OC, Shiomi T. Dynamic behaviour of saturated porous media; the generalized Biot formulation and its numerical solution. *Int J Numer Anal Meth* (1984) 8(1):71–96. doi:10.1002/nag.1610080106

10. Men F. Wave propagation in a porous, saturated elastic medium. *Acta Geophys Sinica* (1965) 14(02):37–44. (in Chinese).

11. Men F. Problems of wave propagation in porous fluid-saturated media. *Acta Geophys Sinica* (1981) 24(01):65–76. (in Chinese).

12. Men F. On wave propagation in fluid-saturated porous media. *Conf Soil Dyn Earthq Eng* (1982) (1) 225–38.

13. Bowen RM, Reinicke KM. Plane progressive waves in a binary mixture of linear elastic materials. *J Appl Mech* (1978) 45(3):493–9. doi:10.1115/1.3424351

14. Chen S, Liao Z. Study on mechanic models of two-phase media. *Earthq Eng Eng Vib* (2002) 22(04):1–8. doi:10.13197/j.eeev.2002.04.001

15. Gutenberg B. Energy ratio of reflected and refracted seismic waves. *Bull Seismol Soc Am* (1944) 34:85–102. doi:10.1785/BSSA0340020085

16. Geertsma J, Smit DC. Some aspects of elastic wave propagation in fluid-saturated porous solids. *Geophysics* (1961) 26(2):169–81. doi:10.1190/1.1438855

17. Deresiewicz H, Rice JT. The effect of boundaries on wave propagation in a liquid-filled porous solid: V. Transmission across a plane interface. *Bull Seismol Soc Am* (1964) 54(1):409–16. doi:10.1785/BSSA0540010409

18. Hajra S, Mukhopadhyay A. Reflection and refraction of seismic waves incident obliquely at the boundary of a liquid-saturated porous solid. *Bull Seismol Soc Am* (1982) 72(5):1509–33. doi:10.1785/BSSA0720051509

19. Sharma MD, Gogna ML. Reflection and refraction of plane harmonic waves at an interface between elastic solid and porous solid saturated by viscous liquid. *Pure Appl Geophys* (1992) 138:249–66. doi:10.1007/bf00878898

20. Vashisth AK, Sharma MD, Gogna ML. Reflection and transmission of elastic waves at a loosely bonded interface between an elastic solid and liquid-saturated porous solid. *Geophys J R Astron Soc* (1991) 105(3):601–17. doi:10.1111/j.1365-246X.1991.tb00799.x

21. Zhao C, Gao F, Cui J. Boundary effect of wave propagating from liquid-filled porous medium to solid medium. *Earthq Eng Eng Vib* (1999) 19(01):1–6. doi:10.13197/j.eeev.1999.01.001

22. Ye C, Shi Y, Cai Y. Reflection and refraction at the interface when S waves propagate from saturated soil to elastic soil. *J Vib Shock* (2005) 24(2):41–5+147. doi:10.13465/j.cnki.jvs.2005.02.012

23. Yang J. Importance of flow condition on seismic waves at a saturated porous solid boundary. *J Sound Vib* (1999) 221(03):391–413. doi:10.1006/jsvi.1998.2036

24. Yang J. Influence of water saturation on horizontal and vertical motion at a porous soil interface induced by incident P wave. *Soil Dyn Earthq Eng* (2000) 19(8):575–81. doi:10.1016/S0267-7261(00)00067-1

25. Yang J, Sato T. Influence of viscous coupling on seismic reflection and transmission in saturated porous media. *Bull Seismol Soc Am* (1998) 88(5):1289–99. doi:10.1785/BSSA0880051289

26. Yang J, Sato T. Influence of water saturation on horizontal and vertical motion at a porous soil interface induced by incident SV wave. *Soil Dyn Earthq Eng* (2000) 19(5):339–46. doi:10.1016/S0267-7261(00)00023-3

27. Li W. Influence of water saturation on seismic reflection and transmission coefficients at a mainly water-saturated porous soil interface. *Northwest Seismol J* (2002) 24(02):303–9. doi:10.3969/j.issn.1000-0844.2002.04.003

28. Xu P, Xia T. Reflection and transmission of elastic wave at the interface of nearly saturated soil and elastic soil. *Mech Eng* (2006) 28(6):58–63. doi:10.3969/j.issn.1000-0879.2006.06.013

29. Kumar R, Kumar S, Miglani A. Reflection and transmission of plane waves between two different fluid-saturated porous half-spaces. *J Appl Mech Tech Phys* (2011) 59(02):773–82. doi:10.2478/v10175-011-0028-8

30. Wei Z, Wang Y, Zhang Z. Propagating from a single-phase elastic medium to a transversely isotropic liquid-saturated porous medium. *Acta Mech Solida Sin* (2002) 23(02):183–9. doi:10.19636/j.cnki.cjsm42-1250/o3.2002.02.009

31. Singh P, Chattopadhyay A, Srivastava A, Singh AK. Reflection and transmission of P-waves in an intermediate layer lying between two semi-infinite media. *Pure Appl Geophys* (2018) 175:4305–19. doi:10.1007/s00024-018-1896-8

32. Dai Z, Kuang Z, Zhao S. Reflection and transmission of elastic waves at the interface between an elastic solid and a double porosity medium. *Int J Rock Mech Min* (2006) 43(6):961–71. doi:10.1016/j.ijrmms.2005.11.010

33. Chen W, Xia T, Chen W, Zhai C. Propagation of plane P-waves at interface between elastic solid and unsaturated poroelastic medium. *Appl Math Mech* (2012) 33(07):829–44. doi:10.1007/s10483-012-1589-6

34. Kumar M, Singh A, Kumari M, Barak MS. Reflection and refraction of elastic waves at the interface of an elastic solid and partially saturated soils. *Acta Mechanica* (2021) 232:33–55. doi:10.1007/s00707-020-02819-z

35. Goyal S, Tomar SK. Reflection/Refraction of a dilatational wave at a plane interface between uniform elastic and swelling porous half-spaces. *Transp Porous Media* (2015) 109:609–32. doi:10.1007/s11242-015-0539-0

36. Tomar SK, Arora A. Reflection and transmission of elastic waves at an elastic/porous solid saturated by two immiscible fluids. *Int J Sol Struct* (2006) 44(17):1991–2013. doi:10.1016/j.ijsolstr.2007.05.021

37. Kumar M, Saini R. Reflection and refraction of attenuated waves at boundary of elastic solid and porous solid saturated with two immiscible viscous fluids. *Appl Math Mech* (2012) 33(6):797–816. doi:10.1007/s10483-012-1587-6

38. Jiang H, Ma Q, Shao S, Shao S. Characteristic of energy transmission of plane-S-wave at interface between elastic medium and saturated frozen soil medium. *Chin J Rock Mech Eng* (2023) 42(04):976–92. doi:10.13722/j.cnki.jrme.2022.0473

39. Jiang H, Ma Q, Cao Y. Study on the reflection and transmission of P wave on the interface between elastic medium and saturated frozen soil medium. *Rock Soil Mech* (2023) 44(03):916–29. doi:10.16285/j.rsm.2022.0329

40. Ergin K. Energy ratio of the seismic waves reflected and refracted at a rock-water boundary. *Bull Seismol Soc Am* (1952) 42(4):349–72. doi:10.1785/BSSA0420040349

41. Wang J, Jin F, Zhang C. Dynamic response of ideal fluid layer overlying elastic half-space due to SV-wave incidence. *Eng Mech* (2004) 21(1):15–20. (in Chinese).

42. Wang J, Jin F, Zhang C. Dynamic response of ideal fluid layer overlying elastic half-space due to P-wave incidence. *Eng Mech* (2003) 20(6):12–7. doi:10.3969/j.issn.1000-4750.2003.06.003

43. Awad E, Dai W, Sobolev S. Thermal oscillations and resonance in electron-phonon interaction process. *Z Angew Math Phys* (2024) 75(4):143. doi:10.1007/s00033-024-02277-w

44. Awad E, Samir N. A closed-form solution for thermally induced affine deformation in unbounded domains with a temporally accelerated anomalous thermal conductivity. *J Phys A-math Theor* (2024) 57(45):455202. doi:10.1088/1751-8121/ad878f

45. Chen S. *Numerical simulation for near-field wave motion in two-phase media*. [Dissertation thesis]. Harbin: China Earthquake Administration, Institute of Engineering Mechanics (2002).

46. Chen S, Liao Z, Chen J. A decoupling FEM for simulating near-field wave motions in two-phase media. *Chin J Geophys* (2005) 48(4):909–17. doi:10.3321/j.issn:0001-5733.2005.04.025

47. Jing L, Zhuo X, Wang X. Effect of complex site on seismic wave propagation. *Earthq Eng Eng Vib* (2005) 25(6):16–23. doi:10.13197/j.eeev.2005.06.004

48. Jing L, Zhuo X, Wang X. The effect of complex media on seismic wave propagation. *Chin J Geotech Eng* (2005) 27(04):393–7. doi:10.3321/j.issn:1000-4548.2005.04.006

49. Wang X. *Analysis on wave propagation in two-dimensional saturated media*. [Dissertation thesis]. Harbin: China Earthquake Administration, Institute of Engineering Mechanics (2003).

50. Xiao M, Cui J, Li Y, Jiang J, Shan Y, Duhee P. Propagation characteristics of Rayleigh waves and their influence on seabed dynamics in ocean sites. *J Hunan Univ (Natural Sciences)* (2023) 50(05):191–203. doi:10.16339/j.cnki.hdxbzkb.2023069

51. Zhang B, Chen X, Qiu L, Dong J, Zhou Z, Ji Z, et al. Propagation characteristic of elastic waves in fluid-saturated porous media based on model of soil mechanics. *Pure Appl Geophys* (2023) 180(6):2309–26. doi:10.1007/s00024-023-03269-z

52. Zhang B, Qiu L. Reflection of P_1-wave incident obliquely at the free surface of a fluid-saturated half-space: a comprehensive study via the model of soil mechanics. *Front Phys* (2025) 13:1540732. doi:10.3389/fphy.2025.1540732

53. Cui J. *The wave propagation in saturated soil layer and sand liquefaction*. [Dissertation thesis]. Harbin: China Earthquake Administration, Institute of Engineering Mechanics (2002).

54. Chen W, Men F. Study on FEM to simulate slip and seismic liquefaction of slope-field by theory of two-phased dynamics. *Earthq Eng Eng Vib* (2002) 22(01):132–40. doi:10.13197/j.eeev.2002.01.023

55. Chen W. A direct differential method for nonlinear dynamic response of sand layer under water. *Rock Soil Mech* (2007) 28(s1):698–702. (in Chinese).

56. Li Y. *Analysis on nonlinear ground response in one dimension based on the theory of wave propagation in two-phase media*. [Dissertation thesis]. Harbin: China Earthquake Administration, Institute of Engineering Mechanics (2008).

57. Pujol J. *Elastic wave propagation and generation in seismology*. Cambridge, UK: Cambridge University Press (2003). p. 53–72.

58. Seth S, Michael W. *An introduction to seismology, earthquakes, and earth structure*. Oxford, UK: Blackwell Publishing Ltd (2003). p. 114–64.

59. Philippacopoulos AJ. Waves in a partially saturated layered half-space: analytic formulation. *Bull Seismol Soc Am* (1987) 77(5):1838–53. doi:10.1785/BSSA0770051838

60. Deresiewicz H, Skalak R. On uniqueness in dynamic poroelasticity. *Bull Seismol Soc Am* (1963) 53(4):783–8. doi:10.1785/BSSA0530040783

61. Singh J, Tomar SK. Reflection and transmission of transverse waves at a plane interface between two different porous elastic solid half-spaces. *Appl Math Comput* (2006) 176(1):364–78. doi:10.1016/j.amc.2005.09.027

62. Wu K, Qiang X. Reflection and transmission of elastic waves at the interface of two fluid-saturated, porous media. *J China Univ Sci Technol* (1992) 22(1):44–50. (in Chinese).

63. Gurevich B, Radim C, Denneman AIM. Simple expressions for normal-incidence reflection coefficients from an interface between fluid-saturated porous materials. *Geophysics* (2004) 69:1372–7. doi:10.1190/1.1836811

64. Wang J, Feng J, Zhang C. Reflection and transmission of plane waves at an interface of water/porous sediment with underlying solid substrate. *Ocean Eng* (2013) 63:8–16. doi:10.1016/j.oceaneng.2013.01.028

65. Barak MS, Kumari M, Kumar M. Effect of local fluid flow on the propagation of plane waves at an interface of water/double-porosity solid with underlying uniform elastic solid. *Ocean Eng* (2018) 147:195–205. doi:10.1016/j.oceaneng.2017.10.030

66. Chen W, Jeng D, Zhao H, Chen G, Li X. Motion at surface of a gassy ocean sediment layer induced by obliquely incident P waves. *Ocean Eng* (2018) 149:95–105. doi:10.1016/j.oceaneng.2017.12.005

Appendix

In the 5 × 5 matrices, the elements m_{ij} (i = 1 to 5, j = 1 to 5) and $\overline{m}_{ij}$ (i = 5, j = 1 to 5) are given below:

$$[S_{\text{P-SV}}] = \begin{bmatrix} m_{11} & m_{12} & m_{13} & m_{14} & m_{15} \\ m_{21} & m_{22} & m_{23} & m_{24} & m_{25} \\ m_{31} & m_{32} & m_{33} & m_{34} & m_{35} \\ m_{41} & m_{42} & m_{43} & m_{44} & m_{45} \\ m_{51} & m_{52} & m_{53} & m_{54} & m_{55} \end{bmatrix};$$

$$[\overline{S}_{\text{P-SV}}] = \begin{bmatrix} m_{11} & m_{12} & m_{13} & m_{14} & m_{15} \\ m_{21} & m_{22} & m_{23} & m_{24} & m_{25} \\ m_{31} & m_{32} & m_{33} & m_{34} & m_{35} \\ m_{41} & m_{42} & m_{43} & m_{44} & m_{45} \\ \overline{m}_{51} & \overline{m}_{52} & \overline{m}_{53} & \overline{m}_{54} & \overline{m}_{55} \end{bmatrix}$$

where, $m_{11} = -\left(\lambda'\left(k^{\text{I}}\right)^2 + 2\mu'\left(k_z^{\text{I}}\right)^2\right)$, $m_{12} = 2\mu' k_x^{\text{R}} k_z^{\text{R}}$,

$$m_{13} = \left(\lambda + \frac{1\text{-}n}{n}E_{\text{w}} + \delta_1 E_w\right)\left(k_1^{\text{T}}\right)^2 + 2\mu\left(k_{1z}^{\text{T}}\right)^2,$$

$$m_{14} = \left(\lambda + \frac{1\text{-}n}{n}E_{\text{w}} + \delta_2 E_w\right)\left(k_2^{\text{T}}\right)^2 + 2\mu\left(k_{2z}^{\text{T}}\right)^2,$$

$$m_{15} = 2\mu k_{sx}^{\text{T}} k_{sz}^{\text{T}}, m_{21} = 2\mu' k_x^{\text{I}} k_z^{\text{I}},$$

$$m_{22} = \text{-}\mu'\left(\left(k_x^{\text{R}}\right)^2 \text{-} \left(k_z^{\text{R}}\right)^2\right), m_{23} = 2\mu k_{1x}^{\text{T}} k_{1z}^{\text{T}},$$

$$m_{24} = 2\mu k_{2x}^{\text{T}} k_{2z}^{\text{T}}, m_{25} = \mu\left(\left(k_{sx}^{\text{T}}\right)^2 \text{-} \left(k_{sz}^{\text{T}}\right)^2\right), m_{31} = \text{-}k_x^{\text{I}},$$

$$m_{32} = \text{-}k_z^{\text{R}}, m_{33} = k_{1x}^{\text{T}}, m_{34} = k_{2x}^{\text{T}}, m_{35} = \text{-}k_{sz}^{\text{T}}, m_{41} = k_z^{\text{I}},$$

$$m_{42} = \text{-}k_x^{\text{R}}, m_{43} = k_{1z}^{\text{T}}, m_{44} = k_{2z}^{\text{T}}, m_{45} = k_{sx}^{\text{T}},$$

$$m_{51} = 0, m_{52} = 0, m_{53} = \left(\frac{1\text{-}n}{n} + \delta_1\right)E_{\text{w}}\left(k_1^{\text{T}}\right)^2,$$

$$m_{54} = \left(\frac{1\text{-}n}{n} + \delta_2\right)E_{\text{w}}\left(k_2^{\text{T}}\right)^2,$$

$$m_{55} = 0, \overline{m}_{51} = 0, \overline{m}_{52} = 0, \overline{m}_{53} = (1\text{-}\delta_1)k_{1z}^{\text{T}},$$

$$\overline{m}_{54} = (1\text{-}\delta_2)k_{2z}^{\text{T}},$$

$$\overline{m}_{55} = (1\text{-}\delta_{\text{s}})k_{sx}^{\text{T}}.$$

frontiers | Frontiers in Physics

TYPE Original Research
PUBLISHED 15 July 2025
DOI 10.3389/fphy.2025.1627649

OPEN ACCESS

EDITED BY
Yifei Sun,
Taiyuan University of Technology, China

REVIEWED BY
Xiaodong Ni,
Hohai University, China
Zhigao Dong,
Nanjing Vocational Institute of Railway Technology, China

*CORRESPONDENCE
Xiaosan Tao,
txs3880@126.com

RECEIVED 13 May 2025
ACCEPTED 02 July 2025
PUBLISHED 15 July 2025

CITATION
Tao X and Gao Z (2025) Study on seismic response characteristics of the suction bucket group foundation in liquefiable sites.
Front. Phys. 13:1627649.
doi: 10.3389/fphy.2025.1627649

Study on seismic response characteristics of the suction bucket group foundation in liquefiable sites

Xiaosan Tao* and Zhibing Gao

Jiangsu Earthquake Disaster Risk Mitigation Center (Jiangsu Province Earthquake Engineering Research Institute), Nanjing, China

The multi-suction bucket foundation has the potential to enhance anti-overturning capacity by converting the overturning moment of the entire system into axial push-pull forces of individual buckets. In recent years, offshore wind turbines with multi-bucket suction bucket group foundations have been successively put into production and use in China. However, research addressing the seismic dynamic performance of quad-bucket suction foundations embedded in saturated sandy strata remains scarce. Therefore, studying the seismic dynamic response of suction bucket group foundations is of significant practical importance. Based on the finite-element software OpenSees and focusing on the characteristics of liquefiable sites, this paper establishes a numerical model of a four-bucket suction bucket group foundation in saturated sand using an actual engineering project as the background. Considering the effects of earthquake and sand liquefaction, the seismic dynamic response and displacement variations of the four-bucket foundation in liquefiable sites are investigated. The results show that: under seismic action, the peak horizontal displacement of the suction buckets occurs synchronously with the peak ground acceleration; vertical settlement exhibits nonlinear growth with increasing peak ground acceleration, and differential settlement of the foundation is significantly aggravated in liquefiable sites; the excess pore water pressure ratio γ_u serves as a key index for quantifying soil liquefaction, and when $\gamma_u \geq 1$, the soil inside the buckets is completely liquefied, leading to a sudden drop in foundation bearing capacity.

KEYWORDS

suction bucket group foundation, seismic dynamic response, liquefaction site, influencing factors, OpenSees

1 Introduction

With the global energy transition and intensifying climate change, the development of renewable energy has attracted significant attention. Offshore wind power, due to its vast development potential and abundant resource capacity, has emerged as a research hotspot both domestically and internationally. The multi-suction bucket group foundation, which enhances anti-overturning capacity by converting the system overturning moment into axial push-pull forces on individual buckets, has been progressively implemented in China's offshore wind turbine projects in recent years. However, current research on seismic responses of suction bucket foundations primarily

focuses on single-bucket structures, with limited studies addressing the dynamic characteristics of multi-bucket group foundations. Therefore, investigating the seismic dynamic response of suction bucket group foundations holds substantial academic and engineering significance.

Considering that some offshore wind turbines are constructed in seismically active regions, the seismic response of offshore wind turbine structures is of paramount importance [1]. Wang et al. [2] validated the seismic response characteristics of suction bucket models with varying geometric parameters in saturated sandy soils, demonstrating the reliability of the experimental methodology. Zhu et al. [3] analyzed centrifuge experimental data to investigate the influence of a clay layer underlying sandy strata on the cyclic response of suction buckets. Latini and Zania [4] identified structural configuration as a critical parameter affecting the dynamic response of suction buckets. Bagheri et al. [5] evaluated the bearing performance of bucket foundations under cyclic and monotonic loading conditions through three-dimensional finite element analysis. Zhang et al. [6] performed lateral cyclic loading tests on a centrifuge, documenting pore water pressure accumulation and soil liquefaction tendencies. Faizi [7] proposed a novel triple-bucket jacket foundation, significantly reducing installation cost. Zhang et al. [8] conducted a seismic response analysis of suction bucket foundations in clay deposits.

Earthquake-induced soil liquefaction may induce severe damage to suction bucket structures [9]. Recent studies have primarily focused on the combined effects of seismic and environmental loads on the seismic dynamic response of suction bucket structures, as well as the influence of liquefaction on the stability of bucket foundations [10]. In experimental investigations, Yu et al. [11] examined the seismic response of gravity-based and monopile foundations under both dry and saturated conditions. Lu et al. [12] identified seismic amplitude as the most influential parameter. Wang et al. [2] compared the seismic responses of suction buckets in dry and saturated conditions. In numerical investigations, Negro et al. [9] emphasized the high liquefaction susceptibility of sandy soils. Zhang et al. [13] employed Abaqus to study the seismic response and liquefaction behavior of prestressed bucket foundations. Ding et al. [14] revealed that the soil inside the bucket exhibits enhanced liquefaction resistance due to lateral confinement from the bucket walls. Barari et al. [15] investigated liquefaction effects on monopile foundations. Nicosia [16] identified liquefaction potential at an OWT site in Taiwan using FLAC. Zhang et al. [17] demonstrated that installation velocity has negligible impact on liquefaction susceptibility. Patra and Haldar [18] analyzed the influence of seismic intensity and liquefaction depth on the dynamic response of wind turbine structures. Kazemi Esfeh and Kaynia [19] studied the combined wind and seismic load responses of suction buckets, monopiles, and anchor piles. Wang et al. [20] proposed methodologies to effectively mitigate soil liquefaction hazards.

Although numerous numerical simulations and experimental analyses have been conducted by domestic and international scholars regarding the dynamic response of suction bucket foundations in liquefiable sites under seismic loading, existing research predominantly focuses on the soil liquefaction behavior of single-bucket structures during earthquakes. Currently, limited attention has been paid to investigating the seismic dynamic response of suction bucket group foundations in liquefiable sites, particularly regarding the coupled dynamic behavior between the group foundation structures and surrounding soil. Therefore, it is essential and practically significant to conduct systematic research on the seismic dynamic response of suction bucket group foundations under various influencing factors in liquefaction-prone sites.

In this study, a numerical simulation model of the suction bucket structural system was established using numerical simulation software. Centrifuge tests were simulated and systematically validated through comparative analyses of soil dynamic responses and structural dynamic responses against experimental results. This process determined appropriate constitutive models for both sand and structural components, confirming the feasibility of numerical simulations. Based on practical engineering requirements, a group foundation model of suction buckets was developed using the same numerical simulation platform. The seismic dynamic response characteristics of suction buckets in liquefiable site conditions were thoroughly investigated, revealing the critical influence of soil liquefaction on suction bucket performance. The findings provide valuable insights into the seismic design optimization of suction bucket foundations in liquefaction-prone areas.

2 Numerical model development and validation

2.1 Development of the numerical model

The numerical simulation based on an actual offshore wind turbine structure engineering project. The foundation of the wind turbine employs a suction bucket jacket structure, comprising four suction buckets and an upper jacket structure. The substructure consists of four identical suction buckets, each with a diameter of 9.5 m, featuring a bottom elevation of −27.47 m and a top elevation of −19.0 m. The center-to-center distance between each suction buckets measures 20 m. The upper jacket structure, with its base rigidly connected to the suction bucket tops, extends to a top elevation of 17 m. A 1-m-high platform was installed atop the jacket structure, with the wind turbine concentrically positioned above this platform. The geometric configuration of the suction buckets was shown in Figure 1a.

According to the engineering geological data, the soil layers at this site are primarily composed of the following three strata: Silty Sand A: Grayish-black in color, saturated, medium-dense, with relatively pure sandy composition. The particles are uniform in size and exhibit fair gradation. This layer is interbedded with thin layers of silt, showing relatively homogeneous soil properties, with a thickness of 3.4 m. Silty Sand B: Grayish-yellow in color, saturated, dense, containing relatively pure sandy material. The particles demonstrate uniformity in size and moderate gradation, presenting generally consistent soil characteristics. The layer thickness measures 6 m. Silty Sand C: Gray/yellow in color, saturated, characterized as medium compressibility soil with favorable engineering properties. This stratum has a thickness of 8.8 m. The physical and mechanical parameters of each soil type were summarized in Table 1.

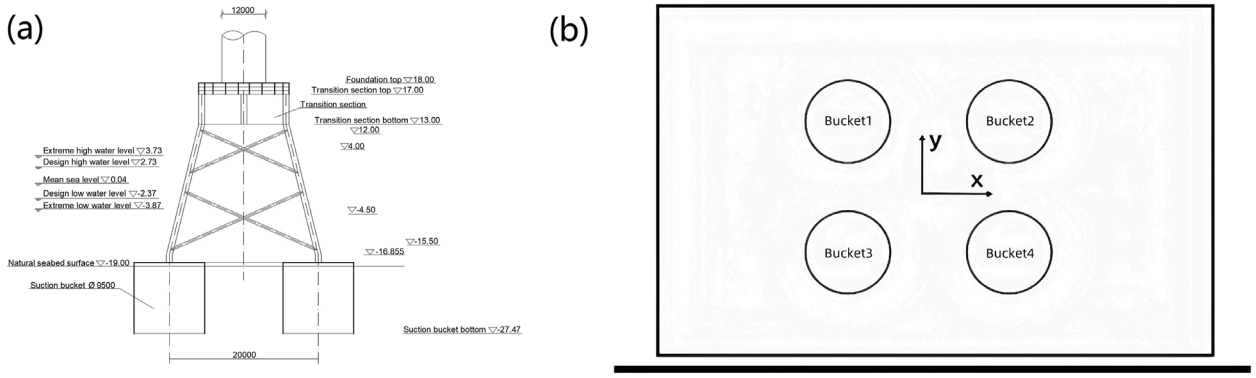

FIGURE 1
(a) Geometric model of suction bucket, **(b)** Top view of the numbering of suction buckets.

TABLE 1 Geological data.

Layer no.	Saturated density (kg/m^3)	Reference shear modulus (kPa)	Reference bulk modulus (kPa)	Cohesion (kPa)	Friction Angle (°)	Layer thickness (m)
Silt A	1700	60	127	0	29	3.4
Silt B	1800	63	189	0	24	6
Silt C	1950	150	437	0	37	8.8

The soil model has a width of 60 m and a length of 100 m. The four suction buckets were sequentially numbered in a clockwise manner according to the plan view, designated as Bucket1, Bucket2, Bucket3, and Bucket4 respectively. Subsequent analyses in this paper will consistently refer to these numerical designations. The spatial arrangement of the numbered suction buckets in the plan view was shown in Figure 1b.

Based on practical engineering parameters of suction bucket foundation structures, the connection between suction buckets and jacket structures was established through a rigid coupling. The inter-tier bracing connections within the jacket structure were modeled using the two NodeLinkMaterial constitutive model from OpenSees. The superstructure platform and wind turbine components were constructed using concrete materials. In numerical simulations, the upper wind turbine structure was simplified as a cylindrical thick pile with equivalent height characteristics. This simplified model incorporates the turbine's self-weight and specified environmental loads to realistically simulate the combined effects of operational loading and seismic actions transmitted to the substructure under actual service conditions.

This study focuses on the seismic sensitivity analysis of suction bucket group foundations under earthquake conditions. The structural models of the suction bucket foundation and group foundation configuration are shown in Figure 2. To better simulate the actual superstructure conditions of wind turbines, a wind turbine tower of defined height was incorporated into the platform model. The turbine assembly was simplified as a spherical mass element, with the total mass of the wind turbine system set at 200 metric tons.

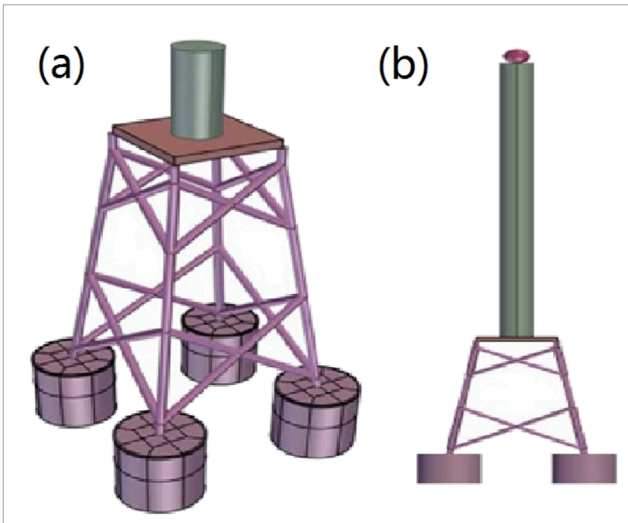

FIGURE 2
Offshore wind power foundation computational model **(a)** structural model of suction bucket, **(b)** front view of numerical model.

To numerically simulate the dynamic response of saturated sand under seismic loading, this study employs OpenSees [21], a renowned analysis platform in earthquake engineering research.

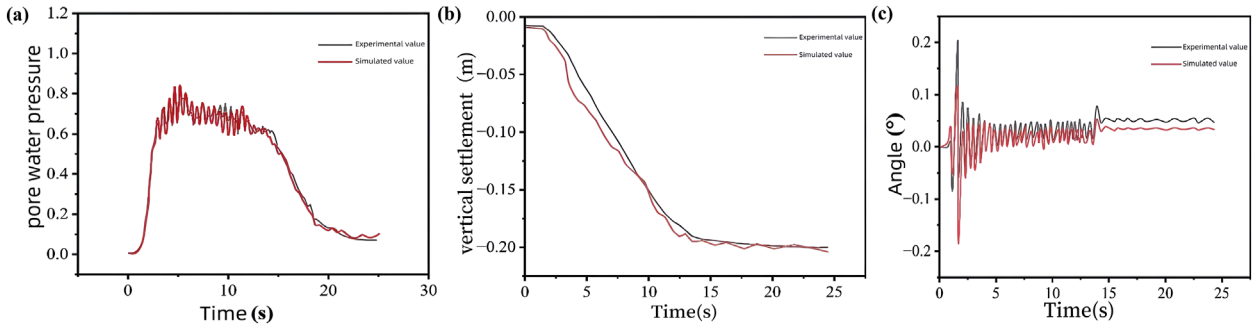

FIGURE 3
(a) Experimental and simulated values of **(a)** pore water pressure, **(b)** vertical settlement, and **(c)** angle.

The soil constitutive model adopts the PressureDependMultiYield material, an elasto-plastic formulation that incorporates confining pressure effects and effectively captures the nonlinear stress-strain behavior of soils. The material parameters for numerical analysis were determined through comprehensive consideration of: fundamental physical properties including relative density and shear wave velocity documented in seismic centrifuge test reports for offshore wind turbine suction bucket foundations; recommended values from the constitutive model developers Yang et al. [22]; and similarity theory principles. This integrated approach ensures the accurate characterization of soil behavior while maintaining consistency with experimental observations and theoretical frameworks.

2.2 Validation of numerical model

Currently, few studies have investigated the seismic dynamic response of suction bucket group foundations in liquefiable sites, with particularly limited research on the coupled seismic behavior of both foundation structures and surrounding soil. To validate the reliability of the numerical simulation model developed in this study, we first established a computational model based on the seismic centrifuge test parameters of offshore wind turbine suction bucket foundations reported by Xuefei Wang et al. [2], including structural configuration and soil properties. Comparative analysis between numerical simulations and experimental observations reveals that the simulated pore water pressure buildup closely matches the experimental data obtained from the centrifuge tests. The numerical simulation results exhibited slightly higher initial vertical settlement of the superstructure compared to experimental measurements, which can be attributed to the idealized soil modeling approach. In reality, soil densification during bucket installation might reduce initial settlement, though the final settlement magnitudes under seismic loading showed good agreement with experimental results. Both numerical simulations and experimental measurements demonstrated comparable structural rotations that were substantially below the critical thresholds specified in relevant design codes. These comparisons confirm the reliability of the suction bucket foundation modeling methodology presented in this study. The quantitative comparisons between numerical and experimental results are graphically shown in Figures 3a–c.

3 Study on seismic response characteristics of the suction bucket group foundation in liquefiable sites

3.1 Liquefaction identification

In engineering, soil liquefaction refers to the phenomenon where originally solid soil transforms into a liquid state or exhibits viscous, fluid-like behavior under seismic action. This geotechnical failure mechanism predominantly occurs in saturated, loose, fine-grained sands or silty sands.

The excess pore water pressure ratio γ_u serves as a common evaluation criterion for assessing sandy soil liquefaction. This ratio is determined by comparing the maximum effective stress (σ_{max}) during seismic action with the average effective stress (σ_0) under initial conditions. When γ_u does not exceed the critical excess pore water pressure ratio γ_{ue}, the soil retains sufficient residual effective stress to prevent liquefaction. A γ_u value of 1 indicates complete liquefaction, signifying zero effective stress within the soil during seismic events. In the transitional range where $\gamma_{ue} < \gamma_u < 1$, the magnitude of γ_u exhibits an inverse correlation with residual effective stress - higher γ_u values correspond to diminished residual effective stress and consequently greater liquefaction severity.

$$\gamma_u = 1 - \frac{\sigma_{max}}{\sigma_0} \tag{1}$$

where γ_u represents the excess pore water pressure ratio under seismic loading, σ_{max} denotes the maximum effective stress during earthquake action, σ_0 indicates the average effective stress in the initial state.

Based on the soil layer information provided in Table 1, the average effective stress σ_0 under initial conditions can be calculated using Equation 2.

$$\sigma_0 = \sigma_{01} + \sigma_{02} + \sigma_{03} \tag{2}$$

where σ_{01} denotes the initial effective stress of the first soil layer, σ_{02} represents the initial effective stress of the second soil layer, σ_{03}

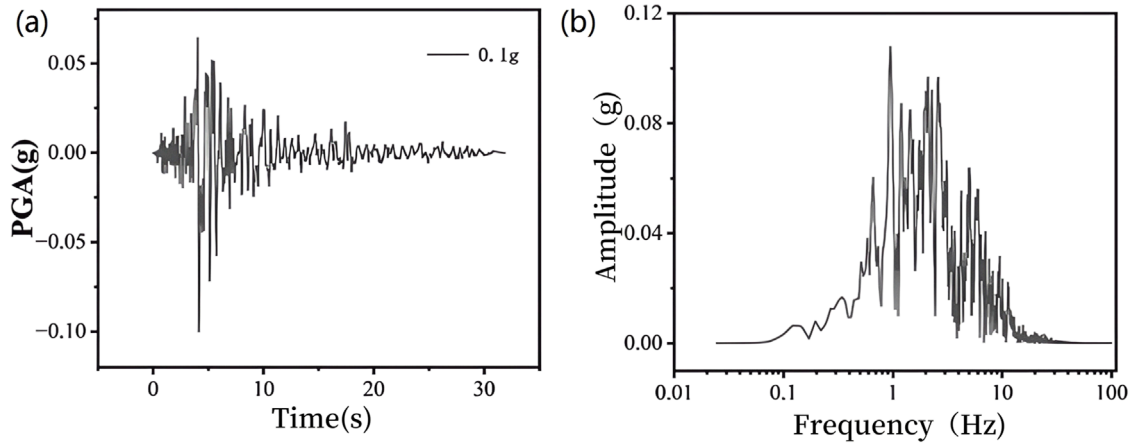

FIGURE 4
(a) Seismic wave, **(b)** seismic spectrum.

indicates the initial effective stress of the third soil layer, σ_{01}, σ_{02}, and σ_{03} can be obtained using Equations 3–5, respectively.

$$\sigma_{01} = Y'_1 \times H_1 \tag{3}$$

$$\sigma_{02} = Y'_2 \times H_2 \tag{4}$$

$$\sigma_{03} = Y'_3 \times H_3 \tag{5}$$

where Y'_1, Y'_2 and Y'_3 represent the buoyant unit weights of the first, second, and third soil layers, respectively; H_1, H_2 and H_3 denote the thicknesses of the first, second, and third soil layers, respectively. Based on the maximum effective stress obtained from numerical calculations, the excess pore pressure ratio γ_u can be determined using Equation 1.

Prior to conducting numerical calculations, a static analysis of the suction bucket foundation within the target soil stratum was performed to obtain the initial stress field of the soil mass.

The selected seismic event was the Parkfield-02. CA earthquake. In accordance with the seismic fortification intensity requirements of the project, the seismic wave was scaled to a peak ground acceleration (PGA) of 0.1 g and applied to the numerical model. The input seismic wave comprise horizontal seismic components exclusively along the west-east (x) direction. The directional relationship between seismic wave propagation and suction bucket foundation orientation is schematically illustrated in Figure 1b. All subsequent seismic inputs maintain this consistent orientation throughout the study. The scaled Parkfield-02. CA seismic wave with 0.1 g PGA and its corresponding fourier amplitude spectrum are shown in Figures 4a,b, respectively.

3.2 Dynamic response of foundation and soil

Figure 5a shows the time-history curves of acceleration responses across different soil layers. As shown in figure, with increasing depth of the soil layer in the model, the saturated density of the soil gradually rises. This enhanced density results in a reduced acceleration amplification coefficient, consequently leading to progressive attenuation of soil acceleration. Although the peak acceleration values of various soil layers occur at similar time instances, they exhibit distinct magnitudes in their peak amplitudes.

A soil layer point with a thickness of 0.5 m inside the suction bucket was selected to analyze the post-seismic pore water pressure. As shown in Figure 5b, the pore water pressure within each suction bucket progressively increases during seismic loading and gradually returns to its initial state following earthquake termination. During the initial phase of seismic excitation, negative pore water pressure emerges in the internal soil of the suction bucket. This phenomenon occurs due to the structural constraints of the suction bucket that prevent immediate drainage of the sheared sand within the bucket, thereby restricting volumetric expansion. As shear deformation continues, water expulsion becomes feasible through the lower section of the suction bucket, leading to subsequent pore water pressure accumulation and the generation of positive pore water pressure. Under the 0.1 g horizontal Parkfield-02. CA ground motion, the maximum pore water pressure recorded at the 0.5 m depth within the suction bucket reaches approximately 180 kPa, which remains insufficient to induce complete liquefaction. Figure 6 shows contour plots comparing the pore water pressure distributions before and during the seismic event.

To investigate the seismic response characteristics of suction bucket foundations, this section focuses on analyzing the horizontal displacement and vertical settlement of suction buckets. A comparative analysis was conducted on the time-history variations of horizontal displacement and vertical settlement for each suction bucket under seismic excitation. Figure 7a shows the time-history variation of horizontal displacement for each suction bucket under the 0.1 g Parkfield-02. CA seismic wave input. As shown in figure, Buckets 1 and 2 exhibit nearly identical horizontal displacement trends, while similar consistency is observed between Buckets 3 and 4. The substantial relative displacements between suction buckets in liquefiable sites may potentially induce damage to connections in the upper truss structure. The horizontal displacement patterns of all suction buckets demonstrate synchronized variations

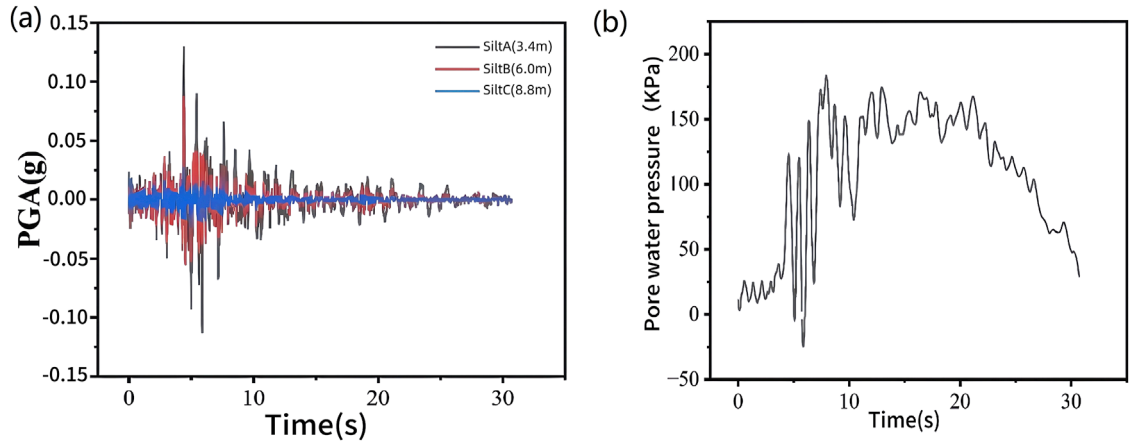

FIGURE 5
(a) Acceleration time history of soil mass, **(b)** pore water pressure.

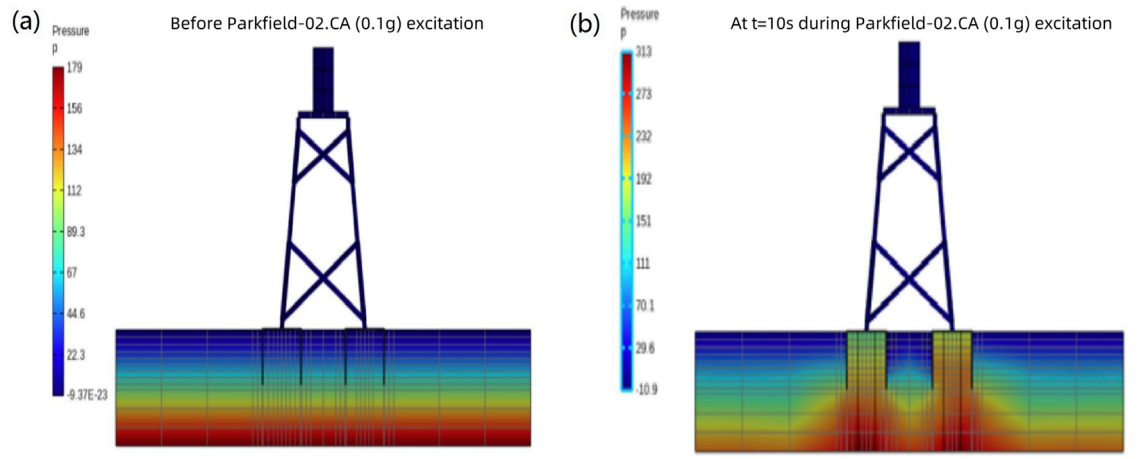

FIGURE 6
Pore water pressure cloud map **(a)** before the earthquake, **(b)** during the earthquake.

with the seismic wave, reaching peak values concurrently with maximum seismic acceleration rather than attaining maximum displacement at seismic termination. Therefore, subsequent studies on suction bucket safety under seismic conditions should prioritize the maximum displacement during seismic events rather than relying solely on residual displacement at motion cessation.

Figure 7b shows the time history of vertical settlements for each suction bucket under the Parkfield-02. CA seismic wave (PGA = 0.1 g). As shown in figure, the vertical settlements of all suction buckets initially exhibit rapid growth during seismic vibration, followed by gradual stabilization after reaching specific thresholds, ultimately maintaining relatively constant values until the earthquake termination. The significantly larger vertical settlements observed across all suction buckets can be attributed to varying degrees of soil liquefaction occurring in the underlying liquefiable site during seismic action. The maximum total settlement of the suction bucket foundation manifests at the conclusion of seismic loading, whereas the peak differential settlement emerges during the earthquake propagation process.

Figure 7c shows the time histories of rotation angles for each suction bucket under the Parkfield-02. CA seismic wave excitation (PGA = 0.1 g). As shown in figure, the rotational variations of all buckets exhibit negligible magnitudes, with peak rotation angles reaching approximately 0.001°, which remains substantially below the code-specified limit value. Consequently, the rotational behavior of suction buckets will not be incorporated into subsequent investigations concerning liquefiable site conditions.

4 Analysis of influencing factors

4.1 Effect of peak ground acceleration

In the study of the influence of peak ground acceleration (PGA) on suction bucket group foundations, the Parkfield-02. CA ground

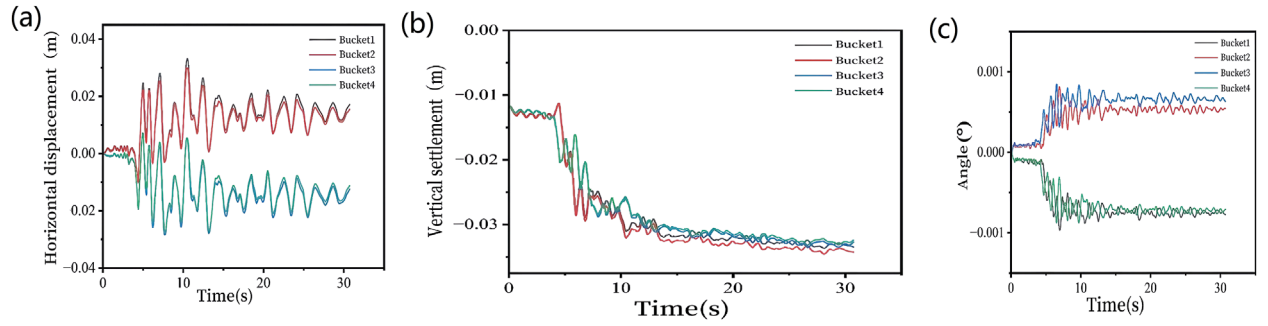

FIGURE 7
(a) Horizontal displacement of each suction bucket, **(b)** vertical settlement of each suction bucket, and **(c)** suction bucket angle.

motion was selected and scaled to 0.1, 0.15, 0.2, 0.25, 0.3, and 0.4 g. To evaluate the liquefaction extent and distribution within the bucket soil, the maximum pore water pressure was measured at 1-m intervals inside the bucket. The excess pore water pressure ratio γ_u was calculated using Equation 1. Envelope curves illustrating the variation of γ_u with soil depth for buckets 2 and 3 under different PGA levels of the Parkfield-02. CA ground motion were plotted. As shown in Figures 8a,b, the excess pore water pressure ratio γ_u in the bucket soil progressively increases with higher PGA levels, indicating an escalation in soil liquefaction severity. When PGA <0.3 g, the γ_u values in Buckets 2 and 3 remain below 1, demonstrating incomplete soil liquefaction. However, at PGA = 0.4 g, γ_u exceeds 1 in both buckets, signifying complete liquefaction. The analysis reveals minimal variation in liquefaction severity across different soil depths within the buckets. Notably, γ_u decreases with increasing soil depth, suggesting that upper soil layers exhibit greater susceptibility to liquefaction compared to deeper strata.

Figures 8c,d and Figures 9d,e respectively show the simulated horizontal displacements and vertical settlements of Buckets 2 and 3 under Parkfield-02. CA ground motion inputs with different peak accelerations. As illustrated, both horizontal displacements and vertical settlements of suction buckets in liquefiable sites progressively amplify with increasing ground motion acceleration amplitude. The maximum horizontal displacements consistently coincide with peak ground acceleration occurrences during seismic events, while vertical settlements exhibit rapid escalation when seismic acceleration attains peak values. As peak acceleration intensifies, varying degrees of liquefaction gradually develop and continuously expand in both internal and external soils surrounding the suction buckets. This liquefaction phenomenon induces partial loss of soil bearing capacity and expansion of interparticle pore spaces (ultimately amplifying horizontal displacements), coupled with progressive reduction of soil foundation stress (driving continual settlement of foundations). Notably, settlement magnitudes display no stabilization tendency upon cessation of ground motion excitation but rather manifest a persistent trend toward continued subsidence.

Based on the bar charts shown in Figures 9a,b illustrating the maximum horizontal displacements and maximum vertical settlements of Buckets 2 and 3 under different peak ground acceleration (PGA) levels, the growth of maximum horizontal displacements and maximum vertical settlements for all suction buckets exhibits a direct proportionality to the PGA. Under liquefiable site conditions where soil liquefaction may occur, notable differences in maximum horizontal displacements between Buckets 2 and 3 emerge under varying seismic amplitudes: the maximum horizontal displacements of Bucket 2 exhibit progressive escalation from 0.026 m at 0.1 g PGA to 0.111 m at 0.4 g PGA, while Bucket 3 displays an increase from 0.020 m to 0.108 m under equivalent excitations, with the maximum differential displacement reaching 0.003 m at 0.4 g PGA. Under progressive PGA amplification, the degree and extent of soil liquefaction inside and around the suction bucket progressively intensify, resulting in a corresponding reduction in the bearing capacity of the surrounding soil; this mechanism induces differential amplification of peak horizontal displacements between Buckets 2 and 3, thereby generating relative horizontal displacements that necessitate special attention to the connection integrity of upper truss structures and require structural reinforcement measures to enhance stability. Furthermore, since the vertical settlements of the buckets under different PGA levels follow similar variation trends with ground motion duration, assessing the differential settlement characteristics across the entire suction bucket foundation becomes essential when investigating structural stability.

The differential settlement under various working conditions was calculated by determining the displacement differences between individual buckets at different peak accelerations. As shown in Figure 9c, the differential settlement of the suction bucket foundation demonstrates a progressive increase with higher peak ground acceleration (PGA) of seismic motions. Notably, the maximum differential settlement occurred during the seismic event rather than at its conclusion. When the seismic acceleration reached its peak value, the differential settlement between buckets simultaneously attained maximum values. The results indicate a positive correlation between PGA magnitude and the induced differential settlement, where greater seismic accelerations produce more pronounced uneven settlement. This phenomenon may pose significant adverse effects on structural stability, particularly under high-intensity seismic conditions.

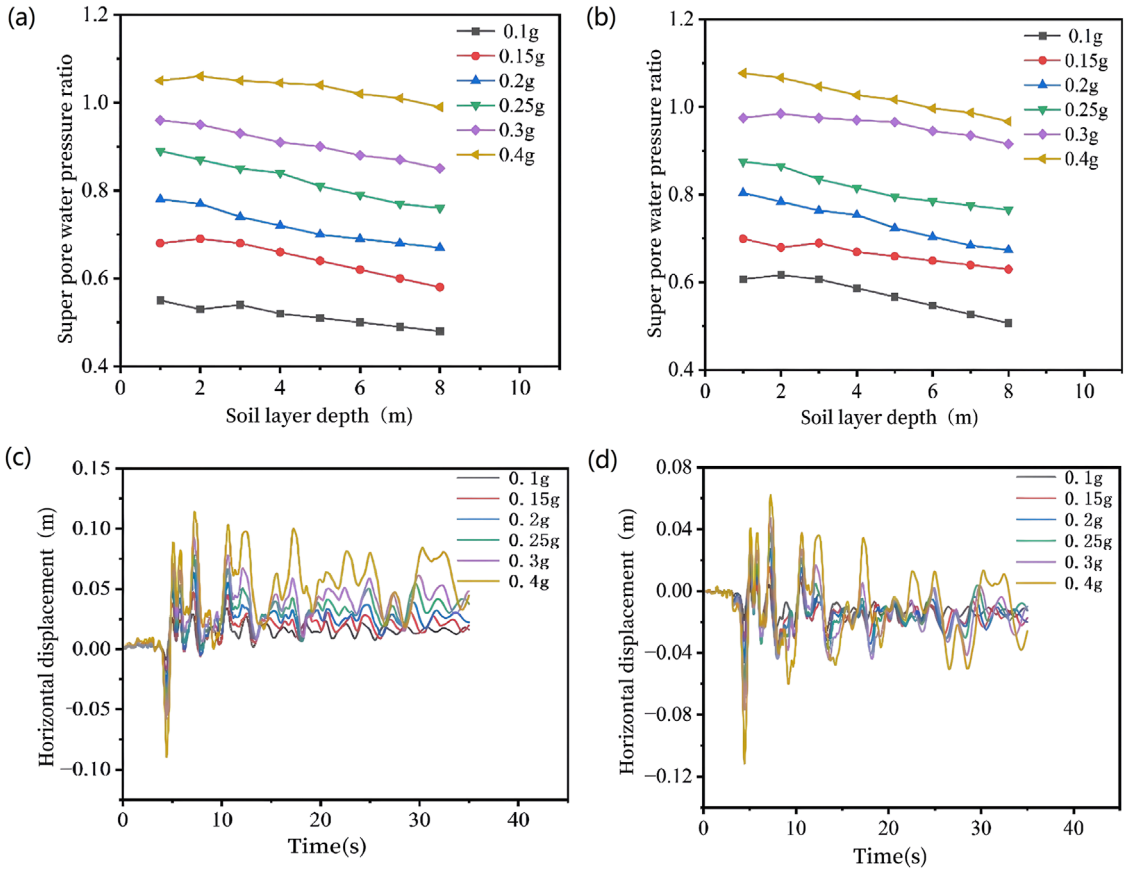

FIGURE 8
Excess pore water pressure ratio envelope diagram **(a)** Bucket 2, **(b)** Bucket 3 and horizontal displacement **(c)** Bucket 2, **(d)** Bucket 3.

4.2 Effects of ground motion spectral characteristics

When investigating the influence of seismic ground motion spectral characteristics on the seismic performance of suction bucket foundations, four earthquake records with distinct spectral differences were selected: Parkfield-02. CA, Irpinia, Whittier, and ChiChi. As established in the previous section, the soil within each bucket of the suction bucket foundation undergoes complete liquefaction when the peak ground acceleration (PGA) reaches 0.4 g. This section employs ground motions with different response spectra but identical amplitude (PGA = 0.4 g) to better observe the effects of soil liquefaction in individual buckets on foundation behavior under varying seismic spectral characteristics. Figures 10a,b show the scaled peak ground accelerations and fourier amplitude spectra of the four amplitude-adjusted seismic waves.

To evaluate the liquefaction degree and distribution range of soil within suction buckets, the maximum pore water pressure was measured at 1-m intervals. The excess pore water pressure ratio γ_u was calculated using Equation 1, and envelope diagrams illustrating the variation of γ_u with soil depth under different seismic motion spectral characteristics were plotted for Buckets 2 and 3, as shown in Figures 11a,b. The maximum γ_u values exhibited significant variations among buckets under different seismic spectral characteristics. Notably, the Parkfield-02. CA motion induced generally lower γ_u values, whereas the ChiChi motion resulted in significantly higher ratios. This discrepancy is attributed to the substantial spectral energy and high energy density of the ChiChi earthquake, which enhanced both the liquefaction degree and affected zone within the buckets. Both Buckets 2 and 3 demonstrated maximum γ_u values exceeding 1 under all examined seismic spectral conditions, indicating complete liquefaction of the contained soil. Under identical seismic peak acceleration inputs, the excess pore water pressure ratio γu of the soil inside the bucket continuously decreases with increasing soil depth, leading to a reduction in soil liquefaction degree. However, soils exhibit a higher likelihood of liquefaction when subjected to ground motions characterized by greater spectral energy intensity.

Figures 11c,d show the horizontal displacements of suction Buckets 2 and 3 under different ground motion inputs, while Figures 12d,e show the vertical settlement time histories of suction Buckets 2 and 3 under four ground motions with distinct spectral characteristics. As shown in these figures, significant variations in both horizontal displacements and vertical settlements are observed among the suction buckets when subjected to ground motions with distinct spectral characteristics. The acceleration time histories and Fourier amplitude spectra differ

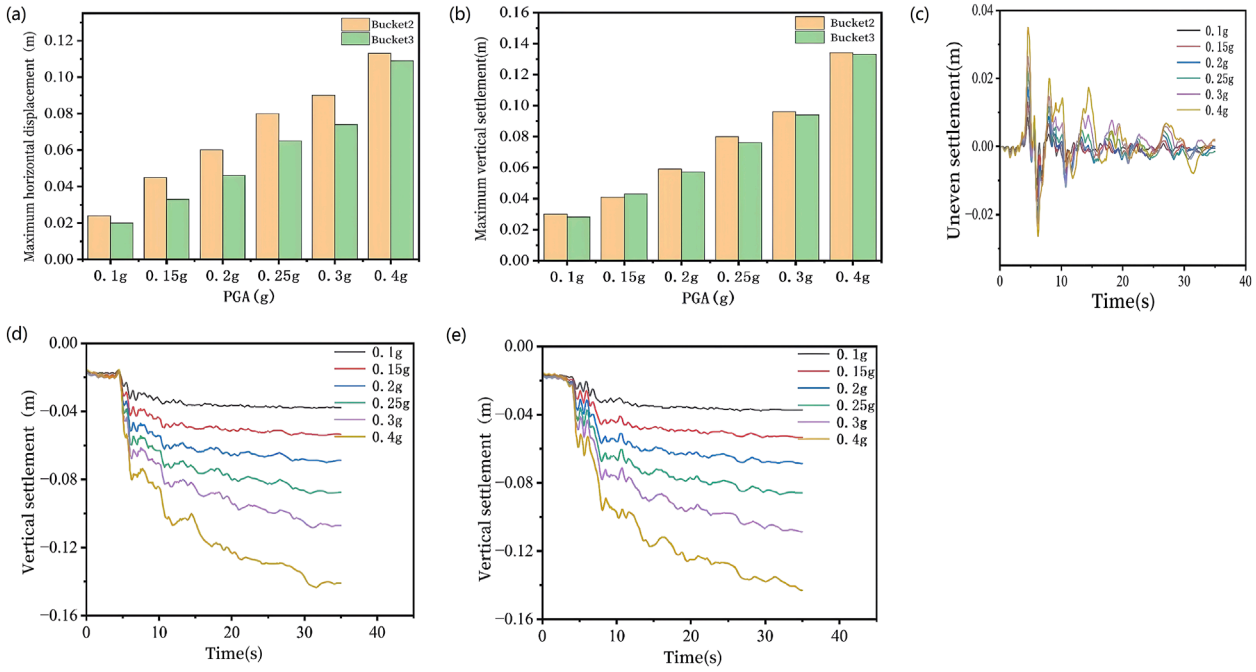

FIGURE 9
(a) Histogram of maximum horizontal displacement, **(b)** histogram of maximum vertical settlement, **(c)** inhomogeneous settlement, and vertical settlement **(d)** Bucket 2, **(e)** Bucket 3.

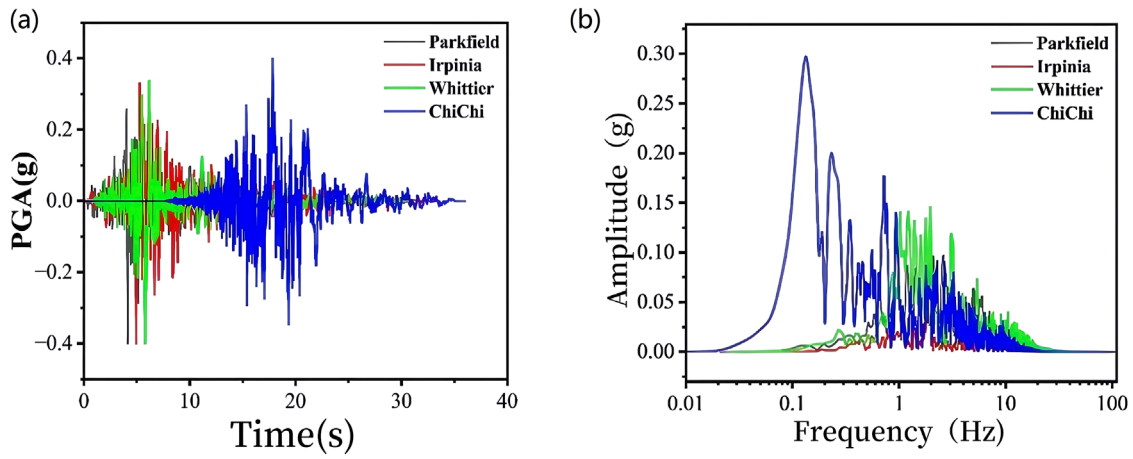

FIGURE 10
(a) Seismic acceleration, **(b)** Fourier amplitude spectrum.

among the four seismic waves, with the ChiChi ground motion deviating significantly from the other three. It exhibits lower energy and smoother waveforms in the initial phase, but higher energy and denser waveforms in the middle-to-late phases. Consequently, both the degree and spatial extent of soil liquefaction within the suction bucket are more extensive. Specifically, the horizontal displacements and vertical settlements of Buckets 2 and 3 under the ChiChi ground motion exhibit substantially smaller values compared to those induced by the other three seismic waves during the initial phase of shaking, while significantly exceeding them during the middle and later stages. This phenomenon can be attributed to the concentrated energy distribution and higher energy intensity inherent in the ChiChi ground motion, which consequently generates the largest maximum horizontal displacement. As the ground motion progresses, all buckets demonstrate continuously increasing vertical settlement. This observation indicates that ground motions with higher seismic spectral energy and greater energy density induce larger displacements in suction bucket group foundations. Given that all input ground motions maintain identical peak accelerations of 0.4 g, resulting in complete liquefaction

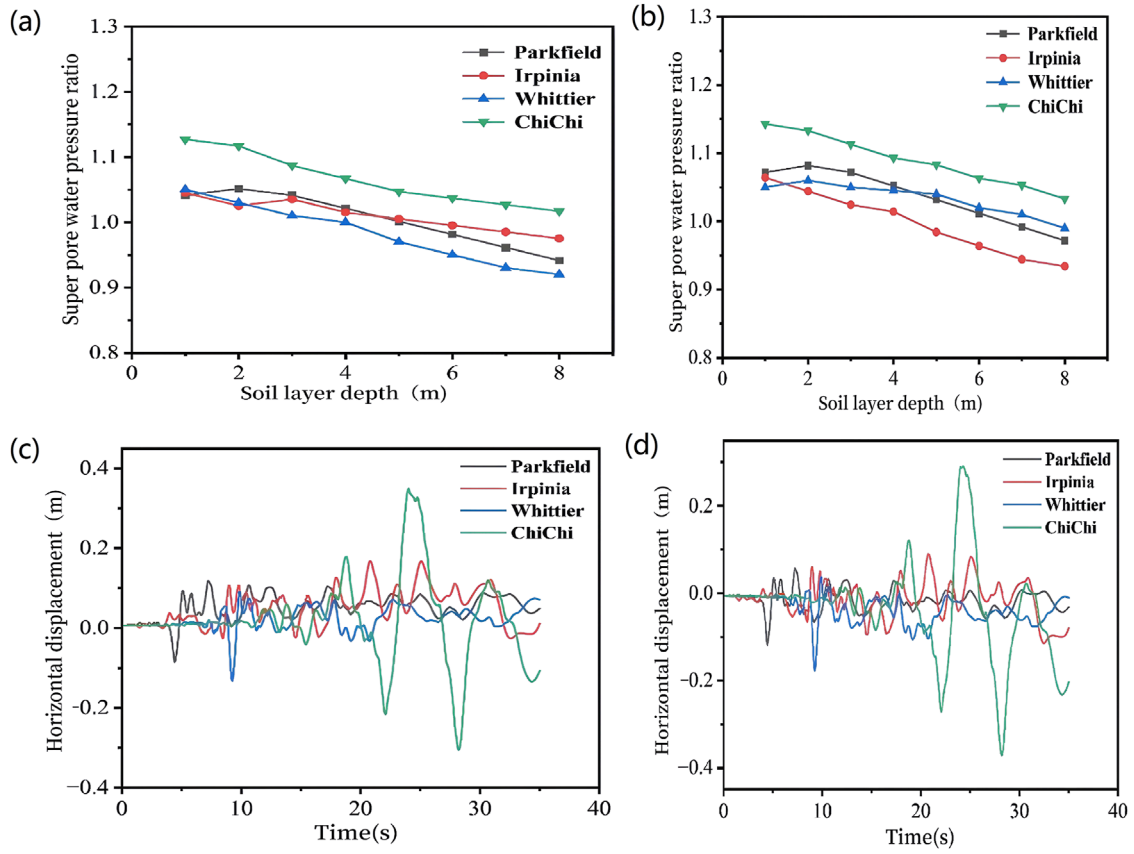

FIGURE 11
Excess pore water pressure ratio envelope diagram **(a)** Bucket 2, **(b)** Bucket 3, and horizontal displacement **(c)** Bucket 2, **(d)** Bucket 3.

of the soil within each bucket, the settlement demonstrates a persistent post-seismic continuation trend after ground motion cessation.

The bar charts illustrating the maximum horizontal displacements of Buckets 2 and 3 under seismic motions with different spectral characteristics and the maximum vertical settlements are shown in Figures 12a,b, respectively. Analysis reveals that the maximum horizontal displacements and maximum vertical settlements of the buckets vary significantly with the spectral characteristics of input ground motions. Notably, ground motions characterized by higher energy content and densely concentrated waveforms tend to generate substantially greater maximum horizontal displacements. Although ground motions with varying spectral properties induce distinct maximum displacements in individual buckets, Buckets 2 and 3 exhibit minimal differences in their maximum horizontal displacements and vertical settlements. This observed similarity is attributed to the symmetric load configuration and the exclusive application of ground motions along the horizontal X-direction, resulting in comparable displacement magnitudes between these two buckets.

Figures 12c shows the differential settlement values under various working conditions obtained through difference calculations of settlement displacement data for suction buckets under ground motions with different spectral characteristics. As shown in figure, the input ground motions with distinct seismic spectral characteristics yield different differential settlement curves for the suction bucket foundation. The ChiChi ground motion exhibits lower energy and gentler waveform characteristics during the initial seismic phase, while demonstrating higher energy and closely spaced waveform patterns during the mid-to-late seismic phase. Consequently, under the ChiChi seismic spectrum characteristics, the differential settlement between Buckets 2 and 3 during the initial earthquake phase was significantly smaller compared to the other three seismic waves. However, during the mid-to-late seismic phase, the oscillation amplitude of differential settlement substantially exceeded that observed under the other three seismic wave conditions.

4.3 Effects of site soil layer liquefaction on foundation displacement

As analyzed in the preceding two sections, the influence of peak ground acceleration (PGA) on soil liquefaction in liquefiable strata significantly outweighs that of ground motion spectral characteristics. This section comparatively examines the displacement patterns of suction bucket foundations in both liquefiable and non-liquefiable sites under Parkfield-02. CA seismic motions with PGAs of 0.1, 0.2, and 0.4 g. For computational

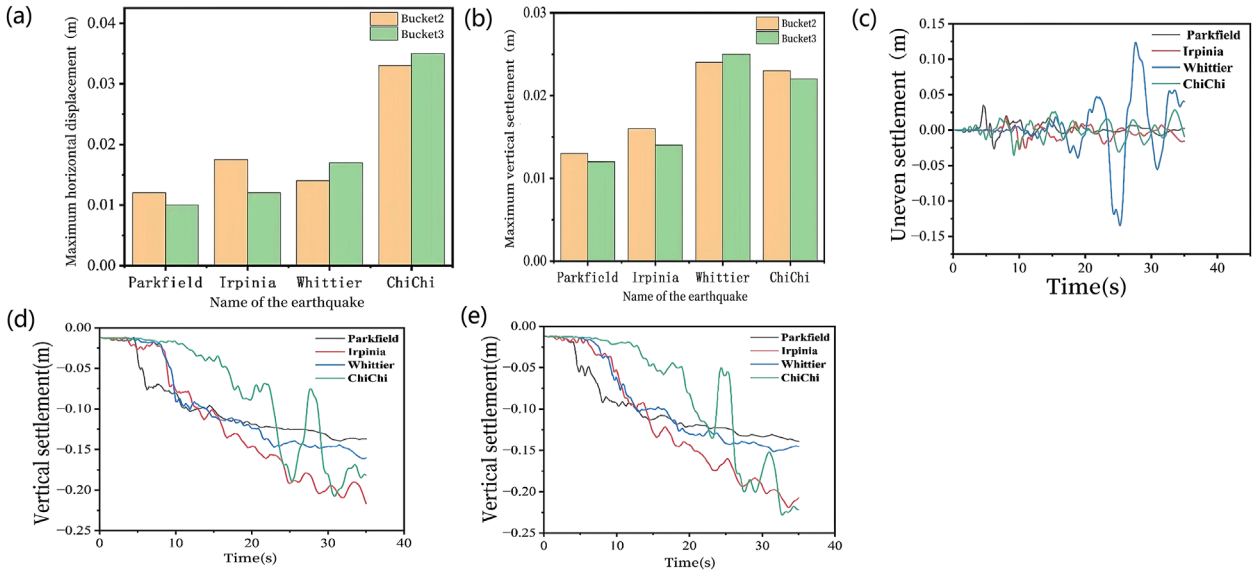

FIGURE 12
(a) Histogram of maximum horizontal displacement, **(b)** histogram of maximum vertical settlement, **(c)** inhomogeneous settlement, and vertical settlement **(d)** Bucket 2, **(e)** Bucket 3.

simplification, bucket No.1 has been selected as the representative subject for this comparative investigation.

Figures 13a–c shows the time-history curves of horizontal displacement for suction bucket foundations in both liquefiable and non-liquefiable sites under Parkfield-02. CA ground motions with varying peak accelerations. As shown in figure, the horizontal displacements of suction buckets in liquefiable and non-liquefiable sites demonstrate negligible differences under 0.1 g peak ground acceleration (PGA). During the initial phase of ground motion, the horizontal displacements in both site conditions remain nearly identical, with minor discrepancies emerging in the later stages of shaking. When the PGA increases from 0.1 g to 0.2 g, a noticeable disparity in horizontal displacements between the two site conditions becomes evident. As the PGA further escalates to 0.4 g, extensive soil liquefaction occurs within the suction bucket embedded in the liquefiable site. This progressive liquefaction directly results in substantial differential horizontal displacements between the two foundation conditions. Specifically, the complete liquefaction of a significant soil portion inside the suction bucket under liquefiable site conditions critically amplifies displacement contrasts compared to its non-liquefiable counterpart.

Figures 13d–f shows the time-history curves of vertical settlement for the suction bucket foundation in both liquefiable and non-liquefiable sites under Parkfield-02. CA ground motions with different peak ground accelerations (PGA). As shown in figure, when subjected to a PGA of 0.1 g, the maximum vertical settlements of the suction bucket foundation show negligible differences between liquefiable and non-liquefiable sites. As the PGA increases to 0.2 g, the discrepancy in vertical settlement displacements between the two site conditions becomes more pronounced. When the PGA reaches 0.4 g, extensive soil liquefaction occurs within the suction bucket foundation in the liquefiable site, resulting in the maximum difference in vertical settlement displacements between the two site conditions. Soil liquefaction significantly impacts structural settlement behavior, generating notable vertical settlement differences between the two site conditions. The maximum vertical settlement displacement difference is observed at the conclusion of the seismic event.

The maximum horizontal displacements and vertical settlements of suction buckets in both liquefiable and non-liquefiable sites under varying peak ground accelerations (PGA) are systematically shown in Figure 14. As the PGA increases, the differential values of horizontal displacement and vertical settlement between suction buckets embedded in liquefiable and non-liquefiable sites exhibit a progressive enlargement. This phenomenon can be attributed to the intensified liquefaction severity and expanded liquefaction zones within the soil surrounding suction buckets in liquefiable sites under elevated PGA, which substantially compromise the horizontal and vertical stability of the suction bucket foundations.

5 Conclusion

This study investigates the seismic response characteristics of suction bucket group foundations in the liquefiable sites. Through the development of numerical models and multi-parametric analysis, the research systematically examines the influence of ground motion parameters on the dynamic response of foundations. The principal research findings are summarized as follows:

(1) Under seismic loading, the pore water pressure within the soil inside the suction bucket initially exhibits transient negative values due to shear-induced contraction effects, subsequently shifting to positive pore water pressure as drainage conditions improve. The excess pore water pressure ratio (γ_u) serves as an effective indicator for quantifying the degree of

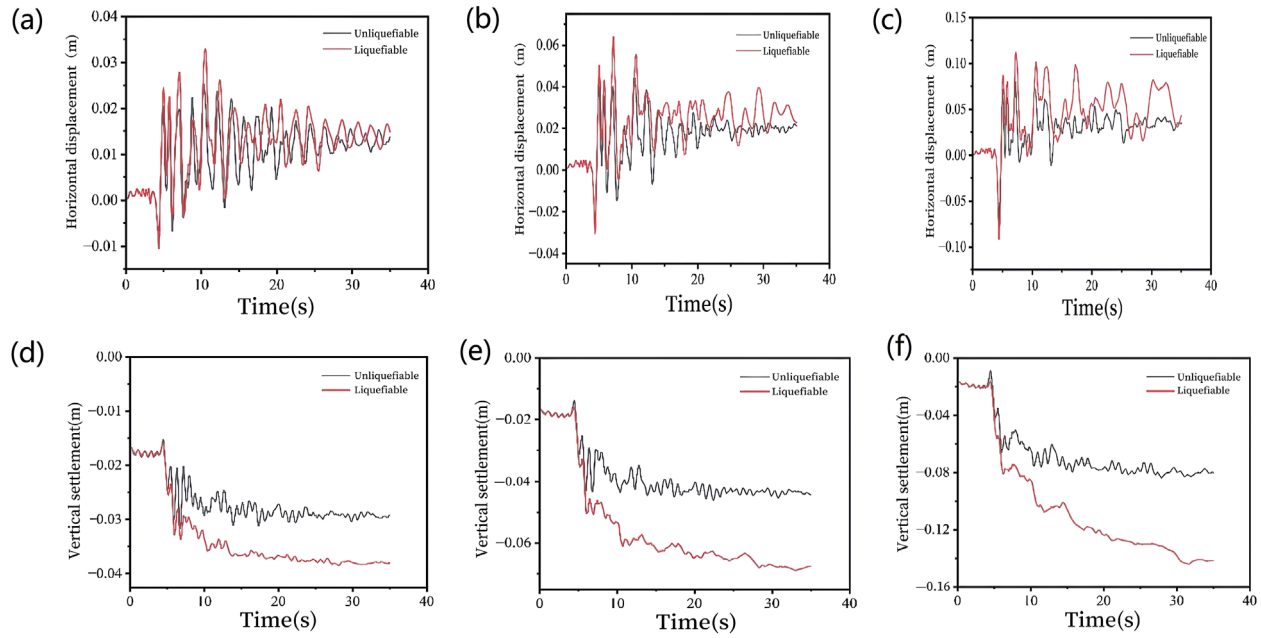

FIGURE 13
Horizontal displacement under both sites **(a)** 0.1 g, **(b)** 0.2 g, **(c)** 0.4 g, and Vertical displacement under two kinds of sites **(d)** 0.1 g, **(e)** 0.2 g, **(f)** 0.4 g.

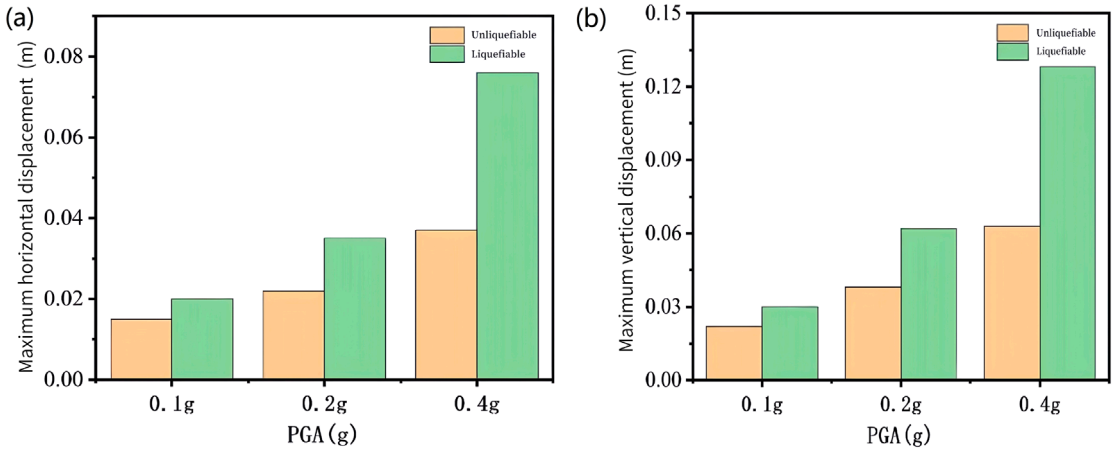

FIGURE 14
Maximum displacement under both sites **(a)** Horizontal displacement, **(b)** Vertical settlement.

soil liquefaction. When $\gamma_u \geq 1$, the soil inside the bucket becomes fully liquefied, resulting in significant reduction in bearing capacity.

(2) The horizontal displacement and vertical settlement of the suction bucket group foundation exhibit distinct patterns under seismic loading, accompanied by the presence of differential settlement. Each suction bucket demonstrates similar variation trends in horizontal displacement corresponding to seismic wave fluctuations, with peak displacements coinciding temporally with maximum seismic accelerations. The maximum overall settlement of the suction bucket group foundation occurs at the earthquake termination phase, while the most severe differential settlement manifests during the seismic excitation process.

(3) The peak ground acceleration (PGA) exhibits a proportional relationship with the horizontal displacement, vertical settlement, and differential settlement of suction bucket foundations. As the PGA increases, these deformation parameters demonstrate corresponding growth. As PGA increases from 0.1 g to 0.4 g, the suction bucket group foundation system exhibits linear amplification of horizontal displacements: Bucket 2 displacement escalates from 0.026 m to 0.111 m, while Bucket 3 increases from 0.02 m to 0.108 m. Concurrently, vertical settlements demonstrate synchronized

growth with mean values rising from 0.03 m to 0.14 m. Differential settlement between the two buckets progressively increases from 0.008 m to 0.036 m. Furthermore, under seismic waves with varying spectral characteristics, structural displacements of the suction bucket group foundation intensify with enhanced seismic spectral energy and increased energy density in the input ground motion. Specifically, seismic waves containing higher spectral energy concentrations induce more pronounced foundation displacements. The Parkfield-02. CA ground motion exhibits the lowest spectral energy among the considered excitations, inducing displacements of 0.10 m (horizontal), 0.12 m (vertical settlement), and 0.037 m (differential settlement) in the suction bucket group foundation. Conversely, the ChiChi ground motion demonstrates the highest spectral energy concentration, generating substantially amplified displacements of 0.35 m (horizontal), 0.22 m (vertical settlement), and 0.14 m (differential settlement).

(4) When the seismic amplitude increases, the degree and extent of soil liquefaction inside and around the suction bucket progressively intensify, resulting in a corresponding reduction in the bearing capacity of the surrounding soil. Under various seismic loadings, the displacement variations of the suction bucket embedded in liquefiable sites exhibit significantly greater magnitudes compared to those observed in non-liquefiable sites under identical conditions.

Data availability statement

The original contributions presented in the study are included in the article/supplementary material, further inquiries can be directed to the corresponding author.

Author contributions

XT: Conceptualization, Software, Supervision, Writing – original draft, Writing – review and editing. ZG: Investigation, Validation, Visualization, Writing – review and editing.

Funding

The author(s) declare that no financial support was received for the research and/or publication of this article.

Conflict of interest

The authors declare that the research was conducted in the absence of any commercial or financial relationships that could be construed as a potential conflict of interest.

Generative AI statement

The author(s) declare that no Generative AI was used in the creation of this manuscript.

Publisher's note

References

1. Kim HD, Lee GS, Lee KI. Seismic fragility analysis of 5 MW offshore wind turbine. *Renew Energy* (2014) 65:65250–6. doi:10.1016/j.renene.2013.09.023

2. Wang X, Yang X, Zeng X. Seismic centrifuge modelling of suction bucket foundation for offshore wind turbine. *Renew Energy* (2017) 114:1013–22. doi:10.1016/j.renene.2017.07.103

3. Zhu F, Bienen B, O'Loughlin C. Suction caisson foundations for offshore wind energy: cyclic response in sand and sand over clay. *Géotechnique* (2018) 69(10):1–25. doi:10.1680/jgeot.17.p.273

4. Latini C, Zania V. Dynamic lateral response of suction caissons. *Soil Dyn Earthquake Eng* (2017) 100:10059–71. doi:10.1016/j.soildyn.2017.05.020

5. Bagheri P, Yoon JC, Park D. Numerical analysis of suction bucket foundations used for offshore wind turbines: energy and geotechnics. (2019).

6. Zhang J, Zhang L, Lu X. Centrifuge modeling of suction bucket foundations for platforms under ice-sheet-induced cyclic lateral loadings. *Ocean Eng* (2006) 34(8):1069–79. doi:10.1016/j.oceaneng.2006.08.009

7. Faizi K, Faramarzi A, Dirar S, Chapman D. Investigating the monotonic behaviour of hybrid tripod suction bucket foundations for offshore wind towers in sand. *Appl Ocean Res* (2019) 89:89176–87. doi:10.1016/j.apor.2019.05.018

8. Jianxin Z, Wenlong C, Xinglei C. Seismic responses analysis of suction bucket foundation for offshore wind turbine in clays. *Ocean Eng* (2021) 232. doi:10.1016/j.oceaneng.2021.109159

9. Negro V, Lopez-Gutierrez J, Esteban DM, Matutano C. Uncertainties in the design of support structures and foundations for offshore wind turbines. *Renew Energy* (2014) 63:125–32. doi:10.1016/j.renene.2013.08.041

10. Kaynia MA. Seismic considerations in design of offshore wind turbines. *Soil Dyn Earthquake Eng* (2019) 124:124399–407. doi:10.1016/j.soildyn.2018.04.038

11. Yu H, Zeng X, Li B, Lian J. Centrifuge modeling of offshore wind foundations under earthquake loading. *Soil Dyn Earthquake Eng* (2015) 77:402–15. doi:10.1016/j.soildyn.2015.06.014

12. Xiaobing L. Centrifugal experimental study of suction bucket foundations under dynamic loading. *Acta Mechanica Sinica* (2007) 06(23):97–106. doi:10.1007/s10409-007-0100-7

13. Zhang P, Ding H, Le C. Seismic response of large-scale prestressed concrete bucket foundation for offshore wind turbines. *J Renew Sustainable Energy* (2014) 6(1):013127. doi:10.1063/1.4863986

14. Ding H, Xiong K, Zhang P. Seismic response of offshore wind structure supported by bucket foundation. *Trans Tianjin Univ* (2016) 22(4):294–301. doi:10.1007/s12209-016-2630-1

15. Ibsen L. Bo. Transient analysis of monopile foundations partially embedded in liquefied soil. *Geomechanics Eng* (2015). doi:10.12989/gae.2015.8.2.257

16. Nicosia GLD. Seismic design of monopile supported offshore wind turbines in presence of extensive liquefaction. (2016).

17. Zhang JF, Yu C, Su DS. Wave-induced seabed liquefaction around the composite bucket foundation of offshore wind turbines. In: *International Ocean and polar engineering conference*. Kona, Hawaii: International Society of Offshore and Polar Engineers (2015).

18. Patra S, Haldar S. Seismic response of monopile supported offshore wind turbine in liquefiable soil. *Structures* (2021) 31:248–65. doi:10.1016/j.istruc.2021.01.095

19. Esfeh PK, Kaynia AM. Numerical modeling of liquefaction and its impact on anchor piles for floating offshore structures. *Soil Dyn Earthquake Eng* (2019) 127:105839. doi:10.1016/j.soildyn.2019.105839

20. Xuefei W, Chengliang M, Jiale L. Seismic response of suction bucket foundation for offshore wind turbines: a parametric study. *Ocean Eng* (2022) 257. doi:10.1016/j.oceaneng.2022.111570

21. Papanikolaou VK, Kartalis-Kaounis T, Protopapadakis E. A new graphical user interface for OpenSees. In: *1st European conference on OpenSees* (2017).

22. Yang CSW, Desroches R, Rix GJ. Numerical fragility analysis of vertical-pile-supported wharves in the western United States. *J Earthquake Eng* (2012) 16(4):579–94. doi:10.1080/13632469.2011.641063

Frontiers in Physics

Investigates complex questions in physics to understand the nature of the physical world

Addresses the biggest questions in physics, from macro to micro, and from theoretical to experimental and applied physics.

Discover the latest Research Topics

See more →

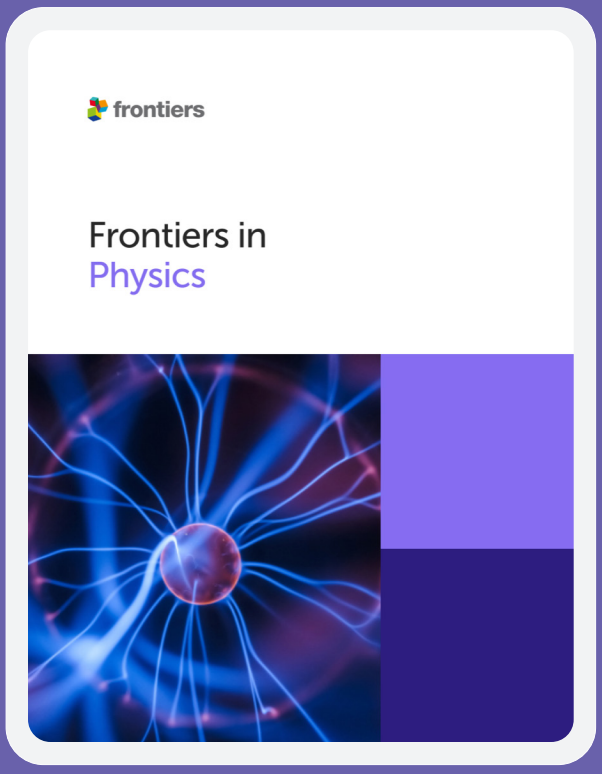

Frontiers

Avenue du Tribunal-Fédéral 34
1005 Lausanne, Switzerland
frontiersin.org

Contact us

+41 (0)21 510 17 00
frontiersin.org/about/contact